

**Ministry of Education and Science of the Russian Federation
Saint Petersburg National Research University of Information
Technologies, Mechanics, and Optics**

***NANOSYSTEMS:
PHYSICS, CHEMISTRY, MATHEMATICS***

2016, volume 7(1)

**Special Issue:
Proceedings of the 12th Biennial International Conference
“Advanced Carbon Nanostructures” (ACNS’2015)**

Наносистемы: физика, химия, математика

2016, том 7, № 1



NANOSYSTEMS:

PHYSICS, CHEMISTRY, MATHEMATICS

ADVISORY BOARD MEMBERS

Chairman: V.N. Vasiliev (*St. Petersburg, Russia*),
V.M. Ievlev (*Voronezh*), P.S. Kop'ev (*St. Petersburg, Russia*), N.F. Morozov (*St. Petersburg, Russia*), V.N. Parmon (*Novosibirsk*), A.I. Rusanov (*St. Petersburg, Russia*),

EDITORIAL BOARD

Editor-in-Chief: I.Yu. Popov (*St. Petersburg, Russia*)

Section Co-Editors:

Physics – V.M. Uzdin (*St. Petersburg, Russia*),
Chemistry, material science – V.V. Gusarov (*St. Petersburg, Russia*),
Mathematics – I.Yu. Popov (*St. Petersburg, Russia*).

Editorial Board Members:

V.M. Adamyan (*Odessa, Ukraine*); O.V. Al'myasheva (*St. Petersburg, Russia*);
A.P. Alodjants (*Vladimir, Russia*); S. Bechta (*Stockholm, Sweden*); J. Behrndt (*Graz, Austria*);
M.B. Belonenko (*Volgograd, Russia*); V.G. Bepalov (*St. Petersburg, Russia*); J. Brasche (*Clausthal, Germany*);
A. Chatterjee (*Hyderabad, India*); S.A. Chivilikhin (*St. Petersburg, Russia*); A.V. Chizhov (*Dubna, Russia*);
A.N. Enyashin (*Ekaterinburg, Russia*), P.P. Fedorov (*Moscow, Russia*); E.A. Gudilin (*Moscow, Russia*); V.K. Ivanov (*Moscow, Russia*),
H. Jónsson (*Reykjavik, Iceland*); A.A. Kiselev (*Houston, USA*); Yu.S. Kivshar (*Canberra, Australia*);
S.A. Kozlov (*St. Petersburg, Russia*); P.A. Kurasov (*Stockholm, Sweden*); A.V. Lukashin (*Moscow, Russia*);
V.A. Margulis (*Saransk, Russia*); I.V. Melikhov (*Moscow, Russia*); G.P. Miroshnichenko (*St. Petersburg, Russia*);
I.Ya. Mittova (*Voronezh, Russia*); H. Neidhardt (*Berlin, Germany*); K. Pankrashkin (*Orsay, France*); B.S. Pavlov (*Auckland, New Zealand*);
A.V. Ragulya (*Kiev, Ukraine*); V. Rajendran (*Tamil Nadu, India*); A.A. Rempel (*Ekaterinburg, Russia*);
V.Ya. Rudyak (*Novosibirsk, Russia*); D Shoikhet (*Karmiel, Israel*); P Stovicek (*Prague, Czech Republic*); V.M. Talanov (*Novocherkassk, Russia*);
A.Ya. Vul' (*St. Petersburg, Russia*); V.A. Zagrebnov (*Marseille, France*).

Editors:

I.V. Blinova; A.I. Popov; A.I. Trifanov; E.S. Trifanova (*St. Petersburg, Russia*),
R. Simoneaux (*Philadelphia, Pennsylvania, USA*).

Address: University ITMO, Kronverkskiy pr., 49, St. Petersburg 197101, Russia.

Phone: +7(812)232-67-65, **Journal site:** <http://nanojournal.ifmo.ru/>,

E-mail: popov1955@gmail.com

AIM AND SCOPE

The scope of the journal includes all areas of nano-sciences. Papers devoted to basic problems of physics, chemistry, material science and mathematics inspired by nanosystems investigations are welcomed. Both theoretical and experimental works concerning the properties and behavior of nanosystems, problems of its creation and application, mathematical methods of nanosystem studies are considered.

The journal publishes scientific reviews (up to 30 journal pages), research papers (up to 15 pages) and letters (up to 5 pages). All manuscripts are peer-reviewed. Authors are informed about the referee opinion and the Editorial decision.

Content

FROM THE EDITORIAL BOARD

International conference “Advanced Carbon Nanostructures”	6
List of Participants ACNS’2015	8
From Guest Editorial	21

PAPERS, PRESENTED AT THE CONFERENCE

V.T. Lebedev, Yu.V. Kulvelis, V.V. Runov, A.A. Szhogina, M.V. Suyasova Biocompatible water-soluble endometallofullerenes: peculiarities of self-assembly in aqueous solutions and ordering under an applied magnetic field	22
A.A. Lebedev Growth, study, and device application prospects of graphene on SiC substrates	30
V.K. Ksenevich, N.I. Gorbachuk, Ho Viet, M.V. Shuba, P.P. Kuzhir, S.A. Maksimenko, A.G. Paddubskaya, G. Valusis, A.D. Wieck, A. Zak, R. Tenne Electrical properties of carbon nanotubes/WS₂ nanotubes (nanoparticles) hybrid films	37
M.V. Kondrin, V.V. Brazhkin Is graphane the most stable carbon monohydride?	44
S.A. Ktitorov, R.I. Mukhamadiarov Electromagnetic radiation by electrons in the corrugated graphene	51
S.A. Ktitorov, R.I. Mukhamadiarov Phenomenology of ripples in graphene	58
R.H. Amirov, M.E. Iskhakov, M.B. Shavelkina Synthesis of high-purity multilayer graphene using plasma jet	60
E.V. Seliverstova, N.Kh. Ibrayev, R.Kh. Dzhanabekova Study of graphene oxide solid films prepared by Langmuir-Blodgett technology	65
E.F. Sheka, I. Natkaniec, N.N. Rozhkova, E.Yu. Buslaeva, S.V. Tkachev, S.P. Gubin, V.P. Mel’nikov Parent and reduced graphene oxide of different origin in light of neutron scattering	71
A.E. Aleksenskii, S.P. Vul’, A.T. Dideikin, V.I. Sakharov, I.T. Serenkov, M.K. Rabchinskii, V.V. Afrosimov Etching of wrinkled graphene oxide films in noble gas atmosphere under UV irradiation	81
O.Yu. Ananina, N.A. Lvova, E.V. Severina The divacancy V₂ and V–C=C–V configurations on the diamond surface: quantum-chemical simulation	87

S.V. Boroznin, I.V. Zaporotskova, N.P. Polikarpova Investigation of the sorption properties of carbon nanotubes with different boron impurity contents	93
N. Jargalan, T.V. Tropin, M.V. Avdeev, V.L. Aksenov Investigation and modeling of evolution of C₆₀/NMP solution UV-Vis spectra	99
I.V. Mikheev, T.A. Bolotnik, D.S. Volkov, M.V. Korobov, M.A. Proskurnin Approaches to the determination of C₆₀ and C₇₀ fullerene and their mixtures in aqueous and organic solutions	104
N.B. Tamm, M.P. Kosaya, M.A. Fritz, S.I. Troyanov Synthesis, isolation, and X-ray structural characterization of trifluoromethylated C₇₈ fullerenes: C₇₈(2)(CF₃)_{10/12} and C₇₈(3)(CF₃)_{12/14}	111
L.V. Vinogradova, A.Yu. Pulyalina, V.A. Rostovtseva, A.M. Toikka, G.A. Polotskaya C₆₀ fullerene-containing polymer stars in mixed matrix membranes	118
K.P. Meletov, J. Arvanitidis, D. Christofilos, G. Kourouklis Comparative Raman study of photo-oligomer stability in the donor-acceptor fullerene complex {Pt(dbdte)₂}•C₆₀ and pristine C₆₀	125
K.P. Meletov, J. Arvanitidis, D. Christofilos, G. Kourouklis Pressure-assisted photopolymerization in the molecular donor-acceptor fullerene complex {Cd(dedte)₂}•C₆₀	133
G.N. Churilov, A.A. Popov, U.E. Guliaeva, N.A. Samoylova, N.G. Vnukova, A.L. Kolonenko, V.G. Isakova, A.I. Dudnik, V.S. Koravanets Express analysis of endohedral fullerenes amount contained at fullerene mixture	140
V.A. Shilin, A.A. Szhogina, M.V. Suyasova, V.P. Sedov, V.T. Lebedev, V.S. Kozlov Fullerenes and fullerenols survival under irradiation	146
I.A. Dubinina, E.M. Kuzmina, A.I. Dudnik, N.G. Vnukova, G.N. Churilov, N.A. Samoylova Study of antioxidant activity of fullerenols by inhibition of adrenaline autoxidation	153
I. Alieva, I. Kireev, A. Rakhmanina, A. Garanina, O. Strelkova, O. Zhironkina, V. Cherepaninets, V. Davydov, V. Khabashesku, V. Agafonov, R. Uzbekov Magnet-induced behavior of iron carbide (Fe₇C₃@C) nanoparticles in the cytoplasm of living cells	158
B. Ortega García, O.V. Kharissova, H.V. Rasika Dias, F. Servando Aguirre T., J. Salinas Hernández Nanocomposites with antibacterial properties using CNTs with magnetic nanoparticles	161
A.D. Bozhko Power-like corrections to the conductivity of Mo-C nanocomposites	169

A.A. Maltsev, S.B. Bibikov, V.N. Kalinichenko An improved adsorption method for the characterization of water-based supercapacitor electrodes	175
M.K. Eseev, A.A. Goshev, P. Horodek, S.N. Kapustin, A.G. Kobets, C.S. Osokin Diagnostic methods for silica-reinforced carbon nanotube-based nanocomposites	180
A.V. Alekseev, M.R. Predtechenskiy Aluminum foil reinforced by carbon nanotubes	185
R.M. Nikonova, V.I. Ladyanov, N.S. Larionova The influence of carbon (fullerite, graphite) on mechanical alloying of Cu-25 at% C composites	190
E.A. Lyapunova, S.V. Uvarov, M.V. Grigoriev, S.N. Kulkov, O.B. Naimark Modification of the mechanical properties of zirconium dioxide ceramics by means of multiwalled carbon nanotubes	198
Yu.S. Nechaev, V.P. Filippova, A.A. Tomchuk, A. Yurum, Yu. Yurum, T.N. Veziroglu On the spillover effect of the solid H₂ intercalation into GNF's	204
V.V. Kovalevski, I.A. Moshnikov TEM study of structure of graphene layers in shungite carbon	210
I.A. Moshnikov, V.V. Kovalevski Electrophysical properties of shungites at low temperatures	214
D. Abramov, S. Arakelian, D. Kochuev, S. Makov, V. Prokoshev, K. Khorkov Interaction of femtosecond laser radiation with carbon materials: exfoliation of graphene structures and synthesis of low-dimensional carbon structures	220
V.S. Neverov, P.A. Borisova, A.B. Kukushkin, V.V. Voloshinov Diffraction-based characterization of amorphous sp² carbon: sensitivity to domain-like packing of nanostructures	226
V.A. Logvinenko, V.G. Makotchenko, V.E. Fedorov Reactivity in combustion process for expanded graphites: influence of dimensional effect	234
M.V. Gudkov, V.P. Melnikov ERP study of graphite oxide thermal reduction: the evolution of paramagnetism and conductivity	244
I. Arkharova, I. Zaporotskova Quantum-chemical study of carbon nanotubes interaction with contaminants of petroleum, oil and lubricants	253

International conference “Advanced Carbon Nanostructures” (ACNS’2015)

Organizers

- **Ioffe Physical-Technical Institute**, St.Petersburg, Russia
- **National Research Centre "Kurchatov Institute", B.P.Konstantinov Petersburg Nuclear Physics Institute**, Russia
- **National Research Center "Kurchatov Institute"**, Moscow, Russia
- **St.Petersburg State Institute of Technology (Technical University)**, Russia

Official Partners

- **Russian Foundation for Basic Research**
- **Government of Saint Petersburg**
- **Fund for Infrastructure and Educational Programs**
- **Dmitry Zimin Dynasty Foundation**
- **Chemical Abstracts Service**

International Advisory Committee

F. Banhart	Strasbourg University, France
J. Davidson	Vanderbilt University, USA
M. Dresselhaus	Massachusetts Institute of Technology, USA
L. Echegoyen	University of Texas At El Paso, USA
T. Enoki	Tokyo Institute of Technology, Japan
D. Gruen	Argonne National Laboratory, USA
D. Guldi	University of Erlangen-Nurnberg, Germany
R. Kalish	Israel Institute of Technology, Technion, Israel
W. Kraetschmer	Max-Plank Institute, Germany
H. Kroto	Florida State University, USA
E. Osawa	Nanocarbon Research Institute Ltd., Japan
H. Shinohara	Nagoya University, Japan
F. Wudl	University of California, USA

Organizing Committee

A.Ya. Vul' (Conference Chair)	Ioffe Institute, St. Petersburg, Russia
S.V. Kidalov (Chair)	Ioffe Institute, St. Petersburg, Russia
B.B. Chaivanov	National Research Center "Kurchatov Institute", Russia
V.F. Ezhov	St Petersburg Nuclear Physics Institute, Russia
A.V. Kirillin	Russian Foundation for Basic Research, Russia
P.S. Kop'ev	Ioffe Institute, St. Petersburg, Russia
V.V. Kveder	Institute of Solid State Physics, Chernogolovka, Russia
V.T. Lebedev	National Research Centre "Kurchatov Institute", B.P.Konstantinov Petersburg Nuclear Physics Institute, Russia
N.V. Lisitsyn	St. Petersburg State Institute of Technology, Russia

O.M. Nefedov Branch of Chemistry and Material Sciences of the Russian Academy of Science, Russia
M.Yu. Romanovsky Department of General Physics, Russian Academy of Science
S.A. Tsyganov Russian Foundation for Basic Research, Russia
A.G. Zabrodsky Ioffe Institute, Russia

International Programme Committee

M.V. Baidakova (Co-Chair) Ioffe Institute, St. Petersburg, Russia
A.T. Dideikin (Co-Chair) Ioffe Institute, St. Petersburg, Russia
A.E. Aleksensky Ioffe Institute, St. Petersburg, Russia
A.S. Artjomov Lebedev Physical Institute, Moscow, Russia
V.Yu. Dolmatov Federal State Unitary Enterprise "Special Design and Technological Office "Technolog", St. Petersburg, Russia
Yu.S. Grushko St. Petersburg Nuclear Physics Institute, Russia
A.V. Eletsii National Research Center "Kurchatov Institute", Russia
M. Korobov Moscow State University, Russia
S.V. Kozyrev Center for Advanced Studies of St. Petersburg State Polytechnical University, St. Petersburg, Russia
A.V. Krestinin Institute of Problems of Chemical Physics, Russia
I.I. Kulakova Moscow State University, Russia
V.L. Kuznetsov Borekov Institute of Catalysis, Novosibirsk, Russia
L.B. Piotrovsky Institute of Experimental Medicine North-West Branch of RAMS, St. Petersburg, Russia
O.A. Shenderova International Technology Center, USA
A.M. Shikin St. Petersburg State University, Russia
V.I. Sokolov Institute of Organoelement Compounds, Moscow, Russia
V.M. Titov Institute of Hydrodynamics, Novosibirsk, Russia
A.P. Vozniakovskii Federal State Unitary Enterprise Scientific Research Institute for Synthetic Rubber, St. Petersburg, Russia
A.Ya. Vul' Ioffe Institute, St. Petersburg, Russia

Local Organizing Committee

I.V. Vorobyova (Chair) Ioffe Institute, St. Petersburg, Russia
T.P. Kazantseva Ioffe Institute, St. Petersburg, Russia
B.M. Silin Ioffe Institute, St. Petersburg, Russia
L.V. Sharonova Ioffe Institute, St. Petersburg, Russia

Technical Group

D.B. Shustov Web-site, Ioffe Institute, St. Petersburg, Russia
A.N. Trofimov Ioffe Institute, St. Petersburg, Russia
K.N. Guliaeva Ioffe Institute, St. Petersburg, Russia

in association with Agency for Science and Technology "Intellect"

List of Participants ACNS'2015

Jean-Charles Marie Arnault

France, CEA LIST
jean-charles.arnault@cea.fr

Olga Aftenieva

Russia, Moscow Institute of Physics and
Technology
aftenieva@phystech.edu

Artjom Vladimirovich Alekseev

Russia, OCSiAl
artem.alekseev@ocsial.com

Belen Aleman

Spain, IMDEA Materials
belen.aleman@imdea.org

Javid Ali

India, Jamia Millia Islamia, New Delhi
javidphy@gmail.com

Mandana Amiri

Iran, University of Mohaghegh Ardabili
mandanaamiri@yahoo.com

Ravil Amirov

Russia, Joint Institute for High
Temperatures of Russian Academy of
Sciences
amirovravil@yahoo.com

Sergey Mikhailovich Andreev

Russia, NRC Institute of Immunology
FMBA
andsergej@yandex.ru

Liubov Yurievna Antipina

Russia, Technological Institute for
Superhard and Novel Carbon Materials
lyuantipina@tisnum.ru

Irina Antonova

Russia, Institute of Semiconductor Physics
SB RAS
antonova@isp.nsc.ru

Sergey Arakelian

Russia, Vladimir State University
arak@vlsu.ru

Sofya Borisovna Artemkina

Russia, Nikolaev Institute of Inorganic
Chemistry SB RAS
artem@niic.nsc.ru

Mikhail V. Avdeev

Russia, Joint Institute for Nuclear Research
avd@nf.jinr.ru

Gleb Yurievich Averchuk

Russia, IT department, Mendeleev
University of Chemical Technology of
Russia
altermn@gmail.com

Marina V Baidakova

Russia, Ioffe Institute,
Organizer
baidakova@mail.ioffe.ru (FTI im Ioffe RAN)

Maxim Viktorovich Barsukov

Russia, National Research University of
Electronic Technology
vakavakav@gmail.com

Elena Bashkatova

Russia, NRC Institute of Immunology,
Moscow, Russia
bashkatova_en@mail.ru

Alexander Nikolaevich Bekhterev

Russia, Magnitogorsk State Technical
University
alexbehterev@yandex.ru

Abolfazl Bezaatpour

Iran, Department of Chemistry, University
of Mohaghegh Ardabili, Ardabil, Iran
a_bezaatpour@yahoo.com

Olga Anatoliivna Biloivan

Ukraine, IMBiG NANU
o.a.biloivan.imbg.org.ua

Oleksandr Bochechka

Ukraine, V. Bakul Institute for Superhard
Materials, Nat. Acad. of Sci. of Ukraine.
bochechka@ism.kiev.ua

Viktor Pavlovich Bogdanov
Russia, Moscow State University, Chemistry
Department
vb@thermo.chem.msu.ru

Svetlana Bogdanova
Russia, Kazan National Research
Technological University
polyswet@mail.ru

Seyed Majid Borghei
Iran, Karaj Islamic Azad University
majid_borghei@yahoo.com

Polina Alekseevna Borisova
Russia, National Research Centre
"Kurchatov Institute"
borisovapa@mail.ru

Sergei Vladimirovich Boroznin
Russia, Volgograd State University
sefm.volsu@gmail.com

Alexey Dmitrievich Bozhko
Russia, A.M. Prokhorov_General Physics
Institute of RAS
bozhko@lt.gpi.ru

Sergey Sergeevich Bukalov
Russia, Scientific and Technical Center on
Raman Spectroscopy RAS, INEOS RAS
buklei@ineos.ac.ru

Galina Konstantinovna Burkat
Russia, Saint Petersburg State
Technological Institute (Technical
University)
DiamondCentre@mail.ru

Nikolay Alexandrovich Charykov
Russia, Public Joint Stock Company
"Scientific and Production Association
"TECHNOLOGIES", Saint Petersburg,
Russia
ncharykov@yandex.ru

Sergey Chupin
Russia, International Scientific Center on
Termophysics and Energetics
info@iscte.ru

Grigory Nikolaevich Churilov
Russia, L.V. Kirensky Institute of Physics of
Siberian Branch of Russian Academy of
Sciences
churilov@iph.krasn.ru

Magdalena Couty
France, CEA, LIST, Diamond Sensors
Laboratory
magdalena.couty@cea.fr

Sergei Yurievich Davydov
Russia, Ioffe Physical-Technical Institute
sergei_davydov@mail.ru

Valeriy Aleksandrovich Davydov
Russia, L.F. Vereshchagin Institute for High
Pressure Physics
vdavydov@hppi.troitsk.ru

Vladimir Yakovlevich Davydov
Russia, Chemistry Department
M.V.Lomonosov Moscow State University
VYaDavydov@phys.chem.msu.ru

Alexey Petrovich Dementjev
Russia, National Research Center
"Kurchatov Institute"
demcarbon@yandex.ru

Victor Demin
Russia, IBCP RAS
demin_v_a@mail.ru

Artur Dideikin
Russia, Ioffe Institute
dideikin@mail.ioffe.ru

Mircea Vasile Diudea
Romania, Department of Chemistry, Faculty
of Chemistry and Chemical Engineering,
"Babes-Bolyai" University
diudea@gmail.com

Anton Yakovlevich Dobrynin
Russia, Volgograd State University
greatanton777@gmail.com

Valerii Yurievich Dolmatov
Russia, FGUP SKTB "Technolog"
DiamondCentre@mail.ru

Irina Alexandrovna Dubinina
Russia, Siberian Federal University
churilov@iph.krasn.ru

Sergey Vladimirovich Dubkov
Russia, National Research University of
Electronic Technology
sv.dubkov@gmail.com

Marc DUBOIS
France, ICCF
marc.dubois@univ-bpclermont.fr

Tran Thi Thuy Duong
Vietnam, D. Mendeleev University of
Chemical Technology, Moscow, Russia
duongtrannho2012@gmail.com

Alexander Valentinovich Dzyabchenko
Russia, L. Ya. Karpov Physico-Chemical
Institute
adz@cc.nifhi.ac.ru

Luis Alberto Echegoyen
United States, University of Texas at El
Paso
echegoyen@utep.edu

Dominik Eder
Germany, University of Münster
dominik.eder@uni-muenster.de

Nikolay Efimov
Russia, Kurnakov Institute
nnefimov@narod.ru

Lusine Elbakyan
Russia, Volgograd state university
lusniak-e@yandex.ru

Alexander Valentinovich Eletsii
Russia, Moscow Power Engineering
Institute (Technical University)
eletsii@mail.ru

Marina Elistratova
Russia, Peter the Great Saint-Petersburg
Polytechnic University
elistratovamari@yandex.ru

Anna Erofeevskaya
Russia, Saint Petersburg State University
anna.erofeevskaya@gmail.com

Sergey Vladimirovich Erohin
Russia, Federal State Budgetary Institution
"Technological Institute For Superhard And
Novel Carbon Materials"
sverohin@tisnum.ru

Denis Erokhin
Russia, Chemical Abstracts Service
derokhin@acsi.info

Igor Ershov
Russia, Don state technical university
iershov86@gmail.com

Marat Kanalbekovich Eseev
Russia, Northern Arctic Federal University
m_eseev@mail.ru

Alfiya Gabdilovna Fazlitdinova
Russia, Chelyabinsk State University
fazlitdinovaag@mail.ru

Vladimir Fedorov
Russia, Nikolaev Institute of Inorganic
Chemistry, Siberian Branch of Russian
Academy of Sciences
fed@niic.nsc.ru

Aleksandr Semenovich Fedorov
Russia, L. V. Kirensky Institute of Physics
SB RAS
alex99@iph.krasn.ru

Natalia Alekseevna Fedosova
Russia, D. Mendeleev University of
Chemical Technology of Russia
sway4ka@gmail.com

Mattia Gianandrea Gaboardi
Italy, Department of Physics and Earth
Sciences, University of Parma
mattiagianandrea.gaboardi@fis.unipr.it

Wilhelm Hans Karl Gaeth

Germany, Gaeth-Diamant
gaeth@wtal.de

Nicolay Rostislavovich Gall

Russia, Ioffe Institute
gall@ms.ioffe.ru

Azat Rustemovich Gataoullin

Russia, Kazan National Research
Technological University
zulfat.azari@yandex.ru

Igor Gayduchenko

Russia, National Research Centre
"Kurchatov Institute"
igorandg@gmail.com

Arsen Shahsenovich Gazaliev

Russia, National Research Centre
"Kurchatov Institute", Moscow State
Pedagogical University
gazaliev@fnbic.ru

Ilya Goldt

Russia, Skolkovo Foundation
igoldt@sk.ru

Alexandre Golub

Russia, INEOS RAS
golub@ineos.ac.ru

Alexey Goryunkov

Russia, Lomonosov Moscow State
University
aag@thermo.chem.msu.ru

Andrey Sergeevich Goryunov

Russia, Institute of Biology, Karelian
Research Centre RAS
ser61953454@yandex.ru

Leonid Vladimirovich Grigoryev

Russia, ITMO University
leonid70@mail.ru

Yulia Gromova

Russia, ITMO University
yulia.a.gromova@gmail.com

Sergey Grudinkin

Russia, Ioffe Institute
grudink@gvg.ioffe.ru

Maksim Vladimirovich Gudkov

Russia, Semenov Institute of Chemical
Physics
GOOD_ok-eee@mail.ru

Steffen Guenther

Switzerland, Reishauer AG
Steffen.Guenther@reishauer.com

Uliana Guliaeva

Russia, Siberian Federal University
churilov@iph.krasn.ru

Sanju Gupta

United States, Western Kentucky University
sgup77@gmail.com

Maxim Georgievich Gushchin

Russia, MIET Institute
magusch@gmail.com

Yuhei Hayamizu

Japan, Tokyo Institute of Technology
hayamizu.y.aa@m.titech.ac.jp

Veli-Pekka Hyttinen

Finland, Chemical Abstracts Service
vhyttinen@cas.org

Levan Pavel Ichkitidze

Russia, National Research University of
Electronic Technology "MIET", MIET,
Zelenograd, Moscow, 124498 Russian
Federation
leo852@inbox.ru

Victor Ilyasov

Russia, Don State Technical University
viily@mail.ru

Alexandra Isakova

Russia, A.N. Frumkin Institute of Physical
Chemistry and Electrochemistry RAS
Isakova_Aleks@list.ru

Elena Borisovna Iudina
Russia, Saint Petersburg State Institute of
Technology (Technical University)
electa@yandex.ru

Anton Ivanovich Ivanov
Russia, Bauman Moscow State Technical
University
ivanovantone@gmail.com

Michail Grigorievich Ivanov
Russia, Ural Federal University
m.g.ivanov@urfu.ru

Igor Leonidovich Jityaev
Russia, Institute of Nanotechnologies,
Electronics, and Electronic Equipment
Engineering, Southern Federal University
jityaev.igor@gmail.com

John Kwadwo Kaabi
Ghana, BLESSING KKB CONSULT
blessing.kkbconsult@aol.com

Sergey Kalyuzhnyi
Russia, Management Company RUSNANO
sergey.kalyuzhnyi@rusnano.com

Aida Razim Karaeva
Russia, FSBI TISNCM
karaevaar@tisnum.ru

Mikhail Katkov
Russia, Nikolaev Institute of Inorganic
Chemistry
katkovmi@gmail.com

Viktor Anatol'evich Keskinov
Russia, Public Joint Stock Company
"Scientific and Production Association
"TECHNOLOGIES"
keskinov@mail.ru

Azat Khadiev
Russia, Kazan National Research Technical
University named after A.N. Tupolev
azat.khadiev@mail.ru

Oxana Vasilievna Kharissova
Mexico, UANL
okhariss@mail.ru

Alexander Kharitonov
Russia, Branch of the Talrose Institute for
Energy Problems of Chemical Physics RAS
khariton@binep.ac.ru

Vasiliy Anatolievich Kharitonov
Russia, Semenov Institute of Chemical
Physics, Russian Academy of Sciences
vch.ost@mail.ru

Pavel Anatolyevich Khavrel
Russia, Moscow State University, Chemistry
Department
khavrel@thermo.chem.msu.ru

Andrew Khomich
Russia, Prokhorov General Physics Institute
antares-610@yandex.ru

Sergey Kidalov
Russia, Ioffe Institute
Kidalov@mail.ioffe.ru

Andrey Knizhnik
Russia, Kintech Lab Ltd
knizhnik@kintech.ru

Dmitrii Andreevich Kochuev
Russia, Vladimir State University
b@mail.ru

Eleonora Koltsova
Russia, Mendeleev University of Chemical
Technology of Russia
kolts@muctr.ru

Dmitry Valentinovich Konarev
Russia, Institute of Problems of Chemical
Physics RAS
konarev3@yandex.ru

Mikhail V. Kondrin
Russia, Institute for High Pressure Physics
mkondrin@hppi.troitsk.ru

Sergei V Koniakhin
Russia, Ioffe Institute
kon@mail.ioffe.ru

Oleg Viktorovich Kononenko
Russia, Institute of Microelectronics
Technology and High Purity Materials
oleg@iptm.ru

Mikhail Valerievich Korobov
Russia, Department of Chemistry, Moscow
State University
mkorobov49@gmail.com

Mariya Petrovna Kosaya
Russia, Chemistry Department, Moscow
State University
maria.cosaya@yandex.ru

Ilya Kostogrud
Russia, Novosibirsk State University,
Institute of Thermophysics SB RAS
ikostogrud@gmail.com

Igor Alekseevich Kotin
Russia, Rzhhanov Institute of Semiconductor
Physics SB RAS
kotin@isp.nsc.ru

Valeri Kovalenko
Russia, A. E. Arbutov Institute of Organic
and Physical Chemistry
koval@iopc.ru

Kirill Kremlev
Russia, Razuvaev Institute of
Organometallic Chemistry
kkremlev@mail.ru

Anatoly V. Krestinin
Russia, Institute of Problems of Chemical
Physics RAS
kresti@icp.ac.ru

Anton Sergeevich Kriukov
Russia, Ioffe Institute
emreu30@gmail.com

Aleksey Andreevich Krutoyarov
Russia, VOLSU
akrutoyarov@yandex.ru

Vitaly Ksenevich
Belarus, Belarusian State University
ksenevich@bsu.by

Sergey Andreevich Ktitorov
Russia, Ioffe Physical-Technical Institute
ktitorov@mail.ioffe.ru

Inna Ivanovna Kulakova
Russia, Lomonosov Moscow State
University
inna-kulakova@yandex.ru

Vladimir Anatolievich Kulbachinskii
Russia, M.V. Lomonosov Moscow State
University
kulb@mig.phys.msu.ru

Aynur Kumarovna Kulbasova
Russia, Volsu
k_a_k_1301@mail.ru

Utkarsh Kumar
India, BABASAHEB BHIMRAO
AMBEDKAR UNIVERSITY LUCKNOW
utkarsh218@gmail.com

Alexey Vasilyevich Kuzmin
Russia, Institute of Solid State Physics
Russian Academy of Sciences
kuzminav@issp.ac.ru

Alexander Kvashnin
Russia, Moscow institute of physics and
technology
agkvashnin@gmail.com

Dmitry G Kvashnin
Russia, Emanuel Institute of Biochemical
Physics RAS
dgkvashnin@gmail.com

Yulia Kvashnina
Russia, Moscow Institute of Physics and
Technology
jakvashnina@tisnum.ru

Kirill Andreevich Laptinskiy
Russia, Moscow State University
laptinskij@physics.msu.ru

Olga Nikolaevna Lavrentieva
Russia, Lomonosov Moscow State
University
lavrolja@mail.ru

Aleksandr Aleksandrovich Lebedev
Russia, Ioffe Institute
shura.lebe@mail.ioffe.ru

Nikolay Gennadievich Lebedev
Russia, Volgograd State University
lebedev.ng@mail.ru

Vasily Timofeevich Lebedev
Russia, Petersburg Nuclear Physics Institute,
NRC Kurchatov Institute
vlebedev@npi.spb.ru

Dmitrii Vladimirovich Leshchev
Russia, CAS of Peter the Great
St.Petersburg Polytechnic University
dimvovich@narod.ru

Hua Li
China, Ningbo Institute of Materials
Technology and Engineering, Chinese
Academy of Sciences
lihua@nimte.ac.cn

Ji Chao Liao
China, Forturn Myriad Diamond Nano Tech
Co.,Ltd
78049623@qq.com

Egor Vladimirovich Lobiak
Russia, Nikolaev Institute of Inorganic
Chemistry Siberian Branch of Russian
Academy of Sciences
lobiakev@niic.sbras.ru

Yurii Efremovich Lozovik
Russia, Institute of Spectroscopy
lozovik@isan.troitsk.ru

Sergei Glebovich Lvov
Russia, Kazan Physical-Technical Institute
sglvov@ya.ru

Natalia Anatolievna Lvova
Russia, TECHNOLOGICAL INSTITUTE
FOR SUPERHARD AND NOVEL
CARBON MATERIALS
nlvova@tisnum.ru

Elena Lyapunova
Russia, Institute of continuous media
mechanics
lyapunova@icmm.ru

Dmitry Makarov
Russia, Northern (Arctic) Federal University
named after MV Lomonosov
makarovd0608@yandex.ru

Ivan Aleksandrovich Makarov
Russia, FGUP SKTB "Technolog"
DiamondCentre@mail.ru

Tatiana Makarova
Russia, Ioffe Institute
tatyana.makarova@lut.fi

Alexander Andreevich Maltsev
Russia, Institute of Biochemical Physics
sadnesscurer@gmail.com

Geza Istvan Mark
Hungary, 1Centre for Energy Research,
Institute of Technical Physics and Materials
Science
mark@mfa.kfki.hu

Alexey Markin
Russia, Nizhny Novgorod State University
markin79@mail.ru

Polina Vladimirovna Matveychikova
Russia, SPbGTI (TU)
matveychikovapolina@gmail.com

Olga Nikolayevna Mazaleva
Russia, Moscow State University
mazaleva.olya@gmail.com

Aleksandr Pavlovich Meilakhs
Russia, Ioffe Institute
mejlaxs@mail.ioffe.ru

Konstantin Meletov
Russia, Institute of solid state physics
Russian academy of sciences
mele@issp.ac.ru

Svetlana Leonidovna Mikhailova
Kazachstan, al-Farabi Kazakh National
University
svetik.mikhailova@gmail.com

Ivan Mikheev
Russia, Lomonosov Moscow State
University
mkheev.ivan@gmail.com

Alexander Sergeevich Minkin
Russia, National Research Center
"Kurchatov Institute"
amink@mail.ru

Yury Mironov
Russia, Bauman Moscow State Technical
University
bmstunc@mail.ru

Edward Mitberg
Russia, Technological Institute for
Superhard and Novel Carbon Materials
mitbergeb@tisnum.ru

Sergei S. Moliver
Russia, Ulyanovsk State University
moliver@sv.uven.ru

Vladimir Zalmanovich Mordkovich
Russia, Technological Institute for
Superhard and Novel Carbon Materials
mordkovich@tisnum.ru

Sergey Morozov
Uzbekistan, Institute of Ion-Plasma and
Laser Technologies, Uzbek Academy of
Sciences, 100125 Tashkent, Uzbekistan
morozov@aie.uz

Stanislav Moshkalev
Brazil, UNICAMP
stanisla@ccs.unicamp.br

Igor Moshnikov
Russia, Institute of Geology Karelian
Research Centre of RAS
igorm@krc.karelia.ru

Eugene Vladimirovich Moskalyov
Russia, SPb Institute of Technology
(University)
evmosk@gmail.com

Ruslan Mukhamadiarov
Russia, Ioffe Institute
mruslani13@gmail.com

Nikolay Nagirny
Russia, Novosibirsk State University
nicholas-nagirny@mail.ru

Arao Nakamura
Japan, Toyota Physical and Chemical
Research Institute
a.nakamura@nagoya-u.jp

Jargalan Narmandakh
Russia, Joint Institute for Nuclear Research
narmandah@jinr.ru

Nadezhda Nebogatikova
Russia, Institute of Semiconductors Physics
SB RAS
nadonebo@gmail.com

Yury Sergeevich Nechaev
Russia, Bardin Institute for Ferrous
Metallurgy, Kurdjumov Institute of Metals
Science and Physics
yuri1939@inbox.ru

Dmitrii Nelson
Russia, Ioffe Institute
d.nelson@mail.ioffe.ru

Roza Muzafarovna Nikonova
Russia, Physical-Technical Institute Ural
Branch of RAS
rozamuz@ya.ru

Anatoliy Petrovich Onanko
Ukraine, Kyiv national university, physical
department
onanko@univ.kiev.ua

Tatiana Sergeevna Orlova
Russia, Ioffe Physical-Technical Institute
orlova.t@mail.ioffe.ru

Beatriz Ortega
Mexico, UANL
beatriz.ortega24@gmail.com

Anton V. Osipov
Russia, Vladimir State University
osipov@vlsu.ru

Tae Hee Park
Korea (South), NeoEnBiz Co.,LTD.
nanodiamond@neomond.com

Andrey Nikolaevich Ponomarev
Russia, Scientific and Technical Centre of Applied Nanotechnologies
info@nanotech.ru

Anna Nikolaevna Panova
Ukraine, V. Bakul ISM
annpanova@ukr.net

Sergey Igorevich Pavlov
Russia, Ioffe Institute
pavlov_sergey87@mail.ru

Yan Peng
China, Pen Tan Technology Company Ltd,
China
goldstone@vip.163.com

Andrey Vitalievich Petrov
Russia, Saint Petersburg State University
andreypetrov@chem.spbu.ru

Anatoliy Evgenievich Petukhov
Russia, Saint Petersburg State University
anatolyptkhv@gmail.com

Levon Borisovich Piotrovskiy
Russia, Institute of Experimental Medicine
levon-piotrovsky@yandex.ru

Alexey Pokropivny
Ukraine, Frantsevich Institute for Problems of Materials Science of NASU
apokr@mail.ru

Natalia Polikarpova
Russia, Volgograd State University
n.z.1103@mail.ru

Galina Andreevna Polotskaya
Russia, Saint Petersburg State University
polotskaya@hq.macro.ru

Kirill Ponkratov
Russia, Renishaw
kirill.ponkratov@renishaw.com

Vladimir A. Popov
Russia, National University of Science and Technology "MISIS"
popov58@inbox.ru

Anna Nickolaevna Popova
Russia, Institute of coal chemistry and materials science SB RAS
h991@yandex.ru

Olesya Posrednik
Russia, Saint-Petersburg Electrotechnical university
lesya1976@mail.ru

Dmitrii Pudikov
Russia, Saint Petersburg State University
dmitrii.pudikov@spbu.ru

Daria Dmitrievna Purgina
Russia, NRC Institute of Immunology FMBA of Russia
purgina_d@mail.ru

Anastasia Dmitrievna Pykhova
Russia, Moscow State University
a.d.pykhova@gmail.com

Marina Pyshniak
Russia, Saint Petersburg State University
marina.pyshnyak@spbu.ru

Maxim Konstantinovich Rabchinskii
Russia, Ioffe Institute
maxraer@mail.ru

Victor Grigorievich Ralchenko
Russia, General Physics Institute of Russian Academy of Sciences
ralchenko@nsc.gpi.ru

Nikolai M. Romanov
Russia, Ioffe Institute,
nikromanov.90@gmail.com

Natalia Andreevna Romanova
Russia, Lomonosov Moscow State
University
natroman1987@yandex.ru

Natalia Nikolaevna Rozhkova
Russia, Institute of Geology, Karelian
Research Centre RAS
rozhkova@krc.karelia.ru

Alexey Vladimirovich Rybalchenko
Russia, Moscow State University, Chemistry
Department
alexry@gmail.com

Anna Alexeevna Rybkina
Russia, Saint Petersburg State University
rybkina-anna@bk.ru

Anton Ryzhov
Russia, Magnitogorsk State Technical
University named after Nosov
antonryzhov.fiz@yandex.ru

Natalia Vladimirovna Sadovskaia
Russia, Karpov Institute of Physical
Chemistry
sadovska@nifhi.ru

Irina Viktorovna Safronova
Russia, FGUP SKTB "Technolog"
DiamondCentre@mail.ru

Nataliya Samoylova
Germany, Leibniz Institute for Solid State
and Materials Research, Dresden
natalivrn@gmail.com

Masahiro Sawada
Japan, Hiroshima Synchrotron Radiation
Center, Hiroshima University
sawa@hiroshima-u.ac.jp

Vadim Stanislavovich Sedov
Russia, A.M. Prokhorov General Physics
Institute, Russian Academy of Sciences
sedovvadim@yandex.ru

Yevgeniya Vladimirovna Seliverstova
Kazakhstan, Institute of Molecular
Nanophotonics, Y.A. Buketov Karaganda
State University
genia_sv@mail.ru

Olesya Olegovna Semivrazhskaya
Russia, Lomonosov Moscow State
University
semivrazhskaya@gmail.com

Mariya Vladimirovna Serova
Russia, Volgograd State University
mari.serova.93@inbox.ru

Marina Borisovna Shavelkina
Russia, Joint Institute for High
Temperatures
mshavelkina@gmail.com

Nikolai Viktorovich Shchankin
Russia, Ioffe Institute
79213878750@ya.ru

Elena Fedorovna Sheka
Russia, Peoples' Friendship University of
Russia
sheka@icp.ac.ru

Ping Sheng
Hong Kong, Hong Kong University of
Science & Technology
sheng@ust.hk

Mikhail Shestakov
Russia, Ioffe Institute
mishavolkin@gmail.com

Victor Olegovich Shevelev
Russia, St. Petersburg State University
victorshevelev@yandex.ru

Vasily Andreevich Shilin
Russia, National Research Centre
"Kurchatov Institute", B. P. Konstantinov
Petersburg Nuclear Physics Institute
shilin@pnpi.spb.ru

Stanislav Alexeevich Shostachenko
Russia, NRNU MEPhi
fizik92@inbox.ru

Filipp Shumilov
Russia, INSTITUTE OF SYNTHETIC
RUBBER
Itachi16@mail.ru

Alex V. Shvidchenko
Russia, Ioffe Institute
alexshvidchenko@mail.ru

Renat Timergalievich Sibatov
Russia, Ulyanovsk State University
ren_sib@bk.ru

Samiksha Sikarwar
India, Babasaheb Bhimrao Ambedkar
University
samiksha9.2009@gmail.com

Sergei Kirillovich Simakov
Russia, LLC "Adamant"
simakov@ap1250.spb.edu

Mikhail Maximovich Simunin
Russia, National Research University of
Electronic Technology
michanel@mail.ru

Alexander Sergeevich Sinita
Russia, NRC "Kurchatov Institute"
alexsinita91@gmail.com

Viktor Sivkov
Russia, Komi Science Centrum Ural
Department RAS
sivkovvn@mail.ru

Evgenii Vyacheslavovich Skokan
Russia, Lomonosov Moscow State
University, Chemistry Department
skokan@phys.chem.msu.ru

Dmitriy Vladimirovich Smovzh
Russia, Kutateladze Institute of
Thermophysics
smovzh@itp.nsc.ru

S. S. Sologubov
Russia, N.I. Lobachevsky Nizhny Novgorod
State University
markin@calorimetry-center.ru

Gennadi Girshevitch Sominski
Russia, St. Petersburg State Polytechnical
University
Postbox@stu.neva.ru

Pavel Sorokin
Russia, Emanuel Institute of Biochemical
Physics of Russian Academy of Sciences;
pbsorokin@gmail.com

Dorin Mihailovici Spoiala
Moldavia, Moldova State University
spodor@usm.md

Anatolii Starukhin
Russia, Ioffe Institute
a.starukhin@mail.ioffe.ru

Yury Victorovich Stebunov
Russia, Moscow Institute of Physics and
Technology
ystebunov@gmail.com

Tatiana Sergeevna Stepanova
Russia, Moscow Institute of Physics and
Technology (State University)
tanja.stepanova36@gmail.com

Dina Yurievna Stolyarova
Russia, National Research Centre
"Kurchatov Institute"
stolyarova.d@gmail.com

Craig Thomas Stoppiello
United Kingdom (Great Britain), University
of Nottingham
pcxcts@nottingham.ac.uk

Nadezhda Sukhinina
Russia, Institute of Solid State Physics RAS
suhinina@issp.ac.ru

Marina Vadimovna Suyasova
Russia, Petersburg Nuclear Physics Institute
marinasuyasova@pnpi.spb.ru

Artem Vladimirovich Sysa
Russia, MIEE
sysa.artem@yandex.ru

Vitalii Igorevich Sysoev
Russia, Nikolaev Institute of Inorganic
Chemistry
sysoev@niic.nsc.ru

Alina Szhogina
Russia, National Research Centre
"Kurchatov Institute", B. P. Konstantinov
Petersburg Nuclear Physics Institute
allin_ok2@mail.ru

Nadezhda Borisovna Tamm
Russia, Moscow State University, Chemistry
Department
tamm@thermo.chem.msu.ru

Evgeni Taradaev
Russia, SPBPU
evgeny_tar@hotmail.com

Konstantin Alekseevich Ten
Russia, Lavrentiev Institute of
Hydrodynamics SB RAS
ten@hydro.nsc.ru

Reshef Tenne
Israel, Weizmann Institute
reshef.tenne@weizmann.ac.il

Maria Letizia Terranova
Italy, University of Rome Tor Vergata ,
Dep. Chemical Sciences and Technologies
terranova@roma2.infn.it

Galina Vladimirovna Tikhomirova
Russia, Ural Federal University
galina.tihomirov@mail.ru

Oleg Tolochko
Russia, Saint Petersburg State Polytechnical
University
tolochko_ov@spbstu.ru

Oleg Borisovich Tomilin
Russia, Mordovian State University
tomilinob@mail.ru

Alexander Trofimov
Russia, Ioffe Institute
trofimov.pti@gmail.com

Sergey Igorevich Troyanov
Russia, Chemistry Department, Moscow
State University
stroyano@thermo.chem.msu.ru

Adis Anisovich Tukhbatullin
Russia, Institute of Petrochemistry and
Catalysis of RAS
adiska0501@gmail.com

Airat Ramilevich Tuktarov
Russia, Institute of Petrochemistry and
Catalysis of RAS
airat_1@mail.ru

Tatiana Alexeevna Tumareva
Russia, Saint Petersburg Polytechnical
University
tumareva@rphf.spbstu.ru

Vladimir Stepanovich Urbanovich
Belarus, SSPA "Scientific-Practical
Materials Research Centre of NAS of
Belarus"
urban@physics.by

Sergei Urvanov
Russia, Technological Institute for
Superhard and Novel Carbon Materials
urvanov@tisnum.ru

Iraida Ushakova
Russia, A. Baikov Institute of Metallurgy
and Materials Science
ush.in@yandex.ru

Rustem Eduardovich Uzbekov
France, Tours University
rustuzbekov@aol.com

Anastasija Viktorovna Valueva
Russia, Pavlov Ryazan State Medical
University
anastacia.lithium90@gmail.com

Ekaterina Vasina
Russia, St-Petersburg State Institute of
Technology (Technical University)
LedyKatrin@mail.ru

Evgeny Aleksandrovich Veretennikov
Russia, Saint Petersburg State
Technological Institute (Technical
University)
eaveret@gmail.com

Dinara Vil'keeva
Russia, Volgograd State University
vidinara@mail.ru

Andrey Yakovlevich Vinogradov
Russia, Ioffe Institute
vingrdov@mail.ru

Anton Vopilov
Russia, Department of Solid State
Electronics, Faculty of Physics, Saint-
Petersburg State University
antonvop@mail.ru

Anton Sergeevich Voronin
Russia, Siberian Federal University
a.voronin1988@mail.ru

Sergey Alexander Voropaev
Russia, GEOKHI RAS
voropaev@geokhi.ru

Vladimir Voroshnin
Russia, Saint Petersburg State University
Vl.Voroshnin@yandex.ru

Alexey Vozniakovskii
Russia, Ioffe Institute
alexey_inform@mail.ru

Alexandr Voznyakovskii
Russia, Lebedev Research Institute for
Synthetic Rubber
voznap@mail.ru

Nikolay Alekseevich Vysochanskiy
Russia, Moscow Institute of Physics and
Technology
n.vysochanskiy@yandex.ru

Yang Xu Xu Yang
China, Forturn Myriad Diamond Nano Tech
Co.,Ltd
78049623@qq.com

Bal Chandra Yadav Yadav
India, B B A UNIVERSITY
nano.lu71@gmail.com

Ishmumin Djabbarovich Yadgorov
Uzbekistan, Institute of Ion-Plasma and
Laser Technologies
iyadgarov@mail.ru

Ruslan Yur'evich Yakovlev
Russia, Pavlov Ryazan State Medical
University
yarules@yandex.ru

Shangfeng Yang
China, University of Science and
Technology of China
sfyang@ustc.edu.cn

Dmitry Vladimirovich Yudaev
Russia, ISCTE
dmitry.yudaev@ocsial.com

Alexander Stepanovich Zolkin
Russia, Novosibirsk State University
zolkinas@gmail.com

Svetlana Zaglyadova
Russia, United research and development
centre
zaglyadovasv@rn-rdc.ru

Irina Zaporotskova
Russia, Volgograd State University
irinazaporotskova@gmail.com

Ekaterina Zhukova
Russia, Technological Institute For
Superhard And Novel Carbon Materials
katyazhu@tisnum.ru

Valery Zhylinski
Belarus, Belarusian State Technological
University
zhilinski@yandex.ru

From Guest Editorial

This special volume of “**NANOSYSTEMS: PHYSICS, CHEMISTRY, MATHEMATICS**” presents the Proceedings of the 12th Biennial International Conference "Advanced Carbon Nanostructures" (ACNS'2015) held June 29 - July 3, 2015 in St.Petersburg, Russia.

The tradition of the Conference is traced to its beginning in 1993 in St.Petersburg as the first International Workshop "Fullerenes and Atomic Clusters" (IWFAC). Since that time, the conference is still held every other year, attracting nanocarbon community from all over in the world. In 2011 the Conference was combined with the International Symposium "Detonation Nanodiamonds: Technology, Properties and Applications" under the title “Advanced Carbon Nanostructures”. In 2015, nearly 200 participants from the leading scientific centers and universities of Russia, Ukraine, Belarus, Kazakhstan, Australia, China, Finland, France, Germany, Hungary, Iran Italy, Israel, Japan, Netherlands, Spain, Mexico, USA and the UK participated in the Conference.

We believe that the ACNS'2015 has become one of the most important meetings in the field of carbon-based nanoscience. All aspects of this modern field were covered at the Conference and appropriate papers were included in the Proceedings. The subjects of these papers not only included many theoretical questions of physics, chemistry of graphene, nanotubes, fullerenes and other nanocarbon materials but also covered the potential applications of these promising materials.

The ACNS'2015, was organized by Ioffe Physical-Technical Institute, St.Petersburg Nuclear Physics Institute, National Research Center "Kurchatov Institute", Moscow, Russia, and St. Petersburg State Institute of Technology (Technical University). We would like to express our gratitude to the official partners of the ACNS'2015 – Russian Foundation for Basic Research, Fund for Infrastructure and Educational Programs the Government of Saint Petersburg, Dmitry Zimin Foundation “Dynasty, Chemical Abstracts Service as well as the Journal “Nanosystems: Physics, Chemistry, Mathematics”. We greatly appreciate the active help of the International Advisory Committee and Program Committee members for their important suggestions in determining of the scope of the ACNS'2015, the list of invited and oral speakers as well as the help in reviewing manuscripts for Proceedings.

Taking into account the wishes of all the participants of our conferences, it was decided to organize the next conference “Advanced Carbon Nanostructures” in July 2017, so we are pleased to welcome the members of the global nanocarbon community to St.Petersburg.

Marina V. Baidakova, Artur T. Dideikin and Larisa V. Sharonova.
Guest editors of ACNS'2015.

Biocompatible water-soluble endometallofullerenes: peculiarities of self-assembly in aqueous solutions and ordering under an applied magnetic field

V. T. Lebedev, Yu. V. Kulvelis, V. V. Runov, A. A. Szhogina, M. V. Suyasova

Petersburg Nuclear Physics Institute, NRC Kurchatov Institute, 188300 Gatchina,
Leningrad distr., Russia

vlebedev@pnpi.spb.ru, kulvelis@pnpi.spb.ru, runov@pnpi.spb.ru,
allin_ok2@mail.ru, marinasuyasova@pnpi.spb.ru

PACS 61.48-c; 36.20.-r; 82.35.Np; 61.25.he

DOI 10.17586/2220-8054-2016-7-1-22-29

The self-organization of water-soluble endometallofullerenes (fullerenols) in solutions has been studied by neutron scattering in connection with their applications (Magneto-Resonance Imaging, *X*-Ray Tomography). Their functional characteristics depend strongly on molecular self-assembly which may be altered by chemical additives, concentration increase or the magnetic field applied. Polarized neutrons have been used to search paramagnetic fullerenols' organization into supramolecular structures influenced by the fullerenol concentration and their intensified interactions in a magnetic field.

Keywords: endofullerene, structure, assembly, biomedicine, neutron scattering.

Received: 20 November 2015

1. Introduction

The application of paramagnetic endometallofullerenes (EMF) [1] such as Gd@C_{82} and similar structures in biomedicine (contrasting agents for magnetic resonance imaging (MRI), *X*-Ray tomography, tracers being the isotopes encapsulated in carbon cages etc.) [2,3] is closely related to the study of various water-soluble EMF derivatives in aqueous solutions to understand mechanisms of molecular assembly altered by the functional properties of these substances [4,5].

For example, there is a remarkable well known acceleration of the spin relaxation for protons in the vicinity of paramagnetic EMF molecules in aqueous solutions or biological tissues (e.g. fullerenols $\text{Gd@C}_{82}(\text{OH})_x$) [6]. This effect is enhanced by the association of EMFs and is dependent upon the size and forms of EMF clusters [7]. This proton relaxivity enhancement effect is induced by dissolved EMF molecules and is of great importance to achieve higher resolution in MRI-diagnostics while simultaneously avoiding toxicity issues associated with heavy metals (e.g. Gd), since their atoms are encapsulated in carbon cages and well-protected against chemical interaction with the surrounding media in living organisms. Along with this, a gain in relaxivity can be expected when one uses paramagnetic EMFs mixed with diamagnetic (empty) EMFs, since their labile π -electrons may be polarized by a neighboring paramagnetic molecule. Thus, one can expect an amplification of fluctuating local fields due to additional effects of proton relaxivity acceleration. However, these inductive effects between paramagnetic and diamagnetic molecules are not yet studied. Additionally, there is only a poor knowledge of the mechanisms for the local ordering of paramagnetic fullerenols in solutions, especially under the influence of applied magnetic fields which can be relatively strong (few Tesla in MRI-tests).

It should be noted that a set of effective experimental methods and instruments to comprehensively analyze the self-organization of water-soluble EMFs in aqueous media still

remains restricted, especially regarding the study of both supramolecular and magnetic ordering in EMF solutions in magnetic fields and by altering other parameters (e.g. concentration of paramagnetic EMFs, pH-factor, temperature).

Among these structural methods (e.g. *X*-ray or light scattering), only the polarized neutron reflectometer is a powerful enough instrument to obtain detailed information on the molecular and magnetic ordering and subtle effects of their interference over a wide range of spatial scales ($10^0 - 10^2$ nm). It is of principal importance that the polarized neutron beam does not disturb the sample and gives information on the size and forms of molecular arrangements, as well as the possible magnetic ordering of EMFs under the applied magnetic field. The polarization of scattered neutrons is very sensitive to fine magnetic correlations in the ensembles of paramagnetic objects [8].

The aim of our experiments on aqueous mixtures of paramagnetic and diamagnetic fullerenols is to study the behavior of these systems under magnetic field to discover original and field-induced mechanisms for the self-assembly of fullerenols by varying their concentration and magnetic induction.

2. Experimental

2.1. Samples and measurements

The samples were synthesized at PNPI for neutron experiments. Mixtures of $\text{Gd}@C_{82}(\text{OH})_X$ ($X = 24 - 30$) and $C_{60}(\text{OH})_X$ were prepared keeping a constant level of paramagnetic component (30 wt%). These mixtures were dissolved in light water to obtain solutions with concentrations $C = 0.044, 0.056, 1.04$ and 2.0 wt% (Samples 1–4) where the upper limit is close the threshold for fullereneol solubility ($C_{\text{max}} = 2.3$ wt%).

Polarized small-angle neutron scattering experiments (PSANS) have been carried out at ambient temperature on the Diffractometer “Vector” (PNPI) [8] over a range of momentum transfer $q = (4\pi/\lambda) \sin(\theta/2) = 0.03 - 0.45 \text{ nm}^{-1}$ where neutron wavelength $\lambda = 0.92 \text{ nm}$ ($\Delta\lambda/\lambda = 0.25$), scattering angles $0 \leq \theta \leq 3^\circ$. The q -interval corresponded to the scales of the fullerenols structures $R \sim 2\pi/q \sim 10^1 - 10^2 \text{ nm}$. In the detector plane (X, Y), the scattering was registered with q -resolution $\delta q_X, \delta q_Y \approx 4.5 \cdot 10^{-3} \text{ nm}^{-1}$.

For the Samples 1–4 (solutions layers, thickness $d_S = 1 \text{ mm}$) an isotropic scattering was observed in the external field $B = 0.01, 0.6, 1.0 \text{ T}$ applied along the vertical axis Y (incident beam along Z -axis). In scattering measurements, the direction of vertical polarization of the beam ($P_0 = 0.94$) was periodically reversed ($\pm \mathbf{P}_0$) to detect the intensities $I^\pm(\mathbf{q})$ which were used to calculate the sums $I_t = I^+ + I^-$ and the differences $\Delta I = I^+ - I^-$ sensitive to interference effects of the scattering on molecules (atomic nuclei) and the magnetic moments of Gd atoms. A measure of such nuclear magnetic interference is the effective polarization $P_{ef} = \Delta I/I_t$. The measured intensities (I_t) were used to determine the scattering intensities (I_S) and the related cross sections, taking into account the neutron transmissions for the samples, the background level and the contribution of the beam that passed through the samples without scattering. Finally, the differential cross sections per unit solid angle (Ω) and cm^3 of sample volume were computed in absolute units, $d\sigma(q)/d\Omega = (I_S/I_W)(d_W/d_S)(d\sigma_W(q)/d\Omega)$, where I_W is the intensity measured for H_2O -standard (layer, thickness $d_W = 1 \text{ mm}$) at the same experimental conditions. Here, the cross section of water $d\sigma_W(q)/d\Omega = 1.089 \text{ cm}^{-1}/\text{cm}^3$ is used [9]. In following treatment the notation $\sigma(q) = d\sigma(q)/d\Omega$ is accepted.

2.2. Discussion

In the experiments, the magnetic field was varied from minimum magnitude $B_1 = 0.01$ T (guide field to keep beam polarization) up to intermediate and maximum magnitudes, $B_2 = 0.6$ T, $B_3 = 1.0$ T. At these induction values, the measurement was organized in such a way that periodically the induction was switched on and after few hours of data collection it was switched off for the measurement at minimum field B_1 . These weakly magnetic substances did not reveal any significant hysteresis and demonstrated a reversible behavior detected in the scattering. In Fig. 1, the cross sections of the solutions with concentrations $C = 0.044$ – 2.0 wt% are shown as dependent on momentum transfer for minimum and maximum fields.

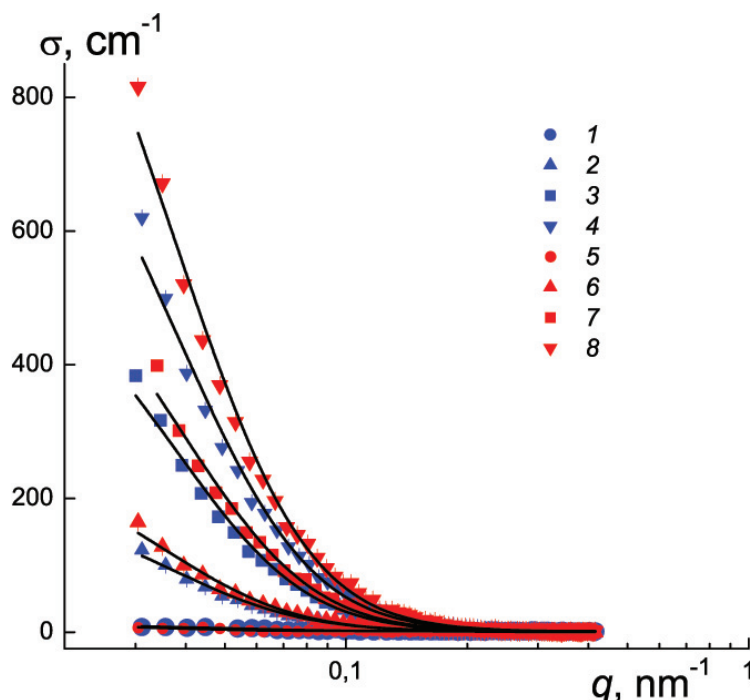


FIG. 1. Scattering cross sections of the solutions with different contents of fullerenols (0.044, 0.056, 1.04 and 2.0 wt%) studied in weak and strong fields (B_1 , B_3) (data 1–4 and 5–8, respectively). Lines are fitting functions (1)

The application of a magnetic field caused a remarkable increase in the scattering without qualitatively altering the cross section's q -dependence, which is clearly visible at concentrations $C = 0.056$, 1.04 and 2.0 wt%. In the most dilute solution ($C = 0.044$ wt%), an opposite situation is observed when the intensity slightly decreases with field application (Fig. 2).

In Fig. 2 the differences of cross section, $\Delta\sigma(q, B) = \sigma(q, B) - \sigma(q, B_1)$, are presented for the dilute system showing a negative effect. Although, in the experimental q -range, the application of moderate and strong fields (B_2 , B_3) does not lead to more intensive scattering, but at the same time, the deficit in cross section means that the scattering redistribution favors lower momentum transfers if the field stimulates aggregation. Indeed, this trend is observed in more concentrated solutions (Fig. 3), where the positive differences of cross sections become greater in the strong field B_3 .

This qualitative analysis has been supplemented by a detailed description of structuring when we used the scattering function :

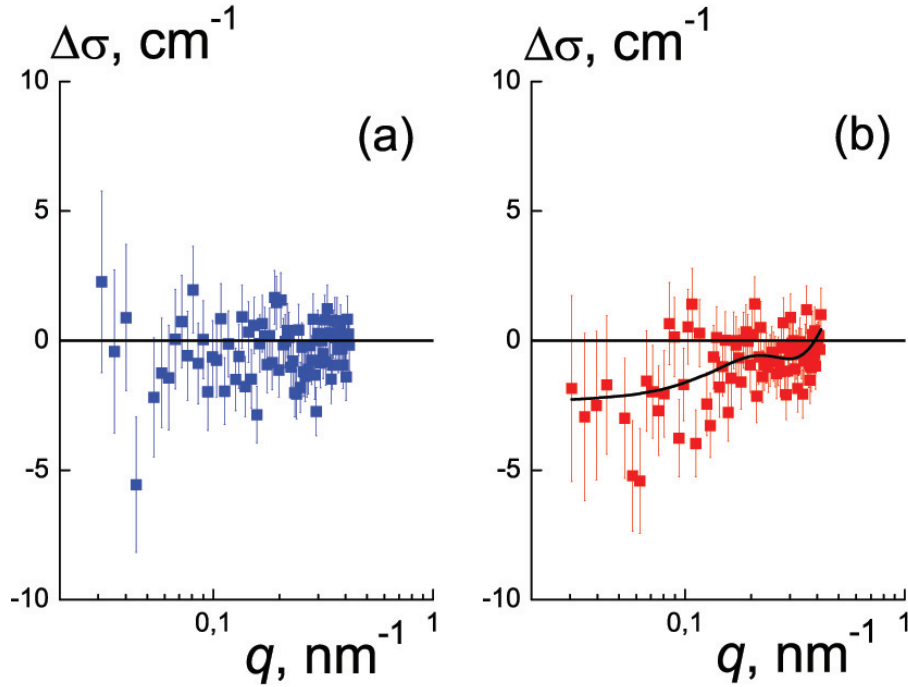


FIG. 2. Differences of cross sections $\Delta\sigma(q, B) = \sigma(q, B) - \sigma(q, B_1)$ in dilute solution ($C = 0.044$ wt%) measured in moderate and strong fields (B_2, B_3) (a, b) as compared to the data obtained in weak field B_1 . Line (b) shows a spline-function

$$\sigma(q) = \frac{\sigma_0}{[1 + (qR_C)^2]^2} + Bg, \quad (1)$$

where $\sigma_0 = \sigma(q \rightarrow 0)$ is forward cross section, R_C is the radius of molecular correlations, the parameter Bg denotes a contribution of incoherent background to the total cross section. The formalism in (1) satisfactorily fits the experimental data for all concentrations and magnetic field strengths.

The parameters $\sigma_0(C)$, $R_C(C)$ showed how the behaviors were modified by the external applied magnetic field (Fig. 4). The forward cross sections demonstrate quite linear growth (Fig. 4a) disturbed by quadratic terms, $\sigma_0(C) = (\alpha_1 C + \alpha_2 C^2)$ where α_1 , α_2 are the fitting parameters. Conversely, the parameter $\sigma_0 = (\Delta K)^2 \varphi(m V_F)$ is proportional to the aggregation number (m). This also includes the contrast factor of fullerolols in water ($\Delta K = 4.8 \cdot 10^{10} \text{ cm}^{-2}$), their total volume fraction $\varphi = (C N_A / M_F) V_F$ which depends on Avogadro's constant (N_A), molecular weight (M_F) and the volume (V_F) of fullerol molecule. Obviously, at a constant aggregation number (m), there should be linear behavior $\sigma_0 \sim \varphi \sim C$. This means an increase in the numbers of clusters with the enrichment of solutions. Additionally, the term $(\alpha_2 C^2)$ arises due to clusters' pair interactions. The increase in the relative rate of aggregation is given by $(1/m) dm/dC = \alpha_2 / \alpha_1$. This ratio rises more than twice from $\alpha_2 / \alpha_1 \approx 9$ to $\approx 19 \text{ cm}^3/\text{g}$ due to the induction enhancement from the minimum to the maximum magnetic field strength. Hence, magnetic field stimulates more dense integration of fullerolols when the size of clusters (R_C) remains fairly constant (Fig. 4b).

At magnetic fields ranging from $B = 0.01 - 1.0$ T the correlation radius takes the value $R_C \sim 18 - 19$ nm for the concentrations $C = 0.056, 1.04$ and 2.0 wt% (Fig. 4b). However, in weak and moderate fields, at the lowest fullerol content, (0.044 wt%) the correlation lengths

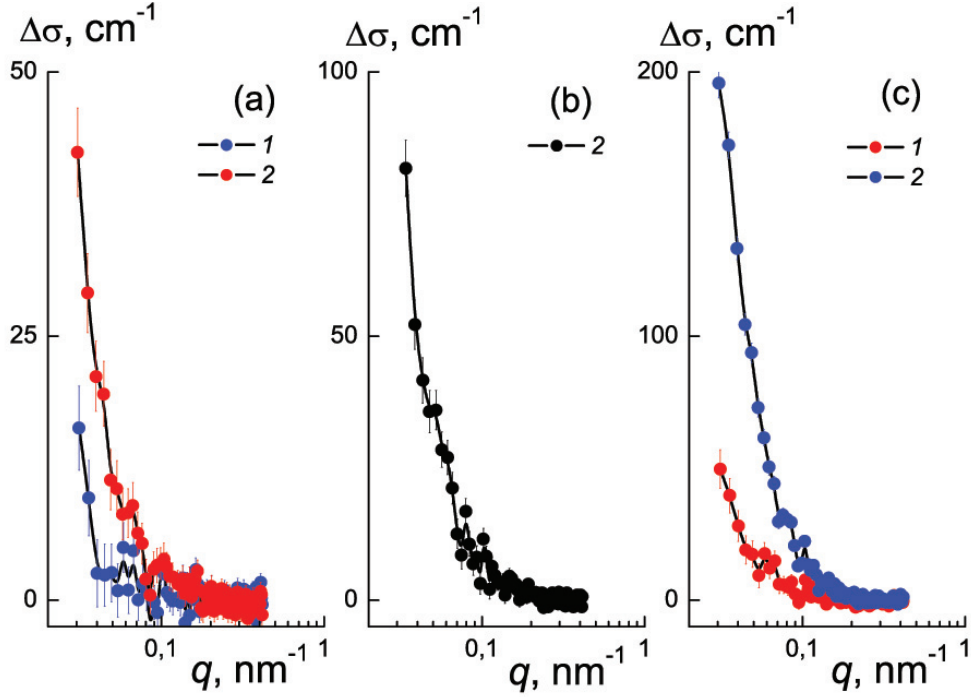


FIG. 3. Field induced gain in cross sections of solutions, $\Delta\sigma(q, B) = \sigma(q, B) - \sigma(q, B_1)$, with fullerenols concentrations $C = 0.056, 1.04$ and 2.0 wt% (a, b, c). Data 1, 2 are related to the experiments at moderate and strong fields (B_2, B_3)

are shorter, $R_C \sim 15$ nm, while a strong field amplifies the correlations, the radius of which becomes larger, $R_C \sim 18$ nm (Fig. 4b). Thus, under the strong field ($B_3 = 1.0$ T), clusters achieve the size $R_C \sim 18 - 19$ nm practically not influenced by fullerenols concentrations. Along with this, the aggregation numbers $m(C)$ found from the forward cross sections grow intensively with the concentration, especially in the strong field B_3 (Fig. 5).

The number of molecules $m \sim (2 - 5) \cdot 10^4$ (Fig. 5) occupies a relatively extended region with gyration radius $R_G = \sqrt{6} \cdot R_C \sim 40$ nm. For instance, a spherical region with such gyration radius has the geometric radius $R_S = (5/3)^{1/2} R_G \sim 60$ nm. In a spherical approximation, one can estimate the average share of occupied volume, $\Phi \sim 3 - 7$ %. Alternatively, a characteristic volume of molecular correlations $V_C = 8\pi R_C^3 \sim 2 \cdot 10^5$ nm³ is smaller, and in this region, the occupied volume is of $15 - 35$ %. This figure increases with the fullerene concentration and becomes higher in a strong field, which stimulates the integration of fullerenols into clustered structures.

The analysis performed above concerned the cross sections corresponding to the sum of scattering intensities $I^+(q), I^-(q)$ obtained by reversing beam polarization ($\pm P_0$) in vertical guide-field. In general, each intensity [8]:

$$I^\pm = I_n(q) + I_m(q) \pm I_{INT}(q), \quad (2)$$

includes the contributions of nuclear and magnetic scattering, $I_n(q) \sim a_N^2$, $I_m(q) \sim [b_M \cdot \sin(\alpha)]^2$, with the amplitudes $a_N(q)$ and $b_M(q) \sin(\alpha)$ where α is the angle between induction \mathbf{B} and scattering vector \mathbf{q} . In addition, it presents the interference part $I_{INT}(q) \sim 2P_0 a_N(q) b_M(q\alpha)$, in our experiments $\mathbf{P} \parallel \mathbf{B}(q)$. This part was extracted as the difference:

$$\Delta(q) = I(q, P^+) - I(q, P^-) \equiv I^+(q) - I^-(q) = 2I_{INT}(q). \quad (3)$$

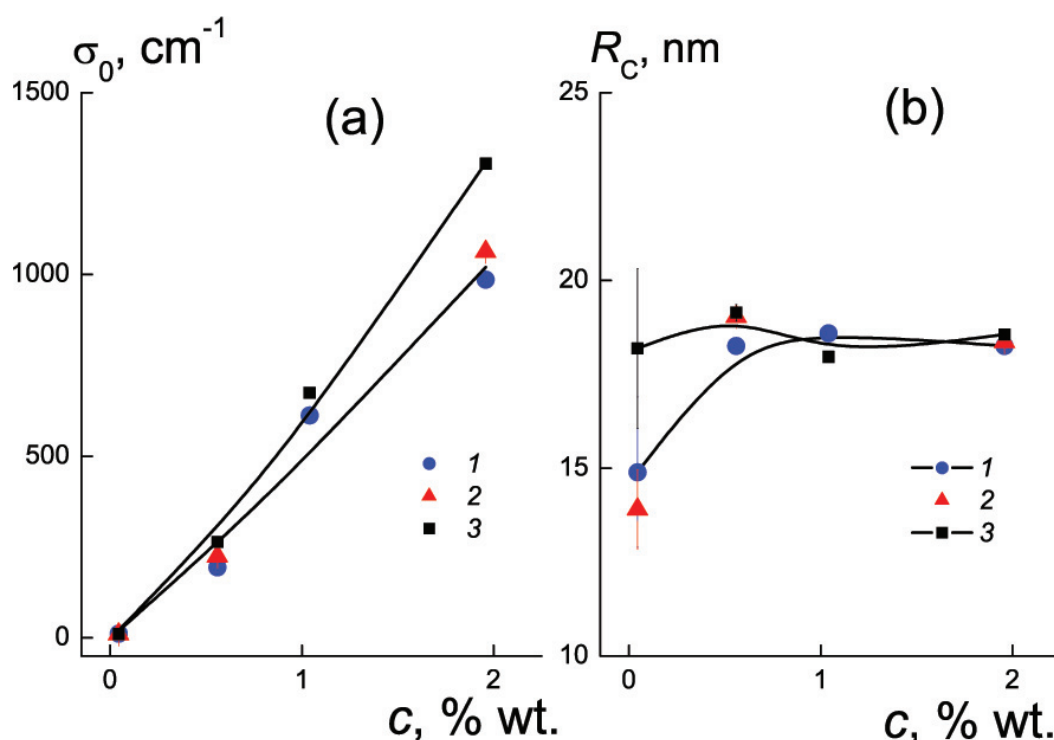


FIG. 4. Concentration and field dependence of the fullerenols clusters parameters: forward cross section $\sigma_0(C)$ and correlation radius of clusters $R_C(C)$ (a, b) at external fields B_1, B_2, B_3 (data 1–3)

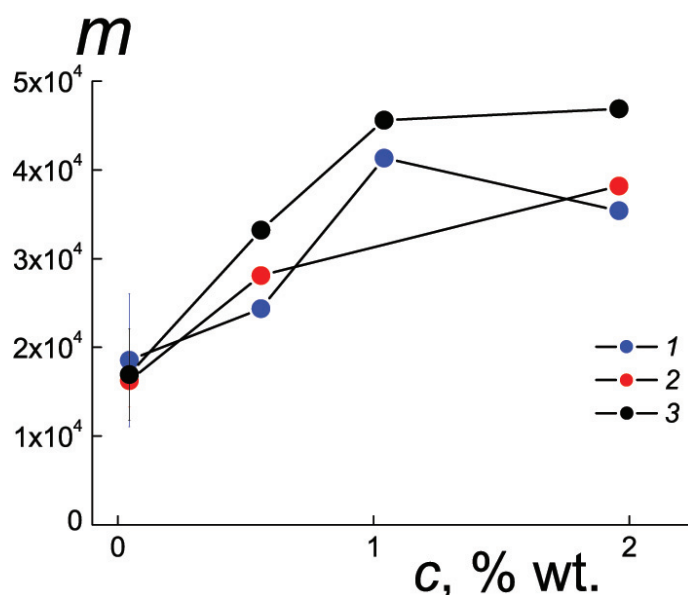


FIG. 5. Aggregation number vs. concentration when magnetic fields B_1, B_2, B_3 are applied (data 1–3)

The relative contribution of interference to the total scattering intensity is given by the effective polarization $P_{ef} = (I^+ - I^-)/(I^+ + I^-)$. In solutions having weakly magnetic properties, a search of nuclear-magnetic interference has shown low effects averaged over q-range, $\langle P_{ef} \rangle = (0.07 \pm 0.05) \%$, even at the maximum concentration $C = 2.0$ wt% (Fig. 6).

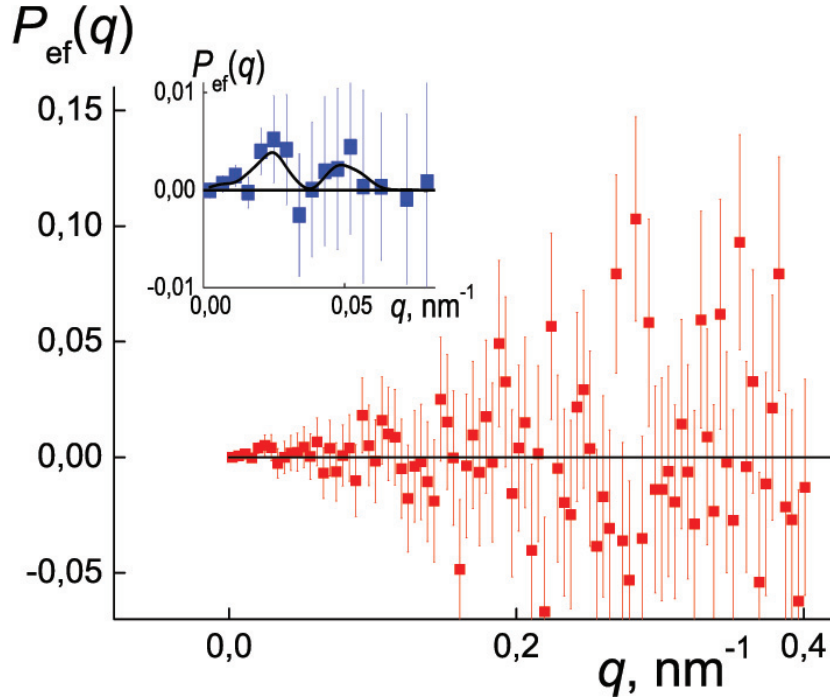


FIG. 6. Effective polarization $P_{ef}(q)$ vs. momentum transfer in fullereneol solutions (concentration $C = 2.0$ wt%). Inset shows the behavior of effective polarization at low q -values

This can be explained as a result of low concentration of paramagnetic Gd atoms in these systems, $N_{Gd} = 2 \cdot 10^{18} \text{ cm}^{-3}$ at $C = 2.0$ wt%. The applied field $B_3 = 1.0$ T did not align the magnetic moments of Gd. For complete magnetization, higher induction is needed (by two orders in magnitude). This would appear to be in contradiction with the observed substantial amplification of the molecular ordering under magnetic field $B_3 = 1.0$ T. Meanwhile, such a discrepancy is eliminated if we consider the induced diamagnetic moments in massive clusters interacting in solutions that stimulates ordering in molecular solutions even at the low diamagnetic susceptibilities of carbon structures ($\chi \sim 5 \cdot 10^{-7}$ for C_{60} fullerite [10]). Indeed, some large-scale effects in effective polarization are visible in the inset shown in Fig. 6 where two maxima are present at $q^* \sim 0.025 \text{ nm}^{-1}$ and $q^{**} \sim 0.05 \text{ nm}^{-1}$. One might suspect that the nuclear-magnetic interference is detected at large scale $R \sim 2\pi/q^* \sim 300 \text{ nm}$ for the superstructures of weakly magnetized clusters.

3. Conclusions

The first scattering experiments with polarized neutrons on the mixtures of paramagnetic and diamagnetic fullereneols have revealed unexpected features in fullereneols behavior. A strong applied magnetic field was shown to stabilize the size of molecular aggregates ($R_C \sim 20 \text{ nm}$) when the concentrations were varied by two orders of magnitude, i.e. the system concentration was changed from very dilute to concentrated (close to the threshold of fullereneol solubility).

The influence of magnetic field does not only involve direct alignment of the paramagnetic atoms' moments. A substantial enhancement of the aggregation numbers was detected under a strong applied magnetic field. In addition, the scattering of polarized neutrons gave specific indications for the correlated spatial organization of molecular and magnetic subsystems at large (submicron) scales where the magnetic domains are visible.

The fundamental importance of the performed experiments is combined with the practical benefits of the possible application of these substances as effective contrast agents in MRI. As a result of these studies, structural stability has been confirmed for EMF aggregates over a broad range of concentrations in solutions under strong applied magnetic fields.

Acknowledgements

The work is supported by Russian Found for Basic Research (grant 14-23-01015 ofi_m).

References

- [1] Heath J.R., O'Brien S.C., et al. Lanthanum complexes of spheroidal carbon shells. *J. Am. Chem. Soc.*, 1985, **107**, P. 7779–7780.
- [2] Piotrovsky L., Eroshkin M., et al. Biological Effects in Cell Cultures of Fullerene C₆₀: Dependence on Aggregation State. In: *Medicinal Chemistry and Pharmacological Potential of Fullerenes and Carbon Nanotubes*. Eds. F. Cataldo, T. Da Ros. Germany: Springer, 2008, P. 139–155.
- [3] Kato H., Kanazawa Y., et al. Lanthanoid endohedral metallofullerenols for MRI contrast agents. *J. Am. Chem. Soc.*, 2003, **125**, P. 4391–4397.
- [4] Yin J.J., Lao F., et al. The scavenging of reactive oxygen species and the potential for cell protection by functionalized fullerene materials. *Biomaterials*, 2009, **30** (4), P. 611–621.
- [5] Grushko Yu.S., Kozlov V.S., et al. MRI-contrasting system based on water-soluble fullerene / Gd-metallofullerene mixture. *Fuller., Nanotub. Carbon Nanostr.*, 2010, **18** (4), P. 417–421.
- [6] Grushko Yu.S., Sedov V.P., Kozlov V.S., Tsirlina E.V. Method of preparation of MRI-contrasting agent. Patent RU 2396207 C2 from 10.08.2010, Bull. No. 22, 2010.
- [7] Toth E., Bolskar R.D., et al. Water-soluble gadofullerenes: toward high-relaxivity, pH-responsive MRI contrast agents. *J. Am. Chem. Soc.*, 2005, **127** (2), P. 799–805.
- [8] Runov V.V., Il'in D.S., Runova M.K., Radzhabov A.K. Study of ferromagnetic correlations caused by the impurities in non magnetic materials by the method of small-angle scattering of polarized neutrons. *JETP Lett.*, 2012, **95** (9), P. 467–470.
- [9] Lindner P. Water standard calibration at D11 verified with polymer samples. *J. Appl. Crystallography*, 2000, **33**, P. 807–811.
- [10] Kitazawa H., Hashi K., et al. Molecular dynamics and structural phase transition in C₆₀ nanowhiskers. *J. Phys.: Conf. Series*, 2009, **159**, 012022 (1).

Growth, study, and device application prospects of graphene on SiC substrates

A. A. Lebedev

Ioffe Institute, St. Petersburg, Russia

Shura.lebe@mail.ioffe.ru

PACS 61.48.Gh, 73.22.Pr

DOI 10.17586/2220-8054-2016-7-1-30-36

It is well known that graphene, which brought the 2010 Noble Prize in physics to Russian scientists Andre Geim and Konstantin Novoselov, exists as two-dimensional carbon layers. The possible range of graphene applications includes development of field-effect transistors for digital and analog electronics, nanoelectromechanical systems, quantum dots, cold cathodes, supersapacitor, gas sensors, and nearly transparent electrodes and coatings. The possibility of using graphene for hydrogen storage and the manufacture of composite materials is also being studied. Being a two-dimensional material, graphene provides ultimate one-dimensional miniaturization and is a convenient basis for manufacture of different nanoelectronic, nanomechanical and nanochemical devices by lithographic methods. The graphene-based device which is closest to being successfully realized for practical application is the gas sensor. The use of graphene makes it possible to achieve a sensitivity exceeding that of all other materials, less than 1ppb. This device combines the comparative simplicity of manufacture with a wide spectrum of possible applications. It should also be mentioned that the structure of the gas sensor actually reproduces the structure of the field-effect transistor. Thus, the gas sensor can be considered the first stage in the development of intricate transistor electronics based on graphene. The paper briefly reviews growth experiments and studies of graphene films on silicon carbide (SiC) and the development of prototype gas sensors based on this material.

Keywords: graphene, silicon carbide, sublimation, gas sensors.

Received: 20 November 2015

1. Introduction

Graphene is a promising material that has unique properties, such as high surface-to-volume ratio, low electrical noise, and exceptional transport properties associated with its two-dimensional structure [1]. After a graphene monolayer was isolated in 2004 [1], much effort has been exerted to study the fundamental properties of this unique structure [2–6]. The most important of these is related to the confinement of carrier motion, which results in nearly linear carrier energy dispersion and, as a consequence, in extremely small effective mass and huge carrier mobility along the 2D graphene plane

Recently, one of the popular methods used to form graphene layers has been the thermal graphitization of single-crystal silicon carbide in a vacuum or under an argon atmosphere [5]. In contrast to the standard approaches, this method can be used to fabricate large graphene samples and allows further lithographic processing. The method utilizes the non-stoichiometric sublimation of silicon from the surface of single-crystal SiC heated to high temperatures, which yields a hexagonal lattice of carbon atoms remaining on its surface. The quality of the layers being obtained is provided by a pre-growth treatment of the SiC substrate. Note that, as far as we know, this method most probably gives a multilayered structure. Thus, we believe that a study of such structures is an important issue for the physics and technology of graphene.

The high adsorption capacity and the large surface-to-volume ratio of graphene make it attractive as a gas sensing material. In recent years, the interest in air pollutants and their monitoring has steadily increased. Nitrogen dioxide (NO_2) is a typical air pollutant that causes environmental and health problems. From this perspective, it is necessary to develop a highly sensitive and an inexpensive gas sensor capable of detecting low concentrations of this gas. Currently, gas sensing experiments demonstrate that epitaxial graphene may be an excellent material for future NO_2 sensors. Graphene layers grown on SiC have demonstrated sensitivities down to the ppb level and a high selectivity for NO_2 detection in the presence of the typical interfering gases [7, 8].

2. Sublimation growth of graphene

It is well known that heating of silicon carbide (SiC) causes the primary sublimation of silicon (Si) atoms and the graphitization of the underlying silicon carbide surface [9] (Fig. 1). After the discovery of numerous forms of nanocarbon (nanotubes, fullerenes, etc.) there appeared an idea of obtaining new carbon structures on silicon carbide via the in vacuo-controlled thermal decay of the crystal's surface [10, 11].

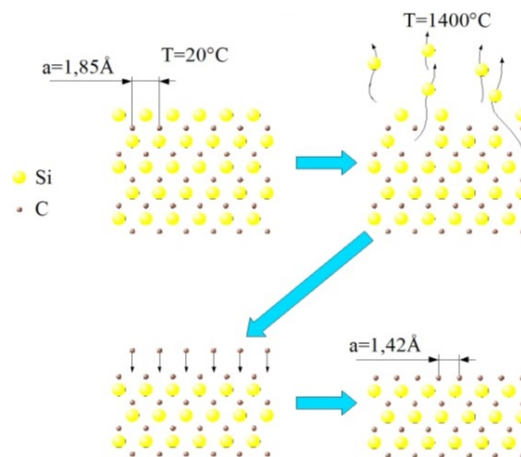


FIG. 1. Diagram of how graphene is formed on the surface of a SiC wafer

After the first planar nanocarbon films (“exfoliated grapheme”) were obtained in 2004 by the laser-mediated peeling from bulk crystalline graphene [1], studies were focused on obtaining a monoatomic layer of carbon on a SiC wafer. There have been several publications reporting that graphene films were obtained on the SiC surface. The communications [12, 13] demonstrated that a graphene film can be obtained in a high vacuum ($\sim 10^{-10}$ Torr) on axis 6H-SiC wafer by the surface thermal decay method. In [14], planar monoatomic carbon films formed on a 4H silicon carbide wafer were also studied.

It was shown in [15, 16] that nanocarbon layers can be formed on the SiC surface by the sublimation method in an open system. At the same time, no additional etching of samples in hydrogen or silicon vapors was required. This significantly simplified the process by which the films were obtained. The thickness of the resulting film was strongly dependent upon the annealing temperature. However, the structural and electrical properties of this film were more variable and sensitive to numerous technological factors, including the pre-growth surface treatment. Some of the existing dependences have been determined, but further analysis of these is required. According to the reflection high-energy electron diffraction (RHEED) method, the film contained two-dimensional graphene crystals. Measurements demonstrated that the films

formed on the carbon face of SiC have a better structural perfection than those formed on the silicon face. The data obtained confirm that the optimal temperature range to form graphene on the SiC surface is 1300 – 1400 °C.

3. Analysis of the films obtained

In addition to the conditions in which planar nanocarbon layers are formed on the SiC surface, various properties of the carbon film and the graphite/silicon carbide system are also being actively studied. The authors of [17] examined the electronic structure of the interface between the 6H SiC (0001) wafers and the graphite film. A structural analysis of the multigraphene (several graphene layers) structure/4H-SiC was made in [18]. The samples were subjected to a surface *X*-ray diffraction analysis. The distance between the wafer and the first monoatomic graphene layer was shown to be only 1.6 Å.

However, in all of the above-mentioned articles, attention was given to the structural analysis of graphene films, without due consideration of their electrical properties. This is partly due to the difficult fabrication of any contacts to such nano-objects as a one-layer-thick carbon film. A technological process for the manufacture of a graphene-based MESFET was suggested in [19]. The only exception is the communication [20], in which the formation of a field transistor structure on a film grown on the SiC surface was reported. As follows from the text of this communication, the carrier mobility in the given film was 535 cm²/(V·s), which is considerably lower than the mobility in the “exfoliated” graphene, where, according to [2], it has a value of 15,000 cm²/(V·s) at room temperature.

A possible reason for this behavior is the low structural perfection of the graphene film studied in [21], which, according to the AFM image, had multiple holes $\sim 0.5 \mu\text{m}$ in diameter. One possible reason why the film is porous is the imperfection of the pre-growth surface treatment, including residual surface impurities (oxygen and other adsorbates), which can react with carbon atoms during the course of thermal destruction to form volatile components (e.g. CO, CO₂). Detailed analyses have been made of Raman spectra of the films [22] and their transport properties [23].

In [24, 25], test structures for electrical measurements were formed the sample surface in the Hall-bar configuration by etching with an argon beam through a photoresist mask. Measurements of the current-voltage characteristics and the Hall effect were made at temperatures ranging from 2 – 300 K. It was stated that at $T < 4$ K, the conductivity weakly depends on temperature and becomes lower with decreasing temperature, in accordance with the weak logarithmic law typical of two-dimensional dirty metals (weak localization mode). According to the theory, the slope ratio of the logarithmic dependence for a two-dimensional system is universal and defined as $e^2/h \sim 4 \cdot 10^{-5} \text{ Ohm}^{-1}$. For the samples under study, this slope ratio is almost the same ($2 - 3 \cdot 10^{-6}$), which is several times less than the universal value. However, the conductivity calculations disregarded the following fact: the samples had a rectangular, rather than square, shape. The resistance for the square should then be reduced by a factor of 5 – 10. Accordingly, the slope ratio for the conductivity temperature dependence should be increased (at the sample length 10 times the width, this slope ratio will be $2 \cdot 10^{-5} \text{ Ohm}^{-1}$, which almost coincides with the theoretical estimation). At low temperatures (1.4 K), the conductivity tends to level-out (“saturate”) for both samples. The observed saturation of the low-temperature conductivity can be attributed to the finite size of the conducting sample ($\sim 10 \mu\text{m}$), compared to the phase fault length L , which at low temperatures may be comparable with the sample size. At the same time, the logarithmic dependence disappears. Multigraphene is characterized by L of $\sim 1 - 10 \mu\text{m}$ at low T . The Hall effect measured at low temperatures, gives for all temperatures the same carrier concentration $n \sim 10^{12} \text{ cm}^{-2}$ for one layer. At the same time, the Hall mobility

is low, about $100 \text{ cm}^2/(\text{V}\cdot\text{s})$. The comparatively high carrier concentration (10^{12} cm^{-2}) and low mobility, $100 \text{ cm}^2/(\text{V}\cdot\text{s})$, confirmed that, rather than being intrinsic, carriers are due to defects in multigraphene or at the SiC-multigraphene interface (GR/SiC).

In [25], the properties of a graphene film grown on SiC were studied “*ex situ*” by atomic force microscopy (AFM), Raman spectroscopy (Fig. 2), low energy electron diffraction (LEED), X-ray photoelectron spectroscopy (XPS), and near edge x-ray absorption fine structure (NEXAFS) spectroscopy. The AFM study showed that the substrate surface consisted of flat and wide ($\sim 1 \mu\text{m}$) terraces covered with sufficiently large and continuous graphene domains. Numerous LEED patterns obtained from different points of the sample demonstrated the concurrent presence of a well-ordered graphite (1×1) pattern and $(6\sqrt{3} \times 6\sqrt{3})R30$ pattern inherent to the underlying buffer layer [26], thus confirming the mainly bilayer nature of the film.

XPS and NEXAFS data obtained on a BESSY II synchrotron (Berlin) specify the chemical composition and electronic structure of the graphene film and confirm its high perfection and mostly bilayer nature. In particular, the bilayer character of the film was confirmed by low energy electron diffraction experiments, as well as by the 0.2 eV shift of the spectrum due to the charge transfer to the substrate, which is typical for bilayer films [27–29]. Considering the bilayer as a quantum well with a SiC bandgap wall, one can assume that the van Hove singularities appear in the density of states because of the quantum confinement in the normal direction. Indeed, two peaks are seen in the valence band spectrum of graphene near the Fermi level. Their energies are $E_1 = 0.5 - 0.2 = 0.3 \text{ eV}$ and $E_2 = 1.5 - 0.2 = 1.3 \text{ eV}$, with consideration for the 0.2 eV spectrum shift due to the charging the layer. The energy ratio ($E_2/E_1 \sim 4 = n_1/n_2$) and values agree with those calculated for the quantum well (Figs. 3, 4).

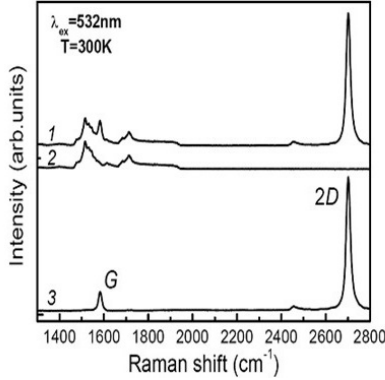


FIG. 2. 1 – Raman spectrum of a graphene layer grown on a 6H-SiC substrate; 2 – second-order Raman spectrum of the substrate 6H-SiC; 3 – differential spectrum obtained by subtracting spectrum 1 from spectrum 2

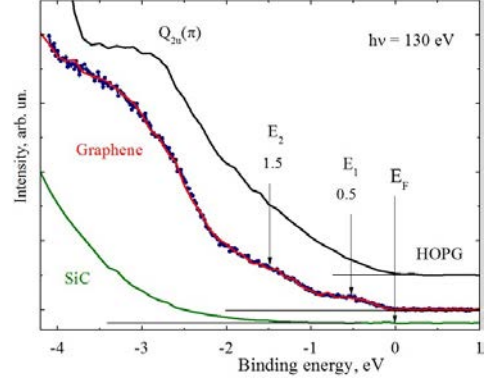


FIG. 3. Valence-band density-of-states spectra of the SiC substrate, bilayer graphene film, and pyrolytic graphite

4. Graphene gas sensors

Currently, there is an increasing demand for a cost-effective sensor for the detection of environmental pollutants like NO_x . Traditionally, transition metal oxides, such as In_2O_3 , SnO_2 , ZnO , and WO_3 , have been used for sensing [30]. However, a serious drawback for

these oxides is that their functional characteristics are strongly dependent upon the conditions used in their syntheses. Recently, epitaxial graphene on SiC has been suggested as a promising route for the mass-production of uniform, wafer-size graphene layers for the detection of gas molecules [7]. At present, this technique can give very high quality graphene films, the size of which is basically limited by the size of the SiC substrate. This technique also provides integration of graphene-based sensors with high-temperature electronics based on SiC. In this communication, we report the fabrication of sensors based on graphene films and their tests in ambient gas sensing.

Gas sensors were fabricated from the epitaxial graphene films grown by annealing of SiC substrates under Ar or vacuum at temperatures of 1200 – 1600 °C. Depending on the annealing time, temperature and atmosphere, the graphene films can contain 1 – 3 layers. The thickness of the graphene films was estimated by Auger and Raman spectroscopy. Patterns for the sensor devices were produced on the graphene surface of the substrate by laser photolithography over AZ5214 resist. Reactive ion etching in argon-oxygen plasma was used to remove the graphene layer from uncoated areas. Ti/Au (5/50 nm) contacts were formed by *e*-beam evaporation and lift-off photolithography with a laser writer over AZ5214 resist. The sample chip was assembled on the holder together with two Pt100 resistors. One of the resistors was chosen for temperature measurements, while the other served as a heater (Fig. 5).

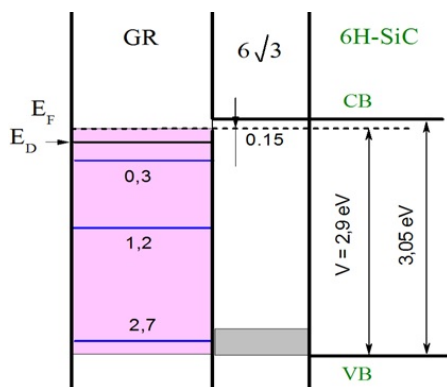


FIG. 4. Scheme of the quantum well for holes, formed on SiC with $6\sqrt{3}$ interface carbon monolayer (buffer layer)



FIG. 5. Sensor device on holder

To measure the gas response of graphene, a custom-made gas system was used. The dilution ratio could be varied from 1:1 – 1:10⁵, which provided an output concentration in the range from 0.1 ppb (parts per billion) to 10 ppm (parts per million). The response r was expressed in percent and defined as the relative change in the resistance of the sample upon its exposure to the gas, $r = (R - R_0)/R_0$, where R is the resistance with the gas, and R_0 is the resistance of the graphene film under the initial conditions defined by the air flow.

In Fig. 6, the relative changes in the resistance of graphene-based sensors upon exposure to NO₂ (exposure periods marked as light grey bands) at 20 °C are presented. Because the desorption rate of NO₂ is very low at room temperature, the sensor was heated at 110 °C after each exposure to restore it to its initial pre-measurement state [8].

The response signs for samples grown by different methods are opposite. According to Raman spectroscopic data, the graphene grown by vacuum annealing is multilayer, while that grown under Ar is single-layer. For multilayer graphene, *p*-type conductivity is expected, whereas *n*-type conductivity is observed for the single-layer material. NO₂ is a strong oxidizer,

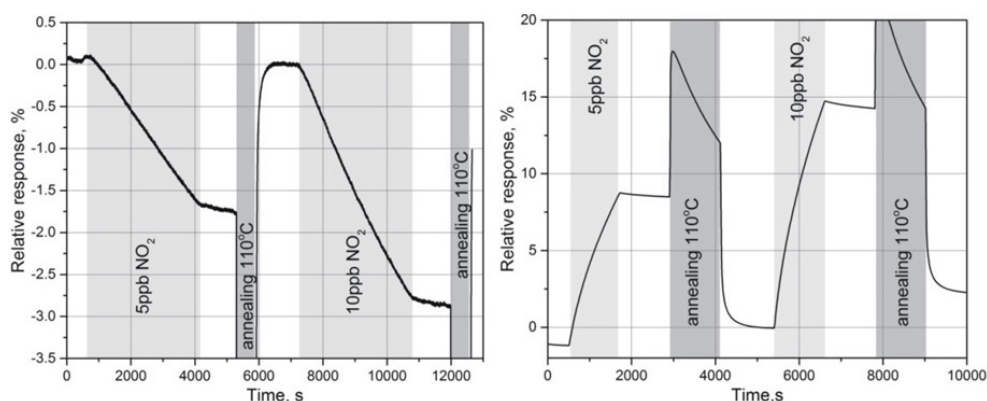


FIG. 6. Response upon exposure of graphene grown by annealing in a vacuum (left) and in argon (right) to a gas mixture containing NO₂ gas at 20 °C. The exposure periods are marked as light gray bands, and the annealing periods, as dark gray bands

withdrawing electrons from the surface on which it is adsorbed. Therefore, its adsorption on the graphene surface is expected to reduce the electron density and raise the hole content. In the case of the *n*-type material, this leads to an increase in resistivity, whereas for the *p*-type, the resistivity decreases. For the NO₂ concentration of 10 ppb, which is typical for environmental monitoring, the response of the multilayer graphene-based sensor is about 3 % upon a 1 h exposure. The response of the single-layer graphene to NO₂ exposure is much stronger and reaches 15 % under the same conditions. This can be accounted for by the screening of the inner layer of the multilayer graphene from adsorbed NO₂ molecules. Nevertheless, the sensitivity of both sensors is sufficient for the environmental monitoring.

5. Conclusion

An analysis of graphene manufacturing methods has shown that the most promising technique for the production of electronic devices from this material is the thermolysis of a silicon carbide surface. However, films formed by this technique have lower carrier mobility than the films obtained by “exfoliation”, but have predictable dimensions and are much more compatible with existing production methods for semiconductor devices. Simple resistive devices based on epitaxially-grown graphene were fabricated and tested for their sensitivity to NO₂ gas. The devices are sensitive to low concentrations of NO₂. The sensor based on the single-layer graphene exhibits a superior performance, compared with the analog that utilized multilayer graphene.

Acknowledgements

Author would like to thanks S.N. Novikov, S.P. Lebedev, Yu.N. Makarov, I.S. Koutousova, A.A. Lavrent'ev, I.V. Makarenko, V.N. Petrov, A.N. Smirnov, V.Yu. Davydov, S.Yu. Davydov, A.M. Strel'chuk,; D.V. Shamshur, N.V. Agrinskaya, V.A. Berezovets, V.I. Kozub, A.A. Sitnikova, R. Yakimova, V.M. Mikoushkin, V.V. Shnitov, S.Yu. Nikonov, T. Iakimov, O.Yu. Vilkov for help in experiments and fruitful discussion.

References

- [1] Novoselov K.S., Geim A.K., et al. Electric field effect in atomically thin carbon films. *Science*, 2004, **306**, P. 666.

- [2] Geim A., Novoselov K. The rise of graphene. *Nature Mater.*, 2007, **6**, P. 183.
- [3] Soldano C., Mahmood A., Dujardin E. Production, properties and potential of graphene. *Carbon*, 2010, **48**, P. 2127–2150.
- [4] Wu Y.H., Yu T., Shen Z.X. Two-dimensional carbon nanostructures: fundamental properties, synthesis, characterization, and potential applications. *J. Appl. Phys.*, 2010, **108**, 071301 (1–38).
- [5] Edwards R.S., Coleman K. Graphene synthesis: relationship to applications. *Nanoscale*, 2013, **5**, P. 38–51.
- [6] Berger C., Song Z., et al. Ultrathin epitaxial graphite: 2D electron gas properties and a route toward graphene-based nanoelectronics. *J. Phys. Chem. B*, 2004, **108**, P. 19912.
- [7] Pearce R., Iakimov T., et al. Epitaxially grown graphene based gas sensors for ultra-sensitive NO₂ detection. *Sensors and Actuators B*, 2011, **155**, P. 451–455.
- [8] Novikov S., Satrapinski A., Lebedeva N., Iisakka I. Sensitivity Optimization of Epitaxial Graphene-Based Gas Sensors. *IEEE Trans. Instrum. Meas.*, 2013, **62** (6), P. 1859.
- [9] Badami D.V. X-ray studies of graphite formed by decomposing silicon carbide. *Carbon*, 1965, **3**, P. 53–57.
- [10] Kusunoki M., Suzuki T., et al. A formation mechanism of carbonnanotube films on SiC (0001). *Appl. Phys. Lett.*, 2000, **77** (4), P. 531–533.
- [11] Kusunoki M., Suzuki T., et al. Aligned carbon nanotube films on SiC (0001) wafers. *Physica B*, 2002, **303**, P. 296–298.
- [12] Rollings E., Gweon G.-H., et al. Synthesis and characterization of atomically-thin graphite films on a silicon carbide substrate. *J. Phys. Chem. Solids*, 2006, **67**, P. 2172–2177.
- [13] Emtsev K.V., Seyller Th., et al. Initial stages of the graphite-SiC(0001) interface formation studied by photoelectron spectroscopy. *Mater. Sci. Forum*, 2007, **556/557**, P. 525–528.
- [14] Hass J., Jeffrey C.A., et al. Highly-ordered graphene for 2D electronics. *Appl. Phys. Lett.*, 2006, **89**, 143106 (3 p).
- [15] Lebedev S.P., Lebedev A.A., et al. Investigation of nanocarbon films on SiC surface Formed by sublimation in vacuum. *Fuller., Nanotub. Carbon Nanostr.*, 2010, **18**, P. 501–504.
- [16] Lebedev S.P., Strel'chuk A.M., et al. Transport properties of multi-graphene films grown on semi-insulating SiC. *Fuller., Nanotub. Carbon Nanostr.*, 2012, **20**, P. 553–557.
- [17] Seyller Th., Emtsev K.V., et al. Electronic structure of graphite/6H-SiC interfaces. *Mater. Sci. Forum*, 2007, **556–557**, P. 701–704.
- [18] Hass J., Feng R., et al. The structural properties of the multi-layer graphene/4H-SiC (0001) system as determined by surface X-ray diffraction. *Phys. Rev. B*, 2007, **75**, 214109 (1–8).
- [19] Ragan-Kelley B.L., Williams J.R., Friend C.M. *Building a Metallic Graphene Transistor*. Harvard DEAS REU Program, 2005, URL: www.yumpu.com/en/document/view/35107623/.
- [20] Gu Gong, Nie Shu, et al. Field effect in epitaxial graphene on a silicon carbide substrate. *Appl. Phys. Lett.*, 2007, **90**, P. 253507.
- [21] Kisoda K., Kamoi S., et al. Few epitaxial graphene grown on vicinal 6H-SiC studied by deep ultraviolet Raman spectroscopy. *Appl. Phys. Lett.*, 2010, **97**, P. 033108.
- [22] Peres N.M.R. The transport properties of grapheme: an introduction. [arXiv:1007.2849v2](https://arxiv.org/abs/1007.2849v2).
- [23] Lebedev A.A., Agrinskaya N.V., et al. Low temperature transport properties of grapheme and multigraphene structures on 6H-SiC obtained by thermal graphitization: Evidence of a presence of nearly perfect Graphene Layer. *J. Mater. Sci. Engin. A*, 2013, **3** (11), P. 757–762.
- [24] Lebedev A.A., Agrinskaya N.V., et al. Low temperature transport properties of graphene and multigraphene layers. *Mater. Sci. Forum*, 2013, **740–742**, P. 137–140.
- [25] Mikoushkin V.M., Shnitov V.V., et al. Size confinement effect in graphene grown on 6H-SiC (0001) substrate. *Carbon*, 2015, **86**, P. 139–145.
- [26] Hass J., de Heer W.A., Conrad E.H. The growth and morphology of epitaxial multilayer grapheme. *J. Phys.: Condens. Matter*, 2008, **20**, P. 323202.
- [27] Lebedev S.P. Petrov V.N., et al. Formation of periodic stepson 6H-SiC (0001) surface by annealing in a high vacuum. *Mater. Sci. Forum*, 2011, **679–680**, P. 437–440.
- [28] Ohta T., Bostwik A., et al. Interlayer interaction and electronic screening in multilayer graphene investigated with angle-resolved photoemission spectroscopy. *Phys. Rev. Lett.*, 2007, **98**, P. 206802.
- [29] Virojanadara C., Yakimova R., Zakharov A.A., Johansson L.I. Large homogeneous mono-/bi-layer graphene on 6H-SiC (0001) and buffer layer elimination. *J. Phys. D: Appl. Phys.*, 2010, **43**, P. 374010.
- [30] Becker T., Muhlberger S., et al. Air pollution monitoring using tin-oxide-based microreactor systems. *Sensors and Actuators B*, 2000, **69**, P. 108–119.

Electrical properties of carbon nanotubes / WS₂ nanotubes (nanoparticles) hybrid films

V. K. Ksenevich¹, N. I. Gorbachuk¹, Ho Viet¹, M. V. Shuba², P. P. Kuzhir², S. A. Maksimenko²,
A. G. Paddubskaya³, G. Valusis³, A. D. Wieck⁴, A. Zak⁵, R. Tenne⁶

¹Department of Physics, Belarusian State University, Minsk, Belarus

²Research Institute for Nuclear Problems, Belarusian State University, Minsk, Belarus

³Center for Physical Sciences and Technology, Vilnius, Lithuania

⁴Department of Physics and Astronomy, Bochum Ruhr-University, Bochum, Germany

⁵Department of Sciences, Holon Institute of Technology, Holon, Israel

⁶Department of Materials and Interfaces, Weizmann Institute of Science, Rehovot, Israel

ksenevich@bsu.by

PACS 73.63.Fg

DOI 10.17586/2220-8054-2016-7-1-37-43

DC and AC electrical properties of hybrid films, consisting of carbon nanotubes and tungsten disulfide nanotubes (and fullerene like nanoparticles) were studied within the 2 – 300 K temperature range and over the 20 Hz – 1 MHz frequency range. The temperature dependences of the resistance $R(T)$ exhibit behavior typical for the fluctuation-induced tunneling model in the intermediate temperature range. Analysis of the dependences of real and imaginary components of the impedance on the frequency ($Z'(f)$ and $Z''(f)$) demonstrates the rising role of the contact barriers between carbon nanotubes inside hybrid films, consisting of the carbon nanotubes and inorganic tungsten disulfide nanotubes as the temperature was decreased. The active component of the impedance was found to prevail in the AC electrical properties of the hybrid films, consisting of multi-wall carbon nanotubes and WS₂ nanoparticles over the entire available temperature range.

Keywords: carbon nanotubes, inorganic nanotubes, tungsten disulfide, impedance, electrical properties.

Received: 20 November 2015

1. Introduction

The electrical and electromagnetic properties of carbon nanotubes (CNT) and tungsten disulfide nanostructures of different morphology (tubular and semi-spherical) are of particular interest, due to the number of their possible applications. Different types of CNT-based structures can be utilized for manufacturing of various integrated-circuit elements and electromagnetic devices, for example, transmission lines [1], interconnects [2], and nanoantennas [3,4]. Undoped WS₂ nanotubes exhibit semiconductor properties with a well-defined band gap and with direct or indirect transition, depending on chirality [5]. High quality field-effect transistors based on WS₂ nanotubes were recently demonstrated [6].

Hybrid materials based on carbon and inorganic nanostructures attracted a lot of interest, due to their unique electrical, mechanical, optical and thermal properties [7]. The multifunctionality of hybrid nanocomposites provides possibility for a number of applications of these materials, including gas sensors, chemical sensors, supercapacitors, batteries and photovoltaic elements [8].

We assume that new class of hybrid materials consisting of organic (carbon nanotubes) and inorganic components (WS_2 nanotubes (NT) or WS_2 nanoparticles (NP)), which are commercially available, can be used for fabricating media with electrical properties and electromagnetic parameters that can be varied over a wide range. In this paper, we have focused our efforts on characterization of low frequency AC and DC electrical properties of such hybrid films.

2. Experimental details

Both single-wall carbon nanotubes (SWCNT) and multi-wall carbon nanotubes (MWCNT) were used as organic components for the fabrication of hybrid films. Commercially available HipCO SWCNT (with diameter of 0.8 – 1.2 nm and length in the range 100 nm – 1 μm) and CVD-produced MWCNT (with diameter of 30 – 50 nm and length in the range 0.5 nm – 200 μm) were utilized for hybrid films fabrication. WS_2 nanotubes were grown in the large-scale fluidized-bed reactor. A detailed description of the growth mechanism was given in [9]. Careful parameterization of the conditions within the reactor allowed the scaling-up of nanotube synthesis to the current level of 150 g/day of pure nanotubes. The synthesized nanotube powder is rather fluffy and can easily be dispersed in different solvents and polymer blends and do not require an additional deagglomeration process. The majority of the WS_2 nanotubes are 1 – 30 μm in length and 20 – 180 nm in diameter. According to the HRTEM analysis tungsten disulfide nanotubes reveal highly crystalline order as one can see also from Fig. 1a. Inorganic fullerene-like WS_2 nanoparticles of 50 – 150 nm in diameter were synthesized by a high temperature (850 °C) reaction using H_2S gas and strongly reducing conditions in a fluidized bed reactor.

SWCNT/ WS_2 -NT and MWCNT/ WS_2 -NP hybrid films were produced on a cellulose acetate membrane filter (Millipore, 0.22 μm pore size) via a filtration process. In a typical procedure, 0.2 mg of each type of CNTs was dispersed into 1 wt% SDS aqueous solution by ultrasonication for 1 h at 44 kHz. In order to remove the remaining CNT agglomerates, thick CNT bundles and catalytic particles, the prepared suspension was subjected to centrifugation for 10 min at an acceleration of 12000 g. The surfactant was washed away with distilled water. CNT and inorganic WS_2 nanotubes (fullerenes) were mixed in the filtration cell. Typical SEM image of SWCNT/ WS_2 -NT hybrid film is shown in Fig. 1b. TEM micrograph of a typical WS_2 NP with fullerene-like structure is shown in Fig. 1c. This nanoparticle consists of some 25 concentric and closed layers of WS_2 , but is not free of point defects, especially at points of acute curvature angles. Typical SEM image of SWCNT/ WS_2 -NP hybrid film is shown in Fig. 1d. In order to determine influence of inorganic nanotubes (nanoparticles) on the electrical properties of hybrid films, pure SWCNT and MWCNT films were fabricated using the same filtration procedure.

After filtration, the films were transferred onto insulating Al_2O_3 substrates for further electrical characterization. Electrical contacts to the films were made by Ag paint. Measurements of the temperature dependences of resistance $R(T)$ were carried out in the temperature range 2 – 300 K using close-cycled refrigerator CFHF of Cryogenics Ltd.

Characterization of AC electrical properties was done by means of impedance spectroscopy using a LCR meter (Agilent 4284A). Measurements of the complex impedance $Z = Z' + iZ''$ of the hybrid films were performed over frequencies ranging from 20 Hz to 1 MHz at 4.2, 77 and 300 K. The amplitude of the sinusoidal signal was 40 mV. DC bias voltage in the range 0 – 5 V was simultaneously applied to the examined samples. Modeling of the experimental results by equivalent circuits was done using an EIS Spectrum Analyzer 1.0 program.

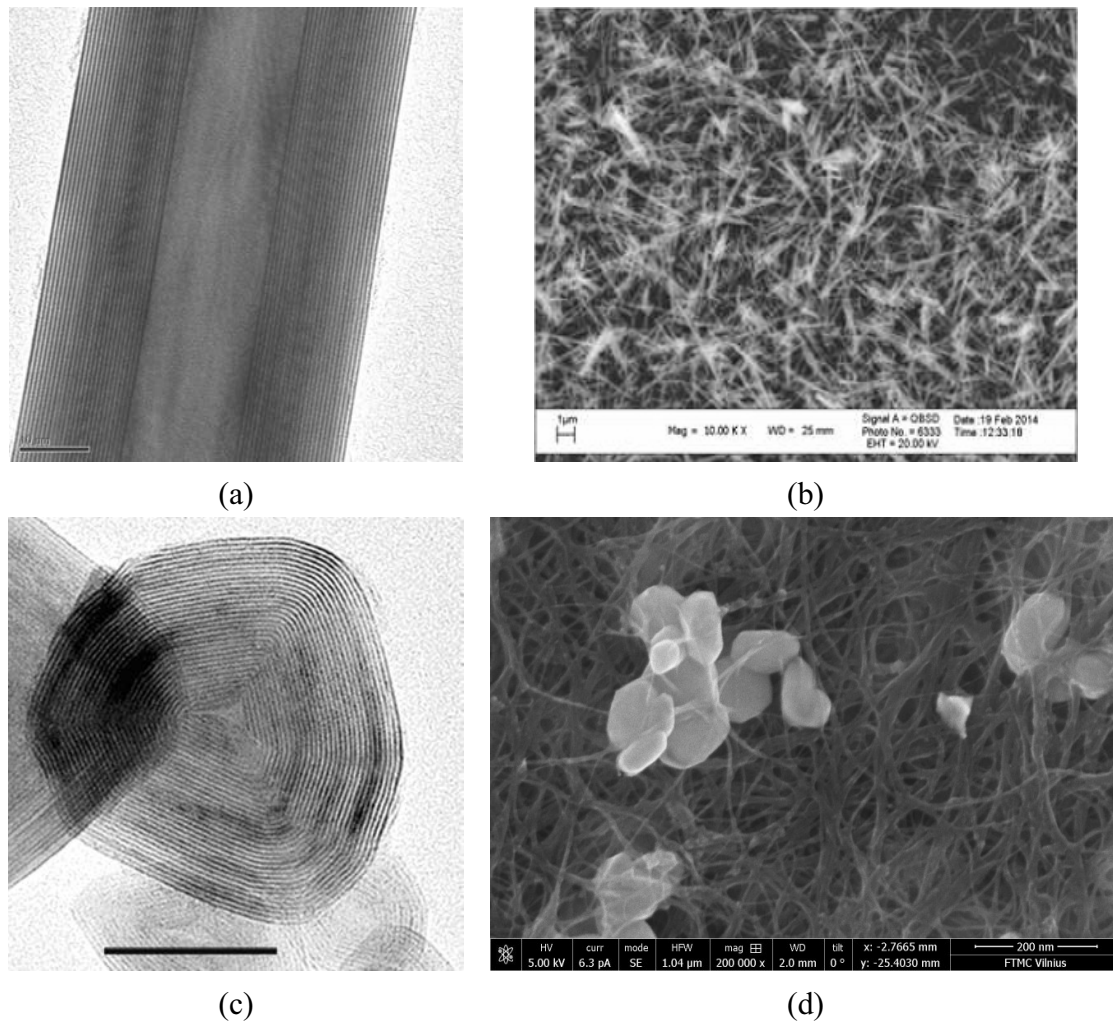


FIG. 1. (a) HRTEM image of WS_2 nanotube, scale bar is 10 nm; (b) SEM image of SWCNT/ WS_2 -NT hybrid film, scale bar is 1 μm ; (c) HRTEM image of a typical fullerene-like nanoparticle of WS_2 , scale bar is 20 nm; (d) SEM image of MWCNT/ WS_2 -NP hybrid film, scale bar is 200 nm

3. Experimental results and discussion

3.1. DC conductivity

Temperature dependences of the resistance $R(T)$ of SWCNT films and SWCNT/ WS_2 -NT hybrid films which have approximately the same geometrical sizes (width, length and thickness of the films) are presented in Fig. 2. $R(T)$ dependences of MWCNT films and MWCNT/ WS_2 -NP hybrid films are shown in Fig. 3. Both types of the samples (pure CNT films and hybrid films) have similar $R(T)$ dependences, characterized by negative temperature coefficient of the resistance ($dR/dT < 0$) over the entire temperature range (2 – 300 K). As one can see from Figs. 2 and 3, hybrid films have higher resistance values in comparison to pure SWCNT and MWCNT films. The difference in the conductivities of pure CNT films and hybrid samples increased as the temperature decreased. In the intermediate temperature range, it was found that the temperature dependences of the resistance $R(T)$ can be approximated by the equation proposed within the framework of inherent for disordered systems fluctuation-induced tunneling model [10]:

$$R = R_0 \exp(T_1/T + T_0), \quad (1)$$

where T_1 , according to [10], is the temperature below which conduction is dominated by the charge carrier tunneling through the barrier and T_0 is the temperature above which fluctuation effects become significant. This model can be applied for fitting of the electrical properties of different types of disordered systems (including carbon nanotubes arrays [11] and CNT based polymer composites [12]) in which large in atomic scale highly conductive regions divided by small insulating barriers.

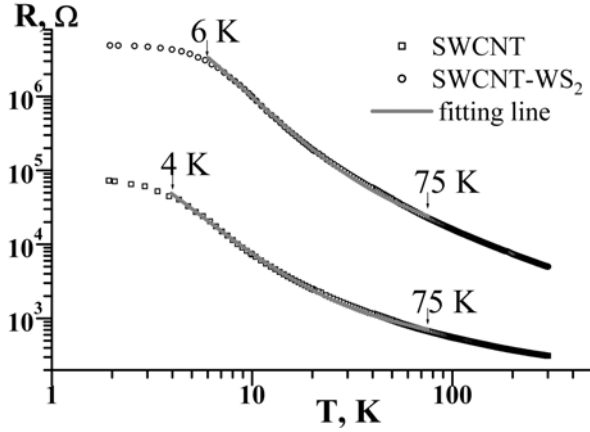


FIG. 2. The temperature dependence of the resistance $R(T)$ (in log – log scale) of SWCNT film and SWCNT/WS₂-NT hybrid film. Solid lines are fitted results from Eq. (1)

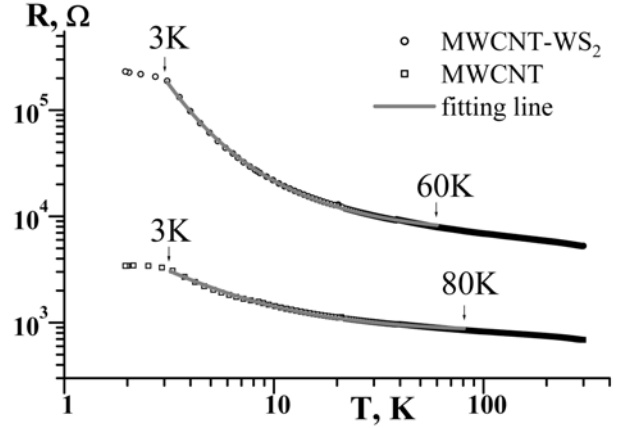


FIG. 3. The temperature dependence of the resistance $R(T)$ (in log – log scale) of MWCNT film and MWCNT/WS₂-NP hybrid film. Solid lines are fitted results from Eq. (1)

The low temperature saturation of the resistance can be explained by the tendency to saturate the dephasing time of the charge carriers inside an individual CNT observed in weakly disordered systems [13]. In order to approximate the experimental data over the entire temperature range, a more complicated analysis is required, which takes into account strong and/or weak localization effects.

3.2. AC conductivity

Impedance spectroscopy is a powerful tool for characterizing different types of disordered structures [14], including nanocomposites and arrays of carbon nanotubes. Measurements of the relationships between the real and imaginary components of the impedance and the frequency, $Z'(f)$ and $Z''(f)$, along with the following of theoretical modeling of experimental results, provides the possibility for dividing the contribution from the nanotubes themselves and the contact barriers between them into the total impedance of the CNT assemblies.

It was found that over the entire temperature range, 4.2 – 300 K, both the pure SWCNT and MWCNT films demonstrate properties inherent for the structures with a prevailing active part of the complex impedance. Incorporation of tungsten disulfide nanotubes into the SWCNT films and tungsten disulfide nanoparticles into the MWCNT films exhibited different influences on the AC electrical properties of hybrid films. Analysis of the $Z'(f)$ and $Z''(f)$ dependences for the SWCNT/WS₂-NT hybrid films clearly demonstrate the increasingly important role of the reactive part of the complex impedance as the temperature decreases. It was found that for

all measurement temperatures (4.2, 77 and 300 K) complex impedance of the SWCNT/WS₂-NT hybrid films can be modeled using an equivalent circuit consisting of the following elements connected in series and parallel: resistance R_1 , capacitance C , resistance R_2 and constant phase element CPE . Impedance diagram of the SWCNT/WS₂-NT hybrid films reconstructed from $Z'(f)$ and $Z''(f)$ dependences measured at $T = 4.2$ K is presented in Fig. 4. Due to the low conductivity of WS₂ nanotubes in comparison to the SWCNTs, we assume that in the equivalent circuit (shown in the inset to Fig. 4), calculated for hybrid film, the resistance R_1 and the capacitance C correspond to the average values of resistance and capacitance for the carbon nanotubes. On the other hand, the resistance R_2 simulates the Ohmic resistance of contact regions between the SWCNTs. The element CPE takes into account the spread in values of the resistance and capacitance of the inter-nanotube contact barriers [14]. The admittance of the CPE is defined as:

$$Y_{CPE} = A_0(i\omega)^\alpha = A_0[\cos(\pi/2\alpha) + i \sin(\pi/2\alpha)], \quad (2)$$

where A_0 is the coefficient with the dimensionality depending on the α value. In the case of $\alpha = 1$, the coefficient A_0 has the dimensionality of capacitance, while in the case $\alpha = 0$, the coefficient A_0 has the dimensionality of resistance. In the intermediate case, the dimensionality of A_0 can be considered as $\Omega^{-1} \cdot s^\alpha$ [15].

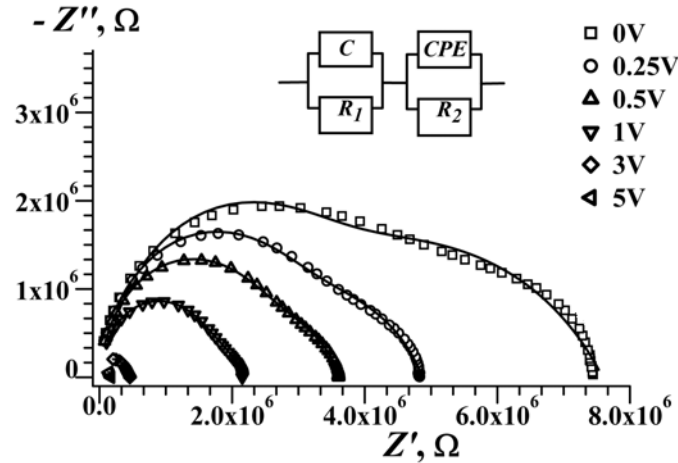


FIG. 4. Impedance diagrams of SWCNT/WS₂-NT hybrid films measured at temperature $T = 4.2$ K and at different value of applied DC voltage. Lines show the approximation of the experimental data by an equivalent circuit, presented in the inset

Unlike the SWCNT films and SWCNT/WS₂-NT hybrid films, the imaginary components of the impedance for both types of MWCNT samples (pure CNT films and hybrid films) were very low in comparison with the active parts of their impedance, even at $T = 4.2$ K and without applied DC bias voltage. The maximum value for the phase shift between voltage and current of about -10° at 1 MHz was observed for MWCNT/WS₂-NP hybrid films at $T = 4.2$ K and at $U_b = 0$ V. This fact indicates that the electrical contacts between individual MWCNT inside pure and hybrid films were good, even in the low temperature range. Thus, the influence of WS₂ nanoparticles incorporation into MWCNT films on the frequency dependence of the impedance is less important in comparison to the case when the WS₂ nanotubes were embedded into the SWCNT films. This can be attributed to a geometrical factor. WS₂ nanotubes and SWCNT are characterized by large difference in sizes (20 – 180 nm vs 0.8 – 1.2 nm in

diameter and 1 – 30 μm vs 100 nm – 1 μm in length, for WS_2 -NT and SWCNT, respectively). Therefore incorporation of poorly conducting WS_2 nanotubes into the matrix consisting of highly conductive SWCNT strongly increases the role of the contact resistance between separate single-wall carbon nanotubes inside the film. Conversely, embedding of the spherical WS_2 nanoparticles with diameter in the range 50 – 150 nm into the film consisting of MWCNT (with diameter of 30 – 50 nm and length in the range 0.5 nm – 200 μm) does not strongly affect the AC conductivity of films.

One of the most interesting features of the AC electrical properties of the examined samples is the existence of a highly reproducible positive value for the imaginary component of impedance observed at $T = 4.2$ K for SWCNT films, MWCNT films and MWCNT/ WS_2 -NP hybrids, as the DC bias voltage was applied. These positive Z'' values (corresponding to the negative part of $-Z''(f)$ plots) are clearly seen in Figs. 5 and 6 and can be explained by the increased role of kinetic inductance for individual carbon nanotubes [16] as the temperature decreased and DC voltage was applied. This effect was not observed for SWCNT/ WS_2 -NT hybrid films due to the high value of negative (capacitive) part of reactive impedance at low temperatures.

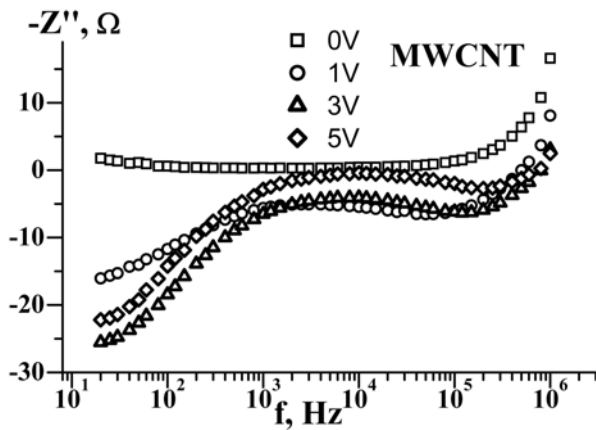


FIG. 5. Frequency dependence of the imaginary component of the impedance $-Z''(f)$ of MWCNT film measured at $T = 4.2$ K

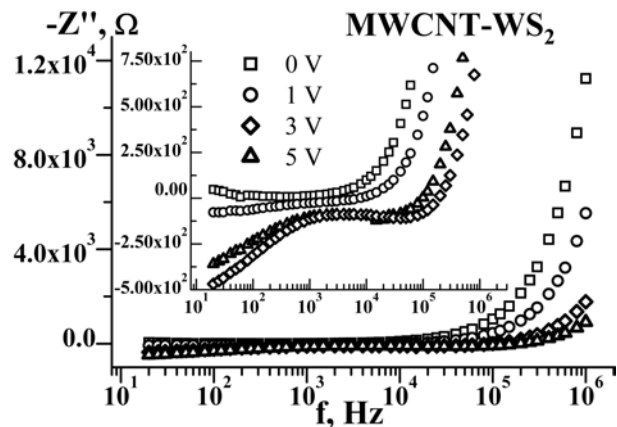


FIG. 6. Frequency dependence of the imaginary component $-Z''(f)$ of the impedance of MWCNT/ WS_2 -NP hybrid films measured at $T = 4.2$ K. Low-ohmic part of $-Z''(f)$ value is shown in the inset

It should be noted, that due to the low value of reactive part of the impedance Z'' in comparison with the active component Z' , the modeling of experimental results for MWCNT films and MWCNT/ WS_2 -NP hybrid films by reasonable equivalent circuits was impossible.

4. Conclusion

Investigation of the AC and DC electrical properties of the nanocomposite materials consisting of carbon nanotubes and inorganic tungsten disulfide nanotubes (nanoparticles) provided evidence for the successful processing of electrically conductive hybrid films using the filtration method. Incorporation of WS_2 nanotubes and nanoparticles into the carbon nanotube arrays was found to reduce strongly the electrical conductivity of fabricated hybrids. Further research will be focused on assessing the possibility of tuning the conductivity and dielectric

constant of composites over a wide range by varying the percentage ratio of the carbon and inorganic components.

Acknowledgments

This work was supported by Belarusian National Research Program “Nanomaterials and Nanotechnologies” (grant No. 2.2.02), by FP7 project PIRSES-2012-318617 FAEMCAR and FP7-316633 POCAONTAS, Tomsk State University Competitiveness Improvement Program, and Federal Focus program of Ministry of Education and Science of Russian Federation # 14.577.21.0006 (project ID RFMEFI57714X0006). We are thankful for Prof. Stefano Bellucci (LNF INFN Italy) for fruitful discussions, valuable comments, and providing us with MWCNT samples.

References

- [1] Slepyan G.Ya., Maksimenko S.A., et al. Electrodynamics of carbon nanotubes: Dynamic conductivity, impedance boundary conditions, and surface wave propagation. *Phys. Rev. B*, 1999, **60** (24), P. 17136–17149.
- [2] Rybczynski J., Kempa K., et al. Subwavelength waveguide for visible light. *Appl. Phys. Lett.*, 2007, **90**, 021104 (1–3).
- [3] Hanson G.W. Fundamental transmitting properties of carbon nanotube antennas. *IEEE Trans. Antennas Propag.*, 2005, **53** (11), P. 3426–3435.
- [4] Slepyan G.Ya., Shuba M.V., Maksimenko S.A., Lakhtakia A. Theory of optical scattering by achiral carbon nanotubes and their potential as optical nanoantennas. *Phys. Rev. B*, 2006, **73** (19), 195416 (1–11).
- [5] Seifert G., Terrones H., et al. On the electronic structure of WS₂ nanotubes. *Solid State Commun.*, 2000, **114** (5), P. 245–248.
- [6] Levi R., Bitton O., et al. Field-Effect Transistors Based on WS₂ Nanotubes with High Current-Carrying Capacity. *Nano Lett.*, 2013, **13** (8), P. 3736–3741.
- [7] Naffakh M., Diez-Pascual A.M., Gomez-Fatou M.A. New hybrid nanocomposites containing carbon nanotubes, inorganic fullerene-like WS₂ nanoparticles and poly(ether ether ketone) (PEEK). *J. Mater. Chem.*, 2011, **21** (20), P. 7425–7433.
- [8] Eder D. Carbon Nanotube – Inorganic Hybrids. *Chem. Rev.*, 2010, **110** (3), P. 1348–1385.
- [9] Zak A., Sallacan-Ecker L., et al. Insight into the Growth Mechanism of WS₂ Nanotubes in the Scaled-Up Fluidized-Bed Reactor. *NANO*, 2009, **04** (02), P. 91–98.
- [10] Sheng P. Fluctuation-Induced Tunneling Conduction in Disordered Materials. *Phys. Rev. B*, 1980, **21** (6), P. 2180–2195.
- [11] Ksenevich V.K., Dauzhenka T.A., et al. Electrical transport in carbon nanotube coatings of silica fibers. *Phys. Status Solidi C*, 2009, **6** (12), P. 2798–2800.
- [12] Kuzhir P., Ksenevich V.K., et al. CNT based epoxy resin composites for conductive applications. *Nanosci. Nanotechnol. Lett.*, 2011, **3** (6), P. 889–894.
- [13] Gershenson M.E. Low-Temperature Dephasing in Disordered Conductors: Experimental Aspects. *Annalen der Physik (Leipzig)*, 1999, **8** (7–9), P. 559–568.
- [14] Barsoukov E., Macdonald J.R. (Eds.) *Impedance Spectroscopy. Theory, Experiment, and Applications*. Wiley, Hoboken, 2005, 616 p.
- [15] Sluyters-Rehbach M. Impedances of electrochemical systems: Terminology, nomenclature and representation – Part I: Cells with metal electrodes and liquid solutions. *Pure and Appl. Chem.*, 1994, **66** (9), P. 1831–1891.
- [16] Burke P.J. An RF Circuit Model for Carbon Nanotubes. *IEEE Trans. Nanotechnol.*, 2003, **2** (1), P. 55–58.

Is graphane the most stable carbon monohydride?

M. V. Kondrin, V. V. Brazhkin

Institute for High Pressure Physics RAS, 142190 Troitsk, Moscow, Russia

mkondrin@hppi.troitsk.ru

PACS 61.50.Ah, 61.41.+e, 62.20.D-, 71.15.Mb

DOI 10.17586/2220-8054-2016-7-1-44-50

We discuss a number of hydrocarbon structures whose cohesive energy is not worse than that of benzene and graphanes. These structures can be regarded as sublattices of known carbon structures so the strain exerted on the crystal lattice is minimal and caused mostly by the steric interactions of hydrogen atoms. Possible synthetic routes are proposed. Due to their exceptional mechanical, structural and electrical properties, these crystal structures may have utility as mechanical, optoelectronic or biological materials.

Keywords: graphane, diamond monohydride, hydrocarbons, nitrogen, high pressures.

Received: 20 November 2015

1. Introduction

In the recent years, the attention of researchers has been drawn to graphane – carbon monohydride theoretically predicted [1, 2] and later experimentally obtained by a complicated synthetic scheme [3]. This compound is interesting due to its exceptional properties (e.g. high temperature superconductivity predicted for properly doped graphane [4, 5]) and as a possible candidate for solid cell hydrogen storage elements [6, 7].

However, it should be noted that graphane is not the only compound with a carbon-hydrogen ratio of C:H=1:1. There are quite a number of other examples: e.g. solid benzene (though at ambient pressure it can exist at low temperatures only [8]), molecular solid phases of cubane/cuneane [9–12] (which can be obtained as metastable forms through complicated organic synthesis), polymeric nanothreads (predicted in [13] and later obtained by high pressure synthesis [14]) and even well-known polystyrene. In the case of carbon, there is nothing astonishing that even its metastable forms can have interesting applications. For example, there are at least 4 hypothetical forms [15–17] (one of them is similar to the cubic-gauche high pressure phase of nitrogen [18]) that has currently never been observed in practice, but according to quantum chemical calculations are more energetically favorable than actually synthesized cubane. It is interesting to note that according to DFT calculations, graphane [2, 19] has the lowest energy among all these allotropes (even lower than benzene).

In this paper, we consider recently proposed 3D hydrocarbon (diamond monohydride/DMH) [20] which can be energetically as viable as graphane. Both can be regarded as sublattices of diamond structure so the internal strain in both is minimal and caused mostly by the steric interactions of hydrogen atoms. We also describe evolution of DMH energy with pressure and discuss its possible analogs among non-organic compounds.

2. The least strained structures

In our previous paper [20], we proposed an heuristic procedure, which can be applied to obtain minimally-strained crystal structures, starting from the known ones (in case of hydrocarbons they are pure carbon structures). To accommodate required number of hydrogen atoms, we need to delete some nodes from the lattice and put hydrogen atom into a bond connecting the deleted node to the nearest carbon atom. From these considerations, restrictions arise. Taking into account relative lengths of C–C and C–H covalent bonds (≈ 1.54 and ≈ 1.0 Å), it is obvious that each unoccupied site can have at most one single occupied node in its vicinity (otherwise the distance between hydrogen atoms on the bonds converging to the same empty node would be too short, resulting in large lattice strain). From this, it immediately follows that the maximum numerical density of structures produced in such a way will be exactly half of the initial amount. Once these conditions are satisfied, it is also clear that the cohesive energies of the proposed structures don't differ much from the initial figures and exact values can be refined subsequently by ab-initio calculations using this postulated structure as a first iteration. However, we would like to stress that even these heuristic considerations will be sufficient to make qualitative predictions about the properties of these structures. We will try to clarify this point in the rest of the paper. Our procedure, to some extent, resembles one adopted previously in the search for zeolite structures [21,22], but we cannot translate it into topological terms of tilings, vertices, etc.

For hydrocarbon structures, one can take diamond and lonsdaleite lattices as starting points. The energy difference between lonsdaleite and diamond is less than 10 meV per bond (it is significantly less than the 20 meV per atom difference between diamond and graphite), so for practical purposes, it can be neglected. There is even a tendency to regard lonsdaleite as a diamond structure, but with a considerable number of stacking faults [23].

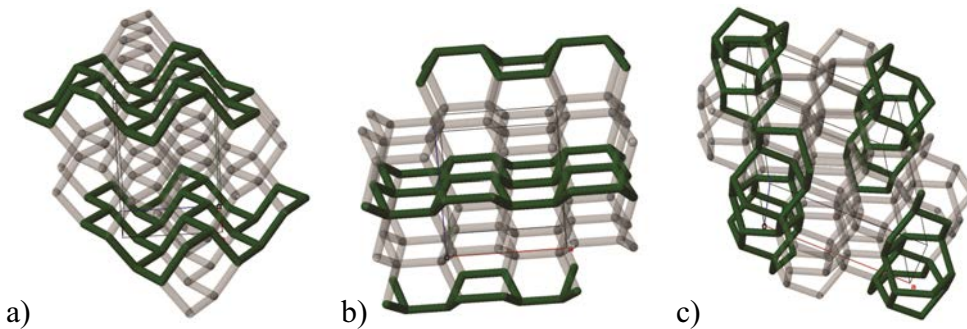


FIG. 1. Diamond-like graphane B (a) and lonsdaleite-like graphane C (b) sheets. c) Hydrocarbon nanothread. Only carbon networks are shown. Translucent bonds demonstrate relations to their respective parent structures

In a more formal way, this procedure can be described as a virtual symmetry breaking operation so the equivalence of lattice nodes in diamond (space group $Fd\bar{3}m$, single Wyckoff position $8a$) and lonsdaleite ($P6_3/mmc$, $4f$) structures aren't retained and their occupancies may vary¹. Well known graphane structures [19,29] can be described in this way. Depending on the initial structure, they can be classified as either diamond- or lonsdaleite-like. Indeed,

¹For details we refer the reader to the book [24], Bilbao server and programs therein [25–27]. Using crystallographic visualization programs (e.g [28]) tremendously helps in understanding the structural transformations.

virtual phase transitions² $Fd\bar{3}m \xrightarrow{(6,4)} Pmna$ and $Fd\bar{3}m \xrightarrow{(6,4)} P\bar{3}m1$ lead to splitting $8a \rightarrow 2 \cdot 4h$ and $\rightarrow 2 \cdot 2d + 1 \cdot 2c$ respectively which correspond to the formation of two graphane sheets types, named B and A in Ref. [19]. Similarly, from lonsdaleite, graphane structures C ($Pm\bar{m}n$ subgroup with index 6, $4f \rightarrow 2 \cdot 4f$) and D ($Pbcm$ with index 12, $\rightarrow 2 \cdot 8e$) can be obtained. Schematically, relations between 2 types of graphane sheets with their respective parent structures are shown in Fig. 1.

However, in all these cases, the resulting structures are not contiguous; that is, they are not completely covalently bonded. Weak van-der-Waals (vdW) forces allow one to somewhat relax positions of the graphane sheets relative to each other to form more energetically-favorable configurations. For example, shifting of every second sheet of B type into base centered positions results in graphane III structure where carbon atoms form black phosphorus structure. An interesting question arises – is it possible to retain the contiguity of the initial lattice? Though we don't know the general answer, in the particular case of hydrocarbons, the search for an answer leads us to new crystal structures.

For lonsdaleite, it is possible to propose the phase transition with prime *klassengleiche* index 7 $P6_3/mmc \xrightarrow{(2,7)} P6_3/m$ which corresponds to the expansion of the unit cell in two dimensions along the basal plane. This transition leads to splitting $4f \rightarrow 2 \cdot 12i + 1 \cdot 4f$, producing a structure (Fig. 1 c) which can be described as a nanothread [13, 14] bundle.

3. DMH structure and its properties

It is remarkable that though nanothread bundle is vdW bonded structure but the procedure similar to described above in case of diamond produces completely covalently bonded DMH crystal. Formally, this is described as a $Fd\bar{3}m \xrightarrow{(8,14)} R\bar{3}$ transition accompanied by splitting $8a \rightarrow 2 \cdot 6c + 4 \cdot 18f$ (in our previous work [20] we have overlooked rhombohedral symmetry). Each of positions' sets can be evenly distributed between occupied and unoccupied nodes. So this structure can be regarded as a result of “halving” of the diamond one. This also dictates the parameters for the resulting conventional unit cell (obtuse hexagonal with $a \approx 6.67 \text{ \AA}$, $c \approx 12.36 \text{ \AA}$ and $Z = 42$ formula units in it).

As an initial estimate for structure optimization, hydrogen atoms are put into this structure 1 Å apart from occupied sites in the direction pointing to the closest unoccupied one (see Fig. 2). The resulting structure turns out to be more energetically favorable than benzene and comparable to diamond-like graphanes. For details of DFT calculation using QuantumESPRESSO software [30] we refer the reader to [20]. Evolution of the energy difference between DMH and graphane with pressure is shown in Fig. 3.

Because carbon atoms in DMH are in the sp^3 -hybridized state, it is not surprising that the substance is good dielectric with quite a large band gap of 4.5 eV (comparable to the theoretical diamond's one but direct). DMH density is somewhat less than half that of diamond's (due to 5 % expansion of covalent bonds) and equals 1.7 g/cm³. Because DMH is related to parent structure through removal of some C–C bonds, the mechanical properties are significantly inferior to that of diamond, but still quite impressive (bulk and shear moduli are $B = 90 \pm 15$ and $G = 60 \pm 15$ GPa respectively). One remarkable DMH feature is the presence of quite spacious “tubes” piercing the bulk of the structure (see Fig. 2). As it was pointed

²The numbers above arrows designate *translationengleiche* and *klassengleiche* subgroup indices t, k . In general such a transition leads to splitting of Wyckoff positions of parent structure into several sets of Wyckoff positions of subgroup. Such a relation we will designate by the notation $4f \rightarrow 2 \cdot 2d + 1 \cdot 2c$, meaning that $8a$ Wyckoff position of the parent group is split into two sets of $2d$ and one set of $2c$ subgroup. The left part can be omitted if it is clear which position is meant.

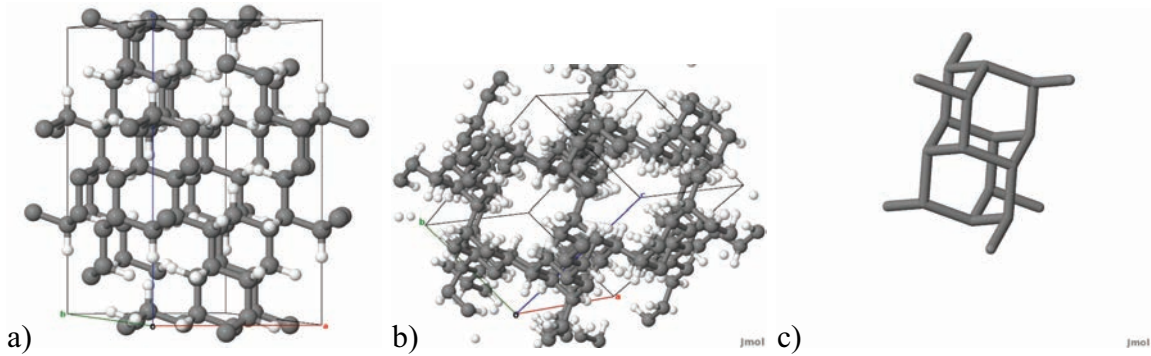


FIG. 2. Structure of DMH. Perspective view along base plane (a) and along pores (b). Grey spheres stands for carbon atoms and white for hydrogen. c) The building block of DMH structure – diamantane molecule with six loose bonds (only carbon framework is depicted)

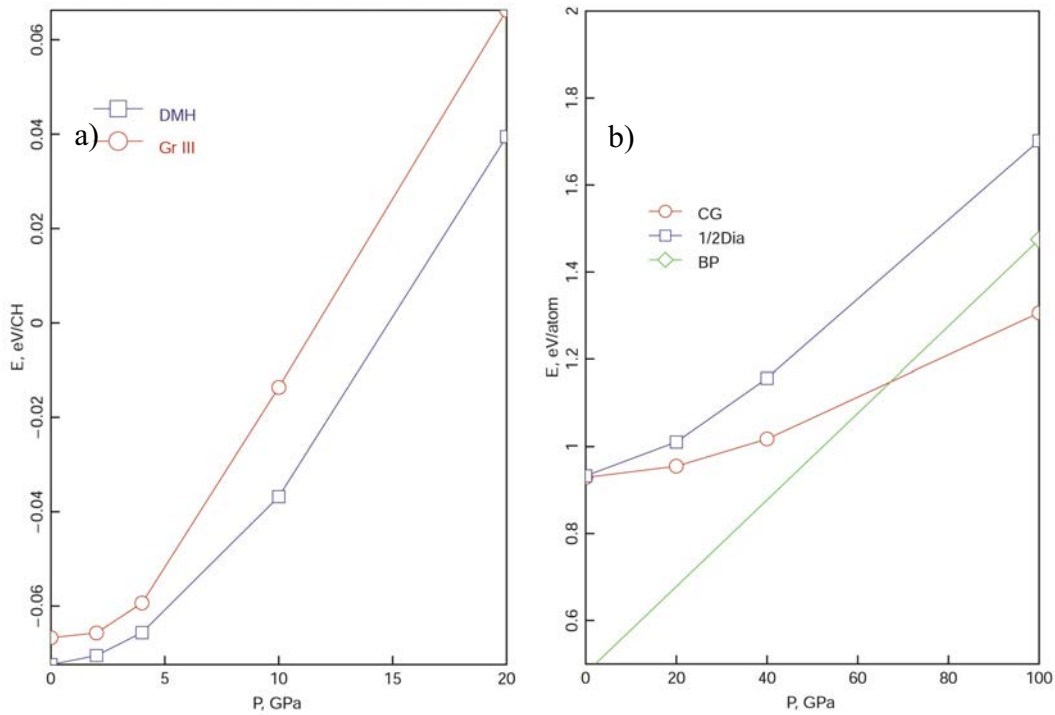


FIG. 3. Pressure evolution of energy in a) hydrocarbon structures (\circ – graphane III and \square – DMH) and b) nitrogen (\circ – cubic gauche, \diamond – black phosphorus and \square – “half-diamond” or DMH-like). In both cases the energy of respective molecular phase (benzene and N_2) at ambient pressure is taken as zero

out in Ref. [31] in the context of carbon-nitrogen compounds the filling of such pores with metallic atoms would lead to almost one dimensional metallic conductivity which in certain circumstances (e.g. strong interaction with phonones of hydrocarbon matrix) could produce high-temperature superconductivity.

Though at first glance, the crystal structure seems extremely complicated, but in reality, this is not true. In fact, it can be thought of as an ordered network of polymerized diamantane molecules ($C_{14}H_{20}$) [32] with six hydrogen atoms removed. So the building block of this structure is a diamantane molecule with six dangling bonds (Fig. 2). Its point group is $\bar{3}$, so naturally

it can be packed in $R\bar{3}$ space group. The diamantane molecule is quite rigid and the DMH structure's unit cell consists of six molecules of such geometry that they are related to each other by crystallographic symmetry.

This observation also gives a clue which possibly will help to produce DMH using properly functionalized/substituted diamantane molecules (this is somewhat similar to considerations present in Refs. [33, 34] but there, adamantane molecules were used as building blocks). If it would be possible to attach some sort of radicals X to secondary carbon atoms in diamantane molecules, such that the hypothetical chemical dimerization $(2 \cdot C_{14}H_{14}X_6 \rightarrow 2 \cdot (C_{14}H_{14}X_5) + 2 \cdot X_2)$ is possible, then the self-organization of these molecules into a crystal structure can be expected.

4. Possible non-organic analogues

Because the DMH structure cannot be readily found in nature (in contrast to benzene and diamantanes which can be separated from the crude oil) it would be worthwhile to look for possible analogs of the DMH structure in the inorganic realm. One possible candidate would be binary sphalerite compounds which are widely used in electronics. For compounds with high enough ionicity (like GaSb or better), a certain reordering of atoms can be expected, which would lead to arrangement with one type of atoms taking positions of occupied nodes in DMH structure while others take positions of empty ones. However, we are not aware of any finding of this kind [35].

Another possibility is the exploiting of the analog between CH radical and group five elements (where a fully occupied orbital plays the role of a C–H bond). In fact, there much similarity between them, for example, in graphane I and III structures, carbon atoms form a network similar to arsenic and black phosphorus structures. As a model object, the nitrogen structures can be extremely educative. For example, the structure of nitrogen at pressures higher than 100 GPa can be considered as “halving” of bC8 structure (observed in the wild in Si, Ge [35], presumably produced under certain conditions in vapor deposited carbon [36] and predicted to be thermodynamically stable in pure carbon at TPa pressures [37]). Here, the symmetry breaking is quite simple and consists of the removal of an inversion center, thus producing a virtual transition $Ia\bar{3} \xrightarrow{2,1} I2_13$. The resulting enantiomorphic crystal structure in the context of nitrogen [38] was named cubic gauche (however one may expect droite conformation too) and was considered previously as a possible candidate for 3D hydrocarbon structures [15]. Although the corresponding hydrocarbon structure significantly loses to DMH and graphanes (about than 0.2 eV per CH group), in the case of nitrogen, the situation is inverted. The relative energies of cubic gauche, DMH-like and black phosphorus type nitrogen crystal structures are depicted in Fig. 3. The behavior of bp- and cg-N generally coincides with the results of Ref. [38] but the energy of DMH-like nitrogen is comparable with that of cg-N only in the low density region and with increased pressure, this difference rapidly increases. It should also be noted that the pressure region in Fig. 3 below 50 GPa has no practical significance because there, molecular nitrogen with triple covalent bond is the unquestionable winner.

Such a difference between DMH and its nitrogen analog is possibly caused by the effective charge of C–H group on the one hand and filled electron orbital in nitrogen on the other. The higher coulomb interaction in nitrogen favors its crystallization in the form where two types of bonds exist (similar to bC8 structure) so the diamond and lonsdaleite structures (where all bonds are equivalent) are simply bad initial approximations.

5. Conclusion

The main conclusion of this paper is fairly obvious and was determined many times before [39,40], however, it is worth repeating once more. That is, the energy considerations are not the decisive factor in the question of viability of some compound (especially an organic one) but the availability of technological process for its fabrication is. The examples considered in this paper include cubane (it even loses to the cubic gauche hydrocarbon structure) and nanothreads, which are of the lonsdaleite type, and such, lose to diamond-type graphanes but nonetheless can be obtained by the high-pressure high-temperature treatment of molecular benzene [14]. A similar consideration applied to DMH structure implies that its manufacturing requires some preliminary steps involving production of suitable precursors. However these efforts may be worthwhile because of its exceptional mechanical, structural and electrical properties. DMH might have utility as a material for biological and optical applications or as a solid hydrogen storage element.

Acknowledgements

The authors acknowledge financial support from the RSF (Grant No. 14-22-00093) and thank Y. B. Lebed for assistance and helpful discussions.

References

- [1] Sluiter M. H. F., Kawazoe Y. Cluster expansion method for adsorption: Application to hydrogen chemisorption on graphene. *Phys. Rev. B*, 2003, **68** (8), P. 085410.
- [2] Sofo J., Chaudhari A., Barber G. Graphane: A two-dimensional hydrocarbon. *Phys. Rev. B*, 2007, **75** (15), P. 153401.
- [3] Elias D. C., Nair R. R., Mohiuddin T. M. G., Morozov S. V., Blake P., Halsall M. P., Ferrari A. C., Boukhalov D. W., Katsnelson M. I., Geim A. K., Novoselov K. S. Control of Graphene's Properties by Reversible Hydrogenation: Evidence for Graphane. *Science*, 2009, **323** (5914), P. 610–613.
- [4] Savini G., Ferrari A. C., Giustino F. First-Principles Prediction of Doped Graphane as a High-Temperature Electron-Phonon Superconductor. *Phys. Rev. Lett.*, 2010, **105** (3), P. 037002.
- [5] Loktev V., Turkowski V. Possible High-Temperature Superconductivity in Multilayer Graphane: Can the Cuprates be Beaten? *Journal of Low Temperature Physics*, 2011, **164** (5-6), P. 264–271.
- [6] Peng Q., Dearden A. K., Crean J., Han L., Liu S., Wen X., De S. New materials graphyne, graphdiyne, graphone, and graphane: review of properties, synthesis, and application in nanotechnology. *Nanotechnology, Science and Applications*, 2104, **7**, P. 1–29.
- [7] Zhou C., Chen S., Lou J., Wang J., Yang Q., Liu C., Huang D., Zhu T. Graphene's cousin: the present and future of graphane. *Nanoscale Research Letters*, 2014, **9** (1), P. 26.
- [8] Ciabini L., Gorelli F. A., Santoro M., Bini R., Schettino V., Mezouar M. High-pressure and high-temperature equation of state and phase diagram of solid benzene. *Phys. Rev. B*, 2005, **72** (9), P. 094108.
- [9] Eaton P. E., Cole T. W. Cubane. *Journal of the American Chemical Society*, 1964, **86** (15), P. 3157–3158.
- [10] Fleischer E. B. X-Ray Structure Determination of Cubane. *Journal of the American Chemical Society*, 1964, **86** (18), P. 3889–3890.
- [11] Yildirim T., Gehring P., Neumann D., Eaton P., Emrick T. Unusual structure, phase transition, and dynamics of solid cubane. *Phys. Rev. Lett.*, 1997, **78** (26), P. 4938–4941.
- [12] Criegee R., Askani R. Octamethylsemibullvalene. *Angewandte Chemie International Edition in English*, 1968, **7** (7), P. 537–537.
- [13] Wen X.-D., Hoffmann R., Ashcroft N. W. Benzene under High Pressure: a Story of Molecular Crystals Transforming to Saturated Networks, with a Possible Intermediate Metallic Phase. *Journal of the American Chemical Society*, 2011, **133** (23), P. 9023–9035.
- [14] Fitzgibbons T. C., Guthrie M., Shi Xu E., Crespi V. H., Davidowski S. K., Cody G. D., Alem N., Badding J. V. Benzene-derived carbon nanothreads. *Nature Materials*, 2015, **14**, P. 43–47.
- [15] Lian C.-S., Wang X.-Q., Wang J.-T. Hydrogenated K4 carbon: A new stable cubic gauche structure of carbon hydride. *The Journal of Chemical Physics*, 2013, **138** (2), P. 024702.

- [16] He C., Sun L. Z., Zhang C. X., Zhong J. Low energy three-dimensional hydrocarbon crystal from cold compression of benzene. *Journal of Physics: Condensed Matter*, 2013, **25** (20), P. 205403.
- [17] Lian C.-S., Li H.-D., Wang J.-T. Crystalline structures of polymeric hydrocarbon with 3,4-fold helical chains. *Sci. Rep.*, 2015, **5**, P. 07723.
- [18] Eremets M. I., Gavriluk A. G., Trojan I. A., Dzivenko D. A., Boehler R. Single-bonded cubic form of nitrogen. *Nat Mater*, 2004, **3** (8), P. 558–563.
- [19] Wen X.-D., Hand L., Labet V., Yang T., Hoffmann R., Ashcroft N. W., Oganov A. R., Lyakhov A. O. Graphane sheets and crystals under pressure. *Proceedings of the National Academy of Sciences*, 2011, **108** (17), P. 6833–6837.
- [20] Kondrin M. V., Brazhkin V. V. Diamond monohydride: the most stable three-dimensional hydrocarbon. *Phys. Chem. Chem. Phys.*, 2015, **17** (27), P. 17739–17744.
- [21] Blatov V. A., Proserpio D. M. Periodic-graph approaches in crystal structure prediction. In *Modern Methods of Crystal Structure Prediction* (Oganov A. R., editor), chapter 1, pp. 1–28. Wiley-VCH Verlag GmbH & Co. KGaA, 2010.
- [22] Delgado-Friedrichs O., Foster M. D., O’Keeffe M., Proserpio D. M., Treacy M. M. J., Yaghi O. M. What do we know about three-periodic nets? *Journal of Solid State Chemistry*, 2005, **178** (8), P. 2533 – 2554.
- [23] Németh P., Garvie L. A. J., Aoki T., Dubrovinskaia N., Dubrovinsky L., Buseck P. R. Lonsdaleite is faulted and twinned cubic diamond and does not exist as a discrete material. *Nat Commun*, 2014, **5**.
- [24] Tolédano P., Dmitriev V. *Reconstructive phase transitions in crystals and quasicrystals*. World Scientific, Singapore, 1996.
- [25] Aroyo M. I., Perez-Mato J. M., Capillas C., Kroumova E., Ivantchev S., Madariaga G., Kirov A., Wondratschek H. Bilbao Crystallographic Server: I. Databases and crystallographic computing programs. *Zeitschrift für Kristallographie*, 2006, **221** (1), P. 15–27.
- [26] Capillas C., Kroumova E., Aroyo M. I., Perez-Mato J. M., Stokes H. T., Hatch D. M. *SYMMODES*: a software package for group-theoretical analysis of structural phase transitions. *Journal of Applied Crystallography*, 2003, **36** (3 Part 2), P. 953–954.
- [27] Kroumova E., Perez-Mato J. M., Aroyo M. I. *WYCKSPLIT*: a computer program for determination of the relations of Wyckoff positions for a group-subgroup pair. *J. Appl. Cryst.*, 1998, **31**, P. 646.
- [28] Jmol: an open-source Java viewer for chemical structures in 3D. <http://www.jmol.org/>.
- [29] Artyukhov V. I., Chernozatonskii L. A. Structure and Layer Interaction in Carbon Monofluoride and Graphane: A Comparative Computational Study. *The Journal of Physical Chemistry A*, 2010, **114** (16), P. 5389–5396.
- [30] Giannozzi P., Baroni S., et al . QUANTUM ESPRESSO: a modular and open-source software project for quantum simulations of materials. *Journal of Physics: Condensed Matter*, 2009, **21** (39), P. 395502.
- [31] Balaban A. T., Klein D. J., Seitz W. A. Holes in diamond or carbon nitride lattices. *International Journal of Quantum Chemistry*, 1996, **60** (5), P. 1065–1068.
- [32] Clay W. A., Dahl J. E. P., Carlson R. M. K., Melosh N. A., Shen Z.-X. Physical properties of materials derived from diamondoid molecules. *Reports on Progress in Physics*, 2015, **78** (1), P. 016501.
- [33] Garcia J. C., Assali L. V. C., Machado W. V. M., Justo J. F. Crystal engineering using functionalized adamantane. *Journal of Physics: Condensed Matter*, 2010, **22** (31), P. 315303.
- [34] Garcia J. C., Justo J. F., Machado W. V. M., Assali L. V. C. Functionalized adamantane: Building blocks for nanostructure self-assembly. *Phys. Rev. B*, 2009, **80** (12), P. 125421.
- [35] Mujica A., Rubio A., Muñoz A., Needs R. J. High-pressure phases of group-IV, III-V, and II-VI compounds. *Rev. Mod. Phys.*, 2003, **75** (3), P. 863–912.
- [36] Johnston R. L., Hoffmann R. Superdense carbon, C₈: supercubane or analog of γ -silicon? *Journal of the American Chemical Society*, 1989, **111** (3), P. 810–819.
- [37] Correa A. A., Bonev S. A., Galli G. Carbon under extreme conditions: Phase boundaries and electronic properties from first-principles theory. *Proceedings of the National Academy of Sciences*, 2006, **103** (5), P. 1204–1208.
- [38] Mailhiot C., Yang L. H., McMahan A. K. Polymeric nitrogen. *Phys. Rev. B*, 1992, **46** (22), P. 14419–14435.
- [39] Brazhkin V. V. Metastable phases, phase transformations, and phase diagrams in physics and chemistry. *Physics-Uspekhi*, 2006, **49** (7), P. 719.
- [40] Brazhkin V. V. Interparticle interaction in condensed media: some elements are ‘more equal than others’. *Physics-Uspekhi*, 2009, **52** (4), P. 369.

Electromagnetic radiation by electrons in the corrugated graphene

S. A. Ktitorov^{1,2}, R. I. Mukhamadiarov¹

¹Ioffe Institute, St. Petersburg, Russia,

²St. Petersburg Electrotechnical University LETI, St. Petersburg, Russia

ktitorov@mail.ioffe.ru

PACS 78.67.Bf

DOI 10.17586/2220-8054-2016-7-1-51-57

The electromagnetic radiation of electrons in the corrugated graphene has been studied in the presence of a transport electric current in the ballistic regime. We considered here the impact of ripples in monolayer graphene on its electromagnetic properties. Electromagnetic radiation was actually calculated with a use of the standard electromagnetic theory. Two cases: those of regular and random structures were analyzed. The nonlinear relationship between the random height function $h(x, y)$ and the gauge field is shown to create a central radiation frequency distribution peak.

Keywords: dipole approximation, graphene, ripples, improper, gauge field.

Received: 20 November 2015

1. Introduction

A recent experimental study has shown that the flat geometry of graphene is unstable, leading to the formation of a corrugated structure: topological defects and ripples [1]. Electron motion through the rippled graphene sheet induces electromagnetic radiation. The mechanism for the formation of bremsstrahlung radiation in graphene is similar to that in an undulator or wiggler [2]. While an electron's trajectory in an undulator and wiggler deviates from a direct line due to a periodic system of dipole magnets, the electron's trajectory in graphene becomes curved due to ripples present on the material's surface. The spatial periodicity of the ripples in graphene could reach several hundreds of nanometers [3], which makes the semiclassical approach feasible. Despite the "quasi-relativistic" character of the spectrum, the ratio of Fermi velocity to the speed of light is much smaller, than unity and we can neglect the retardation of electromagnetic radiation. All these points give us a reason to consider the motion of electrons in graphene within the classical approach. The most important mechanisms are bremsstrahlung, cyclotron, and undulator radiation [4]. The emission mechanism under consideration resembles one in the undulator [5] but practically without retardation. We analyzed radiation using a few distinct models. In the first model, we consider a geometric mechanism, directly connected with the presence of undulations, in the second – the pseudo gauge field effect makes the trajectory become curved in the base plane. Both regular and random ripple structures are considered. In the following sections, we will consider various models of electrons motion in corrugated graphene and will derive a formula for the radiation intensity.

2. Geometric mechanism

Anomalously high electrons mobility in graphene [4] leads to the mean free path of micron value [6]. For the mean ripples period of 50 nanometers, the ratio of the free path to period of the structure is about 20, which leads to the 10 % spectral line broadening. The ballistic regime is implemented for the graphene sample of about several microns. Electrons

motion through the rippled graphene sheet induces an electromagnetic radiation in the terahertz range [4, 7, 8]. The mechanism of formation of the bremsstrahlung radiation in graphene is similar to one in the undulator or wiggler [3]. While the electron trajectory in an undulator and wiggler deviates from the direct line due to the periodic system of the dipole magnets, electron trajectory in graphene is getting curved due to the ripples. A spatial period of ripples in graphene could reach several hundreds of nanometers [1]. This makes the semiclassical approach feasible.

The Fermi velocity vector in the vicinity of the Dirac points in graphene has a constant absolute value of 10^8 cm/s. However, its orientation changes over time, leading to a time dependence of the vector components which is responsible for the emission of electromagnetic waves.

The ripple average amplitude is about 1 nm [9], whereas the period $L \sim 50$ nm. Taking this into account, we could assume that velocity preserves a constant value in the direction of the applied field. In other words, electrons in graphene could be considered as an oscillator having the Fermi velocity. The real graphene sample has a random corrugations period that deviates a little from the mean value. The chaotic surface could be considered as a superposition of sinusoids with their own period and height. This approach is widely used for wave analysis in radiophysics. In order to describe the random process of electromagnetic radiation within a limited spectrum, we introduce the random function $h(x)$ that plays a role of the ripples height relative to the base plane. Assuming the inhomogeneities to be one-dimensional and taking into account small ratio of $\frac{h_m}{L} \ll 1$ we can write the following equation for the velocity:

$$v_x = v_F, \quad v_z = v_F \frac{d}{dx} h(x(t)). \quad (1)$$

That means electromagnetic radiation spreads in a normal direction and infinitesimal changes in the in-plane velocity components are higher order effects [10] and can be neglected. We calculate the magnetic field induced by a moving charge at the deliberately chosen point with use of retarded potentials. The Fourier transform of the vector potential reads:

$$\mathbf{A}_\omega = \frac{e e^{ikr}}{cr} \int_0^\infty \mathbf{v}(t) e^{i(\omega t - \mathbf{k} \cdot \mathbf{r}_0)} dt, \quad (2)$$

where c is the speed of light, e is the electrons charge, \mathbf{r} is the radius vector, \mathbf{r}_0 is the moving charge radius vector.

Taking (1) into account and excluding the retardation effect, we have:

$$A_z = \frac{e e^{ikr}}{cr} v_F \int_0^\infty \frac{d}{dx} h(x(t)) e^{it\omega} dt. \quad (3)$$

The other two components will either be constant or zero and do not contribute to the generation of electromagnetic waves. The Fourier component of the magnetic field becomes:

$$B_y = -ik_x \frac{e e^{ikr}}{cr} v_F \int_0^\infty \frac{d}{dx} h(x(t)) e^{it\omega} dt. \quad (4)$$

The magnetic field enters the intensity formula in squared form:

$$|B_y|^2 = \left(k_x \frac{e}{cr} v_F\right)^2 e^{ikr} e^{-ikr} \int_0^\infty dt \frac{d}{dx} h(x(t)) e^{i\omega t} \cdot \int_0^\infty dt' \frac{d}{dx'} h(x'(t')) e^{-i\omega t'}. \quad (5)$$

In the case of random surface of the graphene, the squared absolute value can be represented as a multiplication of two equations where distribution of random function $h(x)$ could be considered as realizations, which could differ even in the same point [11]. Therefore, while calculating the field intensity, the relationship between them could be represented in terms of the correlation function. We introduce it by averaging (5) over the ripples' configuration:

$$\langle |B_x|^2 \rangle = -k_y^2 \frac{e^2 v_F^2}{c^2 r^2} \int_0^\infty dt \int_0^\infty dt' \frac{d^2}{dx^2} \langle h(x(t)) h(x'(t')) \rangle e^{i\omega(t-t')}, \quad (6)$$

$$\langle |B_y|^2 \rangle = -k_x^2 \frac{e^2 v_F^2}{c^2 r^2} \int_0^\infty dt \int_0^\infty dt' \frac{d^2}{dx^2} \langle h(x(t)) h(x'(t')) \rangle e^{i\omega(t-t')}, \quad (7)$$

where the angle brackets stand for configuration averaging. The random process $h(x)$ could be considered as Gaussian and stationary with the correlator:

$$\langle h(x) h(x') \rangle = K(x - x') = K(\xi). \quad (8)$$

Here, the correlation function value depends on relative coordinate $x - x'$, which means that statistical characteristics are invariant under a shift along the OX . Assuming this process to be one with a narrow band spectrum, we write the correlator in the form:

$$K(\xi) = \langle h^2 \rangle e^{-\alpha|\xi|} \cos \gamma \xi, \quad (9)$$

where $\langle h^2 \rangle$ is the dispersion, α is the inverse correlation radius and γ is the inverse mean period and $\alpha \ll \gamma$. Making the substitution $\xi = x - x'$, $\tau = t - t'$, $T = (t + t')/2$, we can rewrite formula (6) in the form:

$$\langle |B_x|^2 \rangle = \left(\frac{k_y^2 e^2}{r^2} \right) \frac{v_F^2}{c^2} \frac{1}{\alpha^2} \frac{\omega^2}{v_F^2} \langle h^2 \rangle \int_0^\infty dT \int_0^\infty d\tau e^{-\alpha v_F |\tau|} \cos(\gamma v_F \tau) e^{i\omega\tau} e^{iT(\omega - \omega')} e^{i\tau(\omega + \omega')/2}. \quad (10)$$

Integration over the difference variable makes a Fourier transform, whereas integration over sum variable is simply the time required for an electron to travel through graphene sample:

$$\langle |B_x|^2 \rangle = -\delta(\omega - \omega') \frac{k_y^2 e^2 \langle h^2 \rangle \omega^2}{c^2 r^2} \left(\frac{\alpha v_F}{\alpha^2 v_F^2 + (\omega + \gamma v_F)^2} + \frac{\alpha v_F}{\alpha^2 v_F^2 + (\omega - \gamma v_F)^2} \right). \quad (11)$$

Spectral distribution of electromagnetic radiation

$$\frac{d^2 \mathcal{E}}{d\omega d\Omega} = \frac{c}{4\pi^2} \langle |B_x|^2 \rangle r^2. \quad (12)$$

Substituting (11) in (12) we obtain the formula for the spectral intensity of electromagnetic radiation in rippled graphene:

$$\frac{d^2 \mathcal{E}}{d\omega d\Omega} = \delta(\omega - \omega') \frac{k_y^2 e^2 \langle h^2 \rangle \omega^2}{4\pi^2 c} \left(\frac{\alpha v_F}{\alpha^2 v_F^2 + (\omega + \gamma v_F)^2} + \frac{\alpha v_F}{\alpha^2 v_F^2 + (\omega - \gamma v_F)^2} \right). \quad (13)$$

Integrating (13) by frequencies and angle

$$P = \frac{c}{4\pi} \int_{-\infty}^{\infty} d\omega \int_0^{2\pi} d\Omega \langle |B_x|^2 \rangle r^2, \quad (14)$$

we obtain the relation for electromagnetic radiation power per one electron:

$$P_e = \int_{-\infty}^{\infty} d\omega \int_0^{2\pi} d\Omega \cos \theta \frac{e^2 \omega^4 \langle h^2 \rangle}{4\pi c^3} \left(\frac{\alpha v_F}{\alpha^2 v_F^2 + (\omega + \gamma v_F)^2} + \frac{\alpha v_F}{\alpha^2 v_F^2 + (\omega - \gamma v_F)^2} \right). \quad (15)$$

We see that the majority of the electromagnetic radiation comes with a frequency corresponding to the mean period of the ripples structure with some broadening due to its random character. The term in brackets yields the Lorentz distribution.

In the limit of $\alpha \rightarrow 0$ the chaotic surface becomes a regular sine and we obtain the formula:

$$P_e = \int_{-\infty}^{\infty} d\omega \int_0^{2\pi} d\Omega \cos \theta \frac{e^2 \omega^4 h_m^2}{4c^3} \delta(\omega - \gamma v_F) = \frac{\pi e^2 (\gamma v_F)^4 h_m^2}{c^3}. \quad (16)$$

The obtained formulae establish a relationship between the radiation spectral density $\frac{dP}{d\omega}$ and the correlator of ripples. This can be used to investigate of the ripples' morphologies.

For ripples period $L = 50$ nm, maximum amplitude $h_m = 1$ nm and area of graphene membrane $S = 10^{-4}$ cm², we obtain power of electromagnetic radiation of order several mW.

3. Gauge mechanism

In this part of our work, we consider the synthetic gauge field effect on electromagnetic wave emission. The nature of these fields is following. Electronic states in flat graphene can be written by means of the tight binding model equations, which due to linear spectra in Dirac point vicinity take form of Dirac – Weyl equations. The graphene membrane bending modifies the electronic states spectra. Moreover, this influence can be represented by introducing vector potential, rotor of which people called synthetic magnetic field [1]. In fact, these “fields” create new energy levels, similar to Landau levels, and mimics Aharonov – Bohm effect [1]. The elasticity theory gives the following relationships between the out-of-plane displacement $h(y, z)$ and the gauge field vector potential components [12]:

$$A_y = -\frac{\beta}{a} \frac{dh}{dx} \frac{dh}{dy}, \quad A_x = \frac{1}{2} \frac{\beta}{a} \left(\left(\frac{dh}{dx} \right)^2 - \left(\frac{dh}{dy} \right)^2 \right), \quad \mathcal{H}_z = \frac{\partial A_y}{\partial x} - \frac{\partial A_x}{\partial y}. \quad (17)$$

Here, a is the lattice constant and β is a dimensionless parameter. It now becomes apparent that gauge fields in graphene occur only when the structure is inhomogeneous in both in-plane directions. In other words, graphene sheet has to have “humps and hollows” in its structure.

Here, we consider the case of regular undulation in both directions:

$$h(x, y) = h_m \sin \gamma x \sin \gamma y. \quad (18)$$

Substitution of $h(x, y)$ from (18) into (17) gives an expression for the synthetic magnetic field:

$$\mathcal{H}_z = \mathcal{H}_0 \sin(2y\gamma) (-2 + \cos(2x\gamma)), \quad (19)$$

where the amplitude is determined as follows:

$$\mathcal{H}_0 = \frac{h_m^2 \gamma^3}{2a}. \quad (20)$$

The synthetic field \mathcal{H} can be expressed in terms of the “real” field H in the following manner:

$$H = \frac{c\hbar}{e} \mathcal{H}. \quad (21)$$

After this link has been made, we can modify the equations from [11] and define the undulator-like trajectory for “massless” electrons in graphene:

$$\begin{aligned}\frac{\mathcal{E}}{v_F^2} \frac{d^2 x}{dt^2} &= -e \frac{dy}{dt} H \cos \gamma x, \\ \frac{\mathcal{E}}{v_F^2} \frac{d^2 y}{dt^2} &= e \frac{dx}{dt} H \cos \gamma x,\end{aligned}\quad (22)$$

where \mathcal{E} is the electron energy. The solution reads:

$$\cos \gamma x = \cosh \gamma y - \frac{1}{k} \sinh \gamma y. \quad (23)$$

The resulting trajectory differs slightly from a simple sine function. Assuming that $y\gamma \ll 1$, we can simplify the last formula:

$$y = y_m \sin^2 \frac{\gamma x}{2}, \quad (24)$$

where the deviation amplitude is:

$$y_m = \frac{2k}{\gamma} = \frac{2v_F \hbar h_m^2 \gamma}{a\mathcal{E}}. \quad (25)$$

The estimations show the maximum amplitude of in-plane deviations to be much smaller than the mean period for the ripples and have values similar to ripples’ amplitudes. This makes us think that electrons actually move along complex, helix-like trajectory.

These formulae show that gauge fields in graphene have a real influence on an electron’s trajectory and induce in-plane oscillations. The magnitude of the effect depends upon sample parameters and free electron energy.

Now, with (22), we are able to derive the formula for power. Substituting the expression for an oscillating electron’s velocity $v_y = v_F \dot{y}$ into (17), we obtain the formula for the radiation vector potential:

$$A_y = \frac{e e^{ikr}}{cr} \int (y_m \gamma) v_F \sin(\gamma v_F t) e^{i\omega t}. \quad (26)$$

Thus, we have the expression for the radiation power spectral density for the case of harmonic ripple structure:

$$P(\omega, \theta) = \frac{1}{4\pi} \int d\omega \int d\theta \frac{e^2 v_F^2 \omega^2}{2c^3} (y_m^2 \gamma^2) \cos \theta (\delta(\omega + \gamma v_F) + \delta(\omega - \gamma v_F)). \quad (27)$$

Finally, integrating the expression and substituting for y_m , we derive the formula for the electromagnetic radiation power in terms of the sample parameters:

$$P = 2\pi^2 \frac{e^2 v_F^4}{c^3} \frac{h_m^2}{L^4} \left(\left(\frac{v_F \hbar / a}{\mathcal{E}} \right) (h_m \gamma) \right)^2. \quad (28)$$

To understand the role of gauge fields in whole picture of the radiation process, it will be useful to compare power formula obtained in geometric model with (28)

$$\frac{P_{gauge}}{P_{geom}} = \frac{1}{8\pi^3} \left(\frac{v_F \hbar h_m}{a\mathcal{E} L} \right)^2. \quad (29)$$

This ratio would be of order of unity for the same parameters of graphene structure at $\varepsilon = 0.1$ eV energies.

Calculations for the case of the random function $h(x, y)$ are carried out similarly to the case of the geometric mechanism but with one important distinction: a nonlinear relation (17) between the narrow band spectrum random function $h(x, y)$ and the gauge field A induces the

appearance of a central radiation peak of. Really, let us determine the quadratic relation between the random functions:

$$g(t) = (h(t)). \quad (30)$$

When $g(h) = ah^2$, the correlator $\langle g(t)g(0) \rangle$ can be expressed as follows [11]:

$$\langle g(t)g(0) \rangle = a^2\sigma^4 [1 + 2 \langle h(t)h(0) \rangle^2], \quad (31)$$

where σ is the $h(t)$ process variance $\sigma = \langle h^2 \rangle$.

We do not aware about existing experimental data or theoretical results regarding actual correlation function's $\langle h(x)h(x') \rangle$ form. All we can do is estimate dispersion and correlation radius. A reasonable choice would be the simplest form that does not lead to any disagreement. We choose the exponential decay for geometry model, i.e. Lorentz-shaped energy spectra. In case of gauge fields, the exponential correlator yields singularity: it corresponds to infinitely large gradients of random function [14]. Thus, we choose the Gaussian correlator form:

$$K(x) = \frac{\langle h^2 \rangle \alpha^3}{8\pi\sqrt{\pi}} e^{-x^2\alpha^2/4} \cos(\gamma x). \quad (32)$$

Substituting (32) in (31) we have

$$\langle g(t)g(0) \rangle = b^2\sigma^4 \left[1 + 2 \left(\frac{\langle h^2 \rangle \alpha^3}{8\pi\sqrt{\pi}} \right)^2 e^{-2(v_F t)^2 \alpha^2/4} \cos^2(\gamma v_F t) \right]. \quad (33)$$

Taking into account formula (17), we obtain for the gauge field random process:

$$\int_{-\infty}^{\infty} dx e^{ikx} K^2(x) = b^2\sigma^4 \left(\frac{\langle h^2 \rangle \alpha^3}{8\pi\sqrt{\pi}} \right)^2 \int_0^{\infty} dx e^{-(\alpha^2 x^2/2)} [\cos(kx) + [\cos(k+2\gamma)x + \cos(k-2\gamma)x]]. \quad (34)$$

Carrying out the integration, we obtain the spectrum comprising the central and high-frequency components:

$$P \propto P_0 + b^2\sigma^4 \frac{\langle h^2 \rangle^2 \alpha^5 k^3}{16\pi^2\sqrt{\pi}} \left[e^{-k^2/\alpha^2} + \left[e^{-(k+2\gamma)^2/\alpha^2} + e^{-(k-2\gamma)^2/\alpha^2} \right] \right]. \quad (35)$$

The pre-exponent term k^3 in (35) accounts for differentiation in (17) formula. On the Fig. 1 we presented the spectral distribution of a radiation power, divided by k^3 .

Thus, the quadratic relation between velocity and the Monge variable leads to a rise of the electromagnetic radiation central peak.

4. Conclusion

We have considered here the impact of ripples in monolayer graphene on its electromagnetic properties. Two mechanisms of undulator-like radiation are considered: a geometric mechanism, directly connected with the presence of undulations; and the pseudo gauge field effect, which makes the trajectory become curved in the base plane. The electromagnetic radiation was actually calculated using the standard retarded potential. For both of mechanisms, two cases of regular and random structures are analyzed. The nonlinear relation between the random height function $h(x, y)$ and the gauge field A is shown to create a central radiation frequency distribution peak. Our results can be used for study of ripples morphology and for generation of terahertz radiation.

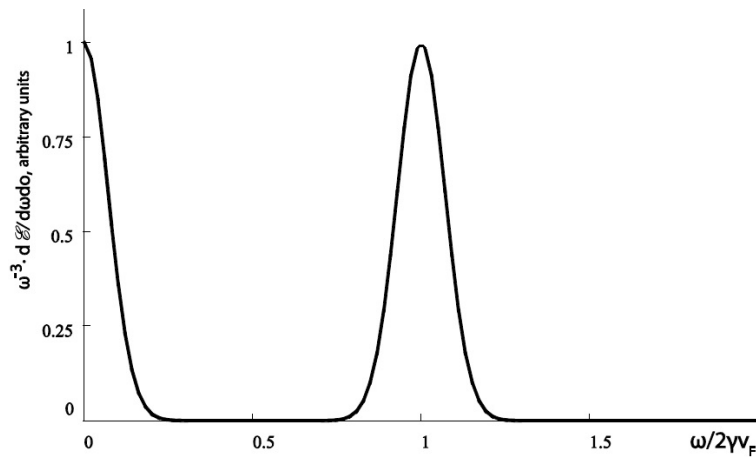


FIG. 1. Central and side radiation peaks in gauge model

References

- [1] Vozmediano M.A.H., Katsnelson M.I., Guinea F. Gauge fields in graphene. *Physics Reports*, 2010, **496**, P. 109–148.
- [2] Alferov D.F., Bashmakov Yu.A., Cherenkov P.A. Radiation from relativistic electrons in a magnetic undulator. *Sov. Phys. Usp.*, 1989, **32** (3), P. 200–227.
- [3] Castro Neto A.H., Guinea F., et al. The electronic properties of graphene. *Rev. Mod. Phys.*, 2009, **81**, P. 109–162.
- [4] Tantiwanichapan K., DiMaria J., Melo S.N. Graphene electronics for terahertz electron-beam radiation. *Nanotechnology*, 2013, **24**, P. 375205–375212.
- [5] Motz H. Applications of the Radiation from Fast Electron Beams. *J. Appl. Phys.*, 1951, **22**, P. 527–535.
- [6] Mayorov A.S., Gorbachev R.V., et al. Micrometer-scale ballistic transport in encapsulated graphene at room temperature. [arxiv:1103.4510](https://arxiv.org/abs/1103.4510), 2011.
- [7] Zhan T., Han D., et al. Tunable terahertz radiation from graphene induced by moving electrons. *Phys. Rev. B*, 2014, **89**, 245434 (1-7).
- [8] Llatser I., Kremers C., et al., Radiation Characteristics of Tunable Graphennas in the Terahertz Band. *Phot. Nanostr.*, 2012, **21**, P. 946–952.
- [9] Castro Neto A.H., Guinea F., et al. The electronic properties of graphene. *Rev. of Modern Phys.*, 2009, **81**, P. 109–162.
- [10] Zulicke U., Winkler R., Bolte J. Nanospintronics meets relativistic quantum physics: Ubiquity of Zitterbewegung effects. *Physica E*, 2008, **40**, P. 1434–1435.
- [11] Stratonovich R.L. *Topics in the theory of random noise*. Gordon and Breach Science Publishers, New York – London, 1963, 216 p.
- [12] Guinea F., Baruch H., Le Doussal P. Gauge field induced by ripples in graphene. *Phys. Rev. B*, 2008, **77**, 205421 (1-8).
- [13] Combe R., Feix M. Mouvement dun electron dans un onduateur magnetique. *Comt. Rend.*, 1953, **237**, P. 1318–1320.
- [14] Chernov L.A. *The waves in randomly inhomogeneous media*. Science, Moscow, 1975.

Phenomenology of ripples in graphene

S. A. Ktitorov^{1,2}, R. I. Mukhamadiarov¹

¹Ioffe Institute, St. Petersburg, Russia,

²St. Petersburg Electrotechnical University LETI, St. Petersburg, Russia

ktitorov@mail.ioffe.ru

PACS 68.65.Pq

DOI 10.17586/2220-8054-2016-7-1-58-59

The ripples are considered an incommensurate superstructure in a two-dimensional crystal, appearing as a result of the formation of periodic solutions in an in-plane optical phonon subsystem. The possible instability of the flexural subsystem is also discussed.

Keywords: Landau functional, graphene, ripples, incommensurate, curvature.

Received: 20 November 2015

1. Introduction

A recent experimental study has shown that the flat geometry of graphene is unstable, leading to the formation of a corrugated structure: topological defects and ripples [1]. Graphene can be viewed as a crystalline membrane. An ideal flat 2D-crystal could not exist at a finite temperature [1], and the long range order in graphene's structure occurs because of ripples and topological defects. Both of these factors facilitate the achievement of thermodynamic stability in graphene [2] and they could be induced to relieve the membrane's strain. As far as we know, no widely accepted model for ripples in monolayer graphene exists. The crumpled membrane theory does not work for graphene at relevant temperatures. Some authors try to obtain a ripple-like solution from the renormalization group approach, but the only result is the appearance of some characteristic length of a correct magnitude. The phenomenon under consideration looks too simple to be described with a use of the sophisticated fluctuation theory: we assume that the ripple theory has to be the mean field one. The somewhat similar problem of undulations in biological membranes was solved by taking into account the internal degrees of freedom [3]. One such fluctuating degree of freedom was the membrane thickness. In the case of graphene, a natural candidate on this position is the in-plane transverse optical phonon. The spatial period of the ripple is determined by the ratio of the coefficients in the thermodynamic potential derivative expansion. The out-of-plane subsystem acquires periodicity due to the interaction between the subsystems. Two interaction mechanisms: bilinear and biquadratic were considered. Only solutions with vanishing Gaussian curvature are admissible. The suggested phenomenological description needs to be justified by future microscopic theory.

2. In-plane phonon instability

The equilibrium state of the membrane is determined by the effective potential in the Monge representation [3]:

$$F[h] = \int d^2x \left[\frac{\kappa}{2} (\nabla^2 h)^2 + \frac{K_0}{8} [P_{\alpha\beta} (\partial_\alpha h \cdot \partial_\beta h)]^2 \right], \quad (1)$$

where κ is the bending rigidity, h is the membrane height relative to the base plane (Monge variable), and the second term is Gaussian curvature.

$$P_{\alpha\beta}^T = \delta_{\alpha\beta} - \frac{q_\alpha q_\beta}{q^2}, \quad K = \frac{2\mu(2\mu + D\lambda)}{2\mu + \lambda}, \quad (2)$$

$P_{\alpha\beta}$ is normal projector, μ and λ are the Lamé elastic moduli. Here, we assume this subsystem to be stable in isolation. In our case, the natural candidate on the symmetry violating system position is the in-plane transverse optical phonon. The simplest Landau functional containing a certain spatial scale (apart from the lattice spacing) in a crystal without the Lifshitz invariant is the one suggested for incommensurate ferroelectrics [4]:

$$F_{\text{incomm}} = \int dx dy \left[\frac{a_2}{2} \varphi^2 + \frac{a_4}{4} \varphi^4 + \frac{c_2}{2} (\nabla \varphi)^2 + \frac{d_2}{2} (\nabla^2 \varphi)^2 \right]. \quad (3)$$

Here, $a_2 < 0$, $a_4 > 0$, $c > 0$, $d > 0$. Varying this functional, we obtain the equilibrium equation:

$$d_2 \frac{d^4 \varphi}{dx^4} + c_2 \frac{d^2 \varphi}{dx^2} + |a_2| \varphi - a_4 \varphi^3 = 0. \quad (4)$$

We consider here unidimensional solutions. For the chosen signature of the coefficients, there exists a periodic solution with the characteristic period value of order $\sqrt{d_2/c_2}$. This violation of the translation symmetry can be transferred to the out-of-plane subsystem by means of an interaction. The simplest interactions that do not break the spatial inversion symmetry read:

$$g \int dx dy \varphi \Delta_2 h, \quad (5)$$

and

$$G \int dx dy \varphi^2 (\Delta_2^2 h)^2. \quad (6)$$

Interaction (5) is more effective, but is not easy to derive. Now, we consider another scenario.

3. Out-plane phonon instability

Corresponding with the Landau-Peierls-Mermin-Wagner theorem, the logarithmic divergencies indicating the instability of the flat state are characteristic for two-dimensional systems. In particular, the bending rigidity constant will be renormalized [3]:

$$\kappa_r = \kappa_0 - \frac{3k_B T}{4\pi} \ln \frac{L}{a}. \quad (7)$$

Here, a is the lattice spacing and L is the sample size. The possible change of sign in (7) induces an instability similar to the case considered above. We believe that fluctuations can make absolute value negative. This may induce instability, which stabilizes by non-linear terms as in phase transitions theory.

References

- [1] Vozmediano M.A.H., Katsnelson M.I., Guinea F. Gauge fields in graphene. *Physics Reports*, 2010, **496**, P. 109–148.
- [2] Mermin N.D., Wagner H. Absence of Ferromagnetism or Antiferromagnetism in One- or Two-Dimensional Isotropic Heisenberg Models. *Phys. Rev. Lett.*, 1966, **17**, P. 1133–1136.
- [3] Nelson D., Piran T., Weinberg S. *Statistical Mechanics of Membranes Surfaces*, World Scientific, New Jersey, 2004.
- [4] Izyumov Y.A., Syromyatnikov V.N. *Phase transitions and symmetry of crystals*. Science, Moscow, 1984, 182 p.

Synthesis of high-purity multilayer graphene using plasma jet

R. H. Amirov¹, M. E. Iskhakov², M. B. Shavelkina¹

¹Joint Institute for High Temperatures, Russian Academy of Sciences, Moscow, Russia

²Dagestan State University, Makhachkala, Russia

amirovravil@yahoo.com, isemarat@mail.ru, mshavelkina@gmail.com

PACS 52.75.Hn, 81.05.ue

DOI 10.17586/2220-8054-2016-7-1-60-64

A method to synthesize graphene materials using a DC high current divergent plasma torch has been developed. Carbon atoms were generated by the decomposition of propane-butane, methane and acetylene in a thermal plasma jet. The graphene materials were characterized by electron microscopy, thermogravimetry, Raman spectroscopy. The influence of the experimental conditions on the morphology and phase composition of the synthesis products was investigated. The optimal conditions for the synthesis of high-purity graphene flakes have been found.

Keywords: graphene materials, flakes, hydrocarbons, synthesis, plasma torch, plasma jet.

Received: 20 November 2015

1. Introduction

Graphene can be produced by variety of techniques, including mechanical exfoliation, growth on the basis of SiC substrates, high-pressure high-temperature growth, chemical exfoliation, and electrostatic deposition [1]. Depending on the synthetic method, graphene may be of three different types: single layer graphene (SLG), bi-layer graphene (BLG) and few-layer graphene ($n \leq 10$) [2]. The quantity and form of graphene required varies according to the application; some applications, such as transparent electrodes and sensors, require thin films of graphene, other applications, such as energy storage devices (such as batteries and supercapacitors) and polymer composites, require relatively large quantities of graphene nanosheets or platelets. Furthermore, the importance of using high quality graphene will vary with application type. For example, no noticeable improvement in electrochemical activity has been observed when going from few-layer- to monolayer-graphene, and defects in the material are thought to enhance both the electrochemical and hydrogen storage ability of graphene sheets [3].

Nevertheless, the issues of large-scale production and process control for graphene, remain essentially unresolved. Thermal plasma, which is produced by high-power discharges at or close to atmospheric pressure, has proven to be an effective tool for the fabrication of nanoparticles and nanostructured films and coatings [4]. Pure layered graphene was produced using a plasma jet reactor based on the DC plasma torch [5]. The number of layers of graphene sheets was controlled by adjusting the rate of ethanol injection.

The main aim of the present study is to obtain experimental data for the synthesis of graphene materials from carbon atoms generated by hydrocarbon decomposition (propane-butane, methane acetylene) in a thermal plasma jet by means of the direct current plasma torch with the extending channel of an output electrode.

2. Experimental setup and procedure

The synthesis of graphene has been investigated using a DC plasma torch with power of up to 40 kW with an expanding channel of the output electrode and the vortex stabilization of the arc [6,7]. A detailed description of the experimental setup was given in the study [8]. The

TABLE 1. Technological conditions

Power	30 – 40
Current	350 – 400 A
Voltage	60 – 110 V
Plasma gas	0.5 – 3.75 g/s
Gas flow rate	0.05 – 0.37 g/s
Pressure	150 – 730 Torr
Duration of the experiment	10 – 20 min

experiment involved simultaneous input of hydrocarbons in a carrier gas (e.g. helium, argon) into the plasma torch, wherein heating and decomposition occurred in the plasma jet and in the region of the arc discharge, followed by condensation of the synthetic product on metallic surfaces. Consumption of carbon, plasma forming gas and plasma torch power were changed independently from one other. For the experimental conditions, the electric power of the plasma torch was set up to 40 kW. Helium and argon were used as plasma gases. The experimental conditions are presented in Table 1.

The main parameters were: varying the pressure and gas flow rate. The hydrocarbon flow rate ranged from 0.11 to 0.3 g/s for a propane-butane mixture; from 0.15 to 0.37 g/s for methane; and from 0.05 to 0.16 g/s for acetylene. Natural gases used as carbon source were: propane-butane in the ratio 30 : 70 %, technical methane and high purity methane (99.99 %). Upon completion of the synthesis, carbon materials samples were collected from the target surface and from the trap. Samples were not purified and were analyzed in the form in which they were synthesized in the reactor.

Methods of electronic microscopy were used to investigate the structure of the synthesized products on a scanning electronic microscope of MIRA 3 TESCAN. Efficiency of synthesis, thermal stability and phase composition of carbon products were evaluated by thermogravimetry and differential scanning calorimetry on a synchronous thermal analyzer STA 409PC Luxx (NETZSCH) with linear heating sample in air at the rate of 10 K/min at temperatures up to 1000 °C. Nano Raman spectroscopy (NTEGRA) was used in the characterization of the graphene with an excitation wavelength of 532 nm under ambient conditions from 300 – 3000 cm^{-1} . The laser power was about 3 mW for a spot size of 1 μm .

3. Results of experiment

Experiments on the decomposition of a propane-butane mixture show that depending on the pressure and the value of plasma gas flow rate, nanostructures in the form of flakes with various geometries are formed. At lower He pressures (200 Torr), a large amount of amorphous carbon (37 %) and graphitized particles are produced. Increasing the pressure led to the formation of graphene flakes. At 350 Torr He, the transverse dimensions of these flakes were in the range of 600 nm. Additionally, the graphene content in the synthetic product increased, although some amorphous carbon was still present in small amounts (Fig. 1).

Further increase of the pressure decreased the content of this phase and reduced the size of the produced graphene flakes. When reaching a He pressure of 710 Torr, the synthetic samples contained 2 % amorphous carbon and 81 % graphene materials. The synthetic products from the propane-butane mixture obtained under argon have transverse dimensions not exceeding 100 nm. As in the case of He, with increased argon pressure, amorphous carbon is present together with graphene materials.

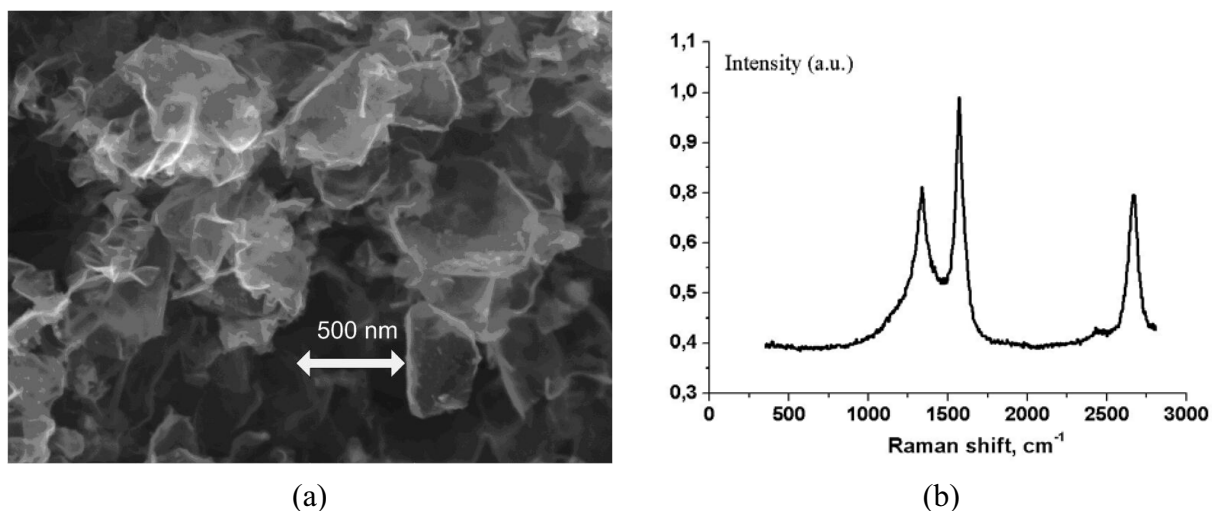


FIG. 1. The morphology (a) and the Raman spectrum (b) of the sample produced from the decomposition of propane-butane in helium plasma at a pressure of 350 Torr. Plasma forming gas is helium

Figure 1(b) shows the Raman spectra of the graphene materials formed from the decomposition of propane-butane in He plasma at 350 Torr. Raman spectra show common features in the 300 – 2800 cm⁻¹ region: the G and D peaks, which lie at around 1560 and 1360 cm⁻¹, respectively, and 2D (2690 cm⁻¹). The number of layers can be derived from the ratio of peak intensities, I_{2D}/I_G , as well as the position and shape of these peaks. Our few-layered graphene materials show a single Lorentzian profile. However, we believe that this measurement was a mixture of graphene flakes with a different number of layers, from 1 to 10.

The best conditions for the synthesis of graphene materials obtained from decomposition of methane differ mainly in higher precursor consumption: pure methane, a pressure of 350 Torr, helium or argon, CH₄ flow rate of 0.75 or 3.5 g/s. Up to 77 % graphene flakes were formed with a transverse dimension of 400 – 600 nm. In helium, the yield of graphene materials was 91 %. The maximum yield of 82 – 88 % of graphene materials with crumpling sheets was observed in argon at 650 – 670 Torr and a high methane flow rate of 0.368 g/s.

Figures 2(a) and 2(b) show the characteristics of the plasma jet-grown multilayer graphene flakes and Raman spectra images under optimized conditions. Fig. 2(a) shows flakes. We believe that the sample used for this measurement may have consisted of a mixture of graphene flakes with differing numbers of layers (from 1 to 10 of graphitic layers formed with various thicknesses). Moreover, the Raman spectra of the image shown in Fig. 2(b) indicates that the graphitic layers observed are similar to the Raman spectra image of the few-layer graphene of [5], whose G and 2D peak intensities lie at 1580 and 2700 cm⁻¹.

It can also be noticed from the image that the shape of the 2D band, particularly the absence of the graphite shoulder, shows a hallmark feature of few-layer graphene. Under our conditions, the samples have less than 10 layers, with the largest shift D line observed for a smaller number of layers. The majority of our samples had 2 – 5 graphene layers. The I_G/I_{2D} ratio of our product is ~ 1.03 , which is comparable to the value for three layers of CVD-grown graphene ($I_G/I_{2D} \sim 1.3$). In our study, we used the well-known approach to make conclusions about the presence of graphene materials and the number of layers in those graphene structures in accordance with previous studies [9].

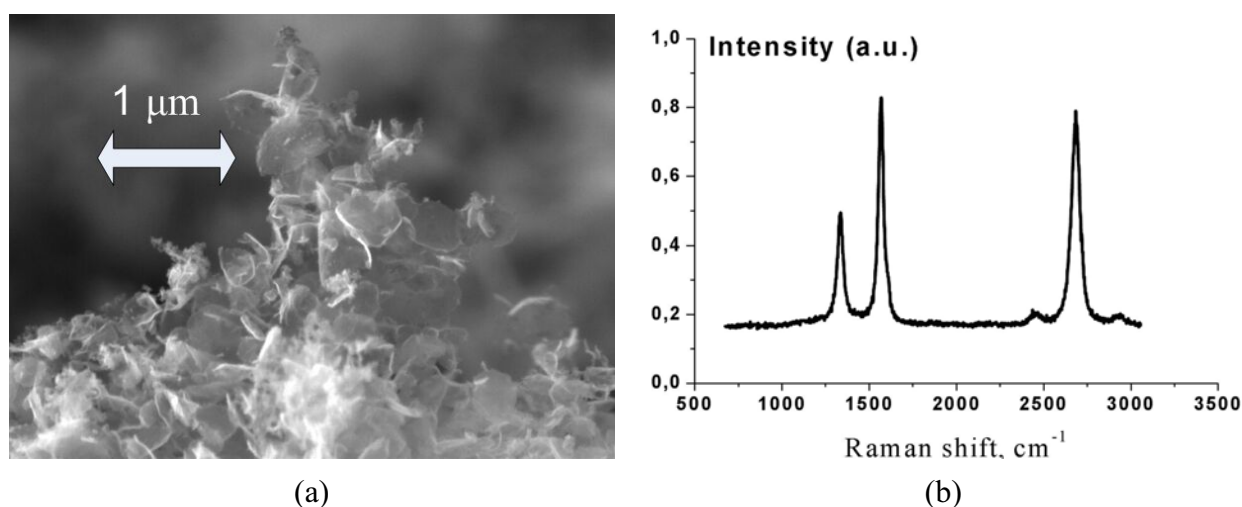


FIG. 2. The morphology (a) and the Raman spectrum (b) of the sample produced from the decomposition of methane at the pressure of 350 Torr. Plasma forming gas is helium

Graphene materials produced from decomposition of acetylene under optimal conditions are less stable at high temperatures than the synthetic products generated using propane-butane. Upon decomposition of acetylene using argon and helium plasma, crumpled graphene structures were produced at pressures ranging from 150 to 350 Torr. In helium, the yield of graphene materials was 81 %. Fig. 3 shows the results of electronic microscopy and thermogravimetric analysis of graphene products. Decreasing the gas pressure to 150 Torr increased the amount of graphite and amorphous carbon phase. Fig. 4 shows a typical Raman spectrum for our product. The three intense features are the D band at 1334 cm^{-1} , the G band at 1577 cm^{-1} and the 2D band at 2662 cm^{-1} . The samples have fewer than 10 layers.

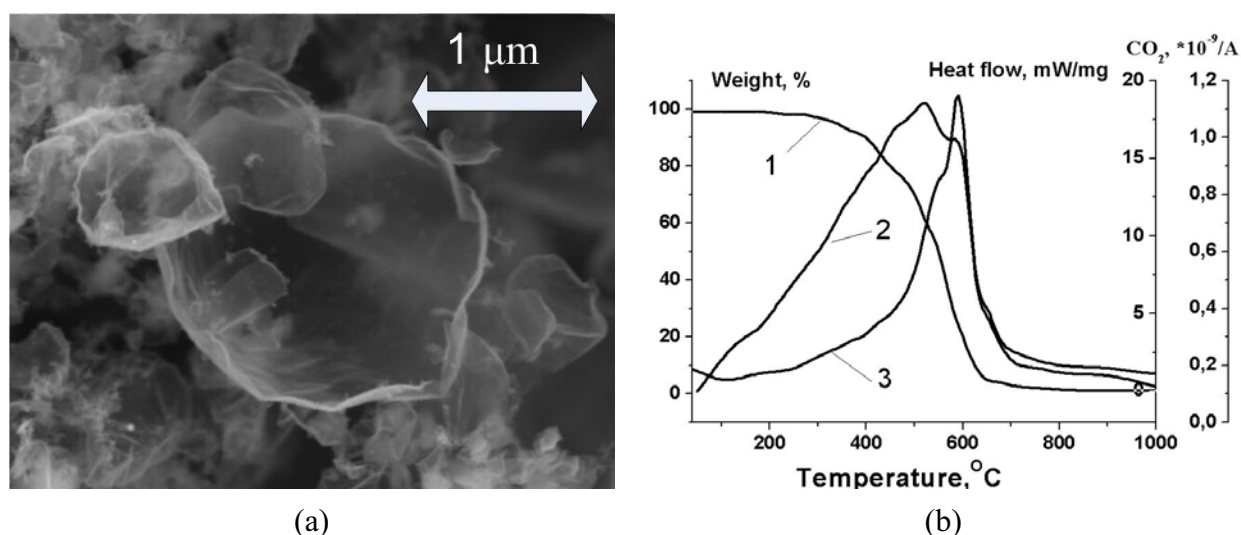


FIG. 3. The morphology (a) and thermogravimetry (b) graphene materials produced from decomposition of acetylene at a pressure of 350 Torr. Plasma forming gas is helium. (1) Loss of weight, (2) heat flow and (3) rate of generation of CO₂

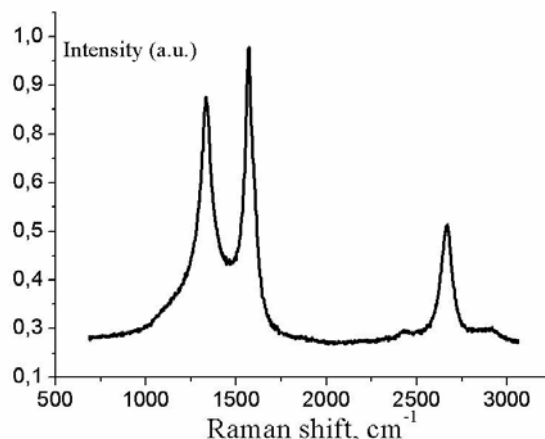


FIG. 4. The Raman spectrum of the sample produced from the decomposition of acetylene at a pressure of 150 Torr. Plasma forming gas is helium

4. Conclusions

Based on the Raman spectra and thermogravimetry for the samples, high-purity multi-layer graphene materials were successfully synthesized using a plasma jet. It has been shown that the selection of hydrocarbon source and their flow rate influenced the quality of the graphene produced. Depending on the synthetic parameters, the geometry of the graphene materials (from curved petals to disk diameter of 100 nm – 1 μ m) and the graphene content in synthesis products (from 58 to 95 %) varied.

In general, the experimental data allowed stepwise scaling of the synthesis so that graphene having the desirable morphology could be obtained.

Acknowledgements

The authors gratefully acknowledge Russian Foundation for Basic Research for the support by grant No. 15-08-00165 and by State Assignments No. 2560 and No. 16.1103.2014/K.

References

- [1] Calizo I., Bejenari I., et al. Ultraviolet Raman microscopy of single and multilayer graphene. *J. Appl. Phys.*, 2009, **106** (4), 043509 (5 p).
- [2] Rao C.N., Sood A.K., Subrahmanyam K.S., Govindaraj A. Graphene: the new two-dimensional nanomaterial. *Angew. Chem. Int. Engl.*, 2009, **48** (42), P. 7752–7777.
- [3] Edwards R.S., Coleman K.S. Graphene synthesis: Relationship to applications. *Nanoscale*, 2013, **5**, P. 38–51.
- [4] Shigeta M., Murphy A.B. Thermal plasmas for nanofabrication. *J. Phys. D: Appl. Phys.*, 2011, **44**, 174025 (16 p).
- [5] Kim J., Heo S., Gu G. Suh J. Fabrication of graphene flakes composed of multi-layer graphene sheets using a thermal plasma jet system. *Nanotechnology*, 2010, **21**, 095601(6 p).
- [6] Isakaev E. Kh., Sinkevich O.A., Tyuftyaev A.S., Chinnov V.F. Thermal fluxes in a generator of low temperature plasma with a divergent channel of the outlet electrode. *High Temperature*, 2010, **48** (1), P. 97–125.
- [7] Isakaev E. Kh., Sinkevich O.A., et al. Study of a Low Temperature Plasma Generator with a Divergent Output Electrode Channel. *High Temperature*, 2010, **48** (6), P. 777–788.
- [8] Amirov R., Isakaev E., Shavelkina M., Shatalova T. Synthesis of Carbon Nanotubes by High Current Divergent Anode-Channel Plasma Torch. *J. Phys.: Conf. Ser.*, 2014, **550**, 012023 (7 p).
- [9] Gupta A. Raman Scattering from High-Frequency Phonons in Supported n-Graphene Laer Films. *Nano Lett.*, 2006, **6** (12), P. 2667–2673.

Study of graphene oxide solid films prepared by Langmuir – Blodgett technology

E. V. Seliverstova, N. Kh. Ibrayev, R. Kh. Dzhanabekova

Institute of Molecular Nanophotonics, Buketov Karaganda State University, Kazakhstan

genia_sv@mail.ru

PACS 81.15.-z, 68.03.cd, 68.60.wm

DOI 10.17586/2220-8054-2016-7-1-65-70

The preparation of Langmuir – Blodgett (LB) films based on graphene oxide and the study of their structure and optical properties are presented. Graphene oxide dispersions were prepared in different solvents and the stability of each solution was studied. The measurements have shown that most stable dispersions were prepared in tetrahydrofuran, but in acetone, the concentration of graphene oxide is higher. Therefore, graphene oxide monolayers were formed from acetone dispersions. The physicochemical properties of graphene oxide monolayers at the water-air interface were studied. The LB films were deposited onto solid substrates according to Y-type (transfer during downward and upward stroke of substrate) and Z-type transfer (deposition during the upward stroke only). The absorption spectra of graphene oxide LB films exhibit a broad band in the ultraviolet and visible region of the spectrum. The optical density of the film obtained according to the Y-type transfer is greater than the optical density of the film prepared according to the Z-type transfer. The transparency of the films in the visible region of the spectrum is greater than 90 %. As it was shown by SEM images, the films obtained according to the Y-type transfer are more uniform in structure.

Keywords: graphene oxide, dispersion, Langmuir – Blodgett films, optical properties.

Received: 20 November 2015

1. Introduction

Currently, the wide use of inorganic solar cells is hindered by the relatively expensive manufacturing technology and processing of inorganic semiconductors, which requires high temperatures and high vacuum. In this regard, interest in organic materials to create new types of cheap solar cells is growing. Organic compounds, being carbon-based, usually do not contain rare chemical elements and can be very manufacturable, and therefore much cheaper in comparison to inorganic materials.

Graphene and its modified derivatives are a new class of carbon materials having high specific surface area and electron mobility, which makes them suitable for use as electrodes in dye-sensitized solar cells. In earlier work [1], it was shown that graphene has a high specific surface area and electron mobility, as well as having a higher oxidation potential than Pt. The wide variety of existing forms of graphene can improve the necessary parameters for counter electrodes. For example, reduced graphene oxide has a surface lattice defects, which implies a higher catalytic activity than the fully reduced defect-free graphene [2, 3]. Additionally, graphene production costs are cheaper than that of other carbon nanomaterials. This combines many useful properties necessary for effective modification of photovoltaical device design. In this aspect, the study of conditions for producing graphene oxide solid films with predictable properties, which is presented in this paper, is particularly relevant.

2. Experimental

Single layer graphene oxide was used for dispersion preparation (SLGO) (Cheaptubes, USA). Graphene oxide suspensions were prepared in acetone, chloroform, tetrahydrofuran (THF) and dimethyl formamide (DMF). All solvents were purchased from Sigma Aldrich and used without purification. The concentration of graphene oxide in solution was equal to $6 \cdot 10^{-4} \text{ mol}\cdot\text{L}^{-1}$. Suspensions were sonicated in ultrasonic bath. The dimensions of the graphene oxide particles were measured by dynamic light scattering method with Zetasizer nano analyzer (Malvern). The graphene oxide particle and film morphologies were obtained with scanning electron microscopy (TESCAN Mira-3) on a glass surface with FTO coating.

Solid films were obtained by Langmuir – Blodgett (LB) technology. Monolayers were formed on the surface of the subphase by spreading of solution throughout the LB trough. The deionized water was purified by AquaMax and was used as the subphase. The resistivity of the deionized water was equal to $18.2 \Omega\cdot\text{m}^{-1}$. The surface tension of water was equal to $72.8 \text{ mN}\cdot\text{m}^{-1}$ at $\text{pH} = 5.6$ and a temperature of $22 \text{ }^\circ\text{C}$.

3. Results and discussion

The conditions for preparation of graphene oxide dispersions were chosen to obtain highly concentrated and stable particle solutions. From the diagram of the size distribution of graphene oxide particles in DMF before sonication, one can see that about 80 % of the particles have a size of 2000 – 3000 nm. Particles with sizes of 2300, 2700 and 3000 nm predominate in the solution. A decrease in the size of the graphene oxide particles was observed after sonication of solution for 30 min: 60 % of particles have a size of 900 – 1000 nm, 15 % – from 850 nm and 17 % of particles – about 1100 nm. Further ultrasonic treatment of the solutions had virtually no effect on the decrease in the average size of particles or the scatter of sizes.

The dependence of the graphene oxide particle size distribution on the sonication time is shown in Fig. 1 (curve 1). At least five measurements were taken to plot the graph.

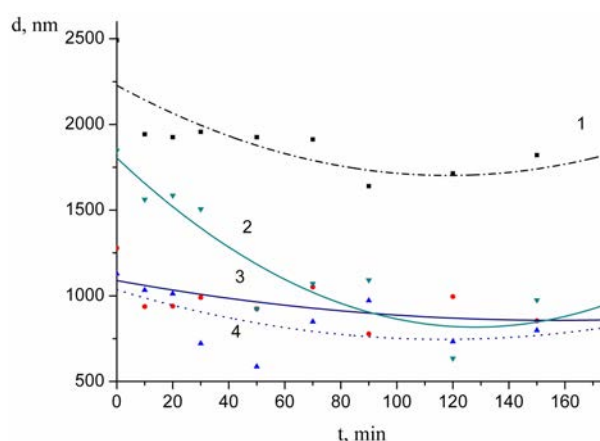


FIG. 1. Dependence of average size of graphene oxide particles over the sonication time in: 1 – DMF; 2 – chloroform; 3 – THF; 4 – acetone

Similar results have been obtained for other solvents. Thus, in THF the particle size also decreased from 2.5 to $1.8 \mu\text{m}$ and from $1.1 \mu\text{m}$ to 750 nm for acetone solution after sonication. In addition, for both solvents, the size of particles remained practically unchanged after 30 min of treatment. Characteristically, that in chloroform ultrasonic treatment of SLGO dispersions has the strongest influence on the particle size. The particle sizes were almost halved with 30 min

of treatment. This behavior for graphene oxide may be associated with the fact that as a result of chloroform's high density, the dissolved particles of SLGO were most strongly affected by the ultrasonic oscillation.

In addition, the size of particles was estimated from SEM images of graphene oxide films obtained by evaporation of SLGO solution in THF on a FTO layer-covered glass surface. Fig. 2 shows that upon drying, the graphene sheets rolled up to form spindle-shaped particles having an average size of ~ 320 nm. The observed conformation of graphene is a result of thermal effects [4].

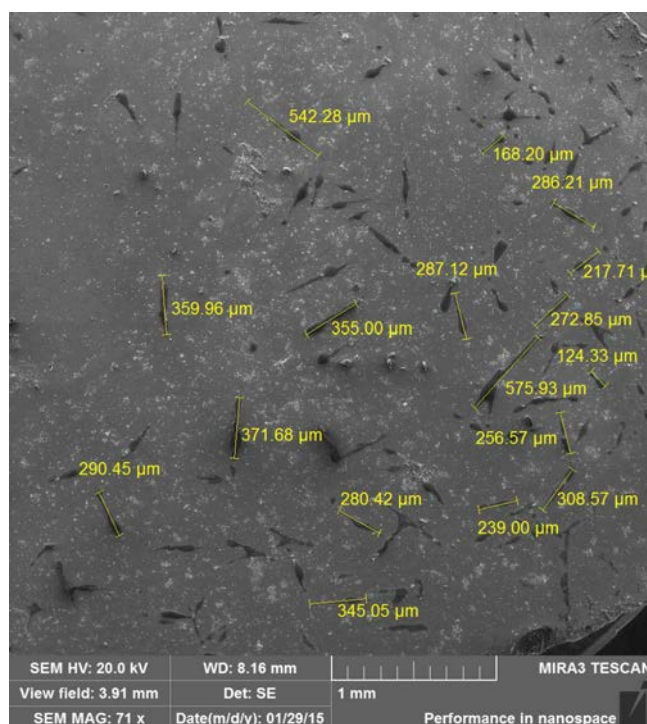


FIG. 2. SEM image of dispersed graphene oxide on the FTO surface

The stability of the graphene oxide dispersion was studied by measuring the optical density of the solutions over various time intervals. Absorption spectra were registered in the UV-Vis spectral region from 290 to 600 nm for DMF and THF and from 320 to 600 nm for acetone. The spectra of SLGO in DMF and THF exhibited a shoulder at ~ 300 nm which was ascribed to $n \rightarrow \pi^*$ transitions of C = O bonds [5]. The dependence of optical density of graphene oxide solutions upon time is shown in Fig. 3. Measurements have shown that the optical density change for graphene oxide in DMF and THF have similar behaviors. The absorption for SLGO in THF was practically unchanged for 48 h after sonication (curve 1). In DMF (curve 2), the optical density was reduced by 15 % within the first hour, additionally, this parameter was decreased by 40 % every 24 h. The strongest changes in the optical density of the graphene oxide solutions were registered for acetone (curve 3). During the first hour, the absorption decreased three-fold. Graphene oxide almost completely precipitated after 24 h of storage in acetone. The most unstable dispersions were obtained in chloroform – SLGO precipitated on the bottom of the cell within 1 hour after preparation.

Subsequently, acetone solutions were used to study the physicochemical properties of graphene oxide, since the solubility of graphene was highest in that solvent. Compression isotherms ($\pi - A$ isotherms) for graphene oxide monolayers are shown on the Fig. 4. The

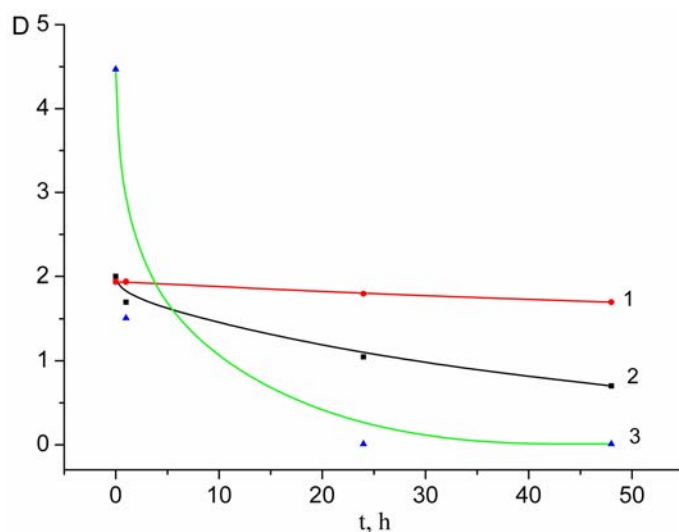


FIG. 3. Time dependence of optical density D of graphene oxide solutions ($\lambda_{\text{reg}} = 340 \text{ nm}$) in: 1 – THF, 2 – DMF, 3 – acetone

minimum volume was deposited onto the subphase monolayer in the “gaseous” state [6] at surface pressures of $2 - 2.5 \text{ mN}\cdot\text{m}^{-1}$ (curve 1). This means that the distance between graphene oxide particles on an aqueous surface is large. With further compression of the monolayer, the particles approach and the film becomes “liquid”. Moreover, this “liquid–expanded” state was preserved with additional compression of the monolayer up to its minimum area.

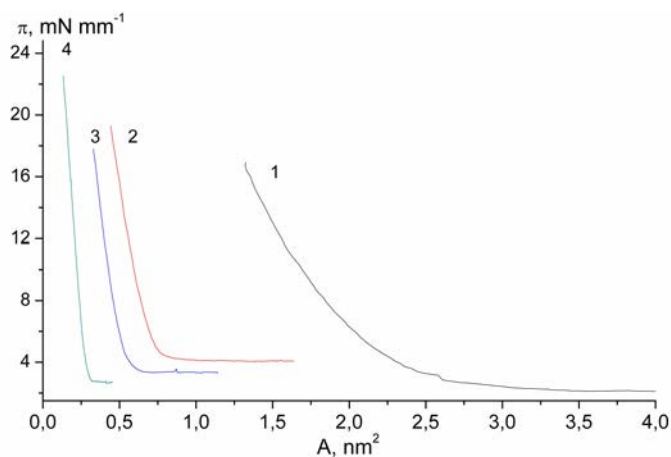


FIG. 4. $\pi - A$ isotherms of monolayers based on graphene oxide. Monolayers were spreaded from acetone, ml: 1 – 0.5, 2 – 1.5, 3 – 3.5, 4 – 5

Spreading a greater volume of substances onto the surface of the subphase (1.5 ml) results in a dense packing of particles within the monolayer (curves 2–4). In this case, the film on the aqueous surface is also initially in the “gaseous” state (curve 2). Transitions of monolayer in “liquid–expanded” and “liquid–condensed” states were observed upon compression of film within the pressure range of $5 - 9$ and $9 - 19 \text{ mN}\cdot\text{m}^{-1}$, respectively.

For monolayers formed from greater volumes of dispersion, an increase in the specific surface area was registered at higher SLGO concentrations. Fig. 5 shows that for the curve 1, the “gaseous state” had an area equal to 1 nm^2 , and 0.8 , 0.5 and 0.3 nm^2 for the curves 2, 3 and 4, respectively. The change of phase states of monolayer upon compression occurs in the

same sequence as that for the curve 2. It should be noted that all monolayers had no collapse, despite the rather large amount of spread solution.

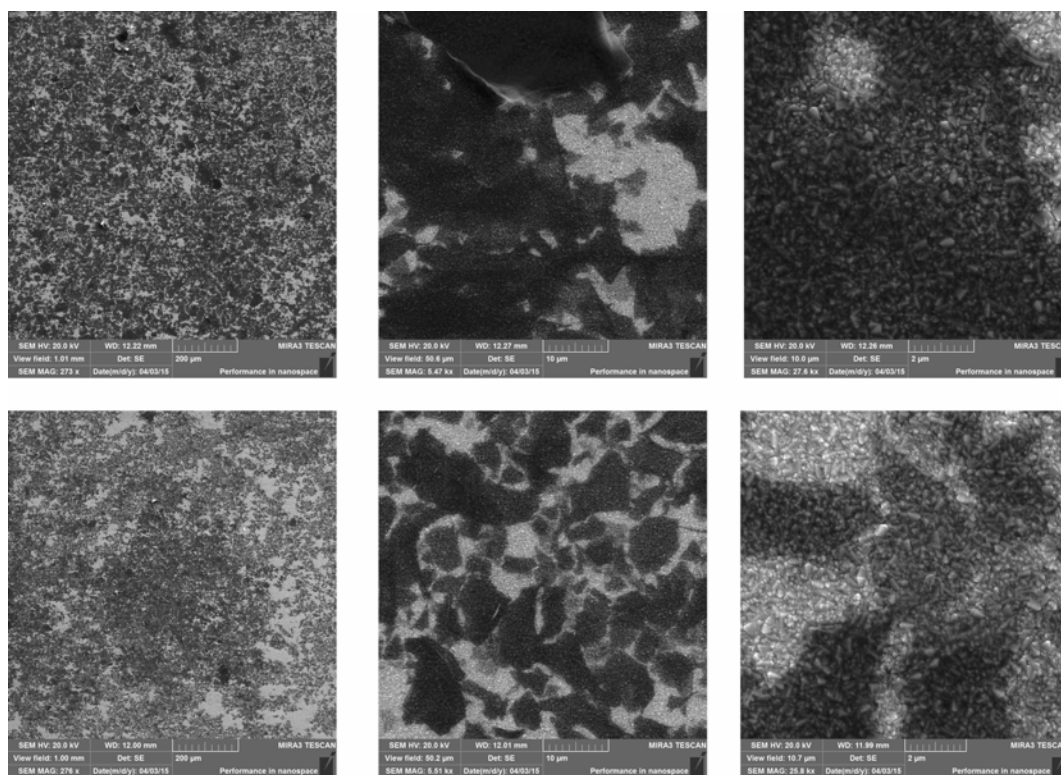


FIG. 5. SEM-images of graphene oxide LB films. At the top – Y-type, at the bottom – Z-type

SEM-images were obtained for graphene oxide LB films (Fig. 5). Monolayers were deposited onto solid substrates according to Z-type (transfer during the upward stroke only) and Y-type transfer (deposition during downward and upward stroke) at surface pressure $\pi = 19 \text{ mN}\cdot\text{m}^{-1}$. The thickness of the films consisted of 4 monolayers.

As can be seen from the figure, the SLGO films on a solid substrate have an island structure. The individual particles of graphene oxide could be distinguished in the SEM-images. Particles were distributed more uniformly across the substrate surface for the film obtained by Y-type transfer than in the film obtained by the Z-type transfer. Upon closer scrutiny, dark areas of varying intensity can be seen on the surface of the film. This fact is evidence for the presence of multilayer graphene oxide particles in the film.

The absorbance and transmittance of the LB films were measured (Fig. 6). Absorption spectra have a typical form and correspond to the spectra obtained by other authors [5]. For films prepared according to the Y-type transfer, the optical density at the maximum absorption band was approximately two times greater than the absorbance than the Z-type prepared films.

In the visible region of the spectrum, both films have high transparency – about 90 % in the wavelength ranging from 400 to 800 nm.

3.1. Conclusion

In this study, we investigated the stability of graphene oxide dispersions in different solvents. The suspensions of graphene oxide were prepared in acetone, chloroform, THF and DMF. Suspensions were sonicated in ultrasonic bath. By measuring the sizes of graphene oxide

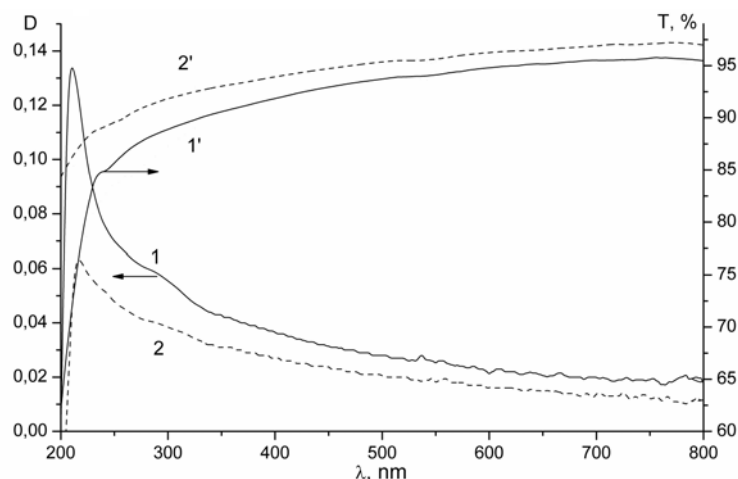


FIG. 6. Absorption $D(1, 2)$ and transmittance $T(1', 2')$ spectra of graphene oxide LB films, deposited according to Y-type (1, 1') and Z-type (2, 2') transfer

particles, it was shown that sonication for 30 min leads to a reduction in the size of graphene oxide particles. Further ultrasonic treatment of the solutions had virtually no effect on the average size of the particles and the distribution of particle sizes. Most stable dispersions of graphene oxide were prepared in THF.

The physicochemical properties of graphene oxide monolayers at the water – air interface were studied. From the compression isotherms of monolayers, it was found that for the pressures in the range of 0 to 2 $\text{mN}\cdot\text{m}^{-1}$ monolayer is predominantly in a gaseous state. With further compression of the monolayer, the particles approach and the film becomes “liquid”. Spreading a greater volume of graphene oxide onto the surface of the subphase results in a denser particle packing within the monolayer. For all monolayers, no collapse was registered, despite the rather large amount of the spread solution.

In the absorption spectra of graphene oxide LB films, a broad band was found in the ultraviolet and visible region of the spectrum with a maximum at 230 nm. The optical density of the film obtained according to the Y-type transfer is greater than the optical density of the film prepared according to the Z-type transfer. The transparency of the films is more than 90 % in the visible wavelength range (from 400 to 800 nm).

SEM-images show that the films have an island structure. In the pictures, the individual particles of graphene oxide are clearly distinguished. The films obtained according to the Y-type transfer were more uniform than films prepared according to than Z-type transfer, which makes them more promising in terms of their use as conductive coatings.

References

- [1] Guo C.X., Guai G.H., Li C.M. Graphene Based Materials: Enhancing Solar Energy Harvesting. *Adv. Energy Mater.*, 2011, **1**, P. 448–452.
- [2] Roy-Mayhew J.D., Bozym D.J., Punckt C., Aksay I.A. Functionalized graphene as a catalytic counter electrode in dye-sensitized solar cells. *ACS Nano*, 2010, **4**, P. 6203–6211.
- [3] Cruz R., Tanaka D.A.P., Mendes A. Reduced graphene oxide films as transparent counter-electrodes for dye-sensitized solar cells. *Solar Energy*, 2012, **86**, P. 716–724.
- [4] Whitby R., Gun'ko V.M., et al. Driving forces of conformational changes in single-layer graphene oxide. *ACS Nano*, 2012, **6** (5), P. 3967–3973.
- [5] Sutar D.S. Spectroscopic studies of large sheets of graphene oxide and reduced graphene oxide monolayers prepared by Langmuir-Blodgett technique. *Thin Solid Films*, 2012, **520**, P. 5991–5996.
- [6] Adamson A. *Physical Chemistry of Surfaces*. A Wiley-Interscience Publication, New York, 1997, 785 p.

Parent and reduced graphene oxide of different origin in light of neutron scattering

E. F. Sheka¹, I. Natkaniec², N. N. Rozhkova³, E. Yu. Buslaeva⁴,
S. V. Tkachev⁴, S. P. Gubin⁴, V. P. Mel'nikov⁵

¹Department of Theoretical Physics and Mechanics, Peoples' Friendship
University of Russia, Moscow, Russia

²Faculty of Physics, Adam Mickiewicz University, Poznań, Poland

³Institute of Geology, Karelian Research Centre RAS, Petrozavodsk, Russia

⁴Kurnakov Institute of General and Inorganic Chemistry, RAS, Moscow, Russia

⁵Semenov Institute of Chemical Physics RAS, Moscow, Russia

sheka@icp.ac.ru, inat@amu.edu.pl

PACS 61.05.fg, 61.46.+w, 63.22.m, 81.05.Uw DOI 10.17586/2220-8054-2016-7-1-71-80

The current paper presents results from an extended neutron scattering study of a three-part set of parent and reduced graphene oxides (GO and rGO, respectively) of different origins. The first part concerns the rGO of natural origin represented by shungite carbon, the second and third parts are related to synthetic GO/rGO pairs with the latter produced during either chemical treatment or via thermal exfoliation of the parent GO, respectively. The study involved both the neutron diffraction and inelastic neutron scattering. The one-phonon amplitude-weighted density of vibrational states $G(\omega)$ represents the inelastic incoherent neutron scattering spectra of the products. Common characteristics and individual distinctions of the studied species are discussed.

Keywords: graphene oxide, reduced graphene oxide, shungite carbon, retained water, inelastic neutron scattering, neutron diffraction.

Received: 20 November 2015

1. Introduction

Graphene oxide and reduced graphene oxide have become the favorite species for neutron scattering study [1–3]. The hydrophilicity of GO and the hydrophobicity of rGO are responsible for the intense responses in both cases. The former is promoted by a considerable retaining of water between individual GO sheets as well as with hydroxyls that are formed during the interaction of the retained water with epoxy groups on the GO basal plane [3]. In the second case, the degree to which the rGO circumference is occupied with hydrogen depends on the rigour of the reduction conditions. C–H bonds formed during the reduction actively participate in scattering via vibrational excitation of both directly bound and involved in the vibrations of the carbon core by ‘riding effect’. Combined with the superb sensitivity for neutron scattering on protium, the above features provide a large hydrogen-sensitive method. In practice, the hydrogen saturation of both GO and rGO is quite variable and dependent on the chemical protocols for its production and conditions of their storage. The current paper presents the main findings related to the response of neutron scattering to high variability of GO and rGO products.

Three types of objects have been studied. The first is the naturally-sourced rGO represented by shungite carbon (sh-rGO below) [1, 2]. The second covers synthetic GO and rGO products of the Akkolab company [5] (Ak-GO and Ak-rGO) with the latter produced in the course of chemical treatment [6]. The third presents a pair of synthetic GO/rGO products, the

former of which is a free standing GO paper (ppGO) while the latter is produced via the thermal exfoliation of the parent ppGO (TErGO) [4]. The atom mass contents of the samples alongside with the per-one-benzenoid-ring chemical formulae are given in Table 1.

TABLE 1. Chemical composition of GO and rGO products, wt%

Products	C	O	H	Chemical formula per one benzoid ring	References
Shungite carbon	95.5 ± 0.6	3.3 ± 0.4	$2.0 - 0.7$	$C_6O_{0.1}H_{1.6-0.7}$	[7]
Ak-rGO	92.0 ± 1.0	5.5 ± 0.5	1.5 ± 0.5	$C_6O_{0.3}H_{1.2}$	[6]
TErGO	87.1 ± 0.3	12.1 ± 0.3	0.5 ± 0.3	$C_6O_{0.7}H_{0.4}$	[4]
Ak-GO	58.0 ± 1.0	39.0 ± 1.0	1.5 ± 0.5	$C_6O_3H_2$	[6]
ppGO	56.2 ± 0.3	40.5 ± 0.3	0.7 ± 0.3	$C_6O_3H_{0.85}$	[4]

The study involved both the neutron powder diffraction (NPD) and inelastic neutron scattering (INS). Both studies were performed using the inverted-geometry time-of-flight (TOF) spectrometer NERA [8] at the high flux pulsed IBR-2 reactor of the Frank Laboratory of Neutron Physics at the Joint Institute for Nuclear Research.

2. General remarks concerning NPD study

Figure 1 shows a typical picture of the NPD patterns related to the GO and rGO samples. The picture is common for all the studied samples in general, while differing slightly in details concerning the width and position of the rGO and GO peaks at ~ 3.5 Å and ~ 7 Å that are equivalent to the allowed Gr(002) and forbidden Gr(001) reflexes of graphite, respectively. Both peaks are broadened, which gives evidence for a stacked structure with a relevant interlayer distance. The obtained data concerning the interlayer spacing in the studied samples, as well as the lateral dimension of the layer, are given in Table 2 (details of the NPD study analysis are given elsewhere [1–4]). As seen in the table, all the studied samples present graphite-like stacked structures differing therewith by both the number of layers in the relevant stacks and the lateral dimensions of the layers. The latter was estimated by the width of Gr(110)-like peaks positioned at ~ 1.2 Å.

TABLE 2. NPD structural data

Samples	Peak position (Å)	Peak width FWHM (Å)	Number of layers	Layer lateral dimension ¹ (nm)
Graphite	3.35 ± 0.0002	0.034 ± 0.001	~ 100	> 20
sh-rGO	3.45 ± 0.0015	0.548 ± 0.006	$5 - 6$	$3 - 4$
Ak-rGO	3.50 ± 0.01	0.30 ± 0.01	7	> 20
TErGO	3.36 ± 0.01	0.26 ± 0.01	8	> 20
Ak-GO	7.00 ± 0.01	1.00 ± 0.01	$2 - 3$	> 20
ppGO	7.21 ± 0.01	0.50 ± 0.01	$4 - 6$	> 20

¹The definition > 20 nm marks the low limit of the lateral dimension of layers pointing that it is bigger than the coherent scattering region of crystalline graphite equal to ~ 20 nm along *c* direction [9]. Actual layer dimensions are of microsize range [3,4].

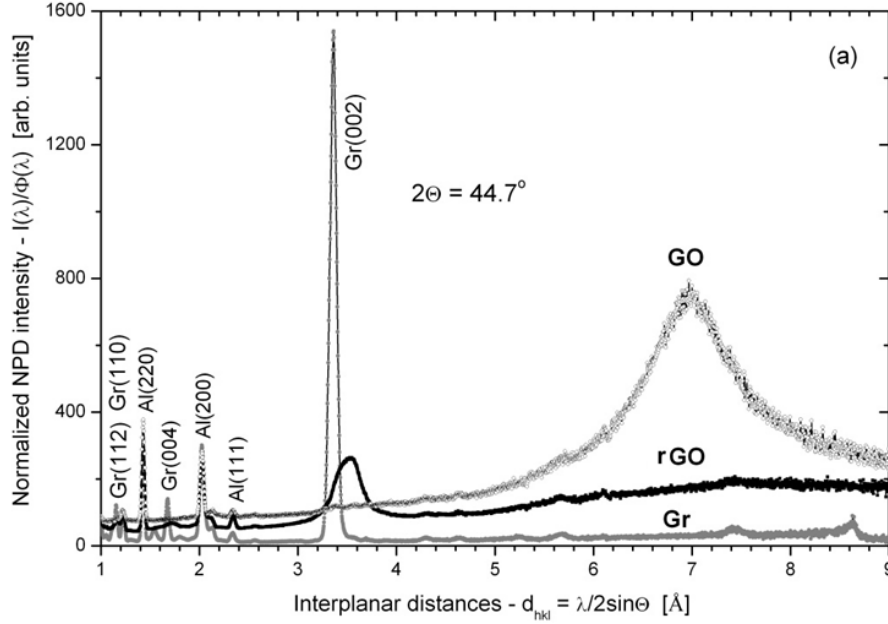


FIG. 1. NPD of spectral graphite (Gr) and Akolab products – graphene oxide (GO) and reduced graphene oxide (rGO), $T = 20$ K [3]. Gr(hkl) (black) and Al(hkl) (gray) denote characteristic diffraction peaks of spectral graphite and cryostat (alongside with sample holder) aluminum at different Miller indexes, respectively

3. General characteristics of the INS study

Typical INS TOF spectra for synthetic GO and rGO versus the incident neutrons' wavelength at low and room temperatures are shown in Fig. 2; the results were exempted from the background and carbon atoms scattering and identically normalized by the monitor counter. The temperature dependence is typical for molecular solids and is provided by considerable enhancement of multi-phonon scattering and a significant smoothing of the entire spectrum as a whole [10–12]. Both species scatter the neutrons quite intensely, indicating to be hydrogen-enriched. However, the hydrogenation is quite different in these two cases. While the hydrogen atoms in retained water play the main role in the hydrophilic GO, whose spectrum is definitely akin to that of wet graphite oxide (GrO) [13], the ones incorporated in the carbonaceous core of hydrophobic rGO are responsible in the second case. Synthetic samples were intensely dried before measuring. As for shungite carbon, the pristine sample contains a considerable amount of retained water (~ 4 wt%) [2] which can be removed by prolonged heating at 100°C under soft vacuum. The transformation of the TOF INS spectrum when passing from wet (1) to dried (2) shungite is well seen in Fig. 3. The difference between the spectra is due to released water.

Experimentally, differential cross-section is the measure of the INS intensity. It consists of two parts:

$$\frac{d^2\sigma}{d\Omega dE} = \left(\frac{d^2\sigma}{d\Omega dE} \right)_{coh} + \left(\frac{d^2\sigma}{d\Omega dE} \right)_{inc} = \sum_n \frac{(b_n^{coh})^2}{M_n} S_n^{coh}(Q, \omega) + \sum_n \frac{(b_n^{inc})^2}{M_n} S_n^{inc}(Q, \omega), \quad (1)$$

that present coherent and incoherent INS [14]. Lengths of neutron scattering, b_n^{coh} and b_n^{inc} , as well as mass of the n -th nucleus M_n , different for atoms and isotopes of the same atoms, determine the contribution of a particular nucleus towards the total INS intensity. The presence

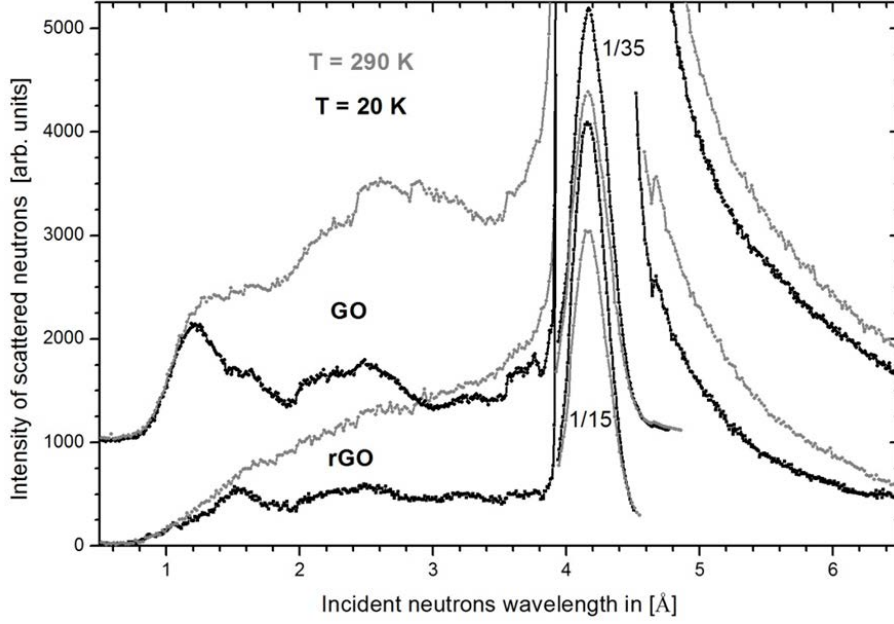


FIG. 2. Time-of-flight INS spectra of Ak-GO and Ak-rGO, recorded at $T = 20$ K (black) and 295 K (light gray) normalized by monitor counter to the same number of incident thermal neutrons flux for the wavelength region (0.8 – 6.8) Å, and exempted of background and scattering spectrum of graphite. The intensity of elastic peaks of Ak-GO and Ak-rGO spectra is 35- and 15-fold reduced, respectively [3]

of hydrogen isotope H^1 in the studied samples, for which b_n^{inc} exceeds that of other nuclei by several times, permits us to use the incoherent inelastic neutron scattering (IINS) cross-section to calculate the INS spectral intensity. In the framework of commonly used inelastic incoherent one-phonon scattering approximation, this is expressed as [14]:

$$\sigma_1^{inc}(E_i, E_f, \varphi, T) \approx \sqrt{\frac{E_f}{E_i}} \frac{\hbar |Q(E_i, E_f, \varphi)|^2}{\omega} \sum_n \frac{(b_n^{inc})^2}{M_n} \frac{\exp(-2W_n)}{1 - \exp\left(-\frac{\hbar\omega}{k_B T}\right)} G_n(\omega), \quad (2)$$

where, $Q(E_i, E_f, \varphi)$ is the neutron momentum transfer; $\omega = (E_i - E_f)$ is the neutron energy transfer; $\exp(-2W_n)$ is the Debye-Waller factor; $G_n(\omega)$ presents the n -th atom amplitude-weighted density of vibrational states (AWDVS):

$$G_n(\omega) = \sum_j [A_j^n(\omega)]^2 \delta(\omega - \omega_j). \quad (3)$$

Here, $A_j^n(\omega)$ is the n -th atom contribution into the eigenvector of the j -th phonon mode expressed as the amplitude of the n -th atom displacement at the vibrational frequency ω_j .

If the matter consists of different nuclei, each nuclear family superpositionally enters the total scattering intensity. The maximum contributions of H^1 , C^{12} , and O^{16} isotopes form a series 639 : 3.7 : 2.1, thus showing that under equal conditions, the scattering from protium atoms are 173 and 304 times stronger than that of carbon and oxygen atoms, respectively. This allows us to neglect the contribution of both heavy atomic families into the total scattering intensity thus presenting it as a mononuclear quantity :

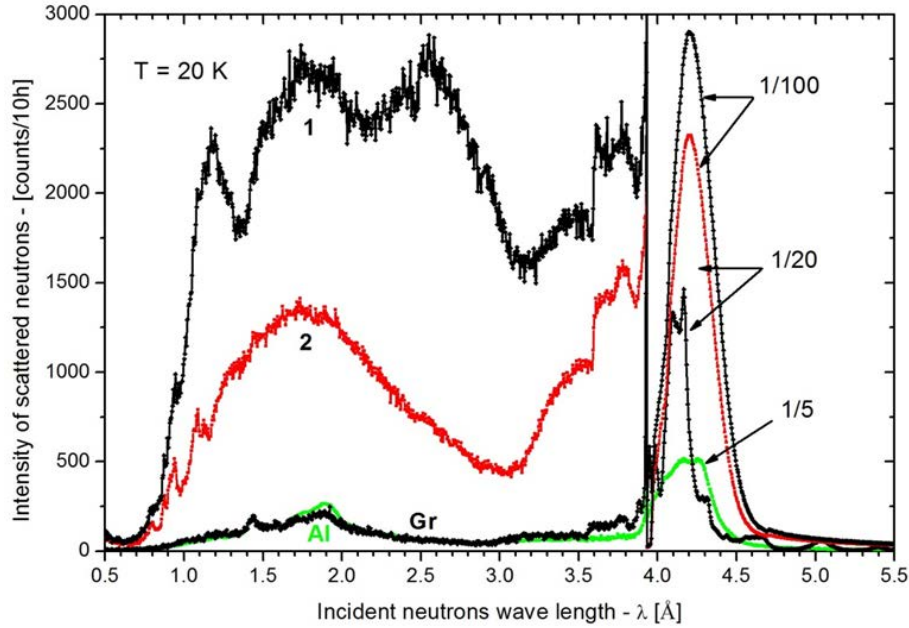


FIG. 3. Time-of-flight INS spectra from wet (1) and dried (2) shungites and spectral graphite (Gr) [1]. Curve Al presents background from Al cryostat and sample holder material. The intensity of elastic peaks is 100-fold, 20-fold and 5-fold reduced for spectra 1, 2, Gr, and background, respectively. Spectra are summarized over 15 scattering angles and normalized per 10 hours exposition time at constant power of the IBR-2 equal 1.9 MW

$$G(\omega) = \sum_n G_n(\omega), \quad (4)$$

which is the hydrogen-partitioned AWDVS. A negligible contribution of carbons atoms in the studied IINS spectra, which cannot be distinguished from background, is amply demonstrated in Fig. 3.

4. Comparative analysis of the experimental $G(\omega)$ spectra

4.1. Retained water spectra

The IINS $G(\omega)$ spectra of the studied samples form two distinct groups. The first is related to GO partners of the synthetic families as well as to the retained water in shungite carbon while the second covers spectra of dried shungite (sh-rGO) and two other synthetic rGOs. Spectra of the first group are given in Fig. 4. The water of shungite carbon (sh-water), presented in Fig. 4b, is the $G(\omega)$ image of the difference between spectra 1 (wet shungite) and 2 (dried shungite) in Fig. 3. Additionally, the NERA spectrum for *Ih* ice is given in Fig. 4a for comparison. Since the relevant GO matrices of Ak-GO and ppGO are not hydrogen-rich and consist of carbon and oxygen atoms [3,4], their IINS spectra should be attributed primarily to confined water, whose $G(\omega)$ spectra are presented in Fig. 4c and d.

As seen in the figure, evidently, the water spectra of the studied samples have much in common: all of them involve three parts characteristic for the bulk water, namely: intensity-dominant B band in the $500 - 600 \text{ cm}^{-1}$ region, less intense A and L bands in the ~ 100 and $200 - 300 \text{ cm}^{-1}$ regions. These peculiarities are undoubted reflections of similar features for bulk water (ice) spectrum and can be attributed to rotational (libration) modes (B) and hindered

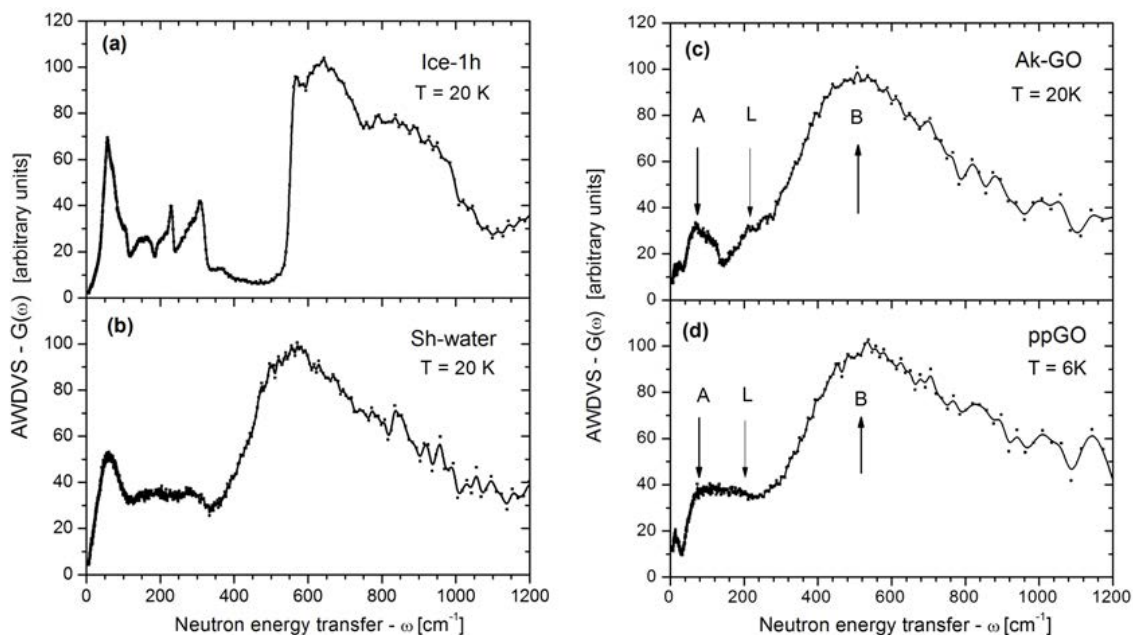


FIG. 4. Experimental amplitude-weighted density of vibrational states (AWDVS) $G(\omega)$ spectra: bulk water (I_h ice) (a) and retained water in shungite (b), Ak-GO (c) and ppGO (d)

translational mode (A and L). As it is well known [15], both the hindered translational and rotational modes are present in bulk water because of intermolecular hydrogen bonds (HB) that are formed by each water molecule surrounded by four other ones. Evidently, the configuration changes when water molecules cannot move freely because of confining geometry due to which it is quite natural to expect a visible modification of water's spectrum when passing from bulk to retained water. As shown in Fig. 4, the spectrum of retained water differs remarkably from that of the bulk compound. However, the less change is characteristic for sh-water spectrum while in the case of the Ak-GO and ppGO spectra of GO samples, the changes are so considerable that one can speak about a drastic modification of the water molecule's behavior (see detailed discussion in [3]); therewith, both latter spectra are quite similar. The observed peculiarities are a result of the confined geometries in which water is bound.

The INS study of retained water has a long history, over the course of which, among other important issues, considerable attention has been given to the topology of its confined geometries [16–20]. According to suggested classification, the sh-water spectrum should be attributed to the spectrum of water retained in pores while Ak-GO and ppGO spectra are characteristic for interlayer confinement. This conclusion is well consistent with our presentation for the sample structure. In reality, the detailed adsorption [21] and small-angle neutron scattering (SANS) [22] studies have shown that shungite carbon is a peculiar porous material with two sets of pores of < 10 nm and ~ 100 nm lateral dimensions formed by stacks (of 4 – 7 layers according to Table 2) of hydrophobic nanosize rGO sheets [23]. Conversely, laterally extended 2 – 4 layer stacks of hydrophilic GO willingly retain water between the layers in a manner similar to GrO [13].

While, as shown [13], the retained water spectrum of GrO remarkably depends on the hydration degree, a general view on $G(\omega)$ spectrum of water retained in a porous matrix [16, 18, 24, 25] does not reveal such an effect. This means that the water interaction with the inner surface of the pores is weak and the molecules can move quite freely both near the surface and

in the pore depth. The latter is supported by the sh-water spectrum which deviates negligibly from the bulk water spectrum (see Fig. 4b). Nevertheless, in spite of weak interaction, the pore topology causes the spectrum deviations that can be observed. They concern fluttering and downshift of bulk HB bends at $\sim 150 \text{ cm}^{-1}$ and HB stretches at ~ 224 and $\sim 296 \text{ cm}^{-1}$. A certain modification of bulk spectrum takes place in the region of librational modes forming a broad band in the $600 - 1200 \text{ cm}^{-1}$ region. The latter is provided with water molecule rotations around three symmetry axes whose partial contribution determines the band shape [16]. The modes conserve their dominant role in the spectra of retained water, despite being downshifted. Obviously, the spectrum three-ax partial contribution is sensitive to the pore size [16]. Thus, the downshift of the red edge of band B from 550 cm^{-1} to 320 cm^{-1} when going from the bulk water to retained one in shungite carbon highlights the shungite pore size of a few nm, which is very consistent with the adsorption and SANS data [21,22].

In contrast with the sh-water spectrum, the Ak-GO and ppGO spectra in Figs. 4c and d considerably deviate in the region of translational modes (covering both HB bending (A) and stretchings (L)) while the intense librational band B is broadened and downshifted in a similar fashion to the B band in the sh-water spectrum. As was shown in [3], the effect is caused by the reconstruction of the HB surrounding caused by the interaction with the GO substrates. Evidently, the effect depends on the chemical composition of the GO basal planes, the number of GO layers in stacks, the shape of the relevant GO sheets, the lateral size of the sheets, and other factors. Due to high variability of GO materials with regards to these parameters [7,26–30], one should expect widely variable INS spectra for samples, which was observed in the two studied cases.

4.2. rGO spectra

By analyzing IINS $G(\omega)$ spectra of rGO samples, one might conclude that a significant portion of the IINS intensity is caused by the hydrogens present on the carbonaceous skeletons. The fixation of the interlayer distance in the rGO stacks in all the studied cases from $3.4 - 3.6 \text{ \AA}$ proves that the relevant hydrogen atoms occupy the circumference (ccf) area of the rGO sheets, and as a result, the latter should be attributed to framed ccf oxyhydrides of graphene (FOHG). Similar to GOs, FOHGs are highly variable by chemical composition, size, and shape [2,7,26–30] and unsurprisingly, their properties also widely change. The latter should be naturally attributed to the IINS spectra as well. However, since the hydrogen contribution mainly provides the IINS spectral data, one should expect some similarity in the spectral behaviors. This turns out to be true, which is illustrated by Fig. 5.

Curves in the left (a – c) panels of Fig. 5 present the $G(\omega)$ spectra for the studied samples recorded with the NERA spectrometer at IBR-2 at JINR (NERA spectra below). The spectra clearly demonstrate a general similarity for the rGO bodies while their difference in details can be considered as convincing proof of the matter variability. Not being satisfied with these general statements, we decided to further scrutinize these results in greater detail. The obtained spectra are provided by the motion of two groups of atoms, namely: hydrogens located in the ccf regions and carbons of the graphene-like cores. Vibrational frequencies follow this division and allow attribution of the spectral region below 800 cm^{-1} to graphite-like modes, and above that region – to vibrations of C–H bonds mainly [3,32]. The fact that the low-frequency vibrational modes are well pronounced in the discussed spectra is associated with the ‘riding effect’ caused by the participation of hydrogen atoms displacements in the wave vectors of the carbon atom modes (see detailed discussion of the effect in [3]). In light of this, the difference in the (a) – (c) spectra may result from two facts related to changes in either the chemical composition of the ccf framing of the studied FOHG or in the graphite-like vibrational modes

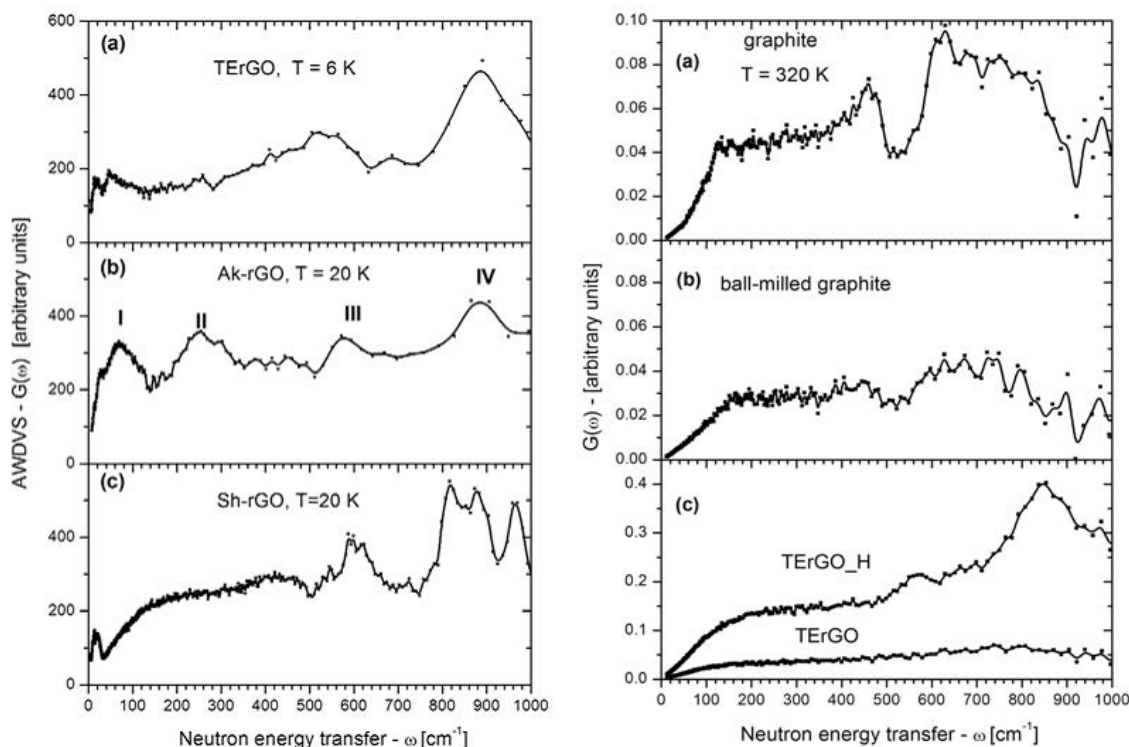


FIG. 5. Experimental amplitude-weighted density of vibrational states (AWDVS) $G(\omega)$ spectra. Left – NERA spectra: (a) TErGO [4]; (b) Ak-rGO [3]; and (c) sh-rGO [1, 2]. Right – ILL spectra: (a) graphite; (b) ball-milled nanographite; (c) thermally exfoliated rGO (TEGO) and hydrogenated TEGO (H-TEGO) recorded at the IN4 spectrometer at the HFR in the ILL [31]

of the relevant carbon cores. Such assessment of the situation has recently obtained serious support based on the study of a set of graphite-like and graphene-like samples at the thermal neutron source of the Institute of Laue and Langevin (ILL) in Grenoble [31].

Thanks to kind permission of the authors (S.R. and C.C.), $G(\omega)$ spectra in the right (a – c) panels of Fig. 5 reproduce data obtained in the ILL (ILL’s spectra below). In contrast to the NERA experimental facilities, the latter related to those at the ILL HFR allowed to fix the coherent INS from carbon atoms, providing parent (a), ball-milled (b) graphite and graphene TEGO (c) scattering to be above the background. The latter sample presents rGO obtained via the thermal exfoliation of GrO (produced from the parent graphite as well) under an inert atmosphere. Taken together, the ILL carbon data exhibit changes in the $G(\omega)$ spectra when going from macroscopic graphite to mesoscopic ball-milled graphite and nanoscopic TEGO, thus disclosing changes in the behavior of graphite-like phonon modes due to decreasing size parameters [31]. Clearly, while $G(\omega)$ spectrum of graphite (a) significantly reproduces all the features of the calculated density of states (DOS) of graphite [33] the reduced dimensions of the grains in ball-milled graphite (b) and TEGO (c) have strong effects on the dynamic properties: peaks in the density of states progressively broaden, with an increased proportion in the low frequency part of the spectrum [31].

When comparing the discussed ILL $G(\omega)$ spectra with the NERA ones present in the left panels of Fig. 5, it is easy to note that the size reduction clearly comes out in the latter when passing from TErGO to sh-rGO within the family. Comparing the spectra of the two sets, it is clearly seen that the TErGO left spectrum is extremely similar to the right spectrum of the

parent graphite while the right TEGO and TEGO-H spectra are very similar to the sh-rGO one. These findings are consistent with microsize lateral dimension of both TErGO and graphite samples while nanosize dimensions of sh-rGO as well as TEGO and TEGO-H are matched quite perfectly, thus making a convincing case for the decisive role of rGO sheet size for the appearance of the DOS of their vibrational states. As for the Ak-rGO spectrum, its changing from that of the TErGO and sh-rGO ones definitely proves the changing dimensions for the sample from the two mentioned above. However, the change is much more significant than caused by ball-milling, while revealing therein a particular change in the DOS spectrum for the carbons' vibrational states.

Considering both the NERA and ILL spectra, until now, we have mainly concentrated on the spectral range below 800 cm^{-1} . However, all the NERA spectra as well as the ILL H-TEGO spectrum (right (c) panel) show well-pronounced features above that region, quite similar to all the other spectra. As is shown in [3,32], the region is characteristic for the non-planar deformational vibrations of C–H units that mainly contribute into framing of FOHG under the presence of hydrogen. The observed transformation of the ILL TEGO and H-TEGO spectra, caused by the additional hydrogenation of TEGO, supports this conclusion directly.

5. Conclusion

The current paper presents results from an extended neutron scattering study of a set of graphene oxide (GO) and reduced graphene oxide (rGO) products of different origins. The neutron diffraction patterns confirmed that the stacking structures of all the species consisted of a number of layers of nanosize (natural product) and microsize (synthetic products) lateral dimension and the interlayer distances of $7.0 - 7.2$ and $3.4 - 3.5$ Å for GO and rGO, respectively. The performed INS study has convincingly shown that neutron scattering clearly distinguishes GO and rGO species and amply exhibits both common features and differences related to the compounds of both families. If the retained water in GOs and graphene-hydride nature of rGOs provide the commonality for dynamic properties within each compound family, the difference in the relevant sheet topology is responsible for a noticeable variability between them. This study has convincingly shown the topochemical nature of large polyvariance of both GO and rGO products.

Acknowledgements

The authors are grateful to S. Rols and C. Cavallari for supplying with the data obtained in the course of experiments at the IN4 spectrometer at the ILL HFR as well as for fruitful discussions and kind permission to use the data at our discretion.

References

- [1] Sheka E.F., Rozhkova N.N., Natkaniec K.I., Holderna-Natkaniec K. Neutron scattering study of reduced graphene oxide of natural origin. *JETP Lett.*, 2014, **99**, P. 650–655.
- [2] Sheka E.F., Rozhkova N.N., Holderna-Natkaniec K., Natkaniec I. Nanoscale reduced-graphene-oxide origin of shungite in light of neutron scattering. *Nanosystems: Phys. Chem. Math.*, 2014, **5** (5), P. 659–676.
- [3] Natkaniec I., Sheka E.F., et al. Computationally supported neutron scattering study of parent and chemically reduced graphene oxide. *J. Phys. Chem. C*, 2015, **119** (32), P. 18650–18662.
- [4] Sheka E.F., Natkaniec I., Mel'nikov V.P., Druzicki K. *Nanosystems: Phys. Chem. Math.*, 2015, **6** (3), P. 378–393.
- [5] AkKoLab LLC, URL: www.akkolab.ru.
- [6] Tkachev S.V., Buslayeva E.Yu., et al. Reduced graphene oxide. *Inorg. Mater.*, 2012, **48**, P. 796–802.
- [7] Sheka E.F., Golubev E.A. About technical graphene – reduced oxide graphene- and shungite – its natural analogue. *Zn. Tehn. Fiz.*, 2016, **86** (submitted).

- [8] Natkaniec I., Chudoba D., et al. Parameters of the NERA spectrometer for cold and thermal moderators of the IBR-2 pulsed reactor. *J.Phys.: Conf. Series*, 2014, **554**, 012002.
- [9] Opalev S.V., Belenkov E.A. Experimental study of changing graphite structure under milling. (in Russ.) *Izvestiya Chelyabinskogo Nauchnogo Centra*, 2004, **3**, P. 27–30.
- [10] Bokhenkov E.L., Natkaniec I., Sheka E.F. Determination of density of phonon states in a naphthalene crystal on basis of inelastic incoherent neutron scattering. *Zh. Exp. Teor. Fiz.*, 1976, **70**, P. 1027–1043.
- [11] Kolesnikov A.I., Bokhenkov E.L., Sheka E.F. Multiphonon coherent scattering of neutrons in a naphthalene crystal. *JETP*, 1984, **57**, P. 1273–1278.
- [12] Johnson M.R., Parlinski K., Natkaniec I., Hudson S. Ab initio calculations and INS measurements of phonons and molecular vibrations in a model peptide compound – urea. *Chem. Phys.*, 2003, **291**, P. 53–60.
- [13] Buchsteiner A., Lerf A., Pieper J. Water dynamics in graphite oxide investigated with neutron scattering. *J. Phys. Chem. B*, 2006, **110**, P. 22328–22338
- [14] Marshall W., Lovesey S.W. *Theory of Thermal Neutron Scattering*, Oxford, 1971.
- [15] Finney J.L. Water? What's so special about it? *Phil. Trans. R. Soc. Lond. B*, 2004, **359**, P. 1145–1165.
- [16] Crupi V., Majolino D., Migliardo P., Venuti V. Neutron scattering study and dynamic properties of hydrogen-bonded liquids in mesoscopic confinement. 1. The water case. *J. Phys. Chem. B*, 2002, **106**, P. 10884–10894.
- [17] Kolesnikov A.I., Zanotti J.-M., Loong C.-K., Thiyagarajan P. Anomalously soft dynamics of water in a nanotube: a revelation of nanoscale confinement. *Phys. Rev. Lett.*, 2004, **93**, 035503.
- [18] Corsaro C., Crupi, V., et al. Inelastic neutron scattering study of water in hydrated lta-type zeolites. *J. Phys. Chem. A*, 2006, **110**, P. 1190–1195.
- [19] Chen S.-H., Loong C.-K. Neutron scattering investigations of proton dynamics of water and hydroxyl species in confined geometries. *Nucl. Eng. Techn.*, 2006, **38**, P. 201–224.
- [20] Bertrand C.E., Zhang Y., Chen S.-H. Deeply-cooled water under strong confinement: neutron scattering investigations and the liquid-liquid critical point hypothesis. *Phys. Chem. Chem. Phys.*, 2013, **15**, P. 721–745.
- [21] Rozhkova N.N., Emel'yanova G.I., et al. From stable aqueous dispersion of carbon nanoparticles to the clusters of metastable Shungite carbon. *Glass Phys. Chem.*, 2011, **37**, P. 613–618.
- [22] Avdeev M.V., Tropin T.V., et al. Pore structures in shungites as revealed by small-angle neutron scattering. *Carbon*, 2006, **44**, P. 954–961.
- [23] Sheka E.F., Rozhkova N.N. Shungite as the natural pantry of nanoscale reduced graphene oxide. *Int. J. Smart Nano Mater.*, 2014, **5**, P. 1–16.
- [24] Hall P.G., Pidduck A., Wright C.J. Inelastic neutron scattering by water adsorbed on silica. *J. Colloid. Interface Sci.*, 1981, **79**, P. 339–349.
- [25] Sheka E.F., Khavryutchenko V.D., Markichev I.V. Technological polymorphism of disperse amorphous silicas: inelastic neutron scattering and computer modelling. *Russ. Chem. Rev.*, 1995, **64**, P. 389–414.
- [26] Kuila T., Bose S., et al. Chemical functionalization of graphene and its applications. *Progr. Mater. Sci.*, 2012, **57**, P. 1061–1105.
- [27] Luo J., Kim J., Huang J. Material processing of chemically modified graphene: Some challenges and solutions. *J. Acc. Chem. Res.*, 2013, **46**, P. 2225–2234.
- [28] Chua C.K., Pumera M. Chemical reduction of graphene oxide: a synthetic chemistry viewpoint. *Chem. Soc. Rev.*, 2014, **43**, P. 291–312.
- [29] Zhao J., Liu L., Li F. *Graphene Oxide: Physics and Applications*. Springer, 2015.
- [30] Kumar P.V., Bardhan N.M., et al. Scalable enhancement of graphene oxide properties by thermally driven phase transformation. *Nature Chem.*, 2014, **6**, P. 151–158.
- [31] Cavallari C., Pontiroli D., et al. Hydrogen on graphene investigated by inelastic neutron scattering. *J. Phys. Conf. Series*, 2014, **554**, 012009.
- [32] Druzbecki K., Natkaniec I. Vibrational properties of water retained in graphene oxide. *Chem. Phys. Lett.*, 2014, **600**, P. 106–111.
- [33] Bousige C., Rols S., et al. Lattice dynamics of a rotor-stator molecular crystal: fullerene-cubane C₆₀·C₈H₈. *Phys. Rev. B*, 2010, **82**, 195413.

Etching of wrinkled graphene oxide films in noble gas atmosphere under UV irradiation

A. E. Aleksenskii, S. P. Vul', A. T. Dideikin, V. I. Sakharov,
I. T. Serenkov, M. K. Rabchinskii, V. V. Afrosimov

Ioffe Institute, St. Petersburg, Russia

Maxrabchinskii@gmail.com

PACS 68.65.Pq

DOI 10.17586/2220-8054-2016-7-1-81-86

We have studied the process of UV reduction of wrinkled graphene oxide films, deposited on silicon substrate from ethanol suspension. In order to avoid destruction of graphene oxide via ozone formation from ambient air, samples were protected by argon atmosphere during UV irradiation. Using the analysis of back scattering spectra for medium energy ions, we have found that the UV irradiation mediated reduction process produced significantly decreased carbon content on the substrate surface. The decrease in the carbon content was accompanied by a smoothing of the films during reduction to graphene. We suppose that the observed effect is related to the oxidation of carbon atoms in the graphene scaffold of graphene oxide to carbon monoxide or dioxide by the oxygen from the graphene oxide (GO) itself. One has to consider this when developing a process for the preparation of graphene films using the UV-mediated reduction of graphene oxide.

Keywords: graphene oxide, reduction, UV irradiation, graphene films.

Received: 20 November 2015

1. Introduction

The reduction of graphene oxide is one of the most promising ways to form large scale conducting transparent films for a variety of applications, including solar cells, displays as well as LED light sources and field emitters [1,2]. Today, effective methods for preparation of high quality large domain graphene oxide in the form of aqueous suspension are ready for industrial application [3]. The only problem still remains is to develop an effective and flexible method for the reduction of graphene oxide (GO) into graphene which obviates the need for high temperature or aggressive reducing agents, such as hydrazine thus avoiding damage to and contamination of the formed graphene film [4]. Using UV irradiation could be a promising approach for the mild preparation of graphene films on a broad variety of substrates [5,6]. Due to relatively low binding energy of epoxy and hydroxyl groups in GO, excitation of the electron structure, resulting from absorption of UV photons is able to release these moieties from the graphene sheet in the absence of a reducing agent or heating. It is also important for future applications of GO/graphene films that UV irradiation is compatible with photolithography techniques currently available in the electronic industry.

Although the UV method of GO reduction does not require heating of the substrate with deposited GO film or exposing it to active chemical reagents, the probability of incidental photochemical reactions with ambient atmosphere or functional groups present in the GO should be considered when devising a practical UV reduction of GO. Thus, it is reasonable to suppose that the results of UV irradiation could be dependent upon the morphology and the chemical composition of GO. One should also take into account the fact that GO itself does not possess the determined ratio between C–O–C and C–OH groups. The composition of the continuous GO sheet (neglecting the edge) can be described by following formula: $(C_2O)_x(COH)_{(x-1)}$ where

$0 < x < 1$. That's why the samples of GO prepared under different oxidation conditions will possess varying compositions and thus abilities for reduction.

Recently, we have developed the method for preparation the large domain single layer GO sheets with perfect crystalline structure [7]. We have also demonstrated the preparation of single layer GO films on silicon substrates as well as the graphene films obtained by thermal reduction of GO films under a hydrogen atmosphere. However, it was later shown that the applied method of reduction provided partially hydrogenated graphene and consequently, did not allow us to obtain products with sheet resistance less than several $k\Omega/\text{sq}$. The reliable method of *in vacuo* thermal treatment [8] requires temperatures exceeding $900\text{ }^\circ\text{C}$, which makes it incompatible with a majority of potential substrates, including organic polymers. In our search for a more effective and flexible method for the preparation of highly conductive graphene layers, we have chosen the UV irradiation of GO films on the surface of silicon substrates.

The goal of the present work was to study the process of preparation the graphene films using UV irradiation for reduction of GO sheets on silicon substrates.

2. Experimental

Graphite Oxide aqueous suspension was prepared by enhanced Hummers method [9] from natural crystalline graphite. In order to remove small particles and residual graphite, the obtained suspension was centrifuged at 1500 RCF, forming 4 wt% solution, which was subsequently diluted by ethanol at ratio 1:500 to obtain the final suspension, suitable for deposition on substrates. Size distribution of Graphite Oxide particles in initial water and final ethanol suspensions was measured by Optical Diffraction method, using Malvern Mastersizer 2000. Preparation of several layer graphene films on the surface of silicon substrates included deposition the droplets of ethanol suspension to the horizontally-positioned substrates and subsequent drying in air at room temperature. Due to excellent wettability of silicon by ethanol suspension, the surface of each sample was fully covered thus forming a continuous GO film after drying without any additional measures like rotation of the substrate. We assumed that applying the freely-spreading ethanol suspension on a silicon surface will allow us to avoid the use of the complicated Langmuir – Blodgett technique for forming several layer GO films. Graphite Oxide films, formed on silicon wafer, were analyzed by scanning electron microscopy with GEOL GSM3001F instrument.

As a source of UV irradiation, we applied the 30 W deuterium lamp with quartz window with wavelengths ranging from 186 – 360 nm. Samples were placed at 5 mm behind the quartz window of lamp in the quartz cylinder with pure argon gas flow at normal pressure. Noble gas is necessary in order to avoid the generation of ozone by UV irradiation from ambient oxygen and therefore prevent damage to the reducing graphene film by the reaction with active oxygen species.

Argon gas also played role of coolant to avoid significant increasing of sample temperature under irradiation. Adjusted gas flow was at 150 cm^3 per minute and the duration of UV irradiation was 1 hour.

Reduction of Graphite Oxide films under UV irradiation was analyzed using: UV-Vis spectroscopy, performed on a Shimadzu UV 2450; IR-spectroscopy, performed on Infracum 08 FTIR spectrometer with attenuation total reflectance attachment, and by analysis and reciprocal modeling of reverse backscattering spectra of medium energy ions (RBS). Medium Energy Ion Spectrometry combined with ion channeling method also provided possibility to estimate the element (C,O) amounts. In our previous work [10], we have demonstrated the usability and high efficiency of applying RBS for observing the structure and composition of atomically thin films on the surface of perfect crystals as a result of the channeling effect.

3. Results and discussion

Figure 1 demonstrates the size distribution of separate graphite oxide platelets in prepared suspension, measured by optical diffraction method (OD), and structure of formed GO film on silicon substrate. One sees, that the average size of graphite oxide particles is about $50 \mu\text{m}$, much larger than that usually obtained using the common Hummers method [11]. This is rather important, especially in the case of following formation of large scale conducting transparent films, due to the decreasing of degree of platelets boundaries influence on optical and electronic properties. A SEM image of the prepared graphite oxide film on silicon wafer, presented at Fig. 1b demonstrates presence of wrinkles on GO flakes deposited onto the silicon surface. However, the presence of wrinkles is unlikely to contribute to the overall resistance of reduced graphene film because, as estimated from the SEM image, the curative radius in each wrinkle is incomparable to the thickness of a single layer of graphene film.

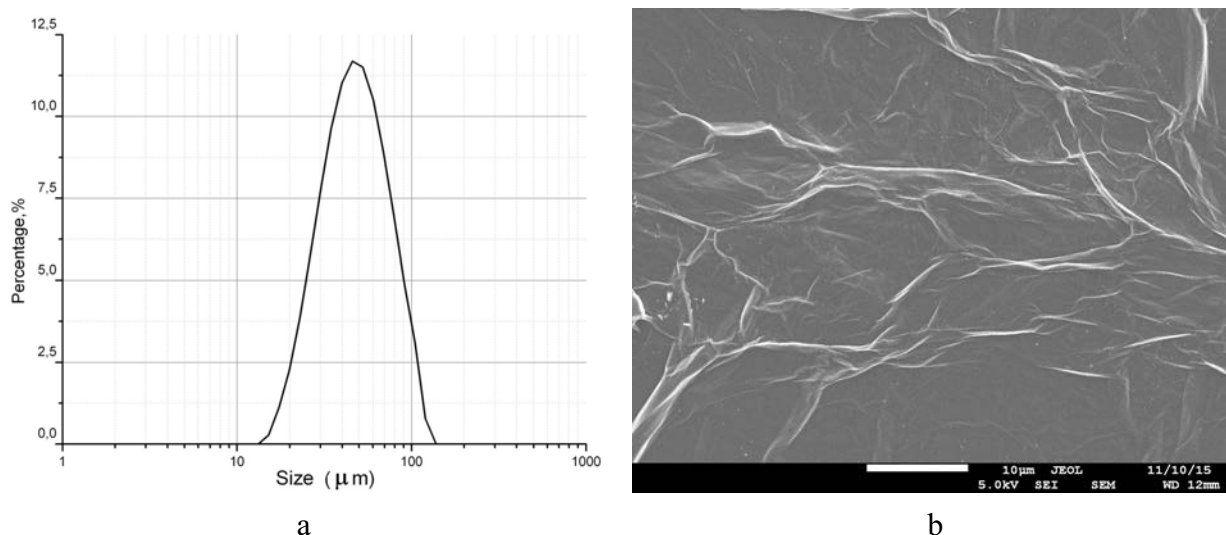


FIG. 1. a) size distribution of GO particles in aqueous suspension; b) SEM image of the GO film deposited on the surface of silicon substrate

Reduction of the graphite oxide film was confirmed by UV-Vis spectroscopy and FTIR spectroscopy, which are presented in Fig. 2. The UV-Vis spectrum of the initial graphite oxide contains two peaks – at 300 nm, attributed to $n-\pi^*$ transitions in $\text{C}=\text{O}$, and 230 nm attributed to $\pi-\pi^*$ transitions of $\text{C}=\text{C}$ in amorphous carbon system [12] – and absence of absorption at wavelengths from 500 to 1000 nm. However, the UV-Vis spectrum of graphite oxide film after 1 hour UV irradiation has specific changes, in particular, the peak at 300 nm has disappeared, the peak at 230 nm has shifted to 260 nm, and absorption at wavelengths from 500 to 1000 nm have significantly increased, which confirms reduction of the sample. In order to prove this fact, we measured IR spectra of initial graphite oxide and graphite oxide film after 1 hour of UV irradiation. The IR spectrum of the initial GO has several distinguishing features, determining presence of functional groups: region at $3000 - 3700 \text{ cm}^{-1}$, corresponding to hydroxyl groups and water molecule deformations, peaks at 1720 cm^{-1} (carboxyl), 1620 cm^{-1} (interlayer water), 1040 and 1365 cm^{-1} (hydroxyl groups), 1160 cm^{-1} and shoulder at 1220 cm^{-1} , corresponding to epoxide groups [13,14]. After treatment, the IR spectrum has significant changes – absorption at $3000 - 3700 \text{ cm}^{-1}$ (hydroxyls, water and carboxyl) are significantly decreased, the peak for interlayer water (1620 cm^{-1}) also disappears and peaks at 1580 and 1430 cm^{-1} , corresponding to $\text{C}=\text{C}$ and $\text{C}-\text{C}$ vibrations, increases. However, peaks that correspond to epoxide and hydroxyl

functional groups still remain almost unchanged. This observation can be explained by the fact that the formed film has a several-layered structure and reduction of the film by UV irradiation occurs only for a finite number of the top layers. During reduction, light absorption of these uppermost layers significantly increases due to the transition from GO to graphene electronic structure. Consequently, the intensity of UV radiation reaching the bottom layers isn't enough to reduce them. As a result, the underlying layers of GO still remain unreduced and maintain their contribution to the averaged data of the FTIR spectrum.

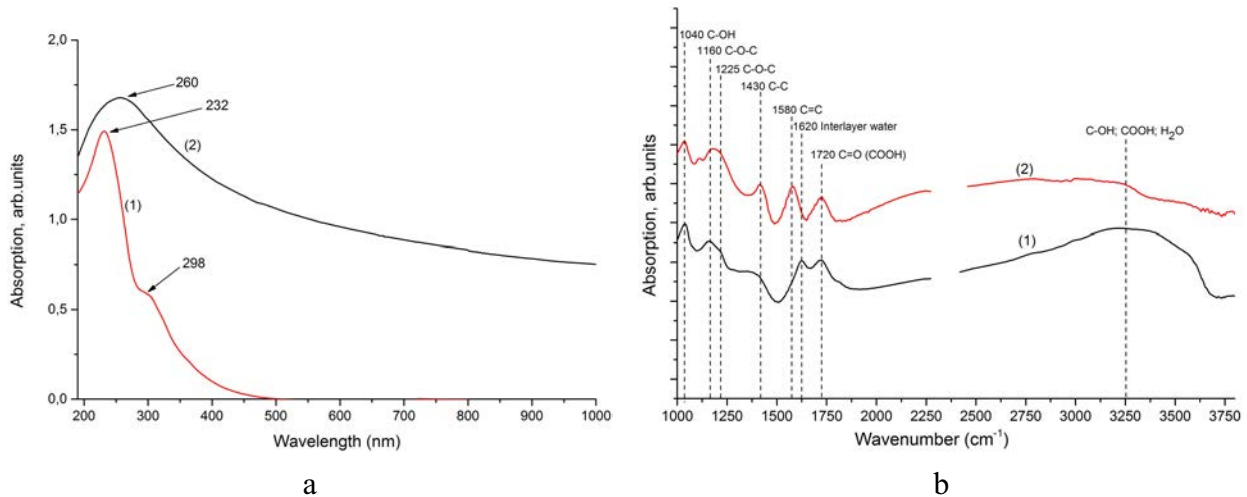


FIG. 2. UV-Vis spectra (a) and IR spectra (b) of initial graphite oxide (1) and reduced graphite oxide (2)

These results are in good agreement with data, reported in [15]. Actually, the energy of UV photons of wavelengths ranging from 186 – 360 nm is enough to overcome the energy barrier for the removal of OH as well as CO groups from the surface of graphene sheet.

For further investigation of structural and chemical changes during reduction process, we utilized Medium Energy Ion Spectrometry with analysis of energy spectra of 96 keV protons, back scattered to 120° from the structure under investigation (silicon single crystal having a natural SiO₂ surface layer of about 1 nm thickness on which GO layer was deposited).

The obtained spectra are presented in Fig. 3. Curve 1 corresponds to the GO film before UV irradiation, while curve 2 corresponds to the film after UV irradiation. The measurements were performed in channeling regime and therefore the signal from bulk silicon was suppressed for about 30 times compared to that in ‘random’ orientation regime. The level of bulk silicon signal is depicted in Fig. 3 by dashed curve. On this pedestal there are three peaks: carbon (73 – 76 keV), oxygen (77 – 80 keV) and silicon (83 – 86 keV), corresponding to amorphous phases of structure. The ion back scattering yield from these phases is insensitive to measurement regime (channeling or ‘random’). Note that besides signal from Si atoms of amorphous SiO₂ layer, the silicon peak contains that from Si atoms, forming so-called surface peak.

Comparison of the carbon peaks in curves 1 and 2 shows a 3-fold carbon content decrease, whereas the corresponding value for oxygen is only 1.2-fold. This is because the basic part of oxygen belongs to SiO₂ layer and is therefore insensitive to UV radiation.

Comparison of the carbon peaks obtained from the films before and after UV irradiation demonstrates the noticeable etching the GO film simultaneously with its reduction. The observed effect can be explained by the fact that graphene oxide is an intermediate state of carbon oxidation. The functional groups that terminate the dangling π -bonds on the surface of graphene

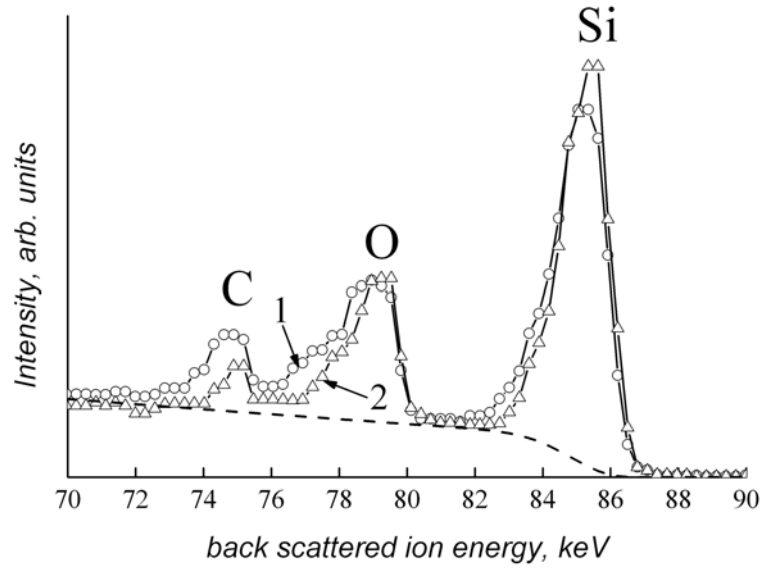
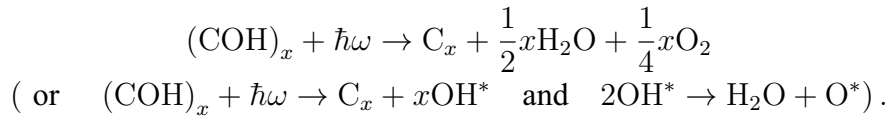
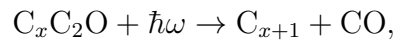


FIG. 3. The energy spectra of H^+ ions having the initial energy of 96 keV back scattered from GO deposited on Si single crystal before (1) and after (2) the UV irradiation

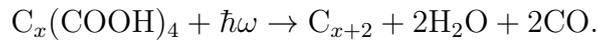
sheet like hydroxyl (OH) and epoxy (C_2O) can be simply removed by excitation in the following process:



As it was demonstrated in [16], this path is related to the extraordinary strength of σ -bonds between carbon atoms inside the graphene plane. The presence of wrinkles or edges can significantly affect the hardness of C–C bonds and give rise for probability of alternative paths for the process in GO films under UV irradiation:



or even



The observed smoothing of the carbon film under UV irradiation shows that the process related to recession of carbon from the graphene film takes place specifically at wrinkles formed by GO during the deposition process.

4. Conclusions

We have demonstrated the successful reduction of GO films by UV irradiation in argon gas atmosphere on silicon substrates at room temperature. We have also observed the effect of smoothing the wrinkled GO films accompanied by the noticeable decrease in the carbon content of the GO film subsequent to UV irradiation. The probable explanation of the observed etching of wrinkled GO films is in further oxidation of the graphene plane of GO by its own oxygen with formation of carbon monoxide or carbon dioxide gases under UV excitation. This effect can be applied for simultaneous smoothing the graphene films while preparation them for optical and electronic applications. It should also be noted that the UV reduction of GO can be used for the preparation of 3D graphene for energy storage of electrochemical applications.

Acknowledgements

M. K. Rabchinsky and A. T. Dideikin are grateful to RFBR (grant No. 15-02-05153) for financial support.

References

- [1] Huang X., Yin Z., et al. Graphene-Based Materials: Synthesis, Characterization, Properties, and Applications. *Small*, 2011, **7** (14), P. 1876–1902.
- [2] Bonaccorso F., Sun Z., Hasan T., Ferrari A.C. Graphene photonics and optoelectronics. *Nature Photonics*, 2010, **4**, P. 611–622.
- [3] Loh K.P., Bao Q., Eda G., Chhowalla M. Graphene oxide as a chemically tunable platform for optical applications. *Nature Chemistry*, 2010, **2**, P. 1015–1024
- [4] Park S., Hu Y., et al. Chemical structures of hydrazine-treated graphene oxide and generation of aromatic nitrogen doping. *Nature Commun.*, 2012, **3**, article number 638. DOI: 10.1038/ncomms1643.
- [5] Gengler Regis Y.N., Badali D.S., et al. Revealing the ultrafast process behind the photoreduction of graphene oxide. *Nature Commun.*, 2013, **4**, article number 2560. DOI: 10.1038/ncomms3560.
- [6] Xue Yuhua, Zhu Lin, et al. Multiscale patterning of graphene oxide and reduced graphene oxide for flexible supercapacitors. *Carbon*, 2015, **92**, P. 305–310.
- [7] Aleksenskii A.E., Brunkov P.N., et al. Single Layer Graphene Oxide Films on a Silicon Surface. *Technical Physics*, 2013, **58** (11), P. 1614–1618.
- [8] Akhavan O. The effect of heat treatment on formation of graphene thin films from graphene oxide nanosheets. *Carbon*, 2010, **48**, P. 509–519.
- [9] Dideikin A., Aleksenskiy A.E., et al. Monolayer graphene from graphite oxide. *Diamond & Related Mater.*, 2011, **20**, P. 105–108.
- [10] Afrosimov V.V., Dideikin A.T., et al. *Nanosystems: Phys., Chem., Math.*, 2014, **5** (1), P. 113–116.
- [11] Zhu Y., Cai W., et al. Transparent self-assembled films of reduced graphene oxide platelets. *Appl. Phys. Lett.*, 2009, **95**, P. 103–104.
- [12] Kumar P.V., Bardhan N.M., et al. Scalable enhancement of graphene oxide properties by thermally driven phase transformation. *Nature Chemistry*, 2014, **6**, P. 151–158.
- [13] Acik M., Lee G., et al. The Role of Oxygen during Thermal Reduction of Graphene Oxide Studied by Infrared Absorption Spectroscopy. *J. Phys. Chem. C*, 2011, **115**, P. 19761–19781.
- [14] Lee D.W., De Los Santos Valladares L., et al. The Structure of Graphite Oxide: Investigation of Its Surface Chemical Groups. *J. Phys. Chem. B*, 2010, **114**, P. 5723–5728.
- [15] Eda G., Fanchini G., Chhowalla M.. Large - area ultrathin films of reduced graphene oxide as a transparent and flexible electronic material. *Nature Nanotechnology*, 2008, **3**, P. 270–274.
- [16] Cote L.J., Cruz-Silva R., Huang J. Flash Reduction and Patterning of Graphite Oxide and Its Polymer Composite. *J. Am. Chem. Soc.*, 2009, **131**, P. 11027–11032.

The divacancy V_2 and $V - C = C - V$ configurations on the diamond surface: quantum-chemical simulation

O. Yu. Ananina¹, N. A. Lvova², E. V. Severina¹

¹Zaporizhzhya National University, Physical Faculty, Zaporizhzhya, Ukraine

²Technological Institute for Superhard and Novel Carbon Materials, Troitsk, Moscow, Russia
ananyina@znu.edu.ua, nlvova@tisnum.ru, sev.l@mail.ru

PACS 68.43.-h, 81.05.ug, 03.67.Lx

DOI 10.17586/2220-8054-2016-7-1-87-92

This paper presents the results for the quantum-chemical modeling of V_2 and $V-C=C-V$ divacancy defects configurations on the $C(111)-2\times 1$ diamond surface. We provide calculations for the geometric, electronic, and energy characteristics for these configurations. Energy characteristics of water and hydrogen molecule adsorption on the surface with divacancy defects are estimated. The presence of V_2 and $V-C=C-V$ divacancy defects are shown to change the mechanism and energy characteristics of molecular adsorption.

Keywords: diamond surface, divacancy defect, electronic properties, adsorption properties.

Received: 20 November 2015

1. Introduction

The properties of diamond are largely determined by its defects, both from its formation and arising during subsequent processing, ion implantation [1]. Vacancy defects are among the most important ones, as they not only have a significant impact on diamond growth, but also can change its optical and electronic properties. When a defect is formed, certain effects such as surface reconstruction, local re-hybridization of electron states, or even binding and bond rupture of the surface atoms may significantly affect the energy and the dynamics of heterogeneous chemical reactions and greatly complicate the existing models of adsorption and desorption. Experimental and theoretical works have mainly been devoted to studying the stability and influence of the vacancy and divacancy defects on the bulk properties of diamonds. Therefore, it is vital to have a comprehensive study of surface defects at the atomic level. Surface point defects can significantly modify the properties of dielectrics and wide-band gap semiconductors. However, it is not always possible to clearly define the structure and properties of the defects based on experimental data. In such a situation, quantum-chemical modeling is of particular interest.

Single vacancies and divacancies on the $C(100)-2\times 1$ diamond surface have been previously studied using density functional theory (DFT) calculations [2]. Calculations indicated that the formation energy of a monovacancy is 2.97 eV, whereas that of a divacancy is 1.28 eV. A theoretical paper [3] found a metastable monovacancy state, and provided research on the adsorption of atomic and molecular hydrogen in the vicinity of the vacancy defects. The results for quantum-chemical calculations of structural, electronic, and energy characteristics of the water chemisorption on the $C(100)-2\times 1$ diamond surface with a vacancy defect are outlined in [4]. The authors of [5] used DFT methods to study the impact of vacancies on the structure of diamond nanoparticles and indicate graphitization of the area around the vacancy. In [6], results were presented for the study of bulk defects in diamond grown by chemical vapor deposition (CVD), using optical absorption, luminescence, and electron spin resonance techniques. The vacancy was shown to lead to the appearance of some permitted levels in the band gap

of diamond ($E_c - 3.2$ eV) and optical absorption, 1.63 eV for vacancies and 2.543 eV for divacancies.

V–C=C–V divacancies in bulk diamond have been investigated in [7] by DFT calculation. An isolated V–C=C–V divacancy was found to be very stable and was separated by a high barrier of 5 eV from the divacancy of two missing adjacent carbons, V_2 . The appearance of these defects on the surface of radiation-damaged diamond is accompanied by the formation of graphitic sp^2 -bonds in the material [1, 5]. Nevertheless, the question of the sp^2 -bond formation effect on the properties of radiation-damaged diamond still remains open.

This paper presents results for calculations of the geometric, electronic, and energy characteristics, adsorption properties of V_2 and V–C=C–V divacancy defects on the diamond (111)– 2×1 surface.

We used a $C_{123}H_{79}$ cluster that reproduces a clean reconstructed C(111)– 2×1 surface and comprises six atomic layers. The dangling bonds of carbon atoms at the edge of the cluster, spreading into volume, were saturated with hydrogen atoms (a monovalent pseudoatom model). Quantum-chemical simulation was performed using the quantum chemical methods: semiempirical – PM6 (MOPAC software package) and Hartree-Fock *ab initio* (PC GAMESS software package). Geometry optimization was carried out by finding the minimum of the total energy by a gradient method. *Ab initio* calculations were performed using RHF approximation which does not lead to the ground state of the system, so the results are estimates. The aim of this work is a comparative calculation of electronic and energy characteristics of divacancy defect configurations on the C(111)– 2×1 surface, as well as energy characteristics of water and hydrogen molecule adsorption on a surface containing divacancy defects. The methodology for this calculation is described in detail in [3, 4].

2. Clean reconstructed C(111)– 2×1 surface

The reconstruction of a clean C(111) diamond surface was found to be in agreement with the model of π -bound Pandey chains [8]. Fig. 1a shows a model of the C(111)– 2×1 surface with Pandey chains (top view). The length of the bonds between the atoms in the chain on the surface is the same for all atoms (1.47 Å), the distance between the chains is 4.37 Å. This leads to a weaker interaction between the atoms of different chains than in the middle of the same chain. The length of the bonds between the atoms in the second-layer chain is 1.56 Å [2].

On the (111) diamond surface, no significant charge sharing between the atoms of the first and second layers is observed. On the surface chain atoms, there is a negative charge $-(0.010 - 0.018)e$, on the second-layer chain atoms there is a positive charge $+(0.008 - 0.016)e$. The bond orders between the carbon atoms in the surface chains are $\sim (1.080 - 1.106)$, in the second-layer rows $\sim (0.952 - 0.966)$, the valence is 3.947 – 3.966.

The orbitals of the atoms in the surface chain have a hybridization close to an $sp^2 + p$ type: 3 low-energy sp^2 -hybrid orbitals with a high s -component form covalent σ -bonds with the adjacent atoms, and a practically unhybridized high-energy p -orbital oriented perpendicular to the plane of the surface is involved in forming a delocalized electron cloud as a result of orbital overlap with first-layer neighboring atoms. Thus, the atoms in the surface chains are bound to each other by π -bonds with the presence of $\pi - \pi$ conjugation. The atoms in the second-layer chains have sp^3 -type hybridization, orbitals with a high s -component form 4 covalent σ -bonds with the neighboring atoms, similar in characteristics to the bonds in a bulk diamond structure.

3. V_2 divacancy defect and V–C=C–V defect on the C(111)– 2×1 surface

A V_2 divacancy defect on a C(111)– 2×1 surface was simulated by the removal of two carbon atoms of the neighboring nodes of the cluster and the subsequent geometry optimization.

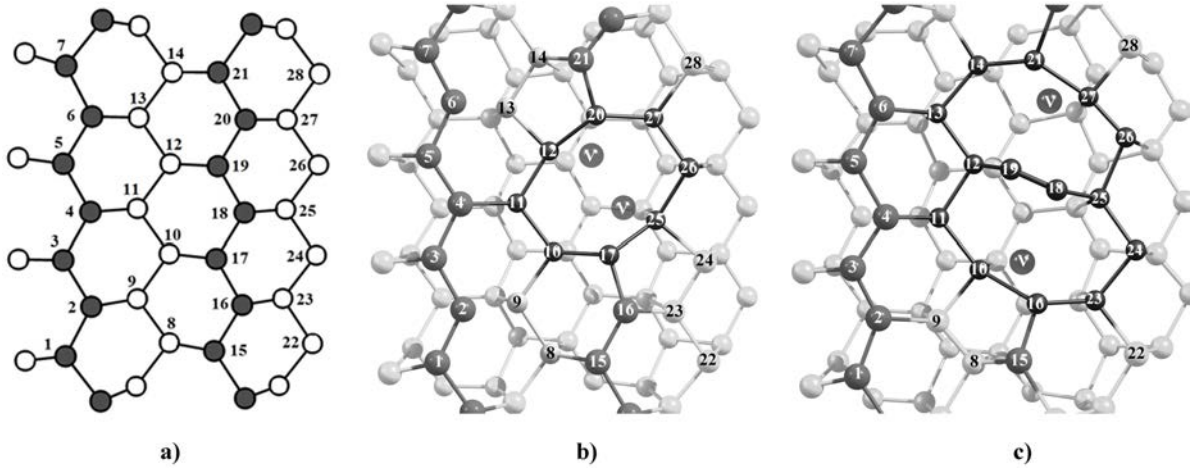


FIG. 1. Fragment of a cluster simulating the C(111)- 2×1 surface: a) a model of a reconstructed C(111)- 2×1 surface with Pandey chains; b) with a V_2 defect, A-configuration; c) with a $V-C=C-V$ defect. Light-gray color indicates the carbon atoms of the cluster, dark-gray indicates the upper surface Pandey chain atoms, black highlights the atoms in the defect, V are vacancies in the upper surface Pandey chain

The search for equilibrium defect geometries was implemented by varying the positions of the atoms surrounding the divacancy within the first and the second atomic layer in directions perpendicular to and along the surface.

We built divacancy models where the vacancies were located in various surface chains. So, we considered the following configurations:

A – the vacancies are located in the neighboring 18 and 19 nodes of the top Pandey chain (V18 and V19); B – in the neighboring nodes of the lower Pandey chain V11 and V12; C – V11 and V in the third layer; D – in the nodes of the upper and lower chains V19 and V12.

Of all the configurations under investigation, the A-configuration had the minimum energy (Fig. 1b). In the B-configuration, the total energy of the surface was 1.67 eV higher, in the C-configuration it was higher by 5.69 eV, and in the D-configuration – by 3.32 eV. Calculation of the activation energy of a V_2 defect migration from the D-configuration to the A-configuration resulted in a value of ~ 4.47 eV.

Now, we consider V_2 vacancy defects in configuration A on the C(111)- 2×1 surface (Fig. 1b). When a divacancy appears, it restructures the surface area around the divacancy, which mainly affects the atoms of the two surface layers, that is, the atoms of the upper and lower Pandey chains. There were two new bonds C12–C20 and C17–C25 between the atoms of the upper and lower chains. It can be assumed that there is greater mobility for atoms in the chains compared to the deeper layers of the surface and the absence of dangling bonds in the A-configuration divacancy which is the cause for the minimum value of the total energy for this configuration.

The lengths of the C–C bonds on the V_2 divacancy perimeter are $d = 1.51 - 1.58$ Å. The C20–C21 and C17–C16 double bonds have an order of 1.43 and a length of $d = 1.41$ Å. There is a charge distribution in such a way that a $-(0.38 - 0.42)e$ negative charge is localized on the C20 and C17 atoms, respectively, and a positive one $+(0.17 - 0.25)e$ is localized on the neighboring atoms. There has been no change in the orbital hybridization of atoms around V_2 : the upper chain atoms C16 ... C21 are in $sp^2 + p$ hybrid state, while the lower chain atoms are

in sp^3 -hybridization. However, both the charge distribution between the atoms and the existence of high-energy p -orbitals in the C17 and C20 atoms are involved in the formation of π -bonds with the C16 and C21 atoms positions these atoms as potential adsorption centers.

When we simulated the $V-C=C-V$ defect, we considered the configurations in which: carbon atoms C19=C18 and vacancies V_{20} and V_{17} are in the upper surface chain nodes (Fig. 1c); carbon atoms C11=C12 and vacancies V_{10} and V_{13} are in the lower surface chain nodes; carbon atoms C11=C12 are in the lower chain and vacancies V_4 and V_{19} are in the nodes of different upper chains; carbon atoms C19=C18 are in the upper chain, V_{17} is in the upper chain and V_{12} is in the lower chain.

The total energy values for the $V-C=C-V$ defect configuration vary in the range of 3.5 eV, the minimum energy corresponds to the configuration shown in Fig. 1 (both carbon atoms and vacancies are in the upper chain).

The lengths of the C-C bonds on the $V-C=C-V$ defect perimeter are $d = 1.42 - 1.64 \text{ \AA}$. The C18-C19 bond has an order of 2.79 and a length $d = 1.22 \text{ \AA}$ indicating a triple bond. It should be noted that there is a slight charge distribution between the carbon atoms in the vacancy. On the atoms belonging to the upper chain, there is a negative charge of $-(0.01 - 0.08)e$, while on the lower chain atoms, there is a positive charge $+(0.03 - 0.10)e$. The orbital hybridization of atoms C18 and C19, having a triple bond between them, is close to the $sp + 2p$ type, and atoms of the upper chain C10 and C21 are in an $sp^2 + p$ hybrid state, while the lower chain atoms have sp^3 -hybridization. Thus, the existence of high-energy p -orbitals involved in the formation of π -bonds between the atoms C18 and C19 makes them preferential sites for active adsorption.

The value of the total energy of the surface with the V_2 defect is 3.8 eV lower than the total energy of the surface with the $V-C=C-V$ defect. In this study, we simulated the transformation (transition) of the $V-C=C-V$ defect into the V_2 divacancy. The activation energy of the transition is 8 - 10 eV, which indicates a very low probability of the $V-C=C-V$ to V_2 conversion by thermal motion of the atoms or even as a result of annealing.

4. Interaction of molecules with divacancy defects

To simulate the adsorption properties of the $C(111)-2 \times 1$ surface with vacancy defects, we selected a nonpolar hydrogen molecule and a dipolar water molecule as adsorbate particles. Adsorption modeling was performed for the ground states of defects shown in Fig. 1b,c.

Adsorption of an H_2 molecule on the ordered $C(111)-2 \times 1$ surface occurs dissociatively, hydrogen atoms form bonds either with the neighboring atoms of the upper surface Pandey chain ($E_{act} = 2.03 \text{ eV}$, $q = -0.47 \text{ eV}$), or with carbon atoms of the adjacent upper Pandey chains ($E_{act} = 2.37 \text{ eV}$, $q = -0.69 \text{ eV}$).

For dissociative adsorption of molecular hydrogen onto the carbon atoms in the V_2 divacancy region, an activation energy $E_{act} = 1.16 \text{ eV}$ is required for adsorption on the atoms C17 and C20; $E_{act} = 1.66 \text{ eV}$ for adsorption on the atoms C17, C16 (C20, C21) and 1.45 eV for adsorption on the atoms C17, C4 (C20, C4). All calculated values of activation energy of hydrogen chemisorption are much lower than the binding energy in the H_2 molecule ($E_b = 4.47 \text{ eV}$), which indicates that there is a weakening (loosening) of chemical bonds in the molecule at the surface. Moreover, in the divacancy area, the weakening of H-H bond in a hydrogen molecule is more pronounced than on an ordered surface.

For dissociative chemisorption of a water molecule, the same pairs of the atoms were chosen as adsorption sites as in the previous case (for a hydrogen molecule). The results for the calculations of energy adsorption characteristics are presented in Table 1.

TABLE 1. Energy characteristics of adsorption of molecules on the $C(111)-2 \times 1$ surface with a V_2 divacancy

Molecule Ads. centers	C17 and C20		C17 and C16		C17 and C4	
	E_{act} (eV)	q (eV)	E_{act} (eV)	q (eV)	E_{act} (eV)	q (eV)
H_2	1.16	-1.42	1.66	-1.18	1.45	-1.28
H_2O	0.31	-1.65	0.43	-1.47	0.40	-1.58

We detected a state of physical adsorption of a water molecule at a distance $r(C-O) = 3.7 \text{ \AA}$, characterized by the activation value $E_{act} = 0.10 \text{ eV}$, and the heat of adsorption $q = -0.12 \text{ eV}$. It should be noted that physical adsorption of water molecules for the ordered $C(111)-2 \times 1$ surface is not observed.

Let us consider the dissociative chemisorption of the molecules on the $C(111)-2 \times 1$ surface with a $V-C=C-V$ defect. The C18 and C19 atoms may form both mono- and dihydride states. In a monohydride state (Fig. 2a), each of the carbon atoms is bonded to one atom of hydrogen and the C18-C19 connection becomes a double bond. When a dihydride state forms, for example, on a C18 atom, the C18-C19 bond becomes single, and the C19 atom forms a new bond with C21, while C18 forms two bonds with hydrogen (Fig. 2b). This state is characterized by the highest value of the heat of adsorption (Table 2).

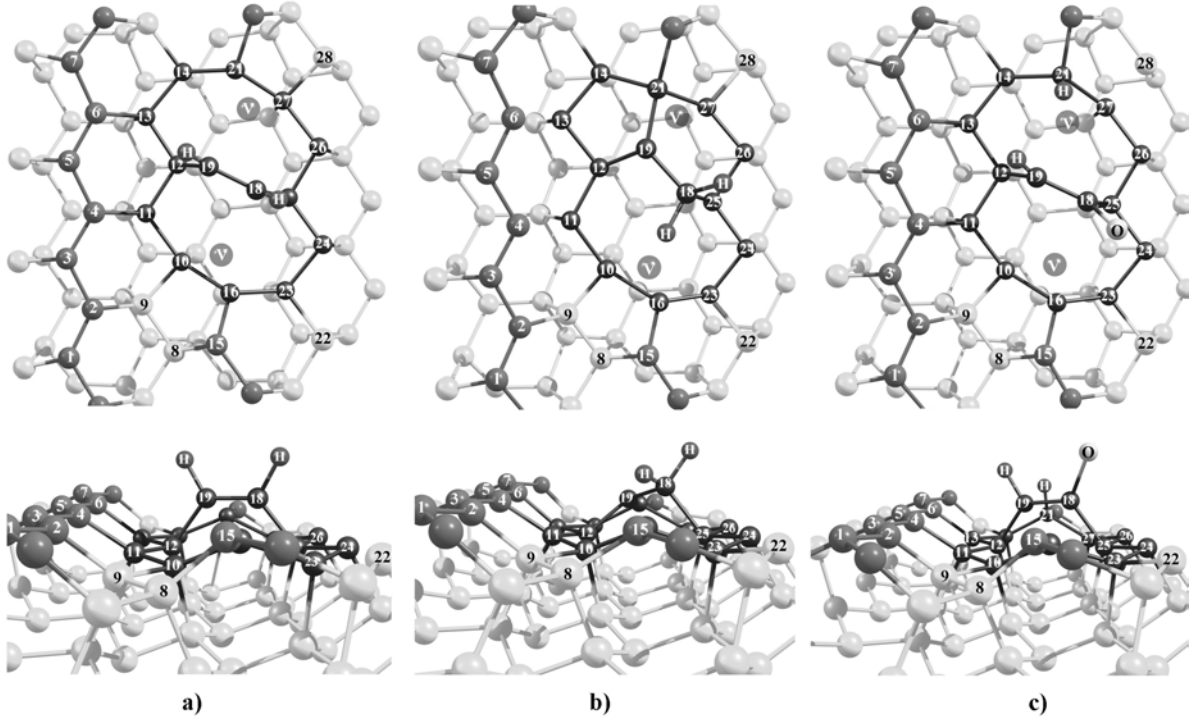


FIG. 2. Fragment of a cluster modeling a $C(111)-2 \times 1$ surface with a $V-C=C-V$ defect: a) monohydride states of atoms C18 and C19; b) dihydride state of the atom C18; c) results of water chemisorption by the $H_2O \rightarrow O + H + H$ mechanism. Light-gray color indicates carbon atoms of the cluster, dark-gray stands for the upper surface Pandey chain atoms, black – atoms in the defect, V are vacancies in the upper surface Pandey chain

TABLE 2. Energy characteristics of adsorption of molecules on the C(111)–2×1 surface with a V–C=C–V defect

Molecule Ads. centers	C18 and C19		C19 and C21		C18 and C16		C18, dihydride	
	E_{act} (eV)	q (eV)	E_{act} (eV)	q (eV)	E_{act} (eV)	q (eV)	E_{act} (eV)	q (eV)
H ₂	1.41	–2.71	1.53	–2.54	1.65	–2.23	1.63	–2.85
H ₂ O	0.12	–3.1	0.09	–2.82	0.07	–2.90	–	–

Dissociative chemisorption of a water molecule by the H₂O → OH+H mechanism on the V–C=C–V defect requires little activation energy (Table 2), indicating the high chemical reactivity of the atoms acting as adsorption sites. The H₂O → O+H+H chemisorption of water is available, however, this process requires an activation energy $E_{act} = 0.52$ eV and heat of adsorption $q = -4.48$ eV. In this case, oxygen binds to one of the C18(C19) atoms forming a double bond with it, and hydrogens saturate the bonds of the neighboring atoms in the defect region (Fig. 2c).

5. Conclusion

Thus, the search for stable configurations of the V₂ and V–C=C–V divacancy defects on the C(111)–2×1 diamond surface leads to states with a minimal total energy where the vacancies are located in the upper surface chain. The total energy of the surface with a V₂ divacancy is nearly 3.8 eV lower than the total energy of the surface with a V–C=C–V defect. However, the divacancy configuration transition from the V₂ to V–C=C–V is not possible due to atomic thermal motion, possibly even as a result of annealing.

Divacancy defects on a diamond surface have an increased reactivity in comparison to an ordered surface. Potential adsorption centers are atoms in the area of divacancies with unsaturated bonds (involved in the formation of delocalized electron clouds) and atoms with a double (triple) bond. It has been found that the C(111)–2×1 diamond surface with a V–C=C–V defect allows for the creation of both monohydride and dihydride states.

References

- [1] Khmel'nitsky R.A., Dravin V.A., et al. Mechanical stresses and amorphization of ion-implanted diamond. *Nucl. Instrum. Meth. Phys. Res. B*, 2013, **304**, P. 5–10.
- [2] Long R., Dai Y., et al. Study of vacancy on diamond (100)(2×1) surface from first-principles. *Appl. Surf. Sci.*, 2008, **254**, P. 6478–6482.
- [3] Filicheva Yu.A., Lvova N.A., Ananina O.Yu. Quantum-Chemical Simulation of Interaction of Hydrogen with Diamond Nanoclusters. *Fuller., Nanotub. Carbon Nanostr.*, 2012, **20** (4–7), P. 616–621.
- [4] Lvova N.A., Ananina O.Yu. Quantum Chemical Simulations of Water Adsorption on a Diamond (100) Surface with Vacancy Defects. *Russian J. Phys. Chem. A*, 2013, **87** (9), P. 1515–1519.
- [5] Barnard A.S., Sternberg M. Vacancy Induced Structural Changes in Diamond Nanoparticles. *J. Comput. Theor. Nanosci.*, 2008, **5**, P. 1–7.
- [6] Iakoubovskii K., Stesmans A. Chemical vapour deposition diamond studied by optical and electron spin resonance techniques. *J. Phys.: Condens. Matter*, 2002, **14**, R467.
- [7] Hyde-Volpe D., Slepetz B., Kertesz M. The [V–C=C–V] Divacancy and the Interstitial Defect in Diamond: Vibrational Properties. *J. Phys. Chem. C*, 2010, **114**, P. 9563–9567.
- [8] Pandey K.C. New p-bonded chain model for Si(111)-(2×1) surface. *Phys. Rev. Lett.*, 1981, **47** (26), P. 1913–1917.

Investigation of the sorption properties of carbon nanotubes with different boron impurity contents

S. V. Boroznin, I. V. Zaporotskova, N. P. Polikarpova

Volgograd State University, Volgograd, Russia

sboroznin@mail.ru, n.z.1103@mail.ru, irinazaporotskova@gmail.com

PACS 61.48.De

DOI 10.17586/2220-8054-2016-7-1-93-98

Since their discovery in the early 1990's, carbon nanotubes (CNTs) have become the subject of numerous investigations into their electronic structure and energy spectrum parameters as well as their physico-chemical properties. Due to their high surface activity, nanotubes can be used as base components for the fabrication of various types of composites. However, along with carbon nanotubes, current research also focuses on theoretical and experimental investigation of non-carbon nanotubes, namely recently discovered boron-carbon nanotubes with different concentrations of boron in them (25 % or 50 %). This article presents the results of theoretical research into the properties of boron-carbon nanotubes (BCNTs) within the framework of an ionic-built covalent-cyclic cluster model and an appropriately modified MNDO quantum chemical scheme, as well as DFT method. The authors studied mechanism of Cl and O atoms sorption onto the external surface of single-walled armchair nanotubes. As result of the study, geometrical optimization of the sorption complexes was defined, and sorption energy values were obtained.

Keywords: nanotechnologies, boron-carbon nanotubes, sorption properties.

Received: 20 November 2015

1. Introduction

Since their discovery in the early 1990's, carbon nanotubes (CNTs) have become the subject of numerous investigations into their electronic structure and energy spectrum parameters as well as their physico-chemical properties. Along with studies of nanotube properties researchers have begun to search for ways to modify NTs and fabricate structures that could possess new mechanical, electronic and other properties. Due to their high surface activity, nanotubes can be used as a base component for the fabrication of various types of composites. In particular, it was found out that pure carbon nanotubes might be used for gas storage because of their excellent adsorption properties [1–3].

As the properties of pure carbon nanotubes are well known, the researchers decided to investigate other types of the nanotube-based structures. One of the most useful type of nanotubes is one based on boron carbide. Earlier studies have shown that the physical and chemical properties of boron-carbon nanotubes (BCNT) are better than those of the corresponding CNTs [4–8].

The nanotube's adsorption process attracts the attention of our research group as well as other researchers around the world [9–13]. The calculations for the adsorption processes of the oxygen atom and O₂ molecule on the surface of BC₃ zig-zag nanotubes have been performed previously [14].

2. Oxygen adsorption on the surface of BCNT

The possibility of interaction between an oxygen atom and the external surfaces of A and B type BC₃ nanotubes was studied. The calculations were carried out using a molecular cluster model with the semi-empirical MNDO scheme. As a cluster model of a boron carbon

nanotube, a fragment that consisted of 30 atoms of boron and 90 atoms of carbon for A type, and 84 atoms of carbon and 36 atoms of boron for B type were chosen. There are four hexagon layers along the nanotube axis, and twelve boron carbon hexagons on its perimeter. The borders of the nanotube are isolated with pseudo atoms – hydrogen atoms. Length of bonds B–C, C–C and B–B totaled 1.44 Å.

The different adatom orientations were simulated: for A type 1) above the boron atom, 2) above the carbon atom, 3) above the B–C bond, 4) above the C–C bond, 5) above the hexagon center, 6) above the B–B bond (see Fig. 1).

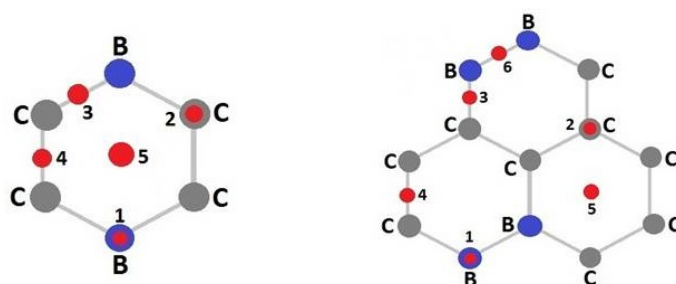


FIG. 1. The different types of adatom orientation were simulated: for A type 1) above the boron atom, 2) above the carbon atom, 3) above the B–C bond, 4) above the C–C bond, 5) above the hexagon center, 6) above the B–B bond

In the first and second types of orientation, the oxygen atom approaches the surface of B or C atoms that are located in the center of the molecular cluster of boron carbon nanotube in order to avoid the influence of edge effects. The boron-carbon nanotube fragment with adsorbed oxygen atom is shown in Fig. 2. The adsorption process was simulated by an oxygen atom in a step-wise approach to the nanotube surface with 0.1 Å increments perpendicular to the axis of the nanotube. The geometry of the system was optimized at each step. The calculations allow one to generate potential energy curves for each type of nanotube (see Figs. 3 and 4). Analysis of the energy curve shows that the oxygen atom is adsorbed onto the nanotube's surface. The minimum on the energy curve proves the fact of adsorption. The type of the bond between the adsorbed atom and the carbon atom of the nanotube surface is chemical. Therefore, the type of adsorption is chemical. The basic characteristics of these processes are shown in Tables 1 and 2. The location of oxygen atom above the B–C for A type and B–B bond for B type is energetically favorable. Geometrical analysis shows that the approaching of the oxygen atom causes a surface deformation for the A type BCNTs. The boron and carbon atoms leave their usual location and approach the adsorbed atom. The chemical bond between oxygen atom and nanotube surface occurs at a distance of 1.3 Å from the nanotube surface by means of so-called 'bridge structure'. Geometrical analysis of B type boron carbon nanotube shows that there is no adsorption above B–B bond at a distance of 3 Å. Further approach causes boron atoms to leave their location: one boron atom penetrates 0.2 Å inside the nanotube, and the other one approaches the adsorbed atom by 0.4 Å. The oxygen atom bonds with boron atom at a distance of 1.5 Å, and then this complex moves 0.5 Å into the nanotube.

The adsorption processes for other types of adsorbed atoms were simulated in the same manner. The oxygen atom approached the fictive atom located above B–C, B–B, C–C bonds or above the hexagon center. The chemical adsorption for these variants is possible, and the energy curves have similar trends (see Figs. 3 and 4). The basic characteristics of the adsorption processes are shown in Tables 1 and 2.

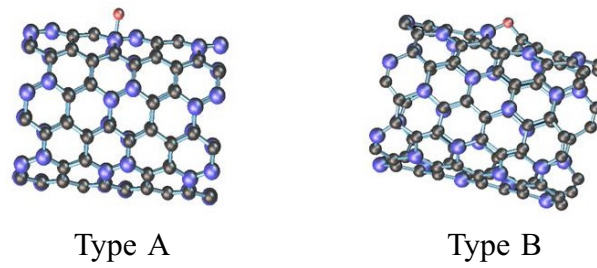


FIG. 2. Fragment of boron-carbon nanotube (6,6) A and B type with adsorbed oxygen atoms

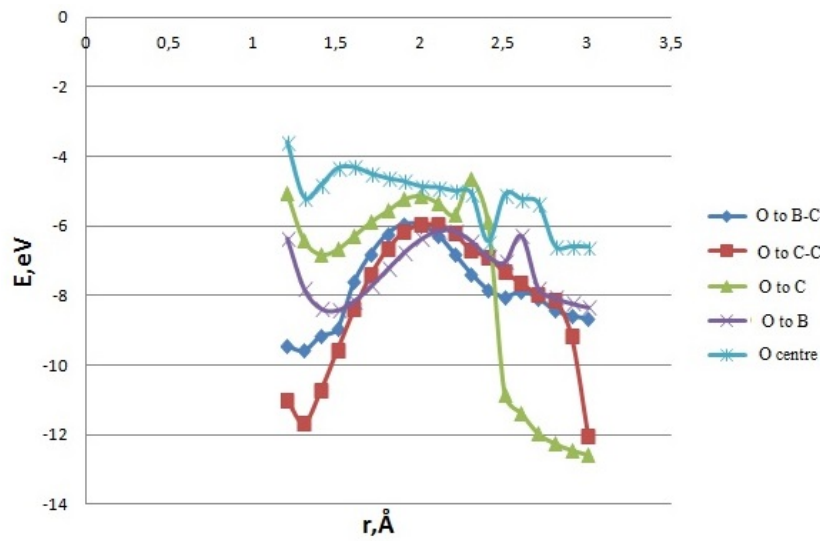


FIG. 3. Potential energy curve of the interaction between oxygen atom and the A type (6,6) BCNT surface for all oxygen atom locations

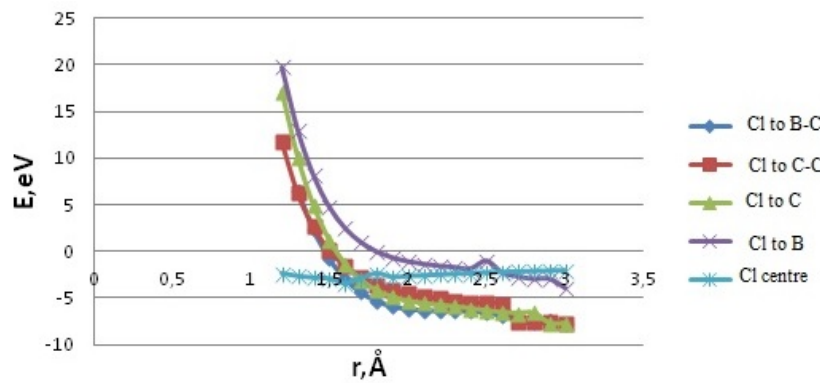


FIG. 4. Potential energy curve of the interaction between oxygen atom and the B type (6,6) BCNT surface for all oxygen atom locations

TABLE 1. Basic electron energy characteristics of oxygen adsorption process on the A type BCNT surface

Variant of adsorption	Activation energy	Adsorption distance	Adsorption energy
B–B	—	—	—
B–C	2.07	1.3	–9.56
C–C	6.09	1.3	–11.66
C	7.94	2.2	–5.67
B	0.89	1.5	–8.4
To center	2.15	2.4	–6.44

TABLE 2. Basic electron energy characteristics of the oxygen adsorption process on the B type BCNT surface

Variant of adsorption	Activation energy	Adsorption distance	Adsorption energy
B–B	—	1.3	–11.69
B–C	2.3	1.3	–9.63
C–C	—	1.3	–11.51
C	1.85	1.4	–6.62
B	—	1.4	–9.54
To center	3.74	2.2	–6.06

3. Chlorine adsorption on the surface of BCNT

The possibility of chlorine adsorption on the external surface of A and B type BCNTs was investigated in the same manner as the oxygen atom. The calculations were made using molecular cluster model with the semi-empirical MNDO scheme. The approaching of the chlorine atom and variants of adsorption were simulated in the same way as for the oxygen atom.

The calculations generated potential energy curves for chlorine adsorption onto the surface of a BCNT.

Analysis of the energy curves shows that there is no adsorption of the chlorine atom onto the external surface of the BCNT (Fig. 5). There are two types of adsorption for the chosen atom: above the hexagon center for nanotube A type, and above the B–B bond for B type (Fig. 6). This type of adsorption is physical.

Geometrical analysis of the system shows that the interaction between chlorine atom and the nanotube surface begins at a distance of 2.5 Å (Fig. 7). Both boron atoms approach the chlorine atom. The chlorine atom moves to one of the boron atoms. The chemical bond between them occurs at a distance of 1.9 Å. Then, the boron atoms return to their initial location. The length of the chlorine–boron bond is 1.2 Å. Therefore, chlorine adsorption does not cause nanotube deformation.

The optimal adsorption distance and activation energy are represented in the Table 3.

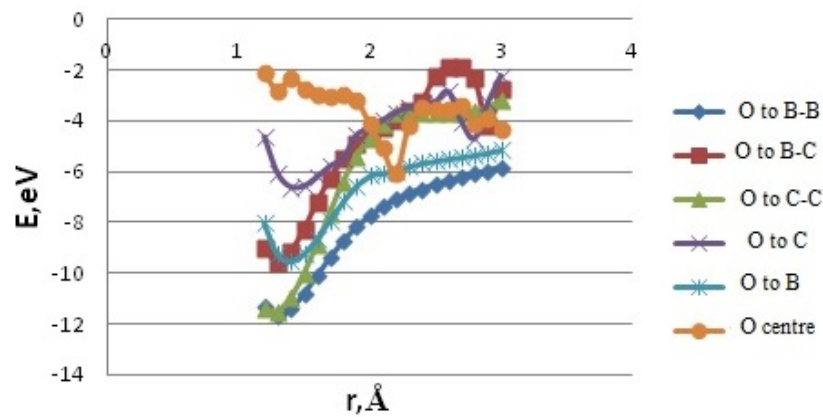


FIG. 5. Potential energy curve for the interaction between chlorine atom and the A type (6,6) BCNT surface for all chlorine atom locations

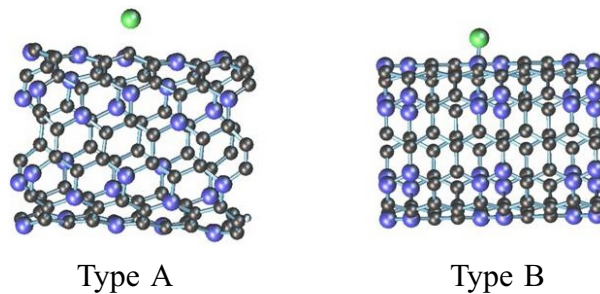


FIG. 6. Fragment of A and B type (6,6) BCNT with adsorbed chlorine atoms

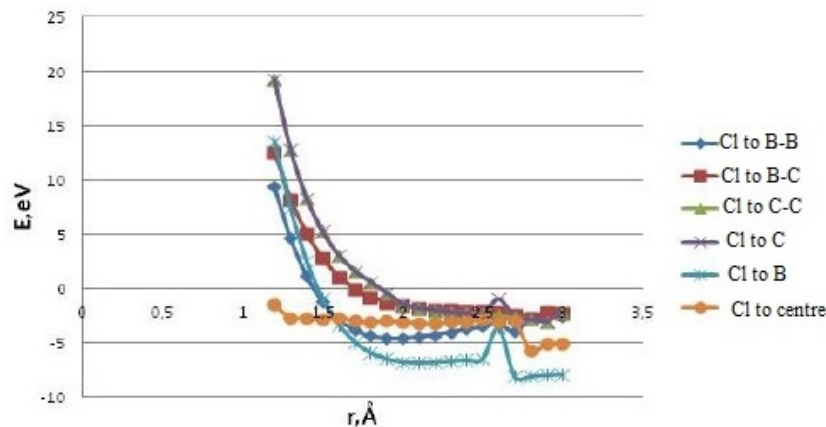


FIG. 7. Potential energy curve for the interaction between a chlorine atom and the B type (6,6) BCNT surface for all chlorine atom locations

4. Conclusion

The MNDO calculations for the adsorption of chlorine and oxygen atoms onto the BCNT surface were carried out. The most energetically favorable mechanisms for these processes were determined.

Oxygen and chlorine atoms were adsorbed onto the BCNT surface. It was determined that these processes depended on the orientations of atoms surface.

TABLE 3. Basic electronic energy characteristics of the chlorine adsorption process on the A type BCNT surface

Variant of adsorption	Activation energy	Adsorption distance	Adsorption energy
To center	0.39	1.6	-3.43
B-B	0.37	1.9	-4.58

There is a high possibility for the adsorption of oxygen atom when the adsorbed atom is located above the B-B bond for the B type BCNT and above B-C bond for A type.

There is a high possibility of adsorption of chlorine atom when the adsorbed atom is located above the B-B bond for the B type BCNT and above the hexagon center for the A type.

References

- [1] Zaporotskova I.V. *Carbon and Uncarbon nanomaterials and composite structures on their base: structure and electronic properties*. Volgograd, VolGU, 2009, 490 p.
- [2] Harris P. *Carbon nanotubes and related structures: New materials for twenty-first century*. oskow, Tehnosfera, 2003, 336 p.
- [3] Lebedev N.G., Zaporotskova I.V., Chernozatonskii L.A. Fluorination of carbon nanotubes within molecular cluster method. *Int. J. Quant. Chem.*, 2004, **100** (4), P. 548–558.
- [4] Zaporotskova I.V., Perevalova E.V. Boron nanotubes: semi empirical investigation of structure and some physics and chemical properties. *Tehnologia metallov*, 2009, **9**, P. 25–29.
- [5] Boroznin S.V., Zaporotskova I.V., Perevalova E.V. About adsorption of molecular oxygen on the external surface of boron and boron-nitrogen nanotubes. *Vestnik of Volgograd state university. Section 10: Innovation activity*, 2011, **5**, P. 18–25.
- [6] McGuire K. Synthesis and Raman Characterization of Boron-Doped Single-Walled Carbon Nanotubes. *arbon*, 2005, **43**, P. 219–227.
- [7] Rubio A. Formation and electronic properties of BC₃ single-wall nanotubes upon boron substitution of carbon nanotubes. *Phys. Rev. B*, 2004, **69**, 245403.
- [8] Zaporotskova I.V., Boroznin S.V., Perevalova E.V., Polikarpov D.I. Electronic structure and characteristics of some types of boron containing nanotubes. *Vestnik of Volgograd state university. Section 10: Innovation activity*, 2012, **6**, P. 81–86.
- [9] Boroznin S.V. Intercalation of lights and transition metal atoms inside the nanotubes as a basis of nanowires. *Fizika Volnovykh Processov i Radiotekhnicheskie Sistemy*, 2010, **13** (4), P. 87–95.
- [10] Boroznin S.V., Prokofieva E.V., Zaporotskova N.P. Composites based on Carbon nanotubes Intercalated with Atoms of Light and Transition Materials. *Nanoscience & Nanotechnology 2010. Book of abstract*, 2010, P. 103–104.
- [11] Zaporotskova I.V., Boroznin S.V., Boroznina E.V., Polikarpova N.P. Boron-carbon Nanotube Modification Using Alkaline Metal Atoms. *J. Nano Electron. Phys.*, 2014, **6** (3), P. 03006(1–2).
- [12] Boroznin, S.V., Zaporotskova I.V., Perevalova E.V. Influence of metal superlattice to boron nanotube. *Fundamental and Applied NanoElectroMagnetics (FANEM'12). Conf. Proc. Minsk. Belarus*, 2012, 43 p.
- [13] Zaporotskova I.V., Lebedev N.G., Chernozatonskii L.A. Electronic structure of carbon nanotubes modified by alkaline metal atoms. *Phys. Solid State*, 2004, **46** (6), P. 1174–1178.
- [14] Zaporotskova I.V., Perevalova E.V., Boroznin S.V. Investigation of oxidation in boron-containing nanotubes. *Nanosci. Nanotechnol. Lett.*, 2012, **4**, P. 1096–1099.

Investigation and modeling of evolution of C_{60} /NMP solution UV-Vis spectra

N. Jargalan^{1,2}, T. V. Tropin¹, M. V. Avdeev¹, V. L. Aksenov^{1,3}

¹Frank Laboratory of Neutron Physics, Joint Institute for Nuclear Research, Dubna, Russia

²Institute of Physics and Technology, Mongolian Academy of Sciences, Ulaanbaatar, Mongolia

³Petersburg Nuclear Physics Institute, National Research Centre ‘Kurchatov Institute’, Gatchina, Russia

narmandah@jinr.ru, ttv@jinr.ru

PACS 78.40.-q, 81.05. ub

DOI 10.17586/2220-8054-2016-7-1-99-103

The kinetics for the dissolution of fullerene C_{60} in N-methyl-2-pyrrolidone (NMP) solvent are investigated through measurements of the stirring speed and temperature dependence of the UV-Vis absorption spectra. We develop a model for the kinetics of simultaneously occurring processes in the solution, employing a system of simple kinetic equations and obtain the corresponding parameters dependence on preparation conditions. The obtained results will allow one in the future to consider these effects when modeling the slow growth kinetics of large clusters in C_{60} /NMP solutions.

Keywords: kinetics of dissolution, fullerene, N-methyl-2-pyrrolidone, UV-Vis.

Received: 20 November 2015

1. Introduction

Presently, a third allotropic form of carbon, called fullerenes, has attracted the interest of scientists in different areas, due to their unusual properties. Fullerenes are soluble in many various liquids, non-polar, organic, polar etc. Much research is being continuously published on the subject [1–4]. One of the most interesting phenomena studied is the cluster formation of fullerenes C_{60} and C_{70} in solutions. The large, stable clusters were detected in nitrogen containing solvents (aggregates size up to 500 nm) [5–7]. In addition to cluster growth, solvatochromic effects are observed, which are associated with complex formation between fullerene and solvent molecules [7–9].

In our previous work [10], the kinetics of fullerene dissolution were investigated in solvents such as benzene, toluene and N-methyl-2-pyrrolidone (NMP) by UV-Vis spectrometry. As is well known, the stable characteristic absorption peaks (e.g. at ~ 330 nm) disappear for C_{60} /NMP solutions, due to the formation of fullerene-solvent complexes. This fact does not allow one to directly measure the kinetics of dissolution in C_{60} /NMP via spectrophotometry. In the present work, we report new results for the analysis of the evolution kinetics of the UV-Vis spectra of C_{60} /NMP solution during the dissolution process.

2. Materials and methods

Solubility of fullerene C_{60} (Neo-Tech Product, purity > 99.5 %) is 0.89 mg/ml [6] in NMP (Merck, purity > 99.5 %). UV-Vis absorption spectra were obtained using Nanophotometer-P330 spectrometer (wavelength range of 200 – 950 nm, quartz cells with 1 mm light path). For this device, the convenient concentration for direct UV-Vis measurements was obtained to be 0.3 mg/ml. During different runs, the solution was stirred at 4 different speeds (V_s of 0, 100,

200, and 400 rpm), various temperatures were applied (room temperature (25 °C), 50, 60, 75 and 100 °C).

3. Method of UV-Vis spectra analysis

The effect of complex formation in C_{60} /NMP on the UV-Vis spectra permits the direct application of the Lambert-Beer law for evaluating the concentration kinetic curves. Thus, if one aims to extract the proper kinetic parameters, some method must be proposed to account for these phenomena.

The typical well-known evolution of the C_{60} /NMP UV-Vis spectra is presented in Fig. 1a for room temperature and a stirring rate of 400 rpm. To extract the kinetic constants from the measurements, we suppose that the dissolution of fullerene is governed by the Noyes-Whitney equation (with dissolution rate k_1), and that the complex formation proceeds simultaneously (rate of reaction k_2). Thus, a system of kinetic equations can be introduced:

$$\begin{cases} \frac{dc(t)}{dt} = k_1(C_s - c(t)), \\ \frac{dy(t)}{dt} = k_2(c(t) - y(t)), \end{cases} \quad (1)$$

where $c(t)$ is the concentration of ‘free’ fullerene molecules in the solution (those, that have not yet formed complexes), $y(t)$ – is the concentration of C_{60} -NMP complexes in the system, C_s – is the saturation concentration or the available concentration of C_{60} , if the solution is unsaturated. For the experiments performed, where the initial stage was the addition of fullerene to NMP, the initial conditions for Eqs. (1) should be: $c(0) = y(0) = 0$.

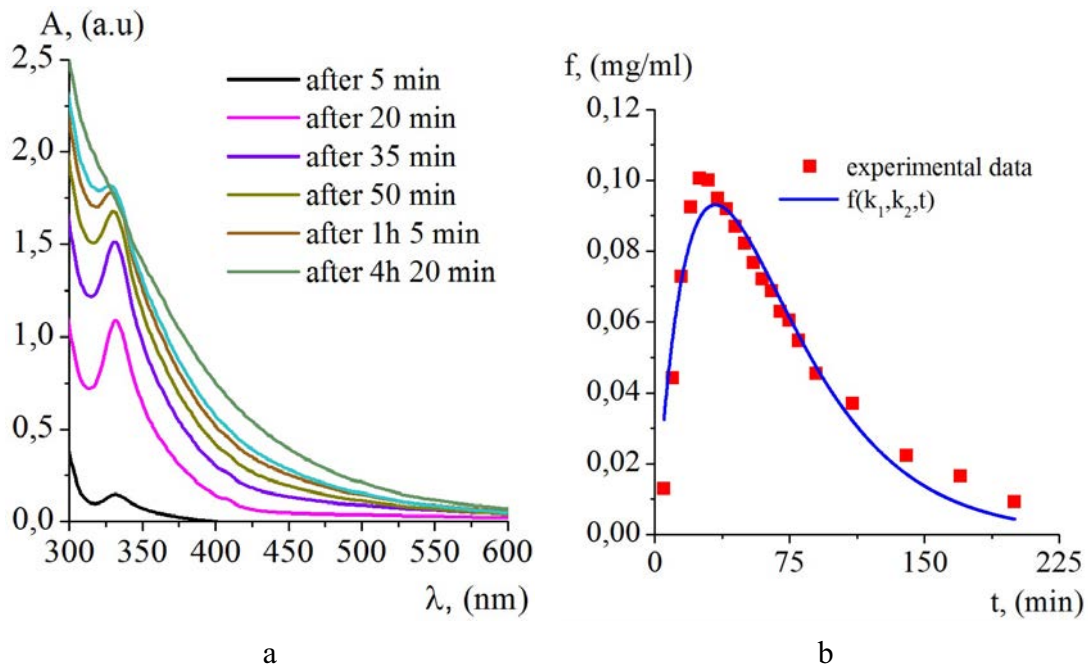


FIG. 1. a – Absorption spectra of C_{60} /NMP for 400 rot/min at room temperature with time, b – Fitting curve for evolution of peak high of C_{60} /NMP for 400 rot/min at room temperature with time

From Fig. 1a, one can see that after all of the fullerene molecules form complexes with NMP in the solution, the UV-Vis spectrum presents a monotonically decreasing curve. The

observed peak at ~ 330 nm corresponds to the concentration of ‘free’ C_{60} molecules. Thus, this peak’s height at any moment of time is proportional to $(\varepsilon_1 c(t) - \varepsilon_2 y(t))$, where ε_1 and ε_2 are the absorption coefficients for the ‘free’ molecules and the complexes, correspondingly. The values of these coefficients are not known, and for the present modeling, we roughly estimate them to be of the same order. This supposition allows one to directly relate the height of the ~ 330 nm peak above the monotonically decreasing type of the UV-Vis spectra to concentration of the ‘free’ C_{60} molecules, equal to $(c(t) - y(t))$. In Fig. 1b, a typical evolution of the respective peaks height is presented for $T = 25$ °C and $V_s = 400$ rpm. The absorption is normalized to the respective solution concentration, thus it estimates the difference $(c(t) - y(t))$, that can be obtained straight from Eqs. (1):

$$c(t) - y(t) = f(k_1, k_2, t) = \frac{C_s k_1 (e^{-k_1 t} - e^{-k_2 t})}{k_2 - k_1}. \quad (2)$$

The quality of the fit of experimental data, presented in Fig. 1b, reflects the applicability of the method proposed. The obtained expression was used for fitting the different experimental curves in order to obtain the values for k_1 and k_2 at various temperatures and stirring rates.

4. Results and discussion

Experimentally, measurements of the absorption spectra were performed apart from the stirred sample. This ensured that the amount of the solution taken for the measurements was small enough to not affect the dissolution kinetics. Measurements were taken at 5, 10, 15, 20, 30, etc. minutes after addition of fullerite soot to the solvent. At high temperatures, especially at $T = 100$ °C the maximum of the dependency of $f(k_1, k_2, t)$, occurs at times prior to 5 minutes, thus only the ‘tail’ of the evolution was captured and the quality of the fit is well reduced. As can be derived from (2), the maximum of $f(k_1, k_2, t)$ occurs at:

$$t_{\max} = \frac{\log(k_1/k_2)}{k_1 - k_2}, \quad (3)$$

i.e. must exist for any rate constant values.

From the performed measurements, it can be concluded, that the typical character of dissolution kinetics, accompanied by the complex formation, takes place for any temperature up to 100 °C and stirring rates up to 400 rpm. Yet, for confident estimates of k_1 and k_2 at various points of this range, a series of reproducible measurements would be required. Moreover, after inspection of Eq. (2) one can conclude, that scaled dependencies $f(k_1, k_2, t)$ can be obtained if one replaces k_1 and k_2 values. This fact shows that additional equation or supposition would improve the quality of the model. With respect to this approach, we depict some of the obtained results in Figs. 2 and 3.

In Fig. 2, typical temperature dependencies of rate constants, introduced in Eqs. (1), are presented for $V_s = 100$ rpm. The expected increase of k_1 and k_2 values with temperature of the Arrhenius type is obtained within experimental error.

The stirring speed dependencies are presented on Fig. 3. Here, we see that the non-stirred solutions tend to dissolve fullerene and form complexes much more slowly than those samples that were subjected to stirring. While the low rate constant values ensure that the peak, similar to the one presented on Fig. 1a, occurs at larger time intervals after initial dissolution, its amplitude, as was observed in the experiments, is very small. Additionally, the solvatochromic effect is not pronounced. For a stirring speed $V_s \geq 100$ rpm, the values of k_1 and k_2 increase by an order of magnitude. As we have obtained, the value of V_s above 100 rpm does not further strongly affect the dissolution character.

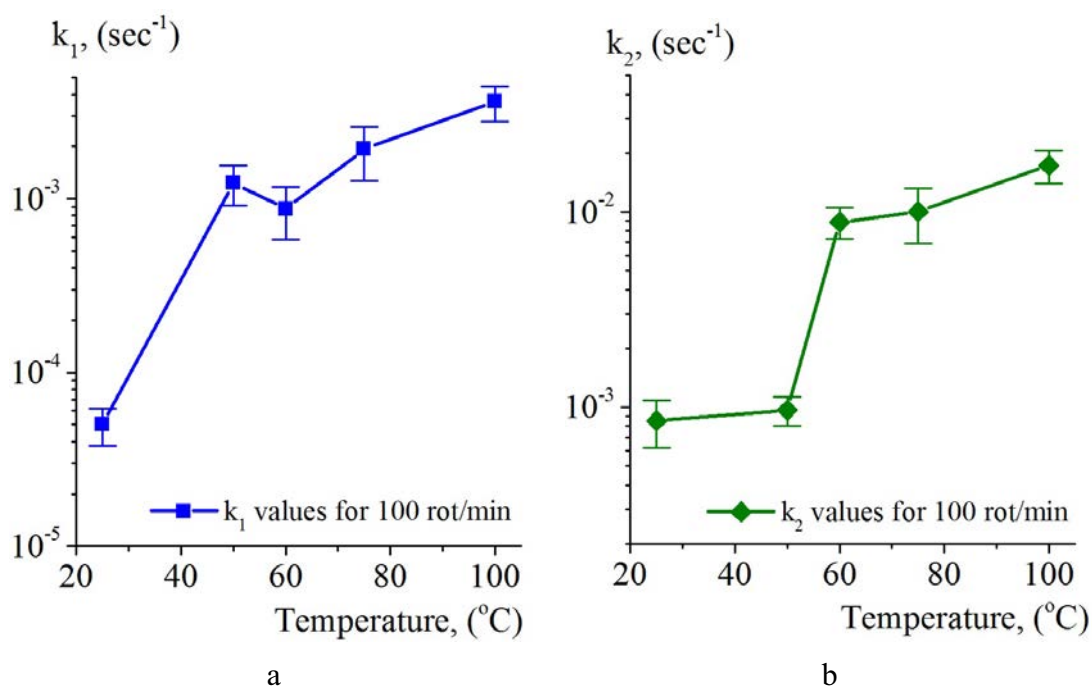


FIG. 2. Temperature dependencies of dissolution rate constant k_1 (a), and rate of complex formation k_2 (b) for the stirring speed of C_{60} /NMP solution equal to 100 rot/min

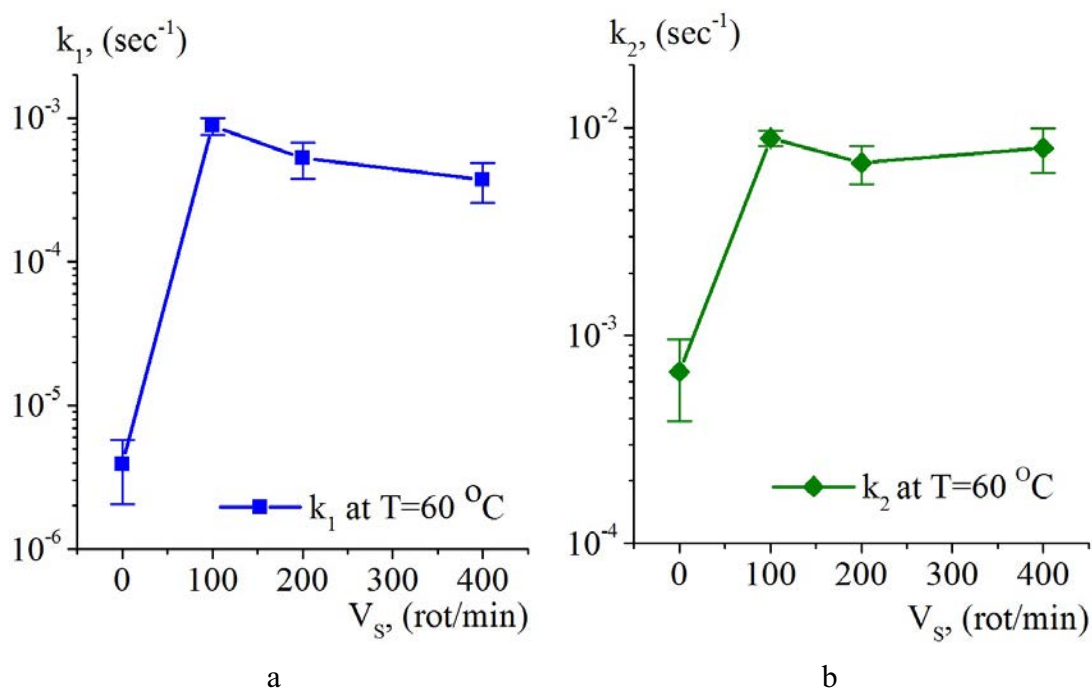


FIG. 3. Stirring speed dependencies of dissolution rate constant k_1 (a), and rate of complex formation k_2 (b) of C_{60} /NMP solution equal at $T = 50$ °C

The obtained values of k_1 and k_2 can also be used in the modeling of cluster growth in the C₆₀/NMP solution. As it was proposed in [11], a model of fullerene aggregation in polar solvents may imply the formation of clusters of C₆₀-solvent molecule complexes. Thus, the kinetic equations developed in [11] directly require one to estimate the rate constant values for a given temperature and other external conditions. As we have obtained here, the approximate values for stirred samples of $k_1 \sim (0.50 \pm 0.15) \cdot 10^{-4} \text{ s}^{-1}$, $k_2 \sim (1.0 \pm 0.2) \cdot 10^{-3} \text{ s}^{-1}$ for room temperature, and $k_1 \sim (0.8 \pm 0.2) \cdot 10^{-3} \text{ s}^{-1}$, $k_2 \sim (0.8 \pm 0.2) \cdot 10^{-2} \text{ s}^{-1}$ for higher temperatures should be used in further theoretical modeling.

5. Conclusions

In the present work, a model for evaluating the C₆₀/NMP dissolution UV-Vis spectra has been proposed, based on the supposition of simultaneous dissolution and complex formation in the solution. The proposed method allows one to estimate the values of the rate constants k_1 and k_2 – the speed of fullerene dissolution, and the rate of new complex formation from the time evolution of the $\sim 330 \text{ nm}$ peak in the absorption spectra. The dependencies of these parameters on the solution stirring speed and temperature were obtained and presented. Further careful measurements in the emphasized ranges of T and V_s can be performed in order to obtain the $k_1(T, V_s)$ and $k_2(T, V_s)$ dependencies.

Acknowledgements

The work was supported by the Russian Foundation of Basic Research, project No. 14-23-01015. The financial support is gratefully acknowledged.

References

- [1] Beck M.T., M'andi G. Solubility of C₆₀. *Fuller. Sci. Technol.*, 1997, **5** (2), P. 291–310.
- [2] Avdeev M.V., Aksenov V.L., Tropin T.V. Models of cluster formation and growth in fullerene solutions. *Russ. J. Phys. Chem. A*, 2010, **84**, P. 1273–1283.
- [3] Wang C.I., Hua C.C., Chen S.A. Dynamic solvation shell and solubility of C₆₀ in organic solvents. *J. Phys. Chem. B*, 2014, **118**, P. 9964–9973.
- [4] Meng Z., Hashmi S.M., Elimelech M. Aggregation rate and fractal dimension of fullerene nanoparticles via simultaneous multiangle static and dynamic light scattering measurement. *J. Colloid Interface Sci.*, 2013, **392**, P. 27–33.
- [5] Aksenov V.L., Avdeev M.V., et al. Formation of fullerene clusters in the system C₆₀/NMP/water by SANS. *Phys. B: Condens. Matter*, 2006, **385–386**, P. 795–797.
- [6] Kyzyma O.A., Bulavin L.A., et al. Aggregation in C₆₀/NMP, C₆₀/NMP/water and C₆₀/NMP/Toluene mixtures. *Fullerenes, Nanotub. Carbon Nanostructures*, 2008, **16**, P. 610–615.
- [7] Yevlampieva N.P., Biryulin Y.F., et al. Aggregation of fullerene C₆₀ in N-methylpyrrolidone. *Colloids Surfaces A: Physicochem. Eng. Asp.*, 2002, **209**, P. 167–171.
- [8] Kyzyma O.A., Korobov M.V., et al. Solvatochromism and fullerene cluster formation in C₆₀/N-methyl-2-pyrrolidone. *Fullerenes, Nanotub. Carbon Nanostructures*, 2010, **18**, P. 458–461.
- [9] Kyzyma O.A., Korobov M.V., et al. Aggregate development in C₆₀/N-methyl-2-pyrrolidone solution and its mixture with water as revealed by extraction and mass spectroscopy. *Chem. Phys. Lett.*, 2010, **493**, P. 103–106.
- [10] Jargalan N., Tropin T.V., Avdeev M.V., Aksenov V.L. Investigation of the dissolution kinetics of fullerene C₆₀ in solvents with different polarities by UV-Vis spectroscopy. *J. Surf. Investig. X-Ray, Synchrotron Neutron Tech.*, 2015, **9**, P. 16–20.
- [11] Tropin T.V., Jargalan N., et al. Kinetics of cluster growth in polar solutions of fullerene: Experimental and theoretical study of C₆₀/NMP solution. *J. Mol. Liq.*, 2012, **175**, P. 4–11.

Approaches to the determination of C₆₀ and C₇₀ fullerene and their mixtures in aqueous and organic solutions

I. V. Mikheev^{1,2}, T. A. Bolotnik^{1,2}, D. S. Volkov^{1,2}, M. V. Korobov¹, M. A. Proskurnin^{1,2}

¹Chemistry Department, Lomonosov Moscow State University, Moscow 119991, Russia

²Agilent Technologies Authorized Partner Laboratory / Analytical Centre of Lomonosov Moscow State University Moscow 119991, Russia

mikheev.ivan@gmail.com, timab@tut.by, dmsvolkov@gmail.com,
mkorobov49@gmail.com, proskurnin@gmail.com

PACS 78.40.Ri, 82.70.Gg

DOI 10.17586/2220-8054-2016-7-1-104-110

The solvent-exchange process from toluene was used for preparing aqueous dispersions of C₆₀ and C₇₀ without preconcentration with final concentrations of 180 ± 2 and 62 ± 1 μM , respectively, which exceeds the previously reported maximum concentrations for C₆₀ more than 6-fold; for C₇₀ such an aqueous dispersion is prepared for the first time. The residual quantity of the organic solvent and low-molecular compounds determined by headspace GC-MS was not more than 1 ppb. The procedure for the determination of fullerenes in aqueous dispersions is developed using a total organic carbon analyzer and absorption spectra; LOD, 50 nM, LOQ, 200 nM by TOC. Spectrophotometric determination of fullerenes in their aqueous dispersions was optimized: for C₆₀ at 268 nm: LOD, 0.1 μM , LOQ, 0.3 μM , for C₇₀ at 218 nm: LOD, 0.1 μM , LOQ, 0.3 μM . RSD mixture quantification by Vierordt's method in the range of 2 – 20 μM does not exceed 0.14 for C₆₀ and 0.09 C₇₀. RSD for toluene fullerene mixtures by Vierordt's method in the range of 2 – 20 μM does not exceed 0.10 for C₆₀ and 0.06 for C₇₀.

Keywords: fullerene C₆₀, fullerene C₇₀, fullerene mixture, UV/vis. spectroscopy, GC/MS.

Received: 20 November 2015

1. Introduction

Aqueous fullerene dispersions (AFDs) are powerful antioxidants that adsorb free radicals and possibly prevent various pathologies [1–3] and might have utility at the cellular and organism levels for the immobilization and transport of medicines [1, 4, 5]. However, the relevant question is to understand the composition of the initial and target fullerene materials [6]. Currently, the most common approaches are UV/vis-spectrometry and liquid chromatography; for mixture analysis in organic solvents, UV/vis and Raman spectroscopies are also used [7, 8]. However, these approaches were not used for AFDs. In addition, the use of organic solvents in AFD production calls for controlling the residual solvent and low-molecular compounds as these components contribute to the chemical behavior and safety of the materials [9–12]. Thus, the aim of this study is to (i) develop procedures for the determination of fullerenes and their mixtures in AFDs and (ii) to carry out the chromatographic characterization of the dispersions and residual solvents.

2. Experimental

2.1. Materials and methods

Fullerene C₆₀, 99.5 % and fullerene C₇₀, 99 %, (LLC Neo Tech Product, Russia), and an unseparated extract (technical mixture, lot PD-1) of fullerenes C₆₀ (90 ± 5 %, estimated value) and C₇₀ (10 ± 5 %, estimated value) from Fullerene Technology Company (Russia) were used.

Chemically pure toluene and benzene (Reakhim, Russia) were used throughout. Reagents were weighed on an Ohaus Discovery analytical balance (Switzerland). Solution preparation and sampling were done with Biohit Proline Plus mechanical automatic dispensers (Biohit Group, Finland). All solutions were prepared in Class A glass volumetric flasks with volumes of 25 and 50 mL (Labtekh, Russia). For sampling, 15 mL polypropylene test tubes were used (Axygen, Mexico). A GRAD 180-35 ultrasonic bath (Grad-Technology, Russia) was used to improve the dissolution of fullerenes and to prepare aqueous fullerene dispersions. Dynamic light scattering was measured using a Malvern Zetasizer nano ZS. Spectrophotometric measurements were made using an Agilent Cary 60 spectrophotometer (Australia). A liquiTOC II from Elementar Analysensysteme GmbH (Germany) was used for total organic carbon analysis and calibrated with standard solutions of potassium hydrogen phthalate in the range of 1 ppm to 200 ppm. The calibration plot of total organic carbon is $c(\text{ppm}) = (10.3 \pm 0.1)S$ ($P = 0.95$, $n = 7$, $r = 0.9986$), where S is the area of the peak of carbon, a.u. The limits of detection (3σ) were calculated using a standard protocol. The measurement results are presented in accordance with the requirements of ISO 5725:1994 (2012) [13].

2.2. Experimental Techniques

Procedure 1. Solvent-exchange aqueous fullerene dispersions [6]. A weighed portion of fullerene (0.5 – 0.6 g) was placed into a 200 mL volumetric flask, dissolved in 100 mL of toluene, and sonicated at 0.30 kW for 2 h at 353 K; next, the solution was diluted to mark with toluene. After sonication, the toluene solution was placed into a conical flask, 1 L of Milli-Q water was added, and the solution was sonicated at 0.90 kW for 3 days (12 h per day) at 353 K until complete elimination of toluene. Next, the solution was heated for 30 min, boiled for 15 min, and filtered through a Schott filter followed by a 0.45- μm microporous membrane filter. The concentration of fullerene was measured by the total organic carbon technique. Additionally, the residual toluene was measured by headspace gas chromatography technique.

Procedure 2. Analysis of residual organic solvent in aqueous fullerene dispersion by headspace gas chromatography. The test specimen (2 ml) was placed into a vial which was then sealed by a crimper. The instrumental parameters were as follows: temperature control time for sample – 20 min; thermostat temperature – 80 °C; sample injection volume – 1 ml. *Conditions of gas chromatographic separation:* column ZB-5 MS (30 m \times 0.25 mm \times 0.25 μm). Injector temperature – 250 °C; volumetric flow rate – 1 ml/min; septum purge flow – 6 ml/min. The initial column temperature was 40 °C (isothermal for 3 minutes), then the temperature was raised at a gradient of 2 °C/min to 60 °C (1 min isothermal). Sample input was done without dividing the carrier gas flow. *Conditions of mass spectrometric detection:* chromatograms registration mode by selected ion m/z 78 (benzene), 91 (toluene); the registration data 0.2 s. Source temperature 200 °C; interface temperature 250 °C.

Procedure 3. Stock fullerene C_{60} and C_{70} solutions preparation in (a) aqueous media (b) toluene media for the analysis by Vierordt's method.

- (a) Aqueous dispersions were analyzed using TOC and GC-MS to determine fullerene concentration. Next, the aqueous samples were diluted to 10 μM . The aqueous fullerene mixture solutions were prepared with the following ratios of C_{60} : C_{70} fullerenes: 1 : 1, 1 : 2, 2 : 1, 1 : 3, 3 : 1 in deionized water (Table 1). Next, the *Vierordt's method* for analysis at wavelengths 420 and 320 nm was used. The content of fullerenes in the mixture was checked by UV/vis spectroscopy.
- (b) A weighed portion of fullerene C_{60} (21.6 mg) and C_{70} (25.2 mg) was placed into a 100 mL volumetric flask, dissolved in 50 mL of toluene, and sonicated at 0.30 kW for 0.5 h

at 353 K. Next, the sample was cooled to room temperature and diluted up to volume with toluene. For analysis, solutions were diluted 10-fold. The concentration of fullerene was 30 μM . The toluene fullerene mixture solutions were prepared with the following ratios of $\text{C}_{60} : \text{C}_{70}$ fullerene: 1 : 1, 1 : 2, 2 : 1, 1 : 3, 3 : 1 in toluene (Table 1). Next, Vierordt's method was used to determine fullerene content by UV/vis spectroscopy at 337 and 406 nm.

TABLE 1. Composition of working solutions of fullerenes in toluene and aqueous mixtures for the analysis by UV/vis for Vierordt's method

Ratio		$c(\text{C}_{60}) \cdot 10^5, \text{M}$	$c(\text{C}_{70}) \cdot 10^5, \text{M}$	$c(\text{C}_{60}) \cdot 10^5, \text{M}$	$c(\text{C}_{70}) \cdot 10^5, \text{M}$
C_{60}	C_{70}	Toluene		Aqueous	
1	1	1.50	1.50	0.500	0.500
1	2	1.00	2.00	0.333	0.667
2	1	2.00	1.00	0.667	0.333
1	3	0.75	2.25	0.250	0.750
3	1	2.25	0.75	0.750	0.250

Procedure 4. Preparation of the toluene solution of technological mixture of the C_{60} and C_{70} for the analysis by Vierordt's method. A weighed portion of C_{60} and C_{70} mixture (30.2 mg) was added to a 100 mL volumetric flask, dissolved in 50 mL of toluene, and sonicated at 0.30 kW for 0.5 h at 353 K. The sample was then cooled to room temperature and diluted to volume with toluene. For the analysis, solutions were diluted 10-fold.

3. Results and discussion

3.1. Characterization of aqueous fullerene dispersions

The aqueous fullerene dispersions were made by the standard protocol [6] from toluene by a solvent-exchange process. The fullerene concentrations were 180 ± 2 and $62 \pm 1 \mu\text{M}$, respectively, which exceeded the previously-achieved maximum concentrations for C_{60} by more than 6-fold, and for the C_{70} fullerene, this was the first time that such an aqueous was prepared. This was confirmed by the TOC-analyzer. We postulate that the high fullerene concentrations were achieved by optimization of the sonication conditions and ratio of the organic to the aqueous phase. The total yields were calculated for C_{60} and C_{70} $54 \pm 2 \%$ and $45 \pm 1 \%$, respectively. The absorption spectra are in a good agreement with existing data for C_{60} (see Fig. 1A), C_{70} (see Fig. 1B). The absorption spectra for the aqueous fullerene dispersion of the technical mixture were obtained for the first time (see Fig. 1C). The AFD were characterized in terms of the physico-chemistry parameters: size clusters distribution, ζ -potential, PDI-indices (see Table 2). These data are in good agreement with existing data for the solvent-exchange process [9, 14–16]. The slight differences may be a result of different preparation conditions or changes in the preparation technique.

3.2. Residual organic solvent analysis in aqueous fullerene dispersions

The residual organic solvent content has an effect not only on human health, but also on the total fullerene concentration in aqueous dispersions (TOC-analysis). We estimated the residual quantity of the solvents by GC-MS analysis. The organic compounds in AFD hardly ever detect and quantify. However, in [17] an effort was made to quantify the residual solvents

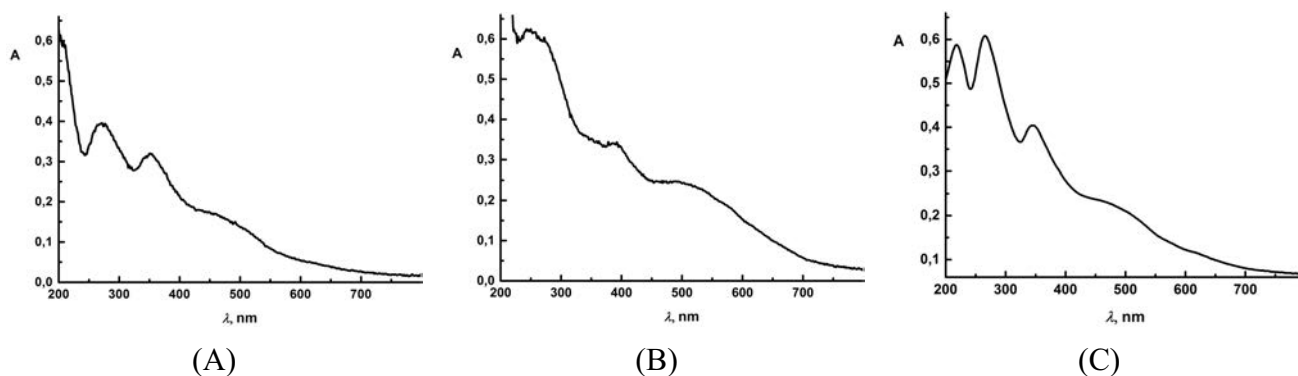


FIG. 1. Absorbance spectra $A(\lambda)$ of the aqueous fullerene dispersions: (A) $35 \pm 2 \mu\text{M}$; (B) $23 \pm 2 \mu\text{M}$; (C) $\text{C}_{60} 59 \pm 2 \mu\text{M}$, $\text{C}_{70} 4.4 \pm 0.3 \mu\text{M}$

TABLE 2. The main colloidal parameters of the aqueous fullerene dispersions

Characteristics	AFD-60	AFD-70	AFD ($\text{C}_{60}/\text{C}_{70}$)
c , μM	180 ± 2	62 ± 1	60 ± 1 ($\text{C}_{60} + \text{C}_{70}$)
ζ , mV	-32.9 ± 1.4	-34.4 ± 0.7	-41.8 ± 1.2
%RSD(ζ)	1.24	1.58	0.65
d , nm	145 ± 3	175 ± 5	89 ± 5
%RSD (d)	1.98	1.32	0.56
PDI	0.10 ± 0.01	0.11 ± 0.02	0.26 ± 0.01

TABLE 3. The GC-MS analysis of the aqueous fullerene dispersions ($n = 3$, $P = 0.95$)

c , ppt	Retention time, min	AFD-60	AFD-70
<i>Toluene</i>	2.38	97 ± 8	69 ± 6
<i>Benzene</i>	4.15	55 ± 5	46 ± 6

using solid-phase extraction with GC-analysis. The LOD of the THF was 1 ppb. Analysis of the samples showed that the AFDs samples contained solvents (benzene and its derivative toluene) below 100 ppt (see Table 3 and amount in AFDs by TOC (*vide infra*) Fig.2). Thus, the solvent analysis allowed us to determine the total fullerene levels much more precisely.

3.3. UV/vis Spectroscopy of individual aqueous fullerene dispersions

The concentrations of fullerenes in the resulting aqueous dispersions were determined by TOC-analyzer with preliminary residual solvent characterization by GS-MS (*vide supra*). The parameters of the fullerene determination are LOD, 50 nM, LOQ, 200 nM by TOC. Comparison of the calculated LOD and LOQ (see Table 4) at 268 and 349 nm shows a decrease in the LOD 3 times at 268 nm, and at 349 nm, the LOD was the same, as was discussed in [18, 19] for C₆₀.

3.4. Application of Vierordt's method for C₆₀, C₇₀, and their technological mixtures

The dependences obtained for $\varepsilon_1^\lambda/\varepsilon_2^\lambda = f(\lambda)$ rely on the absorbance spectra of the fullerene in neat solvent over the range of 300 – 850 nm according to procedure 3b. It is characterized by the following extreme points, maximum at 355, 406 nm, a minimum at 320 and 337 nm, at these wavelengths, the ratios of the molar absorption coefficients have maximum great

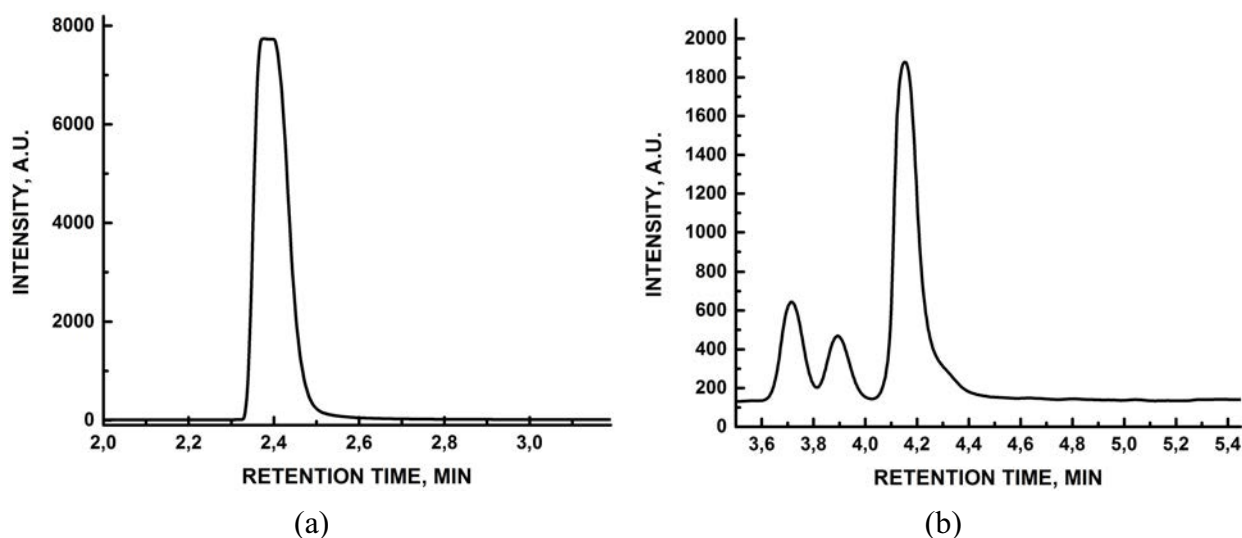


FIG. 2. GC-MS analysis of the aqueous fullerene dispersions sample. Characteristic chromatogram obtained by m/z analysis (a) m/z 78 benzene; (b) m/z 92 toluene

TABLE 4. Metrological parameters for the aqueous fullerene dispersion determination ($P = 0.95$, $n = 10$)

AFD 60				
λ , nm	Calibration curves	$LOD \cdot 10^7$,	$LOQ \cdot 10^7$,	
220	$A = (6.0 \pm 0.6) \cdot 10^4 c$, $r = 0.9977$	2	8	
268	$A = (6.7 \pm 0.6) \cdot 10^4 c$, $r = 0.9975$	1	3	
349	$A = (4.9 \pm 0.2) \cdot 10^4 c$, $r = 0.9969$	4	10	
AFD 70				
218	$A = (7.5 \pm 0.2) \cdot 10^4 c$, $r = 0.9970$	1	3	
248	$A = (6.4 \pm 0.6) \cdot 10^4 c$, $r = 0.9916$	3	12	
387	$A = (3.5 \pm 0.3) \cdot 10^4 c$, $r = 0.9940$	5	16	
486	$A = (2.5 \pm 0.2) \cdot 10^4 c$, $r = 0.9934$	8	25	

difference between $\varepsilon_1^{\lambda_1}/\varepsilon_2^{\lambda_1} - \varepsilon_1^{\lambda_2}/\varepsilon_2^{\lambda_2}$ [20]. Analysis of the mixture by Vierordt's method at 355, 406 and 320, 337 nm showed that the deviation of the calculated concentration in the mixture was more than 15 %. For 337 and 406 nm, the relative error (δc %) concentration ranged from 5 – 10 % (see Table 5). Therefore, for analysis of selected absorption maxima, the fullerene mixture in toluene was evaluated at 337 and 406 nm. Currently, the combination of UV/vis and cumbersome calculation permitted an accuracy of a hundredth of a percent [8]. However, for the technological purposes, such a value for the relative error is sufficient for monitoring fullerene mixture composition after synthesis. We confirmed this by analyzing a real sample of an unseparated fullerene mixture with a known mass ratio. We have calculated the ratio as $C_{60} 92 \pm 3$ % and $C_{70} 8 \pm 2$ %, and this data was in a good agreement with the real sample's certificate. Thus, analysis of the organic solutions permitted expansion to the analysis of the aqueous dispersions. The usage of a TOC-analyzer allowed to us to determine the fullerene content in the dispersions. The combination of the TOC and UV/vis-spectroscopy allowed calculation of the apparent molar absorptivity and then analysis of the aqueous dispersion mixture

TABLE 5. C₆₀ and C₇₀ determination in aqueous dispersion by Vierordt's method at 320/420 nm

Concentration		Calculation		$\delta C, \%$	
$c(C_{60}) \cdot 10^6, M$	$c(C_{70}) \cdot 10^6, M$	$c(C_{60}) \cdot 10^6, M$	$c(C_{70}) \cdot 10^6, M$	C ₆₀	C ₇₀
5.14	5.30	5.75	5.14	11.9	3.0
5.14	2.65	5.70	2.38	10.9	10.2
2.57	5.30	2.91	5.10	13.3	3.9
6.17	2.12	6.82	1.92	10.5	9.3
2.06	6.36	2.32	6.25	12.9	1.7

by Vierordt's method. The dependences $\varepsilon_1^\lambda/\varepsilon_2^\lambda = f(\lambda)$ were obtained based on the absorbance spectra of the fullerene in neat solvent from 300 – 850 nm according to procedure 3(a). This was characterized by maxima at 241, 320, 420 nm, and at these wavelengths, the ratios of molar absorptivities had the maximum difference between $\varepsilon_1^{\lambda_1}/\varepsilon_2^{\lambda_1} - \varepsilon_1^{\lambda_2}/\varepsilon_2^{\lambda_2}$ [20]. Analysis of the mixture by Vierordt's method at 241 and 320 nm showed that the deviation of the calculated concentration in the mixture was more than 25 %. Therefore, analysis was done at 320 and 420 nm for the selected absorption maxima of the fullerene mixture in toluene. For the maxima at 320 and 420 nm, the value of relative error ($\delta c \%$) was below 15 % over the of 2 – 7 μM range (see Table 5).

The determination of fullerenes in toluene by Vierordt's method enabled us to proceed with our mixture analysis of the AFDs. Data obtained for the fullerenes in AFD showed that the relative error in the determination of fullerenes was higher than for toluene solutions of (1.5 times), due to the high light scattering by clustered structures in the AFDs. However, this relative error is acceptable to aim at biology and medicine for establishing the reinforcing action of fullerene in the mixture [21,22]. This was the first time Vierordt's method for analysis was applied to a two-component system of AFDs (C₆₀ and C₇₀).

4. Conclusions

The technique of organic solvent determination is applicable for biological purposes and total AFDs characterization, which can be successfully used for a number of biomedical applications. The results obtained here indicate that we may apply the developed technique for mixture analysis with satisfactory accuracy. Continuing research into this field appears fully justified because no one method totally characterized such object akin to AFDs; rather, this was accomplished by applying a few physico-chemical analytical methods. In our opinion, for biological purposes, we should apply a number of physico-chemical methods to completely describe these aqueous fullerene systems.

Acknowledgements

The work is supported by The Russian Science Foundation, grant no. 14-23-00012. We are grateful to Agilent Technologies – Russia and its CEO, Dr. Konstantin Evdokimov, for the equipment used in this study.

References

- [1] ISO 5725:1994. Accuracy (trueness and precision) of measurement methods and results, 1994 (revised and confirmed in 2012).
- [2] Andrievsky G., Klochkov V., Derevyanchenko L. Is the C₆₀ Fullerene Molecule Toxic?! *Fuller., Nanotub. Carbon Nanostr.*, 2005, **13**, P. 363–376.
- [3] Brant J.A., Labille J., Bottero J.-Y., Wiesner M.R. Characterizing the Impact of Preparation Method on Fullerene Cluster Structure and Chemistry. *Langmuir*, 2006, **22**, P. 3878–3885.
- [4] Chen H.C., Ding W.H. Determination of Aqueous Fullerene Aggregates in Water by Ultrasound-Assisted Dispersive Liquid-Liquid Microextraction with Liquid Chromatography-Atmospheric Pressure Photoionization-Tandem Mass Spectrometry. *J. Chromatography A*, 2012, **1223**, P. 15–23.
- [5] Chen K.L., Elimelech M. Aggregation and Deposition Kinetics of Fullerene (C-60) Nanoparticles. *Langmuir*, 2006, **22**, P. 10994–11001.
- [6] Chen Z.Y., Mao R.Q., Liu Y. Fullerenes for Cancer Diagnosis and Therapy: Preparation, Biological and Clinical Perspectives. *Current Drug Metabolism*, 2012, **13**, P. 1035–1045.
- [7] Chen Z., Westerhoff P., Herckes P. Quantification of C₆₀ Fullerene Concentrations in Water. *Environmental Toxicology and Chemistry*, 2008, **27**, P. 1852–1859.
- [8] Cicek B., Kenar A., Nazir H. Simultaneous Determination of C-60 and C-70 Fullerenes by a Spectrophotometric Method. *Fullerene Sci. Technol.*, 2001, **9**, P. 103–111.
- [9] Dhawan A., Taurozzi J.S., et al. Stable Colloidal Dispersions of C₆₀ Fullerenes in Water: Evidence for Genotoxicity. *Environmental Science & Technology*, 2006, **40**, P. 7394–7401.
- [10] Fortner J.D., Lyon D.Y., et al. C₆₀ in Water: Nanocrystal Formation and Microbial Response. *Environmental Science & Technology*, 2005, **39**, P. 4307–4316.
- [11] Hilburn M.E., Murdianti B.S., et al. Synthesizing Aqueous Fullerene Colloidal Suspensions by New Solvent-Exchange Methods. *Colloids and Surfaces A: Physicochemical and Engineering Aspects*, 2012, **401**, P. 48–53.
- [12] Kato S., Kikuchi R., et al. Defensive Effects of Fullerene-C₆₀/Liposome Complex against Uva-Induced Intracellular Reactive Oxygen Species Generation and Cell Death in Human Skin Keratinocytes Hacat, Associated with Intracellular Uptake and Extracellular Excretion of Fullerene-C₆₀. *J. Photochem. Photobiol. B-Biology*, 2010, **98**, P. 144–151.
- [13] Mikheev I.V., Volkov D.S., Proskurnin M.A., Korobov M.V. Monitoring of Aqueous Fullerene Dispersions by Thermal-Lens Spectrometry. *Intern. J. Thermophys.*, 2014, DOI: 10.1007/s10765-014-1814-y, 11 p.
- [14] Nakamura E., Isobe H. Functionalized Fullerenes in Water. The First 10 Years of Their Chemistry, Biology, and Nanoscience. *Accounts of Chemical Research*, 2003, **36**, P. 807–815.
- [15] Niu S., Mauzerall D. Fast and Efficient Charge Transport across a Lipid Bilayer Is Electronically Mediated by C₇₀ Fullerene Aggregates. *J. Am. Chem. Soc.*, 1996, **118**, P. 5791–5795.
- [16] Pycke B., Chao T.-C., et al. Beyond Nc60: Strategies for Identification of Transformation Products of Fullerene Oxidation in Aquatic and Biological Samples. *Analyt. Bioanalyt. Chem.*, 2012, **404**, P. 2583–2595.
- [17] Sene J.A., Pinheiro M.V. B., Krambrock K., Barbeira P.J.S. Quantification of Fullerene Nanoparticles Suspensions in Water Based on Optical Scattering. *Talanta*, 2009, **78**, P. 1503–1507.
- [18] Torpe A., Belton D.J. Improved Spectrophotometric Analysis of Fullerenes C₆₀ and C₇₀ in High-Solubility Organic Solvents. *Analytical Sciences*, 2015, **31**, P. 125–130.
- [19] Tzirakis M.D., Orfanopoulos M. Radical Reactions of Fullerenes: From Synthetic Organic Chemistry to Materials Science and Biology. *Chem. Rev.*, 2013, **113**, P. 5262–5321.
- [20] Wróbel D., Graja A. Modification of Electronic Structure in Supramolecular Fullerene-Porphyrin Systems Studied by Fluorescence, Photoacoustic and Photothermal Spectroscopy. *J. Photochem. Photobiol. A: Chemistry*, 2006, **183**, P. 79–88.
- [21] Xiao L., Takada H., et al. Antioxidant Effects of Water-Soluble Fullerene Derivatives against Ultraviolet Ray or Peroxylipid through Their Action of Scavenging the Reactive Oxygen Species in Human Skin Keratinocytes. *Biomedicine & Pharmacotherapy*, 2005, **59**, P. 351–358.
- [22] Bernstein I.Ya., Kaminsky Y.L. *Spectrophotometric analysis in organic chemistry Chemistry*, 1986 (in Russian).

Synthesis, isolation, and X-ray structural characterization of trifluoromethylated C_{78} fullerenes: $C_{78}(2)(CF_3)_{10/12}$ and $C_{78}(3)(CF_3)_{12/14}$

N. B. Tamm, M. P. Kosaya, M. A. Fritz, S. I. Troyanov

Department of Chemistry, Moscow State University, Moscow, Russia

tamm@thermo.chem.msu.ru, stroyano@thermo.chem.msu.ru

PACS 61.48.-c

DOI 10.17586/2220-8054-2016-7-1-111-117

Four CF_3 derivatives of C_{78} , $C_{78}(2)(CF_3)_{10/12}$ and $C_{78}(3)(CF_3)_{12/14}$, have been isolated via HPLC from the products of high-temperature trifluoromethylation of a C_{76} – C_{96} fullerene mixture or a C_{78} fraction. Their molecular structures were determined by single crystal X-ray crystallography using synchrotron radiation. The addition patterns of the new compounds are compared with each other and with the previously known $C_{78}(2)(CF_3)_{10}$ and $C_{78}(3)(CF_3)_{12}$.

Keywords: higher fullerenes, C_{78} , trifluoromethylation, HPLC, structure elucidation.

Received: 20 November 2015

1. Introduction

Higher fullerenes are characterized by the existence of multiple cage isomers and relatively lower abundance compared to those of C_{60} and C_{70} , and thus their isolation and further study of their structure and properties are much more difficult. Among the family of higher fullerenes, C_{78} is present in moderate abundance in fullerene mixtures because it, along with C_{84} , C_{90} , and C_{96} , belongs to the group of C_{6n} fullerenes, which have richer isomeric distribution and have been more comprehensively investigated [1]. The C_{78} fullerene possesses five topologically-distinct isolated pentagon rule (IPR) isomers, D_3 - $C_{78}(1)$, C_{2v} - $C_{78}(2)$, C_{2v} - $C_{78}(3)$, D_{3h} - $C_{78}(4)$, and D_{3h} - $C_{78}(5)$ [2]. The $C_{78}(2)$ – $C_{78}(5)$ isomers can be converted into each other by Stone – Wales rearrangements (SWR) of the pyracylene type, whereas $C_{78}(1)$ cannot be transformed into other isomers of C_{78} by SWRs. The abundances of $C_{78}(1)$ – $C_{78}(3)$ isomers in the fullerene soot are comparable, being dependent on the method of fullerene synthesis [3, 4]. The D_3 - $C_{78}(1)$ and C_{2v} - $C_{78}(2)$ isomers were isolated chromatographically and their cage structures were confirmed by ^{13}C NMR spectroscopy [3]. At the same time, isomer D_{3h} - $C_{78}(5)$ is elusive because of a small band gap resulting in a very low solubility; its presence in the fullerene soot could be unambiguously confirmed by the structural study of a CF_3 derivative, $C_{78}(5)(CF_3)_{12}$ [5]. The D_{3h} - $C_{78}(4)$ isomer possesses the lowest stability; it has never been found in the fullerene soot. These differences are satisfactorily explained by the differences in the relative formation energies of the $C_{78}(1)$ – $C_{78}(5)$ isomers [3].

The chemical reactivity of C_{78} fullerene was studied in cyclopropanation, halogenations, trifluoromethylation, and other reactions [6–14]. Structural characterization of the derivatives was carried out by 1H , ^{13}C , and ^{19}F spectroscopy as well as by X-ray crystallography. Among the most structurally investigated compounds are the bromides, $C_{78}(2,3)Br_{18}$ [8], chlorides, $C_{78}(2,3,5)Cl_{18}$ [9–11] and $C_{78}(1,2)Cl_{30}$ [12, 13], and several trifluoromethylated derivatives, $C_{78}(CF_3)_{2n}$ [14]. For the latter group, structural data obtained by ^{19}F NMR spectroscopy and/or X-ray studies are available for compositions $C_{78}(3)(CF_3)_8$, $C_{78}(1,2)(CF_3)_{10}$,

and $C_{78}(3,5)(CF_3)_{12}$. The only structural X-ray study of a pentafluoroethyl derivative concerns the compound $C_{78}(2)(C_2F_5)_{10}$ [15]. Investigations of the structural chemistry of CF_3 derivatives have been restricted to only several examples, which hampers a comprehensive comparison, even within the derivatives of a distinct isomer of C_{78} . The aim of the present study is to expand the chemistry of trifluoromethylated C_{78} derivatives for different isomers. The synthesis, HPLC isolation, and X-ray crystallographic study was performed for several CF_3 derivatives of $C_{78}(2)$ and $C_{78}(3)$ with 10 – 14 CF_3 groups, which enables comparison with previously known $C_{78}(2,3)(CF_3)_n$ isomers. Addition patterns are discussed in terms of the partial of full occupation of 12 pentagons and formation of aromatic substructures and isolated double C=C bonds on the fullerene cage.

2. Results

Two different starting higher fullerene mixtures were used for trifluoromethylation with gaseous CF_3I in quartz ampoules following a previously described procedure [16–18]. The mixture of higher fullerenes $C_{76} - C_{96}$ (45 mg; MER Corp.) was trifluoromethylated at 560 °C for 1 h, whereas a C_{78} fraction (60 mg) obtained by HPLC from the $C_{76} - C_{90}$ mixture (Suzhou Dade Carbon Nanotechnology Co.) was reacted at 450 °C for 1.5 h. In both cases, the trifluoromethylation products were sublimed into the colder parts of the ampoules and were collected from there. The products obtained from the $C_{76} - C_{96}$ mixture contained a complex mixture of fullerene $(CF_3)_{2n}$ compounds with $2n$ in the range of 12 – 20 according to MALDI TOF mass spectrometric analyses, whereas CF_3 derivatives of C_{78} were represented by $C_{78}(CF_3)_{10-16}$ with the maximum abundance of $C_{78}(CF_3)_{12}$ species. Trifluoromethylation of the C_{78} fraction gave a mixture of $C_{78}(CF_3)_{12-18}$ with the highest abundance of $C_{78}(CF_3)_{14}$ and $C_{78}(CF_3)_{16}$. It can be concluded that the lower reaction temperature (450 vs. 560 °C) somewhat shifts the composition in the mixture to the compounds with a large number of CF_3 groups. This effect can be explained by the increase of the compound volatility with the increasing number of CF_3 groups which influences the kinetics of sublimation in the reaction ampoule [19].

Both products were dissolved in toluene and subjected to HPLC separation in toluene (Buckyprep column, 10 mm i.d. \times 250 mm, Nacalai Tesque Corp.) with a flow rate of 4.6 mL \cdot min $^{-1}$ monitored at 290 nm. A typical HPLC trace for the $C_{76-96}(CF_3)_n$ product is shown in Fig. 1a. The fractions obtained were further separated by HPLC using toluene/*n*-hexane mixtures or pure *n*-hexane. The second-step separation of the toluene fraction, which eluted at 6.4 min, was carried out in a toluene/hexane mixture with $v/v = 1/1$ and a subfraction eluted at 20.2 min gave a compositionally pure $C_{78}(CF_3)_{10}$ compound. Recrystallization from *o*-dichlorobenzene and *p*-xylene afforded small crystals which were then investigated by X-ray diffraction with the use of synchrotron radiation, thus revealing molecular structures of $C_{78}(2)(CF_3)_{10}$ in the form of solvates with *o*-dichlorobenzene and *p*-xylene, respectively. HPLC separation of the toluene fraction eluted at 6.8 min was performed in a toluene/hexane ($v/v = 1/1$) eluent and a subfraction eluted at 23.1 min afforded a compositionally pure $C_{78}(CF_3)_{12}$ compound. Slow evaporation of solvent gave small crystals which were studied by X-ray crystallography revealing the molecular structure of $C_{78}(2)(CF_3)_{12}$.

Trifluoromethylation products of the C_{78} fraction were also separated by two-step HPLC using the same Buckyprep column. The second-step HPLC of the first toluene fraction in a toluene/hexane 15/85 v/v mixture (not shown) gave a compositionally pure $C_{78}(CF_3)_{12}$ fraction according to MALDI TOF mass-spectrometry. Recrystallization from toluene afforded small crystals of $C_{78}(3)(CF_3)_{12} \cdot 1.5$ (toluene). Finally, the second-step HPLC separation of the first toluene fraction in hexane at flow rate of 1.5 mL \cdot min $^{-1}$ allowed the isolation of several $C_{78}(CF_3)_{12-18}$ compounds (Fig. 1b). A fraction eluted at 17.7 min (indicated by the arrow),

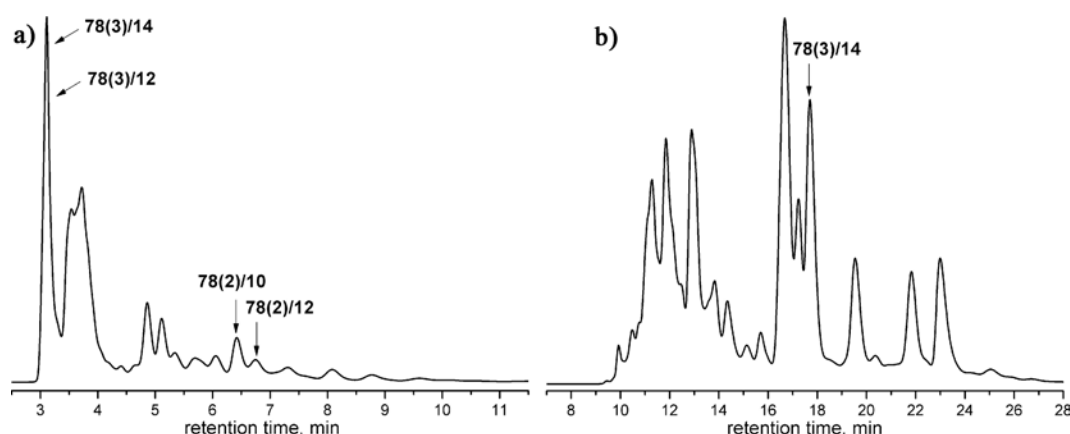


FIG. 1. HPLC trace of a fullerene(CF_3) $_{2n}$ mixture in toluene (a) and of a $C_{78}(CF_3)_{2n}$ mixture in hexane (b). The collected $C_{78}(CF_3)_{2n}$ fractions are indicated by arrows. The compositions of $C_{78}(CF_3)_{2n}$ derivatives are given as $78(N)/2n$, where N denotes the number of a C_{78} isomer according to the spiral algorithm

which contained predominantly $C_{78}(CF_3)_{14}$ admixed by small amount of $C_{78}(CF_3)_{16/18}$, afforded crystals after recrystallization from *p*-xylene. X-ray diffraction revealed the structure of a solvate, $C_{78}(3)(CF_3)_{14} \cdot 2.5$ (*p*-xylene). Most other peaks of this separation also gave crystals which were shown to be CF_3 derivatives of $C_{78}(1)$ with 12 – 18 attached groups. These data will be presented in a separate publication elsewhere later.

Synchrotron X-ray data for the obtained crystals were collected at 100 K at the BL14.2 at the BESSY storage ring (PSF at the Free University of Berlin, Germany) using a MAR225 CCD detector. Crystallographic data, along with some details of data collection and structure refinements, are presented in Table 1. The structures were solved with SHELXD and anisotropically refined with SHELXL [20]. All crystal structures except $C_{78}(2)(CF_3)_{12}$ show disordering phenomena, most of which concern disorder of solvent molecules and CF_3 groups. The latter was caused by the librational movement of CF_3 groups around the C– CF_3 bonds or due to statistical overlap of similar molecules in the same crystallographic site. In the crystal structure of $C_{78}(2)(CF_3)_{10} \cdot 0.5$ (*o*-dichlorobenzene), one CF_3 group and the solvated molecule of *o*-dichlorobenzene are disordered over two positions each. In the crystal structure of $C_{78}(2)(CF_3)_{10} \cdot p$ -xylene, the molecule of solvation is strongly disordered over several positions. In the crystal structure of $C_{78}(3)(CF_3)_{12} \cdot 1.5$ (toluene), there is a disorder of two CF_3 groups and one toluene molecule. In the crystal structure of $C_{78}(3)(CF_3)_{14} \cdot p$ -xylene, there is an overlap of the main molecule with its enantiomer (ca. 16 %) and the molecule of an epoxide, $C_{78}(3)(CF_3)_{14}O$ (ca. 33 %), in the same crystallographic site, which is accompanied by a disorder of seven CF_3 groups. Crystallographic data are deposited under CCDC 1408116 – 1408120.

3. Discussion

Mass spectrometric MALDI TOF analyses of the raw trifluoromethylation products demonstrate the presence of $C_{78}(CF_3)_{2n}$ species with $2n$ ranging from 10 to 18, however, without information concerning C_{78} cage connectivity and CF_3 addition patterns. HPLC separation supported by subsequent MALDI MS analyses of separated fractions indicated the presence of several different $C_{78}(CF_3)_{2n}$ isomers of the same composition, whereas their assignment to specific C_{78} frameworks remained unknown. Crystal growth from separated fractions, followed by

TABLE 1. Crystallographic data and details of data collection and refinement for $C_{78}(CF_3)_{2n}$ compounds

Compound	$C_{78}(2)(CF_3)_{10}$	$C_{78}(2)(CF_3)_{10}$	$C_{78}(2)(CF_3)_{12}$	$C_{78}(3)(CF_3)_{12}$	$C_{78}(3)(CF_3)_{14}$ ¹
Solvate	0.5 <i>o</i> -C ₆ H ₄ Cl ₂	<i>p</i> -C ₆ H ₄ (CH ₃) ₂	—	1.5 C ₆ H ₅ (CH ₃)	2.5 <i>p</i> -C ₆ H ₄ (CH ₃) ₂
Mr	1700.38	1733.04	1764.90	1903.10	2174.44
Crystal system	triclinic	orthorhombic	monoclinic	triclinic	monoclinic
Space group	$P\bar{1}$	$P2_12_12_1$	$P2_1/n$	$P\bar{1}$	$C2/c$
<i>a</i> [Å]	11.537(1)	11.218(1)	11.490(1)	11.878(1)	21.280(2)
<i>b</i> [Å]	14.421(1)	19.022(1)	26.243(1)	12.374(1)	17.637(1)
<i>c</i> [Å]	18.038(1)	28.842(2)	19.154(1)	24.267(2)	42.567(3)
α [°]	85.60(1)	90	90	89.485(9)	90
β [°]	84.155(9)	90	91.409(10)	86.869(8)	90.02(1)
γ [°]	73.83	90	90	66.236(8)	90
<i>V</i> [Å ³]	2863.7(4)	6174.6(8)	5773.8(6)	3259.1(5)	15976(2)
<i>Z</i>	2	4	4	2	8
<i>D_c</i> [g·cm ⁻³]	1.972	1.870	2.030	1.939	1.807
Crystal size [mm]	0.02×0.02 ×0.01	0.03×0.03 ×0.01	0.03×0.02 ×0.01	0.03×0.03 ×0.01	0.03×0.03 ×0.01
λ [Å]	0.9050	0.8434	0.8434	0.8434	0.8551
Temperature [K]	100	100	100	100	100
$\theta(\text{max})$ [deg]	36.66	33.70	34.21	34.74	34.75
Refls collected/ <i>R</i> (int)	37547 / 0.064	87675 / 0.025	91568 / 0.028	51625 / 0.026	84029 / 0.073
Data / parameters	10391 / 11148	14259 / 1144	13460 / 1135	13634 / 1252	18585 / 1463
R_1 [$I \geq 2\sigma(I)$]/ <i>wR</i> ₂ (all)	0.087 / 0.233	0.048 / 0.114	0.054 / 0.135	0.077 / 0.174	0.116 / 0.290
$\Delta\rho(\text{max} / \text{min})$ [e Å ⁻³]	0.90 / -0.49	0.57 / -0.44	0.56 / -0.39	0.55 / -0.55	0.67 / -0.50

¹The crystal structure contains ca. 30 % admixture of an epoxide, $C_{78}(3)(CF_3)_{14}O$, localized in the same crystallographic site.

single crystal X-ray structure determination using synchrotron radiation was successful for only some cases of $C_{78}(CF_3)_{10-14}$, which are additional examples of unambiguous structural characterization of CF_3 derivatives for the most abundant isomers 1 – 3 of C_{78} fullerene (Fig. 2). CF_3 derivatives of the elusive $C_{78}(5)$ have not been detected, most probably, due to its very low content (or perhaps very low solubility), whereas the isolation of CF_3 derivatives of $C_{78}(4)$ was not even expected because of its obvious absence in the fullerene soot.

Two of the three CF_3 derivatives of $C_{78}(2)$ isolated and structurally characterized in this work contain the same C_s - $C_{78}(2)(CF_3)_{10}$ molecule, which is known from Ref. [14] and designated there as 78-10-2. The differences concern only the solvate molecules, *o*-dichlorobenzene,

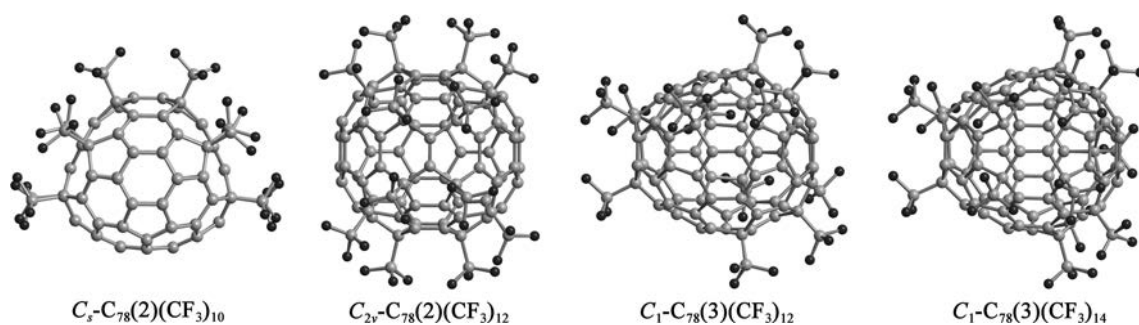


FIG. 2. Projection of the $C_s-C_{78}(2)(CF_3)_{10}$ molecule parallel to the mirror plane; the $C_{2v}-C_{78}(2)(CF_3)_{12}$ molecule is shown along the C_2 axis, whereas the $C_1-C_{78}(3)(CF_3)_{12}$ and $C_1-C_{78}(3)(CF_3)_{14}$ molecules are presented along the C_2 axes of the $C_{78}(3)$ carbon cages

p-xylene, and toluene in [14]. The formation of a toluene solvate with similar unit cell parameters and the space group $P2_1/m$ was also observed in one of our crystallization experiments. The addition pattern of 10 CF_3 groups contains a single ribbon of *para* attachments in nine edge-sharing $p-C_6(CF_3)_2$ hexagons, which is designated as p^9 (Fig. 3). This addition pattern is additionally stabilized by the formation of two nearly isolated benzenoid substructures on the fullerene cage. An isomeric p^4 , p^4 structure of C_2 symmetry (78-10-3), which differs by the position of only one CF_3 group (in the same pentagon near the C_2 axis), has been proposed in [14] based on ^{19}F NMR spectroscopy data. Note that the proposed 78-10-3 also contains two stabilizing nearly isolated benzenoid substructures. According to DFT calculations, $C_s-C_{78}(2)(CF_3)_{10}$ is $21.3 \text{ kJ}\cdot\text{mol}^{-1}$ more stable than the isomer with C_2 symmetry.

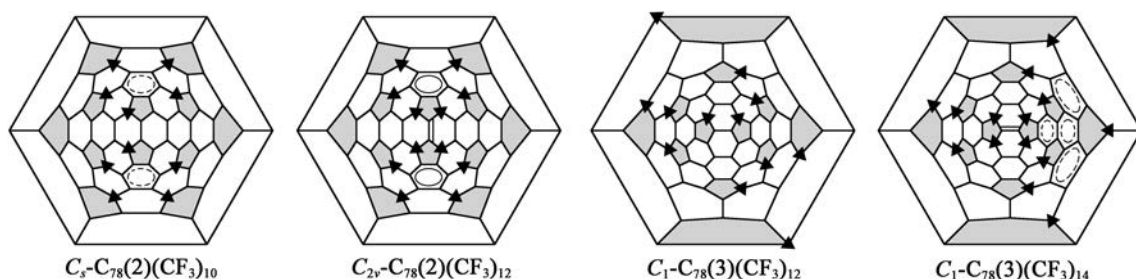


FIG. 3. Schlegel diagrams of $C_s-C_{78}(2)(CF_3)_{10}$, $C_{2v}-C_{78}(2)(CF_3)_{12}$, $C_1-C_{78}(3)(CF_3)_{12}$, and $C_1-C_{78}(3)(CF_3)_{14}$ molecules. Cage pentagons are highlighted with gray. Black triangles denote the positions of attached CF_3 groups. The isolated $C=C$ bonds are denoted by double lines. Aromatic nearly isolated and isolated benzenoid as well as triphenylene substructures are also indicated

The addition pattern of 12 CF_3 groups in the structure of $C_{2v}-C_{78}(2)(CF_3)_{12}$ is interesting in several aspects. Importantly, the structure of $C_{2v}-C_{78}(2)(CF_3)_{12}$ retains the symmetry of the pristine $C_{2v}-C_{78}(2)$ cage (Fig. 3). Its addition pattern contains the addition patterns of both $C_s-C_{78}(2)(CF_3)_{10}$ and $C_2-C_{78}(2)(CF_3)_{10}$ as substructures. Most probably, both molecules serve as precursors of $C_{2v}-C_{78}(2)(CF_3)_{12}$ in the course of trifluoromethylation. The attachment of two CF_3 groups transforms the p^9 ribbon into a p^{12} loop. At the same time, two nearly isolated benzenoid rings become fully isolated and one carbon-carbon bond becomes an isolated double $C=C$ bond, both acting as additional stabilizing factors. It should be noted that the addition pattern of $C_{2v}-C_{78}(2)(CF_3)_{12}$ exhibits an extremely rare example of a fullerene(CF_3)₁₂ structure

where not all pentagons are occupied by CF_3 groups. In fact, two pentagons remain unsubstituted in the experimentally determined structure. If the addition of two more groups occurs in these pentagons (for example, in the left-most and right-most positions of free pentagons), the hypothetical $C_s\text{-C}_{78}(2)(\text{CF}_3)_{12}$ molecule with all 12 pentagons occupied by CF_3 groups would contain two groups attached in isolated positions, which can be considered as a destabilizing feature. Indeed, DFT calculations of the formation energies of the hypothetical and the experimentally determined $\text{C}_{78}(2)(\text{CF}_3)_{12}$ molecules revealed that the former is $10.1 \text{ kJ}\cdot\text{mol}^{-1}$ less stable than the latter.

Structural relations between $\text{C}_{78}(2)(\text{CF}_3)_{10}$ and $\text{C}_{78}(2)(\text{CF}_3)_{12}$ molecules are very similar to those reported for $\text{C}_{84}(18)(\text{CF}_3)_{10}$ and $\text{C}_{84}(18)(\text{CF}_3)_{12}$ [18]. The addition pattern of $C_s\text{-C}_{84}(18)(\text{CF}_3)_{10}$ contains a single p^9 ribbon which is very similar to that in $C_s\text{-C}_{78}(2)(\text{CF}_3)_{10}$. Though the experimentally determined structure of $C_s\text{-C}_{84}(18)(\text{CF}_3)_{12}$ is characterized by the attachment of twelve CF_3 groups in all pentagons (with two additional groups in a separate $p\text{-C}_6(\text{CF}_3)_2$ hexagon), a theoretically predicted structure with a p^{12} loop ($84(18)/12 - 3$ in [18]), i.e., an analog of $\text{C}_{78}(2)(\text{CF}_3)_{12}$, is only $6 \text{ kJ}\cdot\text{mol}^{-1}$ less stable so that its presence in the trifluoromethylation products of $\text{C}_{84}(18)$ cannot be excluded. In fact, the only example of addition-free pentagons in the molecule with more than 12 addends on a fullerene cage has been reported for $\text{C}_{88}(17)\text{Cl}_{16}$ containing two such pentagons [21]. The stabilizing factors of this structure include the formation of one isolated benzenoid ring and three isolated $\text{C}=\text{C}$ bonds on the fullerene $\text{C}_{88}(17)$ cage.

The crystal structure of $\text{C}_{78}(3)(\text{CF}_3)_{12} \cdot 1.5(\text{toluene})$ contains the $C_1\text{-C}_{78}(3)(\text{CF}_3)_{12}$ molecule, which is known from the previous structure determination for a solvate with bromobenzene (78-12-2) [14]. Its asymmetric addition pattern of 12 CF_3 groups occupying all 12 pentagons is characterized by the presence of a short p^3 ribbon and a longer p^5mp ribbon (m for a $meta\text{-C}_6(\text{CF}_3)_2$ hexagon) on the fullerene cage (Fig. 3). Thus, it differs considerably from the additions pattern of $\text{C}_{78}(2)(\text{CF}_3)_{12}$ which comprises a loop of exclusively $para$ additions in $\text{C}_6(\text{CF}_3)_2$ hexagons (p^{12}) and containing two unoccupied pentagons. For comparison, the addition pattern of $C_2\text{-C}_{78}(5)(\text{CF}_3)_{12}$ [5] contains a single p^{11} ribbon of 12 CF_3 groups on the $\text{C}_{78}(5)$ cage which differs from the $\text{C}_{78}(3)$ cage by the position of only one $\text{C}-\text{C}$ bond.

The molecular structure of $\text{C}_{78}(3)(\text{CF}_3)_{14}$ was determined for the first time. Its addition pattern consists of a short pmp ribbon and a long p^{10} ribbon of edge-sharing $\text{C}_6(\text{CF}_3)_2$ hexagons (Fig. 3). There is an isolated double $\text{C}=\text{C}$ bond and an isolated triphenylene-like substructure on the fullerene cage. 13 of 14 CF_3 groups are arranged mirror-symmetrically on the cage. This feature explains the existence of packing errors with a number of enantiomeric molecules located in the same crystallographic sites as the main molecules in the crystal structure. $C_1\text{-C}_{78}(3)(\text{CF}_3)_{14}$ and $C_1\text{-C}_{78}(3)(\text{CF}_3)_{12}$ possess only seven CF_3 groups attached in common positions. Therefore, the latter cannot be regarded as a precursor of the former.

4. Conclusions

Trifluoromethylation of a higher fullerenes mixture and a C_{78} fraction followed by HPLC separation, crystallization, and X-ray diffraction studies resulted in structure determination of several CF_3 derivatives, $\text{C}_{78}(2,3)(\text{CF}_3)_{10-14}$. Although the carbon cages of $C_{2v}\text{-C}_{78}(2)$ and $C_{2v}\text{-C}_{78}(3)$ differ by the position of only one $\text{C}-\text{C}$ bond [2], the addition patterns of the derivatives with equal numbers of CF_3 groups, $\text{C}_{78}(2,3)(\text{CF}_3)_{12}$, differ significantly. A similar phenomenon has also been found for $(\text{CF}_3)_{12}$ derivatives of isomers $\text{C}_{84}(22)$ and $\text{C}_{84}(23)$, which also differ by the position of one bond on the carbon cages [16, 17]. In contrast, the addition patterns of $\text{C}_{78}\text{X}_{18}$ ($X = \text{Cl}, \text{Br}$) are the same for isomers $\text{C}_{78}(2)$, $\text{C}_{78}(3)$, and even $\text{C}_{78}(5)$ [8–11] which give rise to co-crystallization phenomena for these halides [8, 11] thus demonstrating the

levelling effect for a large number of addends on the addition patterns of fullerene derivatives with similar carbon cages. The existence of similar effects for CF_3 derivatives of isomers of C_{78} could be clarified by structural study of compounds with 16 – 18 attached groups.

Acknowledgements

This work was supported in part by the Russian Foundation for Basic Research (grant 15-03-04464).

References

- [1] Yoshida M., Aihara J. Validity of the weighted HOMO-LUMO energy separation as an index of kinetic stability for fullerenes with up to 120 carbon atoms. *Phys. Chem. Chem. Phys.*, 1999, **1**, P. 227–230.
- [2] Fowler P.W., Manolopoulos D.E. *An Atlas of Fullerenes*. Clarendon, Oxford, 1995, 392 p.
- [3] Diederich F., Whetten R.L., et al. Fullerene Isomerism: Isolation of C_{2v} - C_{78} and D_3 - C_{78} . *Science*, 1991, **254**, P. 1768–1770.
- [4] Wakabayashi T., Kikuchi K., et al. Pressure-Controlled Selective Isomer Formation of Fullerene C_{78} . *J. Phys. Chem.*, 1994, **98**, P. 3090–3091.
- [5] Shustova N.B., Newell B.S., et al. Discovering and verifying elusive fullerene cage isomers: structures of C_2 - p^{11} -(C_{74} - D_{3h})(CF_3)₁₂ and C_2 - p^{11} -(C_{78} - $D_{3h}(5)$)(CF_3)₁₂. *Angew. Chem. Int. Ed.*, 2007, **46**, P. 4111–4114.
- [6] Herrmann A., Diederich F. Synthesis, separation and characterisation of the first pure multiple adducts of C_{2v} - and D_3 - C_{78} . *J. Chem. Soc., Perkin Trans. 2*, 1997, P. 1679–1684.
- [7] Han A.H., Wakahara T., et al. A new method for separating the D_3 and C_{2v} isomers of C_{78} . *New J. Chem.*, 2009, **33**, P. 497–500.
- [8] Troyanov S.I., Kemnitz E. The first crystal structure of a halogenated higher fullerene, $C_{78}Br_{18}$, obtained by bromination of a fullerene mixture. *Eur. J. Org. Chem.*, 2003, P. 3916–3919.
- [9] Simeonov K.S., Amsharov K.Yu., Jansen M. Chlorinated derivatives of C_{78} -fullerene isomers with unusually short intermolecular halogen-halogen contacts. *Chem.-Eur. J.*, 2008, **14**, P. 9585–9590.
- [10] Simeonov K.S., Amsharov K.Yu., Krokos E., Jansen M. An epilogue on the C_{78} -fullerene family: The discovery and characterization of an elusive isomer. *Angew. Chem. Int. Ed.*, 2008, **47**, P. 6283–6285.
- [11] Burtsev A.V., Kemnitz E., Troyanov S.I. Synthesis and structure of fullerene halides $C_{70}X_{10}$ (X= Br, Cl) and $C_{78}Cl_{18}$. *Crystallogr. Rep.*, 2008, **53**, P. 639–644.
- [12] Troyanov S.I., Tamm N.B., et al. Synthesis and structure of a highly chlorinated C_{78} : $C_{78}(2)Cl_{30}$. *Z. Anorg. Allg. Chem.*, 2009, **635**, P. 1783–1786.
- [13] Kemnitz E., Troyanov S.I. Chlorides of isomeric C_{78} fullerenes: $C_{78}(1)Cl_{30}$, $C_{78}(2)Cl_{30}$, and $C_{78}(2)Cl_{18}$. *Mendeleev Commun.*, 2010, **20**, P. 74–76.
- [14] Kareev I.E., Popov A.A., et al. Synthesis and X-ray or NMR/DFT structure elucidation of twenty-one new trifluoromethyl derivatives of soluble cage isomers of C_{76} , C_{78} , C_{84} , and C_{90} . *J. Am. Chem. Soc.*, 2008, **130**, P. 13471–13489.
- [15] Tamm N.B., Troyanov S.I. Isomer $C_{78}(2)$ captured as the perfluoroethyl derivative $C_{78}(C_2F_5)_{10}$. *Mendeleev Commun.*, 2009, **19**, P. 198–199.
- [16] Chang K., Fritz M.A., et al. Synthesis, structure, and theoretical study of trifluoromethyl derivatives of $C_{84}(22)$ fullerene. *Chem. -Eur. J.*, 2013, **19**, P. 578–587.
- [17] Romanova N.A., Fritz M.A., et al. Synthesis, structure, and theoretical study of trifluoromethyl derivatives of $C_{84}(23)$ fullerene. *Chem. -Eur. J.*, 2013, **19**, P. 11707–11716.
- [18] Romanova N.A., Fritz M.A., et al. Synthesis and structure of trifluoromethyl derivatives of fullerenes $C_{84}(16)$ and $C_{84}(18)$. *Russ. Chem. Bull. Int. Ed.*, 2014, **63**, P. 2657–2667.
- [19] Kareev I.E., Shustova N.B., et al. Thermally stable perfluoroalkylfullerenes with the skew-pentagonal-pyramid pattern: $C_{60}(C_2F_5)_4O$, $C_{60}(CF_3)_4O$, and $C_{60}(CF_3)_6$. *J. Am. Chem. Soc.*, 2006, **128**, P. 12268–12280.
- [20] Sheldrick G.M. A short history of SHELX. *Acta Crystallogr. A*, 2008, **64**, P. 112–122.
- [21] Yang S., Wei T., Kemnitz E., Troyanov S.I. The most stable isomer of C_{88} fullerene, C_s - $C_{88}(17)$, revealed by X-ray structures of $C_{88}Cl_{16}$ and $C_{88}Cl_{22}$. *Chem. Asian J.*, 2012, **7**, P. 290–293.

C₆₀ fullerene-containing polymer stars in mixed matrix membranes

L. V. Vinogradova¹, A. Yu. Pulyalina², V. A. Rostovtseva², A. M. Toikka², G. A. Polotskaya^{1,2}

¹Institute of Macromolecular Compounds RAS, Saint Petersburg, Russia

²Saint Petersburg State University, Institute of Chemistry, Saint Petersburg, Russia

vinogradovalv@rambler.ru, a.pulyalina@spbu.ru, valfrank56@gmail.com, a.toikka@spbu.ru,
g.polotskaya@spbu.ru

PACS 81.05.ub

DOI 10.17586/2220-8054-2016-7-1-118-124

Star-shaped macromolecules with C₆₀ fullerene branching centers were used as modifiers of poly(2,6-dimethyl-1,4-phenylene oxide) matrix to obtain mixed matrix membranes. Two types of star modifiers were synthesized *i*) six-arms star with six polystyrene arms grafted onto C₆₀ center and *ii*) twelve-arms hybrid star with six polystyrene arms and six copolymer poly(2-vinylpyridine)-*block*-poly(*tert*-butylmethacrylate) arms grafted onto C₆₀ center. The membrane structures were studied by scanning electron microscopy. The transport properties of the membranes were determined by using sorption and pervaporation tests toward methanol and ethylene glycol over a wide concentration range. All membranes showed high affinity for methanol. The separation factor reached its maximum level at 5 wt% modifier concentration in the membrane. Polar hybrid arms were shown to change the membranes' morphologies and considerably improve their transport properties.

Keywords: applications of carbon nanostructures, fullerenes, star-shaped polymers, mixed matrix membrane, pervaporation.

Received: 20 November 2015

1. Introduction

The development of membrane technologies promotes the search for novel effective membranes to solve important industrial ecological problems. The up-to-date methods consist of creating mixed matrix membranes generally obtained by the inclusion of nanoparticles into a polymer matrix. However, agglomeration of small nanoparticles (fullerenes, nanotubes, etc) may create selective delamination on the interface between the polymer matrix and the agglomerated nanoparticle phase, which can result in membrane structural defects. To prevent the agglomeration, different methods of nanoparticle modification could be applied.

In the present work, a C₆₀ fullerene molecule was modified by anionic polymerization in order to serve as a branching center for polymer stars with six or twelve arms; these star-shaped macromolecules were used as fillers for mixed matrix membranes for pervaporation. In recent years, pervaporation, a widely-used membrane technique for the separation of nearly inseparable liquid mixtures (e.g. isomeric, azeotropic, etc.) [1]. The mechanism of the pervaporation process consists of the following steps: selective sorption of liquid molecules into the membrane surface on the feed side, selective diffusion of them through the membrane and desorption from the permeate side of the membrane as a vapor. Separation of organic liquids by pervaporation is based upon the selective permeation of one of the components.

Among the industrially important tasks that can be solved by pervaporation is the separation of methanol – ethylene glycol mixtures, regeneration of these alcohols, and their utilization. This task arises from the joint involvement of these alcohols in a number of syntheses or

technological processes; it is aggravated by the fact that these alcohols are very toxic. To separate the methanol – ethylene glycol mixture, membranes based on homopolymers (cellophane, polyphenylene oxide) [2,3], copolymers [4], and binary polymer blends with additional chemical linkage [5] were proposed. The most simple and available of them is poly(2,6-dimethyl-1,4-phenylene oxide) (PPO), however, it is not effective enough as membrane material [3].

To improve the membrane transport properties, a novel approach based on physical modification of PPO matrix by including C₆₀ fullerene containing star-shaped macromolecules with arms of a different nature is proposed in the present work. Two samples of modifier were used. They are *i*) six-arms star with six polystyrene (PS) arms grafted onto the C₆₀ branching center (C₆₀(PS)₆) [6, 7] and *ii*) twelve-arms hybrid star with six PS arms and six copolymer poly(2-vinylpyridine)-*block*-poly(*tert*-butylmethacrylate) (P2VP-PTBMA) arms grafted onto C₆₀ branching center (C₆₀(PS)₆(P2VP-PTBMA)₆) [8].

2. Experimental

PPO with molecular weight 172,000 and density 1.06 g/cm³ (Brno, Czech Republic) and C₆₀ fullerene of 99.9 % purity (Neo Tech Product, Research & Production Company, Russia) were used. Chloroform, methanol, and ethylene glycol were purchased from Vecton (Russia).

The six PS arms star on C₆₀ branching center C₆₀(PS)₆ and twelve-arms hybrid star C₆₀(PS)₆(P2VP-PTBMA)₆ (Fig. 1) were prepared by synthesis [9, 10].

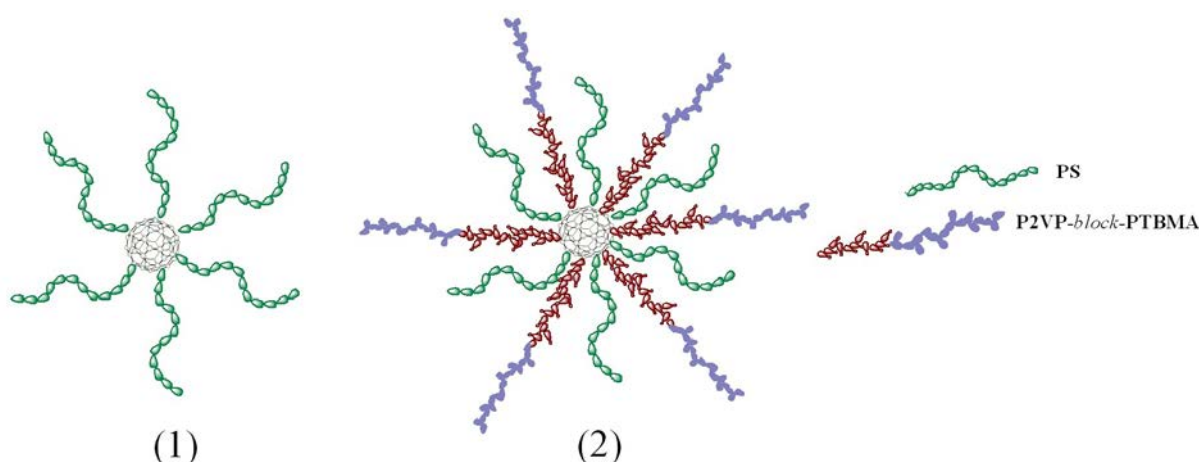


FIG. 1. C₆₀ fullerene-containing polymer stars (1) C₆₀(PS)₆ and (2) C₆₀(PS)₆(P2VP-PTBMA)₆

The composites containing 1, 3, and 5 wt% PPO/C₆₀(PS)₆ or PPO/C₆₀(PS)₆(P2VP-PTBMA)₆ were prepared by mixing solutions of 3 wt% PPO in chloroform and 3 wt% star-shaped polymer in chloroform. Thin film membranes (~ 40 μm thickness) were obtained by casting the 3 wt% polymer solution in chloroform on a cellophane surface. Membrane morphology was studied by scanning electron microscope (SEM) Zeiss SUPRA 55VP (Carl Zeiss AG, Germany).

Pervaporation experiments were performed using a laboratory cell with an effective membrane area of 14.8 cm² at 50 °C, downstream pressure below 10⁻² mm Hg was maintained. The permeate was collected into a liquid nitrogen-cooled trap, weighed and analyzed by chromatography “Chromatec–Crystal 5000.2” (Chromatec, Russia) with a thermal conductivity detector and refractometer IFR–454B2M. The total flux through the membrane was determined as the amount of liquid penetrated through the membrane area per time unit. The separation factor $\alpha_{\text{methanol/EG}}$ was defined by the following equation:

$$\alpha_{\text{methanol/EG}} = \frac{Y_{\text{methanol}}}{Y_{\text{EG}}} / \frac{X_{\text{methanol}}}{X_{\text{EG}}}, \quad (1)$$

where Y and X are the weight fraction of component in the permeate and feed, respectively.

Sorption experiments were performed by immersion of membrane samples in the individual liquid (methanol or ethylene glycol) at 20 °C. The weight change was determined gravimetrically. The sorption degree S was calculated by equation:

$$S = \frac{M_s - M_d}{M_d} \cdot 100, \quad (2)$$

where M_s is the weight of a swollen membrane upon equilibrium state and M_d is the weight of a dry membrane.

Kinetic curves for the sorption as a function of $M_t/M_\infty = f(t^{1/2}/l)$ were plotted, where M_t is the amount of desorbed substance per time t , M_∞ is the equilibrium amount of desorbed substance that was determined as the difference between the weight of a swollen membrane and the weight of membrane dried to a constant weight, and l is the membrane thickness. The effective diffusion coefficient D was calculated by the equation:

$$D = \frac{\pi}{16} (\tan \beta)^2, \quad (3)$$

where $\tan \beta$ is the initial linear slope of the desorption kinetic curves when $M_t/M_\infty < 0.4$.

3. Results and discussion

Preparation of $C_{60}(\text{PS})_6$ and $C_{60}(\text{PS})_6(\text{P2VP-PTBMA})_6$ star shaped macromolecules through covalent binding of the fullerene molecule with polymer chains prevents agglomeration of the modified nanoparticles and leads to their dispersion on the molecular level in the PPO matrix. PS and PPO blends are completely inter-soluble and the phase separation of these blends does not occur up to the temperature of their thermal destruction [11]. Therefore, one can expect that PS arms of both star types will be compatible with PPO matrix and this will facilitate the uniform distribution of star modifiers in the film.

The morphologies of the membranes containing 1, 3, and 5 wt% star modifiers were studied by scanning electron microscopy. Fig. 2 shows that the inclusion of star modifiers in the PPO matrix leads to changes in the top surface and cross-section structures of membranes containing 5 wt% $C_{60}(\text{PS})_6$ or $C_{60}(\text{PS})_6(\text{P2VP-PTBMA})_6$.

Figure 2(b) shows that the inclusion of $C_{60}(\text{PS})_6$ stars in the PPO matrix does not affect the top surface structure as compared to the PPO membrane (Fig. 2(a)). On the contrary, inclusion of $C_{60}(\text{PS})_6(\text{P2VP-PTBMA})_6$ hybrid stars changes the membrane's morphology considerably (Fig. 2(c)). One can observe domain structures of a rounded shape formed due to the segregation of hybrid star-shaped macromolecules. In the previous work, data from small-angle neutron scattering analyses gave evidence for supramolecular structure formation in the case of these types of hybrid star-shaped macromolecules [10]. As can be seen from micrographs of the membrane cross-section (Fig. 2(d, e, f)), they acquire a cellular structure after modification.

The transport properties of hybrid membranes were studied by pervaporation and sorption tests toward two elementary alcohols: monohydric methanol and dihydric ethylene glycol (EG). The separation of a methanol – ethylene glycol mixture by pervaporation was studied over a wide concentration range of feed mixtures for both mixed-matrix membrane types at 50 °C. All membranes were more permeable for methanol than for ethylene glycol, thus the permeates were enriched by methanol. For both membrane types, the effect of methanol concentration in the feed was the same, namely, the growth of methanol concentration led to a decrease in the

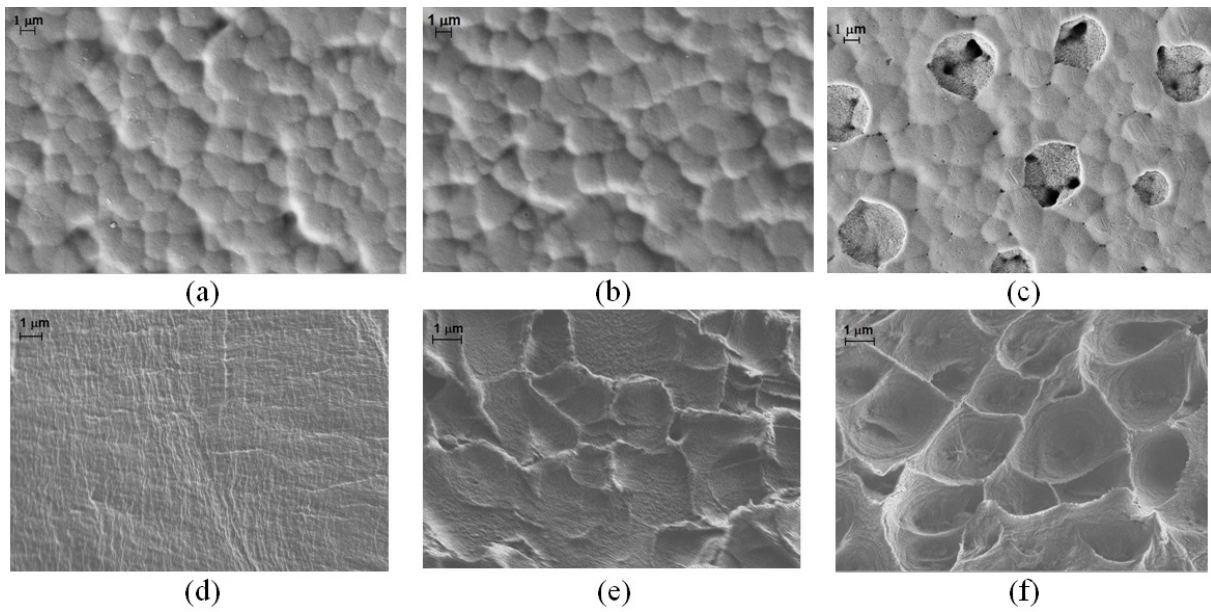


FIG. 2. SEM micrographs of (a, b, c) top surface and (d, e, f) cross-section of three membranes: (a, d) PPO, (b, e) PPO/C₆₀(PS)₆ (5 %), and (c, f) PPO/C₆₀(PS)₆(P2VP-PTBMA)₆ (5 %)

separation factor and increasing flux through membrane. However, the type of star modifier does have an effect on the quantitative characteristics of the membrane’s transport properties. Fig. 3 shows the effect of C₆₀(PS)₆ content on the PPO matrix on the main pervaporation parameters: the total flux through the membrane and the separation factor (methanol/ethylene glycol). One can see that the separation factor increases but the flux through membrane decreases with increased star modifier content in the PPO/C₆₀(PS)₆ membrane.

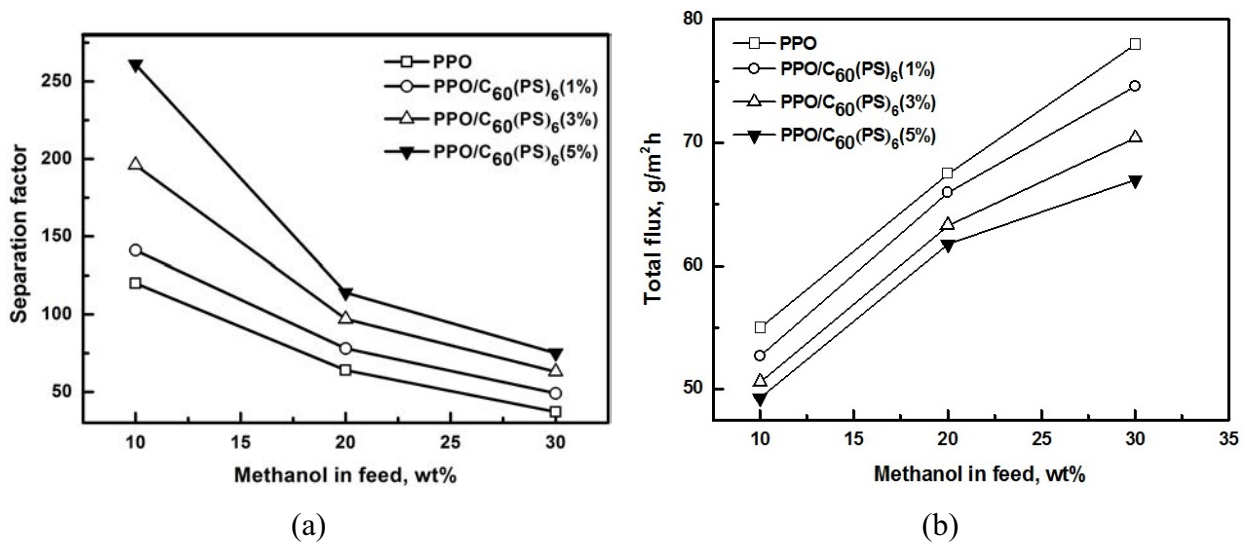


FIG. 3. Dependence of (a) separation factor and (b) total flux on methanol concentration in the feed for pervaporation of methanol – ethylene glycol mixture using PPO and PPO/C₆₀(PS)₆ membranes, 50 °C

A similar study of PPO/C₆₀(PS)₆(P2VP-PTBMA)₆ membranes showed that both the total flux and the separation factor increase with the inclusion of the hybrid stars. It should be noted that the magnitudes of both flux and separation factor are higher for membranes containing C₆₀(PS)₆(P2VP-PTBMA)₆ as compared with PPO/C₆₀(PS)₆. The best separation properties were obtained for membranes containing 5 wt% star modifiers. The PPO/C₆₀(PS)₆ (5 %) membrane exhibits a separation factor of 260, which is more than twice the level for the unmodified membrane (125).

Figure 4 shows data on the total flux and separation factor for the most efficient membrane, PPO/C₆₀(PS)₆(P2VP-PTBMA)₆ (5 %). The use of this membrane makes it possible to double the value of the total flux and to raise the separation factor more than four-fold in pervaporation of the feed containing 10 wt% methanol as compared with the unmodified membrane. The preparation and properties of PPO/C₆₀(PS)₆(P2VP-PTBMA)₆ membranes are claimed in the RU patent [12].

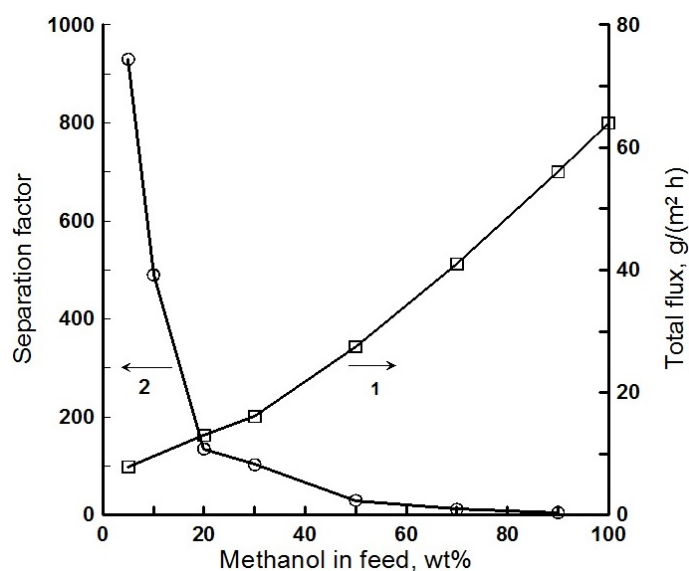


FIG. 4. Dependence of (1) total flux and (2) separation factor on methanol concentration in the feed for pervaporation of methanol – ethylene glycol mixture through PPO/C₆₀(PS)₆(P2VP-PTBMA)₆ (5 %) membrane, 50 °C

In pervaporation, the transport of small molecules through a membrane proceeds according to the “solution-diffusion” model i.e. the permeability is directly proportional to the solubility (sorption) and diffusivity [1]. Therefore, to explain pervaporation results, sorption and diffusion characteristics were determined on the basis of sorption experiments. Table 1 lists the data obtained for the sorption degree and diffusion coefficient for membranes containing 5 wt% star modifiers. The inclusion of C₆₀(PS)₆ stars into PPO matrix resulted in decreased values for the sorption degree and the diffusion coefficient for both methanol and ethylene glycol. Conversely, the inclusion of C₆₀(PS)₆(P2VP-PTBMA)₆ hybrid stars into the PPO matrix resulted in an increase in these parameters. The increase of the sorption degree may be related to the composition of hybrid stars which contain arms of copolymer poly(2-vinylpyridine)-*b*-poly(*tert*-butylmethacrylate) that are capable of higher affinity for alcohols than the PPO matrix.

Table 1 shows that the sorption degree for methanol is more than twice that of ethylene glycol for all mixed matrix membranes. The higher diffusion rate of methanol in comparison with ethylene glycol makes membranes selective for methanol. The enhancement effect is related to the architecture of the C₆₀ containing polymer stars and structural peculiarity of C₆₀

TABLE 1. Membrane sorption and diffusion characteristics for methanol and ethylene glycol

Membrane	Sorption degree (%)		Diffusion coefficient D (m ² /s)	
	Methanol	EG	Methanol, $D \cdot 10^{12}$	EG, $D \cdot 10^{14}$
PPO	14.0	5.2	2.27	0.37
PPO/C ₆₀ (PS) ₆ (5%)	12.4	5.0	2.10	0.05
PPO/C ₆₀ (PS) ₆ (P2VP-PTBMA) ₆ (5%)	16.1	7.0	4.52	0.69

branching centers, which contain attached arms of different chemical nature which confer the ability to form different types of self-organization.

4. Conclusion

Two fullerene C₆₀ containing star-shaped modifiers C₆₀(PS)₆ and C₆₀(PS)₆(P2VP-PTBMA)₆ were used for modification of PPO matrix to develop novel membranes for the pervaporation of methanol – ethylene glycol mixtures. The high affinity of the mixed matrix membranes for methanol and higher selectivity in separation of methanol – ethylene glycol mixtures were established as compared to that of unmodified membrane.

The improvement of transport properties occurs due to the favorable combination of matrix and filler properties. The effect of star-shaped modifier on the structure and transport properties requires an additional study, but the obtained results show that star modifiers provide a good compatibility for PS arms with matrix polymer, moreover, the segregation of C₆₀(PS)₆(P2VP-PTBMA)₆ polar arms promotes the formation of polar zones (domains) that provide high permeability and selectivity.

The fullerene C₆₀ branching center and the nature of polymer arms of star modifiers have an effect on the interaction between the membrane and separable liquids, thereby affecting pervaporation transport properties of membranes. An appreciable effect of the C₆₀ fullerene branching center on gas transport properties of membranes composed of the star shaped PS with C₆₀ center has been established in our previous work [13]. We believe that the introduction of star shaped macromolecules with C₆₀ branching centers in PPO matrix changes the system and the properties of transport channels, which leads to significant improvement of the membrane's transport characteristics.

Acknowledgements

G. A. Polotskaya acknowledges the Russian Foundation for Basic Research (project 15-03-02131). A. M. Toikka acknowledges Saint Petersburg State University (research grant 12.38.257.2014). The work was also supported by Fellowship of the President of Russian Federation (project No. 184, SP-1469.2015.1).

References

- [1] Baker R. *Membrane Technology and Applications*, 3rd edn.; John Wiley & Sons, Ltd. 2012, 588 p.
- [2] Ghosh I., Sanyal S.K., Mukherjee R.N. Pervaporation of methanol-ethylene glycol with cellophane membranes: performance of conditioned membranes. *Ind. Eng. Chem. Res.*, 1989, **28**, P. 757–763.
- [3] Khayet M., Villaluenga J.P.G., et al. Preparation and application of dense poly(phenylene oxide) membranes in pervaporation. *J. Colloid Interface Sci.*, 2004, **278**, P. 410–422.

- [4] Ray S.K., Sawant S.B., Joshi J.B., Pangarkar V.G. Methanol selective membranes for separation of methanol-ethylene glycol mixtures by pervaporation. *J. Membr. Sci.*, 1999, **154** (1), P. 1–13.
- [5] Zhang Q.G., Hu W.W., Liu Q.L., Zhu A.M. Chitosan/polyvinylpyrrolidone-silica hybrid membranes for pervaporation separation of methanol/ethylene glycol azeotrope. *J. Appl. Polym. Sci.*, 2013, P. 3178–3184.
- [6] Weber V., Duval M., Ederle Y., Mathis C. Physico-chemical behavior in solution of star-shaped polystyrene with C₆₀ core. *Carbon*, 1998, **36** (5–6), P. 839–842.
- [7] Lavrenko P.N., Vinogradova L.V. Hydrodynamic properties of star-shaped polystyrenes with a fullerene nucleus. *Polym. Sci. (Russ) Ser. A*, 2000, **42** (7), P. 726–730.
- [8] Vinogradova L.V. Star-shaped polymers with fullerene C₆₀ branching center. *Russ. Chem. Bull.*, 2012, **61** (5), P. 907–925.
- [9] Ederle Y., Mathis C. Addition of “living” polymers onto C₆₀. *Fullerene Sci. Technol.*, 1996, **4**, P. 1177–1793.
- [10] Lebedev V.T., Török Gy., Vinogradova L.V. Structure and supramolecular structures of star-shaped fullerene-containing heteroarm polymers in deuterotoluene. *Polym. Sci. (Russ) Ser. A*, 2011, **53** (1), P. 12–23.
- [11] Paul D.R., Newman S. *Polymer Blends*. Academic Press, New York, 1978, 435 p.
- [12] Polotskaya G.A., Vinogradova L.V., Krasnopeeveva E.L. Pervaporation membrane for mono- and bihydric alcohol mixture separation. Patent 2543203 Russia. MPK B01D 71/64, No. 2013111205/05, Issue No. 6, 2015.
- [13] Vinogradova L.V., Polotskaya G.A., Shevtsova A.A., Alent’ev A.Yu. Gas separating properties of membranes based on star-shaped fullerene (C₆₀)-containing polystyrenes. *Polym. Sci. (Russ) Ser. A*, 2009, **51** (2), P. 209–215.

Comparative Raman study of photo-oligomer stability in the donor-acceptor fullerene complex $\{\text{Pt}(\text{dbdtc})_2\}\cdot\text{C}_{60}$ and pristine C_{60}

K. P. Meletov^{1*}, J. Arvanitidis², D. Christofilos², G. Kourouklis²

¹Institute of Solid State Physics, Russian Academy of Sciences, Chernogolovka, Moscow region, Russia

²Aristotle University of Thessaloniki, GR-54 124 Thessaloniki, Greece

*mele@issp.ac.ru

PACS 78.30.Na

DOI 10.17586/2220-8054-2016-7-1-125-132

The photopolymerization process and the stability of the C_{60} photo-oligomers at elevated temperature in the molecular donor-acceptor fullerene complex $\{\text{Pt}(\text{dbdtc})_2\}\cdot\text{C}_{60}$ (C_{60} complex with platinum dibenzylidithiocarbamate) and pristine fullerite C_{60} are studied by Raman spectroscopy. Fast polymerization, manifested by the appearance of additional peaks in the frequency region of the $A_g(2)$ pentagon-pinch (PP) mode of the C_{60} molecule, was observed upon sample illumination at 514.5 and 532 nm, even at low laser power density as well as at 785 nm at higher power density. The frequencies of the new peaks are in accordance with the empirical dependence of the PP-mode frequency on the number of the sp^3 -like coordinated carbon atoms per molecular cage. The temperature dependence of the polymer content under constant laser power density reveals the decomposition of the photo-oligomers to monomers at ~ 350 K in the fullerene complex $\{\text{Pt}(\text{dbdtc})_2\}\cdot\text{C}_{60}$ and at ~ 410 K in the case of the pristine C_{60} . These values are considerably smaller than the decomposition temperature of 525 – 565 K for the crystalline polymers of C_{60} .

Keywords: fullerene, molecular complexes, Raman spectroscopy, photopolymerization.

Received: 20 November 2015

1. Introduction

The photo-induced polymerization of C_{60} was observed, for the first time, under intense illumination by visible light. To explain this reaction, a [2+2] cyclo-addition mechanism was proposed for the creation of covalent bonds among adjacent fullerene molecules [1,2]. The photopolymerization effectively occurs in thin films or surfaces of bulk samples, owing to the small light penetration depth ($\sim 1 \mu\text{m}$ near 500 nm), resulting in rather disordered materials consisting of various oligomers [3,4]. Therefore, structural analysis techniques are relatively inefficient for studying the photopolymers and thus, Raman spectroscopy become very important. In contrast to photopolymers, *X*-ray diffraction (XRD) measurements are very effective in the study of the ordered crystalline C_{60} polymers obtained by the treatment of C_{60} fullerite under various conditions of high pressure and high temperature (HPHT) [5,6]. XRD studies of the polymeric phases prepared under carefully controlled conditions of HPHT treatment have identified their crystal structures as follows: one-dimensional orthorhombic (1D-O), two-dimensional tetragonal (2D-T) and two-dimensional rhombohedral (2D-R). IR absorption and Raman scattering studies have revealed important changes in the vibrational spectra of the HPHT polymers with respect to that of the C_{60} fullerite precursor, related to the splitting and softening of the intramolecular modes due to the lowering of the C_{60} molecular symmetry caused by intermolecular covalent bonding [5–9]. The spectroscopic identification of the C_{60} polymers is mainly based on the behavior of the $A_g(2)$ PP-mode of the C_{60} cage, corresponding to the in-phase stretching vibration that involves tangential displacements of carbon atoms with a contraction of the pentagonal rings

and an expansion of the hexagonal rings. The PP-mode downshifts in all C_{60} polymers are due to the decrease of the mean intramolecular bond strength. Its softening depends on the number of the sp^3 -like coordinated carbon atoms per C_{60} molecular cage that arise due to intermolecular covalent bond formation. In the case of the *fcc* crystal structure of the C_{60} monomer, the $A_g(2)$ mode is observed at 1468 cm^{-1} . In the 1D-O polymer (linear polymer, 4 sp^3 -like coordinated carbon atoms) this mode is observed at 1458 cm^{-1} . In the 2D-T polymer (planar tetragonal polymer, 8 sp^3 -like coordinated carbon atoms), the peak downshifts to 1446 cm^{-1} , while in the case of the 2D-R phase (planar rhombohedral polymer, 12 sp^3 -like coordinated carbon atoms) the $A_g(2)$ mode exhibits the strongest softening and is observed at 1408 cm^{-1} [9].

The stability of the HPHT C_{60} polymers at elevated temperature has been studied by differential scanning calorimetry (DSC) [10–12]. Under a heating rate of 10 – 20 K/min, DSC measurements show a strong endothermic peak between 525 and 565 K, but no signal was observed during the cooling scan [10]. The transition temperature depends on the polymeric phase and somewhat on the scanning rate, indicating that the polymer decomposition process is kinetically-controlled. The change of enthalpy related to the complete polymer decomposition is the highest for the C_{60} dimers, decreases for the linear polymeric chains and attains its smallest value for planar polymeric networks. The decomposition kinetics of the planar C_{60} polymers was studied by IR absorption and Raman scattering and the formation of intermediate oligomeric states was observed in the case of the rhombohedral polymer [12, 13]. Note that in the case of photopolymers, their small amount on the surfaces of bulk samples makes the DSC measurements practically impossible. Thus, Raman spectroscopy becomes very important in the study of their stability at elevated temperatures.

We report the comparative Raman study of photopolymerization in the molecular donor-acceptor fullerene complex $\{\text{Pt}(\text{dbdtc})_2\}\cdot C_{60}$ and pristine C_{60} . The fullerene complex $\{\text{Pt}(\text{dbdtc})_2\}\cdot C_{60}$ possesses a layered structure in which the close-packed fullerene layers with nearly hexagonal arrangement of C_{60} molecules alternate with layers of molecular donor. In the fullerene layer, each C_{60} molecule is surrounded by six C_{60} neighbors with the shortest distances between the centers of molecules being 9.97 \AA (four neighbors) and 10.02 \AA (two neighbors). Fast photopolymerization, manifested by the appearance of a number of new peaks in the frequency region of the PP-mode, was observed in the fullerene layers of the $\{\text{Pt}(\text{dbdtc})_2\}\cdot C_{60}$ under low laser power density at $\lambda_{\text{exc}} = 514.5\text{ nm}$ which becomes much slower under $\lambda_{\text{exc}} = 785\text{ nm}$ even at high laser power. The frequencies of the new bands are in accordance with the empirical dependence of the crystalline polymer's PP-mode frequencies on the number of the sp^3 -like coordinated carbon atoms per C_{60} cage [14]. The polymer content can be inferred by the ratio of the sum of the integrated intensities for the new PP components to the total spectral intensity in the frequency region of the PP-mode. This value grows exponentially with laser exposure time while the time constant decreases with increasing laser power. The stabilities of the photo-induced oligomers in the fullerene complex $\{\text{Pt}(\text{dbdtc})_2\}\cdot C_{60}$ and pristine C_{60} were studied at elevated temperatures after saturation of the phototransformation process under constant laser power density. The temperature dependence of the polymer content probed by the same constant laser power density shows the decomposition of photo-oligomers to monomers near $\sim 350\text{ K}$ in the fullerene complex and at $\sim 410\text{ K}$ in the pristine C_{60} . These values are considerably smaller than the decomposition temperature of 525 – 565 K for crystalline polymers of C_{60} [10].

2. Experimental details

The samples of the donor-acceptor complex $\{\text{Pt}(\text{dbdtc})_2\}\cdot C_{60}$ were obtained by evaporating solutions containing fullerene C_{60} acceptors and platinum dibenzylthiocarbamate donors by

the technique described in Ref. [15]. The $\{\text{Pt}(\text{dbdtc})_2\}\cdot\text{C}_{60}$ complex adopts a monoclinic structure (space group $P2_1/c$). The parameters of the unit cell are $a = 15.957(5)$, $b = 17.241(5)$, $c = 10.018(5)$ Å, $\beta = 92.356(5)$ °, $V = 2753.7(5)$ Å³. The fullerene molecules are in monomeric form under ambient conditions. No covalent or coordination bonds were found between the platinum dibenzylthiocarbamate molecules and the fullerenes; furthermore these structures were arranged such that the benzyl substituents of $\text{Pt}(\text{dbdtc})_2$ were adjacent to the C_{60} [16].

The samples of the $\{\text{Pt}(\text{dbdtc})_2\}\cdot\text{C}_{60}$ complex were flat, well-faceted crystals with typical in-plane dimension of ~ 50 μm. The samples of 99.98 % purity pristine C_{60} were vapor-grown small single crystals with typical dimensions of ~ 100 μm, nearly mirror-like surface and truncated cubic outline. The crystal structure of the C_{60} fullerite at room temperature is face-centered cubic with lattice parameter 14.17 Å and a nearest-neighbor $\text{C}_{60} - \text{C}_{60}$ distance of 10.02 Å [17]. The Raman spectra were recorded in the back-scattering geometry using LabRam HR and LabRam ARAMIS micro-Raman setups as well as an Acton SpectraPro-2500i spectrograph, all equipped with Peltier cooled (-70 °C) CCD detectors. The 514.5, 532 and 785 nm laser lines and Olympus $50\times/100\times$ objectives were used for the Raman scattering excitation and activation of the phototransformation.

3. Results and discussion

Raman data related to the phototransformation in the $\{\text{Pt}(\text{dbdtc})_2\}\cdot\text{C}_{60}$ complex are shown in Fig. 1. The top right inset shows five Raman spectra in the PP-mode region recorded consecutively at $\lambda_{\text{exc}} = 785$ nm, laser power 16 μW and $100\times$ objective during 3000 s with 600 s exposure time for each spectrum. These spectra do not show any changes while the spectra recorded under similar conditions but with a laser power of 160 μW (bottom right inset) clearly show the appearance of new bands at lower frequencies. These bands are related to various photo-oligomers of C_{60} with different number of the sp^3 -like coordinated carbon atoms per molecular cage. The phototransformation is accompanied by the splitting of the Hg degenerate modes of the C_{60} molecule (not shown in the figure). The ratio of the sum of the integrated intensities for the new PP components to the total spectral intensity in the frequency region of the PP-mode provides a measure for the polymer content. The dependence of the photopolymer content on the laser exposure time is shown in Fig. 1 (circles) along with the fitting of the data by an exponential growth function (dotted line):

$$P(t) = P_{\text{sat}}\{1 - \exp(-t/\tau)\}. \quad (1)$$

Here, $P(t)$ is the time-dependent content of the photopolymer, P_{sat} is the content of the photopolymer attained after saturation of the phototransformation, and τ is the exponential growth time constant. The phototransformation parameters are $P_{\text{sat}} = 44.5$ % and $\tau = 320$ s for the illumination conditions shown in the bottom right inset, while the increase of the laser power results in an increase in P_{sat} and a decrease in τ . In fact, the time constant τ depends on the laser power density, which implies the necessity for careful and reproducible focusing of the laser beam on different sample sites. The top left inset of Fig. 1 shows the Raman spectrum of the $\{\text{Pt}(\text{dbdtc})_2\}\cdot\text{C}_{60}$ complex recorded under $\lambda_{\text{exc}} = 514.5$ nm, laser power 25 μW and $100\times$ objective. Four spectra recorded consecutively under continuous laser illumination during 360 seconds with 60 seconds exposure time for each spectrum show very fast transformation despite the relatively low laser power. In this case, the polymerization rate increases drastically due to the considerably higher absorption of the C_{60} layers near 514.5 nm than at 785 nm, leading to a vanishingly small exponential growth time constant while the saturated polymer

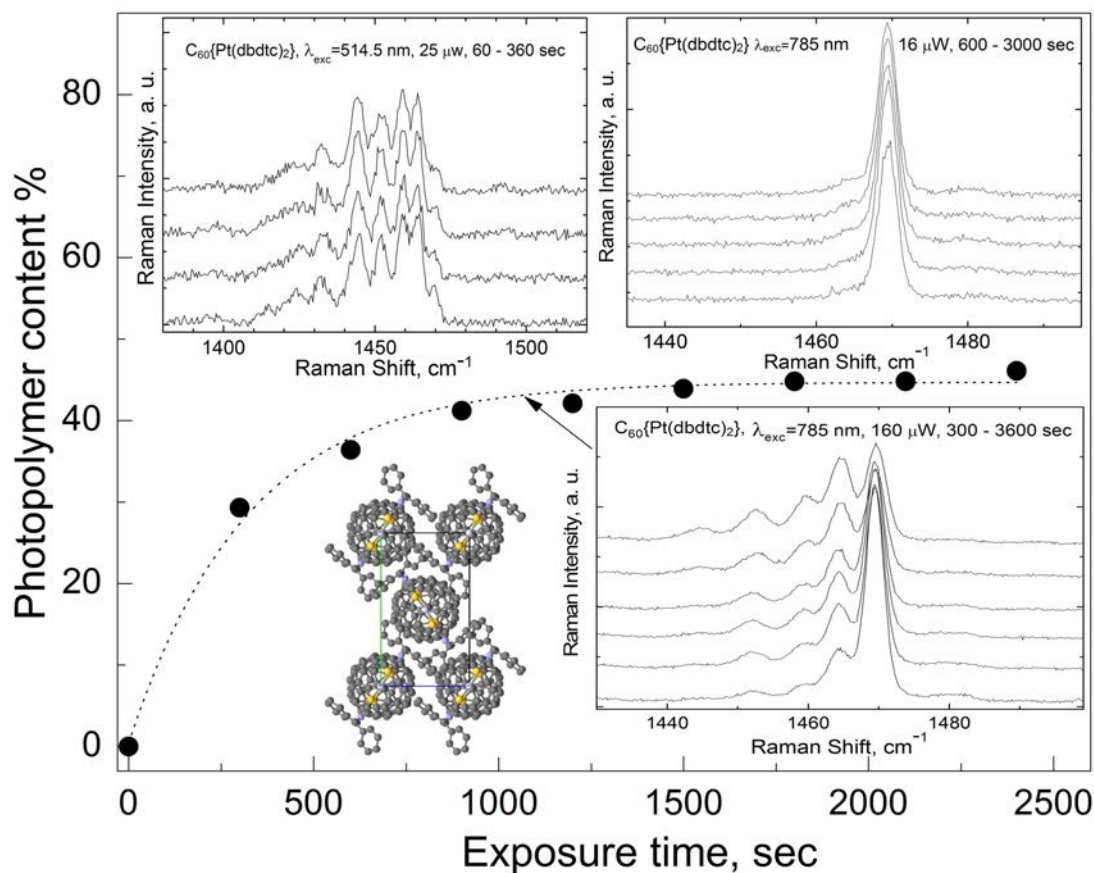


FIG. 1. Photopolymer content in the $\{\text{Pt}(\text{dbdtc}_2)\} \cdot \text{C}_{60}$ complex, excited at $\lambda_{\text{exc}} = 785 \text{ nm}$ and a power of $16 \mu\text{W}$, as a function of the illumination time (circles) fitted by an exponential growth function (dotted line). The molecular arrangement in the fullerene complex viewed along the a -axis of the unit cell is also included. Insets: Time evolution of the Raman spectra of the $\{\text{Pt}(\text{dbdtc}_2)\} \cdot \text{C}_{60}$ complex in the region of the PP-mode excited through a $100\times$ objective and $\lambda_{\text{exc}} = 785 \text{ nm}$, laser power $16 \mu\text{W}$ (top right), $\lambda_{\text{exc}} = 785 \text{ nm}$, laser power $160 \mu\text{W}$ (bottom right), as well as $\lambda_{\text{exc}} = 514.5 \text{ nm}$, laser power $25 \mu\text{W}$ (top left)

content reaches $P_{\text{sat}} = 96.1 \%$. This is in accordance with the much smaller penetration depth for C_{60} crystals at 514.5 nm than at 785 nm [18].

It is interesting to compare the photopolymerization in the $\{\text{Pt}(\text{dbdtc}_2)\} \cdot \text{C}_{60}$ complex with that of the pristine C_{60} with respect to the photo-oligomer content and stability at elevated temperatures. The Raman spectra recorded in the region of the $A_g(2)$ PP-mode under excitation by $\lambda_{\text{exc}} = 532 \text{ nm}$, laser power $60 \mu\text{W}$ and $50\times$ objective are shown in the bottom right inset of Fig. 2. The initial spectrum recorded with 600 s exposure time contains only the $A_g(2)$ PP-mode of the C_{60} monomer. The following spectra recorded with 3600 s exposure time after continuous laser illumination for 7200 , 14400 , 21600 and 28800 s show a gradual decrease of the PP-mode intensity of the monomer as well as the appearance and gradual increase in the intensities of the corresponding photo-oligomer modes. The intensity distribution between the PP-modes of the photo-oligomers differs from that of the $\{\text{Pt}(\text{dbdtc}_2)\} \cdot \text{C}_{60}$ complex but the peak frequencies for both materials are similar. The experimental dependence of the photopolymer content on the laser exposure time is shown in Fig. 2 by circles while the dotted line is the exponential growth

fitting. Its time constant is relatively high (~ 6000 s), suggesting that the almost instantaneously transformed complex is more sensitive to light. However, the time constant of C_{60} being longer, may also be partly related to the larger laser spot under the $50\times$ objective focusing as well as to the somewhat higher transmittance of C_{60} near 532 nm with respect to 514.5 nm. The dependence of the exponential growth time constant on the laser power is shown in the bottom left inset. The measurements were performed at a number of neighboring sites of the same C_{60} sample and under reproducible focusing conditions. The dependence is quasi-linear and the time constant decreases with increasing laser power as in the case of the fullerene complex.

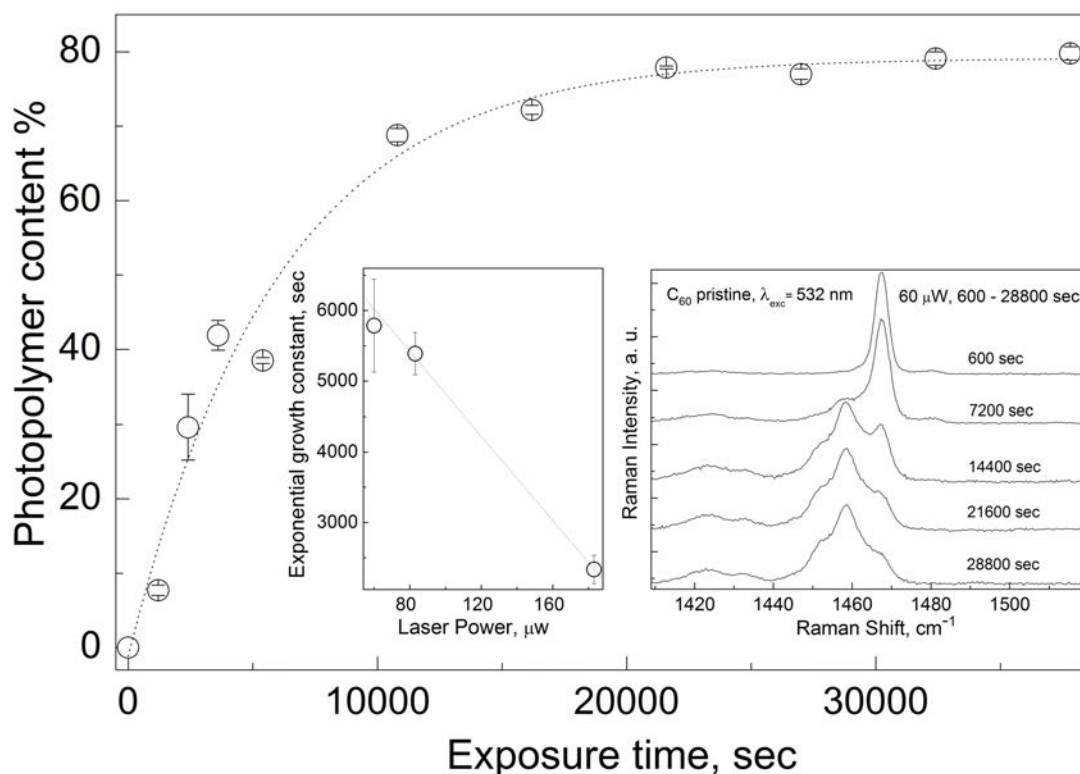


FIG. 2. Photopolymer content in the fullerite C_{60} , excited through a $50\times$ objective at $\lambda_{\text{exc}} = 532$ nm and laser power $60 \mu\text{W}$, as a function of the exposure time (circles) fitted by an exponential growth function (dotted line). Right inset: Time evolution of the Raman spectra in the region of the PP-mode. Left inset: Laser power dependence of the exponential growth time constant (circles) fitted by a linear function (dotted line)

Figure 3 shows the frequencies of the PP-mode for various crystalline polymers of C_{60} (circles) vs. the number of the sp^3 -like coordinated carbon atoms per fullerene molecular cage [7–9, 19]. The Raman frequencies of the photo-oligomers in the pristine C_{60} crystal (squares) and $\{\text{Pt}(\text{dbdtc})_2\}\cdot C_{60}$ complex (open stars) are also shown in Fig. 3. The structural arrangements of the intermolecular covalent bonds in the different HPHT crystalline polymers, as deduced by detailed XRD measurements, are also illustrated [5,6,20]. The empirical dependence of the PP-mode frequency of the crystalline C_{60} polymers shows a gradual decrease with an increase in the number of the sp^3 -like coordinated carbon atoms per C_{60} molecule. The Raman data for the photo-oligomers in the $\{\text{Pt}(\text{dbdtc})_2\}\cdot C_{60}$ complex and pristine C_{60} agree well with those of crystalline polymers, which clarifies the origin of the new PP-modes as dimers, fragments of linear chains, conjugated linear chains, planar tetragonal and rhombohedral

polymeric networks. Note, that the Raman band $\sim 1452\text{ cm}^{-1}$ observed in the Raman spectra of the phototransformed $\{\text{Pt}(\text{dbdtc})_2\}\cdot\text{C}_{60}$ complex and pristine C_{60} does not exist in the crystalline C_{60} polymers and is related to conjugated linear chains that were observed under pressure- and photo-induced transformations in the linear orthorhombic C_{60} polymer [19–21]. In addition, the phototransformed $\{\text{Pt}(\text{dbdtc})_2\}\cdot\text{C}_{60}$ complex and pristine C_{60} exhibit a Raman band near $\sim 1432\text{ cm}^{-1}$ which may be related to the PP-mode of an exotic photo-oligomer with 10 sp^3 -like coordinated carbon atoms per fullerene molecular cage.

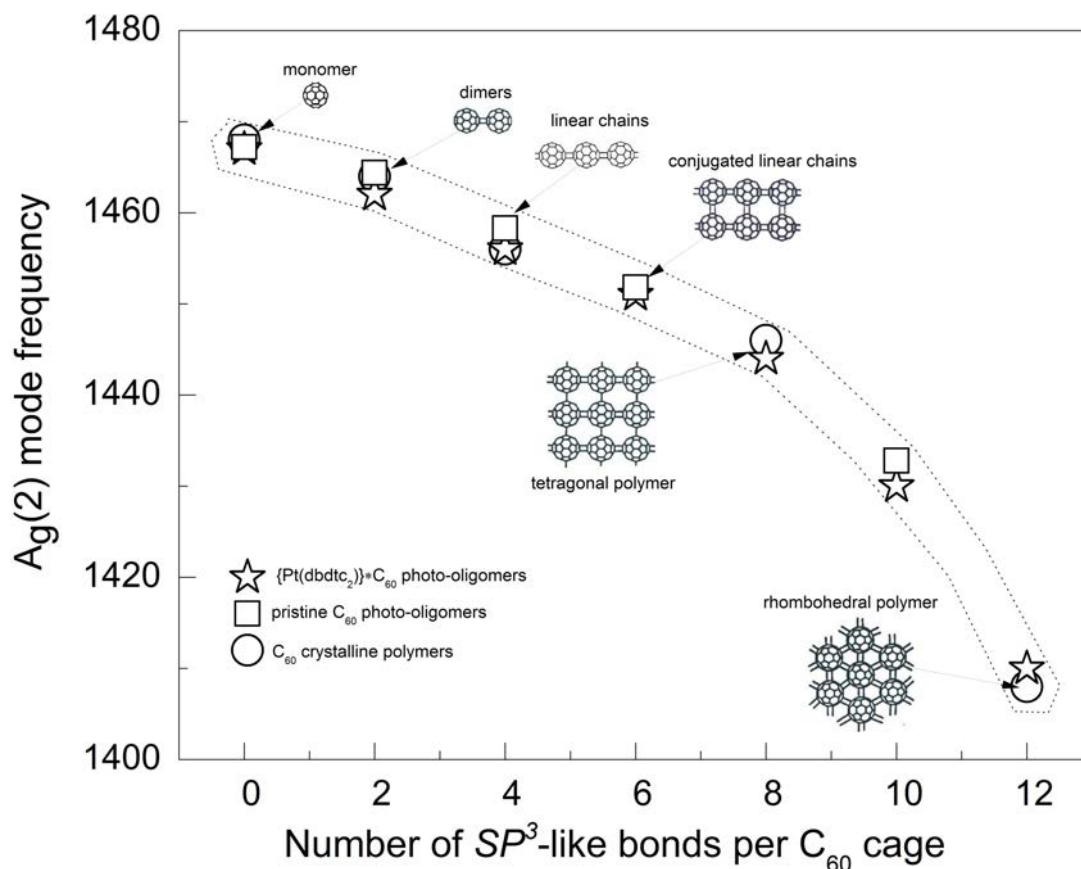


FIG. 3. The frequencies of the PP-mode of the HPHT crystalline polymers of C_{60} (circles), the photo-transformed pristine C_{60} (squares) and $\{\text{Pt}(\text{dbdtc})_2\}\cdot\text{C}_{60}$ complex (stars) vs. the number of the sp^3 -like coordinated carbon atoms per C_{60} molecular cage. The arrangement of the intermolecular covalent bonds in HPHT crystalline polymers is also shown

The stability of the photo-oligomers at elevated temperatures was also studied in a series of Raman measurements under excitation by $\lambda_{\text{exc}} = 514.5\text{ nm}$, laser power $20\ \mu\text{W}$ and $50\times$ objective. The photopolymer content attained after saturation of the phototransformation process is shown as a function of temperature in Fig. 4 for the $\{\text{Pt}(\text{dbdtc})_2\}\cdot\text{C}_{60}$ complex (solid circles) and pristine C_{60} (open circles). The inset in Fig. 4 shows the Raman spectra of the $\{\text{Pt}(\text{dbdtc})_2\}\cdot\text{C}_{60}$ complex in the region of the PP-mode recorded with 240 s exposure time for each spectrum at various temperatures from 318 to 413 K. The data were acquired after 1440 s illumination time, where the saturation of the photopolymer content has occurred. The spectrum recorded at the lowest temperature of 318 K exhibits the typical photopolymer features and is characterized by a suppressed monomeric PP-mode. The maximum content of

polymer at this temperature is $\sim 90\%$ and decreases to $\sim 7\%$ at the highest temperature of 413 K, where the PP-mode of the monomer becomes dominant. The rapid reduction of the photopolymer content begins at ~ 340 K and is halved at ~ 350 K. This temperature can be considered as the temperature limit of the photo-oligomer stability in the $\{\text{Pt}(\text{dbdtc})_2\}\cdot\text{C}_{60}$ complex. Similar Raman measurements were also performed at elevated temperatures for the pristine C_{60} . The photo-oligomers in pristine C_{60} show somewhat higher stability: the rapid decrease of the photopolymer content begins near ~ 400 K and becomes half at 410 K. These data are very close to those obtained in a previous Raman study of the thermal decomposition of photopolymerized C_{60} thin films [22].

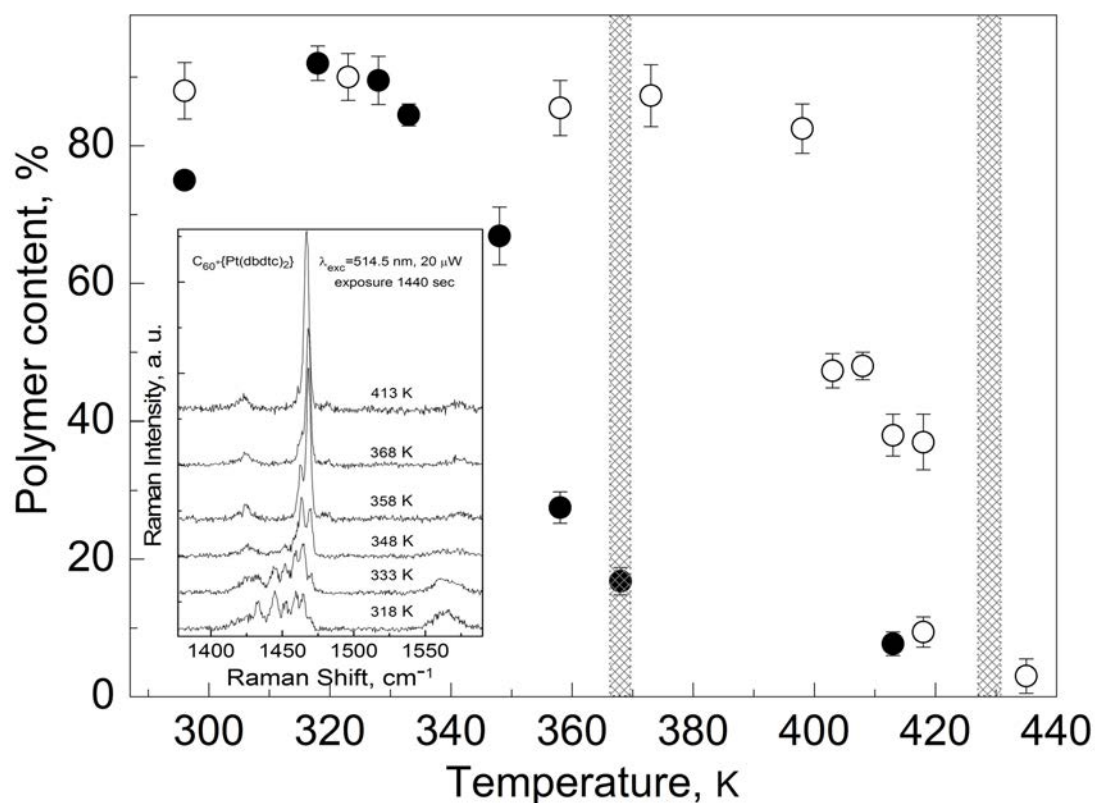


FIG. 4. The photopolymer content attained after saturation of the phototransformation process as a function of temperature for the $\{\text{Pt}(\text{dbdtc})_2\}\cdot\text{C}_{60}$ complex (solid circles) and pristine C_{60} (open circles). Shaded areas indicate the decomposition temperature of the photo-oligomers. Inset: Raman spectra of the $\{\text{Pt}(\text{dbdtc})_2\}\cdot\text{C}_{60}$ complex in the PP-mode region recorded at various temperatures

Summarizing, we have revealed the photopolymerization of the C_{60} layers in the molecular donor-acceptor complex $\{\text{Pt}(\text{dbdtc})_2\}\cdot\text{C}_{60}$. Various aspects of this process were comparatively studied by Raman spectroscopy with those of the pristine C_{60} . The photopolymerization rate and polymer content attained after phototransformation saturation depended on the laser excitation wavelength, laser power and focusing. The photo-oligomers are, most likely, dimers, fragments of linear chains, conjugated linear chains, as well as planar tetragonal and rhombohedral polymeric networks. The stability study of photo-oligomers at elevated temperatures showed that their decomposition to a monomer occurred near 350 K in the fullerene complex $\{\text{Pt}(\text{dbdtc})_2\}\cdot\text{C}_{60}$ and at ~ 410 K in pristine C_{60} . These values are considerably smaller than

the decomposition temperature 525 – 565 K for crystalline C₆₀ polymers [10]. This difference, to a significant extent, may be related to the structural transformations and the deformation of the fullerene molecular cage during the creation of the HPHT crystalline polymers, whereas the photopolymerization is less energetically demanding because of the disordered structure of the photo-oligomers and their small fragment size.

Acknowledgements

The support by the Russian Foundation for Fundamental Research, grant No. 15-02-01495, and the RAS Presidium Program “Physics of compressed matter” are greatly acknowledged. The authors are grateful to Dr. D. Konarev for providing the fullerene complexes.

References

- [1] Rao A.M., Zhou P., et al. Photoinduced polymerization of solid C₆₀ films. *Science*, 1993, **259**, P. 955–957.
- [2] Zhou P., Dong Z.H., Rao A.M., Ecklund P.C. Reaction-mechanism for photopolymerization of solid fullerene C₆₀. *Chem. Phys. Lett.*, 1993, **211**, P. 337–340.
- [3] Pusztai T., Oszlanyi G., et al. Bulk structure of phototransformed C₆₀. *Solid State Commun.*, 1999, **111**, P. 595–599.
- [4] Karachevtsev V.A., Mateichenko P.V., et al. Effective photopolymerization of C₆₀ films under simultaneous deposition and UV light irradiation: Spectroscopy and morphology study. *Carbon*, 2004, **42**, P. 2091–2098.
- [5] Iwasa Y., Arima T., et al. New phases of C₆₀ synthesized at high pressure. *Science*, 1994, **264**, P. 1570–1572.
- [6] Nunez-Regueiro M., Marques L., et al. Polymerized fullerite structures. *Phys. Rev. Lett.*, 1995, **74**, P. 278–281.
- [7] Rao A.M., Ecklund P.C., et al. Infrared and Raman studies of pressure-polymerized C₆₀. *Phys. Rev. B*, 1997, **55**, P. 4766–4773.
- [8] Senyavin V.M., Davydov V.A., et al. Spectroscopic properties of individual pressure-polymerized phases of C₆₀. *Chem. Phys. Lett.*, 1999, **313**, P. 421–425.
- [9] Davydov V.A., Kashevarova L.S., et al. Spectroscopic study of pressure polymerized phases of C₆₀. *Phys. Rev. B*, 2000, **61**, P. 11936–11945.
- [10] Iwasa Y., Tanoue K., Mitani T., Yagi T. Energetics of polymerized fullerites. *Phys. Rev. B*, 1998, **58**, P. 16374–16376.
- [11] Korobov M.V., Senyavin V.M., et al. Phase transformations in pressure polymerized C₆₀. *Chem. Phys. Lett.*, 2003, **381**, P. 410–415.
- [12] Korobov M.V., Bogachev A.G., et al. Relative stability of polymerized phases of C₆₀: Depolymerization of a tetragonal phase. *Carbon*, 2005, **43**, P. 954–961.
- [13] Meletov K.P., Arvanitidis J., et al. Raman study of the temperature-induced decomposition of the two dimensional rhombohedral polymer of C₆₀ and the intermediate states formed. *Carbon*, 2005, **48**, P. 2974–2979.
- [14] Meletov K.P., Kourouklis G.A. Pressure and temperature induced transformations in crystalline polymers of C₆₀. *JETP*, 2012, **115**, P. 707–723.
- [15] Konarev D.V., Khasanov S.S., et al. Fullerene complexes with divalent metal dithiocarbamates: structures, magnetic properties, and photoconductivity. *Russ. Chem. Bull. Int. Ed.*, 2007, **56**, P. 2145–2161.
- [16] Meletov K.P., Konarev D.V. Raman study of the pressure-induced phase transitions in the molecular donor-acceptor complex {Pt(dbdtc)₂}C₆₀. *Chem. Phys. Lett.*, 2012, **553**, P. 21–25.
- [17] Moret R. Structure, phase transitions and orientational properties of the C₆₀ monomer and polymers. *Acta Cryst. A*, 2005, **61**, P. 62–76.
- [18] Meletov K.P., Dolganov V.K., et al. Absorption Spectra of Crystalline Fullerite C₆₀ at Pressures up to 19 GPa. *J. de Physique I*, 1992, **2**, P. 2097–2105.
- [19] Meletov K.P., Davydov V.A., et al. High pressure photoinduced polymerization of the orthorhombic polymeric phase of C₆₀. *Chem. Phys. Lett.*, 2005, **416**, P. 220–224.
- [20] Le Parc R., Levelut C., et al. In situ X-ray powder diffraction study of the one-dimensional polymeric C₆₀ phase formation under high-pressure. *Chem. Phys. Lett.*, 2007, **438**, P. 63–66.
- [21] Meletov K.P., Davydov V.A., et al. The influence of pressure on the photopolymerization rate of linear orthorhombic polymer of C₆₀. *Chem. Phys. Lett.*, 2006, **428**, P. 298–302.
- [22] Wang Y., Holden J.M., Bi X., Ecklund P.C. Thermal decomposition of polymeric C₆₀. *Chem. Phys. Lett.*, 1994, **217**, P. 413–417.

Pressure-assisted photopolymerization in the molecular donor-acceptor fullerene complex $\{\text{Cd}(\text{dedtc})_2\}_2 \cdot \text{C}_{60}$

K. P. Meletov^{1*}, J. Arvanitidis², D. Christofilos², G. Kourouklis²

¹Institute of Solid State Physics, Russian Academy of Sciences, Chernogolovka, Moscow region, Russia

²Aristotle University of Thessaloniki, GR-54 124 Thessaloniki, Greece

*mele@issp.ac.ru

PACS 78.30.Na

DOI 10.17586/2220-8054-2016-7-1-133-139

The pressure-assisted photopolymerization in the fullerene complex $\{\text{Cd}(\text{dedtc})_2\}_2 \cdot \text{C}_{60}$ (fullerene complex with cadmium diethyldithiocarbamate) observed in the pressure region between 2.24 and 5.99 GPa was studied in detail. After a phase transition near ~ 2 GPa, the Raman spectra exhibit time-dependent changes under prolonged laser illumination regarding the appearance of new peaks in the frequency region of the $A_g(2)$ mode of the C_{60} monomer. These peaks are related to the fullerene oligomers with a different number of sp^3 -like coordinated carbon atoms per molecular cage. The polymer content increases with the laser power density and exposure time, while for a fixed laser power, its saturated value is independent of pressure. Outside the pressure range 2.24 – 5.99 GPa, photopolymerization is suppressed.

Keywords: high pressure, fullerene, molecular complexes, Raman scattering, photopolymerization.

Received: 20 November 2015

1. Introduction

The high pressure behavior of donor-acceptor fullerene complexes is of interest due to their layered structure in which the close-packed fullerene layers are alternated with layers of the molecular donor. At high pressures, the reduction of intermolecular distances in fullerene complexes increases the overlap of the highest occupied molecular orbital (HOMO) of the molecular donor and the lowest unoccupied molecular orbital (LUMO) of the fullerene acceptor. This may cause charge transfer, particularly in the case where the molecular complex at ambient conditions is close to the ionic state. Alternatively, the decrease of intermolecular distances within the fullerene layers may result in the formation of covalent inter-cage bonds. The X-ray diffraction (XRD) and Raman studies of ionic and neutral donor-acceptor complexes of C_{60} have revealed the formation of covalent bonds between fullerene molecules at low temperature or elevated pressure [1–8]. Recently, the photo-induced transformations at high pressure were observed in the Raman spectra of the molecular complex $\{\text{Cd}(\text{dedtc})_2\}_2 \cdot \text{C}_{60}$ which take place immediately after the pressure-induced phase transition near 2 GPa [9]. The time-dependent changes in the $A_g(2)$ mode region are reminiscent of those in the Raman spectra of C_{60} fullerene under light irradiation [10].

The ability of C_{60} to form inter-cage covalent bonds is due to the existence of 30 unsaturated double $\text{C}=\text{C}$ bonds in the C_{60} molecule. C_{60} fullerite polymerizes under illumination [10], alkali metal doping [11] and high-pressure/high-temperature (HPHT) treatment [12, 13]. The polymerization of C_{60} is realized through the creation of covalent bonds among adjacent fullerene molecules via a [2+2] cyclo-addition mechanism that necessitates the rotation of molecules to attain a suitable mutual orientation [10, 14]. The photopolymerization is efficient in thin films or the surfaces of bulk samples, owing to the small light penetration depth

($\sim 1 \mu\text{m}$ near 500 nm); the photo-transformed material is rather disordered and contains various oligomers [15, 16]. For these reasons, the XRD method is unsuitable for the analysis of the photopolymers and the role of the Raman spectroscopy becomes crucial. Unlike the case of the photopolymers, XRD is very useful in the study of the ordered crystalline C_{60} polymers obtained by HPHT treatment of the C_{60} fullerite whose structures have been identified as one-dimensional orthorhombic (1D-O), two-dimensional tetragonal (2D-T) and two-dimensional rhombohedral (2D-R) [12, 13]. The Raman spectra of the crystalline polymers exhibit splitting and softening of the bands related to the lowering of the C_{60} molecular symmetry caused by the intermolecular covalent bonds [12, 13, 17]. An important probe of the C_{60} polymers is the behavior of the $A_g(2)$ pentagonal pinch (PP) mode of the C_{60} molecule, related to the in-phase stretching vibration that involves tangential displacements of carbon atoms with contraction of the pentagonal rings and expansion of the hexagonal rings. The PP-mode frequency is downshifted due to the lowering of the average cage stiffness with an increase in the number of the sp^3 -like coordinated carbon atoms per C_{60} molecule, associated with the inter-cage bonds. Thus, the $A_g(2)$ mode of the C_{60} monomer, observed at 1468 cm^{-1} , shifts to 1458 cm^{-1} in the linear chains (1D-O polymer, 4 sp^3 -like coordinated carbon atoms), while in the planar polymers, the peak downshifts further to 1446 cm^{-1} (2D-T polymer, 8 sp^3 -like coordinated carbon atoms) and 1408 cm^{-1} (2D-R polymer, 12 sp^3 -like coordinated carbon atoms) [17].

In this paper, we present the detailed study of the pressure-assisted photopolymerization in the fullerene complex $\{\text{Cd}(\text{dedtc})_2\}_2 \cdot \text{C}_{60}$. We have carefully defined the pressure region in which the phototransformation takes place; we have studied the photopolymerization kinetics and its dependence on pressure, and identified the final products of the reaction as fullerene photo-oligomers. Starting at a pressure of 2.24 GPa, immediately after the pressure-induced phase transition [9], photopolymerization occurs up to 5.99 GPa, after which it is abruptly suppressed. In this pressure range, the Raman spectra exhibit time-dependent changes associated with the appearance of new bands in the frequency region of the $A_g(2)$ mode of the C_{60} monomer. Their intensity increases exponentially with the laser exposure time and saturates at a value that does not depend on pressure. The peak frequencies indicate that the new peaks are related to photo-oligomers with four and six sp^3 -like coordinated carbon atoms per molecular cage.

2. Experimental details

Samples of the donor-acceptor complex $\{\text{Cd}(\text{dedtc})_2\}_2 \cdot \text{C}_{60}$ were obtained by evaporation of a solution containing fullerene acceptors and cadmium diethyldithiocarbamate donors by the method described in [18]. The XRD data show that the $\{\text{Cd}(\text{dedtc})_2\}_2 \cdot \text{C}_{60}$ complex acquires a monoclinic structure, space group $P2_1/c$ with unit cell parameters $a = 16.368(3)$, $b = 17.056(2)$, $c = 10.6650(15) \text{ \AA}$, $\beta = 100.058(14)^\circ$ and $V = 2931.63 \text{ \AA}^3$ [7]. In the fullerene layers, each C_{60} molecule is surrounded by six neighbors in a nearly hexagonal manner with the shortest distances between the centers of the fullerene molecules being 10.058 \AA (four neighbors) and 10.665 \AA (two neighbors). No C–C bonds were found between the fullerenes and, therefore, the fullerene molecules of the complex are monomeric at ambient conditions. The Raman spectra were recorded in the back-scattering geometry using a LabRam HR micro-Raman setup equipped with a Peltier cooled (-70°C) CCD detector. The 514.5 nm laser line was used for Raman excitation and the activation of the phototransformation. The laser beam was focused on the sample by a 50 objective with a laser power of $\sim 200 \mu\text{W}$, before the diamond-anvil cell (DAC). Measurements of the Raman spectra at high pressure were carried out using a Mao-Bell type DAC. The 4 : 1 methanol/ethanol mixture was used as pressure transmitting medium and the ruby fluorescence technique for pressure calibration [19].

3. Results and discussion

Figure 1 illustrates the peculiarities of the pressure-assisted photo-induced transformation in the $\{\text{Cd}(\text{dedtc})_2\}_2 \cdot \text{C}_{60}$ complex as evidenced in its Raman spectra and their pressure and exposure time dependence. The bottom inset shows the time evolution of the Raman spectra of the $\{\text{Cd}(\text{dedtc})_2\}_2 \cdot \text{C}_{60}$ complex recorded at pressures 1.63, 4.37 and 6.37 GPa in the region of the PP-mode under fixed excitation conditions of $\lambda_{\text{exc}} = 514.5$ nm, laser power 200 μW and 50 objective. For each pressure, a different, fresh site of the sample was used to probe the spectra evolution with the illumination time. Raman spectra were recorded consecutively at 1.63 GPa under continuous laser illumination for 1800 s and with 300 s exposure time for each spectrum. The spectra do not evolve with time regarding their structure and intensity distributions. The Raman spectra at 4.37 GPa, recorded under continuous laser illumination for 9900 s and 900 s exposure time for each spectrum, exhibit gradual time-dependent changes associated with the appearance of new bands shifted to lower energies with respect to the $A_g(2)$ mode of the C_{60} monomer. The initial Raman spectrum, recorded with 900 s exposure time is similar to the Raman spectra at 1.63 GPa, while longer time laser illumination leads to a photo-induced transformation manifested by changes in the band structure and intensity distribution. Similar changes were also observed in a number of the degenerate Hg modes for the fullerene molecule. The Raman spectra at 6.37 GPa were recorded under the same laser illumination conditions as the spectra at 4.37 GPa but they do not show any time-dependent changes. The series of Raman measurements at various pressures have shown that the photo-induced transformation takes place in the pressure region 2.24 – 5.99 GPa. The relative intensities of the new bands increase with exposure time, indicating an increase in the photo-oligomers content in the fullerene layers, as in the case for photopolymerization in pristine C_{60} and $\{\text{Pt}(\text{dbdte})_2\} \cdot \text{C}_{60}$ complex at ambient conditions [14,20]. The ratio for the sum of the integrated intensities of the new PP-mode components to the total spectral intensity in the frequency region of the PP-mode provides a measure for the polymer content. The dependence of the photopolymer content on the laser exposure time is shown in Fig. 1 (circles) along with the fitting of the data by an exponential growth function (dotted line):

$$P(t) = P_{\text{sat}}\{1 - \exp(-t/\tau)\}. \quad (1)$$

where $P(t)$ is the time-dependent content of the photopolymers, P_{sat} is the content of the photopolymer attained after saturation of the phototransformation, and τ is the exponential growth time constant. The phototransformation parameters at 2.77 GPa are $P_{\text{sat}} = 64$ % and $\tau = 889$ s. As shown earlier in the photopolymerization study of $\{\text{Pt}(\text{dbdte})_2\} \cdot \text{C}_{60}$ complex at ambient conditions [20], the parameter P_{sat} increases, while the time constant τ decreases with an increase in the laser power. In fact, these parameters depend on the laser power density, which implies that it is necessary to carefully focus the laser beam during measurements. The top inset shows the dependence of the photopolymer content P_{sat} on pressure. The Raman measurements in all pressure values were performed under the same conditions. The photopolymerization was initiated abruptly at 2.24 GPa after the phase transition near 2 GPa [9], occurs up to 5.99 GPa and disappears at 6.37 GPa. The value of P_{sat} varies between 60 % and 80 % despite the fixed illumination conditions, which may be attributed to somehow different focusing of the laser beam in different measurements.

Figure 2 illustrates the pressure dependence of the Raman bands of the $\{\text{Cd}(\text{dedtc})_2\}_2 \cdot \text{C}_{60}$ complex at pressures up to 6.5 GPa. The open circles mark the frequencies of the peaks related to the $H_g(7)$ and $A_g(2)$ modes recorded after short exposure time in the time-dependent set of Raman measurements, whereas the semi-filled circles correspond to the frequencies of the

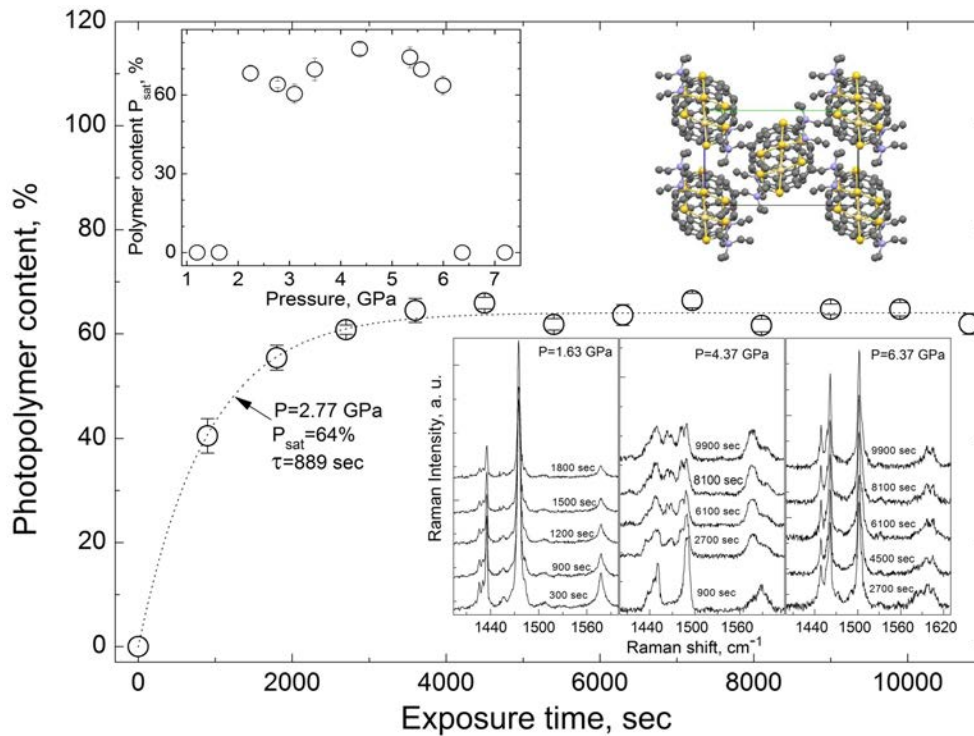


FIG. 1. Photopolymer content in the $\{\text{Cd}(\text{dedtc})_2\}_2 \cdot \text{C}_{60}$ complex at 2.77 GPa, excited with $200 \mu\text{W}$ at 514.5 nm, as a function of the illumination time and fitted by an exponential growth function (dotted line). The molecular arrangement in the fullerene complex viewed along the a -axis of the unit cell is also included. Bottom inset: Time evolution of the Raman spectra of the $\{\text{Cd}(\text{dedtc})_2\}_2 \cdot \text{C}_{60}$ complex in the region of the PP-mode at 1.63 GPa (left), 4.37 GPa (center) and 6.37 GPa (right). Top inset: Pressure dependence of the saturated photopolymer content

split PP-mode components recorded after long exposure time when the photopolymer content is saturated. The solid lines are linear fits of the experimental data related to the $H_g(7)$ and $A_g(2)$ modes, while the dotted lines are fits of the split PP-mode components. Stars denote the frequencies of the split PP-mode components extrapolated to ambient pressure. The pressure evolution of the main PP-mode frequency exhibits an irregularity near ~ 2 GPa: the pressure coefficient between 2 and 3 GPa is almost zero, whereas before and after this region it is $\sim 5 \text{ cm}^{-1}/\text{GPa}$. Thus, the Raman data recorded after short laser exposure time show the pressure-induced phase transition near ~ 2 GPa was most likely associated with covalent bonding between C_{60} molecules in fullerene layers. The phase transition was confirmed independently by XRD measurements which showed a distinct change in the material compressibility along the fullerene layers [9]. The intriguing result of the high pressure Raman study is that the pressure-induced phase transition activates the photo-induced transformation as it follows from the appearance of the split PP-mode components under prolonged laser illumination.

Figure 3 shows the frequencies of the $A_g(2)$ PP-modes of various crystalline polymers of C_{60} (circles) vs. the number of the sp^3 -like coordinated carbon atoms per fullerene molecular cage [17,21]. The Raman frequencies of the photo-oligomers in C_{60} fullerite (hexagons) are also included [20]. The structural arrangements of the intermolecular covalent bonds in different HPHT crystalline polymers, as deduced by detailed XRD measurements, are also illustrated in the insets [12, 13, 22]. The empirical dependence of the PP-mode frequencies of crystalline

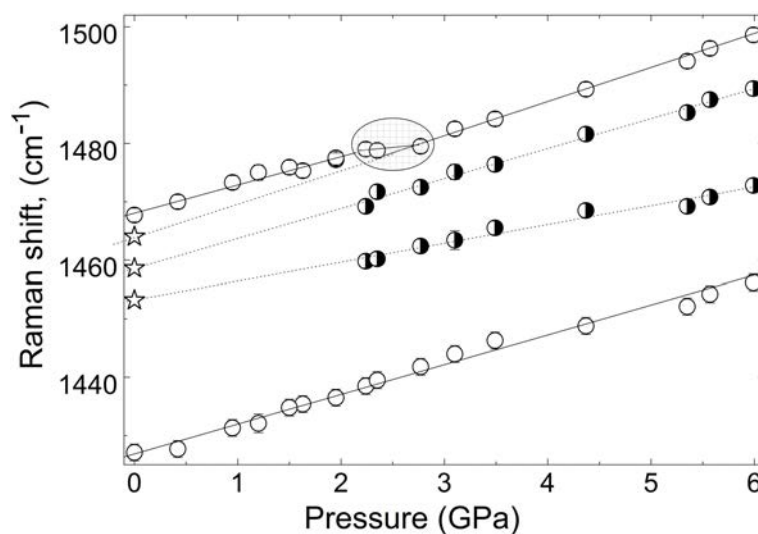


FIG. 2. Pressure dependence of the $\{\text{Cd}(\text{dedtc})_2\}_2 \cdot \text{C}_{60}$ complex Raman peaks related to the $H_g(7)$ and $A_g(2)$ modes of the C_{60} molecule at pressure up to 6.1 GPa. The open circles denote the peak frequencies recorded under short exposure time, while the semi-filled circles the frequencies of the split components of the PP-mode recorded under long exposure time. The lines are linear fits of the experimental pressure dependencies, while the stars show the extrapolated frequencies of the split PP-mode components to ambient pressure

C_{60} polymers and the photo-oligomers in C_{60} fullerite exhibits a monotonic decrease with an increase in the number of the sp^3 -like coordinated carbon atoms per C_{60} molecule. Note, that the Raman band at $\sim 1452 \text{ cm}^{-1}$ in phototransformed C_{60} is related to the conjugated linear chains that were first observed in the pressure-assisted photo-induced transformation of the linear orthorhombic C_{60} polymer [21–23]. The frequencies of the pressure-induced dimers, as well as the pressure-assisted photo-induced oligomers in the $\{\text{Cd}(\text{dedtc})_2\}_2 \cdot \text{C}_{60}$ complex extrapolated to ambient pressure are also shown in Fig. 3 (stars). These data agree well with those of the HPHT crystalline polymers and the photo-oligomers of C_{60} fullerite and may be attributed to dimers, fragments of linear chains and conjugated linear chains.

Summarizing, we have studied in detail the pressure-assisted photopolymerization of the fullerene molecules in the C_{60} layers of the molecular donor-acceptor complex $\{\text{Cd}(\text{dedtc})_2\}_2 \cdot \text{C}_{60}$, activated immediately after the pressure-induced phase transition near 2 GPa. The phototransformation process occurs at pressures ranging from 2.24 – 5.99 GPa. The photopolymerization rate and the saturated polymer content depend on the laser excitation wavelength, laser power and focusing but they are independent of pressure within this region. The photo-oligomers are, most likely, fragments of linear chains and conjugated linear chains whereas the pressure-induced phase transition results in the creation of C_{60} dimers. The photopolymerization of C_{60} , which requires the rotation of the molecules in order to attain a suitable mutual orientation of the neighboring cages necessitated in the [2+2] cycloaddition reaction [14], may serve as the basis for the interpretation of the observed behavior. Then, the stability of the studied complex upon laser illumination at ambient and low pressure suggests that the molecular rotations are hindered. However, in the high pressure phase (above 2 GPa), the inter-cage distances are redistributed due to the pressure induced formation of dimers, leading to relatively large inter-dimer distances. This may allow some rotational degree of freedom that would explain the

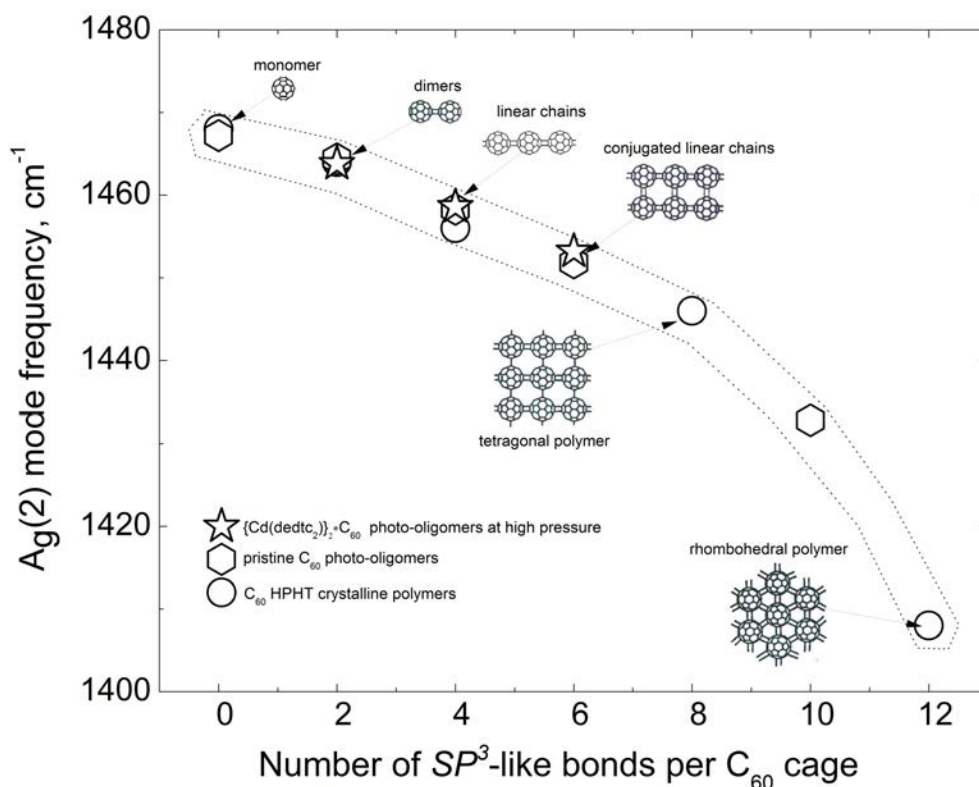


FIG. 3. The frequencies of the PP-modes of the HPHT crystalline polymers of C_{60} (circles), the photo-transformed C_{60} fullerite (hexagons) and the ambient pressure extrapolated frequencies of the photo-induced oligomers in $\{Cd(dedtc)_2\}_2 \cdot C_{60}$ complex at high pressure (stars) vs. the number of the sp^3 -like coordinated carbon atoms per C_{60} molecular cage. The arrangement of the intermolecular covalent bonds in HPHT crystalline polymers is also shown

photosensitivity of the material. Further volume reduction, for pressure above 6 GPa, freezes the rotations and renders the dimer phase immune to the laser irradiation.

Acknowledgements

The support by the Russian Foundation for Fundamental Research, grant No. 15-02-01495, and the RAS Presidium Program “Physics of compressed matter” are greatly acknowledged. The authors are grateful to Dr. D. Konarev for providing the fullerene complexes.

References

- [1] Konarev D.V., Khasanov S.S., et al. Formation of single-bonded $(C_{60}^-)_2$ and $(C_{70}^-)_2$ dimers in crystalline ionic complexes of fullerenes. *J. Am. Chem. Soc.*, 2003, **125**, P. 10074–10083.
- [2] Konarev D.V., Khasanov S.S., et al. Negatively charged π - $(C_{60}^-)_2$ dimer with biradical state at room temperature. *J. Am. Chem. Soc.*, 2006, **128**, P. 9292–9293.
- [3] Meletov K.P., Dolganov V.K., Set al. Pressure-induced charge-transfer phase transition in crystalline $C_{60} \cdot \{C_{10}H_{12}Se_{42}(CS_2)\}$ molecular complex studied by Raman spectroscopy. *Chem. Phys. Lett.*, 1997, **281**, P. 360–365.
- [4] Cui Wen, Yao Mingguang, et al. Reversible polymerization in doped fullerides under pressure: the case of $C_{60} \cdot \{Fe(C_5H_5)_2\}_2$. *J. Phys. Chem. B*, 2012, **116**, P. 2643–2650.

- [5] Meletov K.P., Konarev D.V. Raman study of the pressure-induced charge transfer transition in the neutral donor-acceptor complexes $\{\text{Ni}(n\text{Pr}_2\text{dtc})_2\}\cdot(\text{C}_{60})_2$ and $\{\text{Cu}(n\text{Pr}_2\text{dtc})_2\}\cdot(\text{C}_{60})_2$. *Full. Nanotub. Carbon Nanostr.*, 2012, **20**, P. 336–340.
- [6] Meletov K.P., Konarev D.V. Raman study of the pressure-induced phase transitions in the molecular donor-acceptor complex $\{\text{Pt}(\text{dbdtc})_2\}\text{C}_{60}$. *Chem. Phys. Lett.*, 2012, **553**, P. 21–25.
- [7] Meletov K.P. Phase transitions at high pressure in the donor-acceptor complexes of C_{60} studied by Raman spectroscopy. *High Pressure Research*, 2013, **33**, P. 114–118.
- [8] Meletov K.P. Phase transitions at high pressure in the fullerene C_{60} molecular donor-acceptor complex $\{\text{Hg}(\text{dedtc})_2\}_2\cdot\text{C}_{60}$. *Physics Solid State*, 2014, **56**, P. 1689–1695.
- [9] Meletov K.P., Konarev D.V., Tolstikova A.O. Phase transitions and photoinduced transformations at high pressure in the molecular donor-acceptor fullerene complex $\{\text{Cd}(\text{dedtc})_2\}_2\cdot\text{C}_{60}$. *JETP*, 2015, **120**, P. 989–997.
- [10] Rao A.M., Zhou P., et al. Photoinduced polymerization of solid C_{60} films. *Science*, 1993, **259**, P. 955–957.
- [11] Stephens P.W., Bortel G., et al. Polymeric fullerene chains in RbC_{60} and KC_{60} . *Nature*, 1994, **370**, P. 636–639.
- [12] Iwasa Y., Arima T., et al. New phases of C_{60} synthesized at high pressure. *Science*, 1994, **264**, P. 1570–1572.
- [13] Nunez-Regueiro M., Marques L., et al. Polymerized fullerite structures. *Phys. Rev. Lett.*, 1995, **74**, P. 278–281.
- [14] Zhou P., Dong Z.H., Rao A.M., Ecklund P.C. Reaction mechanism for photopolymerization of solid fullerene C_{60} . *Chem. Phys. Lett.*, 1993, **211**, P. 337–340.
- [15] Puztai T., Oszlanyi G., et al. Bulk structure of phototransformed C_{60} . *Solid State Commun.*, 1999, **111**, P. 595–599.
- [16] Karachevtsev V.A., Mateichenko P.V., et al. Effective photopolymerization of C_{60} films under simultaneous deposition and UV light irradiation: Spectroscopy and morphology study. *Carbon*, 2004, **42**, P. 2091–2098.
- [17] Davydov V.A., Kashevarova L.S., et al. Spectroscopic study of pressure polymerized phases of C_{60} . *Phys. Rev. B*, 2000, **61**, P. 11936–11945.
- [18] Konarev D.V., Khasanov S.S., et al. Fullerene complexes with divalent metal dithiocarbamates: structures, magnetic properties, and photoconductivity. *Russ. Chem. Bull. Int. Ed.*, 2007, **56**, P. 2145–2161.
- [19] Jayaraman A. Ultrahigh pressures. *Rev. Sci. Instrum.*, 1986, **57**, P. 1013–1031.
- [20] Meletov K.P., Arvanitidis J., Christofilos D., Kourouklis G. Comparative Raman study of the photo-oligomers stability in the donor-acceptor fullerene complex $\{\text{Pt}(\text{dbdtc})_2\}\cdot\text{C}_{60}$ and pristine C_{60} . *Nanosystems: Physics, Chemistry, Mathematics*, 2016, **7** (1), P. 125–132.
- [21] Meletov K.P., Davydov V.A., et al. High pressure photoinduced polymerization of the orthorhombic polymeric phase of C_{60} . *Chem. Phys. Lett.*, 2005, **416**, P. 220–224.
- [22] Le Parc R., Levelut C., et al. In situ X-ray powder diffraction study of the one-dimensional polymeric C_{60} phase transformation under high-pressure. *Chem. Phys. Lett.*, 2007, **438**, P. 63–66.
- [23] Meletov K.P., Davydov V.A., et al. The influence of pressure on the photopolymerization rate of linear orthorhombic polymer of C_{60} . *Chem. Phys. Lett.*, 2006, **428**, P. 298–302.

Express analysis of endohedral fullerenes amount contained at fullerene mixture

G. N. Churilov^{1,3}, A. A. Popov², U. E. Guliaeva^{1,3}, N. A. Samoylova², N. G. Vnukova^{1,3},
A. L. Kolonenko¹, V. G. Isakova¹, A. I. Dudnik^{1,3}, V. S. Koravanets³

¹Kirensky Institute of Physic SB RAS, Krasnoyarsk, Russia

²Leibniz Institute for Solid State and Materials Research, Dresden, Germany

³Siberian Federal University, Krasnoyarsk, Russia

churilov@iph.krasn.ru

PACS 32.30; 52.50

DOI 10.17586/2220-8054-2016-7-1-140-145

This paper describes the technique for rapid determination of endohedral metallofullerene (EMF) content in a fullerene mixture (FM). The methods of mass spectroscopy and atom emission element analysis underlay at the technique. By the method of mass spectroscopy, the type of EMF with atom-guest is registered and by the method of emission spectroscopy, the quantity of that element which is contained in the FM is determined. The technique may be used for rapid determination of EMF weight percents in the FM in the specific case if only one type of EMF is present, and of EMF average content if there are different types of EMF are present. The technique is demonstrated through the example of analysis of FM with Y, which was extracted from the carbon condensate (CC) by different solvents (C_5H_5N and CS_2).

Keywords: endohedral fullerene, atom emission spectroscopy, quantitative assessment.

Received: 20 November 2015

1. Introduction

If common fullerenes, such as C_{60} , C_{70} , and type C_{2n} in general are widely studied and have already been frequently used, then we cannot say the same about EMF. Although it is theoretically predicted that they have unique features, able to resolve a number of problems with electronics, computing technologies, medicine, mechanical engineering etc [1]. Of particular significance is the future implementation of EMF with enclosed magnetic and radioactive atoms which may have utility in medicine for diagnostic and therapeutic purposes [2].

Insufficient knowledge of these substances' features is a result of their lack of production in quantities sufficient for full-scale research. In the literature, there are results given for obtaining a carbon condensate (CC) containing EMF, and methods for their isolation [3]. Nevertheless, the search for synthesis and isolation methods is ongoing, as known methods of today are inadequate. The situation is exacerbated by the complexity and significant amount of time required for the analysis of EMF in the selective FM. This slows down the process of determining how synthetic parameters exert influence upon the content of the EMF formed under these parameters and the efficiency of the used fabrication method. The direct method involves chromatographic separation, analysis and determination of the weight fractions by percentage of EMF. There are works in which the extinction of solutions containing a certain type of EMF is determined [4]. However, this method also requires the use of a direct method as well as a chromatographic separation method. Determination of EMF content in the fullerene mixture by our method obviates the need for the time-consuming procedure of chromatographic fractionation with subsequent mass spectroscopic investigation and weighing. The developed

method has been applied by us to study the contents of EMF with Y in fullerene mixture, synthesized at different helium pressures and separated by the solvents C_5H_5N and CS_2 .

2. Experimental part

CC was synthesized using a high frequency (HF) arc plasma for sputter graphitic electrodes (graphitic rods) [5,6]. Graphitic rods, with an axial hole in which Y_2O_3 was placed, were annealed at $1800^\circ C$ for 20 min. Current arc was 190 A, frequency – 66 kHz, and chamber pressure was: 353, 98, 64.8 or 32.4 kPa. CC with Y synthesized under different pressures were portioned into two parts. Extraction of one part was carried out with C_5H_5N and the other – with CS_2 . According to our technique, the FM, after careful filtering, was dried. With the help of emission spectroscopy, the metal content (the atoms of which were the atoms-guests in the EMF) was determined for the FM.

Atomic-emission analysis was performed on the setup, consisting of plasma atomizer – HF discharge in a stream of argon with copper and graphite electrodes, the spectrograph PGS-2 and a computerized spectral registration. Samples were made and concentration-response curves were constructed for Y over a concentration range from $1 \cdot 10^{-5}$ to 1.0 g/l. Samples were made as follows: in graphite rods with a diameter of 6 mm were drilled apertures of 4 mm diameter and 5 mm of depth. Apertures with a solution containing a substance with a known concentration of Y were dried. Thus, prepared samples act as graphite electrodes. Based on the analysis of the emission spectrum at the Y 324.23 nm line, an analytical curve was constructed (Fig. 1). The analytic curve is relevant for all types of compositions because samples are completely atomized during analysis [7].

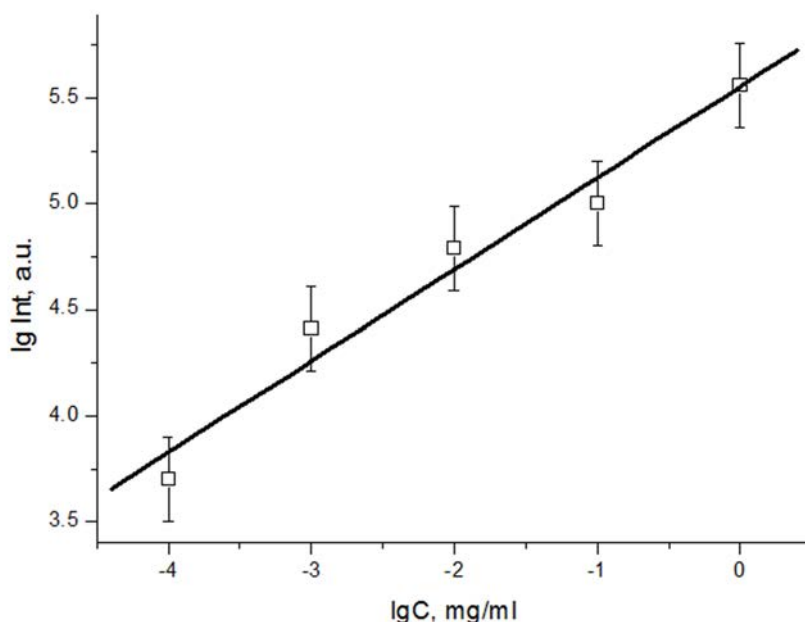


FIG. 1. Analytical curve for Y determination at the carbon

Fullerene extracts from the CC with a known concentration of Y were also applied in the apertures of the graphite rods, as was done in the preparation of samples, and they also acted as graphite electrodes. The content of yttrium in the sample was then determined by the intensity of the yttrium 324.23 nm line and the concentration curve was generated (Figs 3a, 4a).

The mass spectra of FM samples (Bruker BIFLEXTM III Time-of-Flight mass spectrometer with laser desorption) shows the presence of pure fullerenes and fullerene with Y. However, Y(88.9 m/z), YC₂(112.9 m/z), Y₃C (278.7 m/z) and etc. were not registered (Fig. 2)

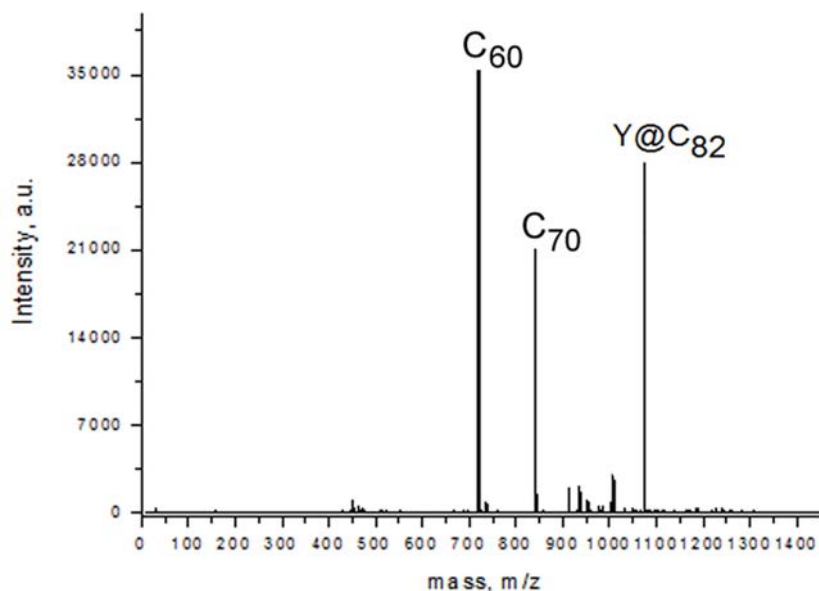


FIG. 2. Mass spectral (positive-ion) analysis of FM synthesized with Y₂O₃

Mass spectroscopic investigation provided information on the qualitative composition of the synthesized EMF (Figs. 3b, 4b). For pressure 353 and 98 kPa, it was discovered that the yttrium occurs in the obtained fullerene mixture only in the form Y@C₈₂. Accordingly, the content of Y@C₈₂ was easily calculated by the content of Y.

This technique allows one to obtain a quantitative assessment, if electromagnetic filter with one metal atom molecule was formed. However, with metal addition, there are often several types of EMF that are formed simultaneously. Mass spectroscopic investigation shows that there are three types of EMF: Y@C₈₂, Y₂@C₈₂, Y₂C₂@C₈₂ (Figs. 5a, 5b and 6a, 6b) in the CC synthesized under 64.8 kPa pressure. In this instance, this technique may also be used, but for average assessment only. We have a qualitative assessment of EMF formation efficiency for those synthesis parameters, but have no information about the amounts of the specific types of EMF synthesized in the process.

Table 1 shows the results of Y and Y@C₈₂ content in the fullerene mixtures extracted from CC synthesized at different pressures and extracted by different solvents (C₅H₅N or CS₂).

Accordingly, the quantitative assessment of EMF may be carried out without fractionation using HPLC, with future determination of fraction characteristics and weighing.

There are the following possible scenarios: 1 – if mass spectral investigation showed that only one type of EMF was formed, then it is easy to calculate the quantitative assessment of EMF by determining the percent content of inputting element; 2 – if mass spectral investigation showed that there are several types of EMF, then to determine the percent content of inputting element, we have only the average assessment of EMF content. In subsequent work, we plan to remove that ambiguity by adding photoelectron spectroscopy to our technique for quantitative assessment of several types of EMF content that was contained in the analyzed FM.

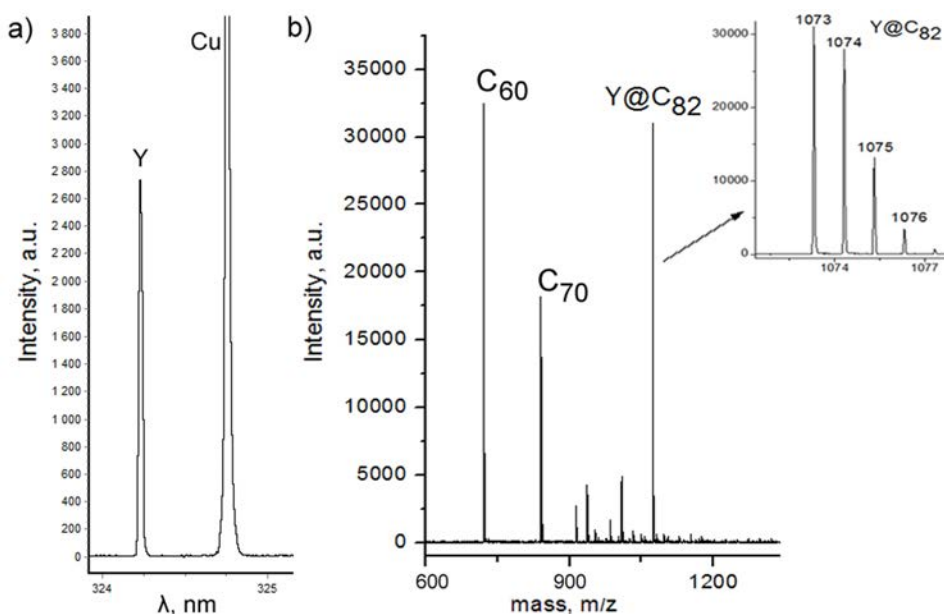


FIG. 3. Results of atom emission and positive-ion mass spectral analysis of FM synthesized with Y_2O_3 under 98 kPa and extracted by C_5H_5N : a) part of atom emission spectrum, b) part of mass spectrum (on insertion – $Y@C_{82}$)

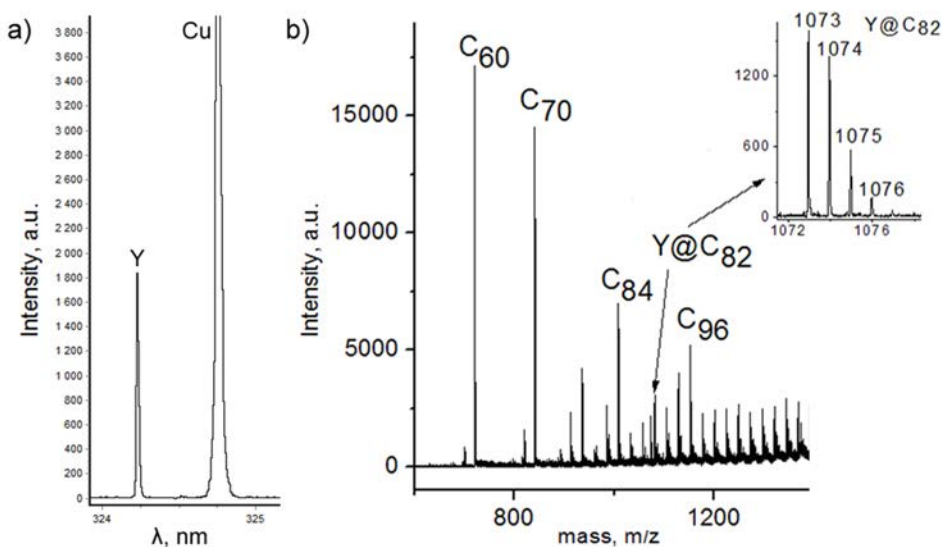


FIG. 4. Results of atom emission and positive-ion mass spectral analysis of FM synthesized with Y_2O_3 under 98 kPa and extracted by CS_2 : a) part of atom emission spectrum, b) part of mass spectrum (on insertion – $Y@C_{82}$)

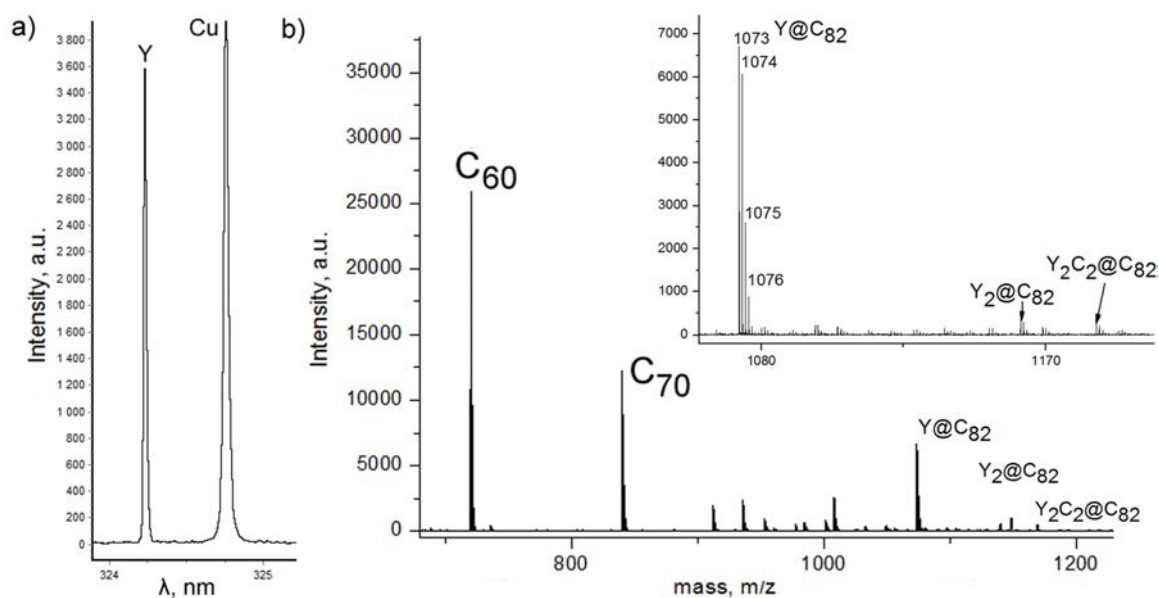


FIG. 5. Results of atom emission and positive-ion mass spectral analysis of FM synthesized with Y_2O_3 under 64.8 kPa and extracted by C_5H_5N a) part of atom emission spectrum, b) part of mass spectrum

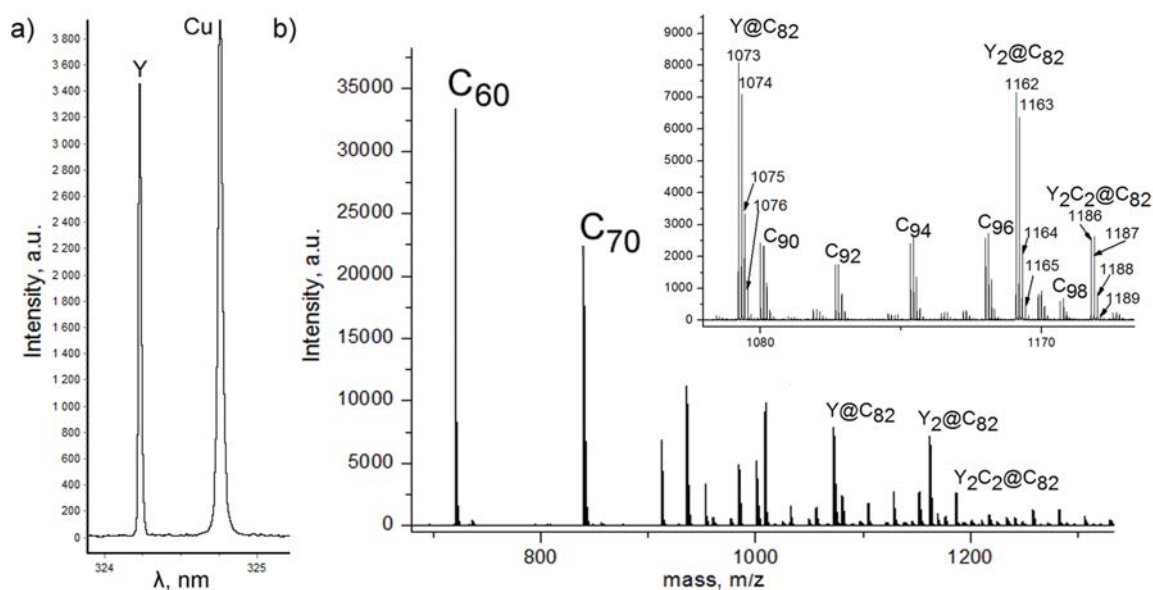


FIG. 6. Results of atom emission and positive-ion mass spectral analysis of FM synthesized with Y_2O_3 under 64.8 kPa and extracted by CS_2 a) part of atom emission spectrum, b) part of mass spectrum

TABLE 1. Analysis results of FM samples contained Y, synthesized under different pressure

Pressure under which EMF synthesis was carried out							
353 kPa		98 kPa		64.8 kPa		32.4 kPa	
C ₅ H ₅ N	CS ₂	C ₅ H ₅ N	CS ₂	C ₅ H ₅ N	CS ₂	C ₅ H ₅ N	CS ₂
Y content at 1 mg FM, mg ¹							
0.99·10 ⁻³	0.41·10 ⁻³	12.1·10 ⁻³	9.7·10 ⁻³	10.6·10 ⁻³	8.0·10 ⁻³	5.17·10 ⁻³	2.4·10 ⁻³
Content Y@C82, wt%				Y@C82, Y2C2@C82, Y2@C82			
1.2	0.5	14.5	11.2	–	–	–	–

¹Methodic error less than 5 %.

Acknowledgements

The work was supported by the Ministry of Education and Science of Russia (Russian-Japanese joined project, Agreement N 14.613.21.0010, ID RFMEFI61314X0010).

References

- [1] Yang S., Liu F., Chen C., Jiao M., Wei T. Fullerenes encaging metal clusters - clusterfullerenes. *Chem. Commun.*, 2011, **47**, P. 11822–11839.
- [2] Meng J., Wang D.L., Wang P.C., J. Biological characterization of [Gd@C₈₂(OH)₂₂]_n nanoparticles as fullerene derivatives for cancer therapy. *Nanosci. Nanotechnol.*, 2010, **10**(12), P. 8610–8616.
- [3] Popov A.A., Yang S., Dunsch L. Endohedral fullerenes. *Chem. Rev.*, 2013, **113**, P. 5989–6113.
- [4] Kareev I.E., Laukhina E., Bubnov V.P., Martynenko V.M., Lloveras V., Vidal-Gancedo J., Mas-Torrent M., Veciana J., Rovira C. Harnessing Electron Transfer from the Perchlorotriphenylmethide Anion to Y@C₈₂(C₂v) to Engineer an Endometallofullerene-Based Salt. *Chem. Phys. Chem.*, 2013, **14**, P. 1670.
- [5] Churilov G.N. Plasma Synthesis of Fullerenes. *Instruments and Experimental Techniques*, 2000, **43**(1), P. 1–10.
- [6] Churilov G.N., Kratschmer W., Osipova I.V., Glushenko G.A., Vnukova N.G., Kolonenko A.L., Dudnik A.I. Synthesis of fullerenes in a high-frequency arc plasma under elevated helium pressure. *Carbon*, 2013, **62**, P. 389–392.
- [7] Terek T., Mika J. Gegush E. *Emission spectrochemical analysis*. MIR, 1982, 464 p.

Fullerenes and fullerenols survival under irradiation

V. A. Shilin, A. A. Szhogina, M. V. Suyasova, V. P. Sedov, V. T. Lebedev, V. S. Kozlov

National Research Centre “Kurchatov Institute” B. P. Konstantinov, Petersburg Nuclear Physics Institute, 188300, Russia, Leningrad district, Gatchina, Orlova Roscha, Russia

shilin@pnpi.spb.ru

PACS 81.05.ub

DOI 10.17586/2220-8054-2016-7-1-146-152

Fullerenes C_{2n} , endometallofullerenes $Gd@C_{2n}$, $Gd@C_{82}$ and water-soluble $Gd@C_{2n}(OH)_{38-40}$ derivatives were synthesized. These substances' survival dependences on the accumulated flux ($10^{16} - 10^{19}$ neutron/cm²) of neutron irradiation over a wide spectrum of energies (from thermal to fast) in the WWR-M reactor zone (Petersburg Nuclear Physics Institute) have been examined.

Keywords: fullerenes, endometallofullerenes, fullerenols, irradiation, survival.

Received: 20 November 2015

1. Introduction

Radiochemical technology allows the creation of new carbon-based materials and the study of their properties, stability and structure. The application of radiolabeled fullerenes, endohedral metallofullerenes (EMFs) and their water-soluble derivatives is of particular importance in modern nuclear medicine and biology, due to their potential utility as radiopharmaceuticals. Fullerene and EMF functionalization, by the attachment of different groups permits the targeted delivery of drug molecules and the use of radioactive EMF properties for diagnostic and therapeutic purposes. There are many published reviews describing endohedral fullerenes and methods for their preparation, for example [1-3].

Recent results from stability studies of endofullerenes and their water-soluble derivatives undergoing irradiation by fast and thermal neutrons in the reactor WWR-M (PNPI) are presented in this article. Non-phonon excitation mechanisms were proposed for understanding the fullerenols' interactions with fast neutrons. In particular, fast electron shaking is suggested as the most probable process [4,5].

It is clear that EMFs irradiations at different neutron fields may lead to their destruction and cause the formation of new chemical substances. A molecule with daughter nucleus may also change the original chemical form leading to such instabilities as oxidation, degradation, crosslinking, etc. For example, there can be a reaction with oxygen due to ionizing radiation accompanied by the formation of reactive radical intermediates.

Although the stabilities of fullerenes and EMFs have been thoroughly investigated [6-9], the stabilities of water-soluble fullerene derivatives are less documented. This is why the present investigation is necessary.

The studies seem to be very prospective for advanced medical applications of metallofullerenes and their isotopic forms for the diagnostics (MRI) and tumor therapy. The active component (heavy metal, isotope) in such molecules is screened from surrounding tissues and toxicity risks are minimized.

2. Experimental and discussions

The substances in the series (C_{2n} , $Gd@C_{2n}$, $Gd@C_{82}$ and $Gd@C_{2n}(OH)_{38-40}$) were synthesized for these studies. The fullerene-containing soot was produced by subjecting graphite rods to electric arc treatment. Subsequently, the soot was extracted with o-xylene. The C_{2n} extract's composition was determined by high-performance liquid chromatography (HPLC).

High purity (99 %) sample $Gd@C_{82}$ was extracted from soot using the solvents o-xylene and N,N-dimethylformamide (DMF). The subsequent transfer of DMF in o-xylene allows the use of chromatographic separation and final $Gd@C_{82}$ purification [10,11].

The $Gd@C_{2n}$ fullerenes were isolated from soot using DMF extraction with the addition of a reducing agent to enhance the ability of the extractant. The $Gd@C_{2n}$ obtained in this manner was the initial compound to yield the hydroxylated $Gd@C_{2n}(OH)_{38-40}$ sample in dilute aqueous hydrogen peroxide solution at 65°C. According to X-ray fluorescence analysis (XRF), water-soluble fullereneols contained 4.8 wt% of gadolinium. The number of hydroxyl groups in a fullereneol molecule ($x = 38-40$) was determined gravimetrically (thermal analysis [12]). The resulting product contained 55% of the gadolinium component according to calculation based on the $Gd@C_{82}(OH)_{38}$ formula.

The powder samples were soldered in quartz ampules and irradiated for 0.5 – 32 h in integral flux of up to 10^{19} neutrons/cm² in the WWR-M. The temperature in the reactor channel was 70 °C.

The irradiated samples stability was determined as follows: the water soluble $Gd@C_{2n}(OH)_{38-40}$ was dissolved in a determined volume of water, assuming the previously-determined solubility. The solution was then stirred for 4 h at 25 °C and was then centrifuged. Irradiated C_{2n} , $Gd@C_{2n}$ and $Gd@C_{82}$ samples were dissolved in o-xylene and stirred for 24 h. The insoluble precipitates were dried and weighted. The differences between the C_{2n} original weights and the insoluble portions, normalized to the initial weights provided product stability data. The stability was defined for the $Gd@C_{2n}(OH)_{38-40}$, $Gd@C_{2n}$ and $Gd@C_{82}$ samples as the radioactivity ratio for the soluble and insoluble portions.

A Shimadzu LC-20 HPLC with Lab Solutions software and system for data processing and output analysis was used for both analysis and separation. The fullerene fractions separation and final purification were performed using three types of chromatographic columns: a BuckyPrep 4.6 × 250 mm analytical column, a Buckyrep 10 × 200 mm semi-prep column, and a Buckyrep 10 × 200 mm semi-prep column. Pure toluene was used as a mobile phase (eluent) in standard analyses. The peaks were detected by the absorption at 330 nm.

Mass-spectrometric analysis of the high-purity $Gd@C_{82}$ sample was performed with a Varian Fourier transform ion cyclotron resonance mass spectrometer and with an Ultraflex extreme device (Bruker), respectively. The $Gd@C_{82}$ sample spectra were recorded at standard device tuning (500 – 4500 Da) without the use of a matrix. The positive ions were recorded at a minimal laser power near the ion appearance threshold, so as to suppress the possible fragmentation. The obtained mass-spectrum is shown in Fig. 1.

Chemical bonding information on the hydroxyl groups was obtained using Fourier transform infrared spectroscopy (FTIR). The measured product FTIR-spectrum showed characteristic frequencies corresponding to chemical bonds in fullereneols. The spectrum is dominated by a broad band at 3412 cm⁻¹, presumably due to the stretching mode of the OH-groups, as well as other peaks at 1620 cm⁻¹ (C=C), 1390 cm⁻¹ and 1150 cm⁻¹ (C–OH).

The γ -spectra were recorded using a semiconductor spectrometer with a detector based on high-pure germanium HPGe (Ortec, EG & G) as done in previous work [13]. The detector

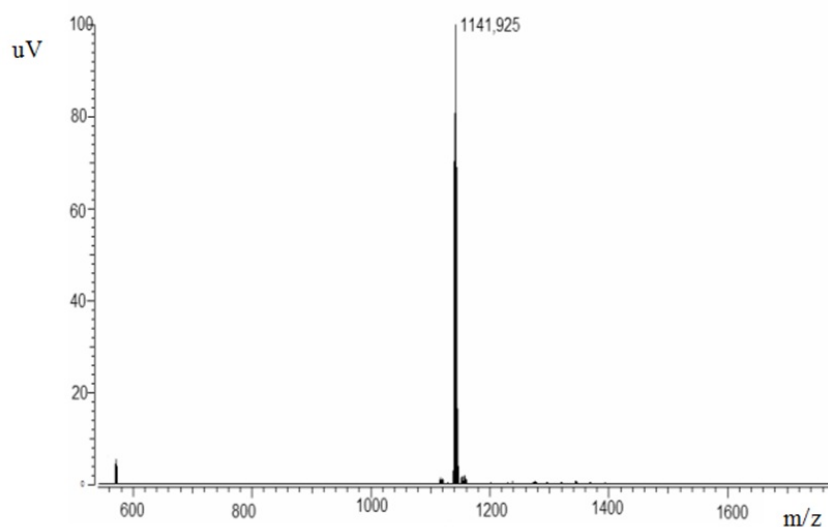


FIG. 1. Mass-spectrum of Gd@C₈₂, Varian mass-spectrometer

efficiency for the 1 MeV range was 5 %. Resolution for 122.06 keV γ -line of ⁵⁷Co was 0.57 keV. The diameter of the detector was 25 mm and the thickness was 13 mm.

The stability dependence of C_{2n}, Gd@C_{2n}, Gd@C₈₂, Gd@C_{2n}(OH)₃₈₋₄₀ upon irradiation time is shown in Fig. 2.

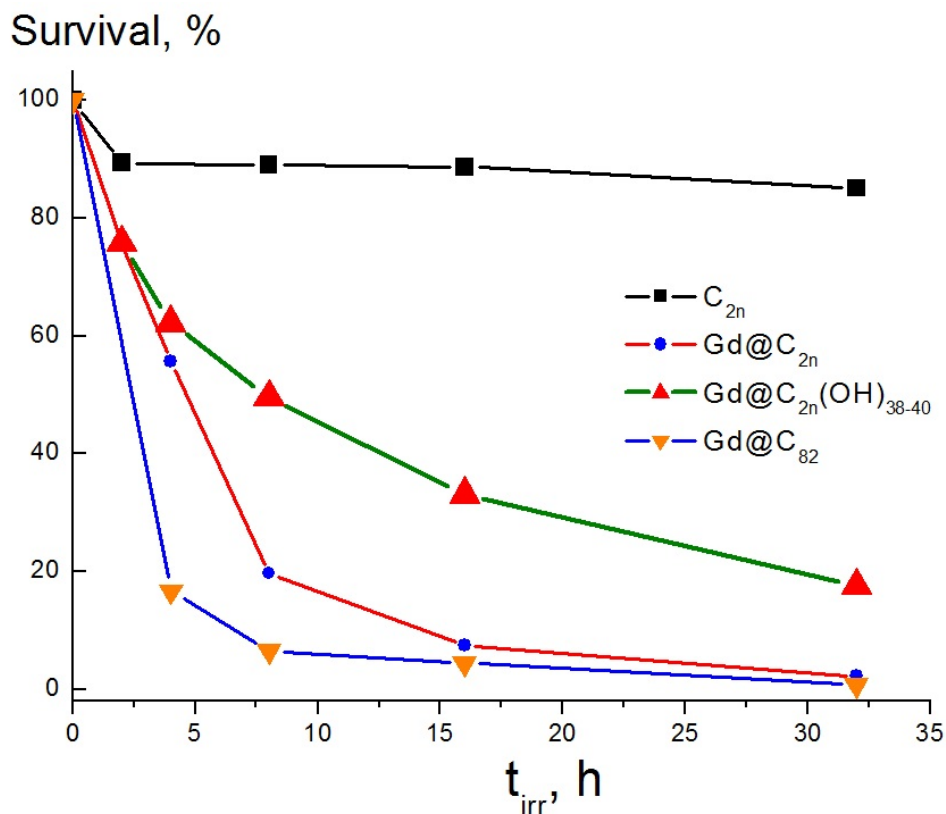


FIG. 2. The fullerenes and fullereneols stability dependence upon irradiation time at an integral flux of $8 \cdot 10^{13}$ neutron/s·cm²

As it can be seen in Fig. 2, the C_{2n} fullerenes have the higher survival as compared with others. It is no wonder, since the C_{2n} composition (Fig. 3) contains predominantly C_{60} and C_{70} [14] possessing a high survival.

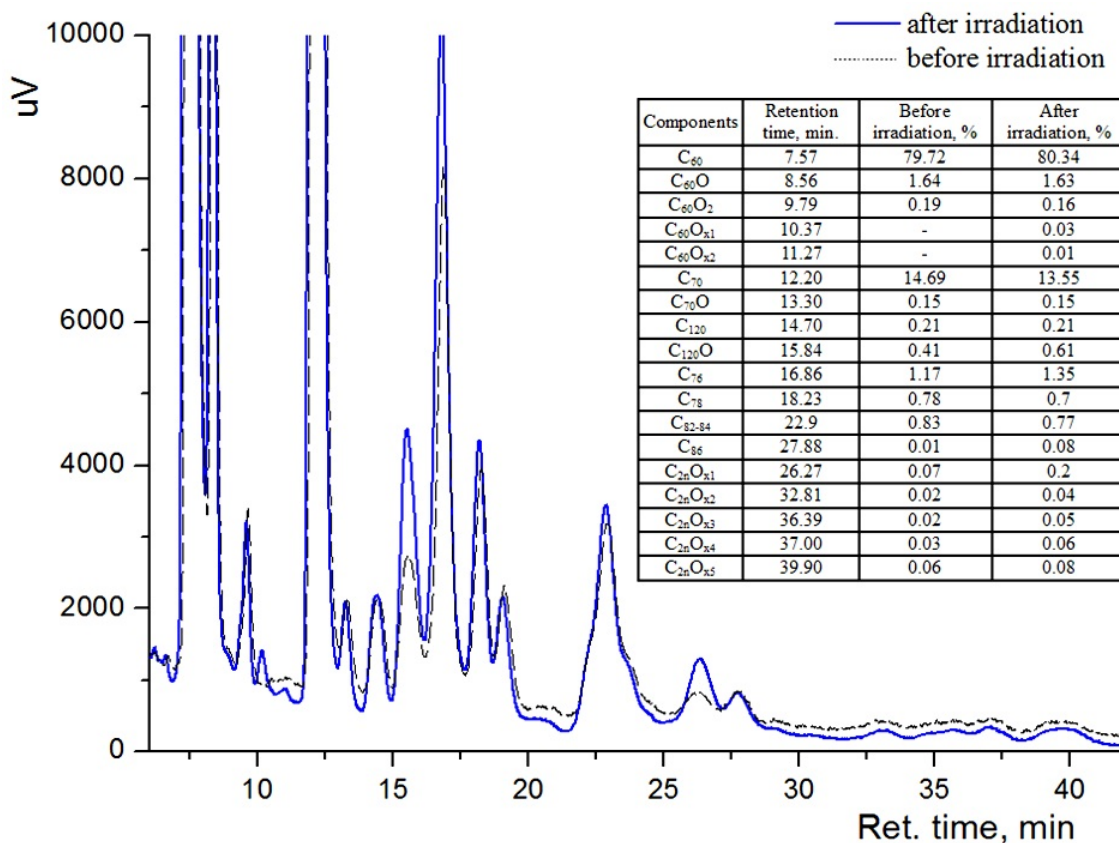


FIG. 3. Fullerenes C_{2n} chromatogram

Meanwhile, the $Gd@C_{2n}(OH)_{38-40}$ has shown a higher survival compared with $Gd@C_{2n}$ and $Gd@C_{82}$. This stability of fullereneol can be interpreted as the effect of its shell containing OH-groups and absorbed water. Really thermal neutrons undergo very intense incoherent scattering on the protons in the shell of fullereneol that prevents neutron absorption by the gadolinium atoms and the subsequent cage destruction due to recoil.

$Gd@C_{2n}$ survives better than $Gd@C_{82}$, because it contains mainly C_{60} which has a more stable framework and lower amounts of higher fullerenes such as C_{82} . This testifies to the fact that the main reason for EMF destruction is a result of the Szilard-Chalmers reaction.

The high survival of $Gd@C_{2n}$ sample as compared to $Gd@C_{82}$ can be associated with a difference in metal atom localization inside the carbon cage, with the electron-donating properties of the surrounding molecular environment and etc. It is known that the EMF properties are strongly dependent upon the metal atom's position inside the carbon cage. It has been noted that even a slight shift inside the carbon atom framework can lead to significant changes in the EMF's molecular properties [15-18].

It should be noted, there is a substantial charge transfer between Gd and the nearest carbon atoms in a $Gd@C_{82}$ molecule. This value was found to be almost 2.5 times higher than in $La@C_{82}$ molecule [19]. Such a high charge density suggests a strong bonding for Gd with the nearest carbon atoms (i.e. covalent bonds). Obviously, this circumstance makes the molecule $Gd@C_{82}$ and $Gd@C_{2n}$ more resistant to various physical and chemical, and, in our opinion,

radiation effects. It should be noted that the charge transfer of Gd, and La are drastically different, even though they have very similar oxidation potentials $\text{Mo}^0/\text{M}^{3+}$ (-2.4 V). It is known that with such potential lanthanides donate three electrons to the fullerene cage and become trivalent.

In EMF molecules and their derivatives [20-22] the electron structure is modified not only via an internal charge transfer but also due to exterior effects, for example, by the presence of attached hydroxyl groups. For fullerenes, EMF and fullerlenols such a combination makes the treatment of their resistance to irradiation very complicated and dependent on molecular symmetry, size, carbon framework electronic structure, the atom's localization inside a carbon cage, the atom's recoil energy, and at last on the presence of impurities and damage in the irradiated material.

It is worth noting that except for destruction, the irradiation may induce opposite processes, i.e. a synthesis of some molecular forms. When the recoil high-energy metal atom can leave molecule and then collide with other molecules to destroy them, this recoil energy of the atom is reduced and it can insert itself into another carbon cage, thus creating a new EMF.

Table 1 shows some previously obtained endometallofullerenols' stability data under different conditions. Such factors are the samples' composition, the metal atom radius, the nuclear recoil energy upon neutron capture. Although the various factors cumulative effect greatly smooths, the presence $\text{C}_{2n}(\text{OH})_x$ fullerlenol influence apparently predominates.

TABLE 1. The endometallofullerenols survival dependence from different factors [23]

Element	Mixture content, %		Atom radius, pm	Recoil energy, eV	Survival, %
	$\text{M}@\text{C}_{2n}(\text{OH})_x$	$\text{C}_{2n}(\text{OH})_x$			
Sm**	17 ($\text{Sm}@\text{C}_{2n}$)	83 (C_{2n})	181	237	85
Tb	81	19	180	136.1	52
Gd	60	40	179	136.4	94.1
Sc	95	5	162	894.1	82.5
Fe	97,6	2,4	126	393.3	47.0
Mo	12	88	139	123.0	87.2
Pr	70	30	182	126.9	45.0
C_{2n}	–	100	–	–	85

*The samples irradiation are proceeded during 8 h in the integral flux $8 \cdot 10^{13}$ neutron/s·cm².

** The sample $\text{Sm}@\text{C}_{2n}$ survival is shown for comparison. The irradiation are proceeded during 2 h in the integral flux $8 \cdot 10^{13}$ neutron/s·cm² [24].

Another feature of endometallofullerenols behavior under neutron irradiation is the relatively high stability value as compared to the EMF. As it is seen from Table 1, all fullerlenols showed significantly greater stability (from 45 to 94 %) than the corresponding $\text{M}@\text{C}_{2n}$ (from 15 to 20 %). We expected to obtain similar results for irradiated C_{60} , C_{70} fullerenes and $\text{C}_{60}(\text{OH})_x$, $\text{C}_{70}(\text{OH})_x$ water-soluble derivatives [14]. However, comparison of the stabilities of C_{60} , C_{70} with their water-soluble derivatives of $\text{C}_{60}(\text{OH})_x$, $\text{C}_{70}(\text{OH})_x$ shows that fullerlenol survival decreases by 2 – 3 times under 32 h irradiation as compared with fullerenes. Fullerlenol molecules under irradiation lose some of the hydroxyl groups and are not destroyed, becoming insoluble. The soluble part weight reduces. The soluble and insoluble parts comparison becomes incorrect. Therefore additional investigations are necessary.

Previously investigated samples $M@C_{2n}$ ($M = Sc, La, Nb, Sm, Eu, Tb, Ho, Yb, Tm, Lu, Pr, Fe, Mo, Gd$) have shown the average survival from 15 to 20 % except $Sm@C_{2n}$ and $Gd@C_{2n}$ [24]. As mentioned earlier, a $Gd@C_{2n}$ high stability to reactor neutron irradiation can be explained by an abnormal feature of Gd-endohedral fullerene's electronic structure. The high stability of $Sm@C_{2n}$ can also be explained in such a way. To determine the anomalous features of how the bivalent $Sm^{+2}@C_{2n}^{-2}$ differs from $Gd^{+3}@C_{2n}^{-3}$, additional investigations are necessary. Although one should bear in mind that under certain circumstances, the bivalent Sm^{+2} can be transformed into trivalent Sm^{+3} [25].

3. Conclusion

The C_{2n} fullerenes, $Gd@C_{82}$, $Gd@C_{2n}$ endofullerenes and $Gd@C_{2n}(OH)_{38-40}$ water-soluble derivatives were synthesized, purified and a comparative analysis of their stabilities under neutron irradiation has been performed at the PNPI WWR-M reactor.

Various factors have defined the fullerenes' and fullereneols' stability to neutron irradiation; among these factors are the Szilard-Chalmers reactions and electronic structural features which give the largest contribution to these compounds' destruction.

The survival of water-soluble Gd-fullereneol was found to be an order of magnitude greater than that of the original EMF which is of substantial importance, assuming fullereneols' biomedical applications as advanced isotopic preparations.

In general, the investigation of fullerenes and fullereneols behaviors under irradiation carries not only theoretical but predominantly practical interests, since the knowledge of their radiation resistance offers a suitable option for a variety of the aforementioned biomedical applications.

Acknowledgements

The work was supported by Russian Foundation for Basic Research (grant 14-23-01015 ofi_m).

References

- [1] Popov A.A., Yang S., Dunsch L. Endohedral Fullerenes. *Chem. Rev.*, 2013, **113**(8), P. 5989–6113.
- [2] Gan L., Yang D., Zhang Q., Huang H. Preparation of open-cage fullerenes and incorporation of small molecules through their orifices. *Adv. Mater.*, 2010, **22**, P. 1498–1507.
- [3] Gan T., Hu C., Hu S. Preparation of graphene oxide-fullerene/phosphotungstic acid films and their application as sensor for the determination of cis-jasmone. *Anal. Methods*, 2014, **6**, P. 9220–9227.
- [4] Grushko Yu.S., Khodorkovski M.A., Kozlov V.S., Kolesnik S.G., Shilin V.A., Grachev S.A., Artamonova T.O. Radioactive Metallofullerenes: Hot Atom Chemistry Aspects. *Fuller., Nanotub. Carbon Nanostr.*, 2006, **14**, P. 249–259.
- [5] Averbukh V., Cederbaum L.S. Interatomic electronic decay in endohedral fullerenes. *Phys. Rev. Lett.*, 2006, **96**, P. 401–405.
- [6] Sueki K., Akiyama K., Zhao Y. L., Ito I., Ohkubo Y., Kikuchi K., Katada M., Nakahara H. Systematic study of lanthanoid endohedral metallofullerenes: Production yields, HPLC retention time and reactor irradiation effects. *J. Radioanalytical Nuclear Chem.*, 2003, **255**(1), P. 159–164.
- [7] Sueki K., Kikuchi K., Tomura K., Nakahara H. Stability of metallofullerenes following neutron capture reaction on the metal ion. *J. Radioanal. Nucl. Chem.*, 1998, **234**, P. 95–100.
- [8] Sueki K., Akiyama K., Kikuchi K., Nakahara H., Tomura K. Stability of Radio-Metallo-Fullerene against Beta-Decay. *J. Radioanal. Nucl. Chem.*, 1999, **239**(1), P. 179–185.
- [9] Nakahara H., Sueki K., Sato W., Akiyama K. Nuclear reactions and radionuclides in study of fullerenes. *J. Radioanal. Nucl. Chem.*, 2000, **243**(1), P. 169–179.

- [10] Kozlov V.S., Suyasova M.V., Lebedev V.T. Synthesis, Extraction, and Chromatographic Purification of Higher Empty Fullerenes and Endohedral Gadolinium Metallofullerenes. *Russian J. Appl. Chem.*, 2014, **87**(2), P. 121–127.
- [11] Suyasova M.V., Kozlov V.S. *Synthesis and Chromatographic Study of Higher Empty Fullerenes and Endometallofullerenes in solutions*. Communication of PNPI 2941. Gatchina, 2014. 20 p. (Rus.).
- [12] Goswami T.H., Singh R., Alam S., Mathur G.N. Thermal analysis: a unique method to estimate the number of substituents in fullerene derivatives. *Thermochimica Acta*, 2004, **419**, P. 97–104.
- [13] Grushko Yu.S., Alekseev E.G., V.V. Voronin et. al. Tracer Study of Smx@C_{2n}. *Mol. Mat.*, 2006, **7**, P. 115–118.
- [14] Shilin V.A., Lebedev V.T., Sedov V.P., Szhogina A.A. Fullerenes and their derivatives synthesis and radiation resistance. *Crystallography* (in press, Rus.).
- [15] Suenaga K., Iijima S., Kato H., Shinohara H. Fine-structure analysis of Gd M45 near-edge EELS on the valence state of Gd@C₈₂ microcrystals. *Phys. Rev. B*, 2000, **62**(3), P. 1627–1630.
- [16] Nishibori E., Takata M., Sakata M., Tanaka H., Hasegawa M., Shinohara H. Giant motion of La atom inside C₈₂ cage. *Chem. Phys. Lett.*, 2000, **330**, P. 497–502.
- [17] Nishibori E., Takata M., Sakata M., Inakuma M., Shinohara H. Determination of the cage structure of Sc@C₈₂ by synchrotron powder diffraction. *Chem. Phys. Lett.*, 1998, **298**, P. 79–84.
- [18] Takata M., Imeda B., Nishibori E., Sakata M., Saito Y., Ohno M., Shinohara H. Confirmation by X-ray-diffraction of the Endohedral Nature of the Metallofullerene Y@C₈₂. *Nature*, 1995, **377**, P. 46–49.
- [19] Nishibori E., Iwata K., Sakata M., Takata M., Tanaka H., Kato H., Shinohara H. Anomalous endohedral structure of Gd@C₈₂ metallofullerenes. *Phys. Rev. B*, 2004, **69**, P. 113412(1-4).
- [20] Tang J.X., Yuan G.M., Cao H., et. al. Tuning electronic properties of metallic atom in bondage to a nanospace. *J. Phys. Chem.*, 2005, **109**, P. 8779–8785.
- [21] Starke K., Navas E., Arenholz E., Hu Z., Baumgarten L., van der Laan G., Chen C. T., Kaindl G. Magnetic circular dichroism in 4d→4f resonant photoemission and photoabsorption of Gd metal. *Phys. Rev. B*, 1997, **55**, P. 2672–2675.
- [22] Tobin J.G., Chung B.W., Schulze R.K., Terry J., Farr J. D., Shuh D. K., Heinzelman K., Rotenberg E., Waddill G.D., Van der Laan G. Resonant photoemission in f-electron systems: Pu and Gd. *Phys. Rev. B*, 2003, **68**, P. 115109(1-11).
- [23] Szhogina A.A., Shilin V.A., Sedov V.P., Lebedev V.T. Endohedral metallofullerenols survival under neutron irradiation. *Crystallography* (in press, Rus.).
- [24] Shilin V.A., Lebedev V.T., Kolesnik S.G., Kozlov V.S., Grushko Yu.S., Sedov V.P., Kukorenko V.V. Investigation of the Neutron Activation of Endohedral Rare Earth Metallofullerenes. *Crystallography Reports*, 2011, **56**(7), P. 1192–1196.
- [25] Okazaki T., Lian Y., Gu Z., Suenaga K., Shinohara H. Isolation and spectroscopic characterization of Sm-containing metallofullerenes. *Chem. Phys. Lett.*, 2000, **320**, P. 435–440.

Study of antioxidant activity of fullerenols by inhibition of adrenaline autoxidation

I. A. Dubinina^{1,2}, E. M. Kuzmina¹, A. I. Dudnik², N. G. Vnukova^{1,2},
G. N. Churilov^{1,2}, N. A. Samoylova³

¹Siberian Federal University, Krasnoyarsk, Russia

²Kirensky Institute of Physics SB RAS, Krasnoyarsk, Russia

³Leibniz Institute for Solid State and Materials Research, Dresden, Germany

churilov@iph.krasn.ru

PACS 81.05.ub

DOI 10.17586/2220-8054-2016-7-1-153-157

In this paper, we describe application of the adrenaline autoxidation reaction to determine the antioxidant activity of fullerenols C_{60} , C_{70} their mixture with higher fullerene and endohedral fullerene $Y@C_{82}$. It was shown that the adrenaline autoxidation reaction can be applied to determine the antioxidant activity of fullerenols. The antioxidant activity of C_{70} fullerene was higher than that of C_{60} fullerene. Additionally, the antioxidant activity of $Y@C_{82}$ fullerene was higher than that of C_{70} fullerene.

Keywords: fullerene, antioxidant activity, endohedral fullerene, adrenaline autoxidation.

Received: 20 November 2015

1. Introduction

Polyhydroxylated fullerenes have been developed as the main derivative of fullerenes with excellent biocompatibility and biofunctionality [1,2]. Indeed, C_{60} fullerenols have been found to have outstanding antioxidant activity, which scavenge almost all reactive oxygen species (ROS) and reactive nitrogen species (RNS) [3].

Endohedral metallofullerenes, i.e. molecules in which a fullerene encapsulates a metal atom(s), have shown great promise for use in biomedical science. Although C_{60} has been the most commonly studied fullerene in biological systems, a few endohedral materials have been synthesized using C_{60} as a cage molecule despite the limited interior volume of C_{60} . Therefore, most endohedral metallofullerenes are synthesized using C_{82} or higher molecular weight fullerenes (presumably with larger interior volumes). Our group has prepared many C_{82} fullerene derivatives. $Y@C_{82}$ is one of the most important molecules in the metallofullerene family [4]. Yttrium endohedral metallofullerene (e.g., $Y@C_{82}(OH)_{22}$) is a functionalized fullerene with yttrium trapped inside the C_{82} fullerene cage. It was reported that the chemical and physical properties of endohedral metallofullerenols depend on the number and position of the hydroxyl groups on the fullerene cage [4]. These results demonstrated that modifying the outer cage of $Y@C_{82}$ with a number of hydroxyl groups tunes the electronic properties of the inner metal atom as well as the electron density and polarizability of the electrons localized on the fullerene's cage.

A number of fullerenes, fullerenols, and endohedral metallofullerenols have been shown to be capable of scavenging free radicals [3,5]. However, much less is known about the antioxidant activity of $Y@C_{82}(OH)_{22}$. It has not been determined if the ROS-scavenging capability of $Y@C_{82}(OH)_{22}$ is higher than that of other functionalized fullerenes. In this work, we applied

the adrenaline autoxidation reaction to determine the antioxidant activity of fullerenols C₆₀ and their mixture with higher and endohedral fullerenols.

2. Methods

2.1. Preparation of fullerenols

Fullerene mixture with endohedral Y-fullerene was synthesized at the set up with high frequency (HF) arc plasma for sputter graphitic electrodes (graphitic rods) [6,7]. Graphitic rods, with an axial hole in which Y₂O₃ was inserted, were annealed at 1800 °C for 20 min. Arc current was 190 A, frequency – 66 kHz, and chamber pressure was 98 kPa. Extraction was carried out using CS₂.

Synthesized fullerenes were separated by liquid chromatography with turbostratic graphite (graphite with an interplanar distance 3.42 Å) as stationary phase and toluene/hexane (4:6) mixture as mobile phase (or pure toluene in case of C₇₀ elution). Endohedral Y-containing fullerene was separated using HPLC chromatography (Agilent 1200-series with Buckyprep column).

The experimental preparation of fullerenols was achieved under acidic conditions by treatment with nitric acid.

2.2. Antioxidant activity study

Antioxidant activity (AA) of fullerenols was measured according to Hasanova et. al [8] by the inhibition of adrenaline autoxidation. The reaction mixture contained 0.1 cm³ of 0.1 % adrenaline hydrochloride, 4 cm³ carbonate buffer, pH 10.55, and 0.1 cm³ of fullereneol solution. The increase in absorbance due to adrenaline autoxidation was monitored at 347 nm and the percentage inhibition of the maximal rate of increase in absorbance was determined. According to [8] more than 10 % inhibition rate shows the AA of investigated solution. This method has been developed for measuring AA of vegetative gathering and for the first time applied for fullerenols. The AA was calculated as follows:

$$AA = \frac{(D1 - D2) \cdot 100}{D1}, \%$$
 (1)

where D1 is optical density of pure adrenaline and D2 is optical density of adrenaline with fullereneol.

3. Results

Synthesized Y-containing fullerene mixture was investigated by HPLC (Fig. 1). We collected fraction with Y-containing endofullerene (30 – 40 min) and investigated it by mass-spectrometry (Bruker BIFLEXTM III Time-of-Flight mass spectrometer with laser desorption) (Fig. 2). The fullerene mixture was shown to consist of only one type of endohedral metallofullerene – Y@C₈₂. The fullerene mixture was separated and 3 fractions were received – pure C₆₀ (99 %), C₇₀ with higher fullerenes (92 and 8 %, respectively), and higher fullerenes with 6 % of Y@C₈₂.

Fullerene fractions were hydroxylated and solutions with concentrations 2 mg/ml of fullerenols were produced.

Figure 3 shows the dynamics for the adrenaline autoxidation reaction. The decrease in the optical density showed the inhibitory effect of the fullerenols. To rate the influence of fullerenols on adrenaline autoxidation process, different exposure times were chosen – 30 s, 3 min, 5 min. Calculation of AA showed that all fullerenols displayed great AA. The AA significantly increased with increasing concentration of higher fullerenols (Fig. 4).

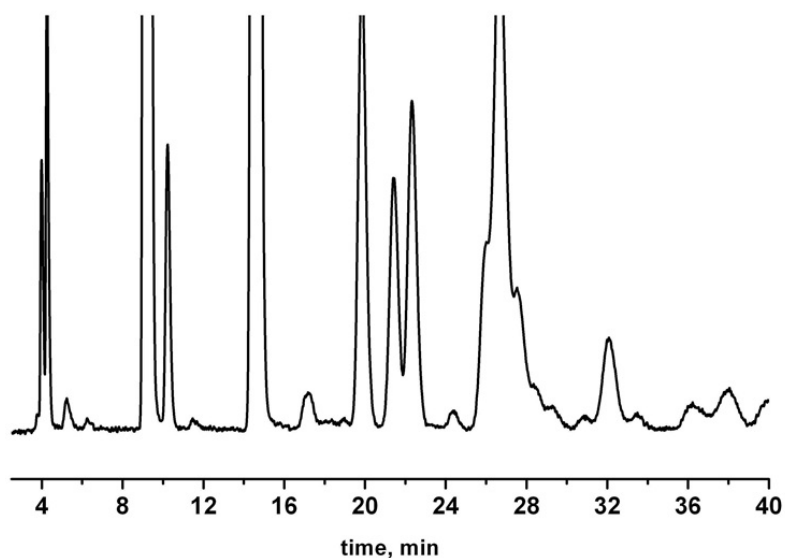


FIG. 1. Chromatogram of fullerene mixture with Y-endofullerene

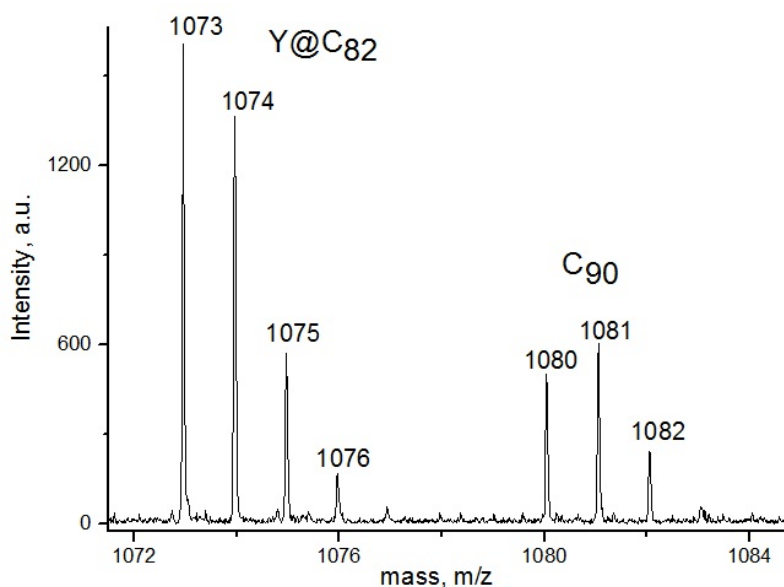


FIG. 2. Mass-spectrum of fullerene fraction with Y-endofullerene (30 – 40 min)

4. Conclusion

Fullerenols were investigated to see if they inhibit the adrenaline autoxidation reaction and thus show great antioxidant activity. Increasing the higher fullerene content, as well as Y@C₈₂ content, resulted in an increase in the antioxidant activity of fullerene solution.

Acknowledgements

The work was supported by the Russian Foundation for Basic Research 15-03-06786.

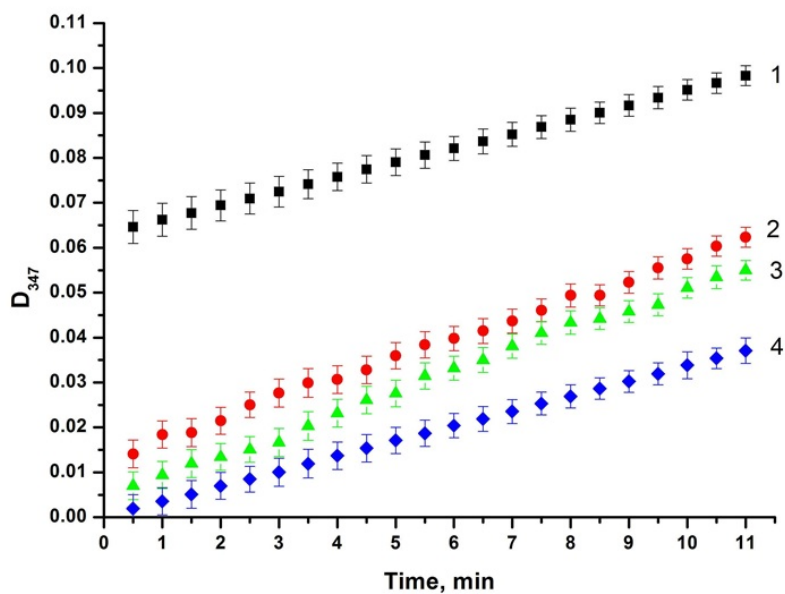


FIG. 3. Optical density dependence on reaction time. 1 – pure adrenaline, 2 – C_{60} fulleranol, 3 – C_{70} and higher fullerenols and 4 – endohedral and higher fullerenols

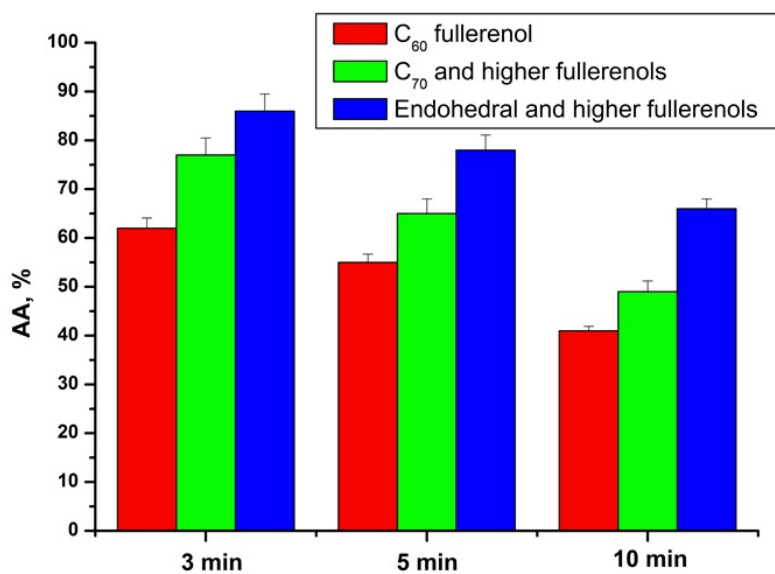


FIG. 4. Comparative antioxidant activity of fullerenols (where 100 % of AA means that adrenaline autoxidation doesn't occur, and 0 % means that there is no inhibitory effect). Statistically significant changes in AA level (ANOVA, $p < 0.05$, $n = 3$)

References

- [1] Chiang L.Y., Swirczewski J.W. Multi-hydroxy additions onto C₆₀ fullerene molecules. *J. Chem. Soc. Chem. Commun.*, 1992, **24**, P. 1791–1793.
- [2] Li J., Takeuchi A. C₆₀ fullerol formation catalysed by quaternary ammonium hydroxides. *J. Chem. Soc. Chem. Commun.*, 1993, **23**, P. 1784–1785.
- [3] Chiang L.Y., Lu F.J., Lin J.T. Free radical scavenging activity of water-soluble fullerenols. *J. Chem. Soc. Chem. Commun.*, 1995, **12**, P. 1283–1284.
- [4] Tang J., Xing G.M., Zhao F., Yuan H., Zhao Y.L. Modulation of structural and electronic properties of fullerene and metallofullerenes by surface chemical modifications. *J. Nanosci. Nanotechnol.*, 2007, **7**(4-5), P. 1085–1101.
- [5] Dugan L.L., Gabrielsen J.K., Yu S.P., Lin T.S., Choi D.W. Buckminsterfullerenol free radical scavengers reduce excitotoxic and apoptotic death of cultured cortical neurons. *Neurobiol. Dis.*, 1996, **3**, P. 129–135.
- [6] Churilov G.N. Plasma Synthesis of Fullerenes. *Instruments and Experimental Techniques*, 2000, **43**(1), P. 1–10.
- [7] Churilov G.N., Kratschmer W., Osipova I.V., Glushenko G.A., Vnukova N.G., Kolonenko A.L., Dudnik A.I. Synthesis of fullerenes in a high-frequency arc plasma under elevated helium pressure. *Carbon*, 2013, **62**, P. 389–392.
- [8] Hasanova S.R., Plehanova T.I., Gashimova D.T., Galiyahmetova E.H., Klysh E.A. Comparative study of antioxidant activity of vegetative gathering. *Proc. Voronezh State University. Series: Chemistry, Biology, Pharmacy*, 2007, **1**, P. 163.

Magnet-induced behavior of iron carbide (Fe₇C₃@C) nanoparticles in the cytoplasm of living cells

I. Alieva¹, I. Kireev¹, A. Rakhmanina², A. Garanina¹, O. Strelkova¹, O. Zhironkina¹, V. Cherepaninets¹, V. Davydov², V. Khabashesku³, V. Agafonov⁴, R. Uzbekov^{5,6}

¹Belozersky Institute of Physico-Chemical Biology, Moscow State University, Moscow, Russia

²L. F. Vereshchagin Institute for High Pressure Physics of the RAS, Troitsk, Russia

³Center for Technology Innovation, Baker Hughes Inc., Houston, TX, 77040, USA

⁴GREMAN, UMR CNRS 7347, Université François Rabelais, 37200 Tours, France

⁵Faculté de Médecine, Université François Rabelais, Tours, France

⁶Faculty of Bioengineering and Bioinformatics, Moscow State University, Moscow, Russia

rustem.uzbekov@univ-tours.fr, viatcheslav.agafonov@univ-tours.fr

PACS 81.40.Rs, 81.07.-b, 87.18.-h, 87.16.Wd, 87.17.Rt, 87.64.Ee, 87.64.M-, 87.64.mh, 87.85.jj

DOI 10.17586/2220-8054-2016-7-1-158-160

The uptake of superparamagnetic Fe₇C₃@C nanoparticles into living cells and their behavior once inside the cell was investigated. The cells used were shown to absorb the nanoparticle aggregates over the first 30 minutes. After absorption, these aggregates moved towards the center of the cell and accumulated near the cell nucleus. No toxic effects on cell physiology were observed. In a magnetic field, the particles aligned in the cells along magnetic lines and shifted to the magnet's side. During long-term cultivation, Fe₇C₃@C nanoparticle aggregates were ultimately discarded via exocytosis.

Keywords: superparamagnetic Fe₇C₃@C nanoparticles, living cells, electron microscopy, magnetic field.

Received: 20 November 2015

1. Introduction

A new type of superparamagnetic nanoparticles (NPs), with chemical formula Fe₇C₃@C was recently obtained by us at high pressure and temperature and studied via physico-chemical and biological methods [1,2]. Prolonged biological exposure demonstrated that Fe₇C₃@C NPs display highly efficient cellular uptake and did not affect cytophysiological parameters for *in vitro* cultured pig kidney epithelial (PK) cells.

2. Experimental section

For live imaging, pig kidney cells were placed on glass-bottomed Petri dishes (LabTek, USA) at a density of 10⁵ cells/ml and incubated with Fe₇C₃@C NPs for 24 h. Cell observation was performed in an environmental chamber kept at 37 °C and under 5 % CO₂. The chamber was mounted on an Olympus IX70 inverted microscope equipped with CCD-camera Orca-RT+(Hamamatsu, Japan) and controlled by Micromanager 1.4 software [1]. Illumination conditions (ND filters, lamp voltage, exposure time) were set to minimize phototoxicity.

For further experiments, PK were washed several times with fresh pre-warmed media to remove free particles, fixed in 2.5 % glutaraldehyde in 100 mM phosphate buffer (pH 7.4)

for 2 h with subsequent post-fixation in 1 % OsO₄ and embedding in Epon (Sigma, USA). Serial ultrathin sections (70 nm) were prepared with Leica ultramicrotome and observed with JEM 1011 (JEOL, Japan) at 100 kV.

3. Results and discussion

Cells were capable of capturing magnetic nanoparticles (MNP) by upper part of the cell membrane, and from the surface of the cultivation substrate during motion process. Immunofluorescence studies using intracellular endosomal membrane marker showed that MNP aggregates can be located in endosomes or lying free in the cytoplasm.

During long-term cultivation, cells discarded Fe₇C₃@C aggregates on the surface of the plasma membrane via exocytosis. These aggregates were reabsorbed later by the same or adjacent cells. In the absence of a magnetic field, Fe₇C₃@C aggregates localized in the central region of the cells around the nucleus with a uniform distribution (Fig. 1).

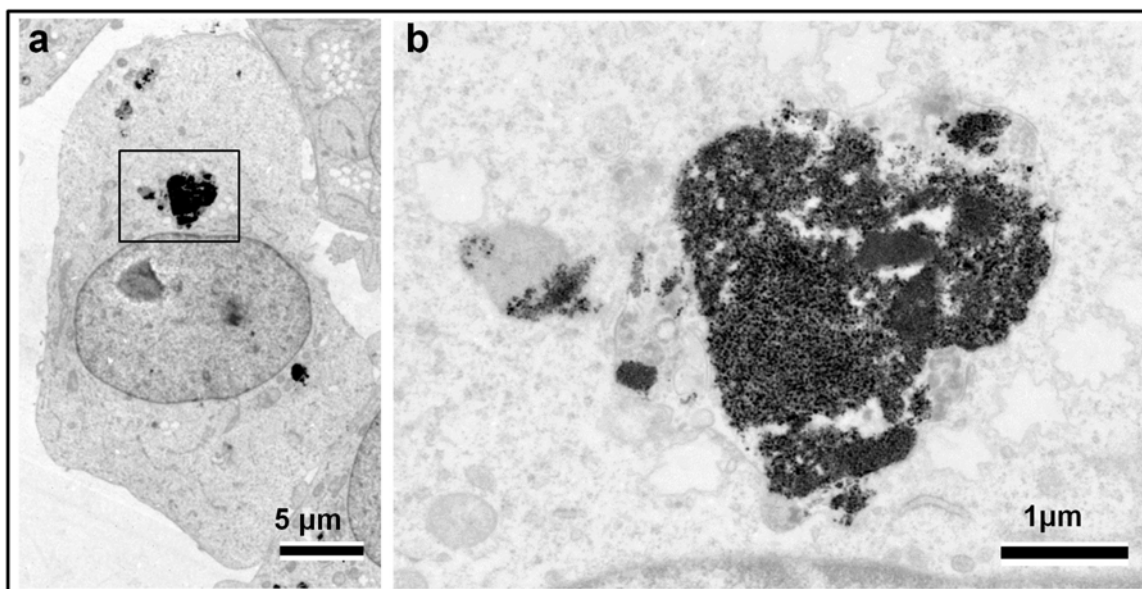


FIG. 1. Transmission electron microscopy photos of the cell with Fe₇C₃@C nanoparticles aggregates. a) Whole cell image on small magnification; b) High magnification of selected region. Scale bar: a – 5 μm, b – 1 μm

In a magnetic field, uneven distribution of Fe₇C₃@C aggregates was observed - it was advantageously arranged on the side of the cell facing the magnet (Fig. 2). Electron microscopy analysis of these cells showed that the aggregates are often located in the cytoplasm of cells along microtubules.

4. Conclusions

Our experiments demonstrated active endocytosis-mediated uptake of Fe₇C₃@C nanoparticles and the absence of any significant effects of it to cell behavior.

The magnetic properties of the Fe₇C₃@C NPs are sufficient for successful manipulation at the intracellular level.

The non-toxic, biologically-compatible paramagnetic Fe₇C₃@C carbide NPs can be used as efficient vectors for the targeted delivery of biologically-active compounds both intracellularly and throughout the entire organism.

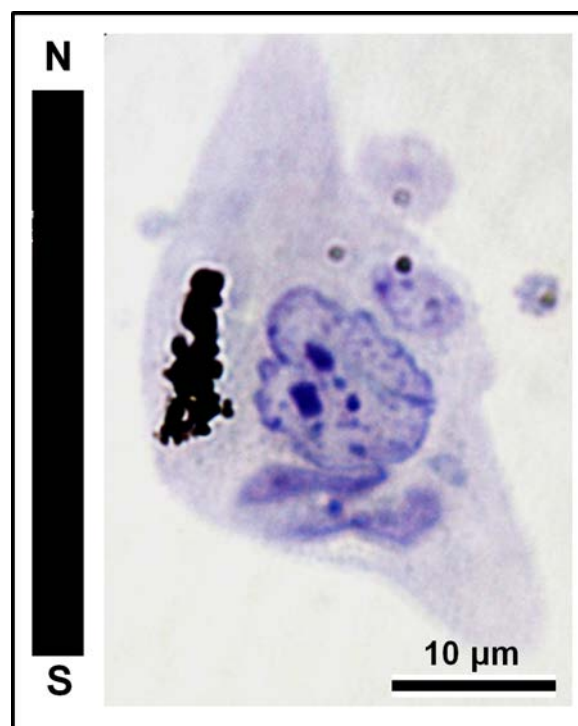


FIG. 2. Light microscopy photo of the cell with Fe₇C₃@C nanoparticles in magnetic field. Nanoparticles aggregate oriented along magnetic field lines and shifted to the magnet side. Scale bar 10 μm

Acknowledgements

This work was supported by Russian Foundation for Basic Research (Grants 12-03-00787, 12-04-00488, 13-04-00885, 15-03-04490) and Moscow State University Development Program PNR 5.13. Our data were obtained with the assistance of the RIO Electron Microscopy Facility of François Rabelais University and CHRU de Tours.

References

- [1] Davydov V., Rakhmanina A., Kireev I., Alieva I., Zhironkina O., Strelkova O., Dianova V., Samani T.D., Mireles M., Hocine Yahia L., Uzbekov R., Agafonov V., Khabashesku V. Solid state synthesis of carbon-encapsulated iron carbide nanoparticles and their interaction with living cells. *J. Mater. Chem. B*, 2014, **2**, P. 4250–4261.
- [2] Uzbekov R.E., Kireev I.I., Alieva I.B., Davydov V. A., Rakhmanina A.V., Agafonov V. Interaction of Iron Carbide Nanoparticles protected by Carbon Shell Onion-like Structure with living Cells. Joint Intern. Conf. “Advanced Carbon Nanostructures” (ACNS’ 2013) St.Petersburg, Russia.

Nanocomposites with antibacterial properties using CNTs with magnetic nanoparticles

B. Ortega García¹, O. V. Kharissova¹, H. V. Rasika Dias²,
F. Servando Aguirre T.³, J. Salinas Hernández⁴

¹Universidad Autónoma de Nuevo León, Facultad de Ciencias Físico-Matemáticas,
Monterrey, Nuevo León, México

²The University of Texas at Arlington, Department Chemistry and Biochemistry,
Arlington, Texas 76019, USA

³Centro de Investigación en Materiales Avanzados (CIMAV),
Monterrey, Nuevo León, México

⁴Centro de Investigación y Desarrollo de Educación Bilingüe (CIDEB),
Monterrey, Nuevo León, México

beatriz.ortega24@gmail.com, okhariss@mail.ru, dias@exchange.uta.edu,
servando.aguirre@cimav.edu.mx, jeannie05@hotmail.com

PACS 81.07.-b, 81.07De, 82.35Cd, 82.35Np

DOI 10.17586/2220-8054-2016-7-1-161-168

In this work, multiwall carbon nanotubes (MWCNT) were functionalized with silver nanoparticles using two different methods of incorporation. Characterization of these composites was done using Raman spectroscopy and Transmission Electron Microscopy (TEM) and the antibacterial properties were measured using method of dilution and plating. The four-point probe method was used to measure the resistivity of the nanocomposite thin films made via the spin coating method.

Keywords: carbon nanotubes, functionalization, silver nanoparticles, polymers, nanocomposites.

Received: 20 November 2015

1. Introduction

It is well-known that diverse polymers possess antibacterial properties [1], however, this also applies to several nanoparticles (for example Ag-NPs [2]) or carbon nanotubes (CNTs) [3]. The CNTs can be magnetic if they contain iron nanoparticles inside as a result of the incorporation of Fe-containing catalysts during their production [4]. It is hoped that once the nanoparticles are integrated into the polymer matrix that all of the NPs properties will be transferred to the polymer, resulting in its antibacterial and magnetic properties. There are many applications reported for polymer-NP nanocomposites with antibacterial properties; however, in the case of also having magnetic properties, there also exists the potential for an alternative means for drug delivery or biosensor applications.

The natural polymer chitosan (CS) belongs to the group of antibacterial polymers [1]; it is compatible with tissues and is utilized in biomedicine. In this work, the functionalization of CNTs with Ag and Fe and their further uniform dispersion in chitosan polymeric matrix is studied.

2. Experimental

2.1. Materials

Multiwall carbon nanotubes (MWCNTs) were prepared by spray pyrolysis method in the presence of iron as a catalyst at two different temperatures, 760 °C and 800 °C. Chitosan (low molecular weight) from Aldrich, AgNO₃ from Fisher, Luperox® LP, Lauroyl peroxide, 97 % from Aldrich, Ethanol 99.2 % from Decon Labs Inc., Acetic Acid (2 %), cetyltrimethylammonium bromide (CTAB) from Aldrich, deionized water (DIW) were used as supplied.

2.2. Functionalization of MWCNTs

Two methods, used for functionalization of carbon nanotubes, were as follows:

For the first functionalization (1NP), the CNTs (0.025 g), synthesized at 800 °C, were ultrasonically dispersed in ethanol (10 mL). Another solution containing DMF (20 mL), silver nanoparticles (0.08 g), prepared by a more environmentally-benign method, and chitosan (2 wt.%), was added to the first solution under nitrogen flow and stirred for 48 hrs (see Fig. 1.1).

For the second functionalization (2NP), the CNTs (0.1 g), synthesized at 760 °C, were ultrasonically dispersed in ethanol (400 mL) and lauroyl peroxide (Luperox® LP, Lauroyl peroxide) (0.5 g) was added for 30 min. Next, the CTAB (0.2 g) was added and the mixture was subjected to ultrasonication for 15 min. After this step, one of previously selected silver compounds (silver(I) acetate, silver(II) oxide or AgNO₃) was added and ultrasonication was continued for an additional 60 min.

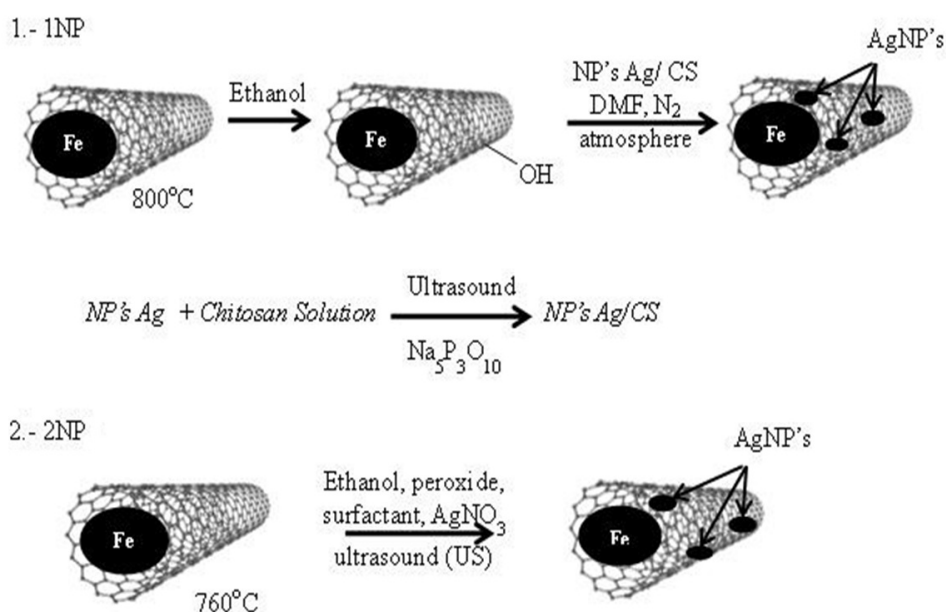


FIG. 1. Two methods for carbon nanotube functionalization with silver nanoparticles

2.3. Preparation of CS/Ag/MWCNT nanocomposite

Carbon nanotubes functionalized with silver nanoparticles were then used (0.02 % wt.%) for the preparation of nanocomposites with different chitosan contents (1 %, 3 % and 5 %) by mixing using ultrasonication for 1 and 5 min. Films of different nanocomposites were obtained by a spin coating technique onto glass slides.

2.4. Characterization

The samples were analyzed by Raman spectroscopy, Transmission Electron Microscopy (TEM); method of dilution and plating was used for measurement of antibacterial property. The four-point probe method was applied to measure the resistivity of the nanocomposites.

2.4.1. Method of dilution and plating:

1. A colony of the strain *Escherichia coli* DH5a was placed in 75 mL of liquid nutrient medium for 12 h at 37 °C (pre-culture).

2. The analyzed samples were Luperox or Lauroyl peroxides, CTAB, mixture of peroxide and CTAB, ethanol, silver nitrate solution as a reference, carbon nanotubes synthesized at 760 °C and carbon nanotubes containing silver nanoparticles. All reagents were introduced into an ultrasonic bath for 5 min for sample dispersion.

3. 1 mL of the pre-culture of *E. coli* DH5a was mixed in 15 – 20 mL of melted nutrient medium agar which was cooled to 40 °C, and allowed to solidify undisturbed on a flat table top.

4. 0.1 mL of the dispersed samples were taken and poured over the filter paper disks and placed in the center of the Petri dish with the bacteria, for this process, sterilization of equipment was done using a Bunsen burner (called “disk technique”).

5. 0.05 mL of the scattered samples were taken and poured into a hole made in the center of the agar plate placed in the center of the petri dish with the bacteria, for this process, sterilization of equipment was done using a Bunsen burner (called agar hole technique)

6. Both plates (paper disks and agar holes) were maintained at 37 °C for 12 h.

Note. The Luperox and CTAB were diluted in absolute ethanol and later dispersed by ultrasonic treatment for 25 min.

3. Results and discussions

Using Raman spectroscopy and TEM analyses, we confirmed the functionalization of the synthesized carbon nanotubes (760 °C). Fig. 2 shows the Raman spectra of MWCNT synthesized at 760 °C and two characteristic peaks are observed: one peak at a Raman shift of 1310 cm^{-1} , called the D-band, which is assigned to the disordered graphitic structure of MWCNTs. The other peak, at a Raman shift of 1600 cm^{-1} , called the G-band, is assigned to the C=C bond in the graphitic plane.

The Raman spectra of both pristine MWCNT and MWCNT/Ag, obtained with an excitation energy of 2.41 eV, are shown in Fig. 2 (an inset in this image corresponds to the reported data for SWCNTs/Ag [5]). The details of sample preparation and Raman experiment have been reported elsewhere [5]. The presence of silver in the Raman spectra is confirmed by the presence of characteristic peaks in the 1100 – 1600 cm^{-1} range. These peaks are slightly shifted and broadened in comparison to the Raman data of the samples without silver. It should be pointed out that the tangential band (at about 1590 cm^{-1}) is composed of several peaks. The downshift in the tangential G^+ -mode from 1600 to 1593 cm^{-1} indicates that electrons are transferred from the silver to the MWCNTs; a similar peak amplification was previously reported for SWCNT/Ag [5].

Figure 3 shows the TEM images of MWCNTs synthesized at 760 °C and MWCNT with silver nanoparticles. Carbon nanotubes synthesized using an iron-containing precursor and functionalized with silver nanoparticles demonstrate magnetic properties. As it is seen in Fig. 4 using a small magnet, the nanotubes are attracted to the magnet. This confirms that magnetic properties are not lost upon functionalization.

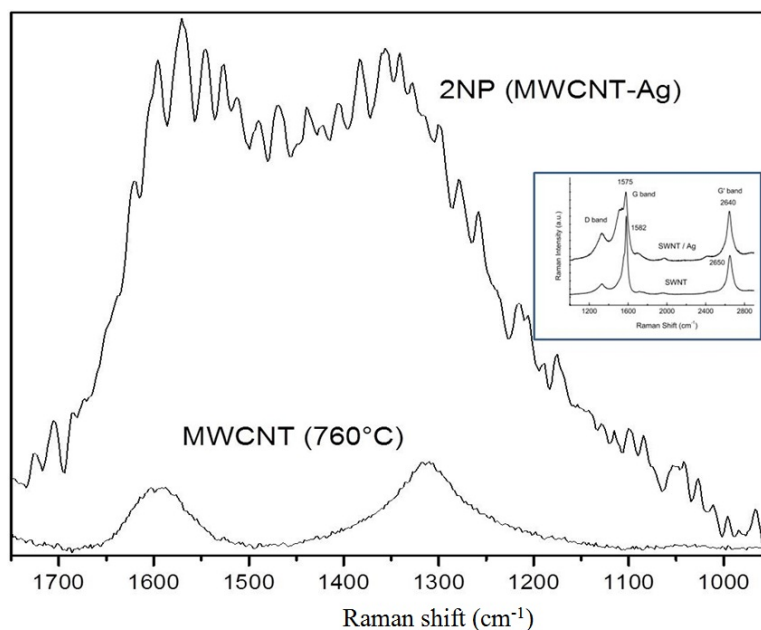


FIG. 2. Raman spectra of MWCNT: Raman spectra of MWCNTs made at 760 °C with Raman spectra of functionalized MWCNTs made at 760 °C and silver nanoparticles. An inset contains earlier reported data for SWCNTs/Ag

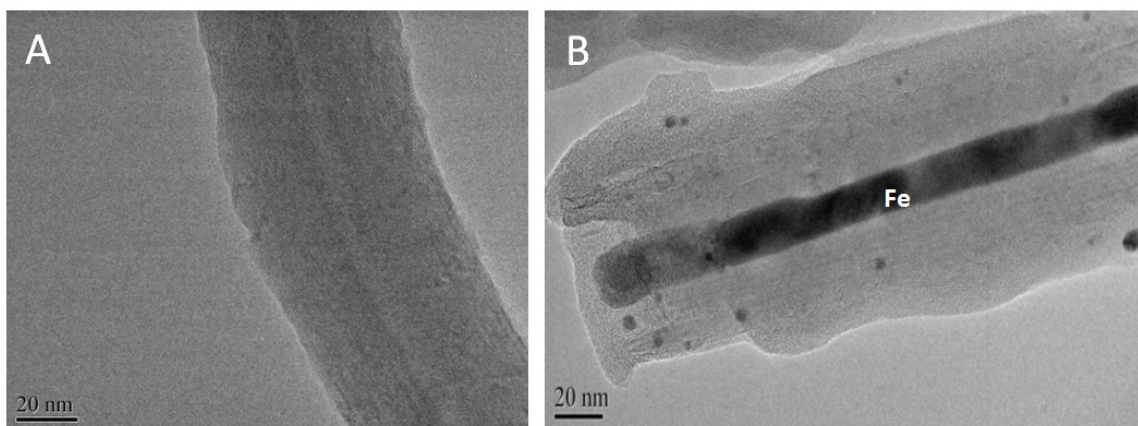


FIG. 3. TEM micrograph: A) MWCNT made at 760°C and B) functionalized MWCNT (760°C) with silver nanoparticles (2NP)

Figure 5 and Fig. 9 show an increase in the resistivity when you increase the number of layers using chitosan solution for 1 % and 3 % and 1NC and 2NC. In Fig. 7, high contents of CS (5 %) were used; one layer presented high resistivity to infinity but increasing other layer resistivity is decreased. In case of addition of nanoparticles (1NC and 2NC), only with 2NC the similar decrease of resistivity takes place.

Figures 8 and 9 show a decrease of resistivity when there is an increase of percentage of CS.

3.1. Antibacterial test of carbon nanotubes with silver

The CNT samples with silver nanoparticles at two concentrations (0.0199 g / 0.5 mL and 0.00199 g / 10 mL) were observed to generate homogeneous foams, while for the remaining



FIG. 4. Carbon nanotubes with magnet nearby

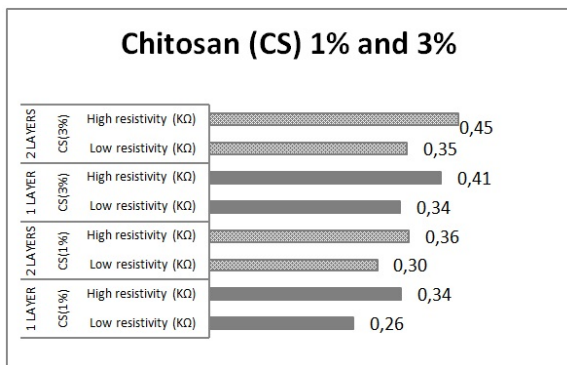


FIG. 5. Results for solutions with different percentages of chitosan

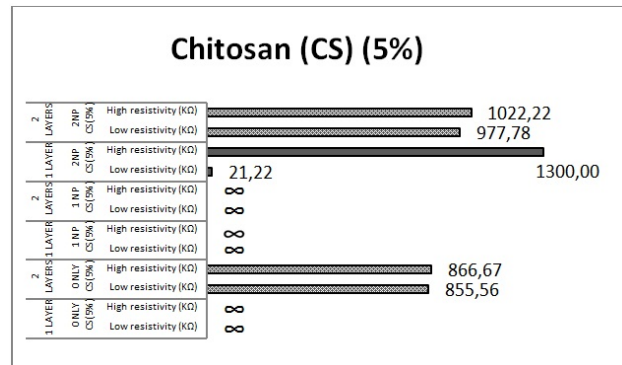


FIG. 6. Results for chitosan solution of 5 % using only chitosan and two different nanoparticles (1NP and 2NP)

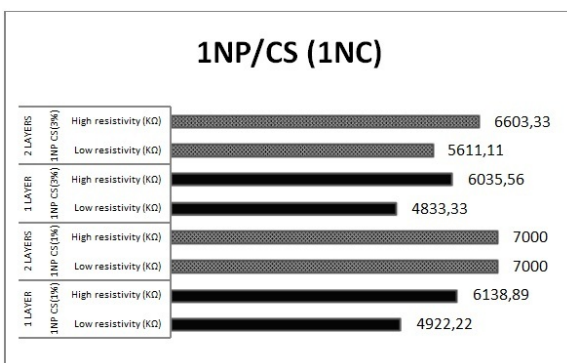


FIG. 7. Decrease in resistivity average (MΩ) of 1NC nanocomposite with CS solution (1 % and 3 %)

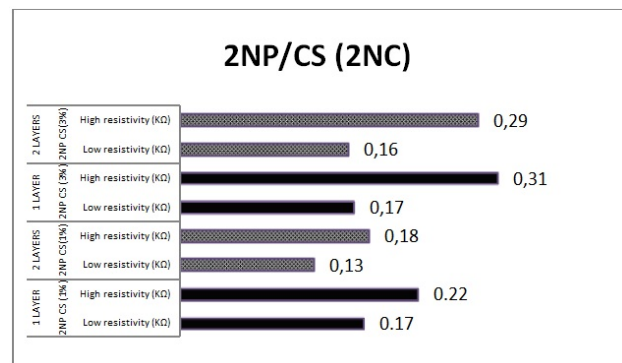


FIG. 8. Decrease in resistivity average (KΩ) of 2NC nanocomposite with CS solution (1 % and 3 %)

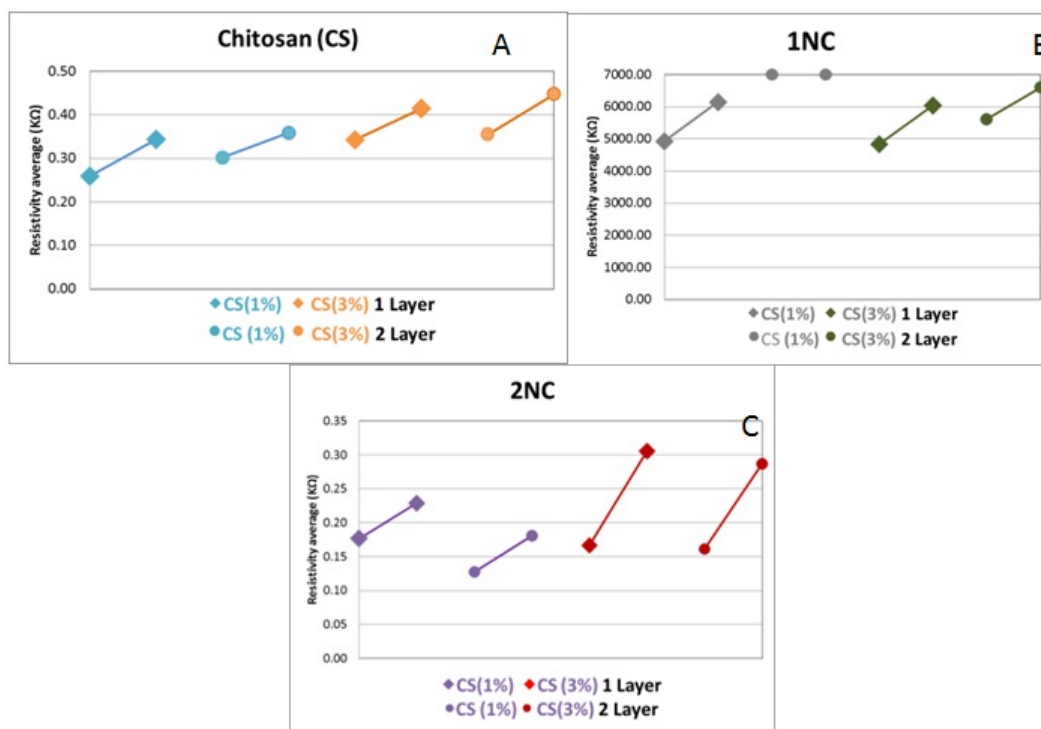


FIG. 9. Resistivity average for 1 layer and 2 layers of A) CS solution (1 % and 3 %) and nanocomposites B) 1NC and C) 2NC

samples, dispersion was difficult. Because this sample showed foaming due to the surfactant CTAB used in the reaction, an experimental design was utilized whereby all reagents were tested in order to rule out that the growth inhibitory activity of *Escherichia coli* DH5 was attributable to the effect of one of them.

The CTAB in agar hole in petri dish showed an inhibition halo of 3.0 cm of diameter. The CTAB in paper filter disk showed in petri dish an inhibition halo of 0.1 cm of diameter.

In Fig. 10, the sample with a concentration of 0.02 g / 0.5 mL in 0.05 mL poured in the agar holes of the sample MWCNT/Ag showed an inhibition halo of 2.3 cm of diameter in the *E. coli* DH5a culture. The samples with a concentration of 0.02 g /0.5 mL in 0.1 mL in disks, only the sample MWCNT/Ag showed an inhibition halo of 0.5 cm of diameter in the *E. coli* DH5a culture (see Table 1).

4. Conclusion

In the present work, we obtained nanoparticles with antibacterial and magnetic properties using an ultrasonic method for functionalization. We confirm the functionalization with Raman analysis by comparing the Raman spectra of MWCNT with and without functionalization. In addition to the antibacterial and magnetic properties of our nanoparticles, we measured the resistivity of chitosan and the nanocomposites. One of the nanocomposites (2NC) decreased the resistivity among 33 % (1 layer) and 58 % (2 layers) less for CS (1 %) and 36 % (1 layer) and 46.6 % (2 layers) less for CS (3 %). These mean that multiwall carbon nanotubes with silver nanoparticles allow increasing the conductivity of the nanocomposite.

TABLE 1. Antimicrobial growth inhibition

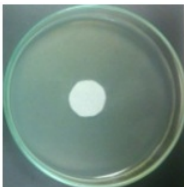
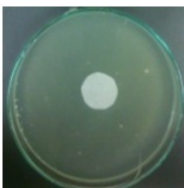
Sample	Antimicrobial growth inhibition		
	Technique:	Agar hole	Disk
Control (only agar with bacteria)	NO		
Peroxide	NO		
CTAB	YES		
Mix of peroxide and CTAB	NO		
Ethanol	NO		
CNT	NO		
CNT with Ag	YES		



FIG. 10. MWCNT with silver nanoparticles (2NP) with a concentration of 0.02 g / 0.5 mL in 0.05 mL poured in the agar holes with a halo of inhibition of 2.3 cm

Acknowledgements

This work was supported by CONACYT and Universidad Autónoma de Nuevo León, and also we are grateful to UTA, CIMAV and CIDEB for their collaboration.

References

- [1] Muñoz-Bonilla A., Fernández-García M. Polymeric materials with antimicrobial activity. *Progr. Polymer Sci.*, 2012, **37**, P. 281–339.
- [2] Simchi A., Tamjid E., Pishbin F., Boccaccini A.R. Recent progress in inorganic and composite coatings with bactericidal capability for orthopaedic applications. *Nanomedicine: Nanotechnology, Biology, and Medicine*, 2011, **7**, P. 22–39.
- [3] Dastjerdi R., Montazer M. A review on the application of inorganic nano-structured materials in the modification of textiles: Focus on anti-microbial properties. *Coll. Surf. B: Biointerfaces*, 2010, **79**, P. 5–18.
- [4] Gui X., Wei J., Wang K., Wang W., Lv R., Chang J., Kang F., Gu J., Wu D. Improved filling rate and enhanced magnetic properties of Fe-filled carbon nanotubes by annealing and magnetic separation. *Mater. Res. Bull.*, 2008, **43**, P. 3441–3446.
- [5] Fagan S.B., Souza Filho A.G., Mendes Filho J., Corio P., Dresselhaus M.S. Electronic properties of Ag-and CrO₃-filled single-wall carbon nanotubes. *Chem. Phys. Lett.*, 2005, **406**(1), P. 54–59.

Power-like corrections to the conductivity of Mo–C nanocomposites

A. D. Bozhko

A. M. Prokhorov General Physics Institute, Russian Academy of Sciences, Moscow, Russia
bozhko@lt.gpi.ru

PACS 72.80.Tm, 72.80.Ng

DOI 10.17586/2220-8054-2016-7-1-169-174

The evolution of the electron transport character in thin films of Mo–C nanocomposites is studied over the metal concentration range 0.14 – 0.3 at temperatures from 4.2 to 400 K. It is shown that conductivity of the Mo–C nanocomposites demonstrates the distinct power-like behavior in the two temperature intervals separated at 20 – 25 K. The concentration dependences of the power exponent in both temperature intervals are characterized by the expressed minimum at Mo content close to 0.2 varying over the range 0.25 – 1.0. The experimental data are discussed and simulated in the model of inelastic tunneling of the electrons in amorphous dielectrics in the framework of the effective medium approximation.

Keywords: metal-carbon nanocomposite, granular materials, amorphous carbon, electron transport, inelastic tunneling.

Received: 20 November 2015

1. Introduction

The interest in nanocomposites is motivated by their potential applications as sensors, optoelectronic devices, *etc.* [1]. The technological flexibility of the synthesis gives an easy way to generate the desired electrical response of the sensors under external excitation. This greatly broadens the field of application for nanocomposites. On the other hand, the competition among the number of physical phenomena such as grain-to-grain tunneling of the electrons, their quantum confinement on a single grain, Coulomb blockade, discrete energy spectrum of the grains, electron-electron interaction, *etc.* gives an opportunity to use the nanocomposites as model objects to study the peculiarities of electron transport in granular materials [1]. The metal-carbon nanocomposites are materials of particular importance. They combine the extraordinary mechanical properties typical for the hard forms of amorphous carbons [2] and the functionality of the nanogranular conducting materials [1]. The complex structure of amorphous carbon allows one to study the influence of the enhanced hierarchically-scaled disorder on the electron transport in the nanogranular matter.

2. Samples preparation and methods used

The films of molybdenum-carbon nanocomposites with a thickness of 1 μm were grown on the polished dielectric substrates in the hybrid deposition setup. The carbon-containing dielectric matrix was deposited by PCVD of siloxane $((\text{CH}_3)_3\text{SiO}(\text{CH}_3\text{C}_6\text{H}_5\text{SiO})_3\text{Si}(\text{CH}_3)_3)$ vapors in DC plasma discharge. The DC magnetron co-sputtering of Mo target was used for the metal phase generation. The substrates were positioned on the RF-biased (1.84 MHz) substrate holder. The detailed description of the deposition process can be found elsewhere [2]. The carbon phase of the deposited films is amorphous [4] and highly insulating ($10^{12} - 10^{14}$ Ohm·cm [3]). In accordance with TEM data, the molybdenum phase has a granular structure with the

typical size of amorphous Mo-rich domains about 1.1 ± 0.3 nm. The peculiarities of the structure allow one to relate the Mo–C nanocomposites to the disordered nanogranular materials.

The DC conductivity of the nanocomposites was measured over 4.2 – 400 K by the routine 4-terminal technique in a gas-flow helium cryostat. The samples were patterned in RF (13.56 MHz) Ar discharge by the use of mechanical mask in a double Hall cross configuration. The elemental composition of the molybdenum-carbon nanocomposites was studied by EPMA JEOL JXA-8200.

3. Results and discussions

The experimental dependences of the scaled conductivity on temperature $\sigma(T)/\sigma(400)$ are shown in Fig. 1 (a) over the Mo concentration range 0.14 – 0.3. The Mo concentration is shown near each curve. It can be seen that conductivity decreases with temperature over the entire range of Mo concentration. In the nanocomposites studied, the transition to the superconducting state is observed. The transition temperature is dependent on the Mo concentration. However, this phenomenon is beyond the scope of this paper.

The $\sigma(T)$ dependences possess the fine structure clearly observed in the temperature dependences of the derivative of the conductivity on temperature. The $\sigma'(T)/\sigma'(400)$ dependences are shown on a double logarithmic scale in the insert to Fig. 1(a). As it can be seen, the temperature dependences of the conductivity derivative are characterized by the existence of two distinct temperature intervals (marked in the insert to Fig. 1(a) as I and II) separated at temperature 20 – 25 K. The extended linear parts of $\sigma'(T)$ dependences within each temperature interval correspond to the power dependences of the conductivity on temperature:

$$\sigma(T) = \sigma_0 + \sigma_1 \left(\frac{T}{T_0} \right)^p, \quad (1)$$

where T_0 is a characteristic temperature.

The principal parameter in the modern models of the electron transport in granular media, which allows one to discriminate the mechanisms of the electron transport, is the value of the power exponent p . In the temperature range $g_T \delta < k_B T < E_C$ the corrections to the conductivity of an ordered granular array assume the logarithmic form (p close to 0) [5]:

$$\Delta\sigma(T) \sim -\frac{1}{g_T d} \ln \left(\frac{g_T E_C}{k_B T} \right), \quad (2)$$

where d is the dimensionality of the sample, the dimensionless intergranular conductance $g_T = G_T/(2e^2/h) \gg 1$, $\delta = (g_F b^3)^{-1}$ – the mean distance between energy levels in a single grain with size b , k_B is Boltzmann's constant, and $E_C \approx e^2/2\epsilon b$ – Coulomb charging energy of a single grain (ϵ is the effective dielectric constant of the media).

At lower temperatures $k_B T < g_T \delta$, the corrections to the conductivity in a 3-dimensional case accept the power form [6]:

$$\Delta\sigma(T) \sim -\frac{1}{g_T} \sqrt{\frac{k_B T}{g_T \delta}}. \quad (3)$$

Figure 1(b) illustrates the concentration dependences of the power exponent p in Mo–C nanocomposites obtained by fitting of the conductivity curves (Fig. 1(a)) in temperature intervals I and II using Eq. (1). The power exponent p varies over the range 0.25 – 1.0 being systematically higher in temperature interval I. Both dependences are characterized by the minimum at Mo concentration around 0.2. It follows from this figure that: a) the logarithmic corrections to the

conductivity (2) are not observed in Mo–C films, b) the square root corrections (3) exist only at certain Mo concentration values.

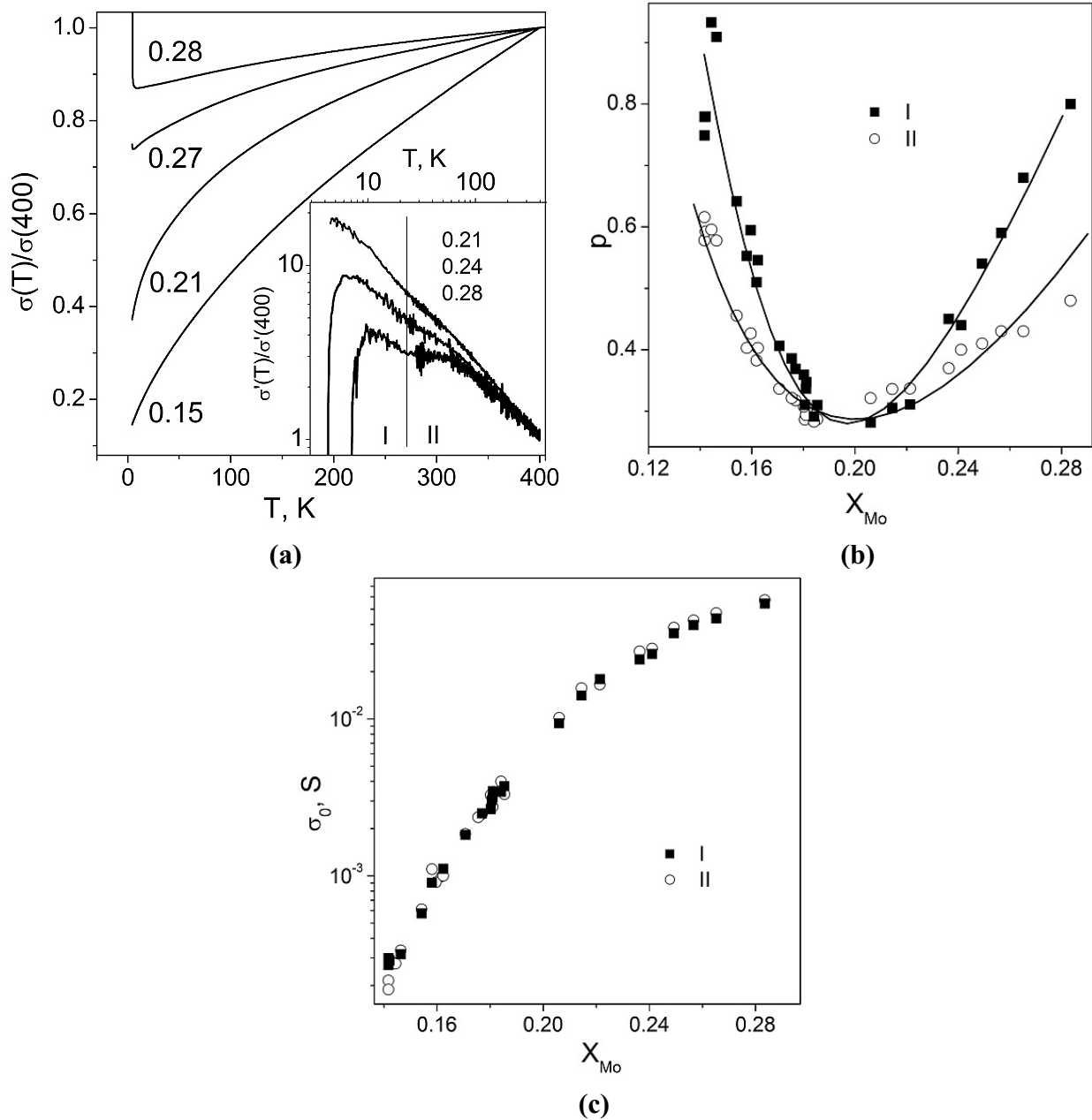


FIG. 1. (a) Normalized conductivity $\sigma(T)/\sigma(400)$ of Mo–C nanocomposite films vs. temperature, insert - normalized derivative $\sigma'(T)/\sigma'(400)$ vs. temperature; (b), (c) Mo concentration dependence of power exponent p (Eq. (1)) (b) and σ_0 (c) of $\sigma(T)$ dependences in temperature intervals I and II; Lines are guide to the eyes only (b). Explanations are given in text

It is generally accepted that the tunneling-percolation model is a good approximation for disordered granular materials [7]. Within this model the charge transfer occurs via tunneling of the electrons between the conducting grains. The temperature dependence of the conductivity of such granular media exists if between at least some conducting grains the temperature-dependent intergrain tunneling takes place.

The candidate for the role of the temperature-dependent tunneling may be the inelastic intergranular tunneling of the electrons proposed as a main charge transfer mechanism in thin films of amorphous dielectrics [8]. Following this model, the conductivity across the thin amorphous dielectric is formed in the tunnel channels via the chains of localized states. The conductivity of the single chain containing more than two localized states n depends on the temperature by the power way:

$$\langle \sigma \rangle_n \sim S e^2 \left(\frac{\Lambda^2}{\rho c^5} \right)^{\frac{n-1}{n+1}} g^n n^{2n} a^{2n-1} l^{n-1} E_0^{\frac{2n}{n+1}} T^{n-\frac{2}{n+1}} \exp \left(-\frac{2l}{a(n+1)} \right), \quad (4)$$

where l is a distance between electrodes, S – cross-section area of the sample, Λ – deformation potential constant, ρ – density of matrix material, c – velocity of the sound in the matrix, g – density of localized states at the Fermi level, a – radius of the localized state, and E_0 is the depth of localized states inside the barrier.

The total conductance of a sample is the sum of the conductance of all the channels. The model of the inelastic tunneling of the electrons gives a good basis for understanding the peculiarities of electron transport in disordered granular materials. In accordance with it, above the metal insulator transition point, the infinite conducting cluster, which consists of tunnel junctions with not more than one localized state in the intergrain potential barriers, exists. The temperature dependence of the conductivity of such a cluster is weak [8]. The parts of the infinite conducting cluster are shunted by the tunnel junctions with more than two localized states, giving the principal contribution to the temperature dependence of the conductivity. In Fig. 1(c), the concentration dependences of the term σ_0 in Eq. (1) in intervals I and II are presented. One can see that both dependences are nearly identical. This means that temperature dependence of the conductivity in both intervals is formed in the current paths shunting the same infinite conducting cluster.

In order to check the applicability of this model the $\sigma(T)$ dependences of the molybdenum-carbon nanocomposites were fitted in the framework of the effective medium approximation [9]. The best results for the fitting were achieved by the following assumptions: the Mo-C nanocomposite was considered as a three-component mixture of the conducting and insulating species; the conducting species represent the intergrain tunnel junctions whose conductivity σ_m does not depend on temperature; the dielectric domains stand for the intergrain tunnel junctions with two or three localized states. Their temperature-dependent conductivities were taken in the form $\sigma_{d1} = \sigma_{11}(T/T_0)^{2.5}$, and $\sigma_{d2} = \sigma_{12}(T/T_0)^{1.33}$ where the power exponents equal to 2.5 and 1.33 appear from the model [8] for the inelastic channels with $n = 3$ and 2, respectively (Eq. (4)). T_0 is the characteristic temperature introduced to retain the parameters σ_{11} and σ_{12} in the units of conductivity. For the simplicity, its value was chosen as 1 K. In the framework of the effective medium approximation, the conductivity of the nanocomposite σ_{eff} , the conductivities of metal σ_m , dielectric σ_{d1} and σ_{d2} species, metal phase fraction X_m , and dielectric phase fraction X_{d1} (3-localized states junction) are interrelated by equation [9]:

$$X_m \frac{3\sigma_{eff}}{2\sigma_{eff} + \sigma_m} + X_{d1} \frac{3\sigma_{eff}}{2\sigma_{eff} + \sigma_{d1}} + (1 - X_m - X_{d1}) \frac{3\sigma_{eff}}{2\sigma_{eff} + \sigma_{d2}} = 1. \quad (5)$$

The model allows one to trace the evolution of the molybdenum-carbon nanocomposites' properties with increasing Mo concentration. The results of the fitting of $\sigma(T)$ dependences for the temperature intervals I and II are summarized in Fig. 2 (a), (b), where the Mo concentration evolution of phase fractions X_m , X_{d1} , $X_{d2} = 1 - X_m - X_{d1}$, and conductivities σ_{11} , and σ_{12} are shown. It follows from the figure that metal fraction X_m monotonically increases while X_{d1} and X_{d2} decrease with an increase in Mo concentration (Fig. 2 (a)). The fractions either of 3-state

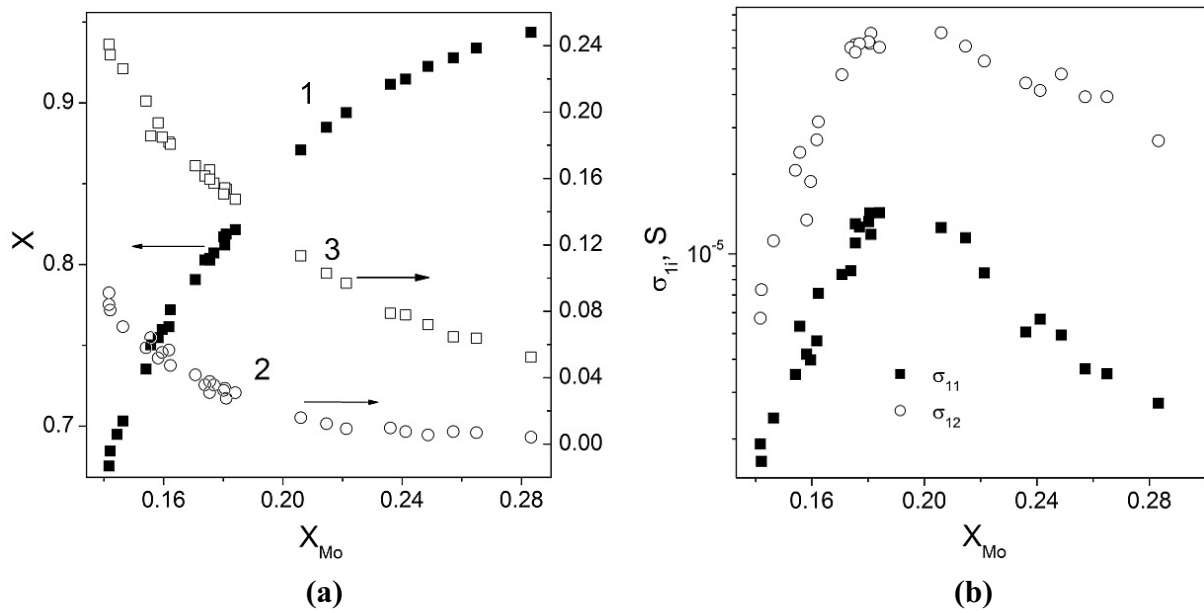


FIG. 2. Mo concentration dependences of: (a) X_m (1), X_{d1} (2), and X_{d2} (3) phase fractions; (b) conductivities σ_{11} and σ_{12} of dielectric species in both temperature intervals. Explanations are given in text

and 2-state barriers remain well below the percolation threshold (~ 0.25) at Mo concentration far from the metal-insulator transition point in the metallic state ($> \sim 0.15$). This means that the temperature-dependent conducting channels do not form the infinite conducting cluster. Thus the corrections to the conductivity of Mo–C nanocomposites are formed in the current paths consisting of the serially-connected elastic and inelastic junctions. The non-monotonic concentration behavior of σ_{11} and σ_{12} prefactors arises from the term $l^{n-1} \exp\{-2l/[a(n+1)]\}$ in Eq. (4) modulated by the possible variation of the parameters of intergranular dielectric space by metal concentration increase.

4. Conclusions

The conductivity of the Mo–C nanocomposites was studied at 4.2 – 400 K over the molybdenum concentration range of 0.14 – 0.3. The conductivity demonstrates the existence of the two distinct temperature intervals separated at temperature 20 – 25 K. Within each temperature interval, the conductivity has a power character with a power exponent non-monotonically dependent on Mo content. It was shown that the model of inelastic tunneling of the electrons between conducting grains in the framework of effective medium approximation can give an adequate description of the electron transport in molybdenum-carbon nanocomposites over the entire metal concentration and temperature ranges.

References

- [1] Beloborodov I.S., Lopatin A.V., Vinokur V.M., Efetov K.B. Granular electronic systems. *Rev. Mod. Phys.*, 2007, **79**, P. 469–518.
- [2] Nalwa H.S. (Ed.). *Handbook of Surfaces and Interfaces of Materials*, Academic Press, San Diego, 2001, Vol. 1, P. 447–508.
- [3] Bozhko A., Ivanov A., Berettoni M. Chudinov S., Stizza S., Dorfman V., Pypkin B. Electroconductivity of amorphous-carbon films containing silicon and tungsten. *Diamond Relat. Mater.*, 1995, **4**, P. 488–491.

- [4] Bozhko A., Takagi T., Takeno T., Shupegin M. Electron transport in W-containing amorphous carbon-silicon diamond-like nanocomposites. *J. Phys.: Condens. Matter*, 2004, **16**, P. 8447–8458.
- [5] Efetov K.B., Tschersich A. Coulomb effects in granular materials at not very low temperatures. *Phys. Rev. B*, 2003, **67**, P. 174205-14.
- [6] Beloborodov I.S., Lopatin A. V., Vinokur V. M. Universal description of granular metals at low temperatures: Granular Fermi liquid. *Phys. Rev. B*, 2004, **70**, P. 205120-5.
- [7] Ambrosetti G., Balberg I., Grimaldi C. Percolation-to-hopping crossover in conductor-insulator composites. *Phys. Rev. B*, 2010, **82**, P. 134201-7.
- [8] Glazman L.I., Matveev K.A. Inelastic tunneling across thin amorphous films. *JETP*, 1988, **67**, P. 1276–1282.
- [9] Vinogradov A.P. *The Electrodynamics of Composite Materials* (in Russian). Editorial URSS, Moscow, 2001, 208 p.

An improved adsorption method for the characterization of water-based supercapacitor electrodes

A. A. Maltsev¹, S. B. Bibikov¹, V. N. Kalinichenko²

¹N. M. Emanuel Institute of Biochemical Physics of RAS, Moscow, Russia

²Semenov Institute of Chemical Physics of RAS, Moscow, Russia

alex.a.maltsev@gmail.com, sbb.12@yandex.ru, kalinval47@yandex.ru

PACS 82.47.Uv, 82.65.+r

DOI 10.17586/2220-8054-2016-7-1-175-179

The specific surface area is a key characteristic of carbon materials used in supercapacitor electrodes. In this paper, the use of a methylene blue technique for specific surface area determination is presented. Values for the specific surface area, determined by a new method, provide better correlation with theoretical values for the specific electrical capacity of highly-porous carbon electrodes than the values measured by the common BET method. Additionally, the methylene blue adsorption method is thought to characterize carbon adsorption activity in relation to a supercapacitor electrolyte.

Keywords: Supercapacitors, specific surface area, methylene blue, aqueous electrolyte.

Received: 20 November 2015

1. Introduction

Supercapacitors, also called ionistors, or electric double layer capacitors (EDLC), are electrochemical energy storage devices. Their application area is rapidly expanding because of their unique power and energy storage properties. A common supercapacitor device contains a pair of highly-porous carbon electrodes immersed in an electrolyte solution and divided by a dielectric membrane. The commonly used electrolyte solutions are aqueous solutions of salts [1], acids [2] and alkalis [3]. Ionic liquids (either neat or dissolved in polar organic solvents) are considered to have promising electrolyte properties [4]. This electrode-electrolyte system forms an electric double layer (EDL) at the interface between conductive electrode and electrolyte. The electric capacitance of the EDL is defined by formula:

$$C = S \frac{\varepsilon \cdot \varepsilon_0}{d}, \quad (1)$$

where C is the specific electrical capacitance, S is the specific surface area, ε is the permittivity, ε_0 is the vacuum permittivity and d is the thickness of adsorption layer. Therefore, it is theoretically possible to reach significant values for the EDL capacitance using a material with larger specific surface area. However, often the real EDL specific capacitance does not correspond to a specific capacitance of the “isolated” electric double layer. This is why we tried to improve the method of measuring of the specific surface area to reach an acceptable correlation between this data and the actual EDLC capacitance.

2. Structure and properties of the used carbon materials

The carbon materials investigated in the work are the highly-porous microstructured forms derived from pyrolyzed rice straw. After the pyrolysis the product was etched in alkali solution to remove residual of SiO₂. All of these materials were prepared and partially characterized in Boreskov Institute of Catalysis, Siberian Branch, Russian Academy of Sciences, Novosibirsk. These materials have different microstructure because of different processing conditions. The main parameters of the materials are given in Table 1, and the micrographs (obtained by SEM method) of some materials are given in Figs. 1 – 3.

TABLE 1. The main parameters of investigated carbon materials

Material (unique name)	BET surface area, m ² /g	Average pore diameter, nm
ME544	544	4.7
ME900	906	3.1
ME991	991	3.0
ME1100	1100	3.0
MI2232	2232	2.2

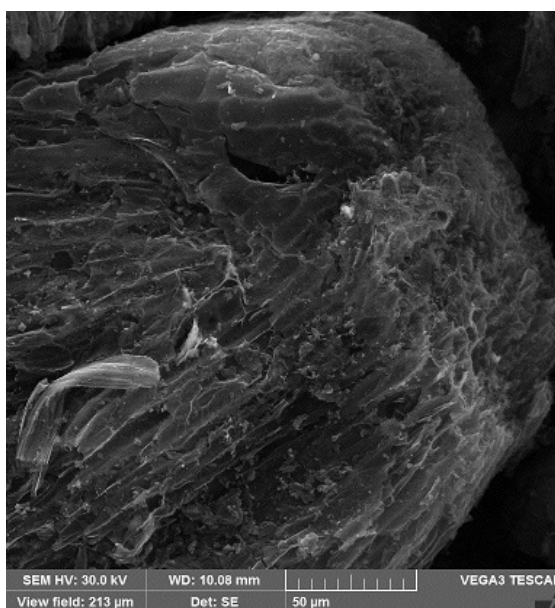


FIG. 1. SEM micrograph of ME991, scale 50 μm

Micrographs of the materials show a highly-porous structure with different pore depths and geometries. These factors, such as the average pore diameter, strongly affect the adsorptive properties of the material.

3. The method of methylene blue adsorption

The conventional method for specific surface area (SSA) measurement is the BET method, named after first letters of its inventors [5]. This method is based on a liquid nitrogen adsorption at a temperature below its boiling point [6]. However, the obtained value for SSA is strongly affected by the capillary condensation, which sometimes gives very large values

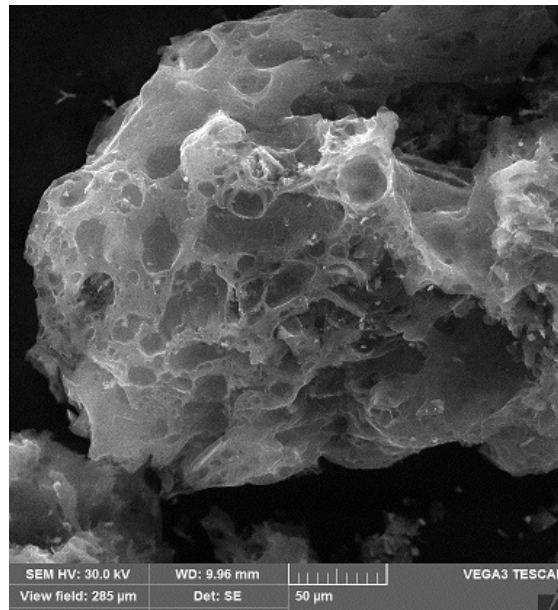


FIG. 2. SEM micrograph of ME2232, scale 50 μm

of SSA. As a result, the material MI3200 (the same type as material MI2232) has shown SSA values near 3200 m^2/g , ranging down to 2600 m^2/g , the highest theoretical value of SSA calculated for single-layer graphene [7]. However, the nitrogen molecule is non-polar, whereas all the electrolyte and solvent molecules used in supercapacitors are all polar in nature. Assuming that the polarity of the adsorbed molecules influences the amount of the material adsorbed, we decided to utilize another method for determining the specific surface area [8]. This method, which is based on the adsorption of methylene blue dye from 0.2 % aqueous solution, is called here the “MetB” method.

To define the SSA by “MetB” method, a minute amount (1 – 10 mg, depending on powder fineness) of the investigated carbon material was added to 5 ml distilled water and 1 drop (approx. 20 mg) 3 M H_2SO_4 solution in a 10 ml flask which was then sealed hermetically. Then, that flask was sonicated in ultrasound bath for 10 minutes to prevent particle agglomeration. Next, an aqueous methylene blue solution was injected into the flask slowly (approx. 0.05 g every 30 min) by a previously weighed syringe. When the suspension’s color change (blue) stopped for 15 min, the syringe was removed and reweighed. The specific surface area (SSA) is defined by the formula:

$$S = \frac{V \cdot C \cdot N \cdot A_m}{m \cdot M}, \quad (2)$$

where V is solution volume (ml), C is concentration of methylene blue (g/ml), N is Avogadro’s constant ($6.023 \cdot 10^{-23} \text{ mol}^{-1}$), A_m is the size of methylene blue adsorption site $1.06 \cdot 10^{-18} \text{ m}^2$, m is mass of carbon material, M is molecular mass of methylene blue (319.9 g/mol). Therefore, when using solution with 0.2 % concentration, the SSA can be calculated with formula:

$$S \left[\frac{\text{m}^2}{\text{g}} \right] = 4.0 \left[\frac{\text{m}^2}{\text{g}} \right] \cdot \frac{M}{m}, \quad (3)$$

where M is mass of methylene blue solution (g), m is mass of carbon material (g).

4. Preparation of the electrodes and specific capacitance measuring

To define the specific capacitance of supercapacitor electrode materials, we used a cyclic voltammetry technique which allowed us to determine the capacitance for our experimental supercapacitor electrodes. A sample supercapacitor consists of two electrodes (placed on stainless steel gauze) separated by a paper membrane and immersed in an electrolyte solution. We used 0.5 M Na_2SO_4 aqueous solution with an additional 2 wt.% ethyl alcohol as surfactant (this was necessary because of the investigated carbon materials' hydrophobicity). To make the electrode, an amount of investigating carbon material (50 mg) was mixed with 0.25 ml 1 % water suspension of PTFE as binder and transferred onto metal gauze. After that, the electrodes were dried for 1 h on an open hot plate at 95 °C to prevent water boiling, and subsequently, the electrodes were formed under 30 MPa pressure. A pair of electrodes made from the same material was assembled in supercapacitor and sealed in polyethylene to prevent electrolyte evaporation and leakage. The capacitance of these model supercapacitors was measured by a cyclic voltammetry method at 5 – 50 mV/s scan rates at 0 – 500 mV voltage window. As an example, the voltammetric curve for ME991 material is shown in Fig. 3.

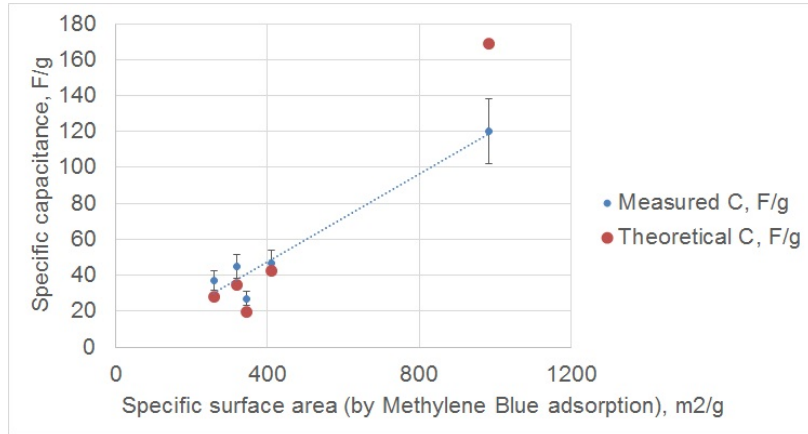


FIG. 3. Comparison of real (blue points) and theoretical (red points) capacitance values of surface area of high-porous carbon materials

To translate the capacitance of supercapacitor into the specific capacitance of the material, one can use a formula:

$$C_s = 2 \cdot \frac{C_{meas}}{m}, \quad (4)$$

where C_s is specific capacitance of material, C_{meas} is measured capacitance of model supercapacitor, and m is full mass of the both carbon electrodes.

To calculate the theoretical value for the specific capacitance of a material, one can use a cylindrical pore model, described in [9]. In this model, the authors used the geometric characteristics of the pore, such as characteristics of the cylindrical capacitor with the solvated ion's diameter as the inner diameter and the average pore diameter as the outer diameter for this cylindrical capacitor:

$$C = S \cdot \frac{\varepsilon \cdot \varepsilon_0}{b \cdot \ln\left(\frac{b}{a_0}\right)}, \quad (5)$$

where ε is permittivity of solvent, ε_0 is vacuum permittivity, b is average pore diameter, a_0 is solvated ion's diameter (0.339 nm for sodium ion), S is full surface area of electrode.

The results for the SSA measured by our “MetB” method corresponded to the measured and calculated specific capacitance of our materials, which are shown in Table 2.

TABLE 2. The measured and calculated parameters of investigated carbon materials

Material	BET surface area, m ² /g	“MetB” surface area, m ² /g	Measured specific capacitance, F/g	Theoretical specific capacitance, F/g
ME544	544	345	27	20
ME906	906	411	47	42
ME991	991	320	45	35
ME1100	1100	259	37	28
ME2232	2232	983	120	169

5. Conclusion

The measured and calculated capacitance of carbon materials with 1000 m²/g (BET) and 300 – 400 m²/g (MetB) specific surface area correlate well. However, highly-porous materials show a worse correlation between these values. We postulate that this divergence is connected either with some kinetic characteristics of the electrochemical system – low diffusion speed in pores, or with inactivation of the surface by a binder or pressure processing.

Though a BET method is fairly convenient, it is not fully appropriate for measuring the specific surface area of highly-porous carbon materials, especially those materials appropriate for supercapacitor electrodes. The method based on methylene blue adsorption yields results that are in better agreement with other experimental data.

References

- [1] Shao J., Li X., Qu Q., Wu Y. Study on different power and cycling performance of crystalline K_xMnO₂·nH₂O as cathode material for supercapacitors in Li₂SO₄, Na₂SO₄, and K₂SO₄ aqueous electrolytes. *J. Power Sources*, 2013, **223**, P. 56–61.
- [2] Chen W., Xia C., Alshareef H.N. Graphene based integrated tandem supercapacitors fabricated directly on separators. *Nano Energy*, 2015, **15**, P. 1–8.
- [3] Wu X., Jiang L., Long C., Fann Z. From flour to honeycomb-like carbon foam: Carbon makes room for high energy density supercapacitors. *Nano Energy*, 2015, **13**, P. 527–536.
- [4] Tsai W.-Y., Lin R., Murali S., Zhang L.L., McDonough J.K., Ruoff R.S., Taberna P.-L., Gogotsi Y., Simon P. Outstanding performance of activated graphene based supercapacitors in ionic liquid electrolyte from –50 to 80°C. *Nano Energy*, 2013, **2**, P. 403–411.
- [5] Fagerlund G. Determination of specific surface by the BET method. *Matériaux et Construction*, 1973, **6**(3), P. 239–245.
- [6] Trunschke A. Surface Area and Pore Size Determination; Modern Methods in Heterogeneous Catalysis Research; 19/10/2007, URL: http://www.fhi-berlin.mpg.de/acnew/departement/pages/teaching/pages/teaching_wintersemester_2007_2008.html
- [7] Hengxing Ji H., Xin Zhaow X., Zhenhua Qiao Z., Jeil Jung J., Yanwu Zhu Y., Yalin Lu Y., Zhang L.L., MacDonald A.H., Ruoff R.S. Capacitance of carbon-based electrical double-layer capacitors. *Nature Commun.*, 2014, **5**, Article number: 3317, DOI: 10.1038/ncomms4317.
- [8] GOST 1. 13144-79. Graphite. Methods for the determination of specific surface. URL: <http://gostexpert.ru/gost/gost-13144-79>.
- [9] Huang J., Sumpter B.G., Meunier V. A Universal Model for Nanoporous Carbon Supercapacitors Applicable to Diverse Pore Regimes, Carbon Materials, and Electrolytes. *Chemistry - A European Journal*, 2008, **14**(22), P. 6614–6626.

Diagnostic methods for silica-reinforced carbon nanotube-based nanocomposites

M. K. Eseev¹, A. A. Goshev¹, P. Horodek^{2,3}, S. N. Kapustin¹, A. G. Kobets^{2,4}, C. S. Osokin¹

¹Northern Arctic Federal University, Arkhangelsk, Russia

²Joint Institute for Nuclear Research, Dubna, Moscow region, Russia

³Institute of Nuclear Physics Polish Academy of Sciences, Krakow, Poland

⁴Institute of Electrophysics and Radiation Technologies NAS of Ukraine, Kharkov, Ukraine

m.eseev@narfu.ru

PACS 62.23.St; 73.63.-b; 61.48.De

DOI 10.17586/2220-8054-2016-7-1-180-184

This paper presents results of the experimental studies of the properties of silica-based nanocomposites with filler in the form of carbon nanotubes by dielectric relaxation and positron annihilation spectroscopy. Based on these results, techniques for diagnosis and control of the investigated materials were proposed.

Keywords: carbon nanotube, nanocomposites, dielectric properties, positron annihilation spectroscopy.

Received: 20 November 2015

1. Introduction

Active research of composite materials, which include nanostructures such as carbon nanotubes (CNTs) as filler, is being conducted globally. Due to the large surface area of CNT, as well as significant differences in the physical properties between nanoobjects and macroscopic material, the properties of nanocomposites are not additive characteristics of each phase and can be radically different from those of each component's [1]. The data on the study of the electrical and other properties of nanocomposites with CNT is provided in these reviews [2,3]. A particularly urgent task is to study the strongly nonlinear dependence of the composite properties on the filler concentration, which is necessary for the selection of the optimum functional properties for the materials (strength, thermal, dielectric and other characteristics). Data on the influence of impurities on the dielectric properties of CNTs of different composites at microwave frequencies, associated with the search for promising materials for “stealth”-technologies, have been presented in the literature [4]. This paper [5,6] investigates the microwave characteristics of nanocomposite materials via controlled modification of the CNTs. We were also interested how the positrons will annihilate in materials reinforced with CNTs.

2. The electrical properties of nanocomposite

Our composite is based on SiO₂. It is reinforced with multi-walled CNTs at different concentrations – 0 %, 0.05 %, 0.1 %, 0.5 % (by weight of silica + water), with an aspect ratio of 10 – 10² (see Fig. 1), obtained by CVD-method.

Silicon was obtained from silicate glue. The chemical reaction is shown below.



Electrical characteristics of the samples were studied by dielectric relaxation spectroscopy, according to which, the sample is placed between the plates of the capacitor (area of $S = 16 \text{ cm}^2$ and the distance between the plates $d = 3.3 \text{ mm}$). The sample was then exposed to an alternating

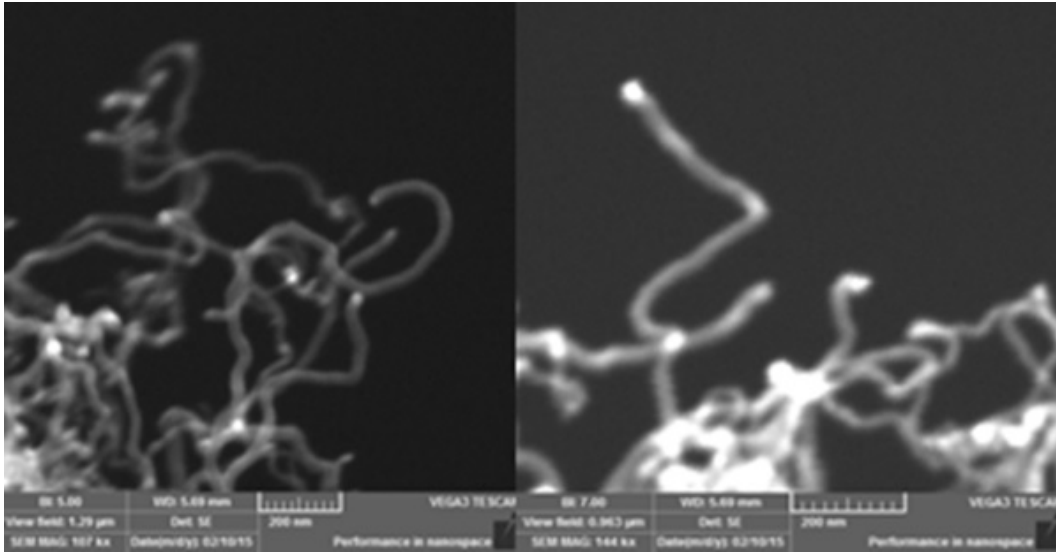


FIG. 1. SEM images of CNTs

electric field with a frequency varying from 25 Hz – 1 MHz. The measured values were: electrical capacitance C , the quality factor Q , and the resistance R . The electrical properties of the composites in electric fields were measured using an immittance meter E7-20.

The microwave properties of the composite are described by the frequency of electrical field f dependence of the complex permittivity and conductivity:

$$\varepsilon = \varepsilon' - i\varepsilon'', \quad \varepsilon'(f) = \frac{(C(f) - C_0)d}{\varepsilon_0 S}, \quad \varepsilon''(f) = \frac{d}{\varepsilon_0 S} \left(\frac{C(f)}{Q(f)} - \frac{C_0}{Q_0} \right), \quad (1)$$

$$\sigma(f) = 2\pi f \varepsilon''(f) \varepsilon_0, \quad (2)$$

where the real and imaginary parts characterize the dielectric polarization and losses in the composite respectively; C , C_0 – capacitance of the cell with the composite and empty cell respectively and Q , Q_0 – quality factor of the filled and empty cells.

According to the table, it can be argued, that there is an optimum concentration at which maximum absorption and scattering of electromagnetic waves at low frequencies occurs. It is known that a change in the CNTs concentration leads to a nonlinear modification of the nanomaterial's functional properties. This dependence is noted for the mechanical properties in [7]. The dependence of the silicon dioxide powder's electrical properties (1), (2) on the concentration of CNTs at different frequencies is shown in Table 1.

TABLE 1. The dependence of electrical properties upon different frequencies

Composition, CNT, n %		REF, 0	0.01	0.05	0.1	0.5
$f = 50$ Hz	$\varepsilon', 10^4$	59.4	53.6	326.3	41.9	8.8
	$\varepsilon'', 10^4$	283	31.5	2331	72.3	8
	$\sigma, 10^{-3}$ Sm/m	7.87	0.88	64.81	2.01	0.22
$f = 500$ Hz	$\varepsilon', 10^4$	0.95	18.4	22.8	13.3	2.3
	$\varepsilon'', 10^4$	23.8	13	243	12.3	2.4
	$\sigma, 10^{-3}$ Sm/m	8.66	3.6	71.2	3.4	0.7

Based on the data (see Table 1) it can be concluded that there is a sharp increase in the absorption properties of the sample at a concentration ~ 0.05 % at lower frequencies. There is also strongly marked maximum in dispersion of electromagnetic waves for all concentrations over a range of ~ 10 kHz. The behavior of ϵ' is associated with a decrease in the electromagnetic field change rate in comparison to the typical recharge time (relaxation time) of effective capacitor consisting of adjacent conductive particles. At higher frequencies, the capacitor does not have time to recharge, and the dielectric permittivity value tends to approach the same composite permittivity value with zero concentration of CNTs.

The dependence of the imaginary parts of permittivity and conductivity on the frequency also shows a clear concentrational nonlinearity. At $n = 0.5$ %, the transition into a zone of agglomerate conductivity occurs where there is deterioration in the conductivity of the sample. With an increase in the electromagnetic field frequency, the conductivity is caused by the bias current and increases for all samples. This nonlinear dependence suggests a restructuring of a complex fine powder $\text{SiO}_2 + \text{multiwalled CNTs} + \text{H}_2\text{O}$ (free and bound) system. Structures are formed (agglomerates) at higher concentrations. The samples dielectric properties support this hypothesis. Their surface areas are less than the total surface area of their components. The reason for the formation of these structures is the large difference between silicon and CNTs surface energies.

Next, we sintered silica powder with CNT in an oven at high temperatures. The conductivity of samples was estimated by the resistance measurement of calibration samples with a cable tester. It is known [1,2], that CNTs themselves could often be quite good conductors.

We determined the concentration dependence of the conductivity σ . The results of these measurements are shown in Table 2.

TABLE 2. The dependence of conductivity upon CNT concentration (%) in a nanocomposite with a SiO_2 matrix

n, %	REF, 0	0.05	0.5	1	3	5
$\sigma, 10^{-3} \cdot \text{Sm/m}$	$< 10^{-6}$	$< 10^{-6}$	$< 10^{-6}$	10	30	30

Based on data acquired, a conclusion about percolation character of direct current conductivity in the obtained samples can be made. Up to a concentration of 0.1 %, there was no direct contact opening the conductivity channel. The conductivity significantly increased at concentrations above 0.1 % . REF is a ceramic sample without CNT. It's worth noting that the percolation threshold is clearly expressed only for direct current conductivity. Previously made alternating current measurements [2], though pointing at a concentration dependence, had no percolation character. This is explained by the absence of necessity for direct contact between CNTs at alternating current conductivity. The tubes are recharging, like the plates of a capacitor separated by an insulator.

3. Positron Annihilation Spectroscopy studies

Positron annihilation spectroscopy (PAS) is a successive method usually recommended for the detection of open volumes in materials. In order to verify the PAS potential application in further studies of our nanocomposites, measurements of the Doppler Broadening of Annihilation Line (DB) were performed. A variable-energy positron beam (VEP), available at the LEPTA facility [8] of the Joint Institute for Nuclear Research in Dubna, was used in this experiment. This is a small linear accelerator (linac) which uses frozen Ne as the moderator of positrons emitted from a ^{22}Na isotope. Then, it allows them to accelerate to the desired energies

ranging from 50 eV to 30 keV and implant them into the sample in the form of a beam. The controllability of positron energies makes it possible to implant the particles at a precise depth. DB measurements, consisting of registration of energetic spectrum of gamma quanta emitted in annihilation processes were done using HpGe detector with energy resolution of 1.2 keV at 511 keV. Analysis of obtained spectra results in extracting so called S parameter. This is defined as the ratio of area under the central part of 511 keV line to the total area below this line. S parameter represents a quantity related to the amount and size of free volume. More information about the method is presented e.g. here [9,10].

In Fig. 2, the S parameter dependence on energy for a reference sample without CNTs (circles) and a sample containing 1 % CNTs (squares) are presented. It should be noted that differences between these dependencies are easily visible. The S parameter values for the specimen containing CNTs are much lower. A similar trend was observed by Chen et. al. [11]. In this case, the decreasing S parameter was explained as the presence of additional carbon nanofiber particles which have no free volume. Further studies in this area are recommended.

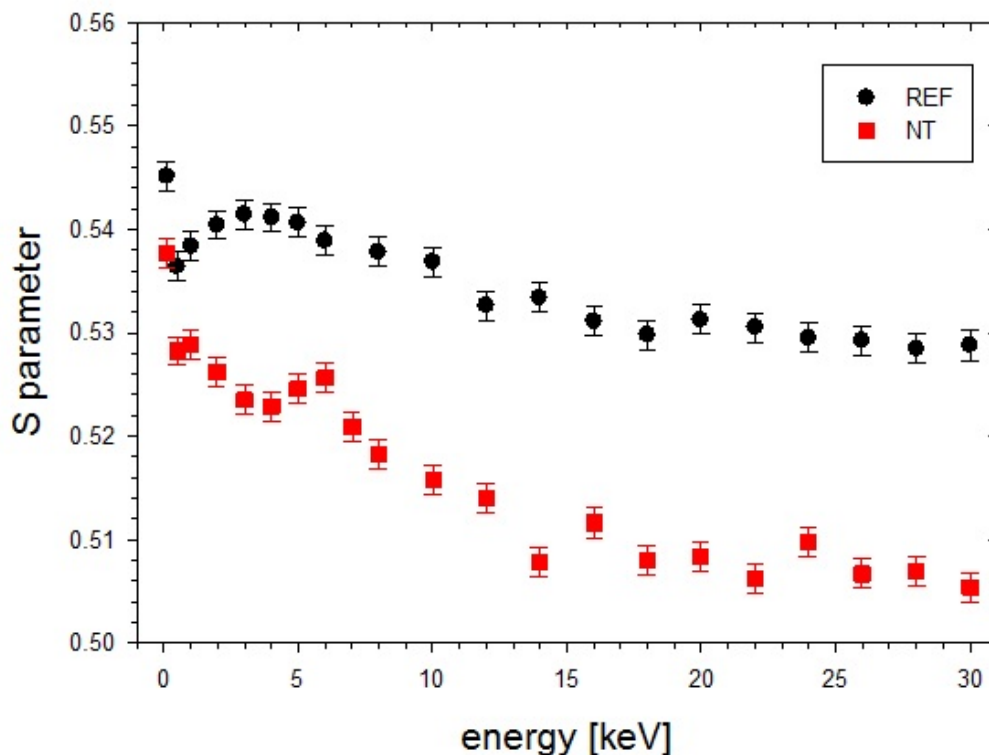


FIG. 2. The dependence of S -parameter of annihilation on positron energy for ceramic samples with CNTs concentration 1 % – ■. REF – sample without CNTs – ●. DALB spectra

4. Conclusions

All the given studies show that a nanocomposites properties are dependent upon the concentration (mass percentage) of CNTs. Although, during the investigation of the direct current conductivity, there was a percolation threshold located between 0.5 and 1 %. Other methods allowed the distinguishing of samples with lower CNTs concentrations.

Acknowledgements

This work was supported by the project of the Ministry of Education of the Russian Federation No. 3635 “Investigation of the nanocomposites properties with controlled modification of the structure reinforced with carbon nanotubes”.

References

- [1] Eletsii A.V. Carbon nanotubes. *Physiks Uspekhi*, 1997, **40**(9), P. 899–924.
- [2] Eletsii A.V., Knizhnik A.A., Potapkin B.V., Kenny J.M. Electrical characteristics of carbon nanotube doped composites. *Physiks Uspekhi*, 2015, **58**(3), P. 209–251.
- [3] Rakov E.G. Carbon nanotubes in new materials. *Russian Chem. Rev.*, 2013, **82**(1), P. 27–47.
- [4] Muradyan V.E., Sokolov E.A., Babenko S.D., Moravsky A.P. Microwave dielectric properties of composites modified by carbon nanostructures. *Techn. Phys.*, 2010, **55**(2), P. 242–246.
- [5] Usanov D.A., Skripal' A.V., Romanov A.V. Complex permittivity of composites based on dielectric matrices with carbon nanotubes. *Techn. Phys.*, 2011, **56**(1), P. 102–106.
- [6] Usanov D.A., Skripal' A.V., Romanov A.V. Effect of annealing on the microwave characteristics of carbon nanotubes and the nanocomposite materials based on them. *Techn. Phys.*, 2014, **59**(6), P. 873–878.
- [7] Kablov E.N., Kondrashov S.V., Yurkov G.Yu. Prospects of using carbonaceous nanoparticles in binders for polymer composites. *Nanotechnologies in Russia*, 2013 **8**(3-4), P. 163–185.
- [8] Sidorin A.A., Meshkov I., Ahmanova E., Eseev M., Kobets A., Lkhmatov V., Pavlov V., Rudakov A., Yakovenko S. The LEPTA facility for fundamental studies of positronium physics and positron spectroscopy. *Mater. Sci. Forum*, 2013, **733**, P. 291–296.
- [9] Puska M.J., Nieminen R.M. Theory of positrons in solids and on solid surfaces. *Rev. Mod. Phys.*, 1994, **66**, P. 841–899.
- [10] Krause-Rehberg R., Leipner S.H. *Positron annihilation in semiconductors*. Springer, Berlin, 1998.
- [11] Chen H.M. Awad S., Jean Y.C., Yang J., James Lee L. Positron annihilation studies in polymer nanocomposites. *Application of Accelerators in Research and Industry*, 2011, **1336**, P. 444–447.

Aluminum foil reinforced by carbon nanotubes

A. V. Alekseev¹, M. R. Predtechenskiy²

¹International Science Centre of Thermal physics and Energetics, Novosibirsk, Russia

²Institute of Thermalphysics, Novosibirsk, Russia
artem.alekseev@ocsial.com, predtechensky.mr@ocsial.com

PACS 81.05.Ni, 81.20.Ev, 81.40.Ef

DOI 10.17586/2220-8054-2016-7-1-185-189

In our research, the method of manufacturing an Al-carbon nanotube (CNT) composite by hot pressing and cold rolling was attempted. The addition of one percent of multi-walled carbon nanotubes synthesized by OCSiAl provides a significant increase in the ultimate tensile strength of aluminum. The tensile strength of the obtained composite material is at the tensile strength level of medium-strength aluminum alloys.

Keywords: carbon nanotubes, aluminum, composite, hot pressing, cold rolling.

Received: 20 November 2015

1. Introduction

The addition of carbon nanotubes can significantly improve the mechanical properties of aluminum and its alloys [1-3]. At the present moment, powder metallurgy methods are mostly used to produce aluminum-based composites reinforced by carbon nanotubes (CNT). These methods include the manufacturing of a powder compact followed by its hot deformation [4]. Compacts are produced by spark plasma sintering [4], cold pressing followed by sintering [5], explosive compacting [6], hot isostatic pressing [7] and hot pressing [8]. The final operation of composite manufacturing is hot extrusion [4] or hot rolling [9]. There are articles in which the authors successfully combined powder compacting and hot extrusion, and thus realized the spark plasma extrusion method [10].

In this work, aluminum composite reinforced by CNT was produced via a hot pressing and final cold rolling operation.

2. Experimental procedure

For powder mixtures, aluminum powder (preparation standard PA-1) (GOST6058-73) and multiwalled carbon nanotubes (MWCNT) manufactured by OCSiAl (see Fig. 1) were used. Powder mixtures containing 1 wt.% CNT were made by high energy milling in planetary ball mill AGO-2S. Thereafter, powder mixtures were compacted by hot pressing at 50 MPa at a temperature of 600 – 670 °C under argon. During cold rolling, 10 % deformation for each pass was produced. Approximately 10 – 15 passes were made to obtain each sample of foil. Part of the foil samples were then annealed at 350 °C for 120 min.

For comparison, we made aluminum foil with additions of 1 wt.% of carbon powder VulkanXC72 and foil without any additives. These foil samples were made in the same way as those with CNT additives. Analysis of composite structure was conducted by scanning electron microscope LEO1430-VP. A Bruker d8 Advance diffractometer with parallel geometry and $\text{CuK}_{\alpha 1} = 1.5406 \text{ \AA}$; $\text{Cu K}_{\alpha 2} = 1.54439 \text{ \AA}$ radiation was used for carbide detection.

Foil samples with 100 μm thickness were cut to obtain samples for tensile strength determinations. Tensile tests were conducted at room temperature by a servo- hydraulic testing machine RPM-50U.

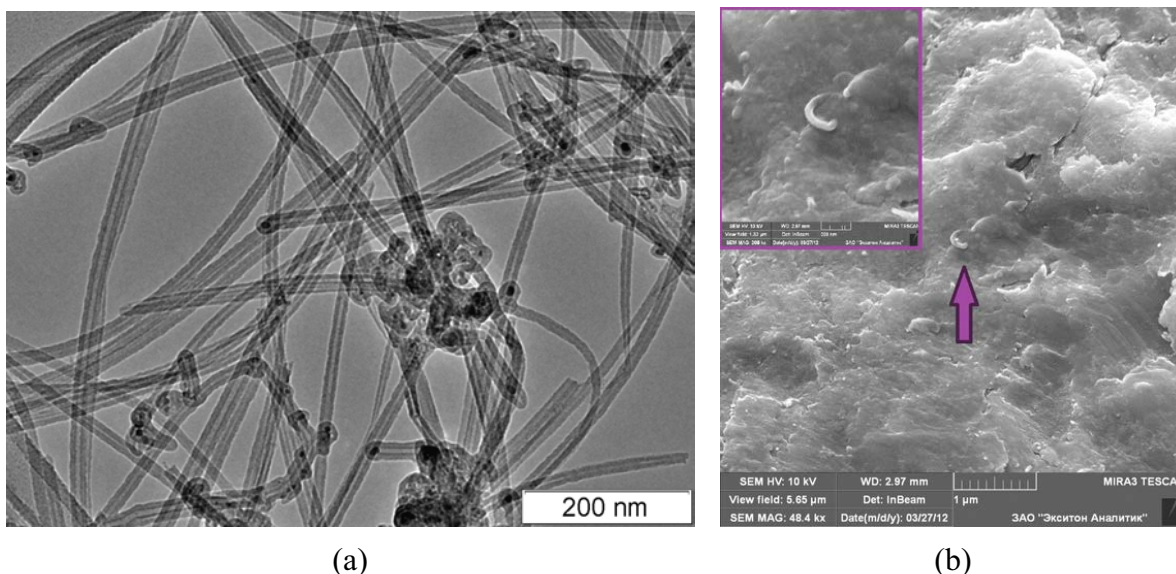


FIG. 1. TEM photographs of MWCNT

3. Results and discussion

SEM photographs of powder mixtures are shown in Fig. 2. The powder mixture containing CNT consisted of mostly spherically-shaped particles. The diameter of powder particles is typically $250 - 270 \mu\text{m}$ and rarely exceeds $900 \mu\text{m}$. Detailed analysis of powder surface by high resolution SEM did not reveal CNT agglomerates but showed separated CNT embedded in the metal particles' surfaces.

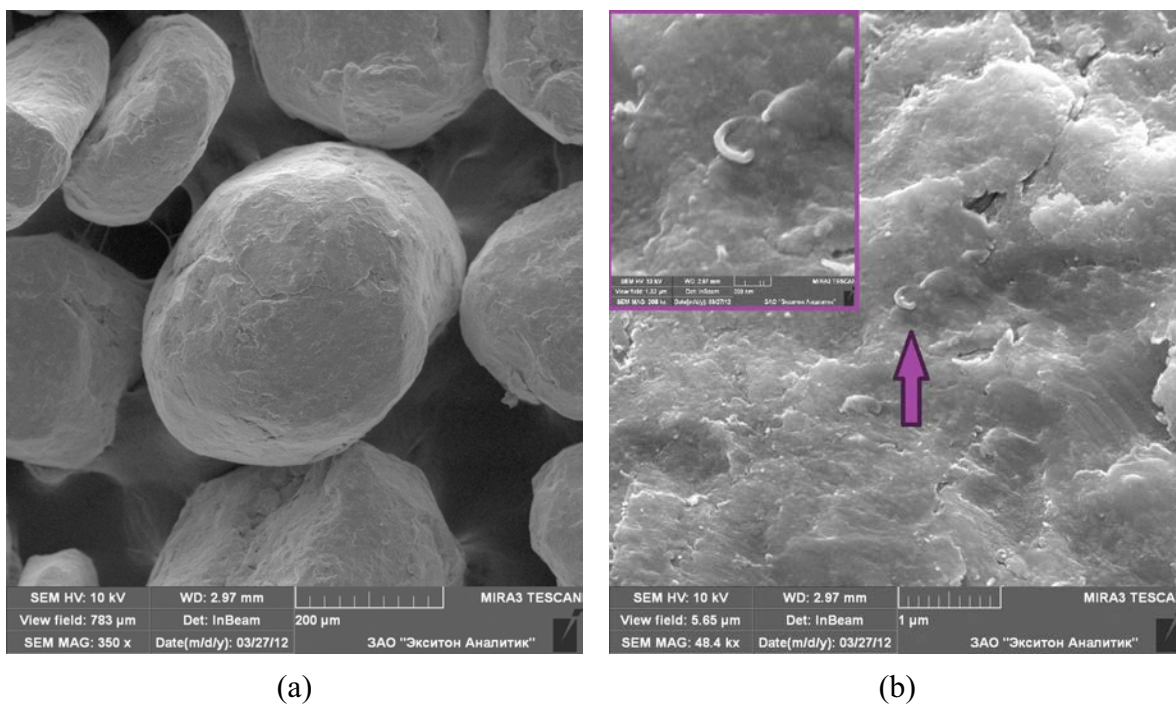


FIG. 2. SEM photographs of powder mixtures containing 1 wt.% CNT

X-ray diffraction spectra of powder mixture containing CNT, and aluminum foil containing CNT are presented in Fig. 3. It is well known that the presence of a large amount of

aluminum carbides decreases the mechanical properties of an aluminum-CNT composite [12]. Consequently, it is preferable to minimize aluminum carbide formation during the composite manufacturing process in order to produce materials with improved mechanical properties.

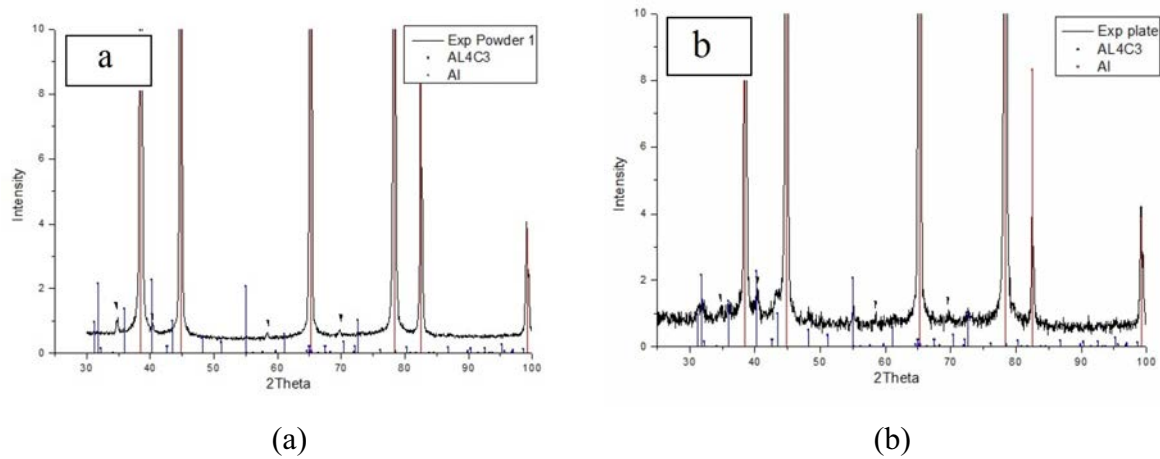


FIG. 3. XRD spectra of powder mixture containing 1 wt.% CNT (a) and composite foil Al – 1 wt.% CNT (b)

Conversely, the existence of a minute amount of aluminum carbide, in the form of nano-sized particles positioned on the CNT-aluminum interfaces can increase the adhesion between CNT and metal matrix [1, 2, 13]. Since aluminum carbide can appear not only during high energy powder mixing [11] but also during the hot pressing of powder mixtures, it is necessary to control its quantity at each step of the composite manufacturing process. As shown in Fig. 3, no aluminum carbide is present in the aluminum-CNT powder mixtures. Only trace amounts of aluminum carbide was shown to be present in our composite foil.

SEM photographs of fracture surfaces from hot pressed powder compacts are shown in Fig. 4. Structures of both compacts are homogeneous. One can see that the length of protruded CNT is not more than 1/10 of the initial CNT length. This indicates good adhesion between the CNT and the metal [13-16].

Table 1 contains the results of the tensile strength test for cold rolled aluminum foils. The tensile strength increase for composite foil can be caused not only by CNT addition, but also by amorphous carbon powder formation during CNT collisions in a high energy ball mill. In this sense, it is more correct to compare composite foil and control samples reinforced by amorphous carbon powder. For this reason, we made two types of control samples. The first one contains amorphous carbon powder additives and the second one has no carbon additives.

TABLE 1. Tensile test results

Sample number	Powder mixture type	Tensile strength, MPa
1	Al + 1 % CNT	441
2	Al + 1 % carbon powder	360
3	Al	357

From Table 1, it is clear that foil samples that contain powder of amorphous carbon have strength similar to that of control foil samples without any additives.

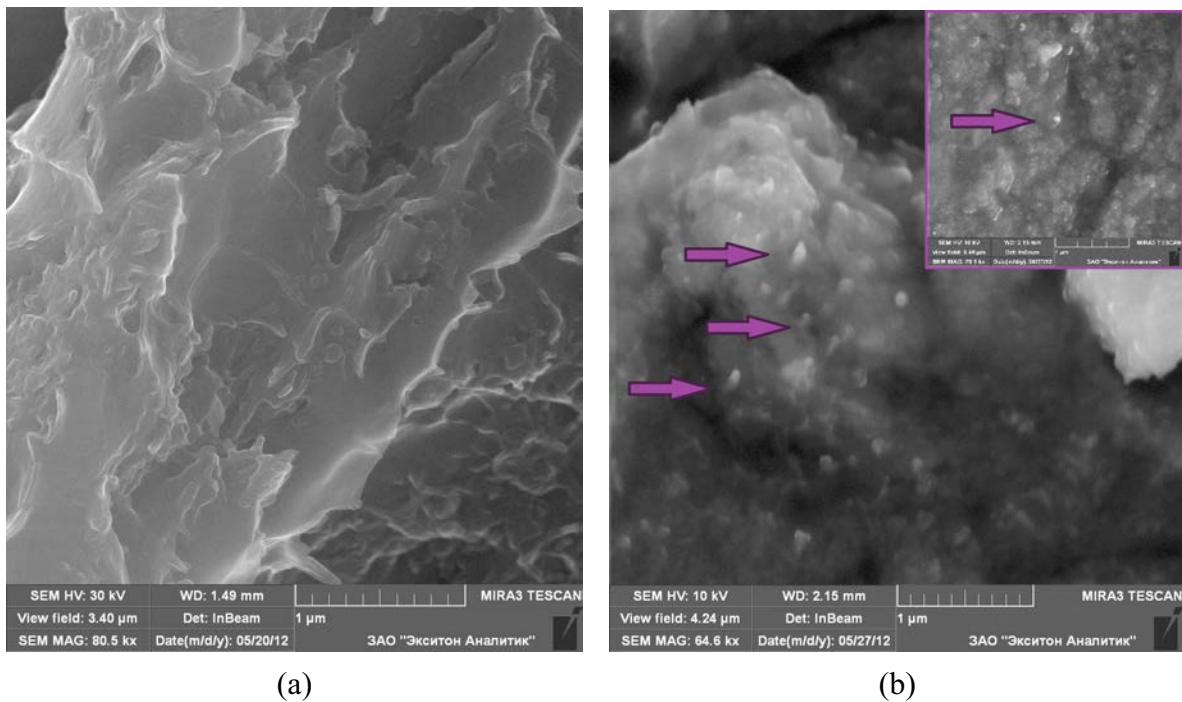


FIG. 4. SEM photographs of hot pressed powder compact with additives of carbon powder (a) and CNT (b)

The tensile strength of aluminum foil with 1 % wt. CNT added was increased by 22 % relative to pure aluminum foil. We can conclude that strength increase is caused only by influence of CNT. All of samples had low plasticity, which may be explained by the high degree of cold working.

Annealed samples of foil with 1 wt.% CNT also had high tensile strength. Comparative diagram of our composite foil and standard aluminum foil GOST618-73 are shown in Fig. 5. These data clearly show that our composite foil surpasses the standard aluminum foil strength by a factor of 3 under both annealed and cold worked conditions.

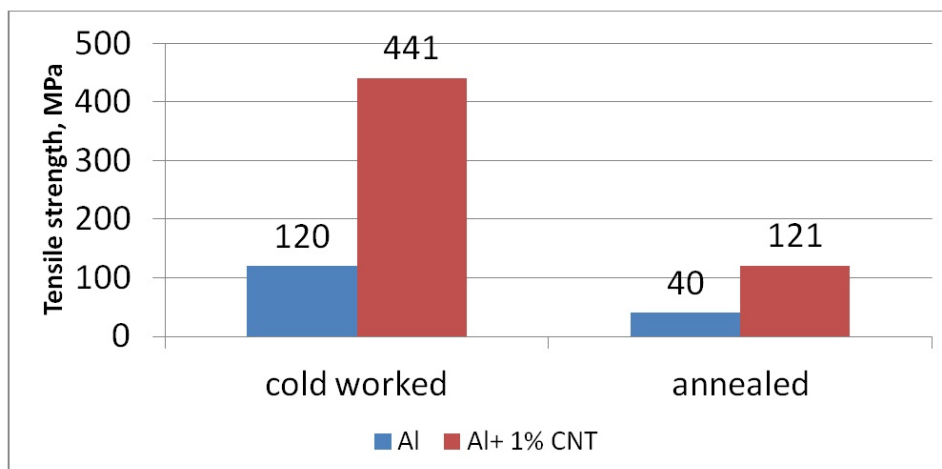


FIG. 5. Comparative diagram of composite foil tensile strength and standard foil tensile strength

4. Conclusion

Composite foil reinforced by CNT was made by hot pressing and subsequent cold rolling. The addition of 1 wt.% of MWCNT manufactured by OCSiAl provided an increase in the tensile strength of aluminum foil by 22 %. Our composite has a tensile strength comparable to that of medium strength aluminum alloys and is 3-fold greater than standard aluminum foil.

References

- [1] Kwon H., Park D.H., Silvain J.F., Kawasaki A. Investigation of carbon nanotube reinforced aluminum matrix composite materials. *Composites Sci. Technol.*, 2010, **70**(3), P. 546–550.
- [2] Bakshi S.R., Agarwal A. An analysis of the factors affecting strengthening in carbon nanotube reinforced aluminum composites. *Carbon*, 2011, **49**(2), P. 533–544.
- [3] Choi H.J., Shin J.H., Bae D.H. Grain size effect on the strengthening behavior of aluminum-based composites containing multi-walled carbon nanotubes. *Composites Sci. Technol.*, 2011, **71**, P. 1699–1705.
- [4] Liao Jin-zhi, Tan Ming-Jen, Sridhar I. Spark plasma sintered multi-wall carbon nanotube reinforced aluminum matrix composites. *Materials & Design*, 2010, **31**(1), P. 96–100.
- [5] Singhal S.K., Pasricha R., Jangra M., Chahal R., Teotia S., Mathur R.B. Carbon nanotubes: Amino functionalization and its application in the fabrication of Al-matrix composites. *Powder Technol.*, 2012, **215–216**, P. 254–263.
- [6] Salas W., Alba-baena N.G., Murr L.E. Explosive Shock-Wave consolidation of Aluminium powder. Carbon nanotube aggregate Mixtures: optical and electron Metallography. *Metallurg. Mater. Trans.*, 2007, **38A**(12), P. 2928–2931.
- [7] Deng C.F., Wang D.Z., Zhang X.X., Ma Y.X. Damping characteristics of carbon nanotube reinforced aluminum composite. *Mater. Lett.*, 2007, **61**(14–15), P. 3229–3231.
- [8] Jafari M., Abbasi M.H., Enayati M.H., Karimzadeh F. Mechanical properties of nanostructured Al2024-MWCNT composite prepared by optimized mechanical milling and hot pressing methods. *Adv. Powder Technol.*, 2012, **23**(2), P. 205–210.
- [9] Esawi Amal M.K., Borady Mostafa A. El. Carbon nanotube-reinforced aluminium strips. *Composites Sci. Technol.*, 2008, **68**(2), P. 486–492.
- [10] Morsi K., Esawi K., Borah P., Lanka S., Sayed A., Tahe M. Properties of single and dual matrix aluminum-carbon nanotube composites processed via spark plasma extrusion (SPE). *Mater. Sci. Engin. A*, 2010, **527**(21–22), P. 5686–5690.
- [11] Kaminsky U.D. Practice and perspectives of implementation mechanoactivation processes in metallurgy. *Nauka-Proizvodstvu*, 2002, **2**, P. 27–34.
- [12] Yufeng Wu, Gap-Yong Kim. Carbon nanotube reinforced aluminum composite fabricated by semi-solid powder processing. *J. Mater. Process. Technol.* Available online 15 March 2011.
- [13] He C.N., Zhao N.Q., Shi C.S., Song S.Z. Mechanical properties and microstructures of carbon nanotube-reinforced Al matrix composite fabricated by in situ chemical vapor deposition. *J. Alloys Compounds*, 2009, **487**(1–2), P. 258–262.
- [14] Deng C.F., Wang D.Z., Zhang X.X., Li A.B. Processing and properties of carbon nanotubes reinforced aluminum composites. *Mater. Sci. Engin. A*, 2007, **444**, P. 138–145.
- [15] Esawi A.M.K., Morsi K., Sayed A., Abdel Gawad A., Borah P. Fabrication and properties of dispersed carbon nanotube-aluminum composites. *Mater. Sci. Engin. A*, 2009, **508**, P. 167–173.
- [16] Singhal S.K., Pasricha R., Teotia S., Kumar G., Mathur R.B. Fabrication and characterization of Al-matrix composites reinforced with amino-functionalized carbon nanotubes. *Composites Sci. Technol.*, 2011, **72**(1), P. 103–111.

The influence of carbon (fullerite, graphite) on mechanical alloying of Cu-25 at % C composites

R. M. Nikonova, V. I. Ladyanov, N. S. Larionova

Physicotechnical Institute, Ural Branch of Russian Academy of Sciences, Izhevsk, Russia

RozaMuz@ya.ru

PACS 61.48.-c, 61.72., 63.22. Kn, 68.35.-, 78.30.Na, 81.05.ub, 81.07.Bc, 82.80.Gk

DOI 10.17586/2220-8054-2016-7-1-190-197

A comparative study of Cu-C_{60/70} and Cu-C_g composites obtained by mechanical alloying has been performed by means of scanning electron microscopy, X-ray diffraction, and Raman spectroscopy. It has been demonstrated that high stress-related effects, which take place during the mechanochemical synthesis of Cu-C_{60/70} and Cu-C_g composites with a nanocrystalline structure, result in the formation of an oversaturated solid solution of carbon in copper, Cu(C). The morphology and the parameters of the crystal lattice $a_{Cu}(t_{MA})$ and the sizes of the crystallites $L(t_{MA})$ of the powders obtained depend on the deformational stability of fullerite and graphite and also on their reactivity to adsorbed oxygen.

Keywords: fullerite, graphite, copper, mechanically alloyed composites.

Received: 20 November 2015

1. Introduction

At present many of researchers' attention is devoted to investigations on the preparation of nanostructured materials for engineering and functional purposes and on the optimization of their physical and technological properties. An upcoming trend here is the synthesis of metal matrix composites modified by carbon nanomaterials (fullerenes, carbon nanotubes, etc.), which have unique physical and mechanical properties.

One of the most widely commercially applied metals is copper – manufacturers like it for its high electrical and thermal conductivity. However its low hardness, and low corrosion resistance limit its use in pure form. To improve its structural characteristics, researchers suggest considering the prospects of preparing of copper-carbon composites. Carbon can protect copper from oxidation and/or regenerate its already oxidized surface. Also, the problem of electrochemical copper erosion can be resolved.

Different carbon forms are used to prepare the Cu-C composites. In most cases, graphite can be utilized [1, 5-8]. Nanotubes [9-13], nanodiamonds [2,5], and fullerites [3, 14-16] are mentioned in the literature as possible carbon sources. Among the methods used for modification of copper with carbon are sintering [6, 13], the formation of film coatings by the joint deposition of Cu and carbon [15, 16], carbon deposition from gaseous phase via the catalytic decomposition of acetylene and ethylene with subsequent compacting and sintering [12], application of ultra-high strain [1], and shock-wave loading [14]. Also, a promising technique is mechanical milling in high-energy ball mills [2,3-5,7]. u-C specimens have higher hardness than that of carbon-free copper [8,12], which is attributed primarily to the stabilization of copper grain boundaries [8].

Since under equilibrium conditions carbon is practically insoluble in copper, mechanochemical synthesis (MS) is considered a promising method for the preparation of such composite materials – it provides the atomic-level mixing of components and thus increases solubility.

Since different forms of carbon have different physico-mechanical and -chemical properties, it is expected that mechanical alloying (MA) of composites with their addition will give different results. In this regard, it would be especially interesting to conduct comparative studies on the effect of allotropic forms of carbon on the formation of the structure of copper-based composites.

So far, comparative studies on the mechanical alloying of copper together with fullerites and graphite have not been performed. However, the authors in [3] assume that the synthesis of composites with fullerene particles in a copper matrix will give better results. The investigations of Fe-C, Al-C, Mg-C systems in papers [14-16] confirm that in contrast with graphite, fullerenes do exert a more significant strengthening effect both immediately after mechanical alloying [16] and after the following spark plasma sintering [14,15].

In this paper, we present the results for the comparative study of mechanically alloyed copper-fullerite and copper-graphite composites.

2. Materials and methods

Copper powders (99.5 %), graphite C_gACS (mechanically crushed rods), and fullerite C_{60/70} were taken as elemental powders for mechanical alloying. Copper powders had a dendrite structure formed by spherically-shaped particles $\sim 3 - 5 \mu\text{m}$ in size, with dendrite branches as long as $\sim 150 \mu\text{m}$ (Fig. 1, 0 h MA). Fullerite C_{60/70} and graphite particles were of a flat and layered ellipsoid shape, respectively, and had a size of $\sim 100 - 200 \mu\text{m}$. The composition of C_{60/70}, according to HPLC and thermal gravitational analysis, was as follows: 82.18 % C₆₀; 14.08 % C₇₀; 2.81 % C₆₀O, C₆₀O₂, and C₇₀O; 0.93 % C₇₆, C₇₈, C₈₂, C₈₄ %; 1.1 % of residual toluene.

For copper-fullerite and copper-graphite composites, the copper and carbon powders were mixed in the proportion Cu-25 at % C (hereafter referred to as Cu-C_{60/70} and Cu-C_g, respectively) with the total weight of 30 g. The samples were mechanically alloyed in a planetary ball-mill AGO-2S (balling drum material was hardened stainless steel, balls 8 mm in diameter were made of ball-bearing steel) in a pre-evacuated inert atmosphere $P_{Ar} = 0.1 \text{ MPa}$ ($P = 10^{-3}$). The duration of mechanical alloying ranged from 15 min to 8 h.

A BRUKER D8 ADVANCE (CuK α radiation) diffractometer was used to perform X-ray diffraction study of the samples. Magnesium oxide (MgO), prepared as described in [17], was taken as a reference specimen to account for instrument broadening. The calculations were made with an error for lattice parameters (a_{Cu}) smaller than 0.002 Å, crystallite sizes (L) 0.5 nm, and the level of microdistortions ($\langle \varepsilon^2 \rangle^{1/2}$) 0.05 %. To measure the changes in particle morphologies (size and shape) a scanning electron microscope QUANTA 200 3D was used. Raman spectroscopy was used to study the structural changes of carbon in the mechanically alloyed Cu-C_{60/70} and Cu-C composites. The measurements were taken with a Labram HR800 (HORIBA) spectrometer with an exciting laser wavelength $\lambda = 632.81 \text{ nm}$.

3. Results and discussion

Fig. 1 includes microimages of the initial copper powders and Cu-C_{60/70} and Cu-C_g samples, and also the images taken after their mechanical alloying for 1 and 8 h. It is seen that in the process of mechanical alloying of copper-carbon powders, different deformation kinetics of Cu-C_{60/70} and Cu-C_g composites are observed, depending on the carbon form. This follows from the different shapes of the resultant particles and their dispersion. After 1 h of milling, the particles of the mechanically alloyed composites represent stone-like agglomerates formed from smaller particles (Fig.1), with Cu-C_{60/70} powders being more finely-dispersed at the beginning

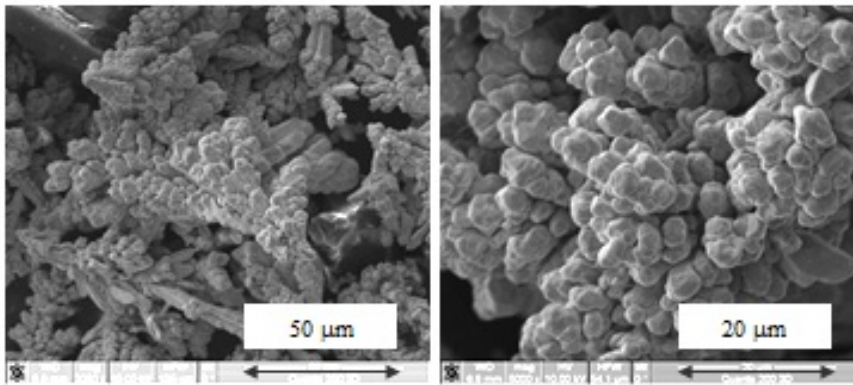
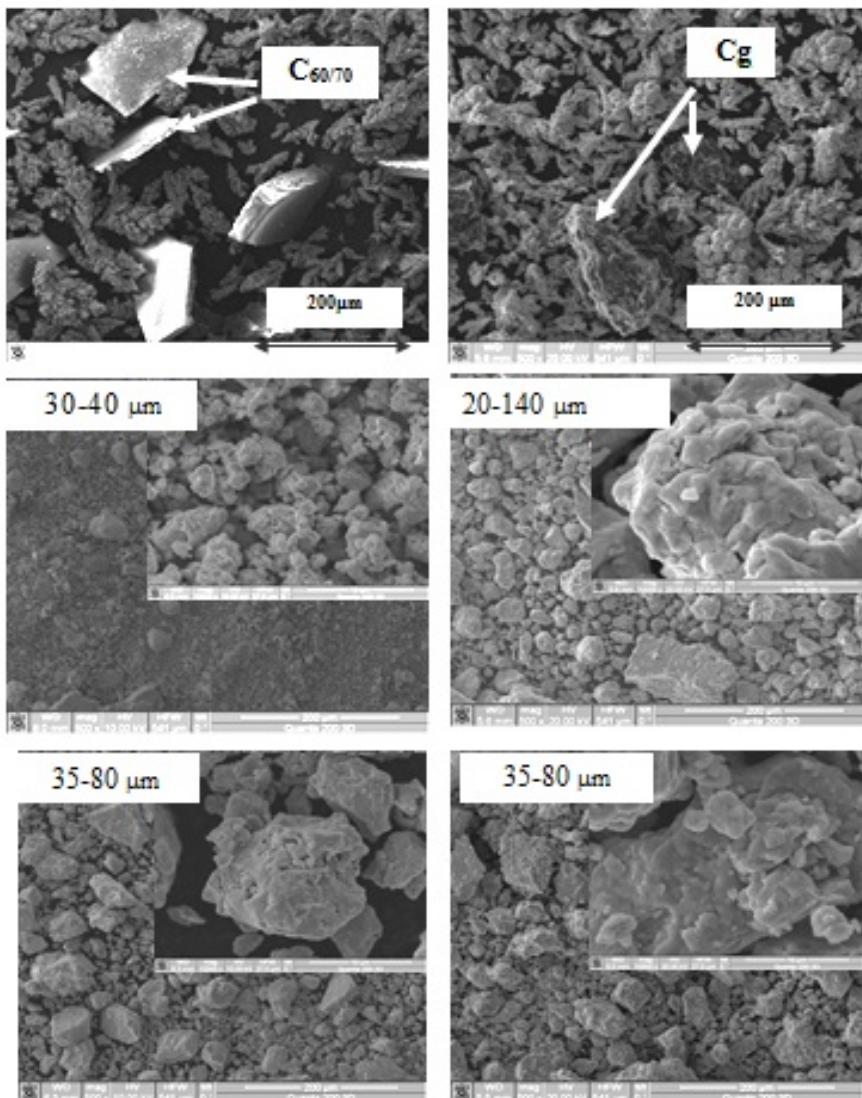
Initial copper**Cu – 25% $C_{60/70}$** **Cu – 25% C_g** **0 h MA****1 h MA****8 h MA**

FIG. 1. SEM-images of particles of Cu-25 %C powders in their initial state and after 1 and 8 h of mechanical alloying

than Cu-C_g powders. With an increase of the mechanical alloying time to 8 h, the particle sizes in the composites compared tend to level off (Fig. 1). It should be noted that with a decrease in the composites' carbon content (to 5 at %), the morphological differences become more expressed.

Figure 2 demonstrates X-ray diffraction patterns for Cu-C_{60/70} and Cu-C_g powders that were mechanically activated for 0.5, 1, 2 and 8 h (t_{MA}). Judging by the appearance of an X-ray amorphous halo in the area of C_{60/70} main reflections at angles $2\theta = 8 - 35^\circ$ (Fig. 2a, insert) an amorphous fullerite-like phase is formed in the Cu-25 % C_{60/70} blend after its mechanical alloying for 0.5 – 2 h. At the same time, Cu₂O is formed. As concerns Cu-C_g, after as early as 0.5 h of mechanical alloying ($2\theta \sim 26^\circ$), the structural maximum of graphite in the X-ray diffraction pattern totally disappears; also, the formation of Cu₂O is no longer observed.

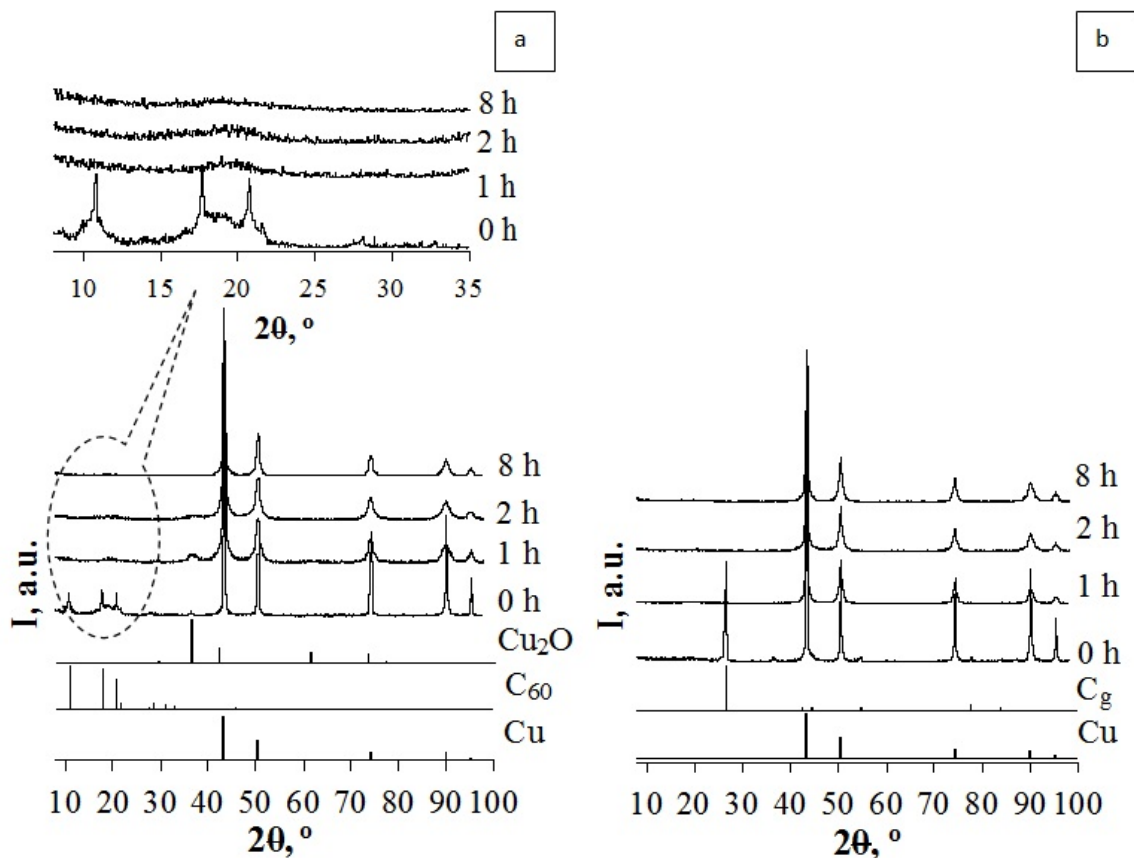


FIG. 2. X-ray diffraction patterns of Cu-C_{60/70} (a) and Cu-C_g (b) powders at different MA times

Figure 3 shows the Raman spectra of Cu-C_{60/70} and Cu-C_g samples after 1 and 8 h of mechanical alloying. Since D-band (1332 cm^{-1}) has a higher intensity in comparison with G-band (1582 cm^{-1}) (Fig. 3, a), we can draw a conclusion that the graphite structure in the Cu-C_g sample after 1 h of mechanical alloying is characterized by a higher number of defects. A considerable intensity decrease and broadening of G-band is a consequence of graphite amorphization [18]. The presence of the main bands of fullerenes C₆₀ and C₇₀ in the Raman spectra of the C_{60/70} composite mechanically milled for 1 h indicates the presence of fullerenes in the sample (Fig. 3, a). Owing to the spherical shapes of C₆₀ molecules, their high compressive strength and weak intermolecular bonds in a crystal, fullerenes in the process of high energy

milling presumably act as “molecular bearings” [19]. Due to this, higher dispersion is attained in the process of mechanical alloying of the Cu-C_{60/70} system.

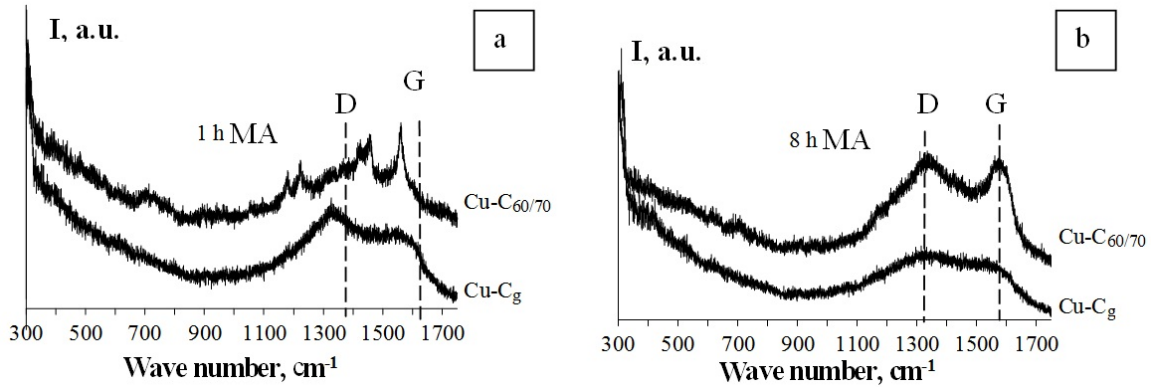


FIG. 3. Raman spectra of Cu-C_{60/70} and Cu-C_g composites after 1 (a) and 8 (b) h of MA

For long periods of mechanical alloying (8 h), the Raman spectra of both Cu-C_{60/70} and Cu-C_g samples correspond to amorphous carbon (Fig. 3, b). This is indicative of the destruction of fullerene molecules and the disordering of graphite’s lamellar structure. As a result, particle sizes in the compared Cu-C_{60/70} and Cu-C_g systems level off (Fig. 1). It is to be noted that smaller particle sizes in Cu-C_{60/70} powders in comparison with Cu-C_g powders can also be explained by the formation of a fragile copper oxide Cu₂O at $t_{MA} = 0.5 - 2$ h (Fig. 2, a).

Thus, based on the results of Raman spectroscopy, it can be stated that the differences observed in the Cu-C_{60/70} and Cu-C_g systems in process of mechanical alloying depend on a higher deformation stability of fullerite in comparison with graphite. The latter was previously shown in our research [20].

According to the diffraction maxima of the Cu-C sample profiles, the dependences of copper crystalline lattice parameter a_{Cu} and crystalline sizes L on the mechanical alloying time (t_{MA}) for Cu-C_{60/70} and Cu-C_g are different (Fig. 4). At $t_{MA} = 1 - 2$ h Cu-C_{60/70} powders have smaller grains, 12 nm, in contrast with Cu-C_g powders, at a maximum value of $a_{Cu} = 3.6169$ Å. In the plot of a_{Cu} versus milling time (t_{MA}) we observe the maximum, and in the plot of L versus milling time, the minimum is observed. In the process of milling for 4 – 8 h crystallite sizes increase and reach values close to those for Cu-C_g composites. At the same time, a_{Cu} decreases to 3.6162 nm. The change of grain sizes in the samples is seen to correlate with the scanning electron microscopy data (Fig. 1) for particle dispersion.

In compliance with [21], from a thermodynamics point of view, the presence of adsorbed oxygen at Cu-C interfaces should not have resulted in the formation of copper oxide, since the latter should have been reduced by carbon. However, since the energy of attachment for oxygen atoms to a C₆₀ molecule exceeds that of the heat of Cu₂O formation (376.8 and 166.6 kJ/mol, respectively [22,23]), it is energetically favorable for oxygen to react with copper. As a result, copper oxide Cu₂O is formed in the sample, with part of oxygen additionally dissolved in the copper matrix to form Cu(C, O). This explains larger value of $a_{Cu} = 3.6169$ Å in comparison with Cu-C_g ($a_{Cu} = 3.6162$ Å). Furthermore, larger a_{Cu} value in the Cu-C_{60/70} system is also determined by smaller grain sizes $\langle L \rangle$, and hence, larger specific surface area for the particles.

Because of this, the solid phase reactions in the Cu-C_{60/70} system proceed in two steps. At the beginning (within 2 h) copper oxide (Cu₂O) is formed, with fullerene molecules remaining uninvolved. At the same time, an oversaturated solid solution of carbon and oxygen

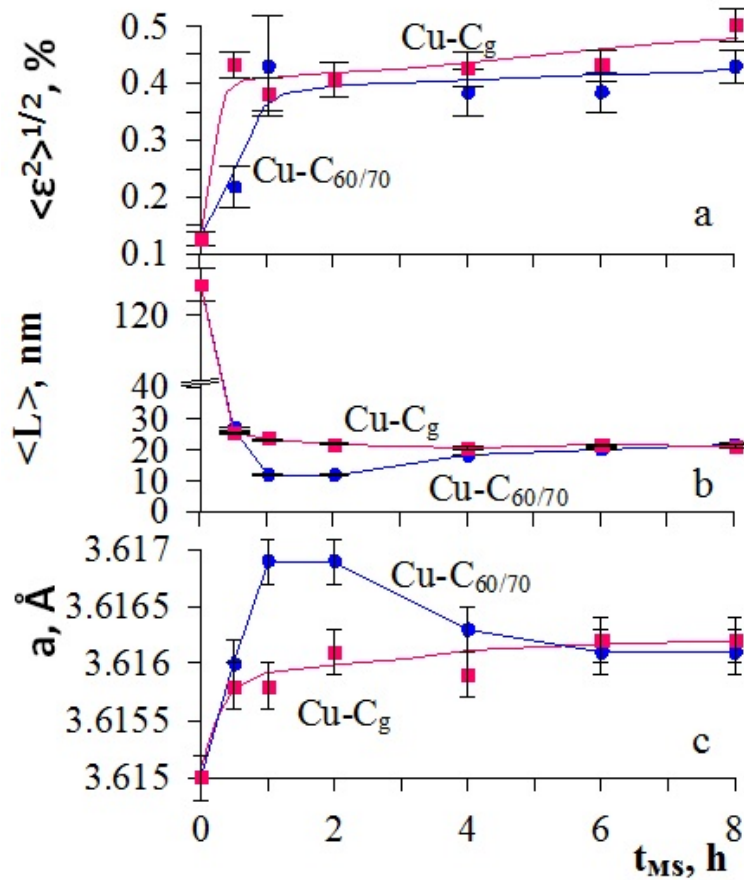


FIG. 4. Dependence of microstress (a), crystallite sizes (b), and lattice parameter (c) of copper in composites Cu-C_{60/70} and Cu-C_g on MA time

in copper Cu(C, O) is formed. The second stage is initiated by the destruction of fullerene molecule frameworks caused by high energy deformation. This results in amorphous carbon formation. At 4 – 8 h of MA, the formed copper oxide is reduced:



and a partial diffusional decay of the oversaturated solid solution Cu(C, O) occurs with the formation of Cu(C). This decay can be explained by the reaction proceeding between its components:



where $[\text{C}]_{\text{Cu}}$ and $[\text{O}]_{\text{Cu}}$ are carbon and oxygen dissolved in copper. As a result, an oversaturated solid solution of Cu(C) is formed with $c_{\text{Cu}} = 3.6161 \text{ \AA}$, and this is accompanied by the recrystallization of the sample ($\langle L \rangle$ increases from 12 to 20 nm).

Unlike the case with Cu-C_{60/70}, the mechanical alloying of Cu-C_g is a one stage process. As a result of this process, an oversaturated solid solution Cu(C) is formed. Because of a faster amorphization of graphite and its high reducibility neither oxide formation nor oxygen dissolution in copper is observed here.

Thus, it can be stated that the differences in the dependence $a_{\text{Cu}}(t_{\text{MC}})$ observed between Cu-C_{60/70} and Cu-C_g at the initial stage of their MA (up to 2 h) are not only determined by the different deformational stability of fullerite and graphite, but also by their different reactivity with oxygen.

4. Conclusion

Regularities of structural and phase conversions in the mechanical alloying processes of copper-fullerite and copper-graphite composites have been identified. It has been demonstrated that the mechanical alloying of Cu-C_{60/70} and Cu-C_g composites with a nanocrystalline structure results in the formation of an oversaturated solid solution of carbon in copper, Cu(C). The formation kinetics of this solution, together with the powder morphology has been shown to depend on the deformational stability of fullerite and graphite, as well as their reactivity with adsorbed oxygen.

Acknowledgements

The work has been carried out under financial support of the program the Presidium of Ural Branch, RAS (grant 15-20-2-22).

References

- [1] Barner A., Mundim K.C., Ellis D.E., Dorfman S., Fuks D., Evenhaim R. Microstructure of Cu-C interface in Cu-based metal matrix composite. *Sensors and Actuators A*, 1999, **74**, P. 86–90.
- [2] Sheibani S., Ataie A., Heshmati-Manesh S., Khayati G.R. Role of process control agent on synthesis and consolidation behavior of nano-crystalline copper produced by mechano-chemical route. *Mater. Lett.*, 2007, **61**, P. 3204–3207.
- [3] Guillet A., Yama Nzoma E., Pareige P. A new processing technique for copper-graphite multilaminary nanocomposite wire: Microstructures and electrical properties. *J. Mater. Process. Technol.*, 2007, **182**, P. 50–57.
- [4] Nunes D., Livramento V., Mateus R., Correia J.B., L.C.Alves, Vilarigues M., Carvalho P.A. Mechanical synthesis of copper-carbon nanocomposites: structural changes, strengthening and thermal stabilization. *Mater. Sci. Engin. A*, 2011, **528**, P. 8610–8620.
- [5] Chu K., Gua H., Jia C., Yin F., Zhang Z., Liang X., Chen H. Thermal properties of Carbon Nanotube-Copper Composites for Thermal Management Applications. *Nanoscale Res. Lett.*, 2010, **5**, P. 969–874.
- [6] Shukla A.K., Nayan N., Murty S.V.S.N., Sharma S.C., Chandran P. Processing of copper-carbon nanotube composites by vacuum hot pressing technique. *Mater. Sci. Engin. A*, 2013, **560**, P. 365–371.
- [7] Yamamoto K., Taguchi T., Hanada K., Osawa E., Inakuma M., Livramento V., Correia J.B., Shohhji N. TEM studies of nanocarbons and nanodiamonds (ND): mechanical milling of ND and Cu. *Diamond Related Mater.*, 2007, **16**, P. 2058–2063.
- [8] Medvedev V.V., Popov M.Y., Mavrin B.N., Denisov V.N., Kirichenko A., Tat'yanin E.V., Ivanov L.A., Akse-nenkov V.V., Perfilov S.A., Lomakin R., Blank V.D. Cu-C₆₀ nanocomposite with suppressed recrystallization. *Appl.Phys.A*, 2011, **105**, P. 45–48.
- [9] Bezruchko G.S., Razorenov S.V., Popov M.Y. The influence of the admixture of the fullerene C₆₀ on the strength properties of aluminum and copper under shock-wave loading. *J. Phys.: Conf. Ser.* 2014, **500**, P. 112008(1-6).
- [10] Kovtun V.A. Investigation of structure and properties of composite materials based on copper-carbon nanoparticles powder systems formed by electrocontact sintering. *Machines, Technologies, Materials*, 2012, **3**, P. 34–38.
- [11] Shpilevsky E.M., Baran L.V., Okatova G.P. Structurally-phase composition of the films Cu-C₆₀, obtained by condensation in a vacuum of a joint atomic-molecular flow. *Adv. Mater.*, 2003, **3**, P. 56–59.
- [12] Larionova T.V., Markina N.V., Petrov N.V., Shapovalov O.S., Afanasev A.A., Koltsova T.S. The structure and hardness of the copper composite materials of carbon. *Vestnik Novgorod State University*, 2012, **68**, P. 15–19.
- [13] Guillet A., Nzoma E.Yama, Pareige P. A new processing technique for copper-graphite multifilamentary nanocomposite wire: Microstructures and electrical properties. *J. Mater. Process. Technol.*, 2007, **182**, P. 50–57.
- [14] Robles Hernandez F.C. Production and characterization of Fe-Cgraphite and Fe-Cfullerene composites produced by different mechanical alloying techniques. *J. Metallurgy*, 2004, **10**(2), P. 107–118.
- [15] Robles Hernandez F.C., Calderon H.A. Nanostructured Al/Al₄C₃ composites reinforced with graphite or fullerene and manufactured by mechanical milling and spark plasma sintering. *Mater. Chem. Phys.*, 2012, **132**, P. 815–822.

- [16] Nikonova R.M., Dorofeyev G.A., Ladyanov V.I., Pushkaryov B.Ye. Mechanical alloying of Mg nanocomposites with different forms of carbon. *Chem. Phys. Mezoscopy*, 2010, **12**(3), P. 382–389.
- [17] Pratapa S., O'Connor B. Development of MgO ceramic standards for X-ray and neutron line broadening assessments. *Advances in X-ray Analysis*, 2002, **45**, P. 41–47.
- [18] Bukallov S.S., Mikhailitzin L.A., Zubavichus Ya.V., Leites L.A., Novikov Y.N. Investigation of the structure of graphite and some other sp² carbon materials by means of micro-Raman spectroscopy and X-ray diffraction. *Russian Chem. J.*, 2006, **L**(1), P. 83–91.
- [19] Shpilevskiy M.E., Stelmakh V.F. Fullerenes and fullerene-like structures as a basis for advanced materials. *J. Engin. Phys.*, 2001, **74**(6), P. 106–112.
- [20] Lad'yanov V.I., Nikonova R.M., Larionova N.S., Aksenova V.V., Mukhalin V.V., Rud A.D. Deformation Induced Changes in the Structure of Fullerites C_{60/70} during Their Mechanical Activation. *Phys. Solid State*, 2013, **55**(6), P. 1319–1324.
- [21] Berner A., Fuks D., Ellis D.E., Mundim K., Dorfman S. Formation of nano-crystalline structure at the interface in Cu-C composite. *Appl. Surf. Sci.*, 1999, **144-145**, P. 677–681.
- [22] Sidorov L.N., Yurovskaya M.A., et al. *Fullerenes*. Moscow: Publishing House "Exam", 2005, 688 p.
- [23] Azarenkov N.A., Litovchenko S.V., Nekludov I.M., Stoyev P.I. *Corrosion and protection of metals. Part 1. Chemical corrosion of metals. Textbook*. Kh.NU, Kharkov, 2007, 187 pp.

Modification of the mechanical properties of zirconium dioxide ceramics by means of multiwalled carbon nanotubes

E. A. Lyapunova^{1,2}, S. V. Uvarov¹, M. V. Grigoriev^{3,4}, S. N. Kulkov³, O. B. Naimark¹

¹Institute of Continuous Media Mechanics, Ural Branch of Russian Academy of Sciences, Perm, Russia

²Ural Federal University, Ekaterinburg, Russia

³Institute of Strength Physics and Materials Science, Siberian Branch of Russian Academy of Sciences, Tomsk, Russia

⁴Tomsk Polytechnic University, Tomsk, Russia

lyapunova@icmm.ru

PACS 62.23.Pq, 62.20.Qp, 63.22.Gh

DOI 10.17586/2220-8054-2016-7-1-198-203

A ceramic matrix composite based on zirconium dioxide doped with carbon nanotubes (CNTs) and metallic silver as a plastic binder was produced by hydrothermal synthesis from ceramic precursor and a CNTs suspension followed by critical point drying of the synthesized hydrogel and metallic silver deposition on ceramic composite aerogel fragments from a AgNO₃ solution. Multi-indentation loading of the composite has revealed two types of mechanical response: 1) hardness decreasing with an increasing of number of cycles and 2) significant increasing of hardness with an increasing number of indentations. Local chemical composition analysis has revealed correlations between the composite hardness and the presence oxygen atoms for first type and silver and yttrium atoms for second type of mechanical response respectively.

Keywords: carbon nanotubes, zirconium dioxide, hydrothermal synthesis, aerogel, nanoindentation.

Received: 20 November 2015

1. Introduction

The production of ceramic composites reinforced by carbon nanotubes (CNTs) is one of rapidly developing area in modern material science because of their ability to enhance ceramic structure, intensify sintering processes and decrease crystallite size [1-3]. Although addition of CNTs can change electromagnetic, electro- and heat-conductive properties of convenient ceramics, the current work is focused on mechanical properties of CNTs-modified zirconia composite. There is discrepancy in the literature concerning the ability of CNTs to improve the mechanical properties of such a composite [4,5], which apparently occurs because complete dispersion of CNTs agglomerates and their optimal arrangement in ceramic matrix can hardly be achieved. That is why reports about several orders of magnitude improvement of mechanical properties (fracture toughness, hardness, etc.) for CNTs-doped ceramics in comparison with conventional ceramics, as well as reports showing the absence of any significant effect of CNTs, can be found in literature. The aim of the present work is the development of the optimal mutual configuration of CNTs and ceramic crystallites in ceramic/CNTs composite and estimation of its mechanical behavior under multiple indentation loading.

2. Composite preparation

Preparation of the composite includes the following steps: hydrothermal synthesis of dense hydrogel from suspension of zirconium salt and CNTs (0.2 wt% concentration of CNTs); critical point drying of hydrogel and thermal treatment of obtained $ZrO_2/CNTs$ aerogel (these steps are described in detail in [6]); addition of metallic binder between aerogel fragments; and final consolidation of them into bulk samples by hot pressing. Critical point drying provided ceramic crystallites size less than 20 nm (Fig. 1, left) and preserves CNTs mutual configuration formed during hydrothermal synthesis.

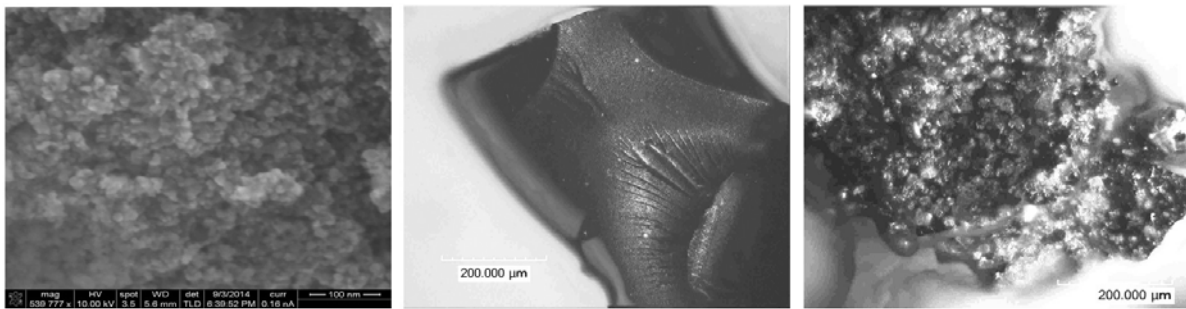


FIG. 1. Crystallite structure of synthesized aerogel (left), aerogel fragments before (center) and after (right) silver deposition

Metallic binder was added to the ceramic composite in order to increase material toughness. Such effect of small amount of titanium in zirconia ceramics was reported more than 50 years ago [7], but at that time, convenient ceramic powder with several hundred micron crystallites size and metallic powder with comparable grain size were used. In our case, with tiny size of ceramic crystallites, another method of metal particle addition was implemented; fragments of $ZrO_2/CNTs$ aerogels were immersed in $AgNO_3$ solution and exposed to ultraviolet radiation with simultaneous sonication for process homogeneity. Such treatment leads to metallic silver precipitation on ceramic fragments (see: Fig. 1, center, Fig. 1, right); metal/ceramics ratio in final composite is controlled by ceramic powder size (its surface area), $AgNO_3$ concentration and ultraviolet radiation intensity.

Consolidation of $ZrO_2/CNTs$ aerogel fragments after metal deposition was carried out by hot pressing in a graphite die at 1500 °C and 53.5 MPa maximum pressing stress with 15 minutes dwelling time at the maximum temperature and pressure. X-ray spectroscopy of the sintered composite samples indirectly confirms the preservation of the ultrathin size of ceramic crystallites; there are peaks which correspond solely to the cubic phase of zirconium dioxide (Fig. 2). Since the sintering temperature was much higher than the melting point of silver, the latter becomes liquid, covering nearby ceramic composite fragments and fills the space between them (Fig. 3). There are different scales of porosity in the sintered composite: the lower scale (from ten to a few hundred nanometer size) which corresponds to the $ZrO_2/CNTs$ aerogel fragments' structure (Fig. 3, right) and is provided in the initial steps of composite production (hydrothermal synthesis and critical point drying of hydrogel). The higher scale of porosity (from a few to several tens of micrometers, Fig. 3, left) is due to incomplete consolidation of ceramic composite fragments during sintering as long as the applied pressure and temperature are not sufficient to reach complete densification of the material.

Transmission electron microscopy (TEM) analysis of composite fragments after hot pressing confirmed the presence of CNTs in the material (Fig. 4, left), however other nanocarbon objects were found, namely carbon nanotoroids (Fig. 4, right). One of the possible reasons

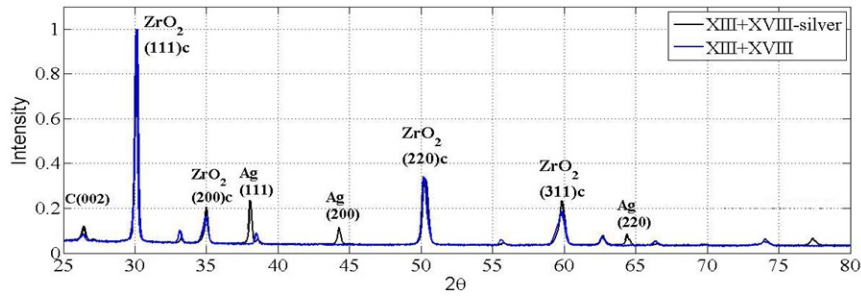


FIG. 2. X-ray spectra of ZrO₂/CNTs composite (blue) and ZrO₂/CNTs aerogel with metallic binder (black)

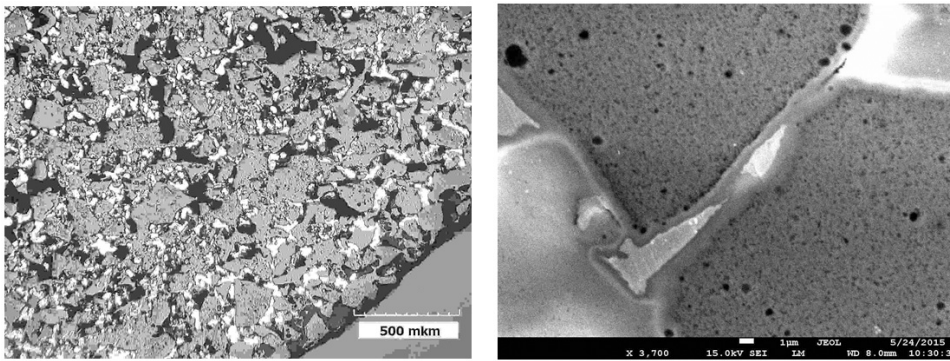


FIG. 3. Polished sample surface. Optical and scanning electron microscopy images demonstrating the common structure on the periphery of the sample (left) and the linkage between two ceramic aerogel fragments (right)

for their appearance is the high gradient magnetic field which occurred during heating of the graphite die by induction currents. CNTs toroidal and coiled structures are under keen investigation, since they are expected to have rather special electromagnetic properties [8].

The synthesis of ZrO₂/CNTs aerogel and its preliminary structural characterization were conducted at the University of Louisville, USA. Metallic silver deposition on ZrO₂/CNTs aerogel fragments was carried out at the Institute of continuous media mechanics, Perm, Russia. Hot pressing of aerogel fragments after silver deposition, X-ray spectroscopy and TEM of the sintered composite were performed at the Institute of Physical Foundations of Strength, Tomsk, Russia.

3. Indentation experiment

Mechanical experiments on multiple indentation of composite were realized on the basis of indentation system NanoTest (Perm State University, Perm, Russia) and consisted of the following steps: loading the sample with Berkovitch indenter to maximum force F_{max} , dwelling the material at this load for 60 seconds, unloading the sample to $0.2F_{max}$, dwelling at this load for 60 seconds and repeating of the loading cycle again. Several series of experiments were produced varying the loading velocity (2, 4 and 8 mN/s) and number of cycles (20 and 40) with the same maximum load 500 mN. For each loading conditions 30 experiments with 50 μm distance were carried out. Fig. 5 shows the scanning electron microscope (SEM) image of the examined composite with a fragment of the indents map. Structural inhomogeneity provides some variation in measurement of mechanical properties, but comparison of force curves with

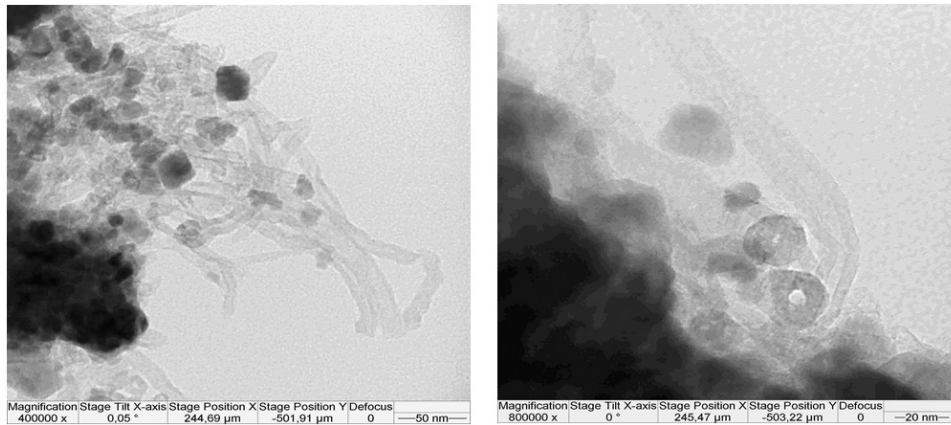


FIG. 4. CNTs with ZrO_2 crystalites (left) and CNTs with carbon nanotoroids (right) in sintered material

SEM images of indents can help to eliminate unreliable points like indentation on the boundary between ceramic fragments and to analyze only the valuable points.

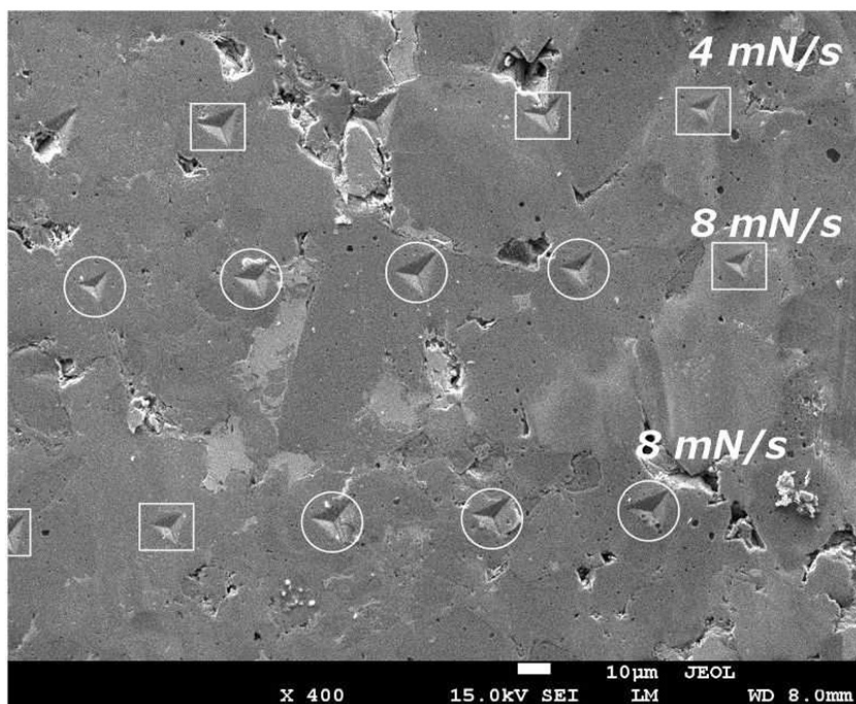


FIG. 5. Three series of indents on the composite produced under different loading conditions. Indents with first and second types of mechanical response are framed in squares and rounds respectively

The synthesized composite exhibits two types of mechanical response under multiple indentation: the first type has decreasing hardness (penetration depth increasing) with each indentation cycle (Fig. 6), and opposite one, namely increasing hardness (penetration depth decreasing) with increasing number of indentation cycles (Fig. 7). Analysis of local chemical composition near indents has shown correlations between the structural elements composition and mechanical properties of the material. Indeed, for the first type of mechanical response, there is a correlation of oxygen concentration with hardness values: the lower the oxygen

concentration, the higher the hardness of material. For the second type of mechanical response, with anomalous composite hardening, the correlation of silver and yttrium concentrations with hardness values has been found, namely, the higher the silver and yttrium percentage, the higher the hardness of material.

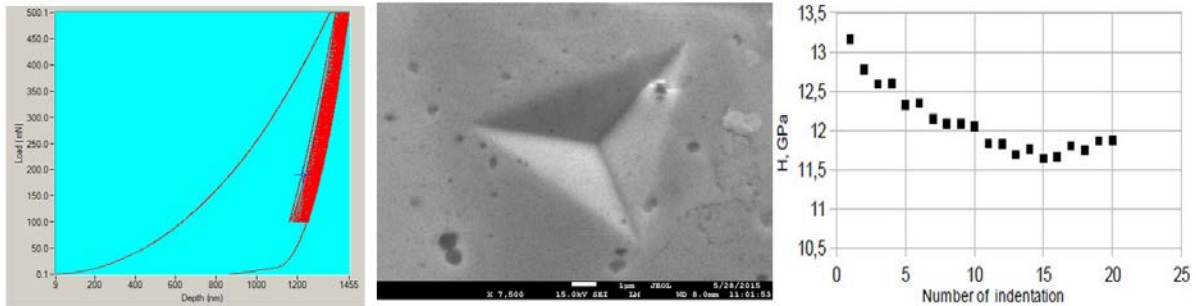


FIG. 6. Force curve (left), SEM image of indent (center) and evolution of hardness during the multiple indentation experiment (right) for the first type of material response

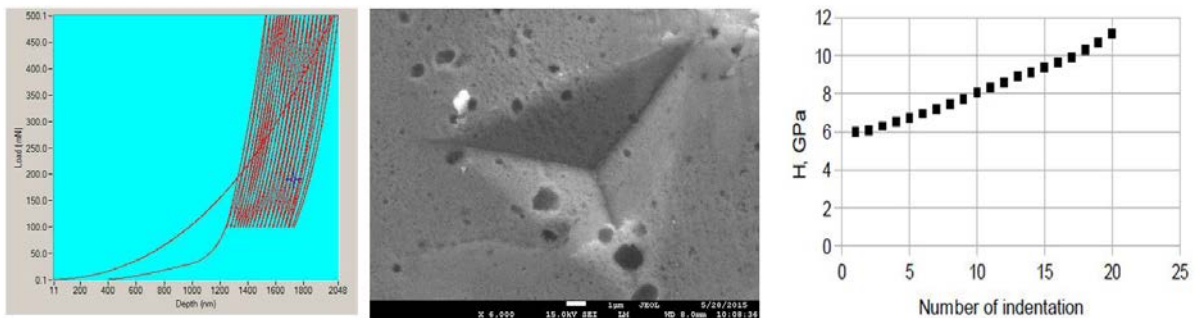


FIG. 7. Force curve (left), SEM image of indent (center) and evolution of hardness during the multiple indentation experiment (right) for the second type of material response

One of the possible explanation for this can be the following: the first type of mechanical response is governed mainly by oxygen vacancies in the ceramic matrix, while anomalous hardening is the result of the phase composition of ceramics composite (which is governed by yttrium concentration) and the presence of silver atoms. Analysis of mutual configuration of metallic particles and CNTs in ceramic matrix as well as investigation of additional chemical bonds forming between them can prove this hypothesis. Also, there is no increasing of hardness during multiple loading of conventional ceramics, so one can conclude that CNTs play a significant role in such type of mechanical response.

4. Conclusions

The ceramic matrix composite based on CNTs-doped zirconium dioxide and metallic silver as a plastic binder was produced. Ultrathin ceramic crystallites (size less than 20 nm) were formed by means of hydrothermal synthesis and critical point drying of the ceramic composite precursor. Multi-indentation loading of composite has revealed two types of mechanical response: 1) hardness decreasing (penetration depth increasing) with each cycle of indentation, and 2) increasing of hardness (penetration depth decreasing) with increasing number of

indentations. Such different mechanical behavior is attributed to both chemical and structural inhomogeneity of material. Local chemical composition analysis has revealed correlations between hardness changes and the presence of silver and yttrium or oxygen atoms for different types of mechanical responses.

Acknowledgements

This work is supported by Russian Foundation for Basic Research (grant N14-01-96015-ural-a).

References

- [1] Xia Z., Riester L., Curtin W.A., Li H., Sheldon B.W., Liang J., Chang B., Xu J.M. Direct observation of toughening mechanisms in carbon nanotube ceramic matrix composites. *Acta Mater.*, 2004, **52**(4), P. 931–944.
- [2] Lyapunova E., Naimark O., Kulkov S., Dedova E., Sobolev I. Structure of zirconium oxide-multiwalled carbon nanotubes composite produced by electrophoretic deposition. *Inorg. Mater.*, 2015, **51**(1), P. 20–24.
- [3] Vasiliev A.L., Poyato R., Pature N.P. Single-wall carbon nanotubes at ceramic grain boundaries. *Scripta Mater.*, 2007, **56**, P. 461–463.
- [4] Curtin W.A., Sheldon B.W. CNT-reinforced ceramics and metals. *Materials Today*, 2004, **7**(11), P. 44–49.
- [5] Peigney A., Laurent C., Flahaut E., Rousset A. Carbon nanotubes in novel ceramic matrix nanocomposites. *Ceramic Intern.*, 2000, **26**, P. 677–683.
- [6] Lyapunova E., Lunegov I., Uvarov S., Naimark O. Structural aspects of zirconium dioxide/MWCNTs composite. *Actual problems of condensed media physics*, 2015, P. 83–90. ICMM UB of RAS, Perm (in Russian).
- [7] Weber B.C., Garrett H.J., Mauer F.A., Schwartz M.A. Observations on the stabilization of zirconia. *J. Amer. Ceramic Soc.*, 1956, **39**(6), P. 197–206.
- [8] Liu L., Liu F., Zhao J. Curved carbon nanotubes: from unique geometries to novel properties and peculiar applications. *Nano Research*, 2014, **7**(5), P.626–657.

On the spillover effect of the solid H₂ intercalation into GNF's

Yu. S. Nechaev¹, V.P. Filippova¹, A. A. Tomchuk¹, A. Yurum², Yu. Yurum³, T.N. Veziroglu⁴

¹Kurdjumov Institute of Metals Science and Physics, Bardin Institute for Ferrous Metallurgy, Moscow, Russia

²Nanoechnology Research and Application Centre, Sabanci University, Istanbul, Turkey

³Falulty of Engineering and Natural Sciences, Sabanci University, Istanbul, Turkey

⁴International Association for Hydrogen Energy, Miami, FL 33155, USA

yuri1939@inbox.ru, varia.filippova@yandex.ru, tomchuk-a@yandex.ru,
ayurum@sabanciuniv.edu, yyurum@sabanciuniv.edu, tnveziroglu@gmail.com

PACS 67.63-Cd, 68.43-Hn, 68.47-Mn

DOI 10.17586/2220-8054-2016-7-1-204-209

Keywords: HOPG, epitaxial graphenes, graphite nanofibers (GNFs), solid H₂ intercalation, spillover effect.

Received: 20 November 2015

1. Introduction

As is known, the hydrogen spillover effect can be characterized by three major steps, the first being where molecular hydrogen is split via dissociative chemisorption into its constituent atoms on a transition metal catalyst surface, followed by migration from the catalyst to the substrate, culminating in their diffusion throughout the substrate surfaces and/or in the bulk materials. The mechanism behind the hydrogen spillover effect has been long disputed, up to currently.

As is noted, for instance in [1-10], the hydrogen spillover effect manifestation in carbon-based nanomaterials has been not studied thoroughly, which is particularly relevant for solving the current problems of on-board hydrogen storage efficiency and safety.

2. Experimental/methodology

A thermodynamic analysis approach [11,12] for the related experimental data (including Figs. 1 – 4 from [12]) has been used.

3. Results and discussion

3.1. The physics for the intercalation of high density H₂ gaseous nanophase into graphene nanoblister in HOPG and epitaxial graphenes (under atomic hydrogen treatment)

Figure 1 shows the two steps ((a) and (b)) of hydrogenation (at 300 K and the atomic hydrogen pressure $P_{(H_{gas})} \approx 1 \cdot 10^{-4}$ Pa, without any catalyst) of surface graphene layers of a highly oriented pyrolytic graphite (HOPG) resulted in intercalation of a high density H₂ gaseous nanophase into surface graphene nanoblister.

If we assume that the nanoblister approximates a semi-elliptical form, we obtain a blister area of $S_b \approx 2.0 \cdot 10^{-11}$ cm² and a volume of $V_b \approx 8.4 \cdot 10^{-19}$ cm³. The amount of retained hydrogen in this sample becomes $Q \approx 2.8 \cdot 10^{14}$ H₂/cm² and the number of hydrogen molecules captured inside the blister becomes $n \approx (QS_b) \approx 5.5 \cdot 10^3$. Thus, within the

ideal gas approximation, and accuracy of one order of the magnitude, the internal pressure of molecular hydrogen in a single nanoblister at near-room temperature ($T \approx 300$ K) becomes $P_{H_2} \approx \{k_B(QS_b)T/V_b\} \approx 1 \cdot 10^8$ Pa. The hydrogen molecular gas density in the blisters (at $T \approx 300$ K and $P_{H_2} \approx 1 \cdot 10^8$ Pa) can be estimated as $\rho_{H_2} \approx \{(QM_{H_2}S_b)/V_b\} \approx 0.045$ g/cm³, where M_{H_2} is hydrogen's molecular mass.

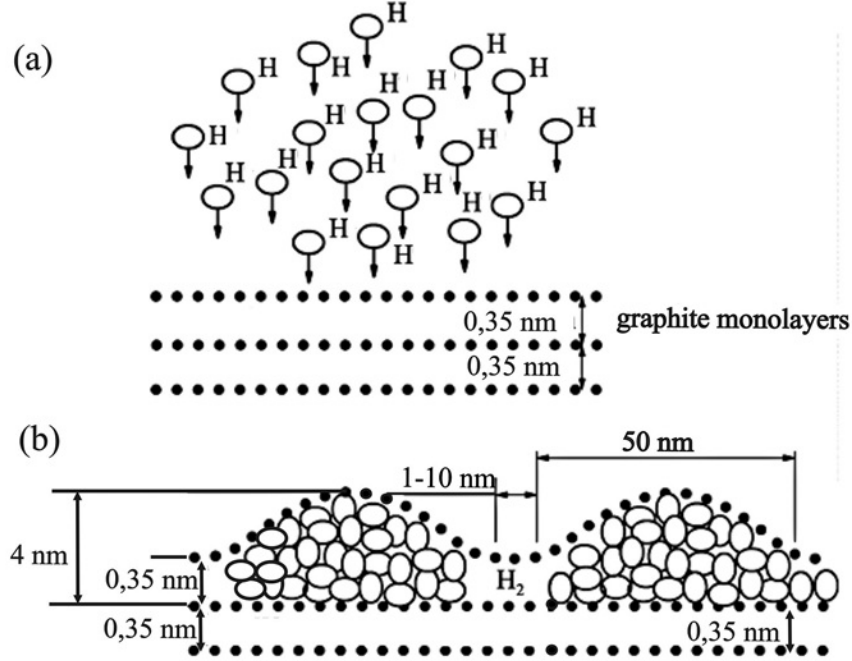


FIG. 1. Model {from STM and AFM data} showing the hydrogen accumulation (intercalation) in HOPG, with the formation of blister-like surface nanostructures; hydrogenation was done at 300 K and the atomic hydrogen pressure $P_{(H_{gas})} \approx 1 \cdot 10^{-4}$ Pa, without any catalyst. (a) Pre-atomic hydrogen penetration (intercalation) step. (b) Molecular gaseous hydrogen, “captured” inside the surface graphene nanoblisters (at $P_{(H_2_{gas})} \approx 1 \cdot 10^8$ Pa), after the intercalation step. Sizes are not drawn exactly in scale. The hydrogen compression effect is of 12 orders (from $P_{(H_{gas})} \approx 1 \cdot 10^{-4}$ Pa to $P_{(H_2_{gas})} \approx 1 \cdot 10^8$ Pa). According to analysis [11,12], it occurs at the expense of the energy of association of hydrogen atoms to the “captured” molecules, Eqs. (1), (2)

These data (Fig. 1) can be quantitatively described, with an accuracy of one order of magnitude, and interpreted within the thermodynamic approach [11,12], by using the conditions of thermo-elastic equilibrium for the reaction of ($2H_{(gas)} \rightarrow H_{2(gas-in-blister)}$), as follows:

$$(P_{H_2}/P_{H_2}^0) = (P_H/P_H^0)^2 \exp \{[\Delta H_{dis} - P_{H_2}^* \Delta V]/k_B T\}, \quad (1)$$

where $P_{H_2}^*$ is related to the blister “wall” back pressure (caused by P_{H_2}) – the so called surface pressure ($P_{H_2}^* \approx P_{H_2} \approx 1 \cdot 10^8$ Pa), P_H is the atomic hydrogen pressure corresponding to the atomic hydrogen flux ($P_H \approx 1 \cdot 10^{-4}$ Pa), $P_{H_2}^0 = P_H^0 = 1$ Pa is the standard pressure, $\Delta H_{dis} = 4.6$ eV is the dissociation energy (enthalpy) of one molecule of gaseous hydrogen (at room temperature), $\Delta S_{dis} = 11.8k_B$ is the dissociation entropy, $\Delta V \approx (S_b r_b/n)$ is the apparent volume change, r_b is the radius of curvature of nanoblisters at the nanoblister edge ($r_b \approx 30$ nm, Fig. 1), N_A is Avogadro's number, and T is the temperature ($T \approx 300$ K). The quantity of

($P_{H_2}^* \Delta V$) is related to the work of the nanoblister surface increasing with an intercalation of 1 molecule of hydrogen.

The value of the tensile stresses σ_b (caused by $P_{H_2}^*$) in the graphene nanoblister “walls” with a thickness of d_b and a radius of curvature r_b can be evaluated from another condition (equation) of the thermo-elastic equilibrium for the system in question, which is related to Eq. (1), as follows:

$$\sigma_b \approx P_{H_2}^*(r_b/2d_b) \approx (\varepsilon_b E_b), \quad (2)$$

where ε_b is a degree of elastic deformation of the graphene nanoblister walls, and E_b is the Young’s modulus for the graphene nanoblister walls.

Substituting in the first part of Eq. (2) the quantities of $P_{H_2}^* \approx 1 \cdot 10^8$ Pa, $r_b \approx 30$ nm and $d_b \approx 0.15$ nm results in the value of $\sigma_b \approx 1 \cdot 10^{10}$ Pa.

The degree of elastic deformation for the graphene nanoblister walls, apparently reaches $\varepsilon_b \approx 0.1$ (Fig. 1). Hence, with Hooke’s law of approximation, using the second part of Eq. (2), one can estimate, with the accuracy of one order of the magnitude, the value of the Young’s modulus for the graphene nanoblister walls: $E_b \approx (\sigma_b/\varepsilon_b) \approx 0.1$ TPa. It is close (within reasonable error) to the experimental value [13, 14] for the Young’s modulus of perfect (that is, without defects) graphene ($E_{graphene} \approx 1.0$ TPa).

Similar STM, AFM and other data from different researchers for epitaxial graphenes (for instance, Fig. 2) can be analyzed and interpreted in a similar manner [11, 12], within the same physical concept (Eqs. 1, 2).

In this connection, it is expedient to note that a number of researchers (for instance, [15, 16]) have not sufficiently considered the “thermodynamic forces” and/or energetics of formation (under the atomic hydrogen treatment) for graphene nanoblisters in the surface HOPG layers and epitaxial graphenes.

It is also expedient to note that very recent experimental data [17] show that a hydrogen atom can not pass through a perfect graphene network. Conversely, the analysis [11, 12] of a number of experimental data (including Fig. 1, 2) shows that a hydrogen atom can pass through permeable defects in graphene, for instance, through triple junctions of grain boundaries. In Fig. 2 a and b, one can imagine some grain boundary network substituted (obviously, in some nano-regions at grain boundaries) by some nano-protrusions.

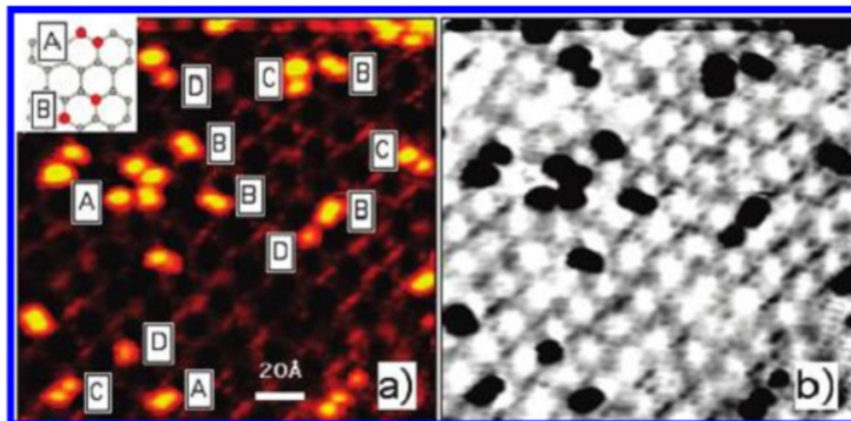


FIG. 2. (a) STM image of hydrogenated graphene/SiC. (b) Same image as in (a) with inverted color scheme, giving emphasis to preferential hydrogen adsorption on the SiC surface. Hydrogen dose at $T_{(beam)} = 1600$ K, $t = 5$ s, $F = 10^{12} - 10^{13}$ atoms/cm² · s ($P_{(Hgas)} \approx 1 \cdot 10^{-4}$ Pa [11, 12])

3.2. The physics of intercalation of the solid H₂ nanophase into hydrogenated graphite nanofibers (with metallic catalysts)

The physics for the intercalation of high density solid molecular hydrogen ($\rho_{H_2} \approx 0.5 \text{ g/cm}^3$, Fig. 3) into closed (in the definite sense) nanoregions in hydrogenated GNFs (Fig. 4) is related to the same concept, Eqs. of type (1), (2) [11, 12].

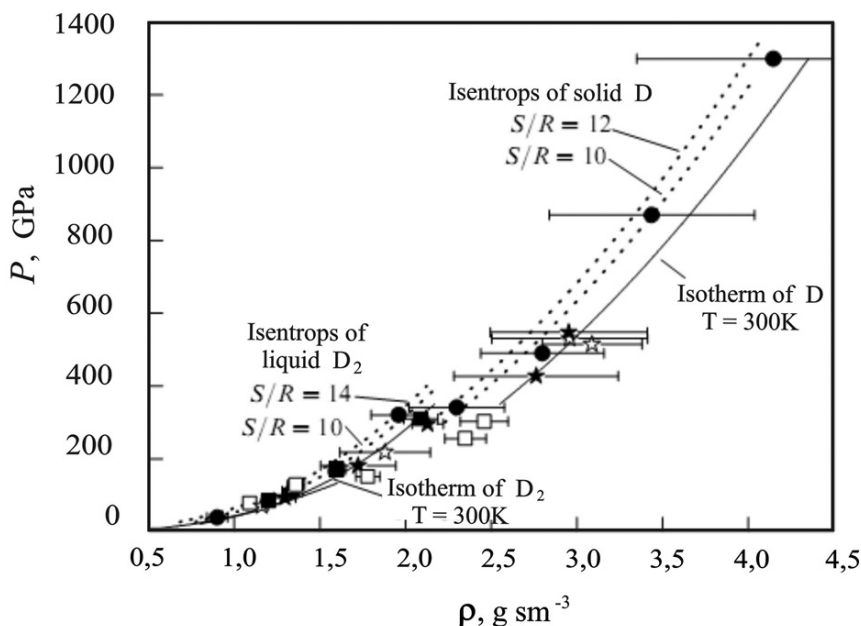


FIG. 3. Data on isentropes (S/R) and isotherms for deuterium and protium. The density (ρ) of protium (H_2 , H) is increased by a factor of two (for the scale reasons). The experimental and theoretical isotherms show that at $T = 300 \text{ K}$ and the external compression pressure of $P = 50 \text{ GPa}$ hydrogen exists in a high density solid molecular state $\rho_{H_2} \approx 0.5 \text{ g/cm}^3$ [12]

Obviously, it is a manifestation of the spillover effect, relevant to providing the necessary partial pressure of atomic gaseous hydrogen (with material hydrogenation at an initial molecular hydrogen pressure $P_{H_2} = 8 \text{ MPa}$).

4. Conclusions

The “thermodynamic forces” and energetics of forming of graphene nanoblister (under atomic hydrogen treatment, without catalysts) in the surface HOPG layers (Fig. 1) and epitaxial graphenes (Fig. 2) are quantitatively described, particularly, two conditions of the thermal-elastic thermodynamic equilibrium – Eqs. (1),(2) – are considered.

The physics for the intercalation of a high density gaseous H₂ nanophase ($\rho_{H_2} \approx 0.045 \text{ g/cm}^3$) into graphene nanoblister (Figs. 1, 2) is considered – Eqs (1), (2). The hydrogen compression effect of 12 orders of magnitude (from $P_{(H_{gas})} \approx 1 \cdot 10^{-4} \text{ Pa}$ to $P_{(H_{2gas})} \approx 1 \cdot 10^8 \text{ Pa}$), at the expense of the energy of association of hydrogen atoms to the “captured” molecules, is shown.

The physics for the intercalation of the high density solid H₂ nanophase ($\rho_{H_2} \approx 0.5 \text{ g/cm}^3$, [18]) into hydrogenated graphite nanofibers with Pd-catalyst (Figs. 3, 4) is considered.

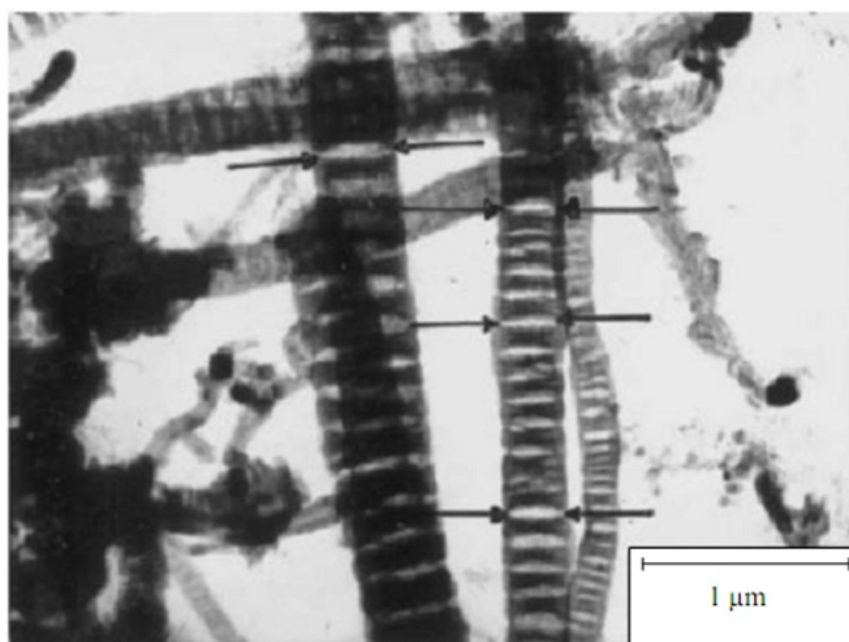


FIG. 4. Micrograph of hydrogenated graphite nanofibers (GNFs), with Pd-catalyst (hydrogenated at 300 K and an initial pressure of $P_{(H_2gas)} \approx 8$ MPa), after release from them, at 300 K, for 10 min, of the intercalated solid H_2 nanophase (17 wt%) of a high density of $\rho_{H_2} \approx 0.5$ g/cm³ (analysis [11, 12]). The arrows in the picture indicate some of the slit-like closed nanopores of the lens shape, where the solid H_2 intercalated nanophase (under pressure of ~ 50 GPa, according to data on Fig. 3) was localized. Such a pressure level can be also evaluated by the consideration of the material deformation and the necessary stresses for forming the lens shape closed nanopores (at the expense of the energy of association of hydrogen atoms to molecules “captured” inside the nanopores, Eqs. of type (1), (2)

In the light of analysis [11,12], the spillover effect is obviously manifested in the extraordinary data [19].

This effect can be used for solving of the current problem of the efficient and safe hydrogen on-board storage [20].

Acknowledgements

This work has been supported by the RFBR (Project #14-08-91376 CT) and the TUBITAK (Project # 213M523).

References

- [1] Juarez-Mosqueda R., Mavrandonakis A., Kuc, A.B., Pettersson L.G. M., Heine T. Theoretical analysis of hydrogen spillover mechanism on carbon nanotubes. *Front Chem.*, 2015, **3**(2).
- [2] Han S.S., Jung H., Jung D. H., Choi S.-H., Park N. Stability of hydrogenation states of graphene and conditions for hydrogen spillover. *Phys. Rev. B*, 2012, **85**, P. 155408.
- [3] Bhowmick R., Rajasekaran S., Friebel D., Beasley C., Jiao L., Ogasawara H., Dai H., et al. Hydrogen spillover in Pt-single-walled carbon nanotube composites: formation of stable C-H bonds. *J. Am. Chem. Soc.*, 2011, **133**, P. 5580–5586.
- [4] Chen L., Cooper A. C., Pez G. P., Cheng H. Mechanistic study on hydrogen spillover onto graphitic carbon materials. *J. Phys. Chem. C*, 2007, **111**, P. 18995–19000.

- [5] Lachawiec A.J., Qi G., Yang R.T. Hydrogen storage in nanostructured carbons by spillover: bridge-building enhancement. *Langmuir*, 2005, **21**, P. 11418–11424.
- [6] Psfogiannakis G.M., Froudakis G.E. DFT study of the hydrogen spillover mechanism on Pt-Doped graphite. *J. Phys. Chem. C*, 2009, **113**, P. 14908–14915.
- [7] Yang F.H., Lachawiec A.J., Yang R.T. Adsorption of spillover hydrogen atoms on single-wall carbon nanotubes. *J. Phys. Chem. B*, 2006, **110**, P. 6236–6244.
- [8] Yang R.T., Wang Y. Catalyzed hydrogen spillover for hydrogen storage. *J. Am. Chem. Soc.*, 2009, **131**, P. 4224–4226.
- [9] Li Y., Yang R.T. Significantly enhanced hydrogen storage in metal-organic frameworks via spillover. *J. Am. Chem. Soc.*, 2006, **128**, P. 726–727.
- [10] Zacharia R., Rather S., Hwang S.W., Nahm K.S. Spillover of physisorbed hydrogen from sputter-deposited arrays of platinum nanoparticles to multi-walled carbon nanotubes. *Chem. Phys. Lett.*, 2007, **434**, P. 286–291.
- [11] Nechaev Yu.S., Veziroglu T.N. On the hydrogenation-dehydrogenation of graphene-layer-nanostructures: Relevance to the hydrogen on-board storage problem. *International J. Phys. Sci.*, 2015, **10**(2), P. 54–89.
- [12] Nechaev Yu.S., Veziroglu T.N. Thermodynamic aspects of the stability of the graphene/graphane/hydrogen systems, relevance to the hydrogen on-board storage problem. *Adv. Mater. Phys. Chem.*, 2013, **3**, P. 255–280.
- [13] Lee C., Wei X., Kysar J.W., Hone J. Measurement of the elastic properties and intrinsic strength of monolayer graphene. *Science*, 2008, **321**(5887), P. 385–388.
- [14] Pinto H.P., Leszczynski J. Fundamental properties of graphene. In: *Handbook of Carbon Nano Materials*. Vol. 5 (Graphene – Fundamental Properties), Eds. F. D'Souza, K.M. Kadish, World Scientific, New Jersey, 2014, P. 1–38.
- [15] Waqar Z. Hydrogen accumulation in graphite and etching of graphite on hydrogen desorption. *J. Mater. Sci.*, 2007, **42**(4), P. 1169–1176.
- [16] Balog R., Jørgensen B., Wells J., Lægsgaard E., Hofmann P., Besenbacher F., Hornekær L. Atomic hydrogen adsorbate structures on graphene. *J. Am. Chem. Soc.*, 2009, **131**(25), P. 8744–8745.
- [17] Hu S., Lozada-Hidalgo M., Wang F.C., Mishchenko A., Schedin F., Nair R.R., Geim A.K. Proton transport through one atom thick crystals. *Nature*, 2014, **516**, P. 227–230.
- [18] Trunin R.F., Urlin V.D., Medvedev A.B. Dynamic compression of hydrogen isotopes at megabar pressures. *Phys. Usp.*, 2010, **53**, P. 605–622.
- [19] Gupta B.K., Tiwari R.S., Srivastava O.N. Studies on synthesis and hydrogenation behavior of graphitic nanofibers prepared through palladium catalyst assisted thermal cracking of acetylene. *J. Alloys Compd.*, 2004, **381**, P. 301–308.
- [20] Nechaev Yu.S., Yurum A., Tekin A., Yavuz N.K., Yuda Yurum, Veziroglu T.N. Fundamental open questions on engineering of super hydrogen sorption in graphite nanofibers: Relevance for clean energy applications. *Am. J. Anal. Chem.*, 2014, **5**(16), P. 1151–1165.

TEM study of structure of graphene layers in shungite carbon

V. V. Kovalevski, I. A. Moshnikov

Institute of Geology, Karelian Research Center, RAS, Petrozavodsk, Russia

kovalevs@krc.karelia.ru, igorm@krc.karelia.ru

PACS 68.37.Og, 61.48.-c

DOI 10.17586/2220-8054-2016-7-1-210-213

Shungites have been studied by high-resolution transmission electron microscopy (HRTEM). Two types of carbon layers have been revealed in shungites by HRTEM. The first type, graphite-like carbon layers are characterized by strongly marked hexagonal symmetry. The second type are remarkable for imperfections connected with insignificant disorder in the direction of fringes and the distance between them, and can result from point defects or the pentagonal and heptagonal carbon rings that are signs of fullerene-like structures.

Keywords: Shungite, High-resolution electron microscopy, Molecular structure.

Received: 20 November 2015

1. Introduction

One of the more intriguing types of non-crystalline carbon occurs in the shungite rocks of Karelia (Russia), from which the first natural occurrence of fullerenes was reported [1] and hollow nanospheres and fibers were described [2]. Shungite rocks are remarkable for very complex genesis defined by an alternation of sedimentary and volcanic processes with diabase and hydrothermal intrusions [3]. There is no consensus in the literature regarding the origin of shungite rocks. Many hypotheses have been proposed, including biogenic, metasomatic, metamorphic and volcanogenic modes of origin together or separately. Shungite rocks are natural composite materials with interpenetrating carbon and mineral matrices. Carbon from shungite rocks is of the non-graphitizable variety and is characterized by turbostratic stacking of the carbon layers. Furthermore, carbon from shungite rocks demonstrates some fullerene-like characteristics on different structural and physical levels. For example, a distinctive feature of some shungites is the considerable increase in the diamagnetism at liquid-nitrogen temperatures with a temperature range and amount of change similar to that of CuC_{60} [4]. The effect is likely sensitive to the structure of the carbon layers and the presence of trace elements and has not been reported for amorphous natural carbon and graphite but has been observed for doped fullerenes. All types of shungite rocks have variable physico-chemical properties depending on the shungite structure, C content, the composition and characteristics of minerals and distribution of carbon and minerals. Unfortunately, there are no direct structural data sustaining an occurrence of faultiness of carbon layers in shungites. The goal of this study is to clarify structural features of carbon layers of the natural carbon.

2. Experimental and results

A JEOL 4000 EX and HB-5 electron microscopes were used for the high-resolution electron microscopy (HRTEM) and for nanodiffraction study [5]. Samples of shungites from Nigozero, Shunga, Maksovo, Zazhogino and Chebolaksha deposits were powdered in water and precipitated onto lacey carbon films placed on copper grids. Images were recorded photographically and processed, as reported elsewhere [5].

All high-resolution transmission electron microscopy (HRTEM) images of shungites contain well-defined fringes, and these occur in packets of 5 to 14 sheets (Fig. 1). Those suggest that some 3-dimensional closed shells occur but, more commonly, there are fractions of such shells or regions of graphene structure that are highly disordered into short bent stacks and enveloped nano-sized pores. Some graphene layers form irregular closed shells, similar to those in carbon nanotubes [5]. A number of nanodiffraction patterns obtained in the stationary beam with a diameter of 0.7 nm, contains several spots corresponding to the distance of 0.34 nm, indicating the presence in the illuminated areas of packages consisting of graphene layers that are almost parallel to the incident beam. For some areas, the obtained nanodiffraction pictures with hkl reflections that meet the 3-dimensional order in the packing of layers, including, for example, hexagonal (ABABA..) and rhombohedral (ABCABC..) graphite [5]. However, their hkl where these reflexes are observed, are weak, diffuse, and are parallel to the 00l reflections, which would seem to indicate poorly structured packing layers. In general, for shungites, there are typical nanodiffraction patterns from graphene layers, approximately perpendicular to the incident beam and containing, reflexes, close to the 100 and 110 reflections of graphite, i.e. azimuthal disordered layers.

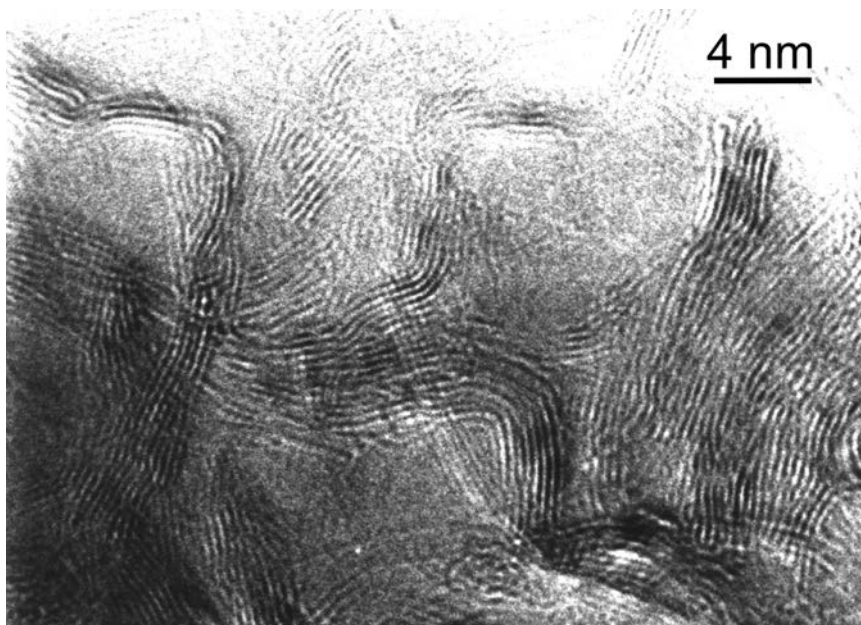


FIG. 1. HRTEM image of a thin region at the edge of Zazhogino shungite

No single extended carbon layers, which could represent graphenes were found. The exception to this were smoothly curved short-length layers up to 10 nm, forming open and closed structures, including, similar in configuration and size, fullerenes C_{240} and C_{560} (Fig. 2) [6].

Two types of carbon layers have been revealed in shungites by HRTEM (Fig. 3). Note that both types of layers in Fig. 3 form packets including at least eight and three layers. The first type, graphite-like carbon layers are characterized by strongly marked hexagonal symmetry, but are corrugated layers. The layers consist of domains about 1 nm in diameter, some of those are elevated and form hillocks and others are down and form hollows. The distance between hillocks and hollows is about 2 nm (left image in Fig. 3).

Imperfections of the latter type of carbon layers on the molecular level connected with irregularities of 100 fringes that suggest a disorder of the carbon layers from HRTEM images. Some of those are connected with essential disorder of fringes that may result from the presence

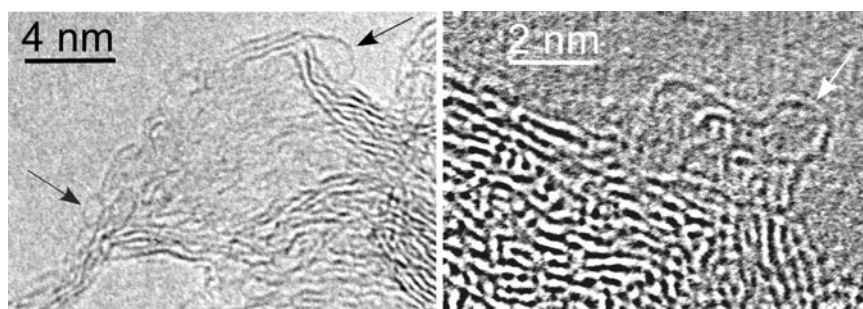


FIG. 2. HRTEM images of a thin regions at the edge of Chebolaksha (left) and Maksovo shungites. The left figure demonstrates smoothly curved short-length carbon layers (arrowed), right one shows objects (arrowed) that are similar in form and size to higher fullerenes

of impurity atoms or clusters in the stack of carbon layers (*i* in Fig. 3). Other imperfections connected with insignificant disorder in the direction of fringes and the distance between them are a result of the pentagonal and heptagonal carbon rings. Those can be deduced from the electron density distribution and the number of adjacent carbon rings bonded with the pentagonal and heptagonal ones (*p* and *h* respectively in Fig. 3). The change of the electron microscopy contrast testifies to the effect that the layers are also corrugated.

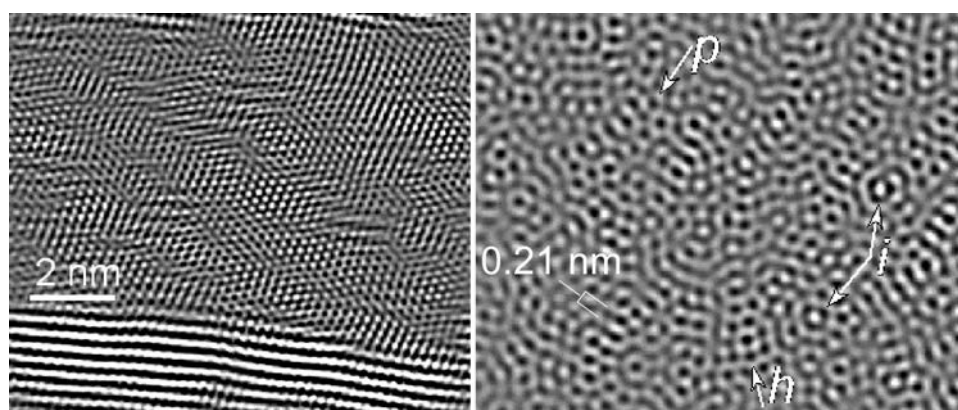


FIG. 3. HRTEM images (after Fourier filtration) of graphite-like (left) and fullerene-like carbon layers (*p* – pentagonal, *h* – heptagonal carbon rings, *i* – noncarbon inclusions) in Maksovo shungite

3. Discussion

HRTEM studies have shown that in shungites, usually 5 to 14 carbon layers are stacked together with 3.4 Å spacing, but no single extended carbon layers were observed at all. There are short-length layers, forming open and closed nano-sized structures, among them similar in configuration and size to higher fullerenes. Extended carbon layers forming packets in shungites are corrugated to a greater or lesser extent. Two types of the carbon layers have been established in shungites by HRTEM. Carbon layers of the first type are characterized by clear two-dimensional hexagonal symmetry without any significant amount of impurity atoms and may be specified as graphite-like ones. It should be noted that the corrugation leads to an increase of the cohesive energy between adjacent carbon layers owing to the formation of potential wells and may result in the characteristic properties of graphene quantum dots [7]. Carbon layers

of the latter type consist of not only hexagonal but also pentagonal and heptagonal carbon rings that are signs of fullerene-like structures [8]. Thus, those may be specified as fullerene-like carbon layers. The left Fig. 3 image offers not a single carbon layer but a packet enclosed three layers. Additionally, the HRTEM image of those demonstrates some clusters that have essentially more electron scattering than an ambient carbon layer and therefore might contain metal atoms. After the Fourier filtration, the clusters present as isolated contrasting dots (i in Fig. 3) that on the basis of their sizes are not only the intralayer, but also interlaminar defects. The clusters also change the band structure of shungites and may alter some physicochemical properties [4, 7].

Acknowledgements

This work was supported in part by the RFBR grant 13-05-98811.

References

- [1] Buseck P.R., Tsipursky S.J., Hettich R. Fullerenes from the geological environment. *Science*, 1992, **257**, P. 215–217.
- [2] Kovalevski V.V., Safronov A.N., Markovski Ju.A. Hollow carbon microspheres and fibres produced by catalytic pyrolysis and observed in shungite rocks. *Mol Mater.*, 1996, **8**, P. 21–24.
- [3] Chazhengina S.Y., Kovalevski V.V. Structural characteristics of shungite carbon subjected to contact metamorphism overprinted by greenschist-facies regional metamorphism. *Eur. J. Mineral.*, 2013, **25**, P. 835–843.
- [4] Kovalevski V.V., Prikhodko A.V., Buseck P.R. Diamagnetism of natural fullerene-like carbon. *Carbon*, 2005, **43**(2), P. 401–405.
- [5] Kovalevski V.V., Buseck P.R., Cowley J.M. Comparison of carbon in shungite rocks to other natural carbons: An X-ray and TEM study. *Carbon*, 2001, **39**, P. 243–256.
- [6] Mordkovich V.Z. The observation of large concentric shell fullerenes and fullerene-like nanoparticles in laser pyrolysis carbon blacks. *Chem. Mater.*, 2000, **12**, P. 2813–2818.
- [7] Razbirin B.S., Rozhkova N.N., Sheka E.F., Nelson D.K., A.N. Starukhin, A. S. Goryunov. Spectral properties of shungite quantum dots. *Nanosystems: Phys., Chem., Math.*, 2014, **5** (2), P. 217–233.
- [8] Cataldo F. The impact of a fullerene-like concept in carbon black science. *Carbon*, 2002, **40**(2), P. 157–162.

Electrophysical properties of shungites at low temperatures

I. A. Moshnikov, V. V. Kovalevski

Institute of Geology, Karelian Research Center, RAS, Petrozavodsk, Russia

igorm@krc.karelia.ru, kovalevs@krc.karelia.ru

PACS 81.05.U, 91.60.Pn

DOI 10.17586/2220-8054-2016-7-1-214-219

The temperature dependence of electrical conductivity and the shielding effectiveness of shungites have been studied at temperatures ranging from 77 to 300 K. The idiosyncrasies of temperature dependences for measuring electrical parameters were determined. Correlations of the $\pi + \sigma$ plasmon energies with changes in the frequency dependence of shielding effectiveness on temperature were determined.

Keywords: shungite rocks, carbon, shielding effectiveness, electrical conductivity.

Received: 20 November 2015

1. Introduction

Shungite rocks are ancient carbonaceous volcanic-sedimentary rocks found in Karelia. Shungite rocks consist of a carbon matrix (shungite) with micro- and nano-dispersed mineral components and can be regarded as carbon-mineral composites. On the assumption of the molecular, permolecular and band structure, shungite can be described as a natural nanostructured fullerene-like carbon with some unique physical and chemical properties [1,2].

Electromagnetic properties are of special interest, as they are the most informative and relevant characteristics of carbon materials necessary for modern technologies. These properties of carbonaceous materials are closely related to their band and atomic structures and are directly determined by the degree of graphitization, the size of the crystallites, the length and imperfection of the graphene layers, etc. For a particular carbon-bearing material, some structural characteristics that largely affect its electromagnetic properties can be distinguished. For example, deficiencies and nanotube chirality have a significant influence on their conductivity type [3]. Also, the deficiencies of carbon nanotubes have an influence on their temperature effect for the transition from metallic to a semiconducting type of conductivity [4].

It is also possible to identify some structural characteristics for shungites which have a great effect on their electromagnetic properties. The conductivity type of shungites, for example, can be significantly determined at low currents by the intercalation of elements on the boundaries of graphene layers [5]. Also, the intercalation of carbon materials may have a significant impact on their electromagnetic properties. For example, the intercalation of pyrolytic graphite with copper and oxygen results in a temperature effect for the transition from metallic to a semiconducting conductivity [6].

One of the most sensitive physical properties to band and atomic structure of solids is magnetic susceptibility [7]. The magnetic susceptibility of shungites with different permolecular structures differed significantly at temperatures from 90 to 150 K [8]. The diamagnetic effect is the greatest for samples with preferable orientation of carbon layers and is not observed for shungites with chaotic layer orientation.

2. Experimental

Shungite rocks with high carbon content (shungites) of different origins from Maksovo, Nigozero, Zazhogino, Chebolaksha and Shunga deposits were selected. The samples were powdered and electrophysical parameters, such as the conductivity and the shielding effectiveness were measured at low and room temperatures. The electrical conductivity (σ) was measured in a coaxial line by the E7-8 meter at a frequency of 1 kHz. The shielding effectiveness (SE) was determined using a selective microvoltmeter SMV 8.5 and SMV 11 at frequencies ranging from 100 kHz to 1 GHz. Cooling of the coaxial line was carried out by liquid nitrogen. For comparison, the same measurements were performed for pyrolytic graphite, pyrobitumen of the “Iron river” deposit and carbonaceous matter of “Erickson gold mine” deposit. The Philips 400 FEG electron microscope with Gatan PEEL spectrometer was used to reveal the $\pi + \sigma$ plasmon energies of various shungites.

The electrical conductivity-temperature dependence of shungite from the Shunga deposit has been defined as a nonmonotonic function. First, the electrical conductivity decreases as temperature increases from 130 to 180 K, which is remarkable for metals, and then it increases from 220 to 260 K, which is typical for semiconductors (Fig. 1). The same effect was also observed for carbonaceous matter from the Erickson deposit with carbon structure similar to that of shungites.

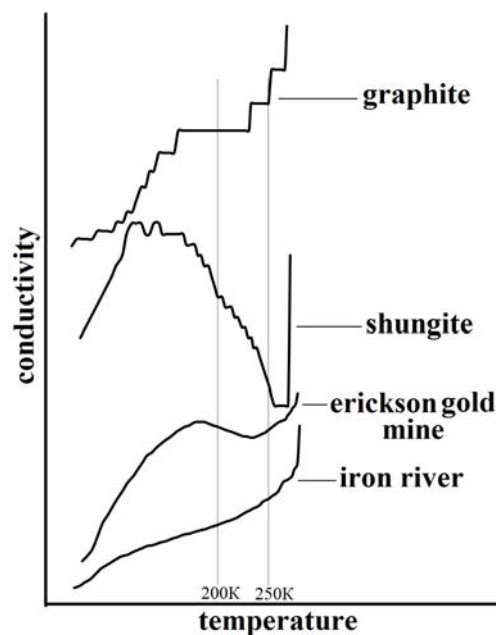


FIG. 1. The electrical conductivity-temperature dependence of pyrolytic graphite, shungite, pyrobitumen of the Iron river deposit and carbonaceous matter of Erickson deposit

Cooling of all samples by liquid nitrogen generally leads to lower values of the shielding effectiveness over the entire measured frequency range. Thus, a slower increase in the shielding effectiveness with electromagnetic field frequency was observed at temperatures less than room temperature. The revealed frequency dependence of shielding effectiveness as function of temperature is different for various shungite rocks as shown in Fig. 2.

To quantify the observed effect, the value Δ as a rate of change of the shielding effectiveness against frequency has been calculated. Those values as a result of the shielding

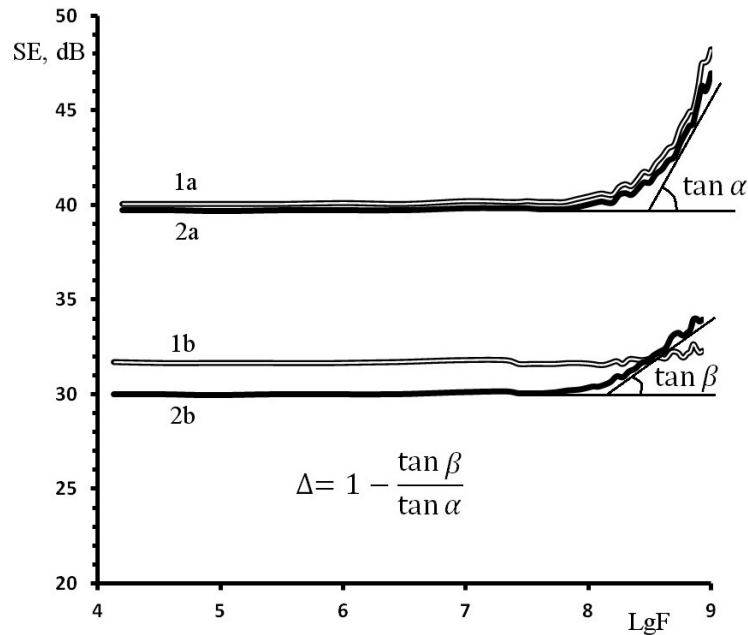


FIG. 2. Dependence of shielding effectiveness of shungite rocks on electromagnetic field frequency. 1a – deposit Maksovo $T \sim 300$ K, 1b – deposit Maksovo $T \sim 77$ K, 2a – deposit Shunga $T \sim 300$ K, 2b – deposit Shunga $T \sim 77$ K

TABLE 1. The shielding effectiveness (SE), the Δ values and the $\pi + \sigma$ plasmon energies for various shungites

Deposit	SE (750 MHz, 300 K), dB	SE (750 MHz, 77 K), dB	Δ	Energy $\pi + \sigma$, V
Maksovo	48	32	0.55	24.9
Nigozero	46	31	0.60	25.1
Zazhogino	60	42	0.70	25.3
Chebolaksha	48	33	0.90	26.3
Shunga	49	32	0.95	26.0

effectiveness – frequency change at different temperatures (Δ in Fig. 2) have a fairly good correlation with the $\pi + \sigma$ plasmon energies of shungites, which are responsible for the bond strengths of valence electrons (Table 1). Namely, as can be deduced from the table, the higher the energy, the slower the shielding effectiveness growth with frequency at lower temperatures.

Studies of the shielding effectiveness at 750 MHz as a function of temperature (ranging from 77 K to 300 K) showed that the change in the shielding effectiveness is not monotonic for the studied shungites. At least three differing regions of the function occur for the shungites and carbonaceous matter from the gold Erickson deposit. An increase in the shielding effectiveness from 77 K to about 180 K was observed, then in the 180 – 200 K temperature range, it decreases, and at about 230 – 250 K temperature it once again increases. Similar variations for the shielding effectiveness versus temperature were not observed for graphite and pyrobitumen from the Iron river deposit, where the shielding efficiency increases for those materials were more monotonous (Fig. 3).

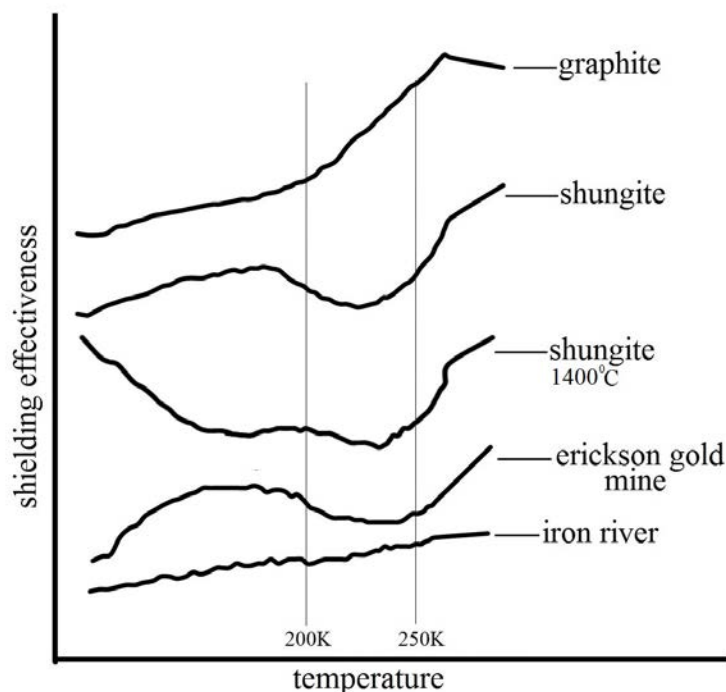


FIG. 3. Temperature dependence of the shielding effectiveness for pyrolytic graphite, shungite, heat-treated (1400 °C) shungite, pyrobitumen of the Iron river deposit and carbonaceous material of the Erickson deposit

To define the possible effect of bound water on the shielding effectiveness growth function, similar studies of the heat-treated shungite (1400 °C) have been performed. The 1400 °C boundary temperature is one that leads to complete water extraction without causing any structural change to the shungite carbon. The shielding effectiveness at 750 MHz from 77 to 300 K for the heat-treated shungite has demonstrated a function similar to that of untreated shungite (Fig. 3). This result provides evidence against water having an effect on the shielding effectiveness growth function.

3. Discussion of the results

Changes in electrical conductivity as a function of temperature obtained in our experiments is similar to that described in [9] for semiconductors, in which the charge carrier can be small radius polarons (Fig. 4). Based on the presented model, it is shown that at low temperatures electrons are mainly related to the donors (area 1). At temperatures below $\frac{1}{2}\Theta$ (where Θ is the Debye temperature) an electron transfers a charge like a heavy particle, being scattered by impurities or lattice vibrations, so the electrical conductivity decreases with increasing temperature (area 2). At temperatures above $\frac{1}{2}\Theta$ the electrical conductivity becomes hopping and increases with temperature increasing (area 3) [9]. Based on values of Θ , determined from the heat capacity curves for Shunga and Maksovo shungites, respectively 420 and 530 K [10], the temperature ranges over which the effect was observed in our experiment and was described in [9] are similar. An anomaly of the temperature dependence of the electrical conductivity has been reported for shungites as a jump in its growth at about 180 K [11]. The effect was accounted for by the occurrence of fullerenes in shungites. In our studies, a jump in the growth of the shungites' electrical conductivity was not observed, rather a smooth change occurred over a similar temperature range.

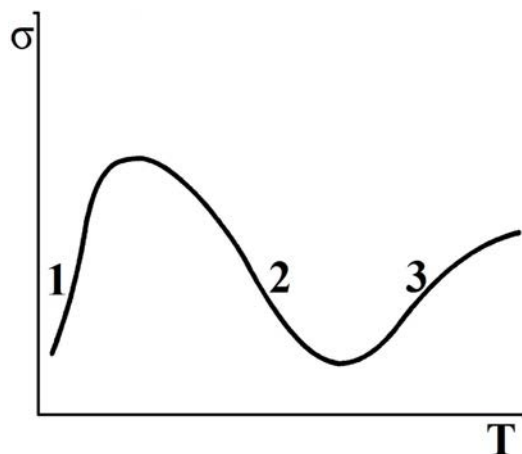


FIG. 4. Typical dependence of electrical conductivity on temperature for a crystalline semiconductor, when the carriers are polarons [9]

We believe that, the behavioral features of the electrical characteristics revealed in our experiments may be a result of many factors. In addition to the influence of structural parameters, such factors as shape and condition of the surface of particles, the presence of moisture and other contact phenomena may also have an effect. The fact that temperature relationships with electrical conductivity and shielding effectiveness were observed only for shungites and Erickson carbonaceous matter (which is similar to shungite in structure) provides evidence for the carbon structure's influence on the effects. The correlation of energy values for the $\pi + \sigma$ plasmon with a change in the frequency dependence of shielding effectiveness on temperature indicates the participation of valence electrons in the shielding mechanism. The similarity of the electrical conductivity dependency on temperature for shungite, and that described for semiconductor materials, in which charge carriers can be polarons, suggests that the detected temperature effect may be associated with the mechanism for the interaction of phonons with charge carriers. Thus, it can be noted that the presence of such temperature effects may be associated with structural features of the shungite carbon, and with the presence of trace elements and non-periodic structural defects in shungite carbon layers, specifically.

Acknowledgements

This work supported in part by the RFBR grant 13-05-98811.

References

- [1] Kovalevski V.V. Shungite or higher anthraxolite? *Zapiski RMO*, 2009, **5**, P. 97–105.
- [2] Augustyniak-Jablokow M.A., Yablokov Y.V., Andrzejewski B., Kempinski W., Los S., Tadyszak K., Yablokov M.Y., Zhikharev V.A. EPR and magnetism of the nanostructured natural carbonaceous material shungite. *Phys. Chem. Minerals*, 2010, **37**(4), P. 237–247.
- [3] Bobenko N.G., Egorushkin V.E., Melnikova N.V., Ponomarev A.V. Low-temperature electrical resistivity in carbon nanotubes. Proc. "Carbon: fundamental problems of science, material science, technology". Troitsk, 2012, P. 65–66.
- [4] Babaev A.A., Hohlachev P.P., Terukov E.I., Nikojev Yu.A., Frenkin A.B., Filippov R.A., Filippov A.K. The temperature dependence of the resistivity of the composite films on the basis of multi-walled carbon nanotubes. *Phys. Solid State*, 2015, **55**(2), P. 404–407.
- [5] Golubev E.A. Electrophysical properties and structural features of shungite. *Phys. Solid State*, 2013, **55**(5), P. 995–1002.

- [6] Masterov M.A., Prichodko A.V., Konkov O.I. The metal-insulator transition and superconductivity in allotropes of carbon intercalated with copper: prediction and experiment. *Fuller. Sci. Technol.*, 1998, **6**(3), P. 481–497.
- [7] Heremans J., Olk C.H., Morelli D.T. Magnetic susceptibility of carbon structures. *Phys. Rev. B*, 1994, **49**(21), P. 15122–15125.
- [8] Kovalevski V.V., Prikhodko A.V., Buseck P.R. Diamagnetism of natural fullerene-like carbon. *Carbon*, 2005, **43**, P. 401–405.
- [9] Mott N.F., Davis E.A. *Electron processes in non-crystalline materials*. Mir, M, 1982, P. 107–108.
- [10] Tupolev A. G., Dukiev E. F. Heat capacity. *The shungit – a new carbonaceous matter*. Petrozavodsk, 1984, P. 84–89.
- [11] Parfenjeva L.S., Smirnov I.A., Zaydenberg, A.Z., Rozhkova N.N., Stefanovich, G.B. Electrical conductivity of shungite carbon. *Phys. Solid State*, 1994, **36**(1), P. 234–236.

Interaction of femtosecond laser radiation with carbon materials: exfoliation of graphene structures and synthesis of low-dimensional carbon structures

D. Abramov, S. Arakelian, D. Kochuev, S. Makov, V. Prokoshev, K. Khorkov

Vladimir State University, Vladimir, Russia

awraam@mail.ru, arak@vlsu.ru, _b_@mail.ru, stephan.makov@gmail.com,
prokoshev_vg@vlsu.ru, freeod@mail.ru

PACS 81.05.-t, 42.62.Cf

DOI 10.17586/2220-8054-2016-7-1-220-225

Carbon is represented in modern nanomaterials by a large variety of modifications. Various methods and technologies have been developed to create these various forms. Methods utilizing laser irradiation constitute a large portion of these techniques. The action of laser pulses upon graphite may result in the exfoliation of graphene layers. This paper presents the results of implementing method of laser-induced cleavage of graphite in liquid nitrogen using femtosecond laser radiation pulses. The process of obtaining graphene from the laser processing of graphite is accompanied by the formation of various types of low-dimensional carbon structures.

Keywords: graphene, carbon nanorods, laser synthesis, femtosecond laser.

Received: 20 November 2015

1. Introduction

Carbon is the basis for many of nanostructures and nanomaterials. Carbon nanotubes, fullerenes and graphene are the most well-known carbon nanostructures, however, this is not an exhaustive list of such materials. Graphene has attracted the attention of many scientists and industrial researchers due to its unique physical and chemical properties. However, the lack of a universal and inexpensive method for its synthesis hampers investigation of its properties and wide application of this promising material. Currently, numerous methods are available for the fabrication of graphene [1]. Among them are such basic techniques as micromechanical exfoliation of graphite, liquid phase exfoliation of graphite, graphite oxidation, chemical vapor deposition method, electric arc graphene production, thermal decomposition of silicon carbide, epitaxial growth of graphene on a metal surface and others. All these methods have their particular advantages and disadvantages. Therefore, research towards the development of methods for graphene fabrication has been extensively carried out.

The liquid phase exfoliation of graphite is a logical development of the classical method of micromechanical graphene fabrication [2]. The use of special chemical and technical conditions makes this method more efficient. Liquid surfactants weaken the bonds between the graphite layers. Ultrasonic treatment or centrifugation are then used to separate the graphene sheets. The development of the liquid-phase graphite exfoliation method has occurred with the aim of finding new solvents which may offer novel approaches for the separation of graphene sheets, which can provide increases in the synthetic yields and purity of the obtained graphene. We propose to use the liquid nitrogen and laser-induced exfoliation for these purposes.

The interaction of femtosecond laser radiation with materials is often accompanied by the formation of micro- and nanostructures on the irradiated surface [3]. The formation of nanorods or nanotips arrays in the case of structuring on the surface of carbon targets is a

distinct sub-interest. Such structures have potential for use in field emission displays or for hydrogen storage [4]. We have registered the formation of arrays of nanorods on the stage preceding the separation of graphene. These results are also presented in this paper.

2. Methods

Laser-induced liquid-phase exfoliation of graphite has been realized using a femtosecond laser radiation pulse. During this exfoliation the aim is to heat only the surface layer of a graphite target with the minimum possible thickness required to separate the surface from the graphene sheet layers underneath. Lasers with the least possible pulse duration of radiation can provide such conditions. Currently, femtosecond-pulse lasers are best suited for this purpose. Two femtosecond laser systems have been used in experiments for the fabrication of graphene. They are ytterbium industrial setup TETA-10 and experimental Ti:sapphire femtosecond laser system.

The irradiation parameters of TETA-10 were as follows: laser radiation wavelength $\lambda = 1029$ nm, pulse with $\tau = 300$ fs, energy per pulse $\varepsilon = 0.15$ mJ and pulse repetition frequency $f = 10$ kHz. This laser system was used in the first series of experiments. The reason for beginning this research with the TETA-10 laser system was because it is widely available for commercial industrial use. The energy characteristics of Ti:sapphire laser are larger and the radiation pulse is shorter than similar parameters for the ytterbium laser. These facts were the basis for theorizing about the possibility of increasing the speed of the graphene generation process when using such laser. Therefore, this latter system was used in the second series of experiments, which was performed to verify of the proposed hypothesis. The irradiation parameters for the Ti : sapphire laser system were as follows: laser radiation wavelength $\lambda = 800$ nm, pulse with $\tau = 50$ fs, energy per pulse $f = 1$ mJ and pulse repetition frequency $f = 1$ kHz. The laser beam was focused on the target surface in a spot with a diameter of $100 \mu\text{m}$ in both series of experiments. The laser beam was moved along the target surface at a speed of 0.01 m/s to 1 m/s.

Samples of the highly oriented pyrolytic graphite (HOPG) and glassy carbon were used as sources for obtaining the graphene. Laser processing of carbon targets was carried out in liquid nitrogen. The depth of a liquid nitrogen layer above the target surface was ~ 10 mm. The liquid nitrogen molecules easily penetrate into spaces between graphite layers. Once in between the graphene layers, the cryogenic liquid then undergoes evaporation during laser exposure. The gas phase expands, thus separating sheets of graphene. Successful application of liquid nitrogen in the liquid phase exfoliation of graphite was displayed in [5]. The authors of this paper used a Q-switched Nd:YAG nanosecond laser system. The process for obtaining graphene material lasted 20 minutes. Using femtosecond laser radiation allowed us to significantly enhance the rate of grapheme fabrication while maintaining comparable characteristics.

Moreover, liquid nitrogen also serves another function; it provides the rapid cooling of the irradiated target surface and attenuates the results of laser irradiation. Thus, potentially destructive laser processing side-reactions are minimized. We have successfully applied this approach to study the interaction of femtosecond laser radiation pulses on metals [6]. This has also shown good results in experiments on the synthesis of graphene and low-dimensional carbon structures.

The structures formed under femtosecond laser irradiation in liquid nitrogen were investigated by analyzing the images obtained using a scanning electron microscope (SEM) Quanta 200 3D.

3. Experimental results

Multi-layer graphene was obtained in both series of experiments. Exposure to a single laser pulse did not exfoliate the graphene sheets. Doing so only modified or destroyed the target surface (depending on the laser radiation intensity). Exfoliation graphene takes place under the influence of four laser pulses. Examples of obtained graphene structures are shown in Fig. 1. Exposure of fifth pulse femtosecond radiation leads to the destruction of obtained nanostructures. Irradiation with a required number of pulses has been provided by appropriate overlap of areas of laser action. The required overlap (75 %) corresponds to the velocity for the movement of the laser beam along the target surface 0.25 m/s at using of a ytterbium laser and 0.025 m/s in the case of treatment of graphite by of Ti : sapphire laser irradiation.

Graphene ribbons with a width up to 50 μm and a length of more than 150 μm and also an arbitrary shape graphene plates with a characteristic size up to 150 μm were registered after treatment of HOPG by ytterbium laser irradiation. The obtained graphene ribbons have folds but also have sufficiently extensive smooth surface portions (an area up to 2000 μm^2).

The graphene material fabricated with the use of Ti : sapphire laser consisted mainly of structures with linear dimensions on the order of a few micrometers. Typically cleaved sheets have numerous folds, although the individual sheets were characterized by a smooth surface and small number of folds. Some registered graphene structures ranged in size from 10 to 30 μm .

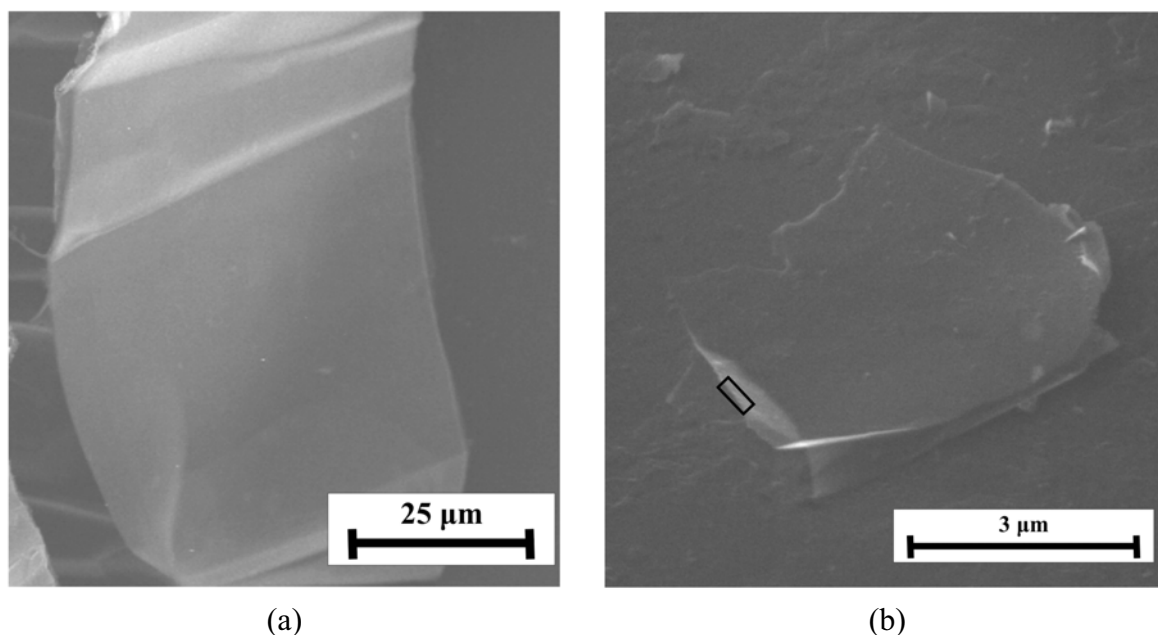


FIG. 1. Graphene structures on the HOPG surface: a – processing of graphite by radiation of ytterbium laser; b – processing of graphite by radiation of Ti : sapphire laser

Analysis of the SEM images of end faces of obtained structures allowed us to estimate their transverse dimensions. Graphene sheets with a thickness of 10 nm were detected (Fig. 2). It should be noted that traditional methods of micromechanical or liquid-phase exfoliation of graphite basically provides fabrication of a multilayer graphene sheets with a thickness of about 16 nm (according to [1]).

Laser treatment of surface of a glassy carbon samples in liquid nitrogen resulted in the fabrication of graphene in the form of crumpled sheets with characteristic structural sizes ranging from 1 to 2 μm and sheet thickness of about 20 nm.

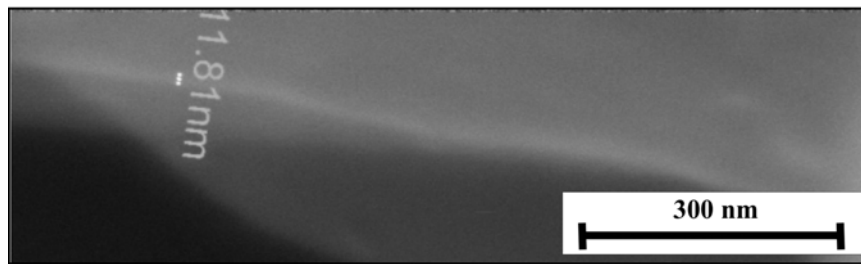


FIG. 2. Measuring the thickness of graphene structures. SEM image corresponds to an area that is highlighted by black rectangle in Fig. 1b

Carbon nanostructures in the form of vertical nanorods were formed on the surface of a graphite target when the number of pulses of laser radiation was less than that necessary for graphene sheet exfoliation. Areas with a random and regular arrangement of the nanorods are registered on the laser modified surface. In the latter case, nanorods are arranged in rows (Fig. 3). Here, nanorods have a diameter of ~ 100 nm, with a distance between rows (period of a total structure) of ~ 100 nm. The distance between the rods in a row is ~ 100 nm. The periodicity of the rows is 8 times smaller than the wavelength of the light used in the laser irradiation experiment. This ratio corresponds to the concept about the discrete changes in the periodicity of the regular structures of the relief, which is formed via the interaction of laser radiation with condensed media. This concept exists in the framework of the universal polariton model (see, for example, the review [7]). Moreover, the spatial changes must be multiples of the main period, which is determined by the wavelength of incident radiation.

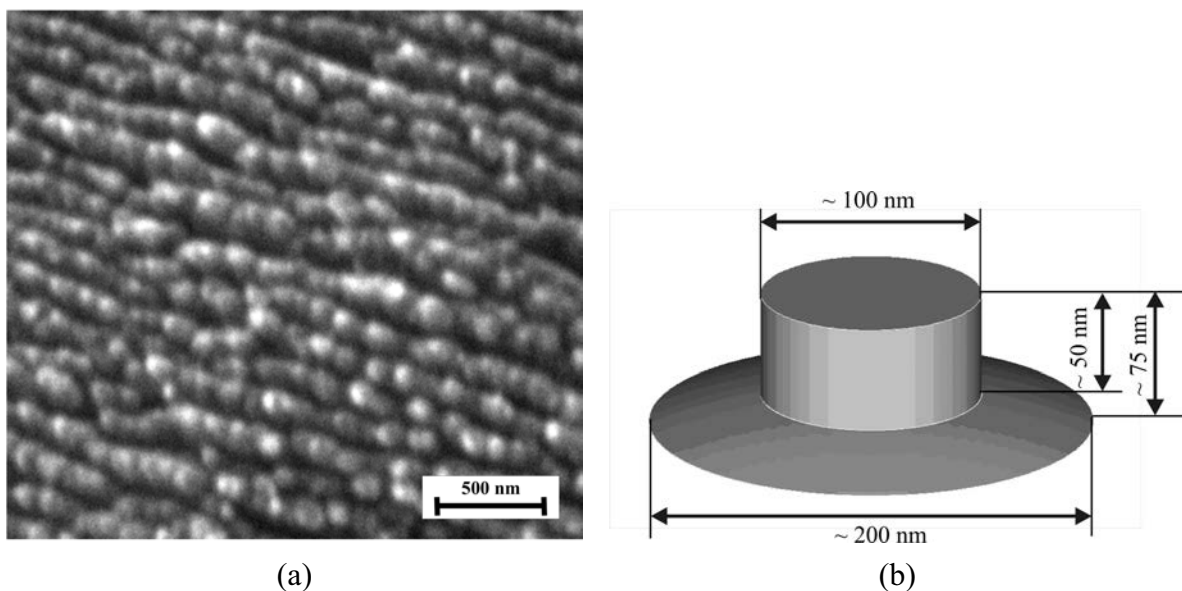


FIG. 3. The array of vertical carbon nanorods: a – SEM image; b – reconstruction of a single nanorod

Nanorods have a diameter of about 30 nm in regions with an irregular arrangement. The distance between the individual rods has a comparable value. Violation of the regularity of the registered nanorods is explained by some deviation from strict linearity, which is always present in the laser-induced periodic structures. For large-scale structures, these deviations

are not critical, but their influence is noticeable with decreasing periodicity of the structures. Nevertheless, the tendency to form rows is visible, even in the system of irregular nanorods.

The produced nanorods have been characterized by means of nanolaboratory Ntegra Spectra (NT-MDT, Zelenograd, Russia). The Raman spectrum for these structures is shown in Fig. 4. The spectrum was recorded under ambient conditions using a He-Ne (632.8 nm) laser source. The strong G-peak (1581 cm^{-1}) corresponds to small crystals of graphite. This significantly exceeds the dispersive D-peak (1344 cm^{-1}), which is dominant for glassy carbon under ambient conditions [8]. Thus, registered nanorods may be characterized as vertical graphite crystals with a small amount of lattice defects. The broadening of the Raman peaks is a consequence of the effect of the numerous edges in arrays of nanorods [9]. The weak 2D-band is shifted to 2700 cm^{-1} . This is typical for small-scale but the multilayer carbon structures [10].

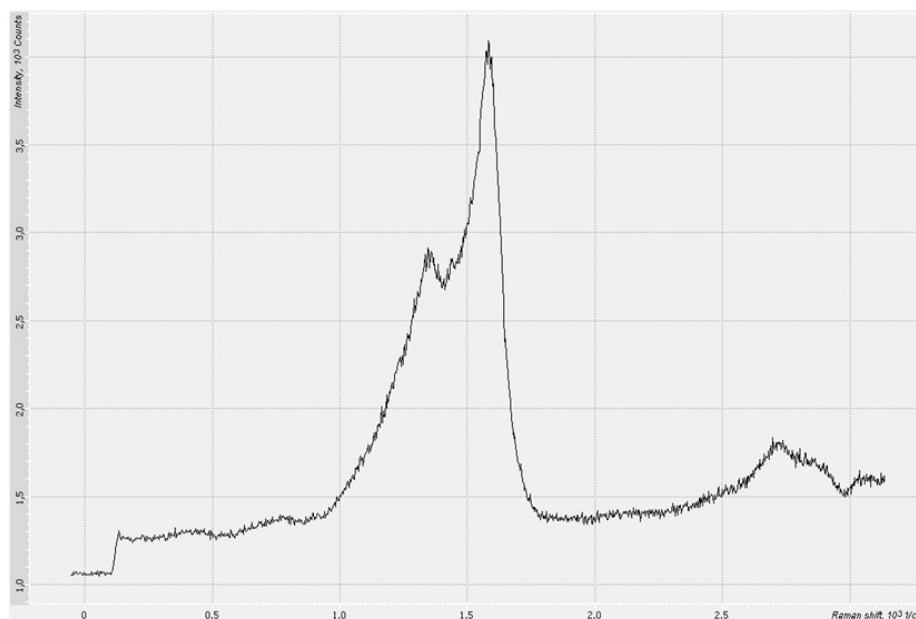


FIG. 4. Raman spectrum for array of nanorods

4. Conclusions

Experiments on the laser-induced liquid-phase exfoliation of graphite have demonstrated the possibility for effective application of femtosecond laser radiation pulses to produce graphene. The proposed approach not only allows short laser processing times, but also, in principle, the exclusion of a purification step for the obtained graphene, which is necessary for other methods which use additional chemical substances in their synthetic scheme. The geometric characteristics of the obtained graphene had similar parameters to that produced using currently-available experimental and commercial large scale syntheses. Also, the femtosecond laser processing of graphite in cryogenic liquids allows the formation of vertical carbon nanorod arrays on its surface.

Acknowledgements

This study was performed as part of the state task VISU 2014/13 to perform state works in the field of scientific studies and also supported under grant of the President of the Russian Federation for state support of the leading scientific schools of the RF NSh-89.2014.2 and grant of the Russian Foundation for Basic Research 14-02-97508.

References

- [1] Eletskiy A.V., Iskandarova I.M., Knizhnik A.A., Krasikov D.N. Graphene: fabrication methods and thermophysical properties. *Phys. Usp.*, 2011, **54**, P. 227–258.
- [2] Novoselov K.S., Jiang D., Schedin F., Booth T.J., Khotkevich V.V., Morozov S.V., Geim A.K. Two dimensional atomic crystals. *PNAS*, 2005, **102**(30), P. 10451–10453.
- [3] Makin V.S., Makin R.S. Nonlinear Interaction of Linearly Polarized Laser Radiation with Condensed Media and Overcoming the Diffraction Limit. *Optics and Spectroscopy*, 2012, **112**(2), P. 162–167.
- [4] Chu J., Peng X., Aldalbahi A., Panhuis M., Velazquez R., Feng P.X. A Simple Route to Carbon Micro- and Nanorods Hybrid Structure by Physical Vapor Deposition. *J. Phys. D: Appl. Phys.*, 2012, **45**(39), P. 395102.
- [5] Mortazavi S.Z., Parvin P., Reyhani A. Fabrication of graphene based on Q-switched Nd:YAG laser ablation of graphite target in liquid nitrogen. *Laser Phys. Rev. Lett.*, 2012, **9**(7), P. 547–552.
- [6] Abramov D.V., Arakelian S.M., Makov S.A., Prokoshev V.G., Khorkov K.S. Formation of a System of Microcraters on a Titanium Surface by Femtosecond Laser Radiation under Rapid Cooling Conditions. *Techn. Phys. Lett.*, 2013, **39**(8), P. 719–722.
- [7] Akhmanov S.A., Emel'yanov V.I., Koroteev N.I., Seminogov V.N. Interaction of powerful laser radiation with the surfaces of semiconductors and metals: nonlinear optical effects and nonlinear optical diagnostics. *Sov. Phys. Usp.*, 1985, **28**, P. 1084–1124.
- [8] Solopova N.A., Dubrovinskaia N., Dubrovinsky L. Raman spectroscopy of glassy carbon up to 60 GPa. *Appl. Phys. Lett.*, 2013, **102**(12), P. 121909.
- [9] Ferrari A.C. Raman spectroscopy of graphene and graphite: Disorder, electron-phonon coupling, doping and nonadiabatic effects. *Solid State Communications*, 2007, **143**, P. 47–57.
- [10] Zheng J., Liu H., Wu B., Guo Y., Wu T., Yu G., Liu Y., Zhu D. Production of high-quality carbon nanoscrolls with microwave spark assistance in liquid nitrogen. *Adv. Mater.*, 2011, **23**(21), P. 2460–2463.

Diffraction-based characterization of amorphous sp^2 carbon: sensitivity to domain-like packing of nanostructures

V. S. Neverov¹, P. A. Borisova¹, A. B. Kukushkin^{1,2}, V. V. Voloshinov³

¹National Research Center “Kurchatov Institute”, Moscow, Russia

²National Research Nuclear University “MEPhI”, Moscow, Russia

³Institute for Information Transmission Problems (Kharkevich Institute),
Russian Academy of Sciences, Moscow, Russia

vs-never@hotmail.com, borisova_pa@nrcki.ru, kukushkin_ab@nrcki.ru,
vladimir.voloshinov@gmail.com

PACS 61.05.F

DOI 10.17586/2220-8054-2016-7-1-226-233

We extend our method formerly suggested for structure refinement of the amorphous sp^2 carbon, based on neutron or x-ray diffraction, and applied to amorphous fullerene and its derivatives produced by vacuum annealing. To diagnose heterogeneous media, the method uses the rigid body molecular dynamics simulations of the domain-like packing for a predefined set of structural blocks. Previously, the sensitivity of the results to the variability of mutual positions of these structural blocks was analyzed in two limiting cases: (A) any domain contains only identical structural blocks and (B) all domains are the identical mixtures of many different structural blocks with variable packing of the blocks. Here, we extend this analysis to intermediate cases which correspond to domains of the type “B” with the subdomains of the type “A”. Such a structuring corresponds to a partial destruction of the nanoscale structure of the sample (e.g. by low-temperature annealing).

Keywords: neutron diffraction, computer simulation, C_{60} fullerenes, annealing, sp^2 carbon structures.

Received: 20 November 2015

1. Introduction

The neutron diffraction study [1] of amorphous C_{60} fullerene derivatives produced by vacuum annealing has shown the complete destruction of the initial sample structure at annealing temperatures higher than 850 °C. To obtain the quantitative characteristics of the resulting sample’s structure for various annealing temperatures, one has to solve an inverse problem, which is known to be a complicated task (see e.g. [2]): the lack of spatial ordering, typical to crystalline media, leaves much freedom in the reconstruction of structural content. The widely used Reverse Monte-Carlo (RMC) method [3], applied to the structure refinement of the similar material (annealed C_{60} fullerenes) [4] enabled the authors to quantify the structure of amorphous samples in terms of the number of edges in its carbon rings. The characterization of the structure on the space scale larger than the distances between neighboring atoms was impossible because the structure, recovered by the RMC modeling, was fully chaotic on that space scale. Despite it being possible to fit the atomic pair-distribution function (or the diffraction pattern) with a model structure of carbon sample, where the order is preserved only on the space scale of the nearest neighboring atoms, the respective model structure is not a unique solution of the original inverse problem.

In [5], we suggested a method for estimating the structural properties of amorphous sp^2 carbon and applied it to the samples studied in [1]. This method enabled us to quantify the

structural properties of the samples in terms of the average size and curvature of the sp^2 carbon structures (graphene-like flakes of 14 – 285 carbon atoms) as well as to estimate the fraction of the intact C_{60} fullerenes in the samples for each annealing temperature.

The main features of the method [5] are as follows: (i) we consider the fitting of the neutron or x-ray powder diffraction patterns for the scattering wave vector's modulus q in the range of a few to several tens of inverse nanometers (the inverse problems are formulated similar to that suggested in [6]); (ii) the sp^2 -structured component of a sample, including the flat and curved carbon flakes with graphene-like arrangement of atoms, is described with a limited number, N_{str} , of structural blocks of a limited number of atoms, N_{atom} ; (iii) the above structural blocks in a sample are packed heterogeneously, in the domains of linear size exceeding 10 nm (for q in the above-mentioned range, the interference of scattering by such separate domains may be neglected), with various average atomic density and various types of spatial ordering of structural blocks, defined by the total potential energy of the ensemble, U_{tot} ; (iv) packing of structural blocks in a domain is modeled using the rigid body molecular dynamics (RBMD) [7] with the Lennard-Jones potential of atom pair interactions in the neighboring rigid-body structural blocks with variable distance R_{opt} at which the potential reaches its minimum. The simulation starts with a random distribution of blocks and the highest value of U_{tot} , and the simulation ends with an ordered steady state which naturally possesses the lowest value of U_{tot} for given initial conditions.

In [5], we interpreted the neutron powder diffraction patterns from [1] for the amorphous C_{60} fullerene obtained by mechanical grinding and subsequent annealing in vacuum at various temperatures (600, 800, 850, 900 and 1000 °C). Hereinafter, we reference the annealed samples as S_{600} , S_{800} , S_{850} , S_{900} , S_{1000} , respectively, and the un-annealed sample (i.e. after mechanical grinding only) as S_{25} . The set of the candidate structural blocks of the total number of $N_{str} = 36$ included the C_{60} fullerene molecules and the sp^2 carbon flakes with graphene-like atom arrangements of various curvatures and sizes. The sensitivity of the results to the mutual positions of these structures was analyzed in [5] in the two limiting cases: (A) any domain (taken as an ensemble ranging in number from a few dozens to several thousand nanostructures) containing only identical structural blocks (mono-structural domains) and (B) all the domains are the identical mixtures of many different structural blocks with the structural content of blocks taken from the solution of the inverse problem in the case "A" (multi-structural domains). All the domains in both cases, "A" and "B", have multiple variants of number of N_{var} , which are generated by the variance of the R_{opt} value (which determines the average density of atoms in the domain) and of the U_{tot} value (which determines both the density and the mutual spatial orientation of structural blocks). The total number of different domains to calculate in the case "A" is equal to $N_{str} \cdot N_{var}$ and N_{var} , in the case "B" (because the structural content of blocks for the multi-structural domains "B" is taken from the solution of the inverse problem in the case "A"). The results for the S_{800} , S_{850} , S_{900} and S_{1000} samples were insensitive to the types of the domains (i.e. the theoretical diffraction pattern in the case "B" fits the experimental one almost as good as in case "A"). At low values of q ($< 25 \text{ nm}^{-1}$), fitting of the diffraction patterns for the S_{25} and S_{600} samples in the case "A" was significantly better than that in the case "B".

Here, we extend our analysis to the intermediate cases that correspond to the type "B" domains with type "A" subdomains. Such a domain-like structuring enables us to analyze the difference of inverse problem solutions in cases "A" and "B" for the S_{25} and S_{600} samples from [1].

2. Sensitivity of characterization to domain-like packing of nanostructures

In [5], we found that the fraction of carbon atoms, which belong to the intact C_{60} fullerenes, in the total number of carbon atoms (we excluded the contribution of gas impurities of N, O and H from our quantitative analysis) in the S_{25} and S_{600} samples is equal to 59 % and 49 %, respectively. For the samples annealed at high temperatures, this fraction is significantly lower. We suggested that the poor fitting of diffraction patterns for the S_{25} and S_{600} samples in the case “B” (multi-structural domains) is caused by the structuring peculiarities of the intact C_{60} fullerenes when their fraction is high. The approach in [5] implies a uniform random distribution of structural blocks in the domain’s volume (and thus in the entire sample) on the space scale of a few-several nanometers. The clustering of structural blocks of the same kind, that can produce a mono-structural subdomain during the RBMD simulation of multi-structural domains, is not possible in the case of such a short-range potential as the Lennard – Jones ones. All the structural blocks from the predefined set, except the C_{60} fullerenes, have the similar structure: carbon flakes of 14 – 285 atoms with a graphene-like atom arrangement. Even if we assume that the samples actually contain the mono-structural domains of some of these structural blocks (except the C_{60} fullerenes), it would be impossible to determine this from the diffraction data only. The latter was proven in [5] for the samples annealed at high temperatures: the theoretical neutron diffraction patterns, calculated in the mono-structural and multi-structural domain cases, appeared to be identical. However, for the samples S_{25} and S_{600} with a high fraction of intact C_{60} fullerenes, the situation is different.

The easiest way to identify the presence of the mono-structural C_{60} fullerene domains in the samples S_{25} and S_{600} is to fit the experimental diffraction patterns with the calculated ones for the multi-structural domains of the sp^2 carbon flakes and mono-structural domains of the C_{60} fullerenes. Since we use the structural content of blocks found in the case of the mono-structural domains, the number of domains in the latter case is equal to $N_{var}(\text{flakes}) + N_{var}(C_{60})$. In [5], it was enough to simulate $N_{var} = 12$ variants of mono- or multi-structural domains (4 different values of R_{opt} parameter and 3 different values of U_{tot} parameter), thus $N_{var}(\text{flakes}) = 12$. For the mono-structural C_{60} fullerene domains, it is enough to model only $N_{var}(C_{60}) = 4$ variants, because, in the case of spherical molecules, the U_{tot} parameter will affect only the mutual orientation of the neighboring fullerenes, that should be taken random to allow for the effects that are visible on the diffraction patterns and caused by thermal rotation of fullerenes. In Figs. 2, 3 and 4, the calculations for this structure of the sample is labeled as “mono (C_{60}) + multi (flakes)”.

Another way is to introduce manually the mono-structural subdomains of the C_{60} fullerenes into the multi-structural domains. In this case, the subdomains should be calculated separately and then introduced into the RBMD simulation of multi-structural domains as rigid bodies in order to prevent subdomain breakdown during the RBMD simulation. Fig. 1 shows the example of the calculated multi-structural domains for ~ 25000 carbon atoms that include the C_{60} fullerenes subdomains of different sizes. The content of the structural blocks in these domains is taken as that obtained in [5] for the S_{600} sample (note that this structural content differs from that for the S_{25} sample) and includes (besides the intact C_{60} molecules) the decomposition products of C_{60} molecules in the amount indicated in the Fig. 1 caption. The domains in Fig. 1 are calculated with the R_{opt} parameter value which, for each pair of structures in the ensemble, is set as random in the range: 0.35 – 0.4 nm. These domains have the lowest value of U_{tot} for given R_{opt} (i.e. correspond to the final time step of RBMD simulation). We also calculated the domains for the following ranges of R_{opt} : 0.25 – 0.3, 0.3 – 0.35, 0.4 – 0.45 nm, for higher values of U_{tot} that correspond to the intermediate stages of

the RBMD simulation. The total number of the calculated domains for each size of the C_{60} subdomains and for each sample is equal to $N_{var} = 12$. Depending on the relative size of the C_{60} subdomains these model samples are labeled in Figures 2, 3 and 4 as follows: “sub XL”, for extra-large subdomains (see Fig. 1 (a)); “sub L”, for large subdomains (see Fig. 1 (b)); “sub M”, for medium subdomains (see Fig. 1 (c)); “sub S”, for small subdomains (see Fig. 1 (d)). The number of C_{60} molecules in each type of subdomain is shown in the captions of Fig. 1 for the S_{600} sample and Fig. 2 for the S_{25} sample. The distances between the C_{60} molecules in the subdomains are different for different values of R_{opt} ; this affects the linear sizes of the subdomains. The linear sizes of the subdomains for the $R_{opt} = 0.35 - 0.4$ nm are approximately 7.5 nm, 5.8 nm, 4.8 nm, 3.8 nm for “sub XL”, “sub L”, “sub M” and “sub S” subdomains respectively. Note, that the sizes of the simulated domains were taken to be large enough (~ 25000 atoms) to avoid disturbance of the diffraction patterns at $q > 5 \text{ nm}^{-1}$, i.e. in the region that is under consideration both in [5] and here. Therefore, no periodic boundary conditions are needed.

Figures 2 and 3 show the results of fitting (by solving the inverse problem (2) – (5) in [5]) the experimental diffraction pattern with theoretical simulations for the S_{25} and S_{600} samples, respectively, for various sample structural contents. The curves for mono-structural (labeled as “mono”) and multi-structural (labeled as “multi”) domains are taken from [5], while the other curves are new. Figs. 2 and 3 show that it is possible to fit the experimental data in the case of mono-structural domains of the C_{60} fullerene and the multi-structural domains of the sp^2 carbon flakes almost as good as in the case of mono-structural domains.

Figure 4 shows the quality of the fitting for different cases in terms of the normalized values of the optimal objective function which describes the difference between the experimental and theoretical data (i.e. the residual, see Eqs. (2) – (5) in [5]). The case of mono-structural domains (“mono”) has the lowest residual among all cases. This is not surprising, because in this case, the solver tries to fit the data with $N_{str} \cdot N_{var} = 432$ calculated curves. The case of mono-structural domains of the C_{60} fullerene and the multi-structural domains of the carbon flakes (“mono (C_{60}) + multi (flakes)”) holds for the second S_{25} and the third S_{600} samples. In this case, the solver tries to fit the data with just 16 calculated curves. The case of multi-structural domains that include the relatively small C_{60} fullerene subdomains (“sub S”) holds for the third S_{25} sample and for the second S_{600} sample. Only 12 curves are used in this case to fit the data. Among four variants of subdomains size, the smallest size provides the best fitting.

From this analysis, we can conclude that the partial destruction of the nanoscale structure of the amorphous C_{60} fullerene sample, resulted from the low-temperature annealing in vacuum, appears to be heterogeneous on the nanoscale. Not only do individual C_{60} molecules survive the annealing at 600 °C, but their clusters of a size of few nanometers also remain intact.

3. Conclusion

The structure refinement method [5] formerly suggested for characterization of amorphous sp^2 carbon, based on the neutron or x-ray diffraction, and applied to amorphous fullerene and its derivatives produced by vacuum annealing [5], has been extended to analyze the partial destruction of a sample’s nanoscale structure (e.g. by the low-temperature annealing). To evaluate heterogeneous media, the method uses rigid body molecular dynamics simulations of the domain-like packing of the predefined set of the structural blocks. Previously, the sensitivity of the results to the variability of mutual positions of these structural blocks has been analyzed in the two limiting cases: (A) any domain containing only identical structural blocks and (B) all the domains are the identical mixtures of many different structural blocks with variable block packing. The extension of this analysis to the intermediate cases that correspond to type “B”

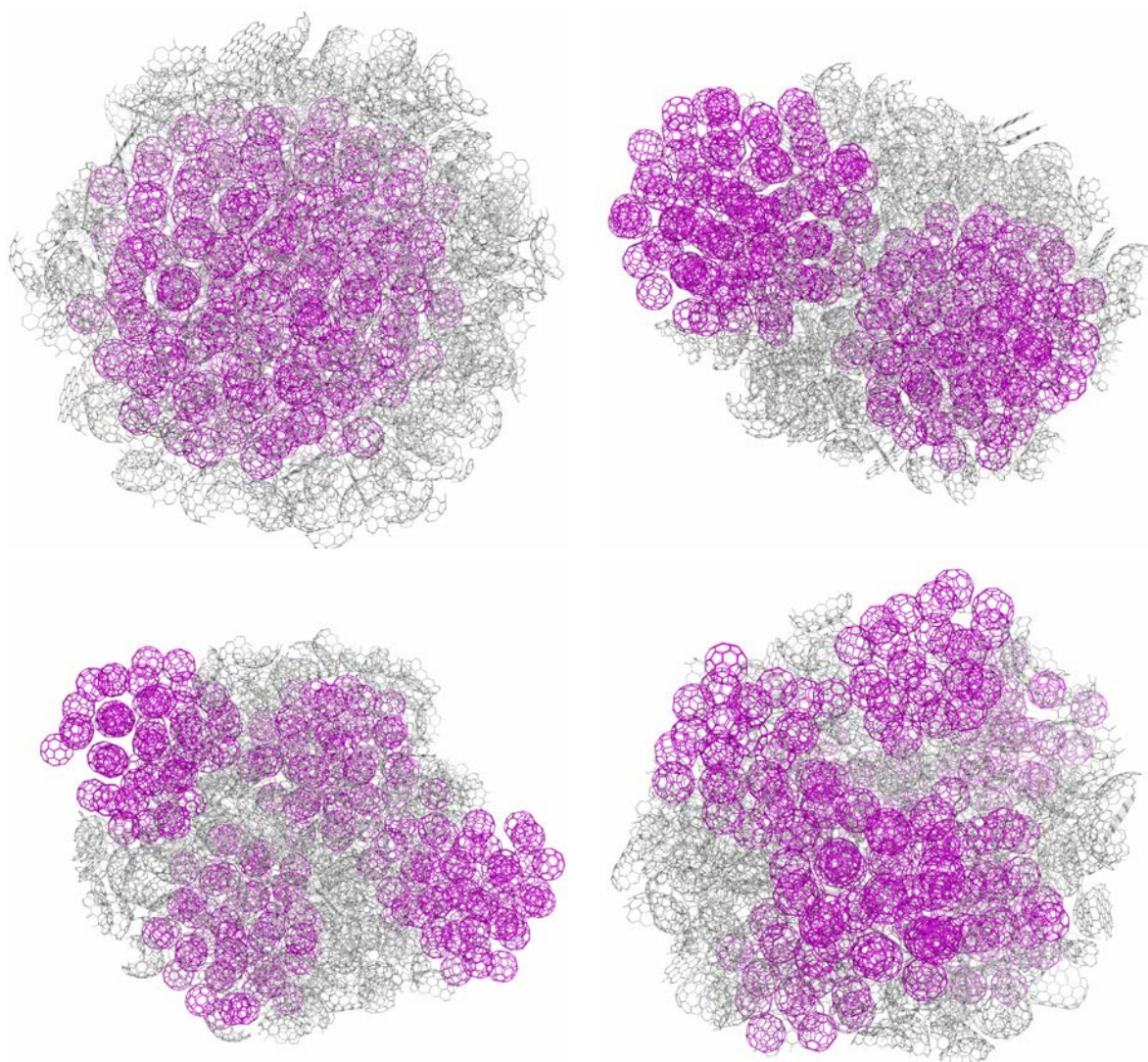


FIG. 1. The model multi-structural domains of ~ 25000 carbon atoms of the following structural content: 49 % C_{60} fullerenes and 51 % products of decomposition of C_{60} in the form of sp^2 carbon flakes (27 % C_{58} molecules, 16 % C_{52} molecules, 6 % C_{34} molecules and 2 % C_{14} molecules). The C_{60} fullerenes are present in these domains in the form of subdomains (highlighted) of different size: one subdomain with 205 molecules (a), two subdomains with 102 – 103 molecules (b), four subdomains with 51 – 52 molecules (c), and eight subdomains with 25 – 26 molecules (d)

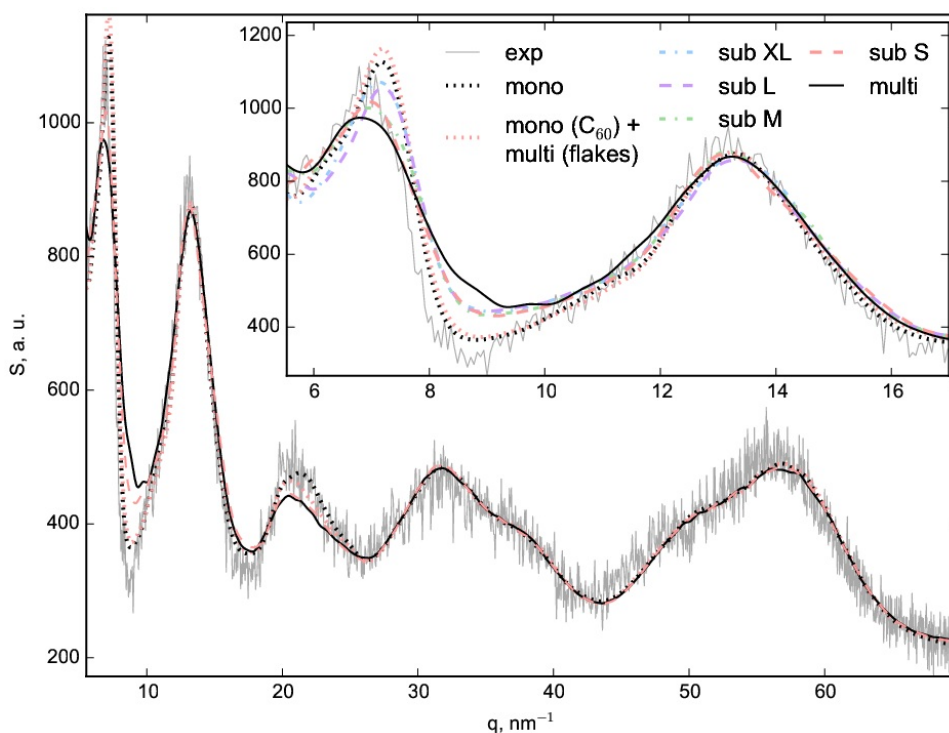


FIG. 2. Fitting of the experimental (“exp”) diffraction pattern for the un-annealed sample (S_{25} sample) with theoretical simulations, in various cases of sample’s structural content: mono-structural domains (“mono”); mono-structural domains of the C_{60} fullerene and the multi-structural domains of the sp^2 carbon flakes (“mono (C_{60}) + multi (flakes)”); multi-structural domains (“multi”); multi-structural domains that include the C_{60} fullerene subdomains of different size: extra-large (as in Fig. 1(a) but for 247 molecules, “sub XL”), large (as in Fig. 1(b) but for 123 – 124 molecules, “sub L”), medium (as in Fig. 1(c) but for 61 – 62 molecules, “sub M”), small (as in Fig. 1(d) but for 30 – 31 molecules, “sub S”). The inset magnifies the results in the range of q values from 5.5 to 17 nm^{-1} . The curves labeled with “sub XL”, “sub L”, and “sub M” are shown in the inset only to ease the readability of the main plot

domains with type “A” subdomains enables us to improve the quantitative description of the structure for amorphous C_{60} samples after the mechanical grinding and subsequent annealing at 600 °C. The partial destruction of the nanoscale structure of the amorphous C_{60} fullerene sample, resulted from the low-temperature annealing in vacuum, appears to be heterogeneous on the nanoscale. Not only do the individual C_{60} molecules survive the annealing at 600 °C, but their clusters of a size of few nanometers also remain intact.

Acknowledgements

The authors are grateful to A. P. Afanasiev, for the support of collaboration between the NRC “Kurchatov Institute” and the Center for GRID-Technologies and Distributed Computing (<http://dcs.isa.ru>) of the Institute for Information Transmission Problems (Kharkevich Institute) of Russian Academy of Science, V. A. Somenkov, for the guidance in the experimental part of the work, O. V. Sukhoroslov, for technical support of MathCloud computing infrastructure, M. S. Blanter and Y. V. Zubavichus, for helpful discussion of results.

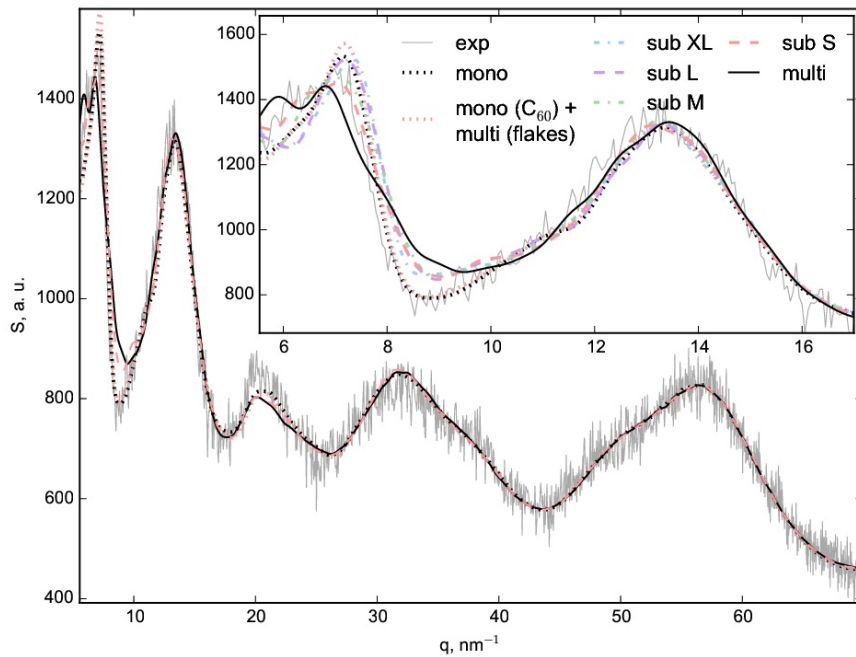


FIG. 3. The same as in the Fig. 2 but for the sample annealed at 600 °C (S_{600} sample). The parameters of the C_{60} subdomains are indicated in the caption of Fig. 1

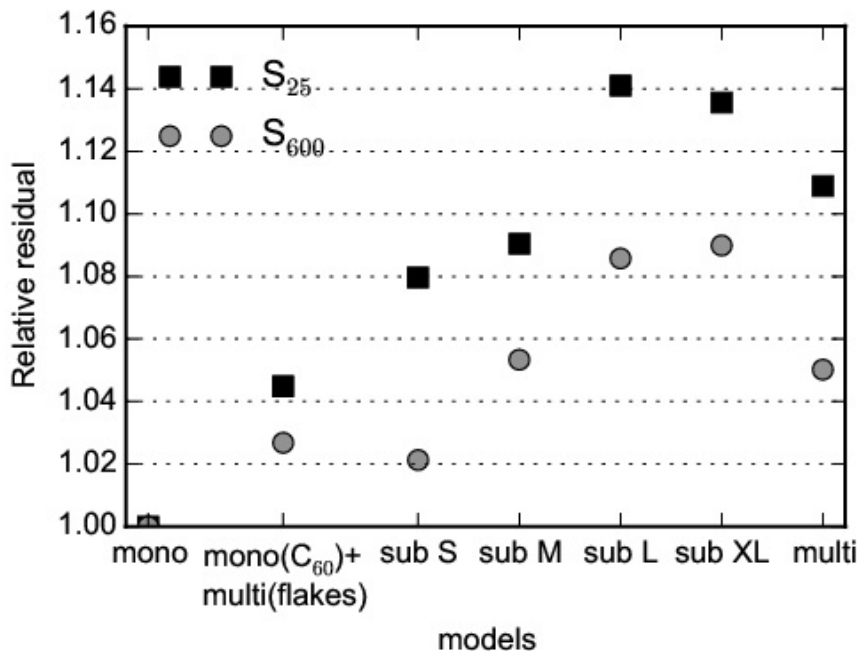


FIG. 4. Normalized values of the optimal objective function (i.e. relative residuals, see Eq. (2) – (5) in [5]) that characterize the quality of fitting the experimental diffraction patterns in different cases of the sought-for structural content of the two analyzed samples. The values are normalized to the minimum, which for both samples is found in the case of mono-structural domains (“mono”). See the caption of Fig. 2 for the annotations

This work is supported by the Russian Foundation for Basic Research (projects RFBR #13-07-00987-a, #13-02-00208-a and #15-07-07901-a). The experimental work was performed using the equipment of Unique Scientific Facility “Research reactor IR-8” supported by the Russian Ministry of Science and Education (project code RFMEFI61914X0002). The most of calculations were carried out using the computational resources of the Multipurpose Computational Complex of the NRC “Kurchatov Institute” (<http://computing.kiae.ru/>).

References

- [1] Borisova P.A., Agafonov S.S., Blanter M.S., Glazkov V.P., Somenkov V.A. Neutron studies of structural changes in amorphous C_{60} fullerite under temperature, pressure, and thermobaric effects. *Bulletin of the Russian Academy of Sciences: Physics*, 2013, **77**(11), P. 1363–1366.
- [2] Juhas P., Cherba D.M., Duxbury P.M., Punch W.F., Billinge S.J.L. Ab initio determination of solid-state nanostructure. *Nature*, 2006, **440**, P. 655–658.
- [3] McGreevy R.L. Reverse Monte Carlo modelling. *J. Phys.: Condens. Matter*, 2001, **13**, P. R877.
- [4] Rud A.D., Kiryan I.M., Nikonova R.M., Lad'yanov V.I., Bilyi N.M., Merzlyakova M.A. Structure Transformation in Fullerenes C_{60} at High Temperature Treatment. Proc. Intern. Conf. “Nanomaterials: applications and properties”. Crimea, Ukraine, 16–19th September 2013, Sumy State University Publishing, 2013, Vol. 2(3), 03NCNN28 (4pp).
- [5] Neverov V.S., Borisova P.A., Kukushkin A.B., Voloshinov V.V. A method for diffraction-based identification of amorphous sp^2 carbon materials. *J. Non-Cryst. Solids*, 2015, **427**, P. 166–174.
- [6] Kukushkin A.B., Neverov V.S., Marusov N.L., Semenov I.B., Kolbasov B.N., Voloshinov V.V., Afanasiev A.P., Tarasov A.S., Stankevich V.G., Svechnikov N.Yu., Veligzhanin A.A., Zubavichus Ya.V., Chernozatonskii L.A. Few-nanometer-wide carbon toroids in the hydrocarbon films deposited in tokamak T-10. *Chem. Phys. Lett.*, 2011, **506**, P. 265–268.
- [7] Ciccotti G., Ryckaert J.P. Molecular dynamics simulation of rigid molecules. *Comp. Phys. Rep.*, 1986, **4**(6), P. 346–392.

Reactivity in combustion process for expanded graphites: influence of dimensional effect

V. A. Logvinenko^{1,2}, V. G. Makotchenko¹, V. E. Fedorov^{1,2}

¹Nikolaev Institute of Inorganic Chemistry, Siberian Branch of the Russian Academy of Sciences, Novosibirsk 630090, Russia

²Novosibirsk State University, Novosibirsk 630090, Russia

val@niic.nsc.ru, mwg@niic.nsc.ru, fed@niic.nsc.ru

PACS 65.80.Ck; 65.80.g; 82.60.Qr

DOI 10.17586/2220-8054-2016-7-1-234-243

Thermal stability in combustion reaction for natural graphite, graphene and several expanded graphite phases were studied; the kinetic parameters of the oxidation reaction were calculated for two samples. Natural graphite (crystalline particles 200 – 300 μm) has the maximum stability ($E_1 = 201 \pm 2$ kJ/mol, $\lg A_1 = 7.1 \pm 0.1$), while multilayer graphene is the most reactive ($E_2 = 120 \pm 1$ kJ mol⁻¹, $\lg A_2 = 4.3 \pm 0.10$). The different sample grain sizes and their different structures result in different thermal stabilities: both in the reaction zones location (i.e. in the topochemical equation forms), and in the kinetic parameters' values.

Keywords: natural graphite, graphene, expanded graphite, thermal stability, non-isothermal kinetics, combustion.

Received: 20 November 2015

1. Introduction

A very noticeable difference is known to exist between a compound's thermodynamic properties for its bulk crystal form versus that of its nanosized particles. For example, the melting point for single nanoparticles of Au with a mean diameter of 4 nm is lower than the bulk value by over 400 °C [1]; the melting temperature of aluminum decreases from 660 °C to 650 °C and to 620 °C respectively for the bulk crystal, 30 nm and 6 nm nanoparticles, respectively [2]. Potassium nitrate nanoparticles melt at a lower temperature (313 °C) than the crystal (333 °C) [3].

It was demonstrated that the intense mechanical treatment of coal (i.e. grinding of particles) causes an increase in its reactivity, which is exhibited both as a decrease in the temperature interval of the combustion, and a decrease in the activation energy [4]. The difference in reactivity can be expected for graphite phases consisting of particles with different sizes and structures.

The oxidation of natural graphite was considered in several detailed papers [5–7]. It was shown that for a prismatic graphite structure, the fraction of edge sites increases, and the fraction of basal plane sites decreases, as the particle size decreases. This confirms that the ratio between edge sites and basal sites has a strong influence on all thermal parameters for graphite oxidation [7].

The activation energy for basic graphite or carbon material follows a distribution similar to that of a probability density function and this will be greatly enhanced by the imperfections in the char structures [5].

There are no direct comparisons of natural graphite, expanded graphites and graphene with regards to the ease of their oxidation in the literature.

2. Experimental

2.1. Synthesis of graphite phases

Dicarbon polyfluoride with the intercalated chlorine trifluoride was synthesized by the vigorous fluorination of graphite with the liquid chlorine trifluoride using the well-known procedure [8]. Graphitic oxide was synthesized by the oxidation of graphite in concentrated sulfuric acid according to the methods of Hummers and Offeman [9]. The syntheses of graphitic nitrate and graphitic bisulfate were carried out by the electrochemical oxidation of the graphite in of sulfuric or nitric acid media [10–12].

The multilayer graphene (phase **I**) was produced by the thermal shock-loading at 800 – 1000 °C. Calculations using the Scherrer equation [13] showed that the graphene stock thickness (along the *c*-axis) was 3 nm. The expanded graphites (phases **II**, **III** and **IV**) were produced from graphitic oxide, nitrate and bisulphate by the thermal shock loading at 800 – 1000 °C. Scherrer equation calculations showed that the graphene stock thicknesses (along the *c*-axes) were 17, 42 and 83 nm, respectively.

The natural graphite (phase **V**) (from Zavaljevskoje deposit) had particles of 200 – 300 μm and the ash content was less than 0.1 wt%.

2.2. Thermal analysis

The oxidation of the graphite phases was studied in the standard experimental conditions: Netzsch thermal analyzer TG 209 F1, corundum crucible, argon + oxygen mixture flow (40 + 10 cm³·min⁻¹), sample masses ≈ 2.0 mg. TG curves were obtained with the heating rates of 3, 5, 10, 20 and 40 K/min.

2.3. Kinetic analysis under non-isothermal conditions

Thermogravimetric data were processed using the computer program Netzsch Thermo-kinetics 2 (Version 2004.05) [14,15]. A special program module, “Model-free”, based on well-known studies [16–25], allows multiple thermogravimetric curves, obtained with different heating rates, to be processed and the activation energy to be calculated without preliminary information about the kinetic topochemical equation. The Friedman method was used to calculate the activation energies for each experimental point of fractional conversion (in the range 0.005 < α < 0.995).

If the activation energy is variable in compliance with the Friedman method, the decomposition process is a multi-step reaction.

We then used the same set of experimental data to search for the corresponding topochemical equation (the selection was made from 16 equations: chemical reaction at the interface, nucleation and diffusion). This calculation was made by the improved differential procedure of Borhardt-Daniels [14, 26] within the multiple linear regression approach. It is very important that the range for the degree of conversion (α) for this calculation be chosen based on the relative constancy of the calculated kinetic parameters from the prior Friedman analysis.

The Fisher test [14] was used to search for the best kinetic description and for statistical control of the obtained equation. This tested the residual variance of the individual models against one another and answers the question of whether the models differ significantly (statistically) or not. If $F_{exp(1)} \approx F_{exp(2)}$ for two equations, there is no reason to assume the first model is better at characterizing the experiment. The statistical quantile F_{crit} is obtained for a level of significance of 0.05.

If the calculation results in two or three kinetic equations with close values in their correlation coefficients and on the F test, but with noticeably different values in kinetic parameters, it is most correct to choose the equation with activation energy values closest to the data from the “Model-free” module program. Discrimination between the two steps is relative in this search for topochemical equations, but helps to identify the most reliable ones. The special program of nonlinear regression is useful in searching for a full set of kinetic parameters for multi-stage processes. The closest fit between the activation energies from the “Model-free” analysis and the nonlinear regression calculation is important from a physicochemical point of view. Therefore, the authors of the computer program used recommend fixing E values (obtained by linear regression and congruent with E from the “Model-free” analysis) in calculations with this program.

The random error in the activation energy values for such a reversible decomposition reaction is usually about 10 % in these experiments, which we took into consideration. The computer program Netzsch Thermokinetics 2 enables estimation for the contribution of each stage (as Δm portion) following this nonlinear regression calculation.

Well-known recommendations for performing kinetic computations on thermal analysis data [27,28] were used; new studies on non-isothermal kinetics were taken into account [29,30].

There were several important assumptions and limitations. The kinetic equations to calculate the kinetic parameters are topochemical and the calculated parameters (E and A) are formal and conventional from the standpoint of the classical chemistry of solids.

However, the general trend in the variation of these values within a specially selected series of compounds (either isostructural or genetically related) is very important because the expected disorder in the reaction zones can be identical for them; all other errors and simplifications will be minimized and smoothed in such a comparison. The best series are coordination compounds with volatile ligands (with one central atom and different ligands or with different central atoms and the same ligand) or inclusion compounds [31–34].

The studied series are several graphite phases with the modified structures; the temperature intervals of the combustion, topochemical equations and the kinetic parameter values can be compared in such series.

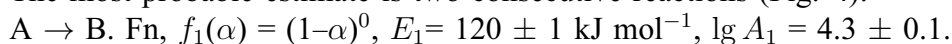
3. Results and Discussion

Thermogravimetric curves for the combustion of several graphite phases are shown in Fig. 1. So, as the curves' temperature intervals are directly connected with the rate constant of the thermal decomposition processes [31,32], the positioning of curves in the temperature series fully correlates with the kinetic stability. Therefore, the thermal (kinetic) stability of the phases under the oxidation (combustion) increases in the series: **I**<**II**<**III**<**IV**<**V** (Fig. 1). This fully correlates with the stock thicknesses of the samples (3, 17, 42, 83 nm and 200 – 300 μm). Two phases, the multilayer graphene and the natural graphite (the leftmost and the rightmost of the series), were chosen for detailed kinetic study.

3.1. Combustion of multilayer graphene (I)

Thermogravimetric curves, obtained using heating rates 10, 20 and 40 $\text{K}\cdot\text{min}^{-1}$, were used for kinetic analysis (Fig. 2). “Model-free” data are given in Fig. 3. The activation energy can be considered a variable in compliance with the Friedman method; therefore, the decomposition reaction is a multi-step process. The best description of the reaction is a two-step process ($A \rightarrow B \rightarrow C$) with an order equation (Fn) and Prout-Tompkins equation (B1) (Table 1).

The most probable estimate is two consecutive reactions (Fig. 4):



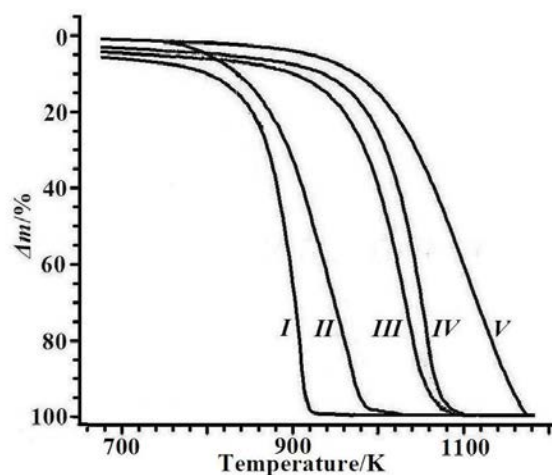


FIG. 1. TG curves of the combustion processes for multilayer graphene (I), the expanded graphite phases (II, III, IV) and natural graphite (V). The heating rate was $10 \text{ K}\cdot\text{min}^{-1}$

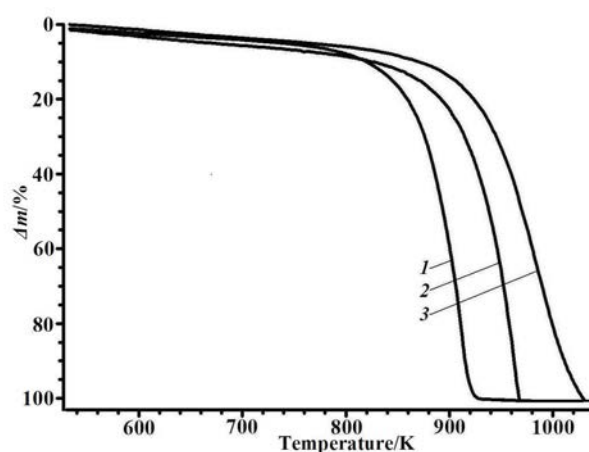


FIG. 2. TG-curves of the combustion process of the multilayer graphene (I). The heating rates were 10 (1), 20 (2) and 40 (3) $\text{K}\cdot\text{min}^{-1}$

$B \rightarrow C$. B1, $f_2(\alpha) = \alpha \cdot (1 - \alpha)$, $E_2 = 31 \pm 5 \text{ kJ mol}^{-1}$, $\lg A_2 = 0.7 \pm 0.3$.
Corr. coeff. = 0.993421.

The time dependencies of the yield for each reactant in the decomposition are shown in Fig. 5. The computer program used enables estimation of the contribution of each stage (as Δm portion) after the nonlinear regression calculation. Therefore, the first stage ($A \rightarrow B$) corresponds to 82 %, and the second stage ($B \rightarrow C$) corresponds to 18 % of this combustion reaction.

The zero order reaction (i.e. the constant decomposition rate) can be connected with the reaction zone, formed on the grain's surface and moving perpendicularly to the graphene layers. The final oxidation step (18 % of the mass loss) was described by the Prout-Tompkins equation ($E_2 = 31 \pm 1 \text{ kJ}\cdot\text{mol}^{-1}$, $\lg A_2 = 0.7 \pm 0.3$); this part of the combustion takes place with the reaction acceleration (as the rapid ignition of the particle nuclei).

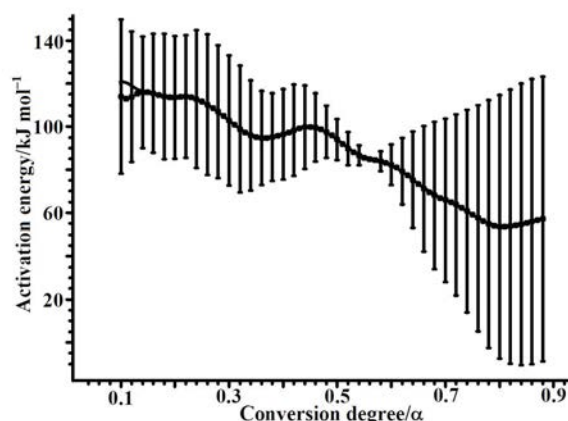


FIG. 3. Friedman analysis of the combustion process of the multilayer graphene (I): activation energies depending on the degree of conversion α . Perpendicular lines SD of calculation

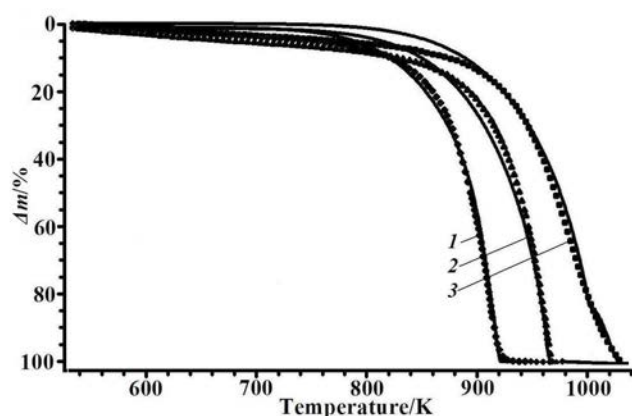
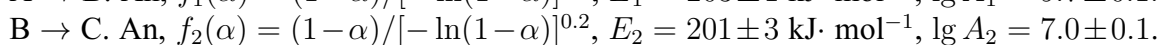
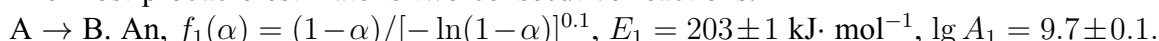


FIG. 4. Data processing for the combustion process of the multilayer graphene (I). TG curve fitting of non-linear regression, simulated with two consecutive reactions (equations Fn and B1). The points are the experimental data; the lines are the calculated data. The heating rates were 10 (1), 20 (2) and 40 (3) $\text{K}\cdot\text{min}^{-1}$

3.2. Combustion of natural graphite (V)

Thermogravimetric curves, obtained with the heating rates 3, 5 and 10 $\text{K}\cdot\text{min}^{-1}$, were used for kinetic analysis (Fig. 6). “Model-free” data are given in Fig. 7. The activation energy can be considered a variable in compliance with the Friedman method; therefore, the decomposition process is a multi-step reaction (Table 2).

The most probable estimate is two consecutive reactions:



Corr. coeff. = 0.998606.

The computer program used enables estimation of the contribution of each stage (as Δm portion) after the nonlinear regression calculation. Therefore, the first step ($A \rightarrow B$) corresponds to 1 %, and the second step ($B \rightarrow C$) corresponds to 99 % of this combustion reaction. So as the first step's contribution is negligible, we recalculate the data as a one-step process (Fig. 8):

TABLE 1. Multilayer graphene combustion. Data on the F-test of fit quality/to identify the best kinetic description

F_{crit}	F_{exp}	F_{act}	Equation A→B	Equation B→C
1.10	1.00	1103	An	An
1.10	1.05	1102	An	Bna
1.10	1.77	1104	An	B1
1.10	2.49	1102	Fn	Bna
1.10	2.49	1104	Fn	B1
1.10	2.50	1103	Fn	An
1.10	2.85	1106	Fn	Fn
1.10	5.25	1107	An	

Notes: F_{exp} – experimental F-value; F_{crit} – critical F-value, calculated for the degree of freedom of current model F_{act} and the degree of freedom of the best model, at the one-sided level of confidence of 0.95. F_{act} is the degree of freedom (number of data points - number of optimized parameters) of the current model.

The used topochemical equations are Avrami-Erofeev (An), n -th order (Fn) and Prout-Tompkins (B1 and Bna) equations [14-15].

The parameter calculation for **An-An**, **An-Bna**, **Fn-An**, **Fn-Fn** equations combination includes both one mass loss stage, and one mass increase stage, so these mathematical solutions have no physical-chemical meaning for the mass loss TG-curves.

TABLE 2. Natural graphite combustion. Data on the F-test of fit quality/to identify the best kinetic description

F_{crit}	F_{exp}	F_{act}	Equation A→B	Equation B→C
1.10	1.00	1174	An	An
1.10	1.05	1178	An	
1.10	1.41	1178	Fn	
1.10	1.45	1178	C1B	
1.10	2.36	1179	D3	
1.10	71.02	1179	B1	

Notes: F_{exp} – experimental F-value; F_{crit} – critical F-value, calculated for the degree of freedom of current model F_{act} and the degree of freedom of the best model, at the one-sided level of confidence of 0.95. F_{act} is the degree of freedom (number of data points – number of optimized parameters) of the current model.

The used topochemical equations are Avrami-Erofeev (An), n -th order (Fn) and Prout-Tompkins (B1) equations [14–15].

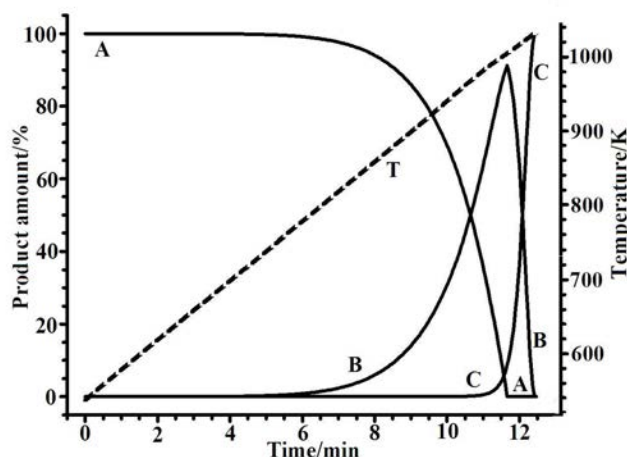


FIG. 5. The combustion process of the multilayer graphene. Time dependence of the yield of each reactant in the decomposition. The calculation corresponds to two-stage consecutive reactions ($A \rightarrow B \rightarrow C$) in Fig. 4. The heating rate was $40 \text{ K} \cdot \text{min}^{-1}$

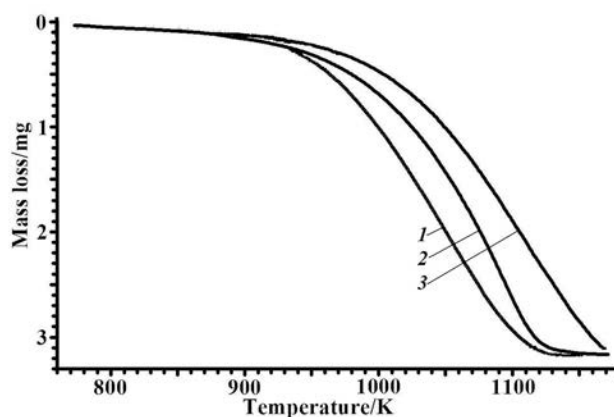


FIG. 6. TG-curves of the combustion process of the natural graphite sample (V). The heating rates were 3 (1), 5 (2) and 10 (3) $\text{K} \cdot \text{min}^{-1}$

$A \rightarrow B$. An, $f(\alpha) = (1 - \alpha)/[-\ln(1 - \alpha)]^{0.2}$, $E = 201 \pm 2 \text{ kJmol}^{-1}$, $\lg A_2 = 7.1 \pm 0.1$.
Corr. coeff. = 0.999120.

Avrami-Erofeev topochemical equation denotes the evident diffusion contribution.

The calculated activation energy stays within the known broad averaged value: $E = 167.5 \pm 50 \text{ kJ} \cdot \text{mol}^{-1}$ for natural graphite oxidation [5,6]. Such a broad estimation of the activation energy can be explained by the different properties of natural graphite samples from different locations.

4. Conclusion

The different sizes of sample particles and their different structures result in different thermal stabilities: both in the reaction zones location (i.e. in the topochemical equation forms), and in the values of kinetic parameters.

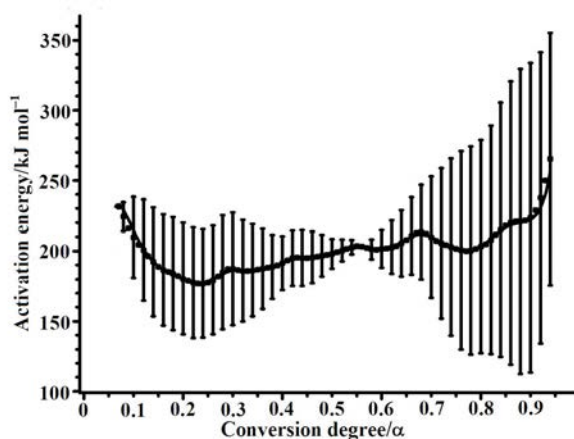


FIG. 7. Friedman analysis of the combustion process of the natural graphite sample (V): activation energies depending on the degree of conversion α . Perpendicular lines SD of calculation

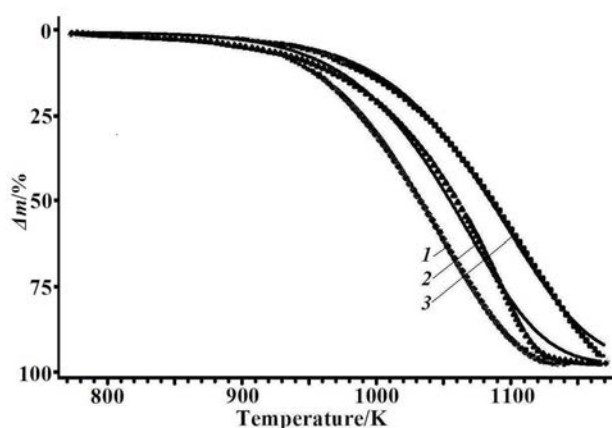


FIG. 8. Data processing for the combustion process of the natural graphite sample (V). TG curve fitting of non-linear regression, simulated with the single stage reaction (equation An). The points are the experimental data; the lines are the calculated data. The heating rates were 3 (1), 5 (2) and 10 (3) $\text{K}\cdot\text{min}^{-1}$

Graphite is a very anisotropic layered substance. For an ideal single crystal, the ratio of the reaction rates on the different crystal faces must reach a factor of 10^{15} times, but for the real graphite single crystal, this ratio is reduced to only 10^2 [35]. This fact can be connected to the reaction zone composition. The actual structure of the crystal surface is disordered; the bond lengths are increased, and the reaction zone formed on different crystal faces is rather uniformly arranged.

Therefore, we can expect the close-ratio kinetic parameters for different crystal faces [31], even through such anisotropic crystals of graphite particles. The calculated kinetic parameters for the natural graphite sample stay fairly close to the known averaged value [56].

The flat (quasi two-dimensional) morphology of the multilayer graphene particles exhibits the peculiarity in the kinetic topochemistry: the zero order reaction (which is the constant rate of the combustion).

We think that the formal kinetic approach used does not give one the possibility to discuss the difference in the kinetic stability based on the distribution of basal and edge active sites with different energies and of the formation of semiquinone and epoxy groups as the reaction progresses [5,7].

The thermal stability of the phases under the oxidation (combustion) increases in the series: **I** < **II** < **III** < **IV** < **V**. This demonstrates the direct influence of the dimensional effect on the kinetic stability in the combustion chemical reaction.

It is worth noting that this generalized series of thermal stabilities is loosely based on the constant rates, but such a series is not the same as for that of the activation energy values. For the extreme terms: $E_I < E_V$ actually, the stability level for the expanded graphites (**II**, **III** and **IV**) can be connected with the entropic contribution (e.g. with the pre-exponential factor value).

Acknowledgements

The work was supported by the Russian Scientific Foundation, Project 14-13-00674.

References

- [1] Buffat Ph., Borel J.P. Size effect on the melting temperature of gold particles. *Phys. Rev.*, 1976, **A 13**, P. 2287–2298.
- [2] Lai S.L., Carlsson J.R.A., Allen L.H. Melting point depression of Al clusters generated during the early stages of film growth: Nanocalorimetry measurements. *Appl. Phys. Lett.*, 1998, **72**, P. 1098–1100.
- [3] Bulavchenko A.I., Demidova M.G., Podlipskaya T.Yu., Tatarchuk V.V., Druzhinina I.A. Alekseev A.V., Logvinenko V.A., Drebuschak V.A. Microemulsion synthesis of powders of water soluble energy saturated salts. *Russ. J. Inorg. Chem.*, 2012, **57**(6), P. 769–776.
- [4] Yusupov T.S., Shumskaya L.G., Burdukov A.P., Logvinenko V.A. Reactivity of coal of different stages of metamorphism in the processes of thermo-oxidative destruction. *Chemistry for Sustainable Development*, 2011, **19**, P. 389–394.
- [5] Backreedy R., Jones J.M., Pourkashanian M., Williams A. A study of the reaction of oxygen with graphite : Model chemistry. *Faraday Discuss.*, 2001, **119**, P. 385–394.
- [6] Bews I.M., Hayhurst A.N., Richardson S.M, Taylor S.G. The order, Arrhenius parameters, and mechanism of the reaction between gaseous oxygen and solid carbon. *Combust. Flame*, 2001, **124**, P. 231–245.
- [7] Jianga W., Nadeaub G., Zaghlibb K., Kinoshitaa K. Thermal analysis of the oxidation of natural graphite – effect of particle size. *Thermoch. Acta*, 2000, **351**, P. 85–93.
- [8] Makotchenko V.G., Grayfer E.D., Nazarov A.S., Kim S.-J., Fedorov V.E. The synthesis and properties of highly exfoliated graphites from fluorinated graphite intercalation compounds. *Carbon*, 2011, **49**(10), P. 3233–3241.
- [9] Hummers Jr.W.S., Offeman R.E. Preparation of graphitic oxide. *J. Am. Chem. Soc.*, 1958, **80**(6), P. 1339.
- [10] Rudorff W., Hofmann U. Uber Graphitsaltze. *Z. Anorg. Allg. Chem. B*, 1938, **238**(1), P. 1–50.
- [11] Metrot A., Fisher J.E. Charge-transfer reactions during anodic oxidation of graphite in H₂SO₄. *Synth. Met.*, 1981, **3**, P. 201–207.
- [12] Avdeev V.V., Monyakina L.A., Nikolskaya I.V., Sorokina N.E., Semenenko K.N. The choice of oxidizers for graphite hydrogen sulfate chemical synthesis. *Carbon*, 1992, **30**(6), P. 819–824.
- [13] Scherrer P. Bestimmung der Größe und der Inneren Struktur von Kolloidteilchen Mittels Röntgenstrahlen, Nachrichten von der Gesellschaft der Wissenschaften, Göttingen. *Mathematisch-Physikalische Klasse*, 1918, **2**, P. 98–100.
- [14] Netzsch Thermokinetics. <http://www.netzsch-thermal-analysis.com/us/products-%20%20solutions/advanced-software/thermokinetics.html>
- [15] Moukhina E. Determination of kinetic mechanisms for reactions measured with thermoanalytical instruments. *J. Therm. Anal. Calorim.*, 2012, **109**, P. 1203–1214.
- [16] Kissinger H.E. Reaction kinetics in differential thermal analysis. *Anal. Chem.*, 1957, **29**, P. 1702–1706.
- [17] Friedman H.L. Kinetics of thermal degradation of char-forming plastics from thermogravimetry. *J. Polym. Sci.*, 1963, **6**, P. 183–195.

- [18] Ozawa T. A new method of analyzing thermogravimetric data. *Bull. Chem. Soc. Japan*, 1965, **38**, P. 1881–1886.
- [19] Ozawa T. Estimation of activation energy by isoconversion methods. *Thermochim. Acta*, 1992, **203**, P. 159–165.
- [20] Flynn J.H., Wall L.A. General treatment of the thermogravimetry of polymers. *J. Res. Nat. Bur. Stand.*, 1966, **70**, P. 478–523.
- [21] Opfermann J., Kaisersberger E. An advantageous variant of the Ozawa-Flynn-Wall analysis. *Thermochim. Acta*, 1992, **203**, P. 167–175.
- [22] Opfermann J.R., Kaisersberger E., Flammersheim H.J. Model-free analysis of thermo-analytical data - advantages and limitations. *Thermochim. Acta*, 2002, **391**, P. 119–127.
- [23] Vyazovkin S. Model-free kinetics: staying free of multiplying entities without necessity. *J. Therm. Anal. Calorim.*, 2006, **83**, P. 45–51.
- [24] Simon P. Single-step kinetics approximation employing non-Arrhenius temperature functions. *J. Therm. Anal. Calorim.*, 2005, **79**, P. 703–708.
- [25] Simon P. The single-step approximation: attributes, strong and weak sides. *J. Therm. Anal. Calorim.*, 2007, **88**, P. 709–715.
- [26] Borchard H.J., Daniels F. The application of differential thermal analysis to the study of reaction kinetics. *J. Amer. Chem. Soc.*, 1957, **79**, P. 41–46.
- [27] Vyazovkin S., Burnham A.K., Criado J.M., Luis A., Perez-Maqueda L.A., Popescu C., Sbirrazzuoli N. ICTAC Kinetics Committee recommendations for performing kinetic computations on thermal analysis data. *Thermochim. Acta*, 2011, **520**, P. 1–19.
- [28] Vyazovkin S., Chrissafis K., Di Lorenzo M.L., Koga N., Pijolat M., Roduit B., Sbirrazzuoli N., Suñol J.J. ICTAC Kinetics Committee recommendations for collecting experimental thermal analysis data for kinetic computations. *Thermochim. Acta*, 2014, **590**, P. 1–23.
- [29] Simon P., Thomas P., Dubaj T., Cibulkova Z., Peller A., Veverka M. The mathematical incorrectness of the integral isoconversional methods in case of variable activation energy and the consequences. *J. Therm. Anal. Calorim.*, 2014, **115**, P. 853–859.
- [30] Sestak J. Is the original Kissinger equation obsolete today: not obsolete the entire non-isothermal kinetics? *J. Therm. Anal. Calorim.*, 2014, **117**, P. 3–7.
- [31] Logvinenko V. Stability and reactivity of coordination and inclusion compounds in the reversible processes of thermal dissociation. *Thermochim. Acta*, 1999, **340-341**, P. 293–299.
- [32] Logvinenko V. Solid state coordination chemistry. The quantitative thermoanalytical study of thermal dissociation reactions. *J. Therm. Anal. Calorim.*, 2000, **60**, P. 9–15.
- [33] Logvinenko V. Stability of supramolecular compounds under heating. Thermodynamic and kinetic aspects. *J. Therm. Anal. Calorim.*, 2010, **101**, P. 577–583.
- [34] Logvinenko V., Drebuschak V., Pinakov D., Chekhova G. Thermodynamic and kinetic stability of inclusion compounds under heating. *J. Therm. Anal. Calorim.*, 2007, **90**, P. 23–30.
- [35] Ginak A.Y., Dimshits V.A., Rosovskiy A.Ya. Kinetics of the anisotropic reactions. Part I. Theoretical model. *Kinetika i katalis*, 1989, **30**, P. 83–91 (in Russian).

ERP study of graphite oxide thermal reduction: the evolution of paramagnetism and conductivity

M. V. Gudkov, V. P. Melnikov

Semenov Institute of Chemical Physics, Moscow, Russia

gudkovmv@gmail.com, melnikov@center.chph.ras.ru

PACS 76.30.Pk, 76.30.Rn

DOI 10.17586/2220-8054-2016-7-1-244-252

The evolution of paramagnetic centers (PMC) and conductivity of graphite oxide (GO) during its thermal reduction has been studied by electron paramagnetic resonance (EPR) at 150 and 165 °C. The GO samples for the study were prepared by systematically varying the KMnO_4 /Graphite weight ratios in the oxidation reaction. It has been shown that the PMC concentration increase in GO correlates with the intense evolution of gaseous products originating from the former oxygen-containing species of GO. The PMC concentration decrease has been described by the kinetic equation of the first order with an effective k_e and an activation energy value of 33 kcal/mol. The values of k_e decreased with increasing the quantities of KMnO_4 used in graphite oxidation reaction. The changes in GO conductivity were followed by measuring the microwave power absorption in the EPR-spectrometer resonator. The conductivity changes correlated with the decay of the radicals and occurred after the decomposition of the oxygen-containing groups was complete.

Keywords: electron paramagnetic resonance, graphite oxide, conductivity, paramagnetic centers, reduction.

Received: 20 November 2015

1. Introduction

The interest in graphite oxide (GO), first synthesized in 1859 [1], has immensely grown in the last decade due to the discovery of graphene's unique properties [2]. The key factors explaining the burst of interest to GO are: (i) simplicity of GO synthesis; (ii) capability of GO to breaking down to few- and even mono-layer particles in proper liquid media; and (iii) practical feasibility of mass production of graphene-like materials from GO by thermal or chemical treatment of the latter. The GO-based materials have already been employed as thin transparent conductive layers, sensors, batteries and capacitors electrodes, etc. [3]. Numerous experimental and theoretical studies have been published regarding GO synthetic procedures, its molecular structure, optimizing the GO reduction and studying the properties of the reduced GO (rGO). The nature of the oxygen-containing groups as well as their formation during the thermal and/or chemical reduction of GO have been investigated with the aid of spectroscopic (IR, Raman, XPS, NMR) and analytical (elemental analysis, XRD, TGA) methods [4]. Owing to their importance in many potential applications, the electrophysical properties of GO-based materials have received much attention recently. In a kinetic study of the monolayer sheet rGO's conductivity, it has been shown [5] that when raising the GO reduction temperature to 200 °C, the conductivity of the product was increased by 3 orders of magnitude. Such conductivity growth infers that polyconjugation of the C=C bonds system was effectively restored during the course of GO reduction. It is also known that under such thermal conditions, the oxygen-containing groups of GO undergo a rapid exothermic decomposition with the release of gaseous CO_2 , CO and H_2O . However, despite much work having already been done to formulate the mechanisms for GO reduction, these potential mechanisms remain a matter of debate and,

in particular, the sequence of steps in chemical reactions or the restructuring of the carbon framework during chemical and thermal treatment of GO still need to be clarified [6-8].

Different samples of GO have been studied by EPR and it has been shown that the paramagnetic centers residing on GO are represented by some localized states and, probably, by dangling bonds. It has also been shown that the concentration of the PMC tends to decrease over the course of thermal or chemical GO reduction processes [9-11].

In the present work, with the aid of EPR spectroscopy measurements at 150 and 165 °C, we have followed the evolution of the PMC in the samples of GO having different degrees of oxidation. The temperature interval for the study was chosen based on the results of our earlier volumetric kinetic study of the gaseous products that were released during the thermally stimulated decomposition of GO and are closely associated with the emission of the oxygen-containing functional groups residing on GO [12]. At the initial stage of thermal treatment, when oxygen-containing groups are undergoing vigorous decomposition, the concentration of PMC was found to increase. Under further heating, a reduction of the PMC concentration was observed. Since the emergence and/or increase in an analyte's conductivity brings about an excess absorption of microwaves within EPR resonator, EPR spectrometry was used in this work to measure the variance of electro conductivity for different GO samples. Accordingly, an apparent correlation between the PMC concentration decay and the growth of GO conductivity has been found. The obtained results infer that radical reactions take an active role in the thermally stimulated reduction of GO.

2. Experimental

2.1. Materials

Graphite powders having the particles size in the range of 10 – 20 μm (ash content <1.0 %) were used throughout this study. Sulfuric acid (94 %), NaNO_3 , KMnO_4 , water and H_2O_2 (3 % water solution) used for GO preparations all had a Reagent Grade purity.

2.2. Preparation of GO

The samples of graphite were oxidized to various predetermined extents via the methods of Hummers [13, 14]. In the standard procedure, 2 g of particulate graphite was charged into a solution of 1 g of NaNO_3 in 46 ml of H_2SO_4 and stirred for 60 minutes at room temperature. Then, the reactor was placed into an ice bath and, under vigorous stirring, a measured quantity of KMnO_4 (3.0, 4.0, 5.0 or 6.0 g) was charged to the suspension in small portions. Thus, in different experiments, the samples of GO with different degrees of oxidation were provided (the samples labeled GO15, GO20, GO25 and GO30, respectively). Upon completion of the permanganate introduction, the reactor temperature was raised to 35 – 40 °C, and stirred at that temperature for additional 30 – 40 minutes. After diluting the reaction mixture with water followed by treatment with hydrogen peroxide, the oxidized graphite was repeatedly washed with distilled water until a GO/water paste having neutral pH was obtained. The resulting paste was freeze-dried in the form of balls (diameter of $\sim 2 - 3$ mm) followed by further vacuum drying at 70 °C. The dried paste was then stored in a sealed container.

2.3. ERP spectroscopy

EPR spectra were acquired with the aid of an EPR-B spectrometer (ICP RAS, X-range) at microwave power less than 2 mW and RF amplitude modulation of 0.1 – 0.2 mT. A small sample of MgO with Mg^{2+} ions was kept in the spectrometer resonator as a lateral calibration standard. For the experiment, a GO sample (2.5 – 3.5 mg) was placed in a short thin-walled

glass capillary (inner diameter of ~ 1 mm) which in turn was placed in a glass ampule having a vacuum joint, the inner diameter of which was close to the outer diameter of the capillary, thus providing precise centering of the sample in the resonator. A pre-vacuumed sample was placed in the thermostat and was held at a constant temperature for a preset period of time (30 – 60 min in different experiments). Before acquiring the spectrum, the sample was subjected to vacuum again to remove the gaseous products.

Registration of the EPR spectrum involved presetting the microwave channel of the spectrometer so that the input to the synchronous detector reference and the reflected power from the resonator balanced each other, the synchronous detector current would thus be zero. When placed into the resonator, the sample absorbs the microwave radiation and a mismatch occurs, producing a synchronous detector current, which is observed and is proportional to the power absorbed by the sample. Thermal reduction of GO leads to lowering of the sample's resistance and the sample begins to absorb microwave radiation. The registration of the EPR spectra proceeds under changing conditions. The changes in the spectra were then corrected for the corresponding signal intensity changes of the lateral standard which was present in the resonator throughout analysis. At the same time, the detector current allows one to estimate the change in the conductivity of GO samples during heating. The conductivity measurement procedure had several steps. In the first step, the ampule with a pristine GO sample was placed in the spectrometer resonator and the power within the microwave tract was adjusted by the attenuator to the desired level. When one cycle of thermal treatment was finished, the sample was cooled to room temperature and then inserted into the spectrometer resonator again. Shortly after the attenuator was reset to the predetermined position, the detector current was observed and fixed. After readjustment, the EPR spectrum was recorded. The above procedure was repeated after every thermal treatment cycle. Thus, in every experiment, not only an EPR spectrum was acquired but also the conductivity variability was registered for GO thermal treatment. The total value of the absorbed power was obtained by summing the detector currents. The power absorbed due to the electro conductivity was divided by the weight of the sample. Obviously, the initial conductivity magnitude taken as the zero at the start of the experiments differed from sample to sample, and, therefore, the registered values of emergence and conductivity increase should be treated only as relative (not absolute) ones.

3. Results and discussion

The GO samples, characterized by different degrees of oxidation, did provide rather similar EPR spectra. In general terms, these are represented by slightly asymmetric singlets having the line width of 2 – 2.5 G, similar to that described in [9]. Comparison of GO samples having various oxidation degrees (Fig. 1) shows that, with increased oxidation, the initial PMC concentration in GO decreases by 4- to 5-fold. Note the high concentration of the localized PMC in the samples amounting to $\sim 10^{18}$ g⁻¹. The latter high value may infer that the PMC can effectively form and be accumulated in GO starting from the very early stages of the oxidation process and, hence, the dependences depicted in Fig. 1 may represent only the falling branch of the whole graphite oxidation process.

Figure 2 below shows two sets of experimental kinetic curves depicting the change of PMC concentration depending on time for the samples of GO subjected to reduction at 150 and 165 °C. It can be seen that (i) indeed, both the formation and the decay of PMC can proceed during the thermal GO treatment at these temperatures; and (ii) in the samples of GO characterized by different oxidation degrees, the processes for PMC accumulation or decay proceed differently. During the initial stage, a significant increase of the PMC concentration was observed for all samples except GO15, the latter being characterized by the lowest oxidation

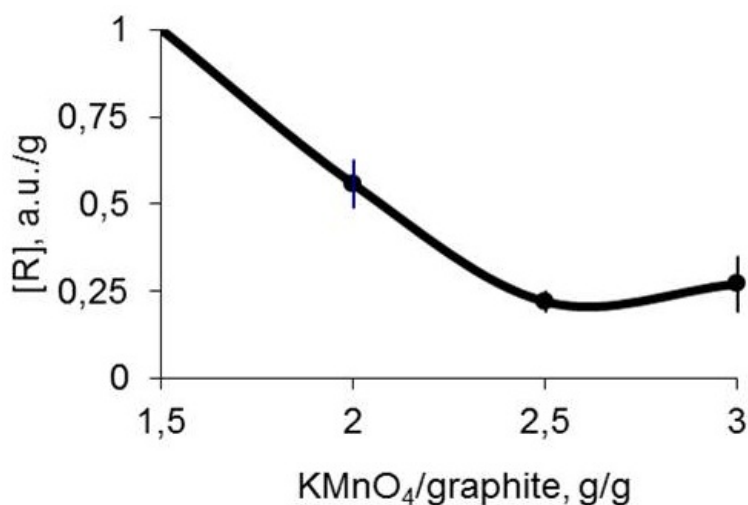


FIG. 1. The dependence of relative PMC concentration in GO samples (two series of measurements) on the relative amount of potassium permanganate used in the oxidation process. The value $[R] = 1$ corresponds to PMC concentration of about $3 \cdot 10^{18} \text{ g}^{-1}$

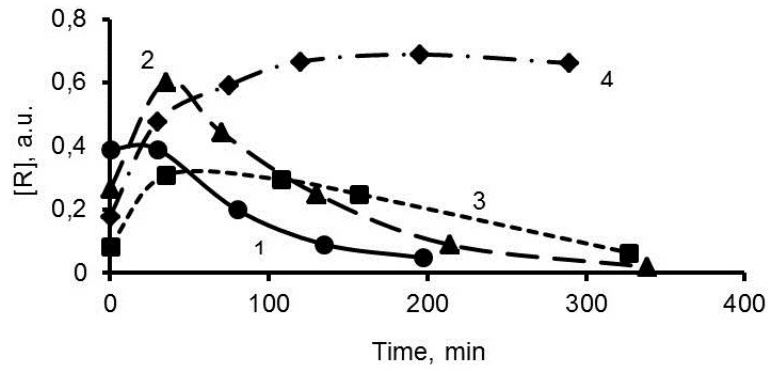
level. The PMC concentration in GO15 began to decrease either from the very beginning of the thermal treatment (at $165 \text{ }^\circ\text{C}$) or after a short delay (at $150 \text{ }^\circ\text{C}$). The ratio of the maximum PMC concentration to the initial one for both temperatures was found to be in the range of 2.3 – 2.6 for GO20, 3.8 – 4.5 for GO25 and 3.8 – 3.9 for GO30. From the data shown in Fig. 2, it also follows that, with increased GO oxidation levels, the time needed to reach the maximum PMC concentration also increases while PMC decay are processes markedly decreased.

The falling branches of the curves shown in Fig. 2 above are presented in Fig. 3a in different coordinates, $\ln[R]/t$. This new representation of the data shows that the PMC decay is described by a first order kinetic equation. The corresponding calculated values for the effective rate constants are shown at Table 1.

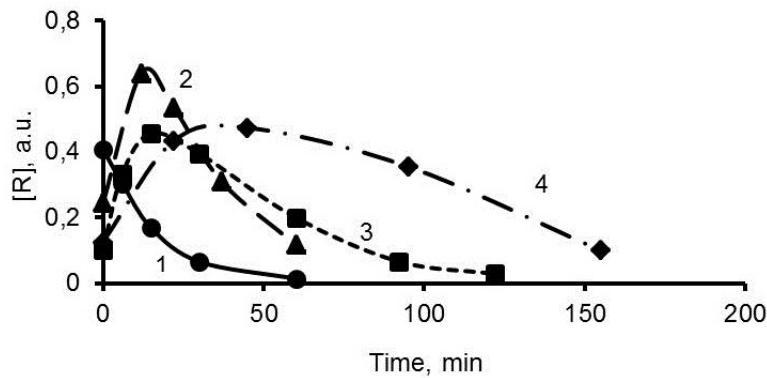
TABLE 1. Values of the effective rate constant

Sample	$K_e 10^3, \text{ s}^{-1}$	
	150 $^\circ\text{C}$	165 $^\circ\text{C}$
GO15	0.23	0.95
GO20	0.16	0.58
GO25	0.13	0.52
GO30	–	–

The data shown in Fig. 3b permits evaluation of Arrhenius parameters for PMC decay processes in GO since the straight line connecting the two temperature points is close to parallel. The evaluation gives an activation energy of, E_a , of $\sim 33 \pm 2 \text{ kcal/mol}$ and a pre-exponential factor, $\lg A \text{ (s}^{-1}\text{)}$, value of $\sim 12.8 - 14.2$. The kinetic aspects of GO reduction processes have been addressed in a few papers only. In one of the above-mentioned works [5], the kinetics of resistance changes and a thermo-programmed desorption of gaseous products have been studied for a monolayer GO. The activation energy values calculated in that work were found to be 38 ± 1 and $32 \pm 4 \text{ kcal/mol}$. Furthermore, the activation energies values of 38.1 and 32.5 kcal/mol

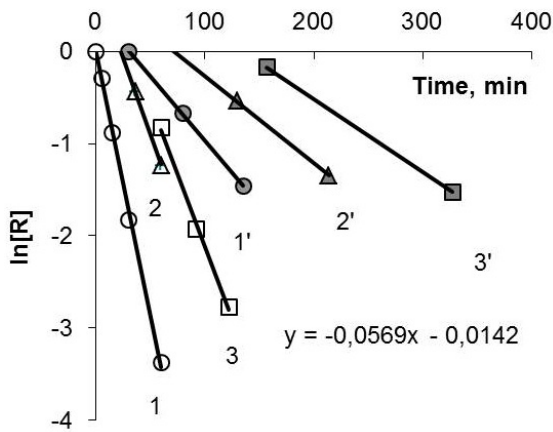


(a)

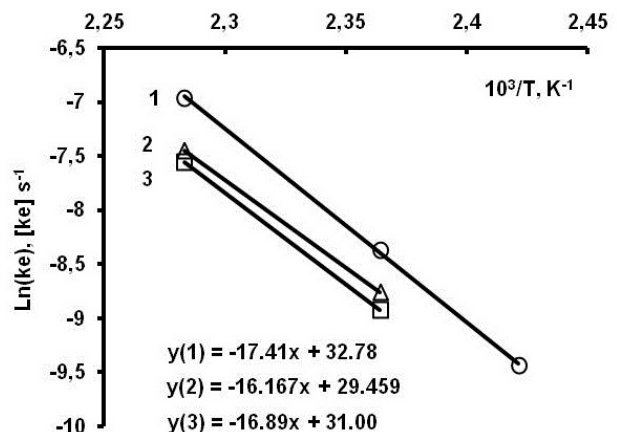


(b)

FIG. 2. The changes of PMC concentration depending on time as measured for different GO samples subjected to thermal treatment at 150 (a) and 165 °C (b). Curves 1 – 4 represent the samples GO15, GO20, GO25, GO30, respectively



(a)



(b)

FIG. 3. Linear anamorphoses of kinetic curves for PMC decay in different samples (a) and the Arrhenius-type dependences of the effective rate constants for corresponding temperatures (b). Line numbers correspond to samples 1, 1' – GO15, 2, 2' – GO20, 3, 3' – GO25

have been reported in another work [15], where thermogravimetric analysis (TGA) data were used for calculations based on diffusion and autocatalytic models for the GO reduction process respectively. In yet another paper [16], an activation energy of 40 kcal/mol has been found based on differential scanning calorimetry (DSC) data interrelating the maximum heat release temperature and the heating rate. Our results are in good agreement with those reported in the literature.

The curves in Fig. 4 depict the observed time dependence of the PMC concentration and that of relative conductivity for different GO samples. The electro conductivity detection, or rather, the conductivity increase of the sample GO15 having the lowest oxidation degree is observed at the initial stage of thermal treatment together with the PMC concentration decrease. The match of the observed conductivity initiation with PMC concentration decrease is also seen for the samples GO20 and GO25, which suggests the existence of a relationship between these two processes. In the case of GO30, which has the highest oxidation degree among all samples, no absorption of microwave power that could be related with the emergence of conductivity was observed. Moreover, the decay of PMC centers at 165 °C proceeds much more slowly in this case than for other samples. Also, the PMC concentration at 150 °C remained at the same level for a long time during treatment, thus qualitatively distinguishing it from other samples.

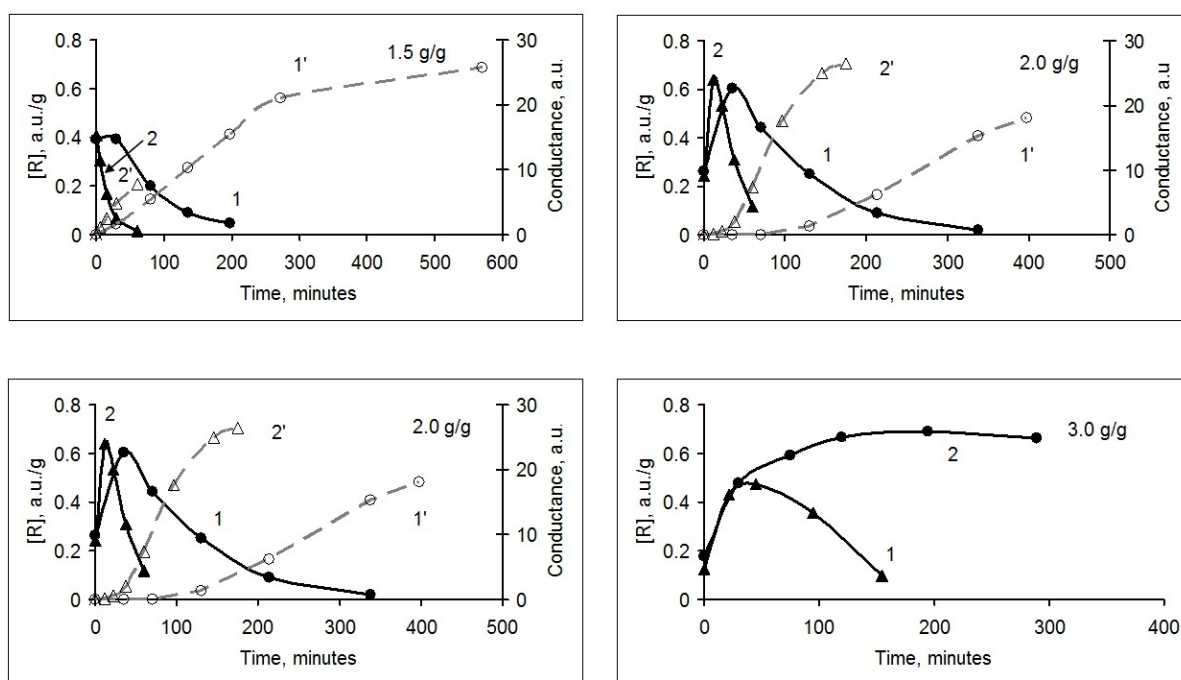


FIG. 4. The dependence of PMC concentration (1, 2) and the relative conductivity (1', 2') of the samples upon the time of heat treatment at two different temperatures of 150 °C (1) and 165 °C (2)

From the very outset of permanganate oxidation, the originally well conductive plane of a single sheet of graphite (consisting almost entirely of sp^2 -hybridized polyconjugated carbons) becomes more and more populated with different oxygen-containing moieties, chemically emerging at the expense of sp^2 -carbons. Thus, eventually more and more carbon atoms within a single "graphene" layer attain sp^3 -hybridization, which leads to a gradual loss of the material's conductivity. Investigations of the resulting GO sheets with the aid of scanning transmission electron microscopy (STEM) and scanning tunneling microscopy (STM) have shown that GO

layer consists of chaotically alternating clusters of oxidized (sp^3) carbons and practically unaffected by oxidation (sp^2) carbon clusters [17-19]. By estimates of various authors based on the intensity ratio of D and G bands in the Raman spectra, the average size of such clusters is around 2.5 – 6.0 nm. It has been noted [20] that the size of these clusters has remained actually the same independently of the thermal or chemical GO reduction mode subsequently employed. The electrical conductivity of graphene (graphite) is attained by virtue of regaining the effective polyconjugation (which was impaired due to oxidation), and hence the GO reduction must be associated with the formation of percolation channels for connecting the separated sp^2 -hybridized domains. Our results suggest that the conductivity recovery is associated with the decay of localized paramagnetic states. It is known that the translational mobility is needed for recombination of unpaired electrons, but the implementation mechanism for this process in GO is not clear. It can be assumed that an unpaired electron's motion becomes feasible owing to thermally-assisted transition (hopping) of the electron onto the conjugation domain with subsequent migrating along the latter. Mono- or bi-molecular processes obey first order kinetic equations. For bi-molecular reactions, it is true only in those cases when the second reactant is present in considerable excess relative to that observed. Under these assumptions, the increase in the graphite oxidation level should lead to a lessening in the total area of polyconjugated carbon domains, that is, the oxidation diminishes the concentration of polyconjugated sites which are potential acceptors of unpaired electrons. This, in turn, leads to lowering the effective rate constants of the radical decay.

The number of the oxygen-containing functional groups in GO is a measure of the oxidation degree of the graphite. In an attempt to quantify this parameter, we have used gas volumetry [12]. The method consisted of collecting and segregating the well-known gaseous products (CO_2 , CO and H_2O) that are released during the thermal treatment of GO at temperatures up to 250 °C, as well as measuring the partial pressures of the gases in a constant volume, i. e., determining the number of moles of each product per the weight of the GO sample (Fig. 5).

The data in Fig. 5 show that the incremental addition of each extra portion of $KMnO_4$ (0.5 g) resulted in an increase in the total amount of released gaseous products from 4.8 (GO15) to 8.7 (GO20), 10.4 (GO25) and finally to 10.7 (GO30) mmol/g, respectively. The first portion of 1.5 g potassium permanganate introduced per 1 g of the graphite has been consumed with rather low efficiency (it was difficult to initiate graphite oxidation). Addition of the next 0.5 g portion of permanganate (GO15→GO20) gave an additional 3.9 mmol/g of oxygen-containing functional groups. Under further incremental additions of $KMnO_4$ oxidative effectiveness of the latter was progressively lowering: GO20→GO25 – 1.7 mmol/g, GO25→GO30 – 0.3 mmol/g. The significant increase in the oxidation efficiency seen after the addition of the second $KMnO_4$ portion (GO15→GO20) may be associated with both physical (facilitated access of oxidant into the interlayer space of graphite) and chemical (increased reactivity of the carbon atoms neighboring the oxidized sites) reasons. The fact that GO sheet surface consists of sporadically spread, strongly-oxidized domains and those unaffected by the oxidation [17-19] provides evidence in favor of the chemical causes. Indirectly, this hypothesis is also supported by the increased reactivity of the carbon atoms located nearby the deformed regions of the graphene sheet, that has been observed experimentally [21].

Figure 5 shows that the largest decrease of the effective radical decay constant is observed when switching from GO15 to GO20, which coincides exactly with the significant in the degree of functionalization for the graphene sheet's surface. Further changes of the effective radical decay constant for the GO20 to GO25 transition were less pronounced because only comparatively small increase in the degree of functionalization of the graphene sheet occurred

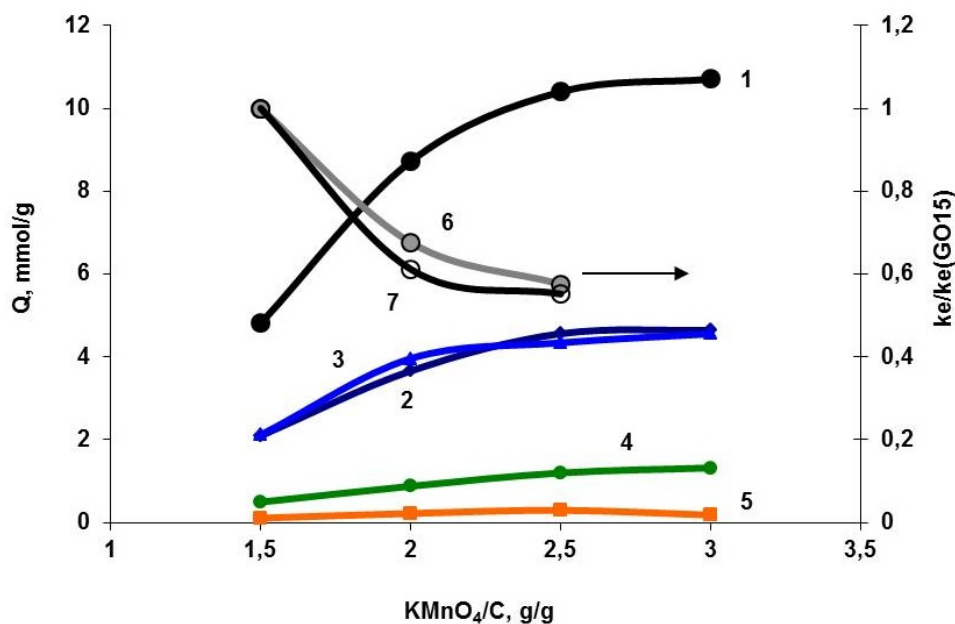


FIG. 5. The yield of typical gaseous products released in the result of thermal reduction of GO by heating the latter at 200 °C: 1 – the total amount of gaseous products, 2 – CO₂, 3 – H₂O, 4 – CO, 5 – unknown impurity. The change of the relative effective radical decay constant on the severity of oxidation of graphite (the amount of KMnO₄, used for graphite oxidation): 6 – at 150 °C, 7 – at 165 °C

at that time. The next increment in the degree of oxidation (sample GO30), having only an insignificant effect on the released gas products leads to a qualitative change: the rate of free radical decay abruptly slows down and the emergence of the electrical conductivity is not detected. This is consistent with the observations of Hummers [13, 14], who pointed out that the use of 3 g of potassium permanganate per 1 g of graphite is optimal for thorough oxidation and the use of an additional amount of oxidizing reagent would be unnecessary.

4. Conclusion

The functional groups arising during graphite oxidation on the periphery as well as on the basal surface of graphene particles emerge arise via the formation of covalent C–O bonds, the new bond formation inevitably accompanied by the appearance of an unpaired electron (PMC) at one of the three neighboring carbon atoms. It is possible that such paramagnetic centers can then participate in certain chemical reactions that take place during the oxidation process, thus justifying the decrease in the PMC concentration observed with increased oxidation. At the early stages of graphite oxidation, these unpaired electrons can be capable of migrating through the polyconjugated sp²-carbon system and have a good chance to recombine since the system is still not badly damaged. At deeper stages of oxidation, when more and more former sp²-carbon atoms have been transformed to oxygen-containing functionalities and thus have attained sp³ hybridization, the above opportunities are lost and the unpaired electrons are stabilized. The growth of PMC content at the initial stages of heat treatment, at temperatures providing the intense release of gaseous decomposition products originating from the oxygen-containing functionalities of GO, reveals the important role of the homolytic bond cleavage during the GO reduction process. Further behavior of the PMC (e.g., their decay under continuing thermal treatment) correlates with the incidence of electrical conductivity that has been detected by

the absorption of microwave radiation in the EPR spectrometer resonator. At the moment, it is difficult to give priority to any single mechanism among all possible ones explaining this relationship. From one side, it well may be a transfer (hopping) of the localized state onto a polyconjugated domain of GO, the migration through the polyconjugation system and the recombination. Alternatively, the occurrence of electrical conductivity may also be induced by the transition of the unpaired electron in the conduction band and by the increase in the carrier number. However, the results of the present work provide evidence that the thermal GO reduction process consists of several consecutive stages and proceeds through intermediates which give rise to paramagnetic states.

References

- [1] Brodie B.C. On the atomic weight of graphite. *Philos. Trans. R. Soc. London*, 1859, **149**, P. 249–259.
- [2] Novoselov K.S., Geim A.K., Morozov S.V., Jiang D., Zhang Y., Dubonos S.V., Grigorieva I.V., Firsov A.A. Electric Field Effect in Atomically Thin Carbon Films. *Science*, 2004, **306**, P. 666–669.
- [3] Zhu Y., Murali S., Cai W., Li X., Suk J.W., Potts J.R., Ruoff R.S. Graphene and Graphene Oxide: Synthesis, Properties, and Applications. *Adv. Mater.*, 2010, **22**, P. 3906–3924.
- [4] Singh V., Joung D., Zhai L., Das S., Khondaker S.I., Seal S. Graphene based materials: Past, present and future. *Progress in Materials Science*, 2011, **56**, P. 1178–1271.
- [5] Jung I., Field D.A., Clark N.J., Zhu Y., Yang D., Piner R.D., Stankovich S., Dikin D.A., Geisler H., Ventrice C.A., Ruoff J.R.S. Reduction Kinetics of Graphene Oxide Determined by Electrical Transport Measurements and Temperature Programmed Desorption. *J. Phys. Chem. C*, 2009, **113**, P. 18480–18486.
- [6] Chua C. K., Pumera M. Covalent Chemistry on Graphene. *Chem. Soc. Rev.*, 2013, **42**(8), P. 3222–3233.
- [7] Acik M., Mattevi C., Gong C., Lee G., Cho K., Chhowalla M., Chabal Y.J. The Role of Intercalated Water in Multilayered Graphene Oxide. *ACS Nano*, 2010, **4**, P. 5861–5868.
- [8] Zhan D., Ni Z., Chen W., Sun L., Luo Z., Lai L., Yu T., Wee A.T.S., Shen Z. Electronic Structure of Graphite Oxide and Thermally Reduced Graphite Oxide. *Carbon*, 2011, **49**, P. 1362–1366.
- [9] Círić L., Sienkiewicz A., Gaál R., Jaćimović J., Vâju C., Magrez A., Forró L. Defects and Localization in Chemically-Derived Graphene. *Phys. Rev. B*, 2012, **86**, P. 195139.
- [10] Ali F., Agarwal N., Nayak P.K., Das R., Periasamy N. Chemical Route to The Formation of Graphene. *Current Science*, 2009, **97**, P. 683–685.
- [11] Rao S.S., Stesmans A., Wang Y., Chen Y. Direct ESR Evidence for Magnetic Behavior of Graphite Oxide. *Physica E*, 2012, **44**, P. 1036–1039.
- [12] Gorshenev V.N., Melnikov V.P. Thermally-assisted expansion of graphites with different degree of oxidation. *Chimicheskaya Fizika*, 2013, **32**, P. 37–43. (in Russian)
- [13] Hummers W.S. Preparation of Graphitic Acid. United States Patent Office, 1957, 2798878.
- [14] Hummers W.S., Offeman R.E. Preparation of Graphitic Oxide. *J. Am. Chem. Soc.*, 1958, **80**, P. 1339.
- [15] Barroso-Bujans F., Alegría A., Colmenero J. Kinetic Study of the Graphite Oxide Reduction: Combined Structural and Gravimetric Experiments under Isothermal and Nonisothermal Conditions. *J. Phys. Chem. C*, 2010, **114**, P. 21645–21651.
- [16] Yin K., Li H., Xia Y., Bi H., Sun J., Liu Z., Sun L. Thermodynamic and Kinetic Analysis of Low Temperature Thermal Reduction of Graphene Oxide. *Nano-Micro Lett.*, 2011, **3**, P. 51–55.
- [17] Erickson K., Erni R., Lee Z., Alem N., Gannett W., Zettl A. Determination of the Local Chemical Structure of Graphene Oxide and Reduced Graphene Oxide. *Adv. Mater.*, 2010, **22**, P. 4467–4472.
- [18] Mkhoyan K. A., Contryman A. W., Silcox J., Stewart D.A., Eda G., Mattevi C., Miller S., Chhowalla M. Atomic and Electronic Structure of Graphene-Oxide. *Nano Lett.*, 2009, **9**, P. 1058–1063.
- [19] Paredes J.I., Villar-Rodil S., Solís-Fernández P., Martínez-Alonso A., Tascón J.M.D. Atomic Force and Scanning Tunneling Microscopy Imaging of Graphene Nanosheets Derived from Graphite Oxide. *Langmuir*, 2009, **25**, P. 5957–5968.
- [20] Mattevi C., Eda G., Agnoli S., Miller S., Mkhoyan K. A., Celic O., Mastrogianni D., Granozzi G., Garfunkel E., Chhowalla M. Evolution of Electrical, Chemical, and Structural Properties of Transparent and Conducting Chemically Derived Graphene Thin Films. *Adv. Funct. Mater.*, 2009, **19**, P. 2577–2583.
- [21] Zhang Y.H., Wang B., Zhang H.R., Chena Z.Y., Zhanga Y.Q., Wanga B., Suia Y.P., Lia X.L., Xiea X.M., Yua G.H., Jinc Z., Liuc X.Y. The Distribution of Wrinkles and their Effects on the Oxidation Resistance of Chemical Vapor Deposition Graphene. *Carbon*, 2014, **70**, P. 81–86.

Quantum-chemical study of carbon nanotubes interaction with contaminants of petroleum, oil and lubricants

I. Arkharova, I. Zaporotskova

Volgograd State University, Volgograd, Russia

arkharova_irina@mail.ru, irinazaporotskova@gmail.com

PACS 61.46.Fq, 61.48.De, 62.23.Pq

DOI 10.17586/2220-8054-2016-7-1-253-259

The article presents the results from the study of carbon nanotube (CNT) interaction with the main products generated in the process of oil “aging”, in particular with a molecule of sulfurous acid, hydroxyl group, ferrous and aluminium oxides. The purpose of the paper is to prove the possibility of oxygen atom adsorption on the outside face of CNT.

Keywords: petroleum, oil and lubricants, nanomaterials, carbon nanotubes, quantum-chemical calculations, DFT.

Received: 20 November 2015

1. Introduction

Oil changes its physico-chemical and functional properties during long-term service (i.e. it “ages”); and its quality parameters reach their limits with respect to the norms [1]. When oil decomposes as a result of oxidation or under the influence of other factors, its acidity increases. Acids are the major products of the aging process for oil. These acidic products can cause metal corrosion, and in order to neutralize generated acids alkali additives are required, therefore negatively affecting the dispersive properties and detergency of oil, as well as its operational life. Active sulfur compounds that penetrate oil after combustion of fuel with high sulfur content frequently cause oil aging [2]. Inorganic contaminants come in contact with oil as a result of mechanical friction of rubbing engine parts and consist mainly of quartz, feldspar, metal oxides and metal particles [3,4]. The detergents, which are the part of engine oil, are organometallic compounds. When oil enters the combustion chamber and is burned, ash particles are formed, consisting of metal oxides and salts belonging to the additives. Ash particles clog the pores of the ash filter, and do not allow it to regenerate completely. For this reason, the search for a means to remove these products of oil aging is relevant and of practical use.

One of the ways of cleaning and removing the undesirable oil by-products which are formed is the introduction of various active additives. It is assumed that carbon nanotubes [5,6] can be used as an admixture that will significantly improve the properties and operational characteristics of lubricating materials. The essential peculiarity of carbon nanotubes arises as a result of their unique sorption characteristics [7-9]. Due to the fact that a nanotube is a surface structure, its weight is enclosed in surfaces of its layers. This defines an abnormally high specific surface area of tubules, and that, in turn, determines their electro-chemical and sorption characteristics [10]. We assume that harmful impurity (acids, oxides of metals, etc.) can be adsorbed onto the nanotubes’ surfaces and subsequently removed from the oil via filtration.

In order to prove the feasibility this process, it is necessary to execute theoretical calculations for the adsorptive interaction of a carbon nanotube and some metal oxides resulting from the degradation of oil and its additives. As a result, different-valence oxides of iron and aluminum were chosen, and interaction process between carbon nanotube and a molecule

of sulfurous acid, hydroxyl group were modeled. The top-priority objective in this case was the calculation of the optimal geometrical structure for a nano-sized molecular cluster, which is clearly considered an important quantum chemistry issue [11-14]. Due to complexity of investigated molecular systems, density functional theory (DFT) has been used in this study to calculate the structure for the molecular cluster [15].

2. Quantum-chemical study of carbon nanotubes interaction with contaminants in petroleum, oil and lubricants

The paper presents the results of a study for modeling the interaction of a type (6,0) carbon nanotube with several base products generated during oil aging, such as a molecule of sulfurous acid, a hydroxyl group, iron and aluminum oxides. The molecular cluster of a nanotube containing 96 atoms of carbon is considered. The clusters' boundaries were closed with pseudo-atoms; in this case, they were hydrogen atoms.

Processes of adsorptive interaction of the chosen type for single-layer nanotubes with a hydroxyl group, with a molecule of sulfurous acid H_2SO_3 , with structural units (elemental fragments) of iron oxides (FeO & Fe_2O_3), with structural units (elemental fragments) of aluminium oxide (Al_2O_3) were also studied. Process was simulated by means of a stepwise approximation (one step equals 0.1 \AA) towards the surface of a carbon tubule, located approximately in the middle of the cluster. Perpendicular connection to the surface of a nanotube with use of active center of a structural unit – an oxygen atom was considered. The oxygen atom, due to the presence of a double bond, can provide adsorptive interaction with the nanotube. Examples of a adsorption complexes “cluster of nanotubulene (6, 0) – molecules (structural units) of harmful components of fuel” are presented in Fig. 1.

Based on the results of theoretical calculations, the potential interaction energy profile for a CNT with a hydroxyl group has been constructed. Analysis of this profile allows one to define the main adsorptive characteristics of this process, which are presented in Table 1.

TABLE 1. General adsorption characteristics of interaction of a single-layer (6,0) CNT with chosen contaminants

Contaminant	Adsorption distance $r, \text{ \AA}$	Adsorption energy $E_{ads}, \text{ eV}$
FeO	3.1	-8.43
Fe ₂ O ₃	2.0	-6.66
OH	2.4	-0.8
H ₂ SO ₃	2.6	-0.51
Al ₂ O ₃	3.1	-0.43

It is stated that hydroxyl group is adsorbed onto the surface of a (6,0) CNT, which is illustrated by the presence of the minimum on the interaction curve (Fig. 2). The distance between the carbon atom of the tube surface and oxygen atom (adsorption distance) amounts to $r = 2.4 \text{ \AA}$; the adsorption energy in this case is $E_{ads} = -0.8 \text{ eV}$. The correlation between our obtained results and those from a study on the adsorption of water molecules onto graphene [16] should be noted. The large value of adsorption energy, in our case in comparison with the values, which are presented in [16], due to the curvature of the nanotube surface, contributing to more active adsorption, and the presence of free communication in the hydroxyl group, which isn't present in the H_2O molecule.

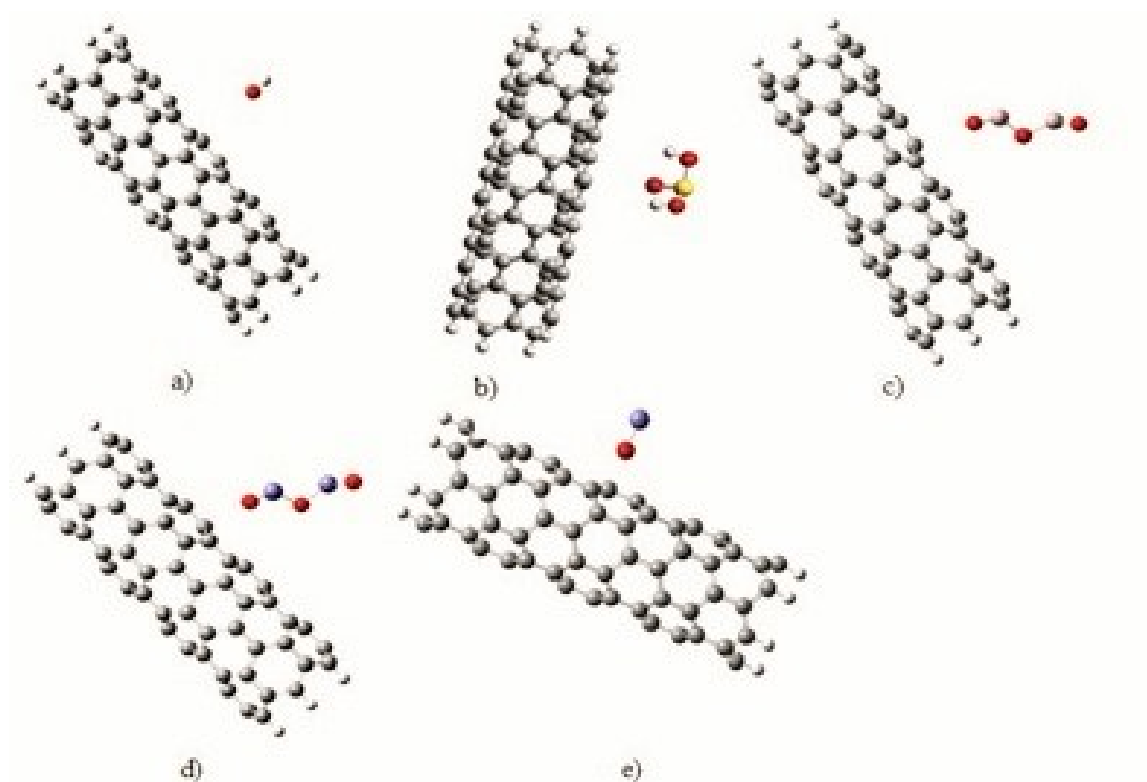


FIG. 1. Model of a single-layer (6,0) CNT molecular cluster interacting with: a) hydroxyl group; b) molecule of sulfurous acid; c) fragment of aluminium oxide Al_2O_3 ; d), e) fragments of aliovalent iron oxides: Fe_2O_3 ; FeO , correspondingly

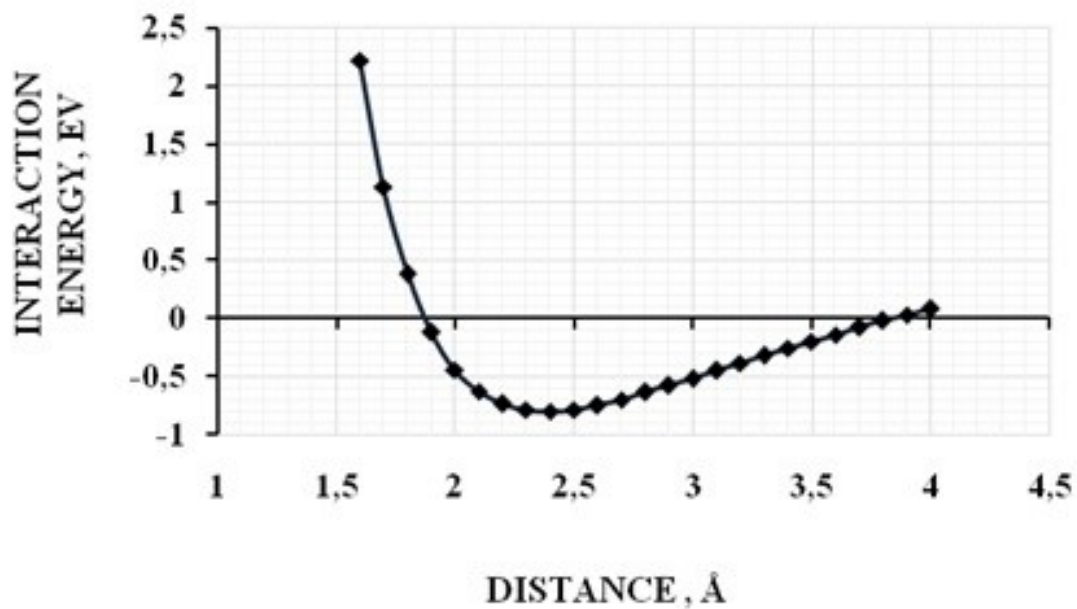


FIG. 2. Surface profile for the potential energy of adsorptive interaction between a (6,0) CNT and a hydroxyl group

As a result of theoretical calculations, the potential interaction energy profile of nanotubule with chosen molecule of sulfurous acid was constructed (Fig. 3). Analysis of this profile allowed definition of the main adsorptive characteristics of the process. The presence of a minimum on the curve indicates the implementation of the adsorption interaction between the H_2SO_3 molecule and the surface of the CNT.

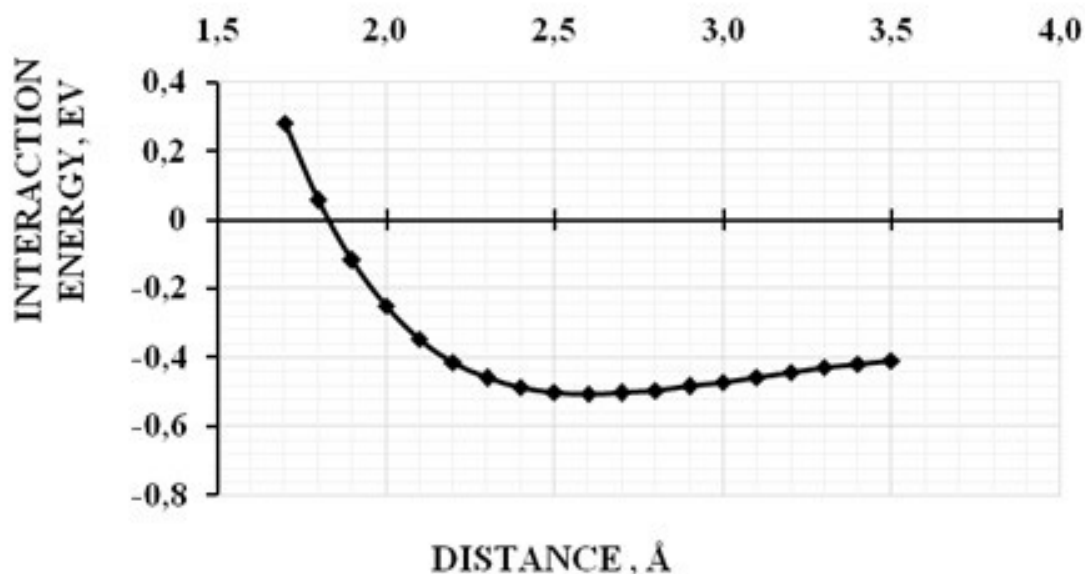


FIG. 3. Surface profile of potential energy of adsorptive interaction between a nanotube (6,0) and sulfurous acid

The adsorption distance was $r = 2.6 \text{ \AA}$, and the adsorption energy in this case was $E_{ads} = -0.51 \text{ eV}$. As a result of theoretical calculations, the potential interaction energy profiles of nanotubules with elemental fragments of iron oxides acid were constructed. It is stated that fragment Fe_2O_3 is adsorbed on the surface of a (6,0) CNT. The adsorption distance was $r = 2.0 \text{ \AA}$, while the adsorption energy was $E_{ads} = -6.66 \text{ eV}$ (Fig. 4).

It is stated that the FeO fragment is adsorbed onto the surface of a (6,0) CNT. The adsorption distance was $r = 2.1 \text{ \AA}$, and the adsorption energy was $E_{ads} = -8.43 \text{ eV}$ (Fig. 5).

Also the interaction process of a (6,0) CNT with an aluminum oxide fragment was investigated. A surface interaction potential energy profile for a CNT with an aluminum oxide fragment was developed (Fig. 6) using a step-by-step approximation of Al_2O_3 approaching to the selected carbon atom on the CNT surface. Analysis of this profile allowed us to define the main adsorptive characteristics of the process. The adsorption distance was $r = 3.1 \text{ \AA}$, and the adsorption energy in this case was $E_{ads} = -0.43 \text{ eV}$.

A summary is shown in Table 1 for the general adsorption characteristics for the interactions between a single-layer (6,0) CNT with contaminants that would be expected to be generated during the normal operation of an oil-lubricated internal combustion engine. The comparison of these adsorption energy values shows that the adsorptive process is most active with ferrous oxide, FeO. This can be explained by the structure of elementary structural units, namely, higher activity of the oxygen atom in the structure. However, other harmful components resulting from the aging of fuel, are also adsorbed onto the CNT surface. Thus, it can

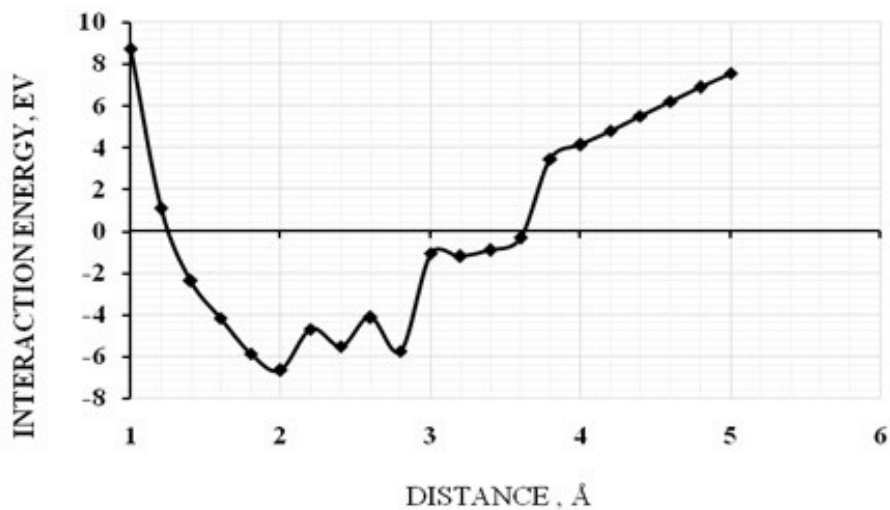


FIG. 4. Surface profile of potential energy for the adsorptive interaction between a (6,0) CNT and a Fe_2O_3 fragment

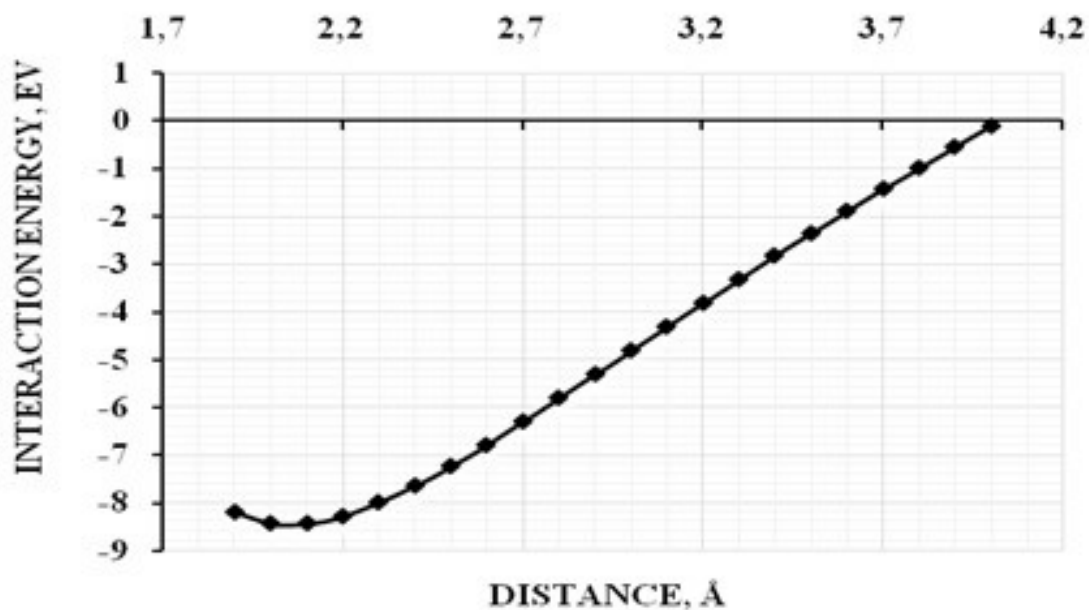


FIG. 5. Surface profile of potential energy of adsorptive interaction between a (6,0) CNT and a FeO fragment

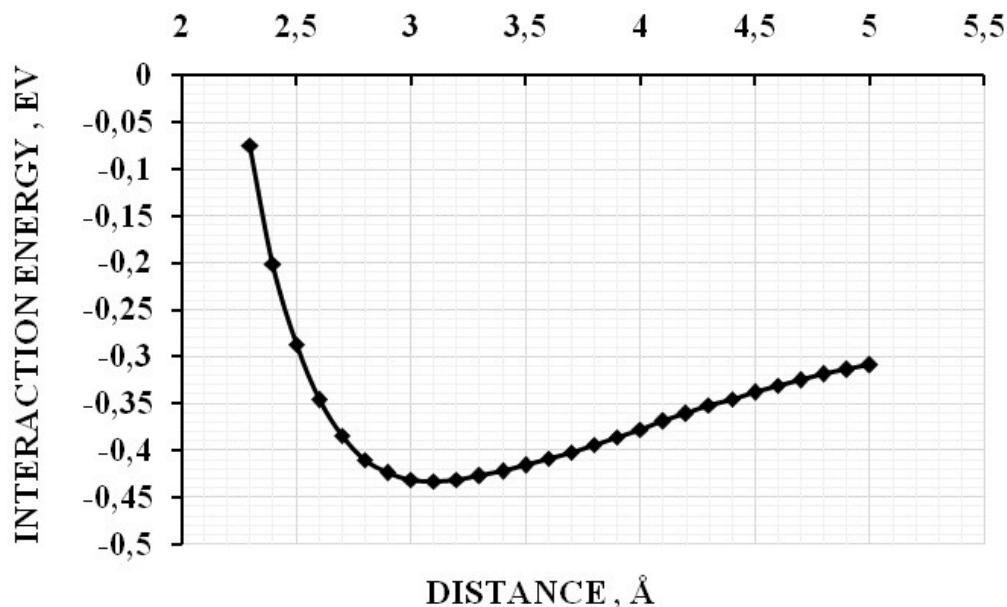


FIG. 6. Surface potential energy profile for the adsorptive interaction between a (6,0) CNT and an Al_2O_3 fragment

be argued that it is possible to use CNTs as active additive in both fuels and lubricants, the main mechanism by which this positive effect on oil is exerted, is the adsorption of harmful components onto the CNT surface.

3. Summary and conclusions

The theoretical quantum-chemical study of the adsorptive interaction of CNTs with a molecule of sulfurous acid, hydroxyl group, ferrous oxides and aluminum oxide proves the possibility CNTs interacting with the contaminants generated during the operation of an internal combustion engine using oil as a lubricant. Analysis of the results shows that the adsorptive process is most active with ferrous oxides. Therefore, the hierarchy for the petroleum oil and lubricant (POL) contaminants chosen with respect to CNT activity can be presented as follows: FeO , Fe_2O_3 , OH , H_2SO_3 , Al_2O_3 . The main mechanism by which the CNTs exert a positive effect upon the lubricant during its degradation via normal operation, is the adsorption of harmful components onto the surface of the CNTs.

References

- [1] Bujanovskij I.A., Fuks I.G., Shabalina T.N. *Boundary lubrication: stages of tribology development*. Nefti gas, Moscow, 2002.
- [2] Badisova K.M., Berstad J.A., Bogdanov S.K., Shkolnikov V.M., Anisimov I.G., Batov S.A. *Fuels, lubricating materials, technical liquids. Variety and application: manual*. Publishing center "Tekhinform", Moscow, 1999.
- [3] Ventsel E.S., Zhalkin S.G., Danko N.I. *Improvement of quality and increase of service life of petroleum oils*. Ukrainian State University of Railway Transport, Kharkov, 2003, 168 pp.
- [4] Grigoriev M.A. *Quality of engine oil and reliability of engines*. Publishing house of standards, Moscow, 1981, 232 pp.

- [5] Ljuty M., Kostyukovich G., Kravchenko V., Struk V., Ovchinnikov E. Tribo-technical characteristics of lubricating materials modified with nanodisperse fillers. Nanostructural materials. Abstr. 2-nd scitech. seminar 24–25 October 2002, IMET RAN, Belorussia - Russia, 2002.
- [6] Lubricating oil composition for friction reduction that includes nanoporous particles: pat. Russian Federation: B82B C10M C10N / Lee Hyeung Jin; Cho Yong Rae; patent applicant and holder SK LubricantsCo., Ltd. - 2012145479/04; applic. 16.03.11; publ. 10.04.14, Journal. 10.
- [7] Eleckij A.V. Sorption properties of carbon nanostructures. *Physics Uspekhi*, 2004, **47**(11), P. 1119–1154.
- [8] Harris P. *Carbon Nanotubes and Related Structures. New Materials for the Twenty-first Century*. Tekhnosfera, Moscow, 2003, 336 p.
- [9] Djachkov P.N. *Carbon nanotubes: morphology, properties, applications*. Binom, Moscow, 2010.
- [10] Zaporotskova I.V. *Carbon and non-carbon nanomaterials and composite structures on its base: morphology and electron properties*. Volgograd State University Press, Volgograd, 2009, 490 p.
- [11] Kotliar G., Savrasov S.Y., Haule K., Oudovenko V.S., Parcollet O., Marianetti C.A. Electronic structure calculations with dynamical mean-field theory. *Rev. Mod. Phys.*, 2006, **78**(3), P. 865–951.
- [12] Wang Z., Gao F., Li N., Qu N., Gou H., Hao X. Density functional theory study of hexagonal carbon phases. *J. Phys.: Condens. Matter*, 2009, **21**, P. 235401–235406.
- [13] Bajsupova E., Aminova R.M. Modelling of molecular nanosize clusters with quantum chemistry methods. *Butlerov's messages*, 2009, P. 10–22.
- [14] Ignatov S.K. *Quantum-chemical modelling of molecular structure, physico-chemical properties and reactive capacity*. Novgorod State University Press, Nizhni Novgorod, 2006, 82 p.
- [15] Reich S., Thomsen C., Maultzsch J. *Carbon nanotubes. Basic concepts and physical properties*. Wiley, VCH Verlag, Berlin, 2003.
- [16] Rangel Cortes E., Magaña Soí L.F., Arellano J.S. Interaction of a water molecule with a graphene layer. *Revista Mexicana de Física*, 2013, **59**(1), P. 118–125.



NANOSYSTEMS:

PHYSICS, CHEMISTRY, MATHEMATICS

Журнал зарегистрирован

Федеральной службой по надзору в сфере связи, информационных технологий и массовых коммуникаций

(свидетельство ПИ № ФС 77 - 49048 от 22.03.2012 г.)

ISSN 2220-8054

Учредитель: федеральное государственное автономное образовательное учреждение высшего образования

«Санкт-Петербургский национальный исследовательский университет информационных технологий, механики и оптики»

Издатель: федеральное государственное автономное образовательное учреждение высшего образования

«Санкт-Петербургский национальный исследовательский университет информационных технологий, механики и оптики»

Отпечатано в Учреждении «Университетские телекоммуникации»

Адрес: 197101, Санкт-Петербург, Кронверкский пр., 49

Подписка на журнал НФХМ

На второе полугодие 2016 года подписка осуществляется через

ОАО Агентство «Роспечать»

Подписной индекс 57385 в каталоге «Издания органов научно-технической информации»